

Wiring variations that enable and constrain neural computation in a sensory microcircuit

William F. Tobin, Rachel I. Wilson, and Wei-Chung Allen Lee

Department of Neurobiology, Harvard Medical School, 220 Longwood Avenue, Boston MA 02115, USA

ABSTRACT

Neural network function can be shaped by varying the strength of synaptic connections. One way to achieve this is to vary connection structure. To investigate how structural variation among synaptic connections might affect neural computation, we examined primary afferent connections in the *Drosophila* olfactory system. We used large-scale serial section electron microscopy to reconstruct all the olfactory receptor neuron (ORN) axons that target a left-right pair of glomeruli, as well as all the projection neurons (PNs) postsynaptic to these ORNs. We find three variations in ORN→PN connectivity. First, we find a systematic co-variation in synapse number and PN dendrite size, suggesting total synaptic conductance is tuned to postsynaptic excitability. Second, we show that PNs receive more synapses from ipsilateral than contralateral ORNs, providing a structural basis for odor lateralization behavior. Finally, we provide evidence of imprecision in ORN→PN connections and show how this can diminish network performance.

INTRODUCTION

The wiring of a neural network is a key determinant of its function. In principle, each synaptic connection might have an optimal strength, as dictated by activity patterns passing through the synapses comprising that connection, as well as the computations that the connection ought to support. The strength of each connection

will depend on many structural features, such as the number of presynaptic neurotransmitter release sites it contains, or the diameter of the postsynaptic dendrite. Therefore, it is fundamentally important to understand how the structure of synaptic connections can be systematically varied to enable specific neural computations, as well as the precision of these systematic variations.

A useful way to study this issue is to examine multiple instances of the same connection type. Studies of isogenic grasshoppers and worms, for example, have discovered anatomical variations in connectivity made by an identifiable neuron in different individuals (Goodman, 1978; Ward et al., 1975). These variations were interpreted as evidence of imprecision in developmental wiring programs (“connection noise”).

However, wiring variations may not necessarily reflect noise. For example, wiring variations might be adaptive if they systematically weight inputs according to their reliability. A recent study in the mouse found that an identifiable motor neuron can make structurally different connections on the left and right sides of the body, and this was suggested to be evidence of an adaptive learning rule that can fine-tune wiring based on neural activity patterns (Lu et al., 2009). Adaptive wiring variations might also emerge from homeostatic processes that systematically compensate for variations in neural activity patterns (Roffman et al., 2012). In short, wiring variations can be substrates for neural computations – rather than simply constraining neural computations.

In this study, we investigated wiring variations in an olfactory glomerulus of the *Drosophila* antennal lobe. The glomerulus is the basic unit of organization in the olfactory system (Chen and Shepherd, 2005; Su et al., 2009; Wachowiak and Shipley, 2006). In the adult fly, there are about 50 glomeruli in total. Each glomerulus receives feedforward sensory input from many olfactory receptor neurons (ORNs), and all the ORNs that project to the same glomerulus express the same odorant receptor, meaning they should all have similar odor responses (Hallem and Carlson, 2004; Vosshall et al., 2000). ORNs synapse onto projection neurons (PNs) that carry signals from the antennal lobe to higher brain regions. The dendritic arbor of a PN is typically confined to a

single glomerulus (Hallem and Carlson, 2004; Stocker et al., 1990). Because a PN pools strong synaptic inputs from all the ORNs that target its cognate glomerulus, the PN can respond relatively quickly and reliably to odor stimuli (Bhandawat et al., 2007; Jeanne and Wilson, 2015).

ORN→PN connections are an ideal setting for studying wiring variations because there are many such connections per glomerulus, each with the same ostensible function. Moreover, these connections have been extensively studied using *in vivo* electrophysiological recordings and calcium imaging (Wilson, 2013). To comprehensively visualize the structure of these connections, we generated a serial section electron microscopy (EM) data set comprising both antennal lobes of an adult *Drosophila* brain. We focused our analysis on a specific glomerulus (DM6) whose cognate ORNs have been well-characterized (Couto et al., 2005; Hallem and Carlson, 2006) and whose postsynaptic PNs have been studied using *in vivo* intracellular recordings (Gaudry et al., 2013; Kazama and Wilson, 2008; Kazama and Wilson, 2009; Kazama et al., 2011; Nagel et al., 2015). We performed a dense reconstruction of all the ORNs and PNs corresponding to DM6 on the left and right sides of the brain. We then integrated our anatomical data with electrophysiological measurements to construct compartmental models of each reconstructed PN. These models allowed us to understand how structure and function are interrelated at individual connections, and how these relationships affect the specific computations that the PN performs.

We discovered three kinds of variations in ORN→PN synaptic connections. First, we found a systematic variation in the number of synapses per ORN→PN connection that compensates for differences in the size of PN dendrites. We used compartmental models to show how this sort of compensation can tightly regulate the postsynaptic impact of each ORN spike. Second, we found a systematic structural difference in the connections made by ORNs onto ipsi- and contralateral PNs. Our compartmental models showed that this systematic structural variation can account for the known physiological differences between ipsi- and contralateral connections. This difference is likely critical to the fly's ability to lateralize odor stimuli. Third, we found some

non-systematic structural variation in ORN→PN connections that does not correlate with variation in ORN activity. We argue that this reflects developmental “connection noise” and we show how it can constrain a PN’s ability to count ORN spikes. Taken together, our results imply that certain structural parameters of these synaptic connections are systematically varied to enable specific neural computations, but the limited precision of synaptic structural control also represents a fundamental constraint on network performance.

RESULTS

Cells comprising the glomerular micro-circuit

We used large-scale serial section transmission EM (Bock et al., 2011; Lee et al., 2016) to collect a volumetric data set comprising the anterior portion of one adult *Drosophila* brain (Figure 1A and 1B, and Movie S1). The series consisted of ~1900 sections acquired at ~4 x 4 x 40 nm/voxel, amounting to ~4 million camera images and ~50 TB of raw data. This data set spans both hemispheres of the brain, and it includes both right and left copies of the antennal lobe.

Three experts independently identified glomerulus DM6 in the EM data set by visual inspection based on a published light-level map (Couto et al., 2005). We then manually reconstructed all the ORNs and PNs targeting glomerulus DM6 (Movie S2) on both sides (Figures 1C-D and S1). In total, 53 ORNs innervated glomerulus DM6. Like most *Drosophila* ORNs, these ORNs project bilaterally (Couto et al., 2005; Stocker et al., 1990; Vosshall et al., 2000). However, we found that one right ORN and one left ORN projected only ipsilaterally. Therefore, each glomerulus contained the axons of 52 ORNs.

Interestingly, we found three “sister” PNs on the left side the brain and two on the right. This is likely to represent a developmental anomaly, because Gal4 lines that label DM6 PNs typically reveal three such cells in each glomerulus (Figure S2). In a later section, we will examine the consequences of this anomaly in more detail.

Profiles not identified as ORNs or PNs are referred to here as multiglomerular neurons. Most of these profiles are probably inhibitory local neurons, because this cell type is the most numerous and broadly-arborizing of the multiglomerular cell types in the antennal lobe (Chou et al., 2010; Lai et al., 2008; Lin et al., 2012; Yu et al., 2010). In addition, some of these profiles may be multiglomerular projection neurons, or neurons that project into the antennal lobe from other regions.

Every segment and synapse of every reconstructed neuron was reviewed by at least two independent annotators. To assess what our reconstructions may be missing, we quantified the percentage of cellular profiles presynaptic to PNs that were “orphans”, i.e. fragments that could be connected to any neuron. Overall, the percentage of orphans was relatively small ($6.8 \pm 1.5\%$, mean \pm SEM). This value was lower for the left glomerulus ($4.4 \pm 0.8\%$) than for the right glomerulus ($10.4 \pm 0.4\%$). Another study using essentially the same reconstruction strategy demonstrated that false continuations between fragments are easily detected and corrected during independent review by a second annotator, and are therefore very rare in the final reconstruction (Schneider-Mizell et al., 2016).

Relative abundance of connection types

In our reconstructions, we identified every connection type known to exist within antennal lobe glomeruli of the adult fly (Rybäk et al., 2016). Beginning with ORN output synapses, we found that ORNs delivered about one-third of their synaptic output to PNs (Figure 1E). Most of the remainder was delivered to multiglomerular

neurons (Figure 1E). Because most multiglomerular neurons are likely inhibitory local neurons, this pattern emphasizes the important role of feedforward inhibition in the antennal lobe circuit.

ORN axon terminals are not just presynaptic elements – they are also postsynaptic to other neurons (Berck et al., 2016; Rybak et al., 2016). We found that DM6 ORN axons received most of their synaptic input from multiglomerular neurons (Figure 1E). This is consistent with physiological studies showing that inhibitory local neurons exert potent control of neurotransmitter release from ORN axon terminals (Olsen and Wilson, 2008; Root et al., 2011; Root et al., 2008). About a third of synapses onto ORN axon terminals originated from PNs and ORNs. It is not known how PN and ORN inputs might affect ORN axon terminals; in principle, they might either facilitate or suppress neurotransmitter release.

Turning to the PN's perspective, we found that the PNs received most of their input (~75%) from ORNs, as expected (Figure 1F). PNs also received a sizeable input (~20%) from multiglomerular neurons. This is also expected, as paired electrophysiological recordings have demonstrated the existence of functional inhibitory synapses from local neurons onto PN dendrites (Liu and Wilson, 2013; Yaksi and Wilson, 2010).

PN dendrites are known to contain presynaptic elements as well as postsynaptic elements (Ng et al., 2002; Wilson et al., 2004). In this regard, PNs are analogous to olfactory bulb mitral/tufted cells, which also release neurotransmitter from their dendrites onto other cells in the same glomerulus (De Saint Jan et al., 2009; Pimentel and Margrie, 2008; Urban and Sakmann, 2002). Within the DM6 glomerulus, we observed that PNs devoted almost all of their output synapses (~90%) to multiglomerular neurons (Figure 1F). PNs devoted a small part of their output to ORN axon terminals. Finally, every PN also made connections with all the other PNs in the same glomerulus, consistent with electrophysiological evidence for reciprocal synaptic interactions between sister DM6 PNs (Kazama and Wilson, 2009).

The structure and strength of excitatory connections

We will use the term “unitary connection” to refer to all the synapses between one presynaptic cell and one postsynaptic cell. Most of the unitary connections we detected were composed of multiple synapses – i.e., multiple contacts at distinct locations, each with its own presynaptic specialization. This is illustrated by the typical ORN-PN pair shown in Figure 1D (Figure S1, shows all ORN-PN pairs).

On average, unitary ORN→PN connections were composed of about 23 synapses (Figure 1G). In principle, a connection composed of so many individual synapses should be both strong and reliable. Indeed, physiological studies have shown that each ORN axon makes a strong and reliable excitatory connection onto every PN in its target glomerulus (Gaudry et al., 2013; Kazama and Wilson, 2008; Kazama and Wilson, 2009). An isolated ORN spike typically depolarizes a PN by about 5 mV, and the size of this unitary excitatory postsynaptic potential (uEPSP) is highly reliable from trial to trial. The average number of synapses that we detected per unitary ORN→PN connection is similar to that predicted by quantal analysis in whole-cell recordings (Kazama and Wilson, 2008) and also by light microscopy methods (Mosca and Luo, 2014).

As compared to ORN→PN connections, the other connections involving ORNs and PNs were weaker, as judged by the number of synapses they contained. Unitary PN→PN connections were composed of about 11 synapses, on average (Figure 1G). ORN→ORN connections and PN→ORN connections typically consisted of just one or two synapses. However, the influence of ORN→ORN connections in particular is likely to be non-negligible, because there are so many ORNs in total, and so ORNs collectively provide a major input to other ORNs (Figure 1E).

Compensatory variations in dendrite size and synapse number

Usually, three PNs reside in glomerulus DM6, with no systematic left-right asymmetry in cell number (Figure S2). However, in the specimen we analyzed, there were only two DM6 PNs on the right side (Figure 2A). The right PNs also had larger dendritic arbors as compared to the left PNs (Figure 2A), possibly because right PNs had fewer sister cells, and so had more space to fill. Because it is atypical to find only two PNs in this glomerulus, we conclude that an error has occurred in its development. Related to this error, we found a number of differences between the left and right versions of DM6 that provide insight into the circuit's developmental program.

First, we found that the number of ORN synapses received by an individual PN was 53% higher on the right than on the left (Figure 2B). Interestingly, the magnitude of this asymmetry produced a similar total number of ORN→PN synapses in the left and right glomerulus. The number of multiglomerular neuron synapses received by an individual PN was also higher on the right than on the left (Figure 2C). Finally, individual PNs on the right formed more presynaptic contacts than did individual PNs on the left (Figure 2D). The differences in ORN→PN synapse number and PN dendrite size resulted in a similar synaptic density in left and right PNs (left PNs had 0.61, 0.63 and 0.57 ORN→PN synapses/ μm ; right PNs had 0.59 and 0.60 ORN→PN synapses/ μm).

What do these findings mean for PN function? In particular, what does the asymmetry in ORN synapse number mean for PNs, given that ORNs are the main drivers of PN activity? To address this question, we constructed a passive compartmental model of each PN's dendritic tree. The length and diameter of each dendritic branch was taken directly from our reconstructions (Figure 3A). The locations of all ORN synapses were also taken from our reconstructions. The specific resistance and capacitance of the PN dendritic membrane were taken from a previous electrophysiological study which measured these values directly (Gouwens and Wilson, 2009). That same study also deduced the conductance produced by a single quantum of neurotransmitter released at

ORN→PN synapses. This measurement was used to model the synaptic conductance, which had the same amplitude and time course at all synapses following a presynaptic spike. In short, all the model parameters were taken directly from data. The model therefore provides a highly-constrained analytical tool for exploring the functional implications of 3-D ultrastructure data.

We used the model to determine if right and left PNs will respond differently to ORN spikes. For each of the 260 ORN→PN connections in our reconstruction, we inferred the corresponding unitary excitatory postsynaptic potential (uEPSP) in the PN cell body (Figure 3B). Surprisingly, the simulated somatic uEPSP amplitudes were almost identical in right and left PNs (Figure 3C). In other words, the overall strength of unitary connections was the same on the right and left. This is notable because of the substantial difference in the number of synapses per ORN→PN connection on the right and the left (Figure 2B).

To better understand this result, we decomposed uEPSPs into their elemental components – i.e., miniature excitatory postsynaptic potentials (mEPSPs). When we measured mEPSPs at the soma, they were much smaller in right PNs than in left PNs (Figure 3D). The difference in mEPSP amplitude also appeared when we measured each mEPSP in the dendrite, at the site of the synapse itself (Figure 3E), reflecting a lower dendritic input resistance in right PNs (Figure 3F). Moreover, in right PNs, mEPSPs also decayed significantly more as they propagated from the dendrite to the cell body (Figure 3G), reflecting a longer average path length from synapse to cell body (Figure 2A). These differences highlight the important effect of the dendrite's overall morphology.

In summary, we find that right and left PNs have uniform average voltage responses to ORN spikes, in spite of their marked differences in dendrite size and synapse number. In principle, synapse number might be altered to compensate for dendrite size, or vice versa. We think it likely that synapse number is altered to compensate for dendrite size (see Discussion). Notably, the functional effects of this compensation could not have been

deduced from simply counting the number of increased synapses: they required us to examine the interactions between different anatomical changes, using the compartmental model.

A basis for odor lateralization in the structure of synaptic connections

Drosophila can lateralize odors by comparing ORN spike trains arising from the right and left antennae. In response to a laterally asymmetric odor stimulus, flies will tend to turn toward the antenna that is stimulated more strongly (Figure 4A; Borst, 1983; Duistermars et al., 2009; Flugge, 1934; Gaudry et al., 2013). Because fly ORNs project bilaterally (Figure 4B), odor lateralization would be impossible unless there were an asymmetry between ORN connections in the ipsi- and contralateral antennal lobes. Electrophysiological recordings have shown that unitary ORN→PN connections are 30 – 40% stronger on the side of the brain ipsilateral to the ORN’s cell body (Gaudry et al., 2013). We therefore asked if there is a structural basis for this ipsi/contra difference.

Indeed, we found that PNs received more input synapses from ipsilateral ORNs than from contralateral ORNs (Figure 4C). Accordingly, our compartmental model predicted a systematic difference in the amplitude of ipsi- versus contralateral uEPSPs (Figure 4D). There was no systematic ipsi-contra difference in the placement of synapses onto the PN’s dendritic tree, as judged by the mean mEPSP amplitude at the PN soma (Figure 4E). There was also no significant difference in the total path length of ipsi- and contralateral ORN axons within the boundaries of glomerulus DM6 (Figure S3).

In short, we find that the difference in the electrophysiological properties of ipsi- and contralateral connections is explained by a single structural difference: PNs receive more synapses from ipsilateral than from contralateral ORNs. This finding represents a case where a particular behavior (odor lateralization) can be traced to a

systematic variation in structure of connections. It also raises the interesting developmental problem of how ORN axons distinguish ipsilateral from contralateral glomeruli and adjust synapse number accordingly.

Inequalities among olfactory receptor neurons

Neural noise represents a fundamental challenge to the computational capacity of the brain. Individual neurons can minimize the impact of electrical noise by pooling many inputs carrying a common signal, but with independent noise (Faisal et al., 2008). The olfactory system is often cited as one of the clearest examples of this strategy. By pooling across many ORNs that express the same odorant receptor, a postsynaptic neuron should be able to dramatically improve the trial-to-trial reliability of its odor responses. If we assume that all sister ORNs are equally reliable, then the optimal strategy is to weight them equally. Alternatively, if some sister ORNs are more reliable than others, then the optimal strategy is to weight these inputs more heavily. We therefore examined the structure of ORN→PN connections for clues as to how ORNs are weighted.

We focused first on connections made by ipsilateral ORN axons, so as to remove the factor of ipsi-contra differences (Figure 5A). Even among ipsilateral ORN axons, we found substantial structural variation among the connections that they formed with PN dendrites. The main source of variation was the number of synapses per connection. This number varied over a wide range: for example, a typical PN received only 10 synapses from one ipsilateral ORN, but 36 synapses from another ipsilateral ORN (left PN1, Figure 5B). The number of synapses per connection was correlated with the physical proximity of ORN axons and PN dendrites (Figure S4), suggesting the number of synapses connecting each ORN-PN pair simply scales with the amount of axonal and dendritic contact.

To normalize for the fact that different PNs receive different total numbers of synapses, we divided the number of synapses per connection by each PN's total synapse count (Figure 5C). This value expresses the contribution of each ORN to a PN's total synapse pool. Across all connections, the coefficient of variation (CV) in this value was 0.31, consistent with previous estimates based on optical methods (Mosca and Luo, 2014).

By comparison, there was little variability among connections in average synapse potency. Synapse potency is defined as the amplitude of a simulated mEPSP at the soma of the compartmental model. Average synapse potency is just the average of all the mEPSP values associated with that connection. We found that average synapse potency was quite uniform across connections (Figures 5D and 5E). This is because each connection comprised many synapses, and there was little systematic variation across connections in the placement of the synapses on the dendrite.

Summation efficacy was also relatively consistent across ORN→PN connections (Figures 5F and G).

Summation efficacy is measured as the amplitude of the uEPSP, divided by the summed amplitudes of all the mEPSPs that contribute to that connection. Most connections had summation efficacies near 0.9, indicating weakly sublinear summation.

Why are average synapse potency and summation efficacy so consistent (Figures 5D-G)? We obtain a similar level of consistency if we randomly allocate synapses to ORN axons. Specifically, we allocate to each ORN axon the same number of synapses as before, but we draw synapses randomly (without replacement) from the pool of ORN→PN synapse locations. After shuffling, average synapse potency is still consistent across connections ($CV_{real} = 0.014$, $CV_{shuffled} = 0.009$), as is summation efficacy ($CV_{real} = 0.041$, $CV_{shuffled} = 0.037$; 1000 shuffles). Because each ORN axon makes synapses at many locations on the dendritic tree, the differences among an ORN's many synapses tend to average out. This makes the qualitative properties of each connection quite similar (i.e., the properties that do not depend on synapse number).

In short, the major source of variation among ORN→PN connections is simply the number of synapses per connection. Our model indicates that this source of variation should produce a relatively large range in uEPSP amplitudes (Figure 5H). Different ORNs in the same antenna should have quite different effects on the PN membrane potential, with the strongest ORNs outweighing the weakest ORNs by almost 10-fold. Thus, it seems that PNs do not assign equal weight to ORNs from the same antenna. Rather, the PN response is likely to be dominated by only a fraction of the ORN population.

Connection noise in olfactory receptor neuron projections

In principle, the variation in ORN→PN connections might be the result of developmental noise. Alternatively, it might represent a strategy to optimize PN signals by weighting the most reliable ORNs more heavily. We cannot know for certain because we cannot compare the spike trains of the ORNs in question. However, we can find a clue by comparing different connections made by the same ORN. Paired electrophysiological recordings from sister PNs show that ORN spikes virtually always produce synchronous synaptic events in all ipsi- and contralateral target PNs (Kazama and Wilson, 2009). In essence, all sister PNs experience the same ORN spike trains. Therefore, if PNs weight ORNs according to their reliability, then those weights should be correlated across all five PNs in our sample. Our analyses thus far have indicated that synapse number is the main correlate of connection strength variability (Figure 5H), so we will focus on synapse number here.

Correlations across PNs are easiest to assess if we first normalize each ORN's contribution by the total contribution from the antenna in question. For example, there are 26 ORNs in the right antenna, which collectively make 893 synapses onto PN1 on the right side. A typical ORN from the right antenna contributes 34 synapses, or 3.81% (34/893) of the total contribution from that antenna. By focusing on these percentages,

we can make a fair comparison between all connections, because this normalization procedure controls for systematic right-left differences as well as ipsi-contra differences.

Using this metric of connection strength, we found correlations between the three PNs on the left side (Figure 6B), and also correlations between the two PNs on the right side (Figure 6C). Specifically, 7 of the 8 ipsilateral comparisons produced a significant correlation (Pearson's r ranged from 0.44 to 0.78, $P < 0.05$; the exception is left PN2 and left PN3, where $r = 0.36$, $P = 0.07$). However, there was no correlation between right and left PNs (Figure 6B and 6C; for the 12 contralateral comparisons r ranged from -0.21 to 0.34, $P > 0.09$)

The failure to find correlations among all PNs argues that ORN→PN connection strengths are not optimized to match some feature of each ORN's spiking behavior. If they were optimized, they would be correlated among all five PNs, because all PNs witness identical ORN spike trains (Gaudry et al., 2013). In other words, if some ORNs are more reliable than other ORNs in the same antenna, then all five PNs should assign greater relative weight to these inputs. Because we do not observe this sort of correlation, then it seems likely that at least some of the variation in ORN→PN connection strengths is due to "connection noise". This connection noise should limit the accuracy of a PNs estimate of the stimulus based on incoming ORN spike trains.

Functional implications of connection noise

Our results imply that at least some of the variation in ORN→PN connection strengths is unrelated to the content of ORN spike trains. Variation that is unrelated to ORN spiking is expected to degrade the performance of the organism on olfactory tasks. To estimate how large this effect could be, we performed an experiment using our compartmental models. Specifically, we asked how accurately an observer can judge the number of ORN spikes fired during a particular time window, based on a model PN's time-averaged voltage response

(Figure 7A). It is important to note that all ORNs fire spontaneously even in the absence of odor (de Bruyne et al., 1999; de Bruyne et al., 2001). Thus, at the perceptual threshold for odor detection, the olfactory system must be able to detect an odor based on an increase in ORN spikes above the expected number of spontaneous spikes.

The perceptual threshold for odor detection is known to be in the regime of low ORN spike numbers (Bell and Wilson, 2016; Gaudry et al., 2013). We therefore first focused on small odor-evoked increases in ORN spiking. We chose a 200-ms window for counting ORN spikes because it can take roughly this amount of time for a fly to show a behavioral response to an odor (Bhandawat et al., 2010; Budick and Dickinson, 2006; Gaudry et al., 2013; van Breugel and Dickinson, 2014). During this counting window, in one antenna, the entire DM6 ORN population fires an average of 12 spontaneous spikes in the absence of an odor (see Experimental Procedures). We want to estimate how connection noise can affect the ability to detect an increase in ORN spiking above this baseline.

We simulated ORNs as independent Poisson spike generators, each with the same average spike rate. Each ensemble ORN spike pattern was fed into a model PN, and we measured the time-averaged voltage response of the PN (Figure 7A). Even when ORN spike numbers are held constant, the model PN voltage responses vary from trial to trial, because the timing of ORN spikes varies. We repeated this procedure many times, and then trained a classifier to use the PN response to discriminate “no odor” trials (12 ORN spikes per antenna) from “odor” trials (13 – 20 spikes per antenna). We repeated this for all five PNs and their associated ipsilateral ORNs. Average performance was poor when the number of “odor-evoked” spikes was small, and performance improved as the number of odor-evoked spikes was increased (Figure 7B, blue lines).

To estimate how much the natural variation in ORN→PN connection strengths degrades PN performance, we repeated this task, but now equalizing the number of synapses per ORN→PN connection. Specifically, we randomly reallocated ORN→PN synapses to presynaptic axons so that the number of synapses per axon was as

equal as possible, but with each PN dendrite receiving synaptic input at all the same physical locations as before. Now performance was markedly improved (Figure 7B, green lines). This simulation shows that the normal variation in the structure of ORN→PN connections can impair the ability of PNs to transmit information about ORN spike counts.

We also considered an odor lateralization task (Figure 7C). This time, the ORN spike count in one antenna was held at the “no odor” level (12 spikes), and ORN spike counts in the other antenna were driven up by a lateralized “odor” (to 13 – 20 spikes). In this simulation, each PN received input from all its presynaptic ORNs (both ipsi- and contralateral ORNs). Based on the difference between the mean voltage in right PNs versus left PNs, we trained a classifier to discriminate “right odor” from “left odor”. Performance in this task was especially poor (Figure 7D, blue lines) because the classifier operates on the difference between two variables (right and left) that are contaminated by independent connection noise. Averaging the activity of PNs on the same side of the brain is of limited benefit because wiring noise is correlated among these PNs. When we artificially equalized the number of synapses per connection by randomly reassigning synapses to ORNs so that the number of synapses per axon was as equal as possible, we found that performance increased dramatically, as expected (Figure 7D, green lines). This simulation shows that the normal variation in the structure of ORN→PN connections can impair the ability of PNs to transmit information about right-left differences in ORN spike counts, particularly because connection noise is correlated within each half of the brain, but uncorrelated across the midline.

DISCUSSION

Strengths and limitations of our data

An olfactory glomerulus represents a discrete and spatially compact neural network. The spatial scale of this network allowed us to comprehensively reconstruct the connections between every excitatory principal cell (i.e., every ORN and PN). Another strength of this data set is the ability to integrate comprehensive structure with *in vivo* electrophysiology. DM6 ORNs and PNs generally have similar physiological properties across different individuals. Therefore, existing electrophysiological measurements of these neurons (Gaudry et al., 2013; Hallem and Carlson, 2006; Kazama and Wilson, 2008; Kazama and Wilson, 2009; Kazama et al., 2011; Nagel et al., 2015) are directly relevant to the anatomical data we analyzed. In particular, because we know the specific resistance and capacitance of the PN membrane, as well as the typical quantal conductance at ORN→PN synapses (Gouwens and Wilson, 2009), we were able to construct highly-constrained compartmental models based on our EM reconstructions. The conclusions we drew from the model were robust to measured variations in the model parameters derived from electrophysiological experiments (Figure S5).

One limitation we faced was our lack of knowledge about the active properties of PN dendrites, if any. In principle, voltage-gated conductances in PN dendrites might alter the integrative properties of PNs. However, active properties are unlikely to play a large role in PN synaptic integration, because the current-voltage relationships in PNs are fairly linear (Gouwens and Wilson, 2009), whereas in other *Drosophila* neurons these relationships can be strongly nonlinear (A.W. Azevedo & R.I. Wilson, in preparation). Thus, our passive models are good first approximations in this case.

Another limitation is the inability to directly measure the synaptic conductance of different synapses. Our model assumes that conductance is identical at every ORN→PN synapse. This assumption is likely reasonable, because a previous quantal analysis predicated on this assumption predicted a number of release sites per unitary connection (12 – 50 sites/connection; Kazama and Wilson, 2008) which is consistent with our observation of about 3 – 52 synapses per connection. In principle, we might be able to examine heterogeneity in synaptic conductance by measuring variations in vesicle numbers at different synapses, or variations in the area

of the postsynaptic density (PSD). However, our aldehyde-based fixation conditions were not optimized to preserve vesicles. Moreover, although indirect evidence exists for the idea that PSD size correlates with synaptic strength at mammalian synapses (Matsuzaki et al., 2001; Nusser et al., 1998; Takumi et al., 1999), it is unclear whether this applies to *Drosophila* synapses. In future, it would be valuable to develop methods to correlate the fine features of *Drosophila* central synapses with synaptic conductance.

Structural correlates of connection strength

We can think of connection strength as being determined by three major factors. The first is the number of synapses comprising that connection. The second is the conductance at each of those synapses. The third is the filtering of those conductances by the postsynaptic dendrite. We cannot measure the conductance at each synapse in our reconstruction, but our reconstruction informs us about the other two factors, and our results imply that the first of these factors is particularly important.

Notably, we found that the number of synapses per connection was strongly correlated with the strength of ORN→PN connections. The comparison between ipsi- and contralateral synapses represents the clearest example of this correlation, because we know from prior electrophysiology experiments that ipsilateral connections are 30 – 40% stronger (Gaudry et al., 2013). Here, we discovered that ipsilateral connections contain ~35% more synapses per connection (Figure 4C). This result argues that the difference in the number of synapses per connection is the main difference between ipsi and contra connections. By extension, we can infer that there is not a sizeable difference in the conductance at ipsi- and contralateral synapses, although we cannot measure the conductance at each synapse directly. We also found no difference in the way that ipsi-contra synapses are filtered by the PN dendritic tree, as evidenced by the fact that there is no ipsi-contra difference in

simulated mEPSP amplitudes (Figure 4E). In short, the number of synapses per connection appears to be the dominant structural feature underlying the systematic difference between ipsi- and contralateral connections.

Interestingly, from the perspective of an individual PN, there was little variation across ORN connections in the average strength of the synapses that comprised each connection (Figure 5E). The efficacy of mEPSP summation at the level of uEPSPs was also notably consistent across these connections (Figure 5G). Thus, insofar as our model accurately represents the structure of each PN dendrite, it predicts that dendritic filtering has an essentially uniform effect on all ORN→PN connections. This uniformity arises because each connection is composed of many synapses, and synapses made by a given ORN axon tend to be placed onto the dendrite in a relatively unbiased fashion. In essence, each connection is composed of many quasi-random “samples” of dendritic filtering properties, and so the average effect of dendritic filtering is similar across connections.

Co-variation in cell number, dendrite size, and synapse number

Although *Drosophila* neural networks are sometimes regarded as highly stereotyped, in fact many networks exhibit slight variations in neuron number. In the optic lobe, a recent EM study analyzed 7 repetitions of a modular neural network that normally contains 23 uniquely identifiable cells. In 3 of the 7 networks, one cell that ought to be present was in fact missing (Takemura et al., 2015). If errors like this were unbiased, then this result would imply that each neuron in the fly brain would be absent about 2% of the time, on average (given 3 missing cells in 7×23 observations). Takemura et al. (2015) found that in the case of one missing cell, a homologous cell in a neighboring column sent an extra branch into the vacated space, where it received synapses from the normal presynaptic partners of the missing cell. Thus, when a cell is missing, there can be compensatory changes in wiring.

Small variations in antennal lobe PN numbers have been inferred previously based on Gal4 expression patterns, which show brain-to-brain variations in PN cell counts on the order of 5% (Tanaka et al., 2004). Indeed, based on Gal4 expression, we find that there are normally 3 PNs in each copy of glomerulus DM6, and only occasionally do we find 2 or 4 (Figure S2). The brain selected for large-scale serial section EM turned out to contain only two PNs on the right side. In this anomalous glomerulus, the dendrites of the remaining PNs were larger, presumably because they had more space to fill. Moreover, there was also a compensatory increase in synapse numbers per PN, so that the total number of synapses per glomerulus was similar on the left and right.

Our compartmental models allowed us to infer the functional consequences of these concerted changes in PN dendrite morphology and ORN→PN synapse numbers. Remarkably, taken together, these anatomical changes created completely normal PN responses to simulated ORN spikes: in the glomerulus where one PN was missing, the up-regulation in synapse number per ORN→PN connection was neatly balanced by the increased size of PN dendrites. As illustrated by classic work at the neuromuscular junction, increasing the size of a postsynaptic compartment produces a lower input resistance, and so each quantum of neurotransmitter produces a smaller depolarization (Katz and Thesleff, 1957). In each of the larger PNs, each presynaptic ORN spike should release more quanta than normal, but the postsynaptic voltage response to each quantum will be smaller. Thus, as a result of the counterbalanced changes in synapse number and dendrite size, the PN response to individual ORN spikes is essentially normal.

Counterbalanced effects like this can result from homeostatic mechanisms in the developing central nervous system. For example, in the larval ventral nerve cord, a decrease in presynaptic neurotransmitter release can elicit compensatory growth in postsynaptic dendrites (Tripodi et al., 2008). Moreover, there is direct evidence that the electrical properties of the dendrites of antennal lobe PNs can instruct changes in ORN→PN connections. One study used cell-specific K⁺ channel overexpression to decrease a PN's input resistance, and found a compensatory increase in unitary excitatory synaptic currents at ORN connections onto that PN

(Kazama and Wilson, 2008). That result argued that PN dendrites can up-regulate synaptic current to achieve sufficient levels of depolarization.

Together, these findings suggest the following scenario. When one PN failed to develop, the remaining PNs grew larger dendrites, and then synapse number increased to compensate for increased dendrite size. This scenario is consistent with the well-described instructive role of PN dendrites in ORN axon development: PN dendrites form a glomerular map prior to the arrival of migrating ORN axon terminals (Jefferis et al., 2004).

This scenario is reminiscent of the “size matching” principle that governs the development of vertebrate neuromuscular junctions, where the size of a muscle is matched to the size of the axon’s terminal arborization, thereby ensuring that large muscles (with low input resistance) receive a larger quantal content per presynaptic spike (Kuno et al., 1971; Lichtman et al., 1987). Here too, the expansion of the postsynaptic cell seems to be primary, with the elaboration of the presynaptic arbor occurring in response (Balice-Gordon et al., 1990; Balice-Gordon and Lichtman, 1990).

Developmental noise in wiring

We found that the number of synapses per ORN→PN connection was quite variable. As a result, ORN→PN connections gave rise to simulated uEPSP amplitudes ranging from 1.6 to 10 mV (Figure 5H). If all ORNs were functionally identical, this sort of variation would be non-optimal, because each PN’s response would be dominated by a relatively small fraction of its presynaptic ORN axons. Indeed, our simulations showed that this sort of variation can substantially impair a PN’s ability to accurately transmit information about total ORN spike counts, as well as right-left differences in ORN spiking (Figure 7). Our simulations suggest that connection noise may be a factor limiting perceptual acuity.

The discovery of connection strength variability *per se* is not surprising: it was already clear that connection weights in the *Drosophila* brain can be variable. In the medulla of the optic lobe, Takemura et al. (2015) tabulated instances of connection motifs repeated across columns, and found that the CV of synapse number per connection ranged from 0.08 to 0.87, depending on connection type. In principle, this sort of variation may be either noise or evidence of adaptive plasticity. For example, systematic variations in upstream input (inherited from earlier layers of visual processing) might drive adaptive activity-dependent changes in the number of synapses per connection. Here, we focused on primary afferent synapses, so any systematic upstream variations are limited to variations in ORN spike trains. Moreover, we know that all DM6 PNs witness identical ORN spike trains, because ORN spikes travel faithfully across the midline to invade both ipsi- and contralateral glomeruli (Kazama and Wilson, 2009). This fact allowed us to test the hypothesis of adaptive plasticity by reconstructing all the synapses that each ORN axon made onto all PNs. We found that the variation in synapse numbers was not faithfully correlated across all PNs (Figure 6), and so some of this variation is likely random – i.e., unrelated to ORN activity.

Intriguingly, we found that synapse number variations were correlated across sister PNs on the same side of the brain, even though they were uncorrelated on the opposite sides of the brain. In principle, this might be evidence of incomplete adaptive plasticity – plasticity that works at ipsilateral connections but somehow fails at contralateral connections. More likely is the scenario of correlated developmental noise – e.g., some ORN axons may simply arrive sooner at the ipsilateral glomerulus, and so may form more physical contact with ipsilateral PNs, and thus more synapses. This sort of correlated developmental noise may be one reason why sister PNs on the same side of the brain display such high levels of correlated electrical noise (Kazama and Wilson, 2009). As we show here, sister PNs on the same side of the brain are dominated by the same pool of ORNs. These ipsilateral sister PNs converge onto higher-order neurons, which are especially sensitive to correlations in sister PN spike times. As a result, sister PN spike timing correlations represent a functionally-

relevant constraint on circuit function which can affect both the speed and accuracy of odor stimulus responses (Jeanne and Wilson, 2015).

Comparison between adult and juvenile networks

In the larval antennal lobe, there are 21 glomeruli, as compared to ~50 in the adult. Each glomerulus in the larva is relatively simple: it contains just one ORN axon and one uniglomerular PN dendrite (Python and Stocker, 2002). The larval antennal lobe connectome has just been reconstructed (Berck et al., 2016), and it is instructive to compare our results with the results of that study. In both the larva and the adult, the pattern of binary connectivity between ORNs and PNs is highly precise: there are almost no “missed” ORN→PN connections. Also, ORNs distribute their synaptic output in a similar way in both the larva and the adult. In both cases, the majority of ORN synapses are formed onto multiglomerular neurons, with approximately a third of ORN output synapses devoted to PNs.

There are also distinct differences between the larva and the adult. In the larva, the average ORN→PN connection contains ~70 synapses, whereas in the adult, it contains 23 synapses. Thus, the increased number of ORNs in the adult is partly compensated by a decrease in the number of synapses per connection. Another distinctive difference is in the control of ORN output. In the larva, almost all synapses onto ORNs arise from multiglomerular neurons. In the adult, most synapses onto ORNs arise from multiglomerular neurons, but a substantial minority arise from PNs and ORNs. This suggests that the adult network may exert more complicated control of ORN neurotransmitter release. In future, it will be interesting to extend these comparisons to the domain of multiglomerular neuron networks, which are complex and intriguing in the larva (Berck et al., 2016).

Variations in the connectome: signal and noise

The brain's computational power would be substantially reduced if all synaptic connections were identical. From this perspective, systematic variations in connection strength are evidence of the brain's functional capacity – the capacity to match a connection's strength to its required function. Our results show how systematic variations in connection strength can arise as a result of systematic differences in the number of synapses per connection.

On the other hand, unsystematic wiring variations ("connection noise") must limit the capacity of every neural system. Some of these noisy variations can be balanced by homeostatic changes to other parameters, including synaptic parameters (Prinz et al., 2004; Roffman et al., 2012). Our findings provide insight into the mechanisms underlying such compensatory changes, but our results also argue for the existence of residual non-optimal wiring variations that can demonstrably impair neural computations.

Large-scale EM offers an unprecedented opportunity to study all these variations – and co-variations – in brain neural network wiring. *Drosophila melanogaster* is likely to be the next organism whose brain is fully mapped at the connectomic level. As such, it provides an opportunity to gain insight into the causes and consequences of systematic and noisy variations in network architecture.

EXPERIMENTAL PROCEDURES

EM material preparation

The brain of an adult *Drosophila melanogaster* female (aged 8-10 days post-eclosion, genotype GH146-GAL4/+; UAS-CD2::HRP+/+) was immobilized by cooling on ice, and then submerged in a drop of fixative (2% paraformaldehyde/2.5% glutaraldehyde in 0.1 M cacodylate buffer with 0.04% CaCl₂ for membrane

stabilization). The head capsule was opened to allow fixative to access the brain before dissection (Meinertzhagen, 1996). Following dissection, the brain was processed for serial-section transmission EM. The dissected brain was post-fixed and stained with 1% osmium tetroxide/1.5% potassium ferrocyanide, followed by 1% uranyl acetate, then lead aspartate (Walton, 1979), then dehydrated with a graded ethanol series, and embedded in resin (TAAB 812 Epon, Canemco). Approximately 1900 serial thin (<50 nm) sections were cut on an ultramicrotome (Leica UC7) using a 35 degree diamond knife (EMS-Diatome) and manually collected on 1×2 mm dot-notch slot grids (Synaptek) that were coated with a pale gold Pioloform support film (Ted Pella), then carbon coated and glow-discharged. Grids were subsequently post-stained with uranyl acetate (saturated) in 50% methanol and 0.2% lead citrate.

Large-scale TEM imaging and alignment

We imaged the ~1900 sections using a custom-built Transmission Electron Microscope Camera Array (TEMCA) (Bock et al., 2011; Lee et al., 2016). Acquired at 4 nm/pixel in plane, this amounted to ~50 terabytes of raw data comprising ~250 million cubic microns of brain and > 4 million (4000×2672 pixel) camera images. Magnification at the scope was 2000×, accelerating potential was 120 kV, and beam current was ~90 microamperes through a tungsten filament. Images suitable for circuit reconstruction were acquired at a net rate of 5-8 MPix/s. The series was aligned using open source software developed at Pittsburgh Supercomputing Center (AlignTK) (Bock et al., 2011; Lee et al., 2016). The aligned series was then imported into CATMAID (Saalfeld et al., 2009) for distributed online visualization and segmentation. Within the portion of the volume spanned by the DM6 glomeruli, there were 9 single-section losses, 2 instances of 2-section losses, 1 instance of 3-section losses, and 2 instances of 4-section losses (losses refer to consecutive sections). Across the entire series of ~1900 sections there were 50 single-section losses, 16 instances 2-section losses, 10 instances of 3-section losses, 3 instances of 4-section losses, 3 instances of 5-section losses, and one instance of a 6-section

loss. Folds, staining artifacts, and cracks occasionally occurred during section processing, but were typically isolated to edges of our large sections and therefore did not usually interfere with manual segmentation.

Reconstruction and verification

We reconstructed the arbors of ORNs and PNs in the EM dataset by using CATMAID to manually place a series of marker points down the midline of each process to generate a wire-frame model of the axonal and dendritic arbors (Lee et al., 2016; Saalfeld et al., 2009). We identified synapses using a combination of ultrastructural criteria – namely, the existence of a presynaptic T-bar, presynaptic vesicles, a synaptic cleft, and postsynaptic densities. The presence of most, though not necessarily all, of these features over multiple sections was required for a synapse to be annotated. PNs were easily identifiable based on having dendrites restricted to DM6 and axons projecting into the inner antennocerebral tract. Annotators began by identifying putative PNs within the DM6 volume (based on their large gauge processes), and then traced the wire-frame structure of each PN dendrite while also comprehensively annotating each PN input synapse and output synapse. This procedure follows a previously described and validated protocol for manual tracing in serial section TEM data sets such as ours (Schneider-Mizell et al., 2016). Subsequently, all profiles presynaptic to each PN were annotated in the same manner. Profiles were categorized as ORNs if they arrived in the antennal lobe from the antennal nerve bundle; all such profiles innervated a single glomerulus either bilaterally (in the case of 51 ORNs) or unilaterally (in the case of 2 ORN). Because ORN axons travel from the antennal nerve to DM6 in a distinctive trajectory, it was clear even before an ORN exited DM6 that it was indeed an ORN. Profiles not annotated as either PNs or ORNs were categorized as multiglomerular neurons; all such profiles presynaptic to PNs were traced until they reached the border of DM6 before their tracing was suspended. The multiglomerular neurons in DM6 likely include local neurons, multiglomerular PNs, and neurons innervating the antennal lobe from other brain regions (extrinsic neurons). For all reconstructed neurons included in our analysis, at least one

additional independent annotator(s) verified the tracing by working backward from the most distal end of every process. Due to the oblique orientation and fine calibre of axons traveling through the anterior commissure, it is formally possible that ORN axon profiles might be mis-traced in this region, and so to verify our reconstructions of ORN axons in the region of the commissure, we re-imaged sections containing DM6 ORN axons in the commissure at higher magnification (20,000 \times). We then aligned the higher-resolution data set to the lower-resolution data set, and an additional independent annotator (who was blind to the original reconstructions) was assigned to trace all the DM6 axons through the commissure.

Labeling DM6 PNs for cell counting

To count the number of PNs that are normally present in a DM6 glomerulus, we labeled and counted these cells in five additional flies. We used *NP3481-Gal4* to drive expression of photoactivatable GFP (PA-GFP) (Datta et al., 2008; Patterson and Lippincott-Schwartz, 2002) in DM6 PNs, along with several other PN types (Tanaka et al., 2012). By selectively photoactivating within the neuropil of DM6, we could photolabel the DM6 PNs alone, and then count the number of PNs innervating that glomerulus. Photoactivation was performed using a custom built two-photon laser-scanning microscope. We first imaged the antennal lobe at 925 nm and low laser power to identify DM6. After defining volumes of interest restricted to the core of the glomerular neuropil based on these images, PA-GFP was photoconverted by imaging through the volume with 710-nm light. In each photoactivation block, we moved through the z depth of the volume of interest with 0.25- μ m steps. Each glomerulus was subject to three photoactivation blocks at intervals of five to ten minutes. After PA-GFP is photoactivated in the glomerular neuropil (i.e., axons and dendrites), it diffuses into the somata of cells. We then imaged each brain using an Andor XD spinning disk confocal microscope equipped with a Yokogawa CSU-X1 spinning disk unit and a Zyla 4.2 CMOS camera. For this imaging we used laser illumination at 488

nm. We found 3.1 ± 0.57 (mean \pm SD) photoactivated DM6 PN somata on each side of the brain in 5 flies (10 glomeruli total).

Compartmental models

To generate compartmental models, we first inflated our wire-frame reconstructions of PNs to create a representation of the entire volume of each dendritic segment. We did this in the CATMAID environment by measuring the average neurite caliber between each pair of skeleton branch points. We then used this value as the radius of the distal branch point (relative to the soma) and all nodes leading up to the proximal branch point. This process was repeated until the entire skeleton was inflated.

Next, we exported PN morphologies along with ORN input synapse locations as neuroML 1.8.1 models (Gleeson et al., 2010). Using the software tool neuroConstruct (Gleeson et al., 2007), we defined PN membrane properties and synaptic conductances, and subsequently exported these models to the NEURON simulation environment (Hines and Carnevale, 1997). Additionally, we used neuroConstruct to remesh the PN models to ensure each segment had an electrotonic length between 0.1 and 0.0001. We gave PN membranes uniform, passive properties. A previous experimental study (Gouwens and Wilson, 2009) used electrophysiological recordings from PNs to derive values for their specific membrane resistance ($20.8 \text{ k}\Omega \text{ cm}^2$), specific membrane capacitance ($0.8 \mu\text{F}/\text{cm}^2$), and specific axial resistivity ($266.1 \Omega \text{ cm}$). The measurements of that study were taken from DM1 PNs, so in order to use these measurements in our study, we assume that the intensive (size-independent) properties of DM6 PNs are similar to those of DM1 PNs. The ORN to PN synaptic conductance waveform we used was also adapted from this study. This was modeled as the sum of two exponentials, with a rising time constant of 0.2 ms and a decay time constant of 1.1 ms. Gouwens and Wilson (2009) modeled the maximum synaptic conductance as having a value of 0.27 nS (it was incorrectly reported in that paper as

2.7×10^{-4} nS, but the value used was actually 0.27 nS); we used a slightly different value here (0.1 nS) because this produced more realistic uEPSP amplitudes (on average roughly 5 mV).

To measure the amplitude of individual mEPSPs, we sequentially activated individual synapses in the modeled PN dendrite, allowing enough time (200 ms) between events for the PN membrane potential to decay to baseline. We recorded PN voltage responses either at the cell body (somatic mEPSPs) or within the compartment where the synaptic conductance was activated (dendritic mEPSPs). To simulate unitary EPSPs, we synchronously activated all synapses from an individual ORN. In this case we always measured the PN voltage response at the cell body (somatic uEPSPs).

Spike Count Discrimination Classifier

We modeled the ORNs ipsilateral to each PN as independent Poisson spike generators. Spike trains in which two spikes in the same neuron occurred at an interval < 4 ms were rejected, in order to create a refractory period. Each modeled ORN spike train was randomly assigned to an ORN axon. The mean spontaneous firing rate of the DM6 ORNs cannot easily be measured from single-sensillum recordings on the antenna because the sensillum which houses DM6 ORNs is the ab10 sensillum (Couto et al., 2005), which is small and has remained undetected in surveys of single-sensillum physiology (de Bruyne et al., 2001; Hallem and Carlson, 2004). We therefore measured the mean spontaneous firing rate of DM6 ORNs by measuring the rate of large spontaneous EPSCs in voltage-clamp recordings from DM6 PNs in a re-analysis of data collected from DM6 PNs for a previously published study (Gaudry et al., 2013). In all recordings we analyzed, the contralateral antenna had been removed just before the recording, so PNs were receiving spiking input from ipsilateral ORNs only. The rate of these events was 58 Hz, and so dividing by 26.5 ORNs, we obtain 2.2 spikes/s/ORN. This method (using spontaneous EPSC rates) has been shown to provide a good agreement with single-sensillum recordings of

ORN spike rates in the case of a different glomerulus, glomerulus DM4 (Kazama and Wilson, 2008).

Multiplying the estimated spontaneous ORN spike rate of 2.2 spikes/s by a window of 200 ms and rounding to the nearest integer yields a basal “no odor” value of 12 spikes.

In each trial, the ipsilateral population of 26 or 27 ORNs fired a specified number of spikes within the first 200 ms, ranging from 12 to 20, and no spikes in the second 200 ms. This allowed the PN membrane potential returned to baseline by the end of each trial. We then used the time-averaged PN membrane potential, recorded at the soma, to train and test a linear classifier to discriminate incoming spike counts. For each of the 5 model PNs, we ran 2500 trials for training and 2500 independent trials for testing. We initially performed this exercise using model PNs based directly on our reconstructions, where each ORN spike activated all synapses attributed to that ORN in our reconstruction. Subsequently, we artificially equalized the number of synapses per ORN axon in the following manner. We defined a pool of synapse locations on the PN dendrite corresponding to all the synapses made by ipsilateral ORNs onto that PN. We then allocated synapses arbitrarily and evenly to ORNs by drawing from this pool (without replacement) until synapses were re-allocated. When the total number of ipsilateral ORN synapses was not evenly divisible by the number of ipsilateral ORNs, the remainders were randomly assigned to simulated ORNs. When synapse numbers are artificially equalized in this manner, summation efficacy increases, and so uEPSP amplitudes increase. In order to keep average uEPSP amplitudes the same as before, the maximum conductance of our synapse model was reduced to 0.0958 nS. Thus, our synapse equalization procedure made uEPSP amplitudes more uniform across connections without changing the mean uEPSP amplitude. As before, for each of the 5 model PNs, we ran 2500 trials for training and 2500 independent trials for testing. Synapses were independently re-allocated in each trial.

Lateralization Classifier

The procedure here was the same as for the spike count classifier, except in every trial we modeled ORNs in the right antenna as well as ORNs in the left antenna, and all PNs received both right and left ORN input. On any given trial, the ORNs in one antenna fired 12 spikes, and the ORNs in the other antenna fired 13 to 20 spikes. In every trial, both right and left ORN spike trains were fed into the dendrites of all 5 PN models. We then used the means of the resulting PN responses to train and test a linear classifier to discriminate trials in which right or left ORNs fired more spikes. In the equalized case, we equalized synapse numbers independently for each PN-antenna combination. For example, we forced all ORNs in the right antenna to have equal contributions to right PN1, and we also forced all ORNs in the left antenna to have equal contributions to right PN1, but the average asymmetry between ipsi- and contralateral connections was preserved. In the equalized case, the maximum conductance of our synapse model was reduced to 0.0958 nS, as before.

Statistics

The number of observations of any given variable was dictated by the number of cells and synapses in glomerulus DM6, and so was not predetermined using statistical methods. Statistical comparisons between sample distributions were done with Permutation tests (i.e. Monte Carlo-based Randomization tests) unless otherwise noted. Permutation test were used because they do not assume the underlying distributions are normal, and because observations do not need to be independent. For Permutation tests, we computed the incidence of differences between means or Pearson's linear correlation coefficient of randomly drawn samples from combined sample distributions exceeding the empirical difference.

Code and Data Availability

Custom code is available upon request. The aligned EM dataset will be made a freely accessible resource at <http://neurodata.io/projects/XXX/>.

AUTHOR CONTRIBUTIONS

W.C.L. processed the tissue for EM and sectioned the series. W.T. and W.C.L. imaged it on the TEMCA. W.T. aligned the EM images into a volume. W.T. annotated the EM dataset and supervised the segmentation effort. W.T. and W.C.L. analyzed the EM reconstruction. W.T. performed the compartmental modeling. W.T., R.W., and W.C.L. designed the study and wrote the paper.

ACKNOWLEDGEMENTS

We thank S. Bellou, R. Caplan, C. Dekker, M. Johnson, P. Starkey, Z. Tweed for primary tracing and reconstruction, E. Raviola for discussions and advice, M. Reed for technical support at the beginning of the study, A. Cardona and S. Saalfeld for making the CATMAID project openly available, and T. Kazimiers for assistance in optimizing our CATMAID instance. We also thank B. Graham and R. Torres for programming, A. Pandya for help with alignment, and G. Hood for alignment pipeline support. J.T. Vogelstein, K. Lillianey, and R. Burns helped make the data freely available. We thank S. Druckmann, M. Pecot, A. Samuel, and members of R.I.W. Lab for feedback on the manuscript. This work was supported by NIH grant R03 DC013622 (to W.C.L.), NIH grant R01 DC008174 (to R.I.W.), a Harvard Brain Initiative Collaborative Seed Grant (to R.I.W. and A. Samuel), the Bertarelli Program in Translational Neuroscience and Neuroengineering, the Edward R. and Anne G. Lefler Center, and the Stanley and Theodora Feldberg Fund. R.I.W. is an HHMI Investigator. The

project is solely the responsibility of the authors and does not necessarily represent the official views of the NIH.

REFERENCES

- Balice-Gordon, R.J., Breedlove, S.M., Bernstein, S., and Lichtman, J.W. (1990). Neuromuscular junctions shrink and expand as muscle fiber size is manipulated: *in vivo* observations in the androgen-sensitive bulbocavernosus muscle of mice. *J Neurosci* 10, 2660-2671.
- Balice-Gordon, R.J., and Lichtman, J.W. (1990). *In vivo* visualization of the growth of pre- and postsynaptic elements of neuromuscular junctions in the mouse. *J Neurosci* 10, 894-908.
- Bell, J.S., and Wilson, R.I. (2016). Behavior reveals selective summation and max-pooling among olfactory processing channels. *Neuron*, In press.
- Berck, M.E., Khandelwal, A., Claus, L., Hernandez-Nunez, L., Si, G., Tabone, C.J., Li, F., Truman, J.W., Fetter, R.D., Louis, M., *et al.* (2016). The wiring diagram of a glomerular olfactory system. *eLife* 5.
- Bhandawat, V., Maimon, G., Dickinson, M.H., and Wilson, R.I. (2010). Olfactory modulation of flight in *Drosophila* is sensitive, selective and rapid. *J Exp Biol* 213, 3625-3635.
- Bhandawat, V., Olsen, S.R., Schlief, M.L., Gouwens, N.W., and Wilson, R.I. (2007). Sensory processing in the *Drosophila* antennal lobe increases the reliability and separability of ensemble odor representations. *Nat Neurosci* 10, 1474-1482.
- Bock, D.D., Lee, W.C., Kerlin, A.M., Andermann, M.L., Hood, G., Wetzel, A.W., Yurgenson, S., Soucy, E.R., Kim, H.S., and Reid, R.C. (2011). Network anatomy and *in vivo* physiology of visual cortical neurons. *Nature* 471, 177-182.
- Borst, A. (1983). Computation of olfactory signals in *Drosophila melanogaster*. *J Comp Physiol [A]* 152, 373-383.

- Budick, S.A., and Dickinson, M.H. (2006). Free-flight responses of *Drosophila melanogaster* to attractive odors. *J Exp Biol* 209, 3001-3017.
- Chen, W.R., and Shepherd, G.M. (2005). The olfactory glomerulus: a cortical module with specific functions. *J Neurocytol* 34, 353-360.
- Chou, Y.H., Spletter, M.L., Yaksi, E., Leong, J.C., Wilson, R.I., and Luo, L. (2010). Diversity and wiring variability of olfactory local interneurons in the *Drosophila* antennal lobe. *Nat Neurosci* 13, 439-449.
- Couto, A., Alenius, M., and Dickson, B.J. (2005). Molecular, anatomical, and functional organization of the *Drosophila* olfactory system. *Curr Biol* 15, 1535-1547.
- Datta, S.R., Vasconcelos, M.L., Ruta, V., Luo, S., Wong, A., Demir, E., Flores, J., Balonze, K., Dickson, B.J., and Axel, R. (2008). The *Drosophila* pheromone cVA activates a sexually dimorphic neural circuit. *Nature* 452, 473-477.
- de Bruyne, M., Clyne, P.J., and Carlson, J.R. (1999). Odor coding in a model olfactory organ: the *Drosophila* maxillary palp. *J Neurosci* 19, 4520-4532.
- de Bruyne, M., Foster, K., and Carlson, J.R. (2001). Odor coding in the *Drosophila* antenna. *Neuron* 30, 537-552.
- De Saint Jan, D., Hirnet, D., Westbrook, G.L., and Charpak, S. (2009). External tufted cells drive the output of olfactory bulb glomeruli. *J Neurosci* 29, 2043-2052.
- Duistermars, B.J., Chow, D.M., and Frye, M.A. (2009). Flies require bilateral sensory input to track odor gradients in flight. *Curr Biol* 19, 1301-1307.
- Faisal, A.A., Selen, L.P., and Wolpert, D.M. (2008). Noise in the nervous system. *Nat Rev Neurosci* 9, 292-303.
- Flugge, C. (1934). Geruchliche Raumorientierung von *Drosophila melanogaster*. *Z Vergl Phys* 20, 463-500.
- Gaudry, Q., Hong, E.J., Kain, J., de Bivort, B., and Wilson, R.I. (2013). Asymmetric neurotransmitter release at primary afferent synapses enables rapid odor lateralization in *Drosophila*. *Nature* 493, 424-428.

- Gleeson, P., Crook, S., Cannon, R.C., Hines, M.L., Billings, G.O., Farinella, M., Morse, T.M., Davison, A.P., Ray, S., Bhalla, U.S., *et al.* (2010). NeuroML: a language for describing data driven models of neurons and networks with a high degree of biological detail. *PLoS Comput Biol* 6, e1000815.
- Gleeson, P., Steuber, V., and Silver, R.A. (2007). neuroConstruct: a tool for modeling networks of neurons in 3D space. *Neuron* 54, 219-235.
- Goodman, C.S. (1978). Isogenic grasshoppers: genetic variability in the morphology of identified neurons. *J Comp Neurol* 182, 681-705.
- Gouwens, N.W., and Wilson, R.I. (2009). Signal propagation in Drosophila central neurons. *J Neurosci* 29, 6239-6249.
- Hallem, E.A., and Carlson, J.R. (2004). The odor coding system of Drosophila. *Trends Genet* 20, 453-459.
- Hallem, E.A., and Carlson, J.R. (2006). Coding of odors by a receptor repertoire. *Cell* 125, 143-160.
- Hines, M.L., and Carnevale, N.T. (1997). The NEURON simulation environment. *Neural Comput* 9, 1179-1209.
- Jeanne, J.M., and Wilson, R.I. (2015). Convergence, divergence, and reconvergence in a feedforward network improves neural speed and accuracy. *Neuron* 88, 1014-1026.
- Jefferis, G.S., Vyas, R.M., Berdnik, D., Ramaekers, A., Stocker, R.F., Tanaka, N.K., Ito, K., and Luo, L. (2004). Developmental origin of wiring specificity in the olfactory system of Drosophila. *Development* 131, 117-130.
- Katz, B., and Thesleff, S. (1957). On the factors which determine the amplitude of the miniature end-plate potential. *J Physiol* 137, 267-278.
- Kazama, H., and Wilson, R.I. (2008). Homeostatic matching and nonlinear amplification at genetically-identified central synapses. *Neuron* 58, 401-413.
- Kazama, H., and Wilson, R.I. (2009). Origins of correlated activity in an olfactory circuit. *Nat Neurosci* 12, 1136-1144.

- Kazama, H., Yaksi, E., and Wilson, R.I. (2011). Cell death triggers olfactory circuit plasticity via glial signaling in *Drosophila*. *J Neurosci* 31, 7619-7630.
- Kuno, M., Turkanis, S.A., and Weakly, J.N. (1971). Correlation between nerve terminal size and transmitter release at the neuromuscular junction of the frog. *J Physiol* 213, 545-556.
- Lai, S.L., Awasaki, T., Ito, K., and Lee, T. (2008). Clonal analysis of *Drosophila* antennal lobe neurons: diverse neuronal architectures in the lateral neuroblast lineage. *Development* 135, 2883-2893.
- Lee, W.C.A., Bonin, V., Reed, M., Graham, B.J., Hood, G., Glattfelder, K., and Reid, R.C. (2016). Anatomy and function of an excitatory network in the visual cortex. *Nature* 532, 370-374.
- Lichtman, J.W., Magrassi, L., and Purves, D. (1987). Visualization of neuromuscular junctions over periods of several months in living mice. *J Neurosci* 7, 1215-1222.
- Lin, S., Kao, C.F., Yu, H.H., Huang, Y., and Lee, T. (2012). Lineage analysis of *Drosophila* lateral antennal lobe neurons reveals notch-dependent binary temporal fate decisions. *PLoS Biol* 10, e1001425.
- Liu, W.W., and Wilson, R.I. (2013). Glutamate is an inhibitory neurotransmitter in the *Drosophila* olfactory system. *Proc Natl Acad Sci U S A* 110, 10294-10299.
- Lu, J., Tapia, J.C., White, O.L., and Lichtman, J.W. (2009). The interscutularis muscle connectome. *PLoS Biol* 7, e32.
- Matsuzaki, M., Ellis-Davies, G.C., Nemoto, T., Miyashita, Y., Iino, M., and Kasai, H. (2001). Dendritic spine geometry is critical for AMPA receptor expression in hippocampal CA1 pyramidal neurons. *Nat Neurosci* 4, 1086-1092.
- Meinertzhagen, I.A. (1996). Ultrastructure and quantification of synapses in the insect nervous system. *J Neurosci Methods* 69, 59-73.
- Mosca, T.J., and Luo, L. (2014). Synaptic organization of the *Drosophila* antennal lobe and its regulation by the Teneurins. *eLife* 3, e03726.
- Nagel, K.I., Hong, E.J., and Wilson, R.I. (2015). Synaptic and circuit mechanisms promoting broadband transmission of olfactory stimulus dynamics. *Nat Neurosci* 18, 56-65.

- Ng, M., Roorda, R.D., Lima, S.Q., Zemelman, B.V., Morcillo, P., and Miesenbock, G. (2002). Transmission of olfactory information between three populations of neurons in the antennal lobe of the fly. *Neuron* 36, 463-474.
- Nusser, Z., Lujan, R., Laube, G., Roberts, J.D., Molnar, E., and Somogyi, P. (1998). Cell type and pathway dependence of synaptic AMPA receptor number and variability in the hippocampus. *Neuron* 21, 545-559.
- Olsen, S.R., and Wilson, R.I. (2008). Lateral presynaptic inhibition mediates gain control in an olfactory circuit. *Nature* 452, 956-960.
- Patterson, G.H., and Lippincott-Schwartz, J. (2002). A photoactivatable GFP for selective photolabeling of proteins and cells. *Science* 297, 1873-1877.
- Pimentel, D.O., and Margrie, T.W. (2008). Glutamatergic transmission and plasticity between olfactory bulb mitral cells. *J Physiol* 586, 2107-2119.
- Prinz, A.A., Bucher, D., and Marder, E. (2004). Similar network activity from disparate circuit parameters. *Nat Neurosci* 7, 1345-1352.
- Python, F., and Stocker, R.F. (2002). Adult-like complexity of the larval antennal lobe of *D. melanogaster* despite markedly low numbers of odorant receptor neurons. *J Comp Neurol* 445, 374-387.
- Roffman, R.C., Norris, B.J., and Calabrese, R.L. (2012). Animal-to-animal variability of connection strength in the leech heartbeat central pattern generator. *J Neurophysiol* 107, 1681-1693.
- Root, C.M., Ko, K.I., Jafari, A., and Wang, J.W. (2011). Presynaptic facilitation by neuropeptide signaling mediates odor-driven food search. *Cell* 145, 133-144.
- Root, C.M., Masuyama, K., Green, D.S., Enell, L.E., Nassel, D.R., Lee, C.H., and Wang, J.W. (2008). A presynaptic gain control mechanism fine-tunes olfactory behavior. *Neuron* 59, 311-321.
- Rybak, J., Talarico, G., Ruiz, S., Arnold, C., Cantera, R., and Hansson, B.S. (2016). Synaptic circuitry of identified neurons in the antennal lobe of *Drosophila melanogaster*. *J Comp Neurol*, in press.

- Saalfeld, S., Cardona, A., Hartenstein, V., and Tomancak, P. (2009). CATMAID: collaborative annotation toolkit for massive amounts of image data. *Bioinformatics* 25, 1984-1986.
- Schneider-Mizell, C.M., Gerhard, S., Longair, M., Kazimiers, T., Li, F., Zwart, M.F., Champion, A., Midgley, F.M., Fetter, R.D., Saalfeld, S., and Cardona, A. (2016). Quantitative neuroanatomy for connectomics in *Drosophila*. *eLife* 5.
- Stocker, R.F., Lienhard, M.C., Borst, A., and Fischbach, K.F. (1990). Neuronal architecture of the antennal lobe in *Drosophila melanogaster*. *Cell Tissue Res* 262, 9-34.
- Su, C.Y., Menuz, K., and Carlson, J.R. (2009). Olfactory perception: receptors, cells, and circuits. *Cell* 139, 45-59.
- Takemura, S.Y., Xu, C.S., Lu, Z., Rivlin, P.K., Parag, T., Olbris, D.J., Plaza, S., Zhao, T., Katz, W.T., Umayam, L., *et al.* (2015). Synaptic circuits and their variations within different columns in the visual system of *Drosophila*. *Proc Natl Acad Sci U S A* 112, 13711-13716.
- Takumi, Y., Ramirez-Leon, V., Laake, P., Rinvik, E., and Ottersen, O.P. (1999). Different modes of expression of AMPA and NMDA receptors in hippocampal synapses. *Nat Neurosci* 2, 618-624.
- Tanaka, N.K., Awasaki, T., Shimada, T., and Ito, K. (2004). Integration of chemosensory pathways in the *Drosophila* second-order olfactory centers. *Curr Biol* 14, 449-457.
- Tanaka, N.K., Endo, K., and Ito, K. (2012). Organization of antennal lobe-associated neurons in adult *Drosophila melanogaster* brain. *J Comp Neurol* 520, 4067-4130.
- Tripodi, M., Evers, J.F., Mauss, A., Bate, M., and Landgraf, M. (2008). Structural homeostasis: compensatory adjustments of dendritic arbor geometry in response to variations of synaptic input. *PLoS Biol* 6, e260.
- Urban, N.N., and Sakmann, B. (2002). Reciprocal intraglomerular excitation and intra- and interglomerular lateral inhibition between mouse olfactory bulb mitral cells. *J Physiol* 542, 355-367.
- van Breugel, F., and Dickinson, M.H. (2014). Plume-tracking behavior of flying *Drosophila* emerges from a set of distinct sensory-motor reflexes. *Curr Biol* 24, 274-286.
- Vosshall, L.B., Wong, A.M., and Axel, R. (2000). An olfactory sensory map in the fly brain. *Cell* 102, 147-159.

- Wachowiak, M., and Shipley, M.T. (2006). Coding and synaptic processing of sensory information in the glomerular layer of the olfactory bulb. *Semin Cell Dev Biol* 17, 411-423.
- Walton, J. (1979). Lead aspartate, an en bloc contrast stain particularly useful for ultrastructural enzymology. *J Histochem Cytochem* 27, 1337-1342.
- Ward, S., Thomson, N., White, J.G., and Brenner, S. (1975). Electron microscopical reconstruction of the anterior sensory anatomy of the nematode *Caenorhabditis elegans*. *J Comp Neurol* 160, 313-337.
- Wilson, R.I. (2013). Early olfactory processing in *Drosophila*: mechanisms and principles. *Annu Rev Neurosci* 36, 217-241.
- Wilson, R.I., Turner, G.C., and Laurent, G. (2004). Transformation of olfactory representations in the *Drosophila* antennal lobe. *Science* 303, 366-370.
- Yaksi, E., and Wilson, R.I. (2010). Electrical coupling between olfactory glomeruli. *Neuron* 67, 1034-1047.
- Yu, H.H., Kao, C.F., He, Y., Ding, P., Kao, J.C., and Lee, T. (2010). A complete developmental sequence of a *Drosophila* neuronal lineage as revealed by twin-spot MARCM. *PLoS Biol* 8.

FIGURE LEGENDS

Figure 1. Cells and connections comprising the glomerular micro-circuit.

- (A) Electron micrograph of a frontal section ($76,000 \times 58,000$ pixels) from the anterior portion of the brain. Glomerulus DM6 is outlined.
- (B) Zoomed-in view of a synapse. Red arrowhead demarcates a presynaptic specialization (T-bar). The long edge of the image measures $2 \mu\text{m}$.
- (C) Schematic of reconstructed cells. All ORNs and PNs within glomerulus DM6 were fully reconstructed. Not shown in this schematic are multi-glomerular neurons (cells that interconnect different glomeruli), which were not fully reconstructed.

- (D) 3-D rendering of a single ORN→PN cell pair viewed frontally. The ORN axon (blue) makes multiple synapses (red) onto the PN dendrite (green). The approximate region occupied by the DM6 glomerulus is circled with dashed lines. The PN cell body is represented as a sphere for display purposes.
- (E) Top: synapses made by ORNs, expressed as a fraction of each ORN's total pool of output synapses. Bottom: synapses received by ORNs, expressed as a fraction of each ORN's total pool of input synapses. "MG" denotes multiglomerular neurons.
- (F) Synapses made by PNs and received by PNs, normalized in the same way.
- (G) Number of synapses between connected pairs of cells, sorted by connection type. Each symbol represents a unitary connection.

Figure 2. Connectivity compensates for a missing cell.

- (A) Skeletonized 3-D renderings of reconstructed PNs. Cells are viewed parasagittally from the left. For each cell, the total path length of all dendrite segments is indicated; note that PNs on the right side of the brain have longer path lengths. Axons are indicated with asterisks.
- (B) Synapses received by each PN from ORNs.
- (C) Synapses received by each PN from multi-glomerular (MG) neurons.
- (D) Output synapses made by each PN within the DM6 glomerulus.

Figure 3. Dendritic arbor size equalizes average unitary responses.

- (A) Volumetric 3-D rendering of an EM reconstructed PN dendrite. (The cell body is represented as a sphere for display purposes.) Compartmental models fit to ultrastructural and electrophysiological data were used to simulate the voltage responses of each PN to synaptic input from ORNs. Synaptic conductances were simulated in the PN dendrite, and voltage responses were recorded in either the cell body or in the dendritic compartment where a given synapse was located. Each of the 5 reconstructed PNs was modeled in this way.

(B) Example voltage responses recorded at the cell body of a model PN. A miniature EPSP (mEPSP) is the response to a quantum of neurotransmitter. A unitary EPSP (uEPSP) is the response to one spike in a single presynaptic axon, i.e. the combined effect of all the mEPSPs generated by that axon. Shown here are the largest and smallest mEPSPs and uEPSPs in this PN. In the model, a spike always produces the same conductance at all synapses, and so variations in mEPSP amplitude must be due to variations in the position of synapses on the dendrite.

(C) There is no left-right difference in the amplitude of uEPSPs, measured at the cell body of each PN. (mean \pm SEM computed across unitary ORN \rightarrow PN connections, $P > 0.7$, permutation test, $n = 156$ left and 104 right unitary connections). Here and elsewhere, box plots show median, 25th percentile and 75th percentile.

Whiskers indicate 2.7 SDs (99.3% coverage of normally distributed data); for clarity, outliers beyond the whiskers are not displayed; notches indicate 95% confidence intervals.

(D) There is a significant left-right difference in the amplitude of mEPSPs, measured at the cell body of the PN (mean \pm SEM computed across all ORN \rightarrow PN synapses, $P < 0.0001$, permutation test, $n = 3013$ left and 3066 right synapses).

(E) There is a significant left-right difference in the amplitude of mEPSPs, measured at the site of each synapse in the dendrite (mean \pm SEM computed across all ORN \rightarrow PN synapses, $P < 0.0001$, permutation test).

(F) There is a significant left-right difference in dendritic input resistance, measured across all model compartments (mean \pm SEM computed across all PN compartments, $P < 0.0001$, permutation test, $n = 5520$ left and 6048 right compartments).

(G) There is a significant left-right difference in the attenuation of mEPSPs as they travel from the site of the synapse to the soma (ratio of somatic to dendritic amplitude, mean \pm SEM computed across all ORN \rightarrow PN synapses, $P < 0.0001$, permutation test).

Figure 4. A basis for odor lateralization behavior in ORN wiring.

- (A) Flies turn toward lateralized odor stimuli, a behavioral response termed osmotropotaxis.
- (B) Schematic of an ORN axon projecting bilaterally. Note that ipsi and contra are defined relative to the location of the ORN cell body. Unitary EPSPs in PNs driven by ipsilateral ORNs are systematically larger than those driven by contralateral ORNs (Gaudry et al., 2013). Successful odor lateralization requires that ipsi- and contralateral synapses are systematically different.
- (C) PNs receive significantly more synapses from ipsilateral ORNs than from contralateral ORNs. Each connected pair of points represents a PN ($P = 0.0032$, paired-sample t-test, $n = 5$ PNs). These 5 PNs collectively have 133 ipsi and 132 contra connections.
- (D) There is a significant ipsi-contra difference in mean modeled uEPSP amplitudes. Each connected pair of points represents a PN, with values averaged across all the connections received by that PN ($P = 0.0059$, paired-sample t-test, $n = 5$ PNs).
- (E) There is no ipsi-contra difference in modeled mEPSP amplitudes. Each connected pair of points represents a PN, with values averaged over all the synapses received by that PN ($P > 0.05$, paired-sample t-test, $n = 5$ PNs). These 5 PNs collectively have 3504 ipsi and 2575 contra synapses).

Figure 5. Wiring inequalities among sister ORNs.

- (A) Schematic of ORNs connected to a PN with different numbers of synapses. Arrow size represents the number of synapses each ORN forms on an ipsilateral PN dendrite.
- (B-G) Histograms showing variation among ipsilateral ORN→PN connections. The histograms are horizontally scaled so that the means of all distributions are aligned, in order to enable a visual comparison of CVs.
- (B) Number of synapses that each ipsilateral ORN makes onto left PN1.
- (C) Analogous to (B) but pooled across all PNs. To enable pooling, we first normalize the number of synapses made by each ipsilateral ORN to the total number of ipsilateral ORN input synapses a PN receives. This yields the percentage contribution of each ORN to the ipsilateral synapse pool. The mean of this value is relatively

consistent across the five PNs (0.037, 0.037, 0.037, 0.039, and 0.039), but there is a large variation within each PN.

(D) Mean mEPSP amplitude for connections made by ipsilateral ORNs onto left PN1. At each unitary connection, the mean mEPSP amplitude is computed across all the synapses that contribute to that connection. This value is relatively consistent across unitary connections.

(E) Analogous to (D) but pooled across all PNs. Each mEPSP value is normalized to the grand average for that PN. This value is consistent across all unitary connections, both within and across PNs.

(F) Summation efficacy at connections made by ipsilateral ORNs onto left PN1. Summation efficacy is computed as the amplitude of the connection's uEPSP, divided by the linearly summed amplitudes of all the mEPSPs that comprise the connection. Again, this value is relatively consistent across unitary connections.

(G) Same as (F) but pooled across all PNs.

(H) Correlation between synapse number per connection and uEPSP amplitude. Each data point is a unitary connection ($n = 260$), with ipsilateral (unfilled) and contralateral (filled) connections indicated. For each PN, there is a strong and significant correlation (Pearson's r ranges from 0.993 to 0.999; P ranges from 9.78×10^{-48} to 1.34×10^{-65} after Bonferroni-Holm correction for multiple comparisons, $m = 5$ tests).

Figure 6: Correlated and independent variation in ORN wiring.

(A) Schematics illustrating alternative scenarios: ORN connection weights may be correlated across PNs or uncorrelated. Arrowhead size represents the strength of ORN→PN connections. ORN spikes faithfully invade both ipsi- and contralateral axonal arbors, and so if connection weights are optimized to reflect the spiking properties of each ORN, then connection weights should be correlated across all ipsi- and contralateral PNs.

(B) Contributions of individual ORNs to each PN's pool of ORN synapses. Values are expressed as the percentage contribution of each ORN to the pool of synapses from that antenna. Within each of these 10 vectors, values sum to 100%. Within an antenna, ORNs are sorted according to the average strength of all the

connections that they form onto left PNs. Note that left PNs are correlated with each other, but not with right PNs.

(C) Same data as in (B), but now sorted by average strength of connections onto right PNs rather than left PNs. Note that right PNs are correlated with each other, but not with left PNs. When we examined pairs of PNs in the same quadrant, we found that 7 of 8 PN pairs were significantly correlated with each other (Pearson's r ranges from 0.44 to 0.78, $P < 0.05$, $n = 27$ or 26 unitary connections for each PN for each test, P values are corrected for multiple comparisons, $m = 8$ tests). The one exception was that left PN2 and left PN3 were not significantly correlated (Pearson's $r = 0.36$, $P = 0.07$ after multiple comparisons correction). When we tested pairs PNs on opposite sides of the midline (again testing separately for correlations among right ORNs and left ORNs), we found that none of the 12 PN pairs were significantly correlated (Pearson's r ranges from -0.21 to 0.34, P always > 0.09 , $n = 27$ or 26 unitary connections for each PN for each test; tests were not corrected for multiple comparisons, as none were significant).

(D) Average contribution of each ORN to the PNs on the right side, plotted against the average contribution of the same ORN to the PNs on the left. Percentages are calculated as in (B) before averaging across all the PNs on the same side of the brain. There is no significant correlation (Pearson's $r = 0.18$, $P = 0.20$, $n = 53$ unitary connections for each PN).

Figure 7: Functional consequences of variability in ORN wiring.

(A) Schematic of total spike count discrimination task. We measured how accurately a binary linear classifier could detect a small increase in ORN spike number, based on the time-averaged voltage in model PNs. Simulated Poisson spike trains were assigned to reconstructed ORN axons and fed into our PN models. Only ORNs ipsilateral to the PN were simulated. Over a 200-ms period, ORNs fired either 12 spikes (the average number of spikes during this time period that DM6 ORNs fire in the absence of an odor), or 13 spikes (representing a minimal odor stimulus). Based on the distribution of the time-averaged PN voltage (μ) in training trials, we classified each test trial as "non-odor" or "odor" (12 or 13 spikes). We repeated this many

times for each of the 5 model PNs. The same procedure was used to measure discrimination accuracy when the “odor” elicited increasing numbers of spikes (14 to 20 spikes).

(B) Performance of the classifier as a function of the number of “odor-evoked” spikes, above the baseline level of 12 spikes. Each blue line represents a different model PN. As in all previous simulations, the PN dendrite morphology and the locations of all ORN synapses are taken directly from our reconstructions. Green lines show that performance increases after we equalize the number of synapses per connection (by randomly reassigning synapses to ORN axons, so that all axons now have essentially equal numbers of synapses).

(C) Schematic of left-right spike count discrimination task. Here we simulated “non-odor” activity (12 spikes) in one antenna and “odor” activity (13-20 spikes) in the other antenna. Classification was based on the difference between the average of the mean PN voltage values on the left, minus the average on the right (mean (μ_{left}) – mean (μ_{right})).

(D) Performance of the classifier as a function of the number of “odor-evoked” spikes (the left-right asymmetry). The two blue lines represent an odor stimulus in either the right antenna or the left antenna. Green lines show that performance increases after we equalize the number of synapses per connection.

LEGENDS FOR SUPPLEMENTAL MOVIES

Movie S1. EM Volume of the anterior fly brain.

The movie shows a fly-through of the aligned EM series. Please see Data Availability for directions to the publicly accessible high-resolution aligned dataset.

Movie S2. Serial EM sections through left glomerulus DM6.

The video shows a fly-through of a cropped ($16.4 \mu\text{m} \times 16.4 \mu\text{m}$) volume traversing 329 of the aligned EM sections containing glomerulus DM6 neuropil in the left hemisphere of the brain.

Figure 1

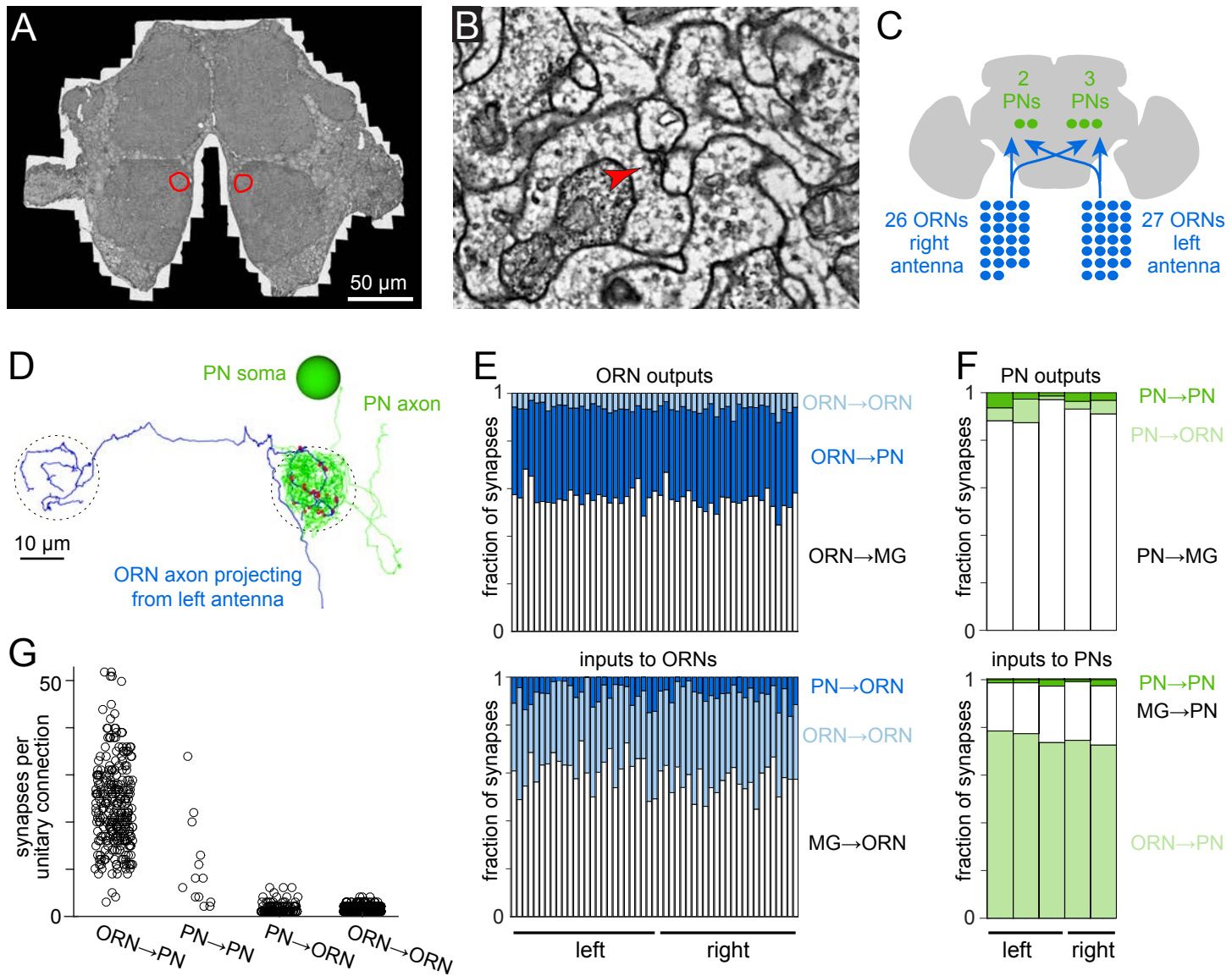


Figure 2

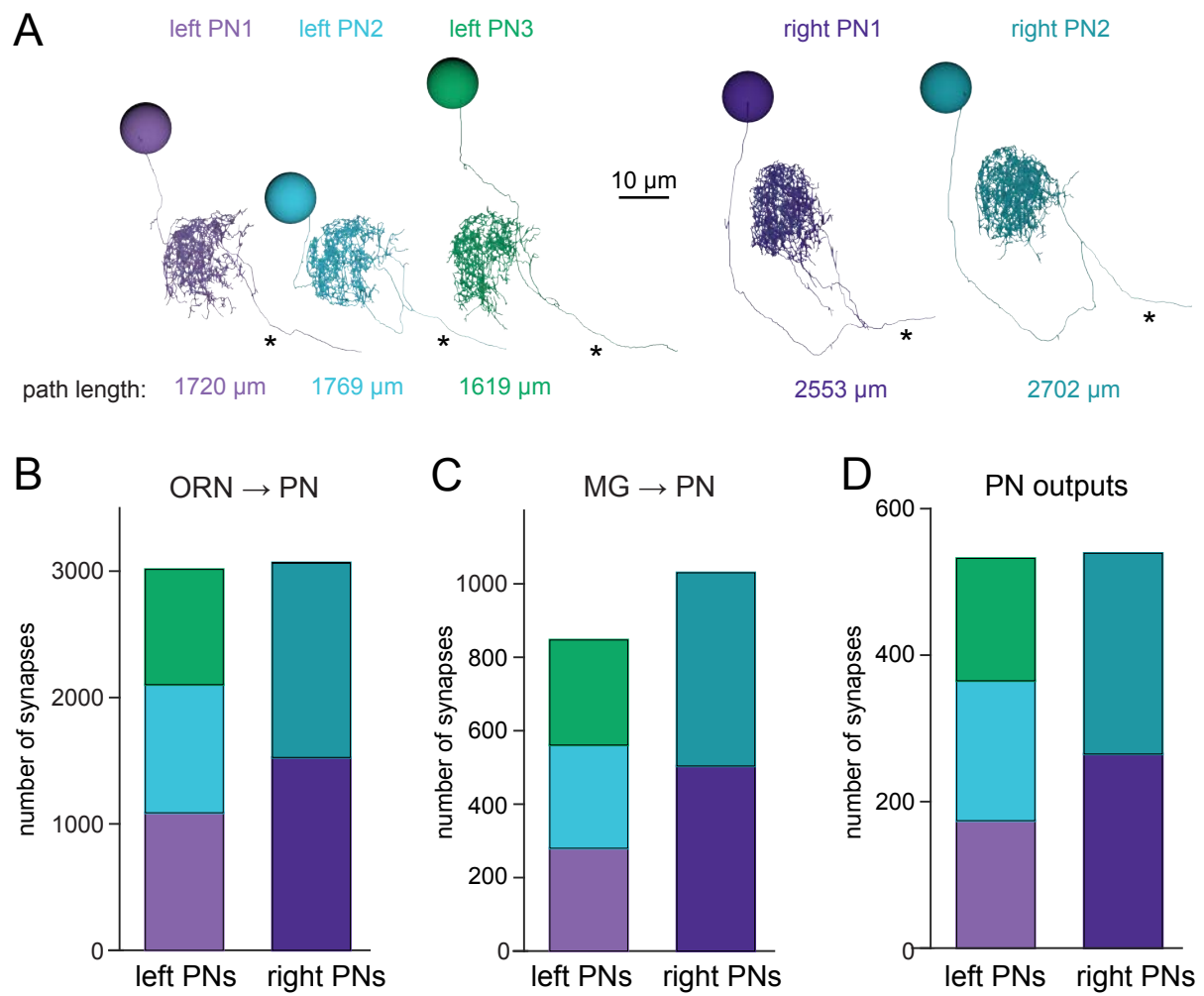


Figure 3

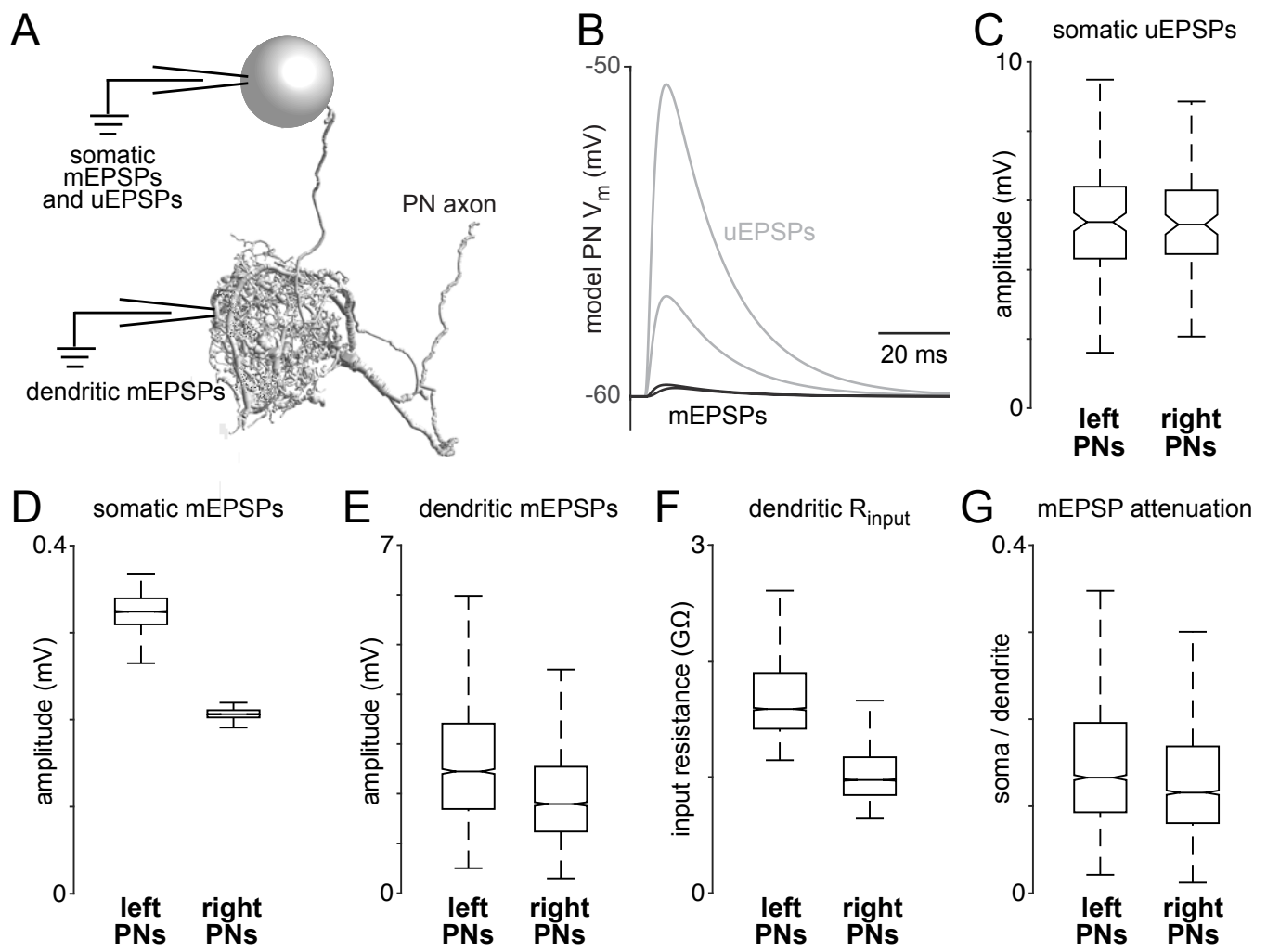


Figure 4

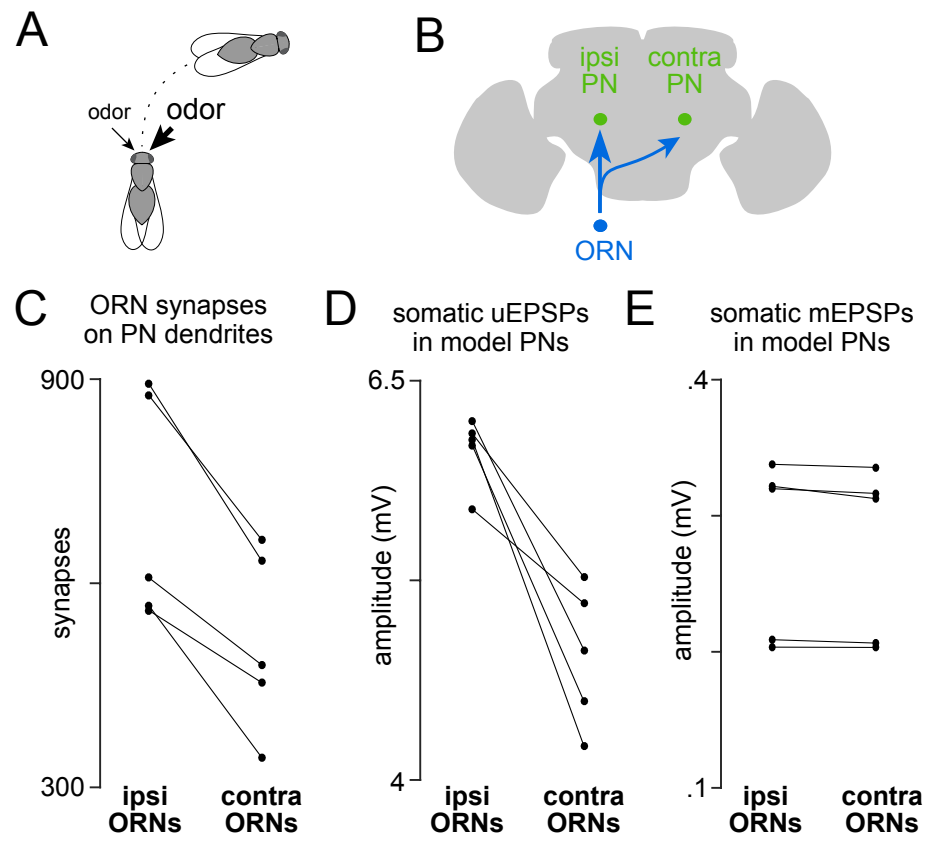


Figure 5

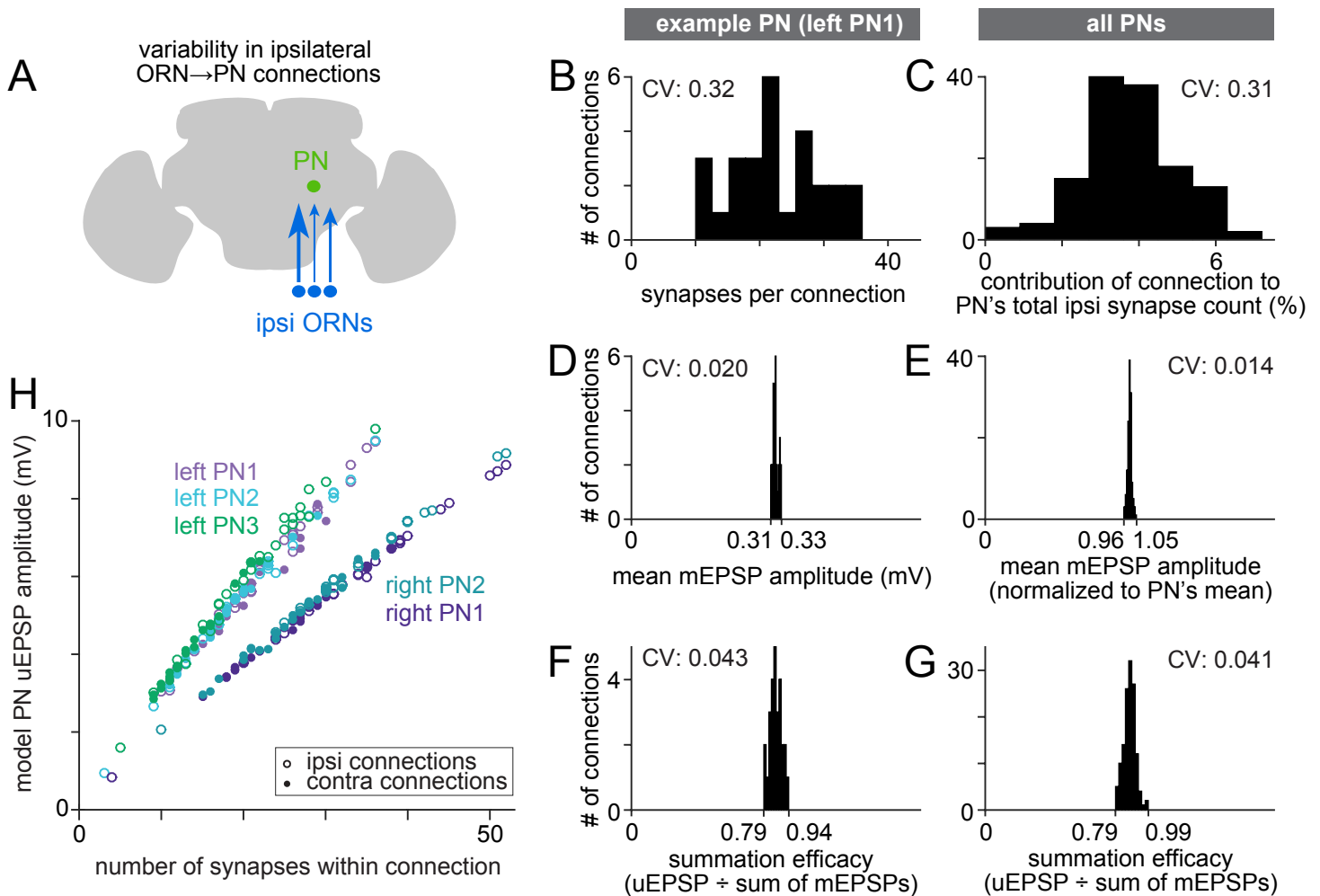


Figure 6

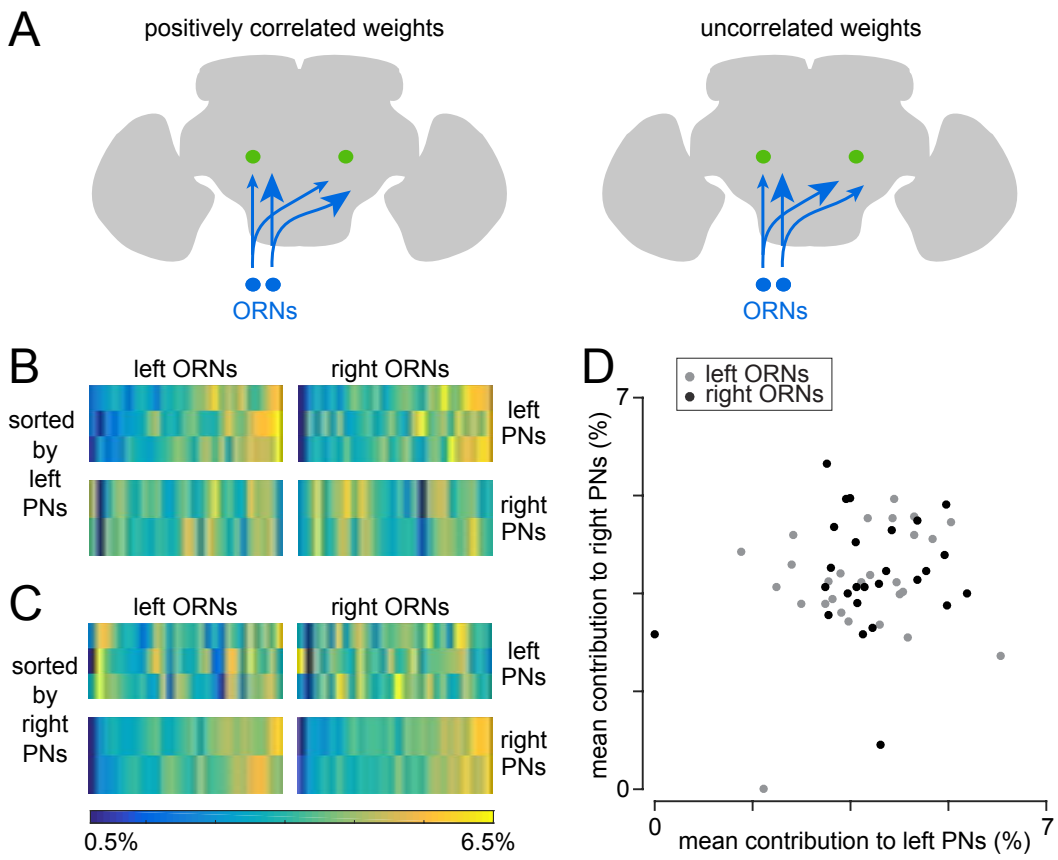


Figure 7

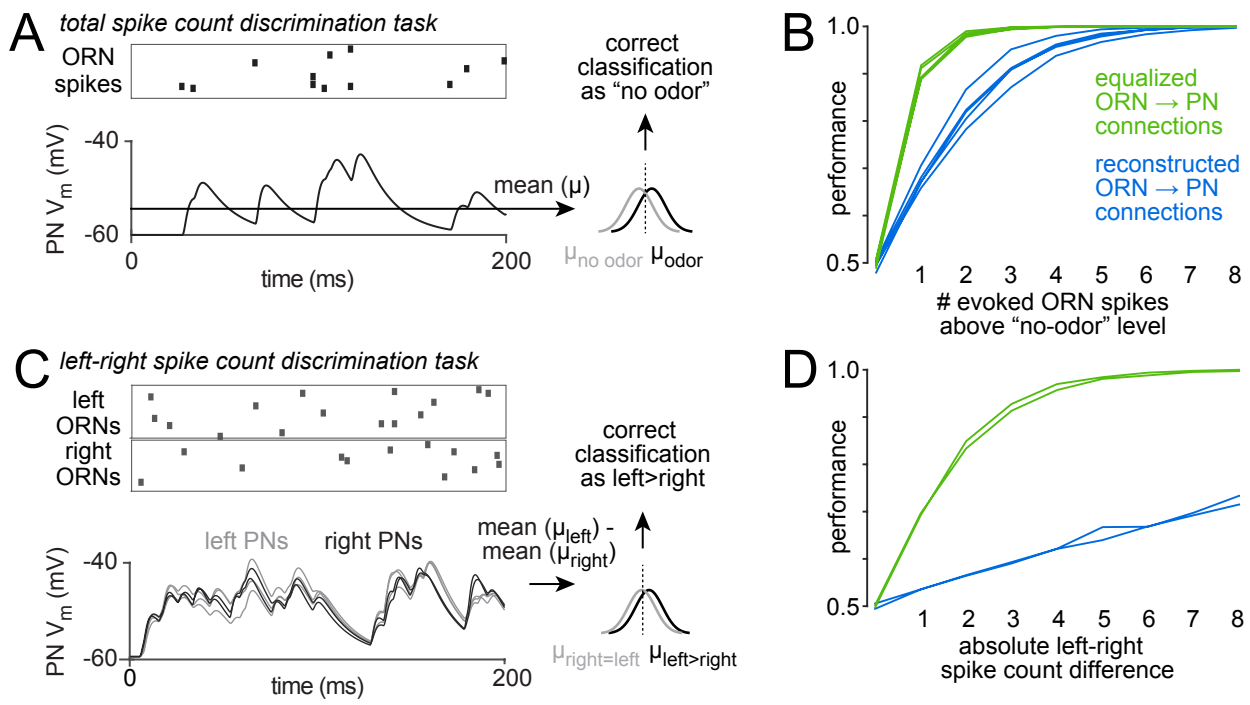
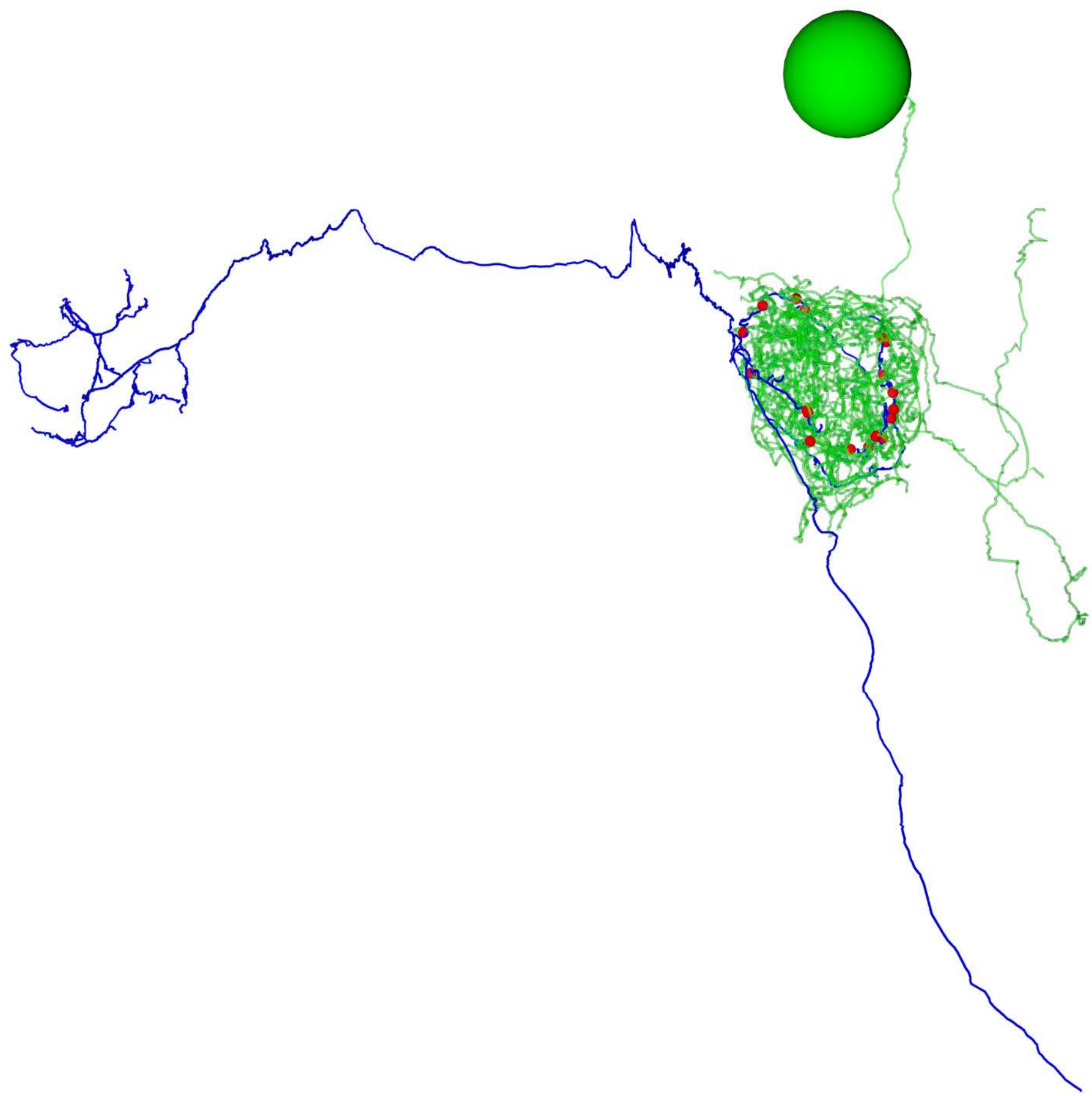
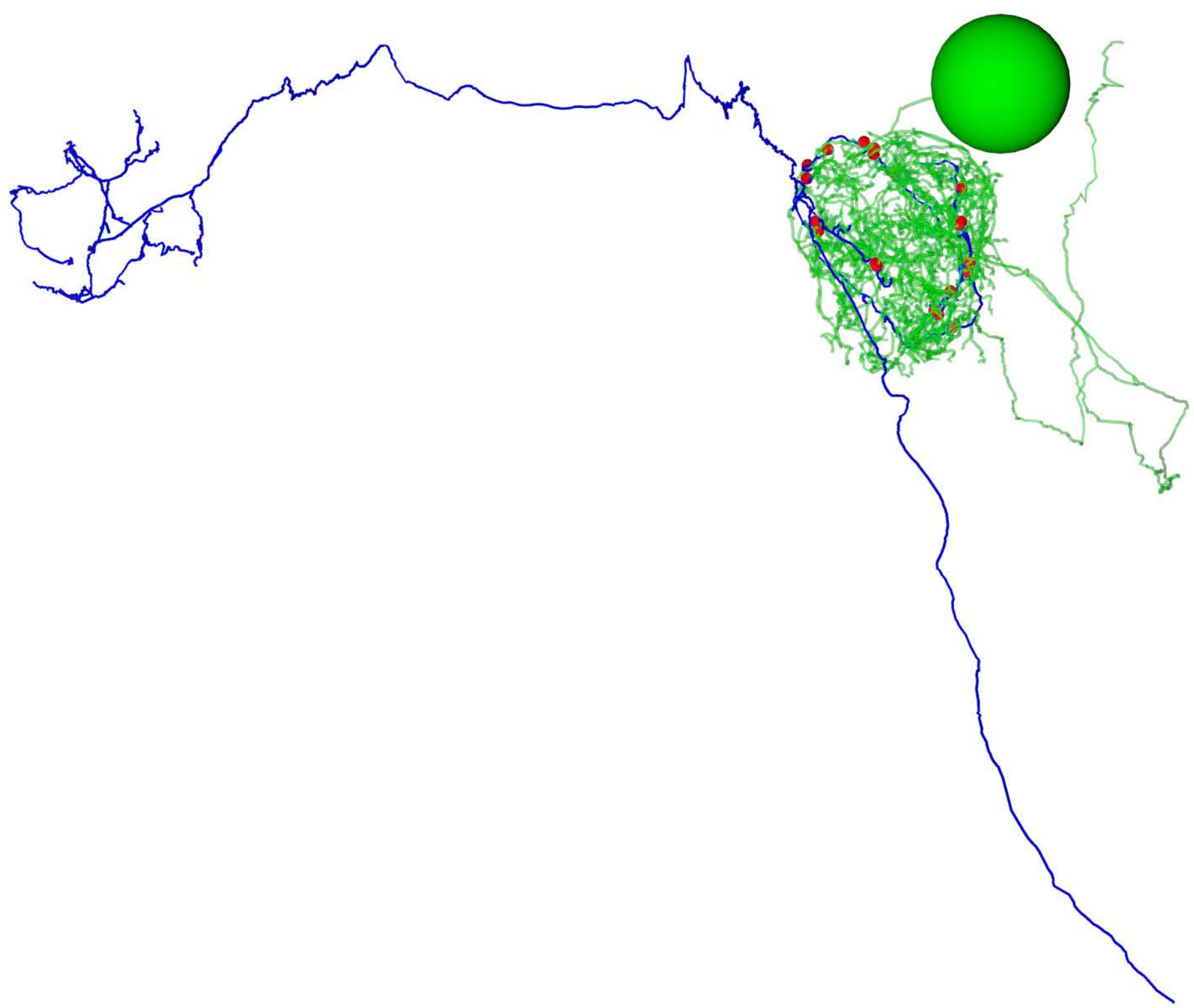
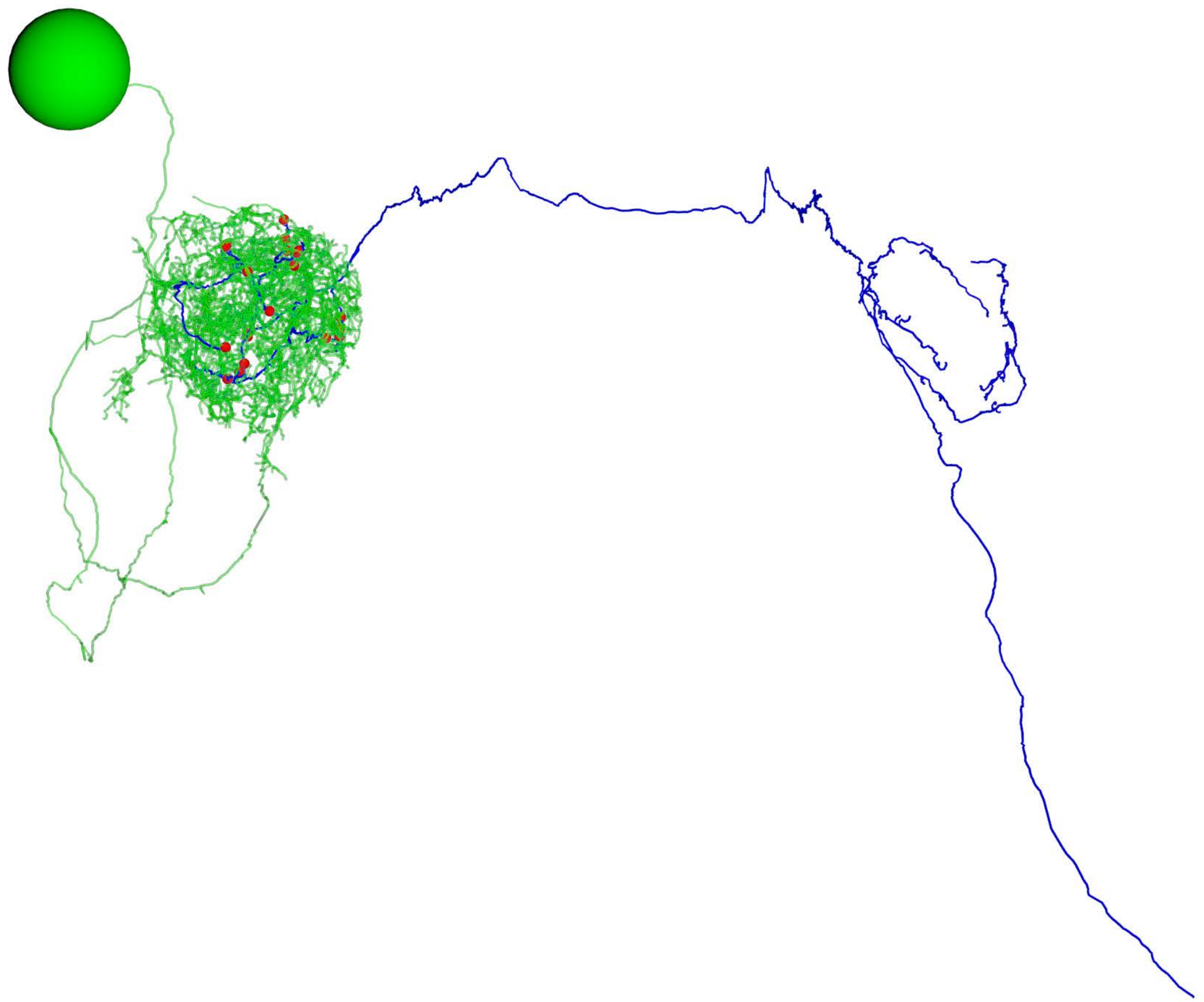


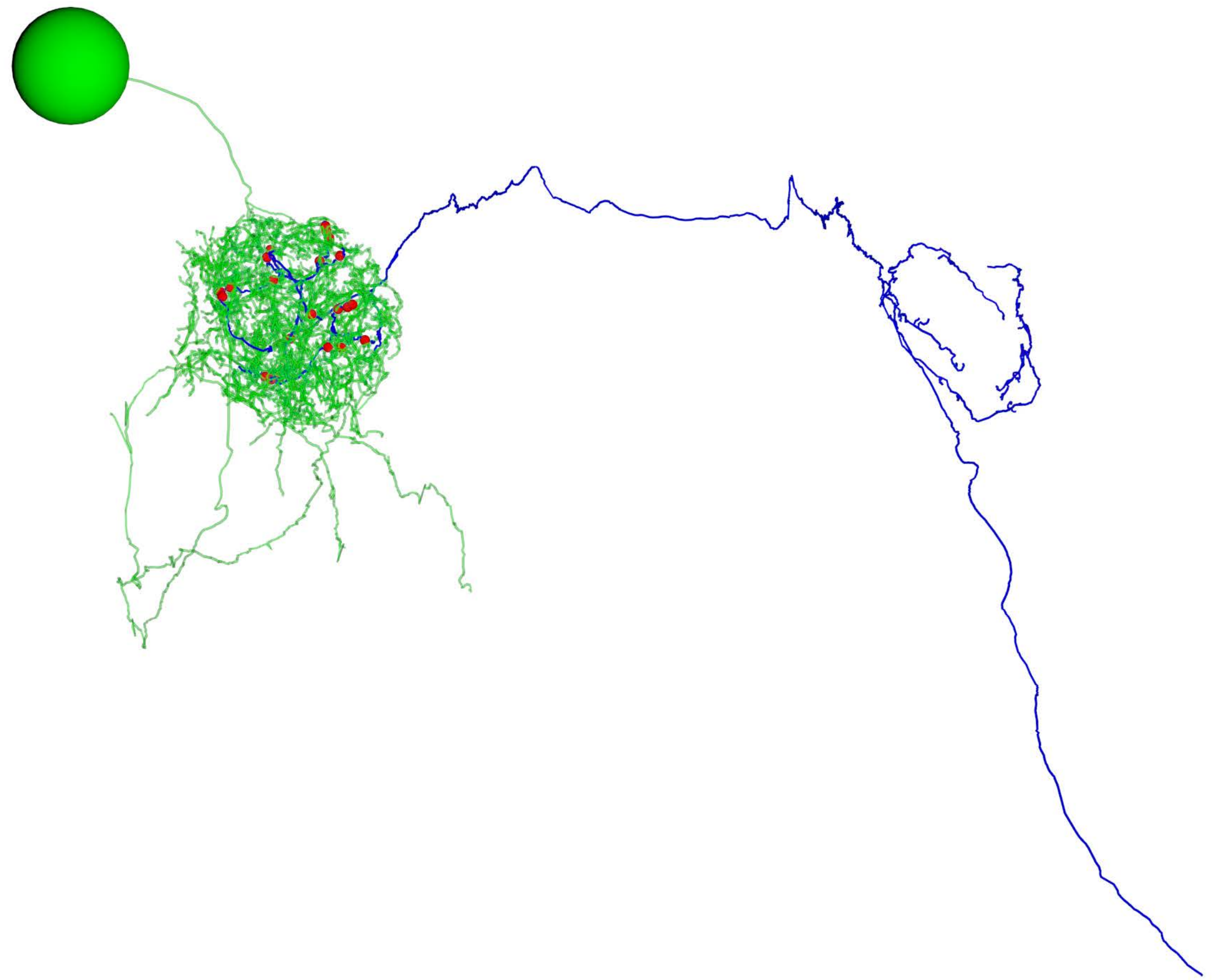
Figure S1. Gallery of anatomical renderings: Connected DM6 ORN and PN pairs.

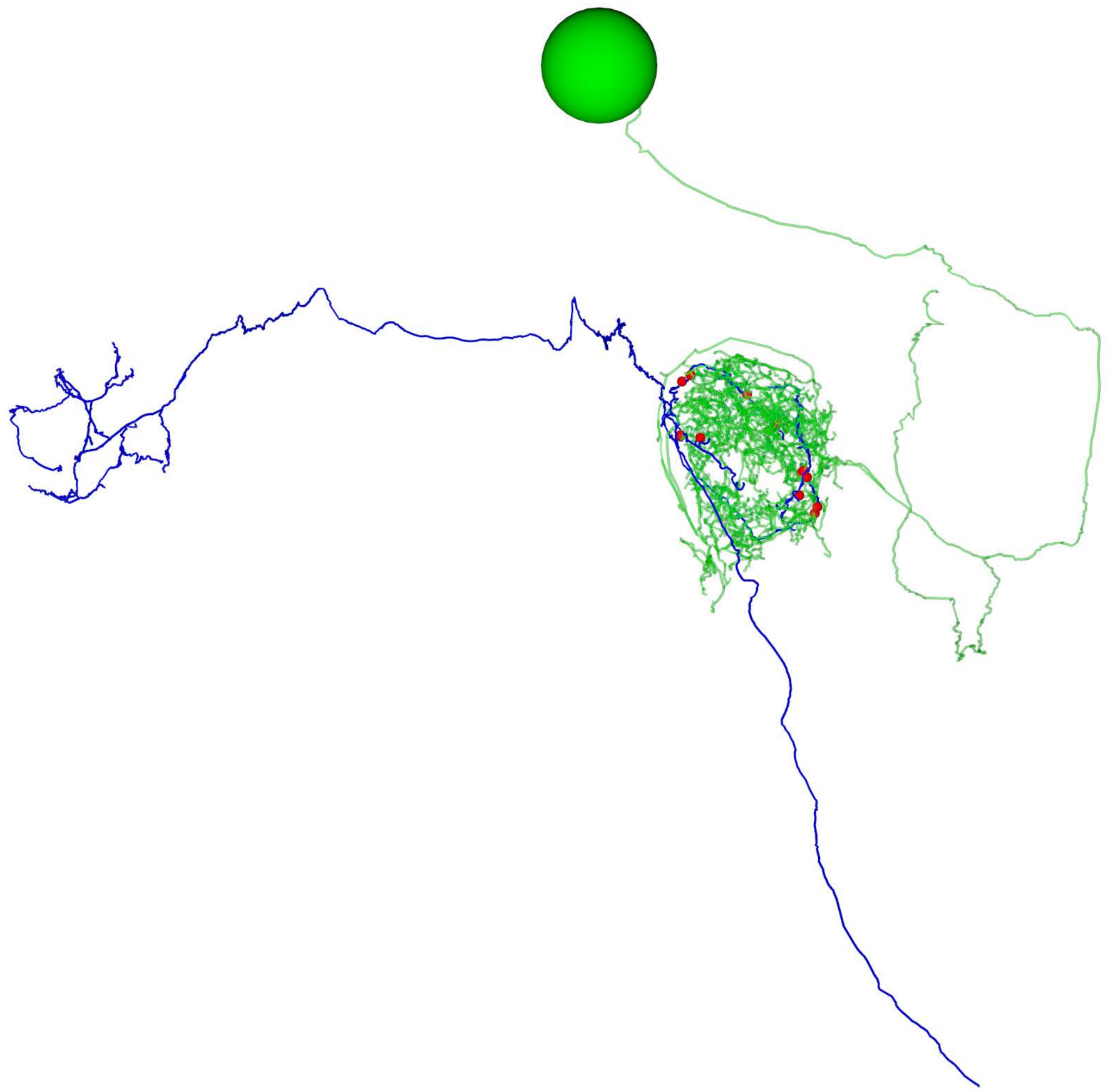
Cell bodies, axons, dendrites and synapses colored, as in Figure 1D. Large balls represent cell bodies (9 μm in diameter) and small red balls represent ORN output synapses. The axonal projection of the PN is omitted.

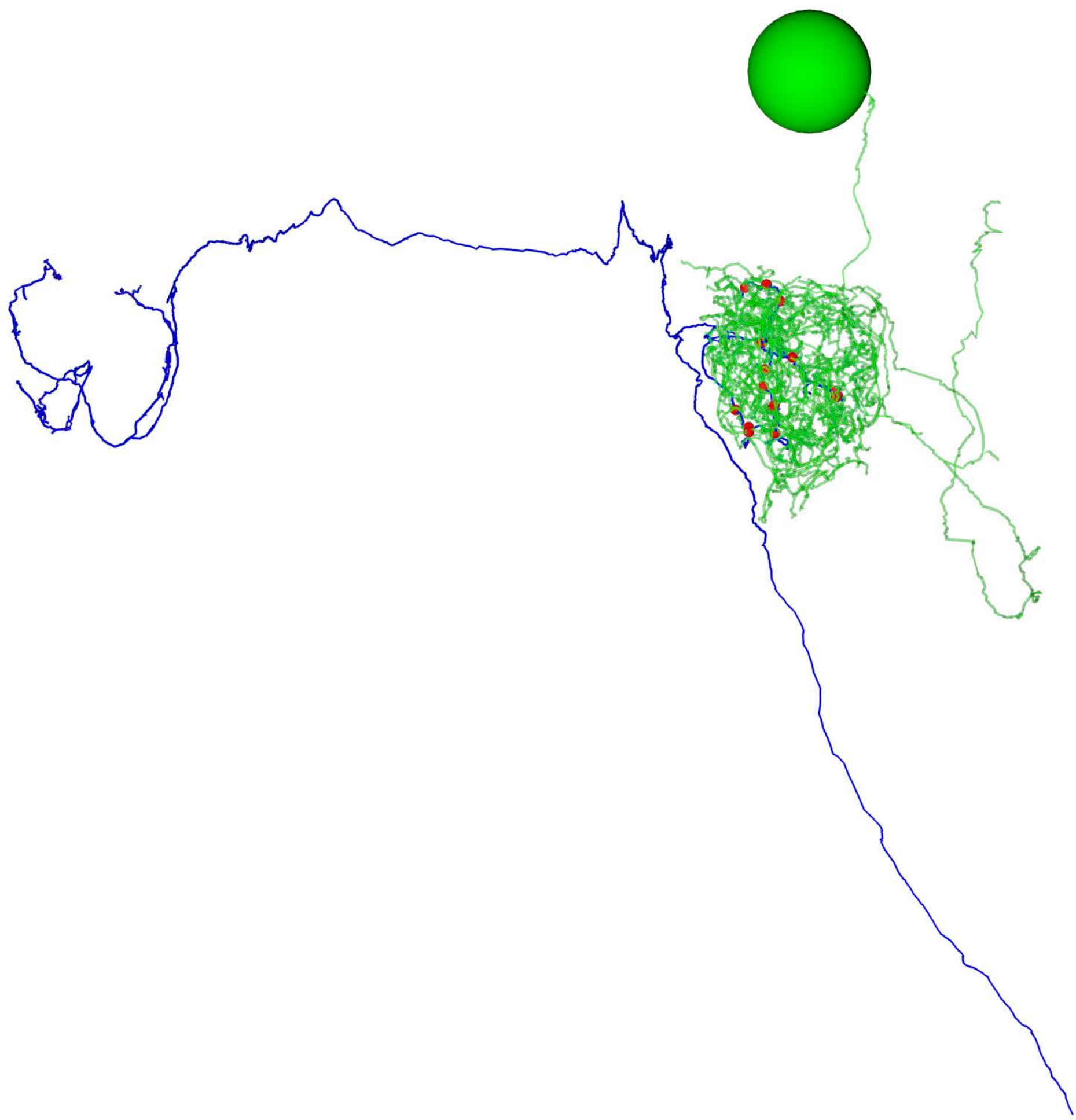


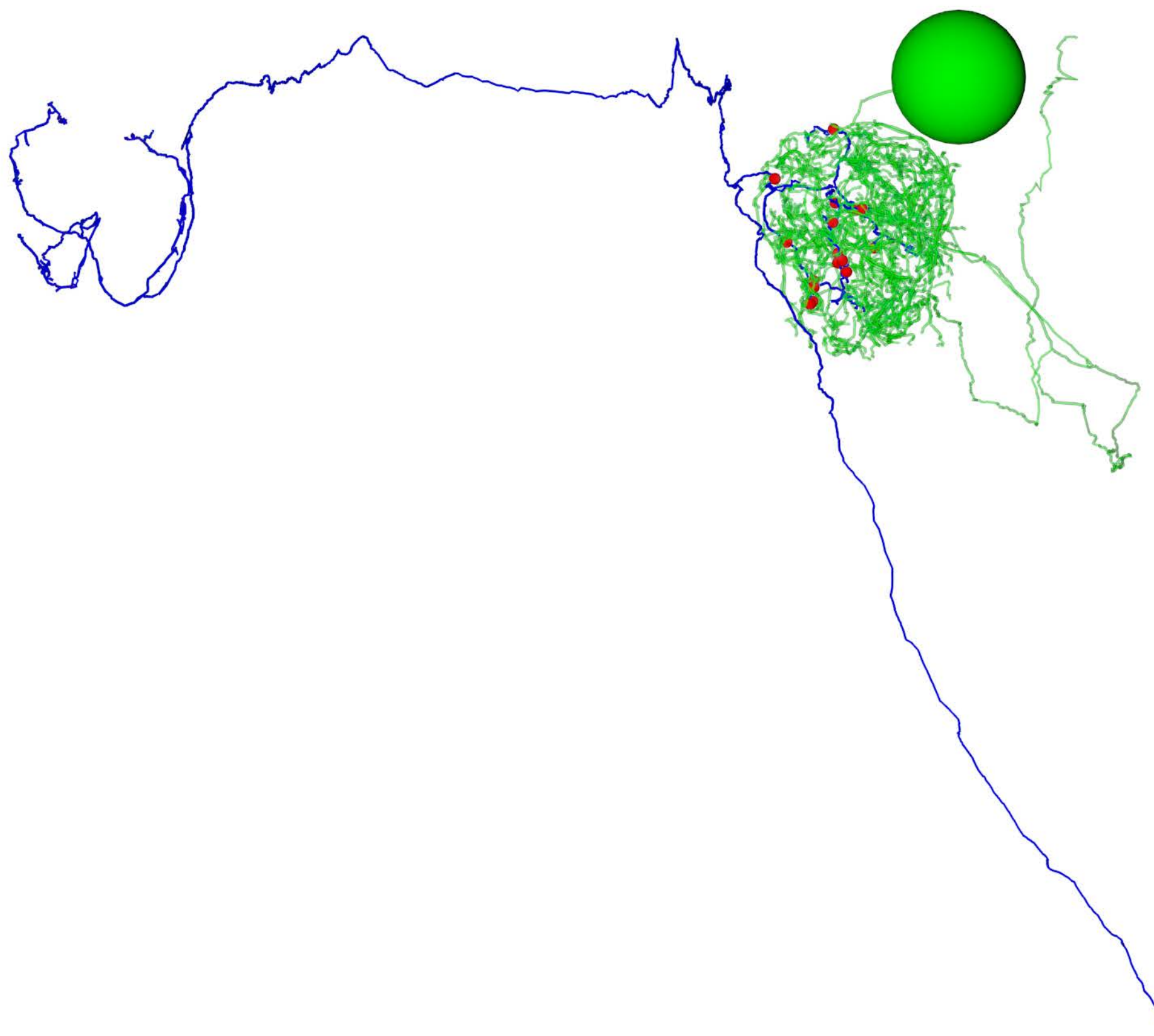


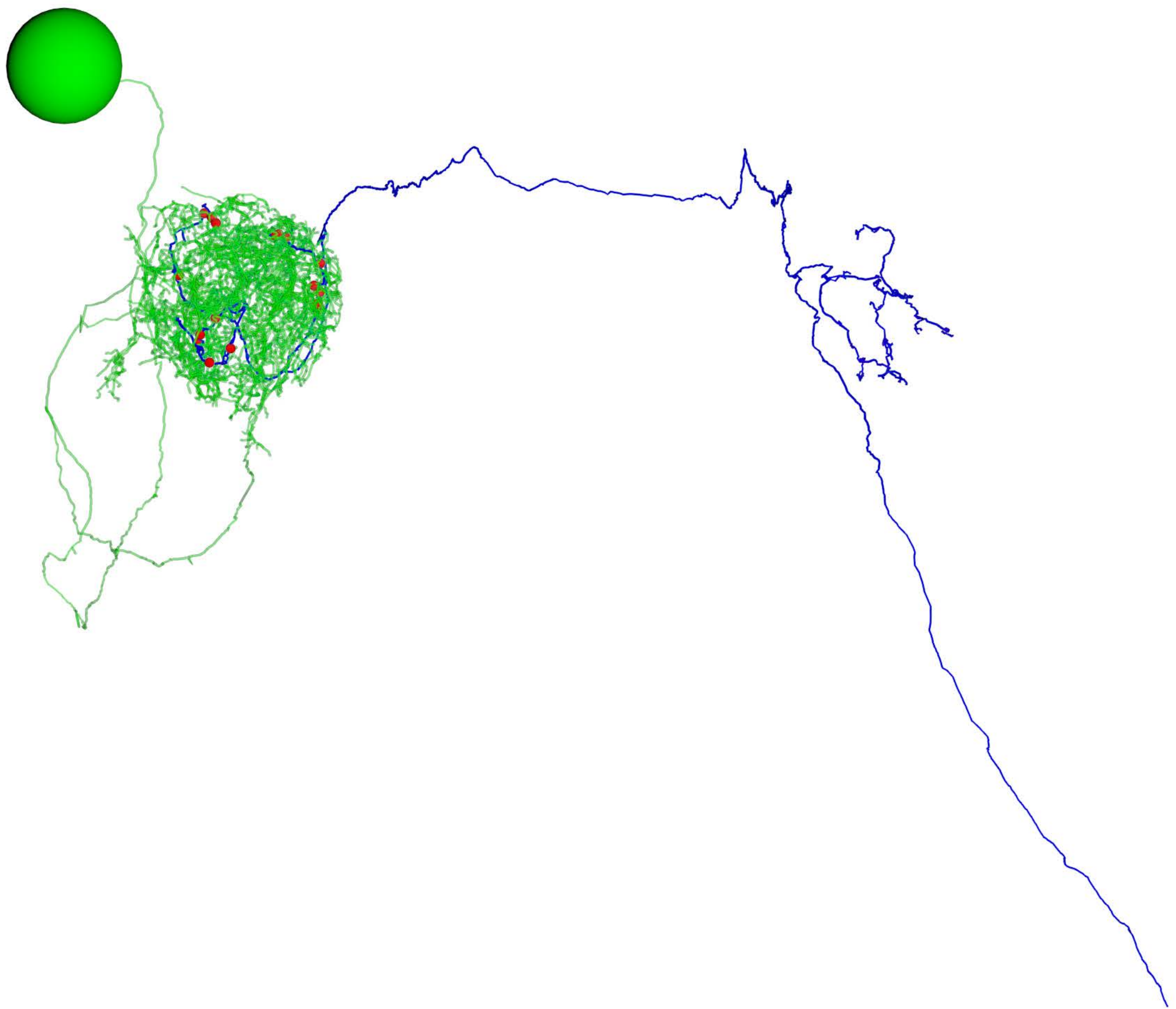


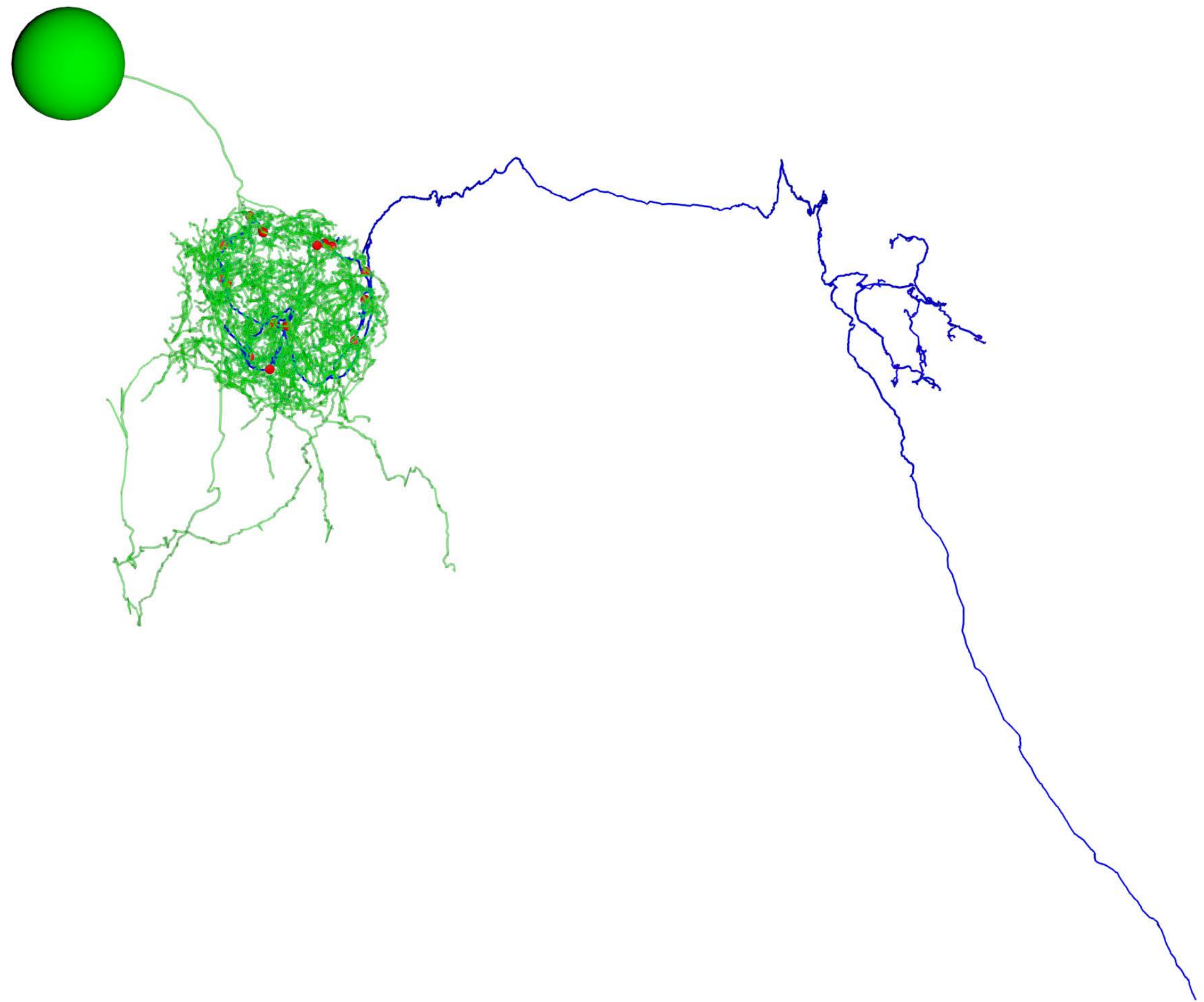


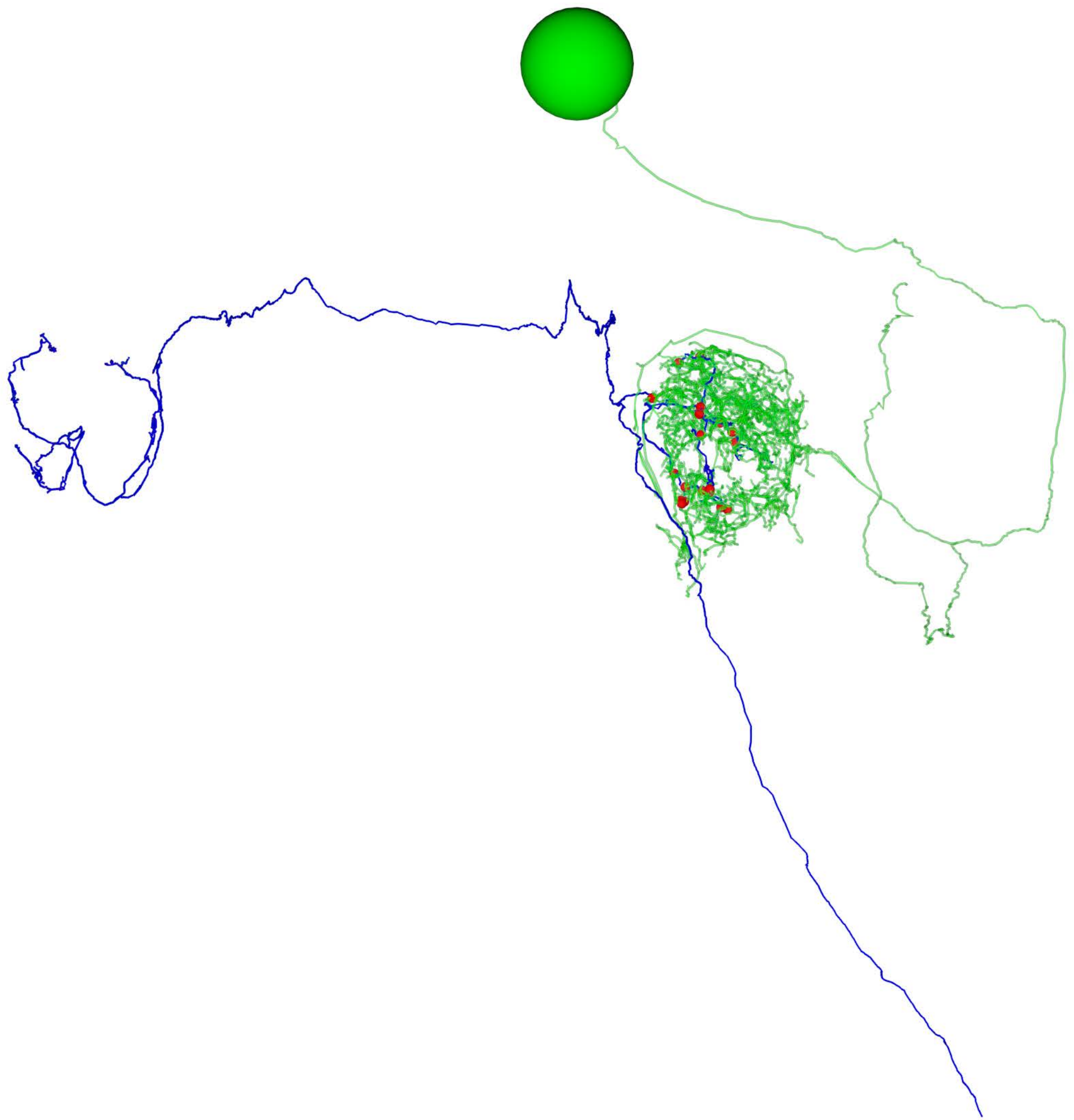


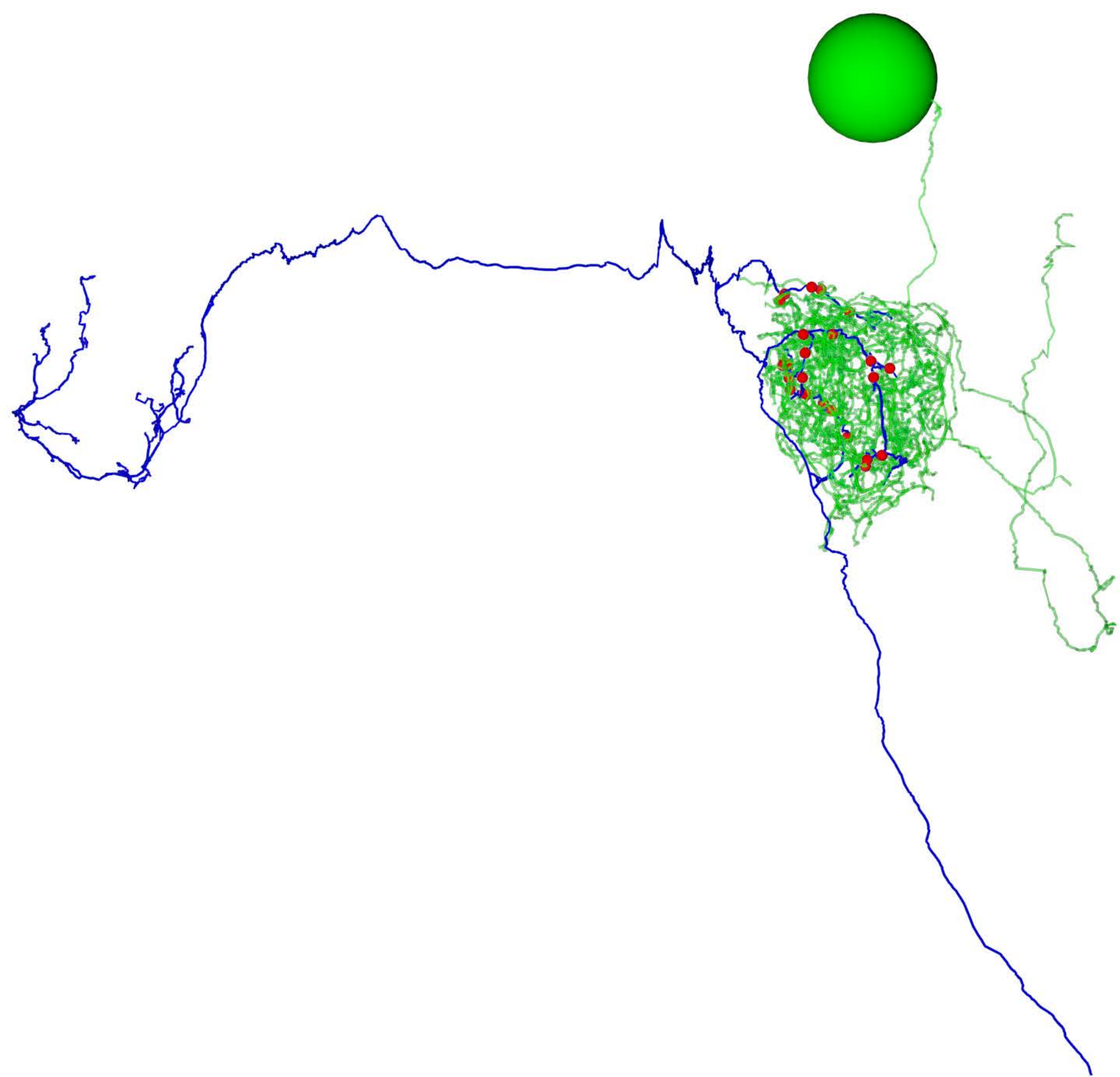


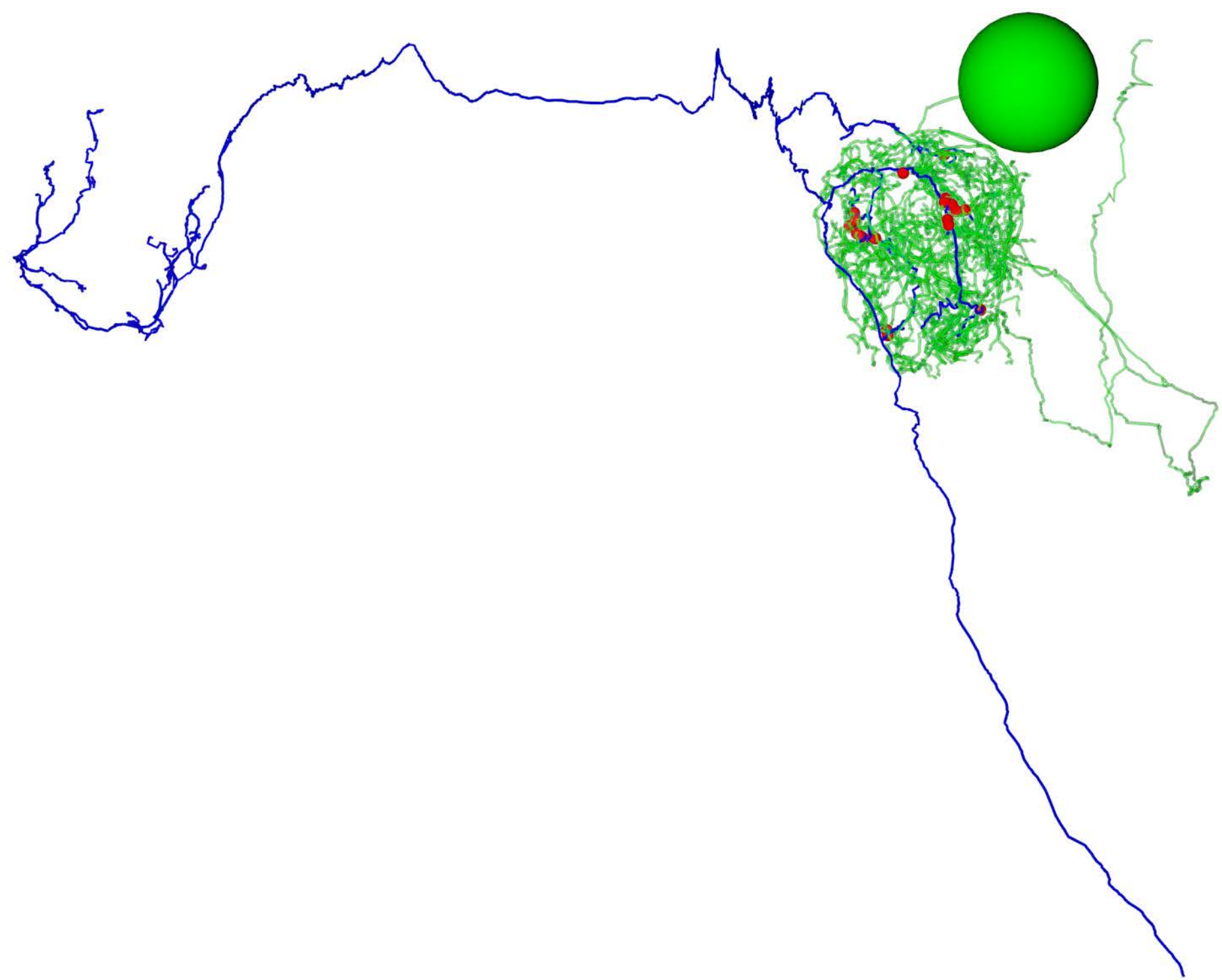


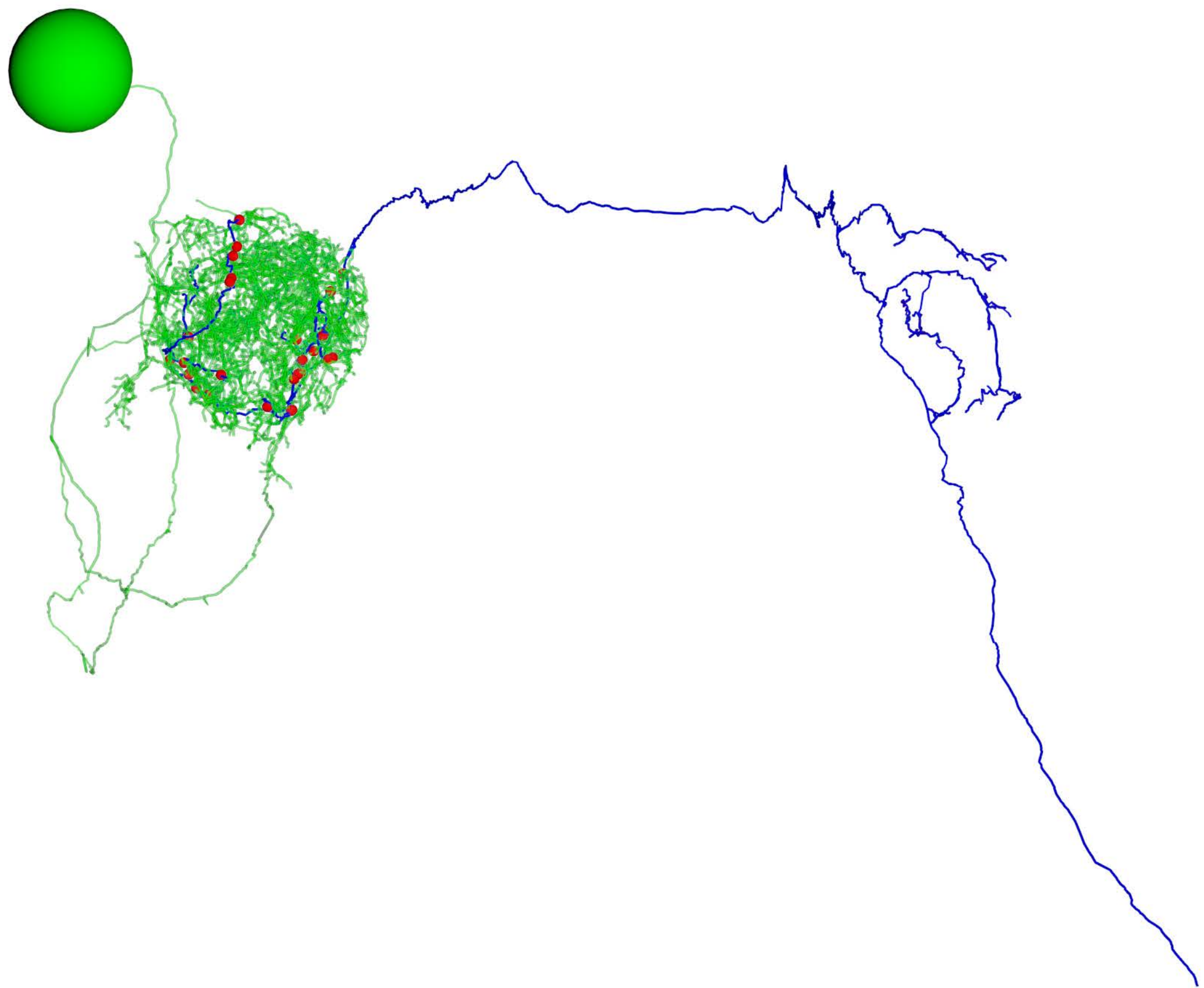


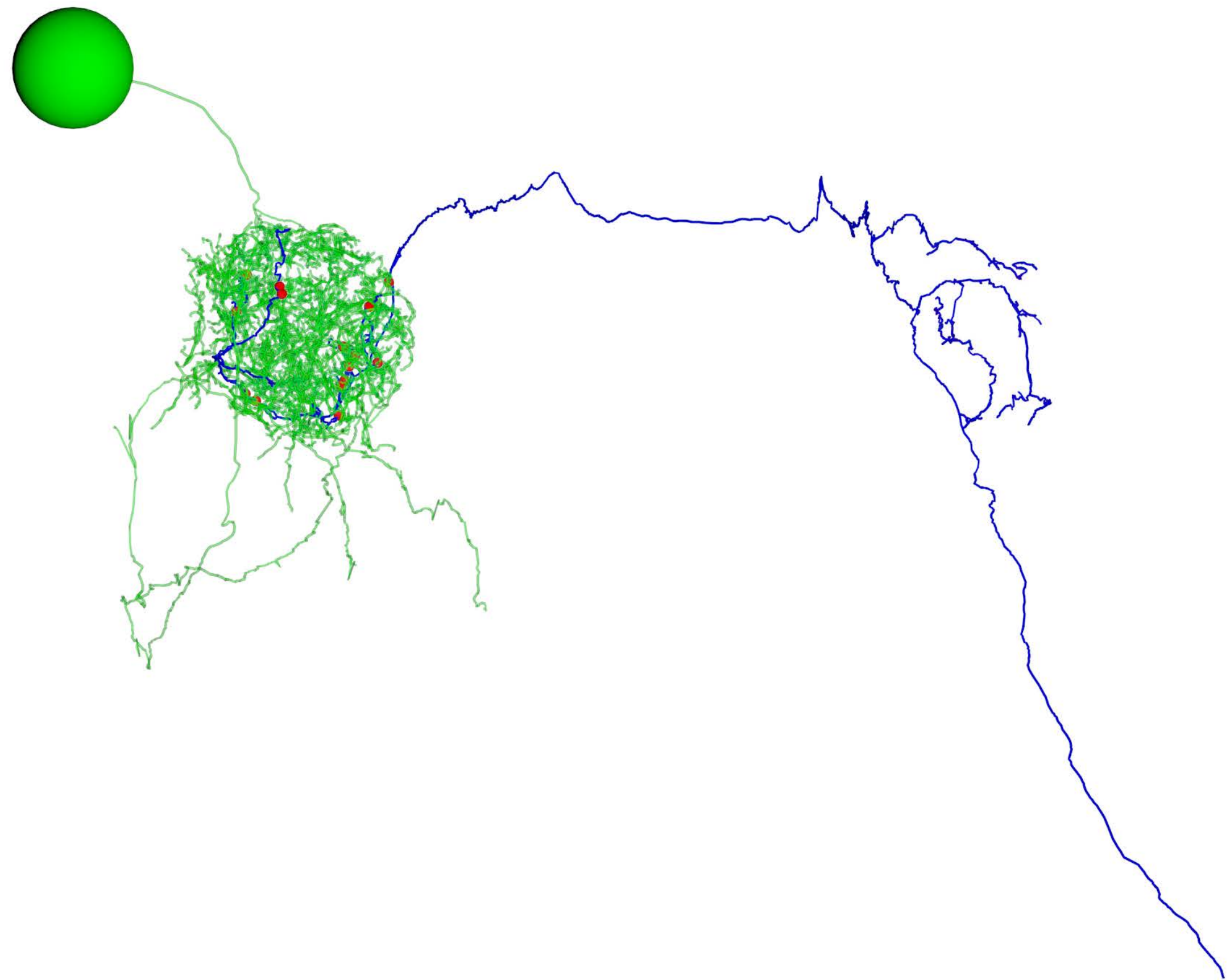


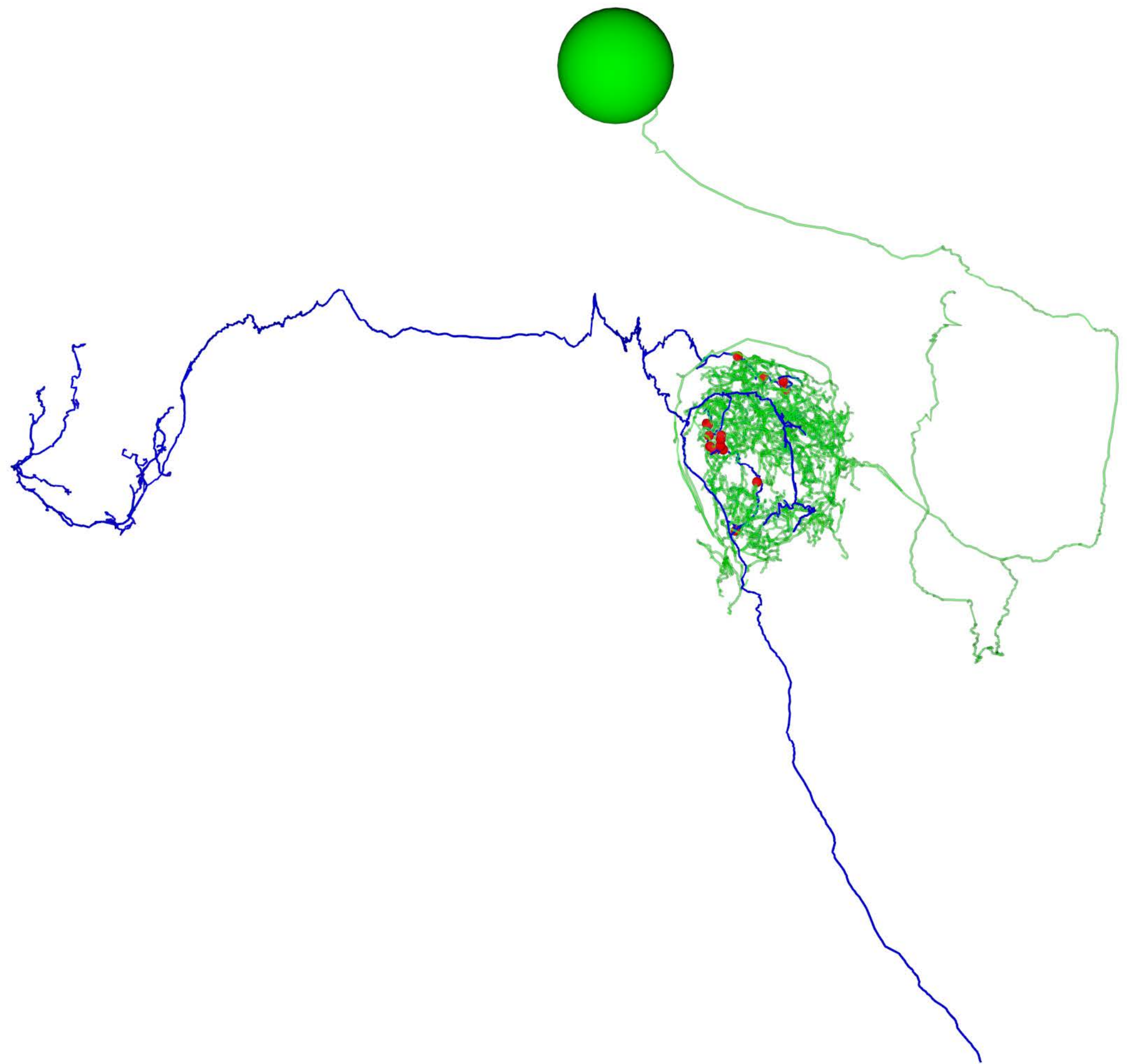


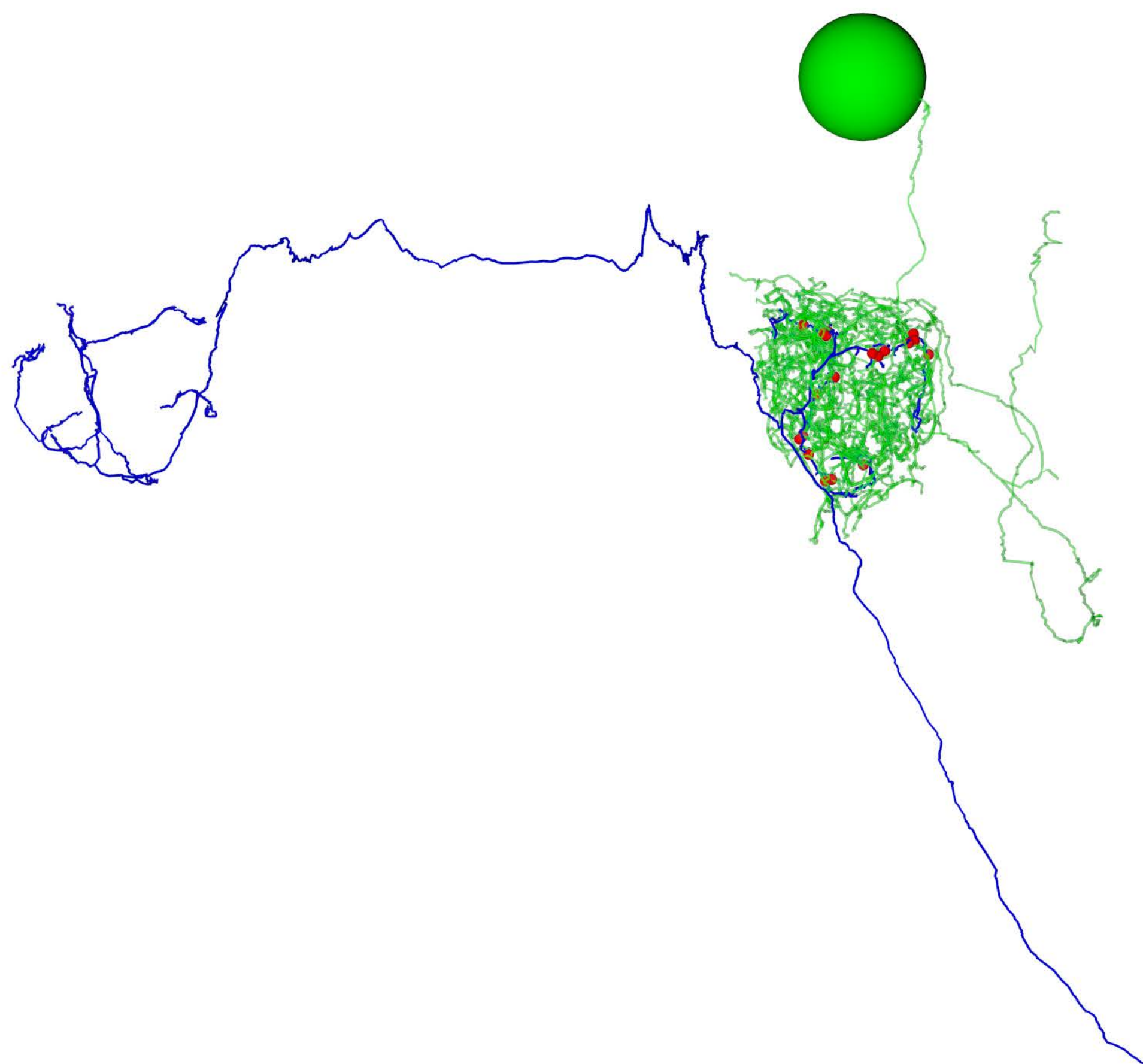


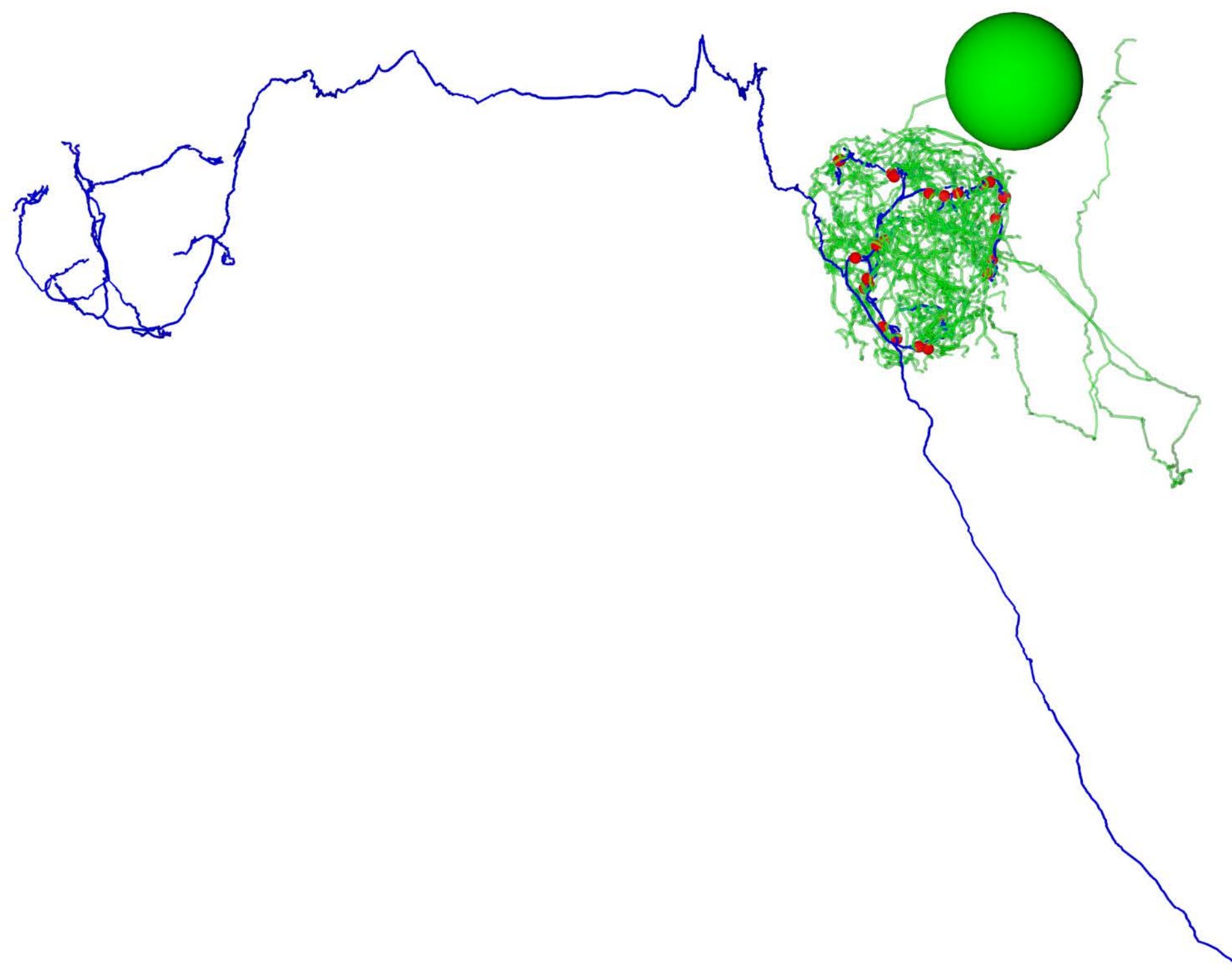


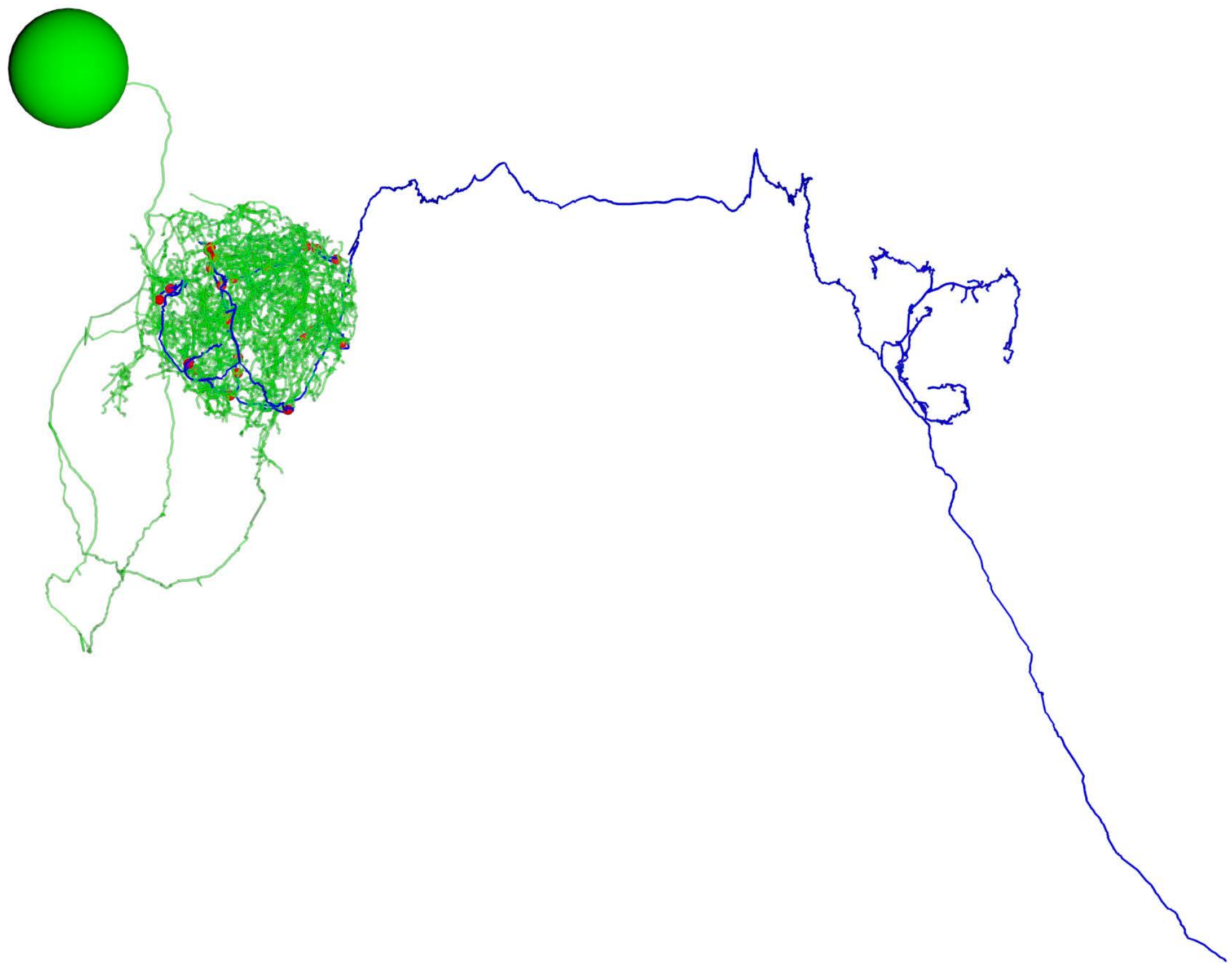


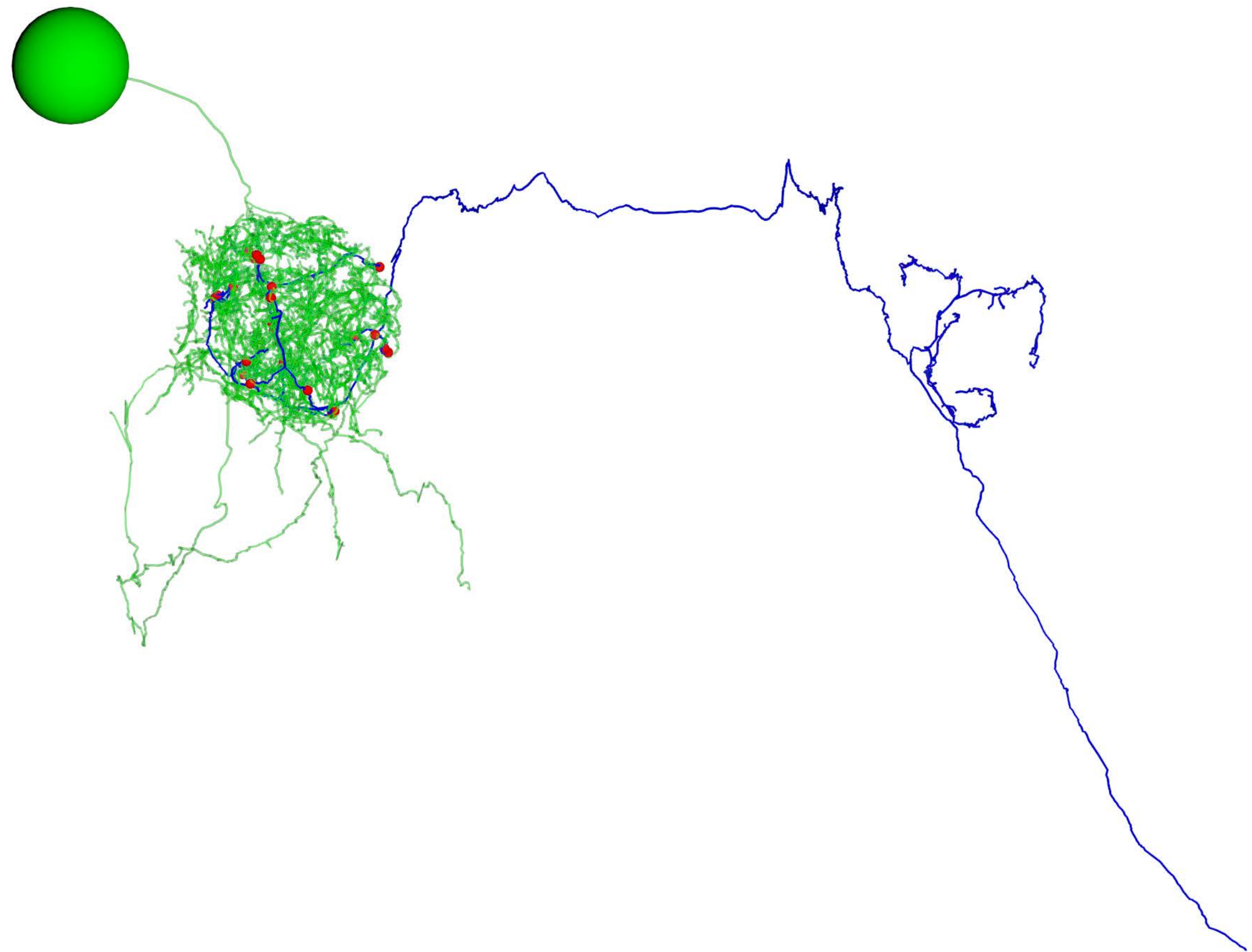


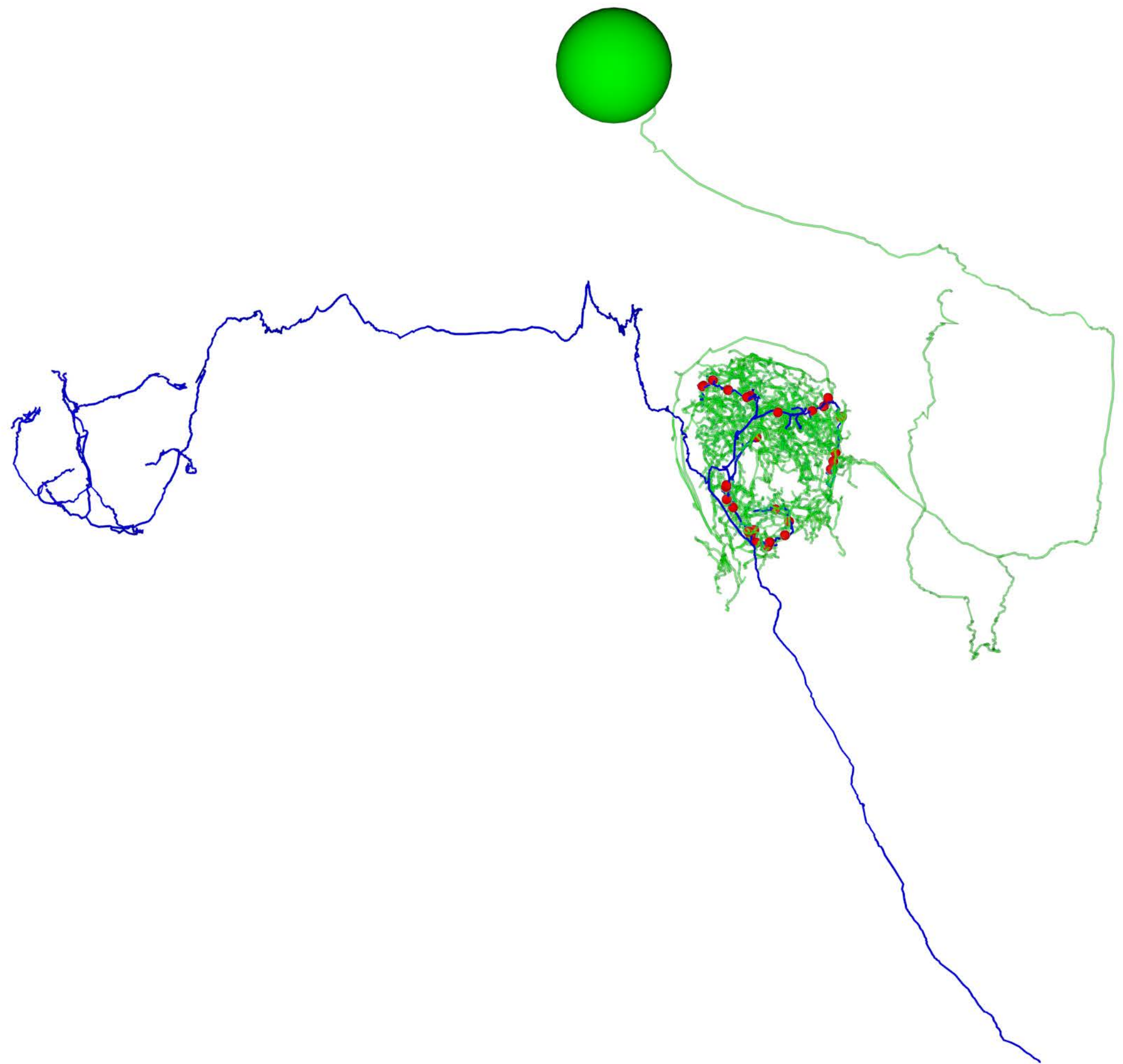


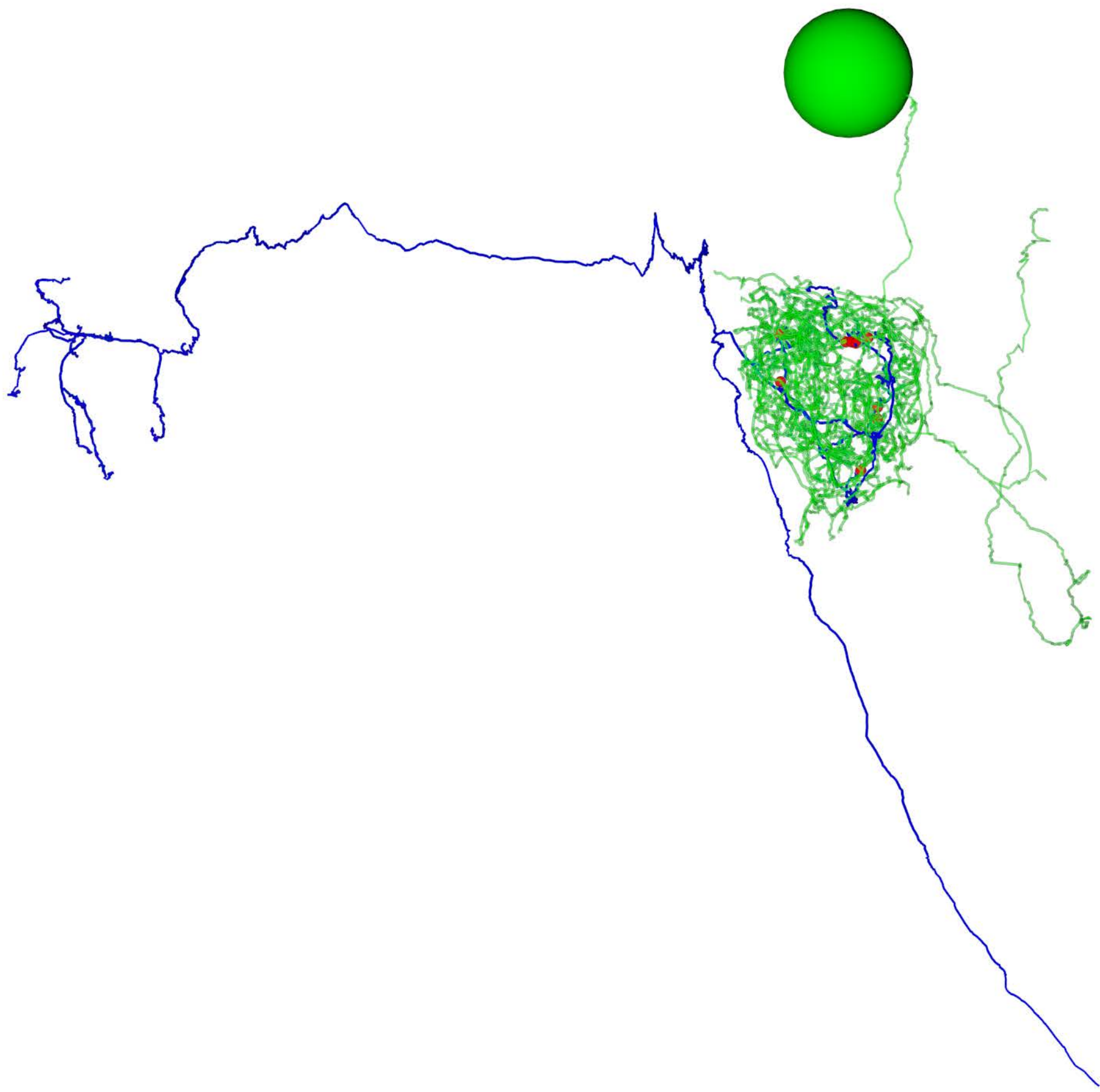


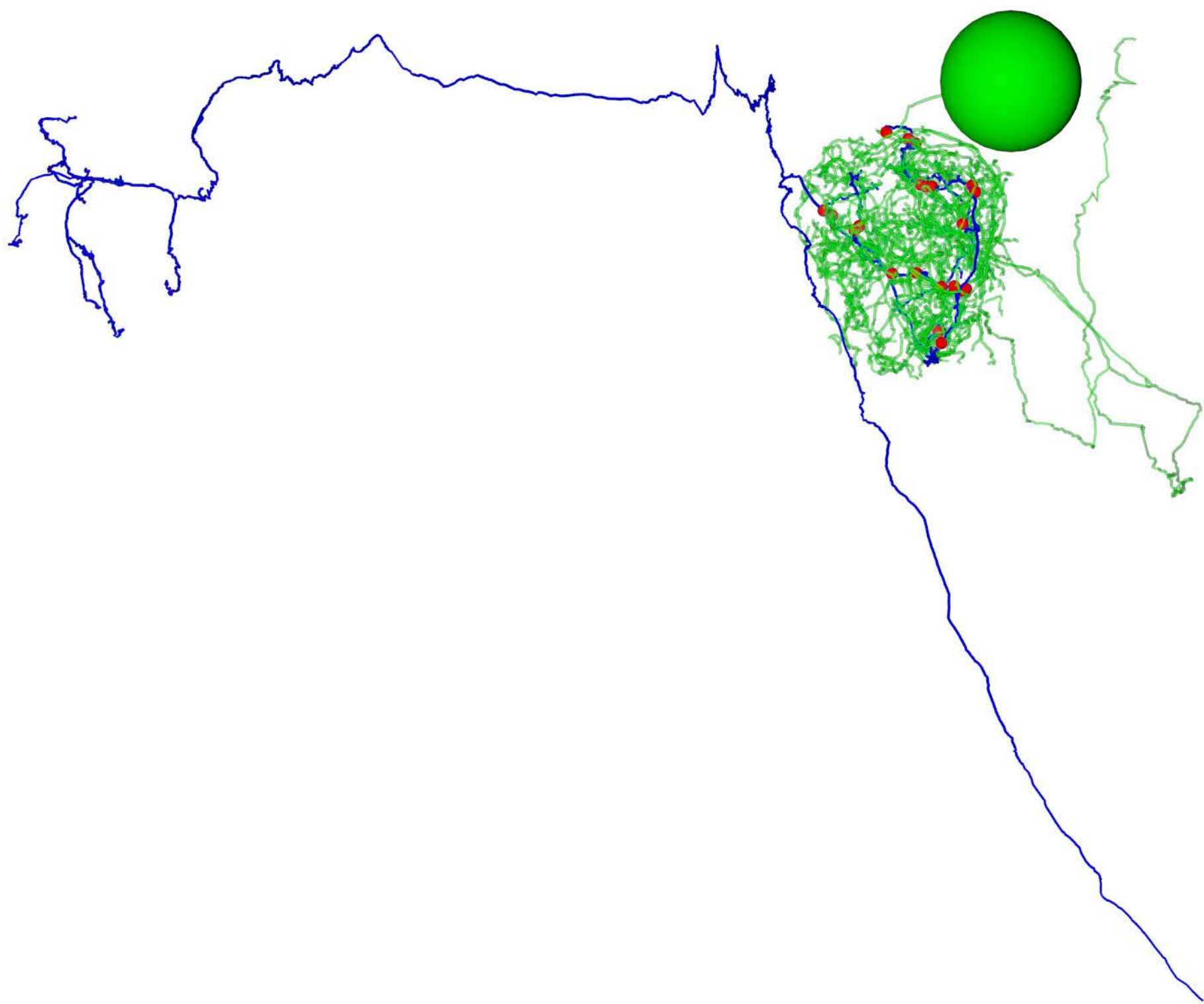


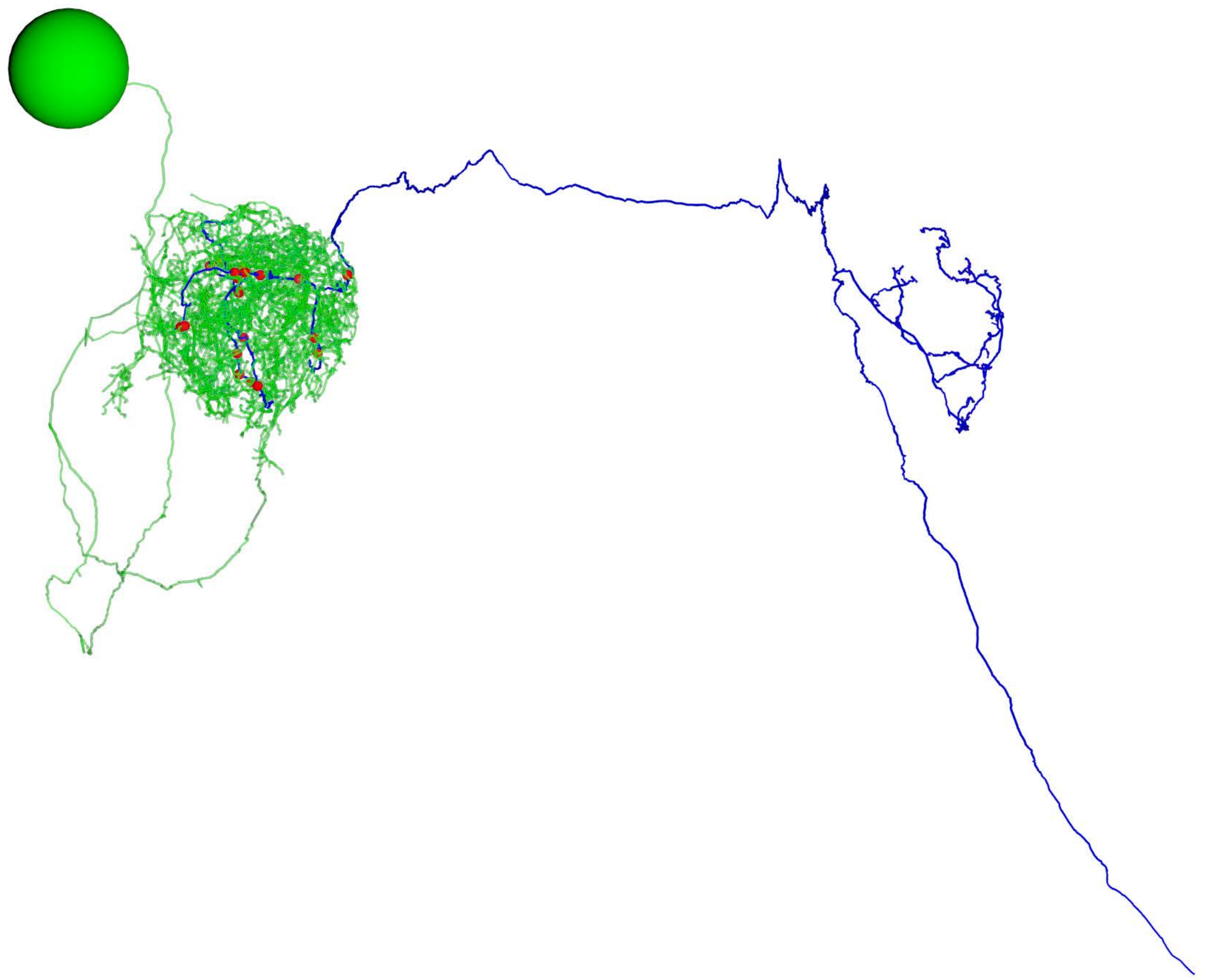


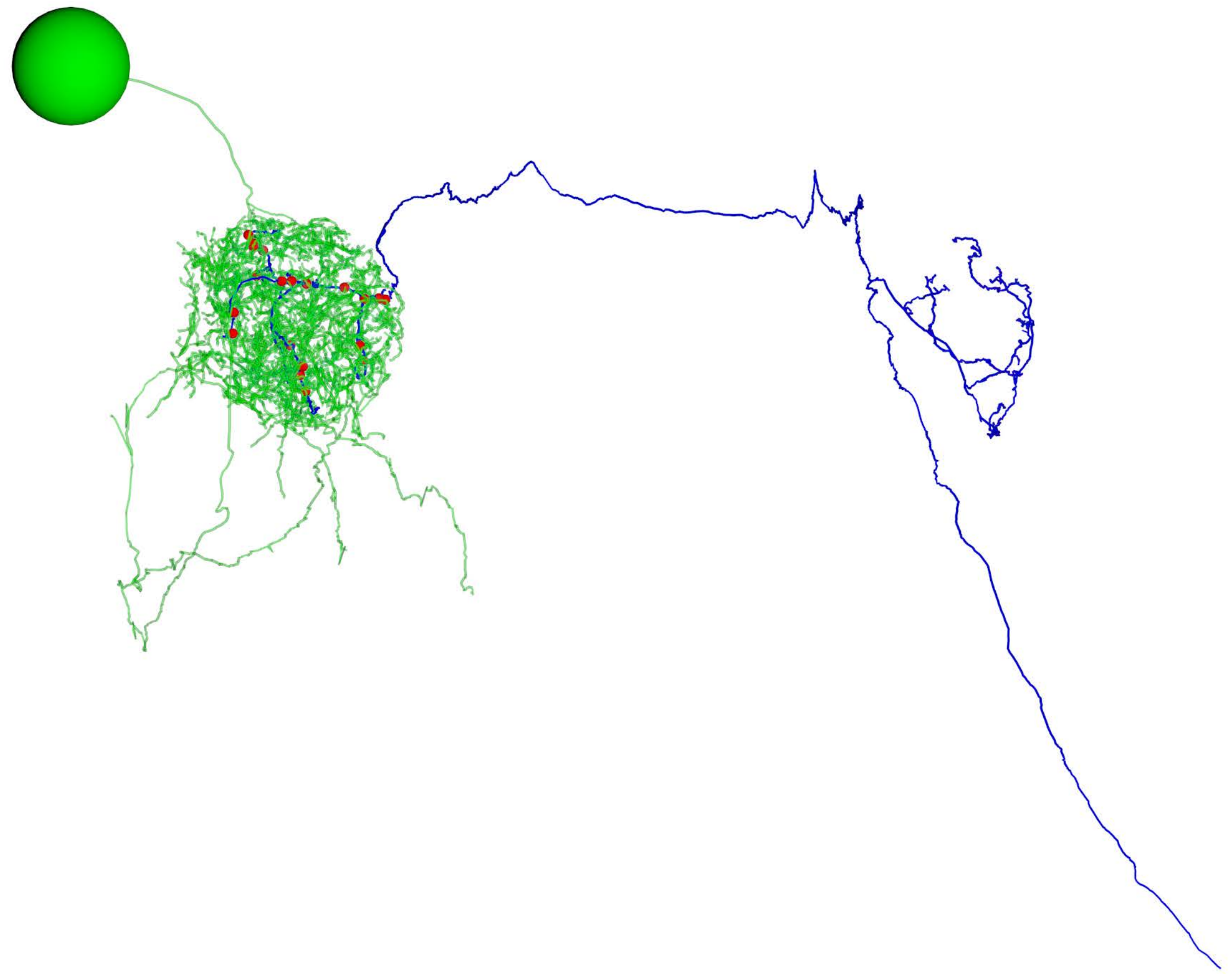


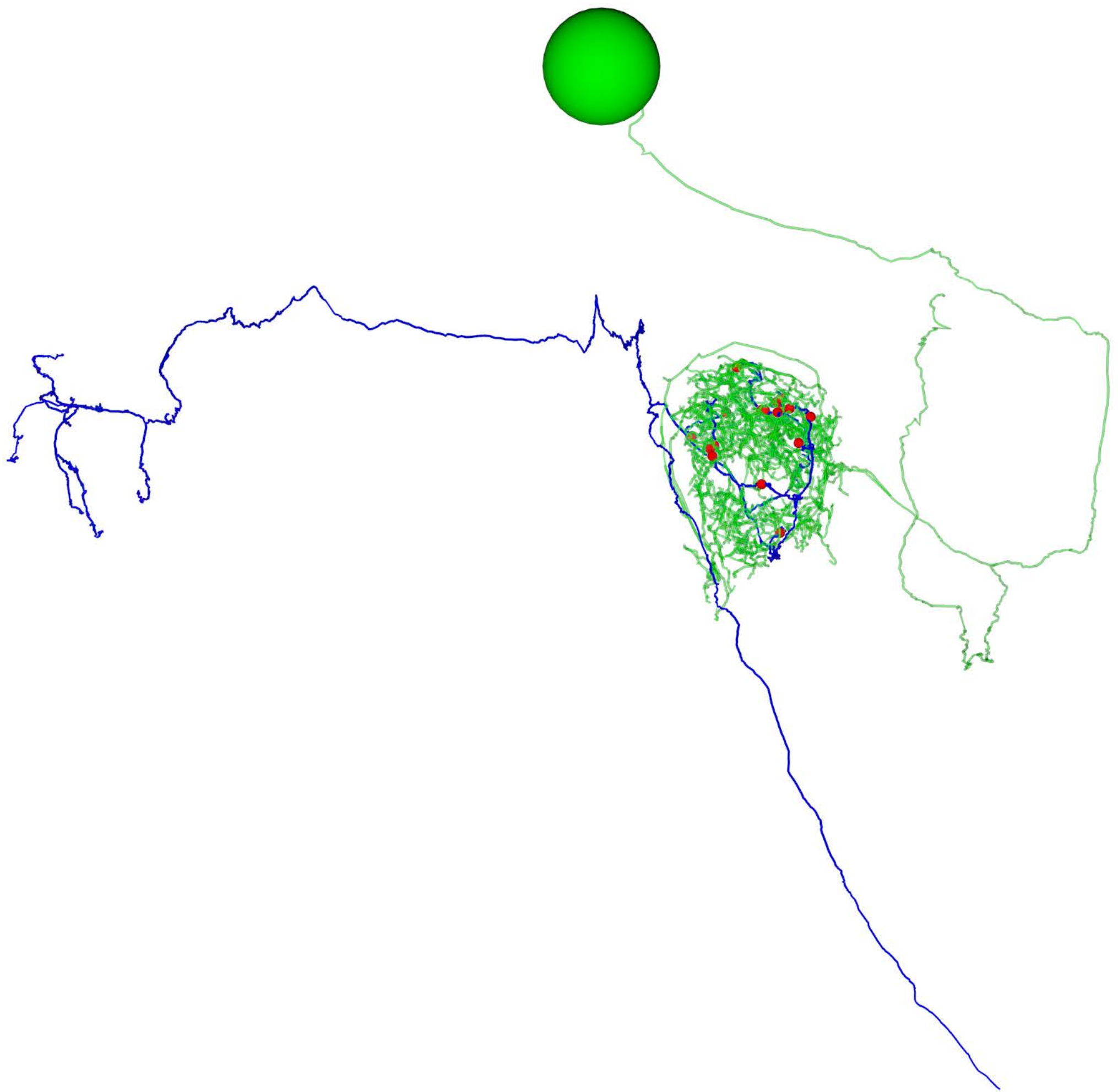


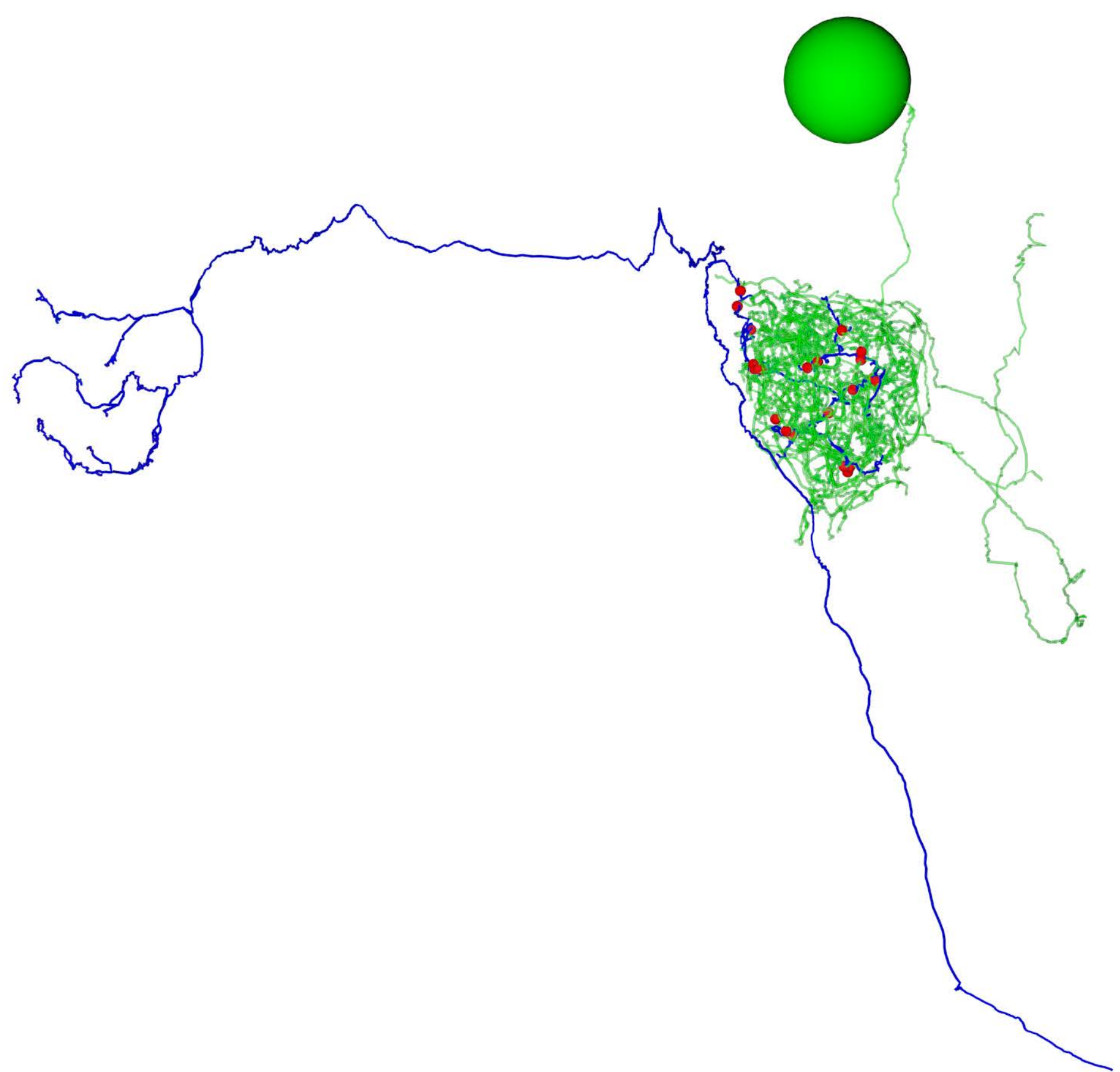


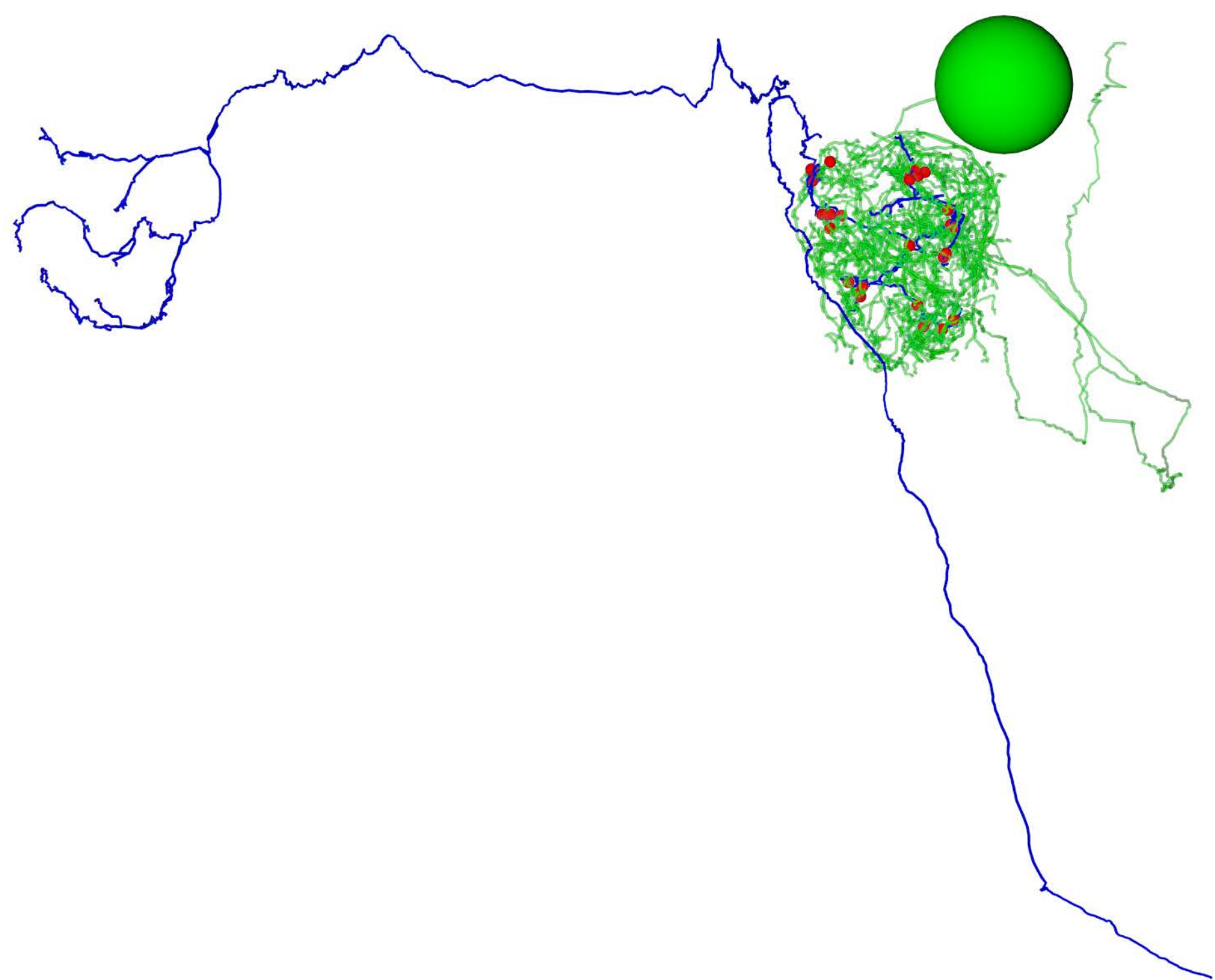


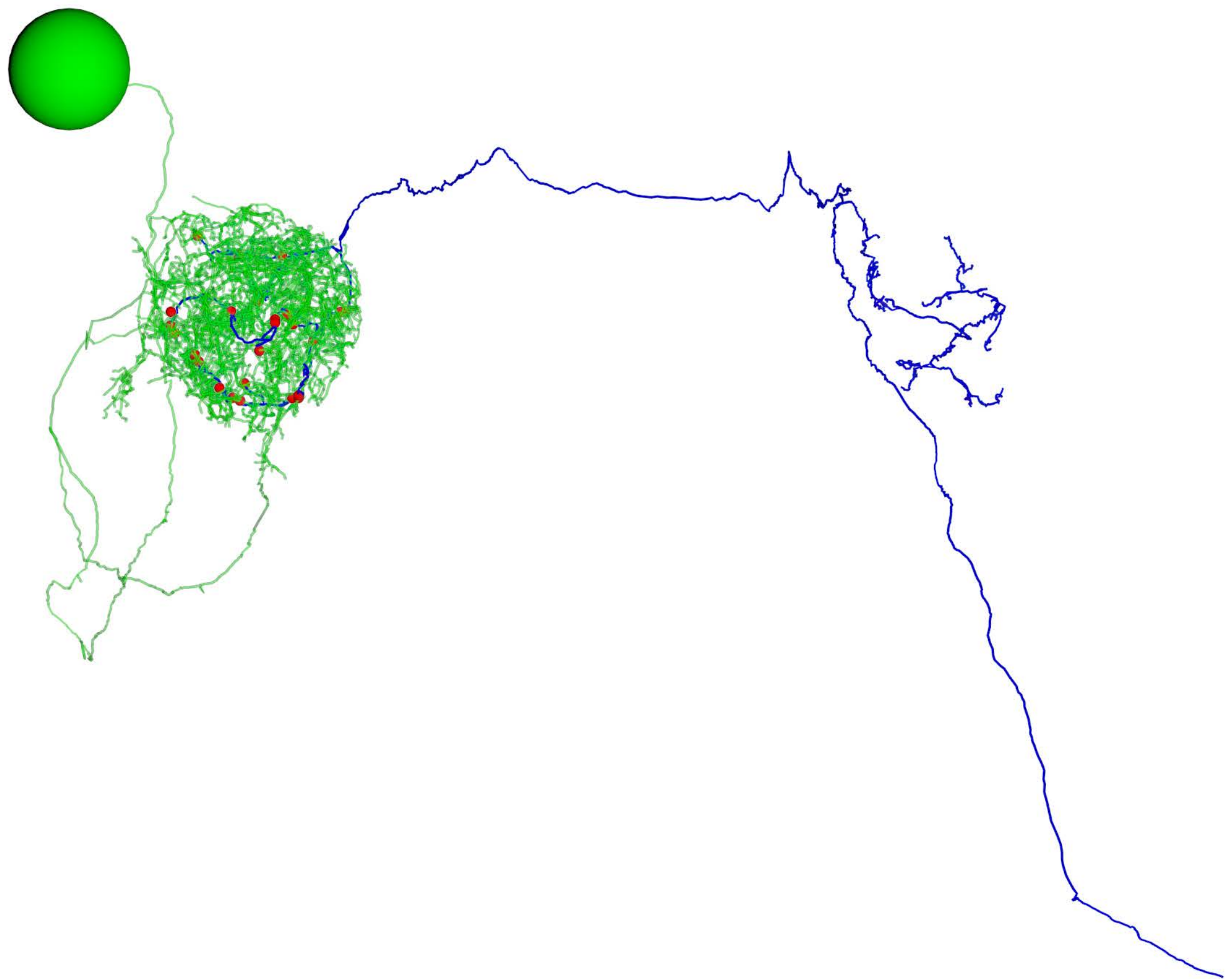


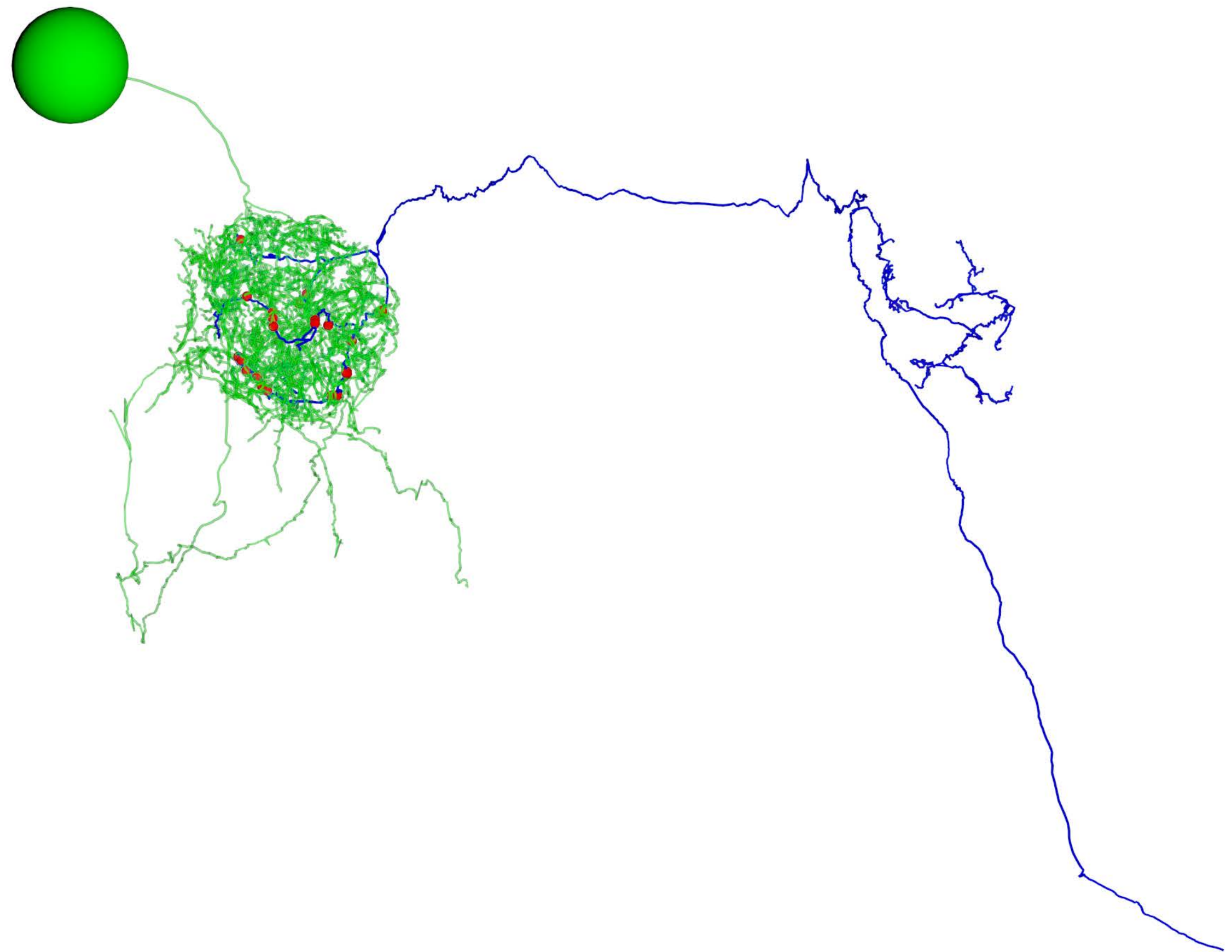


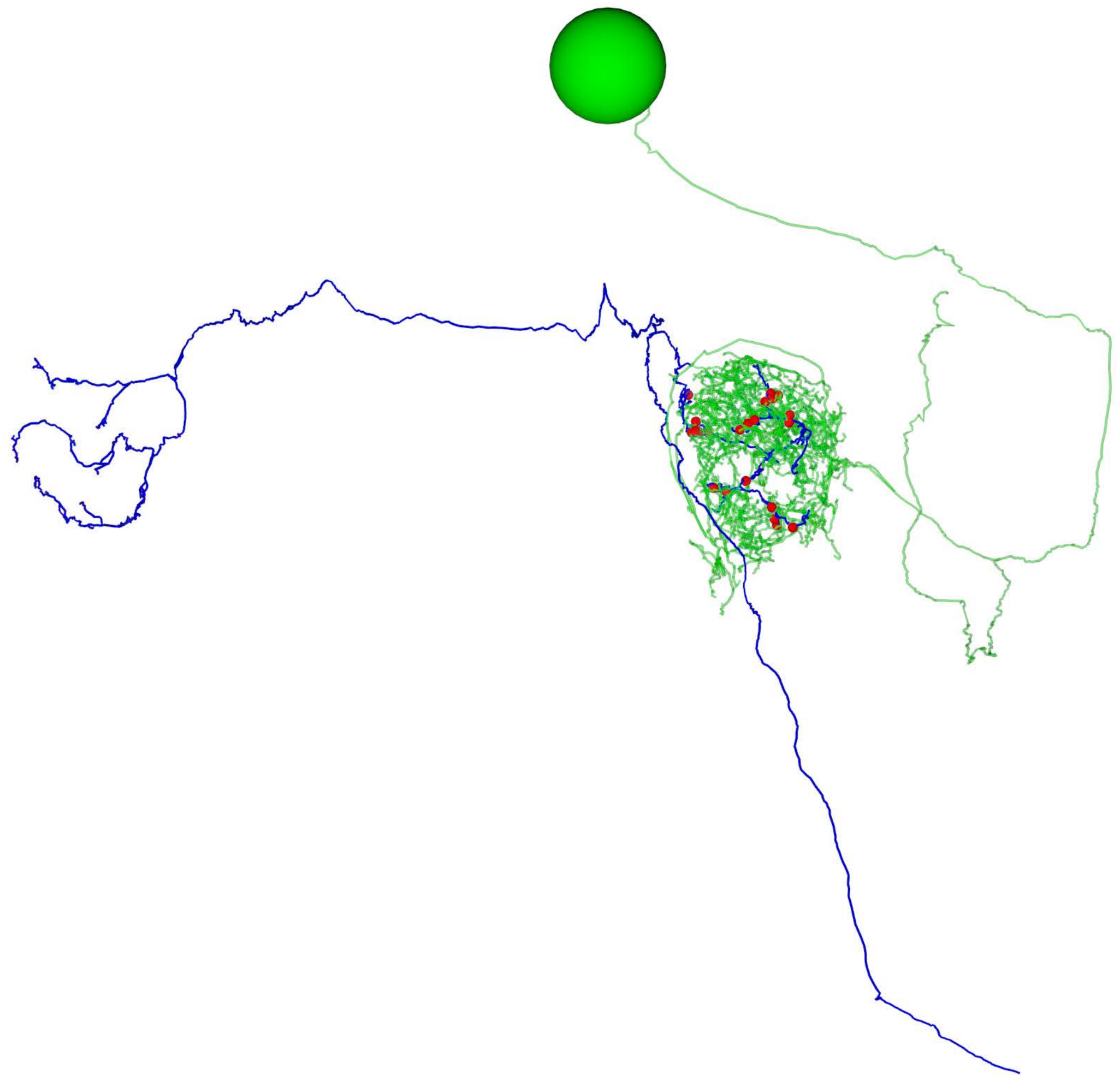


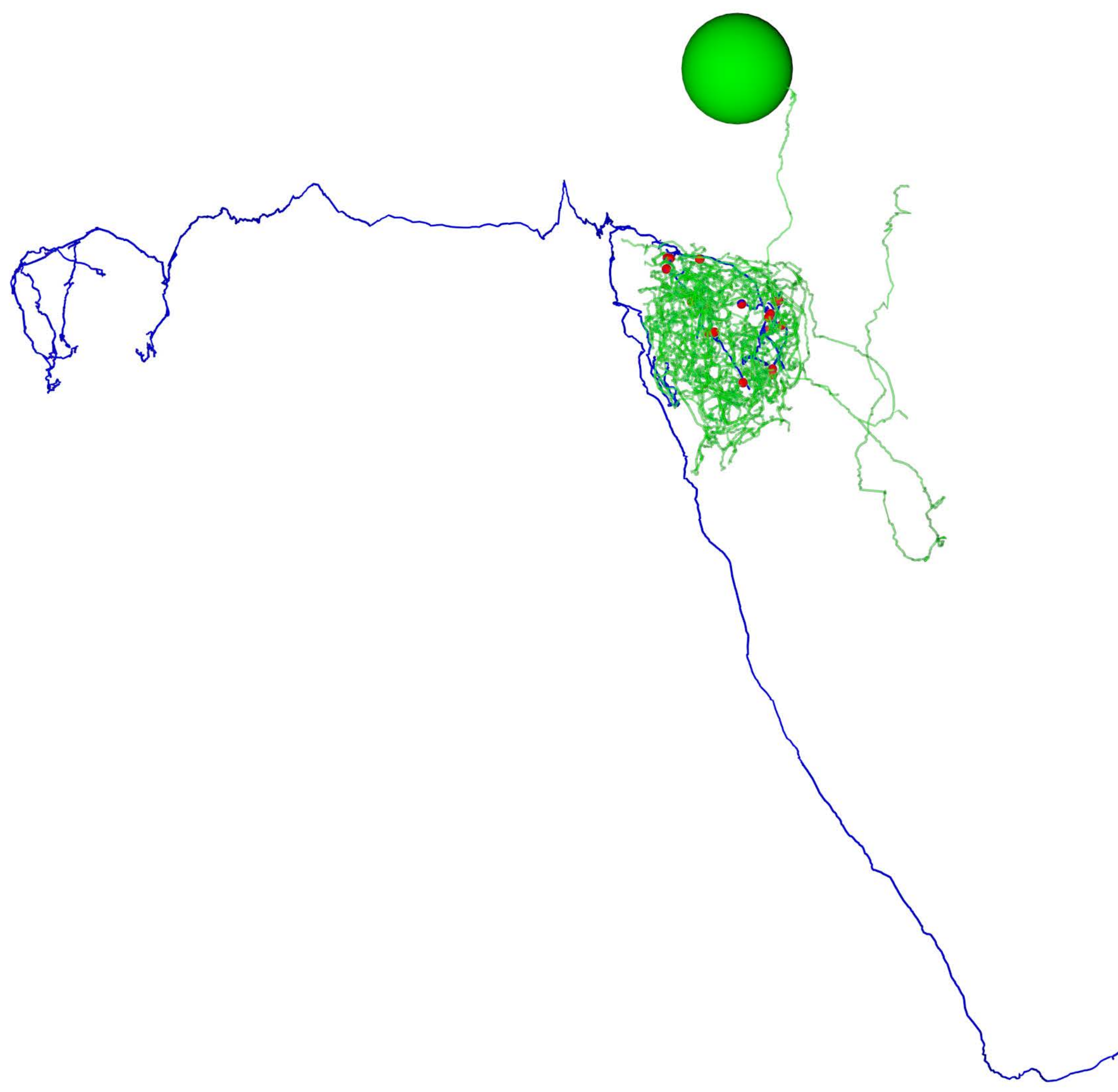


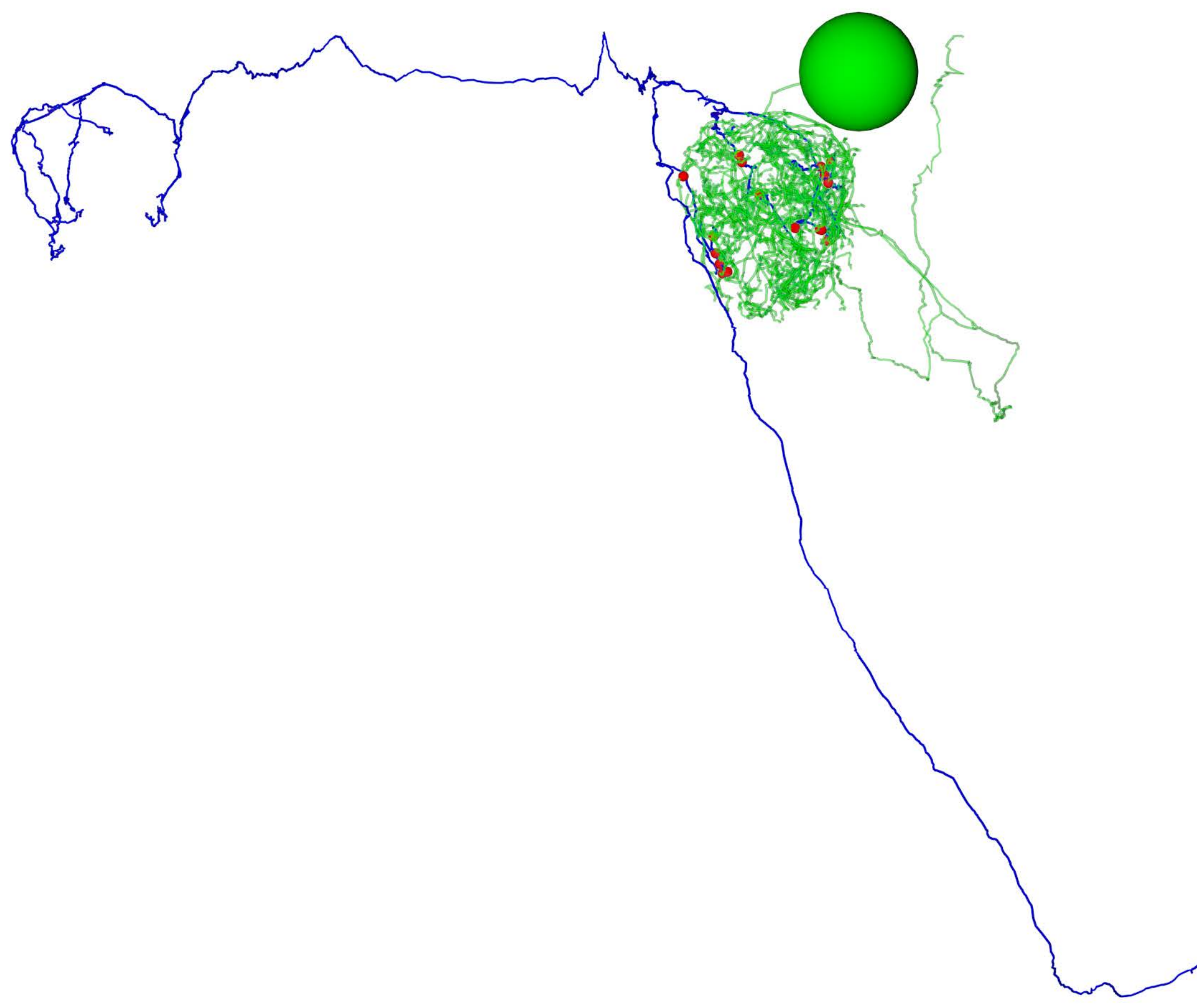


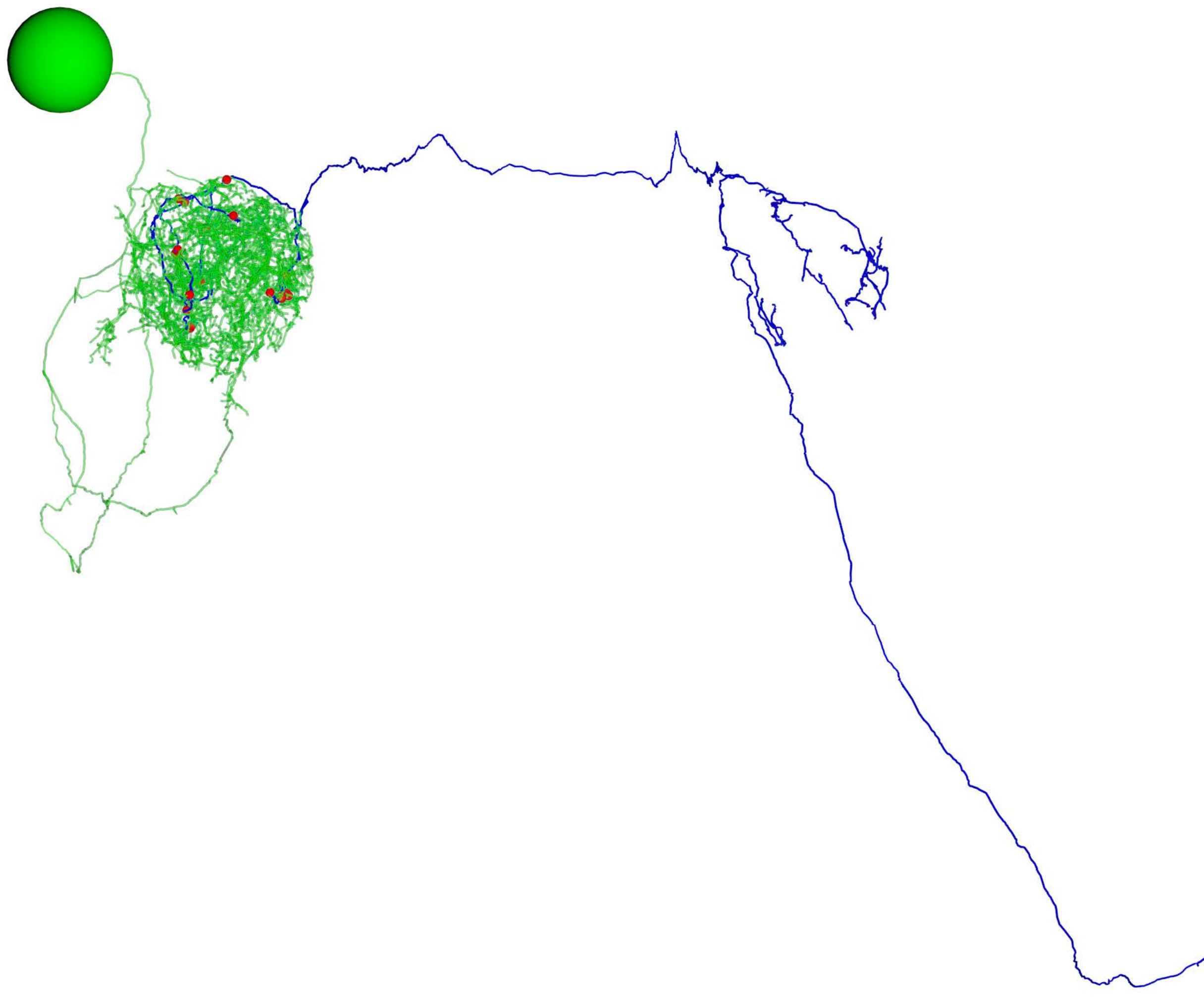


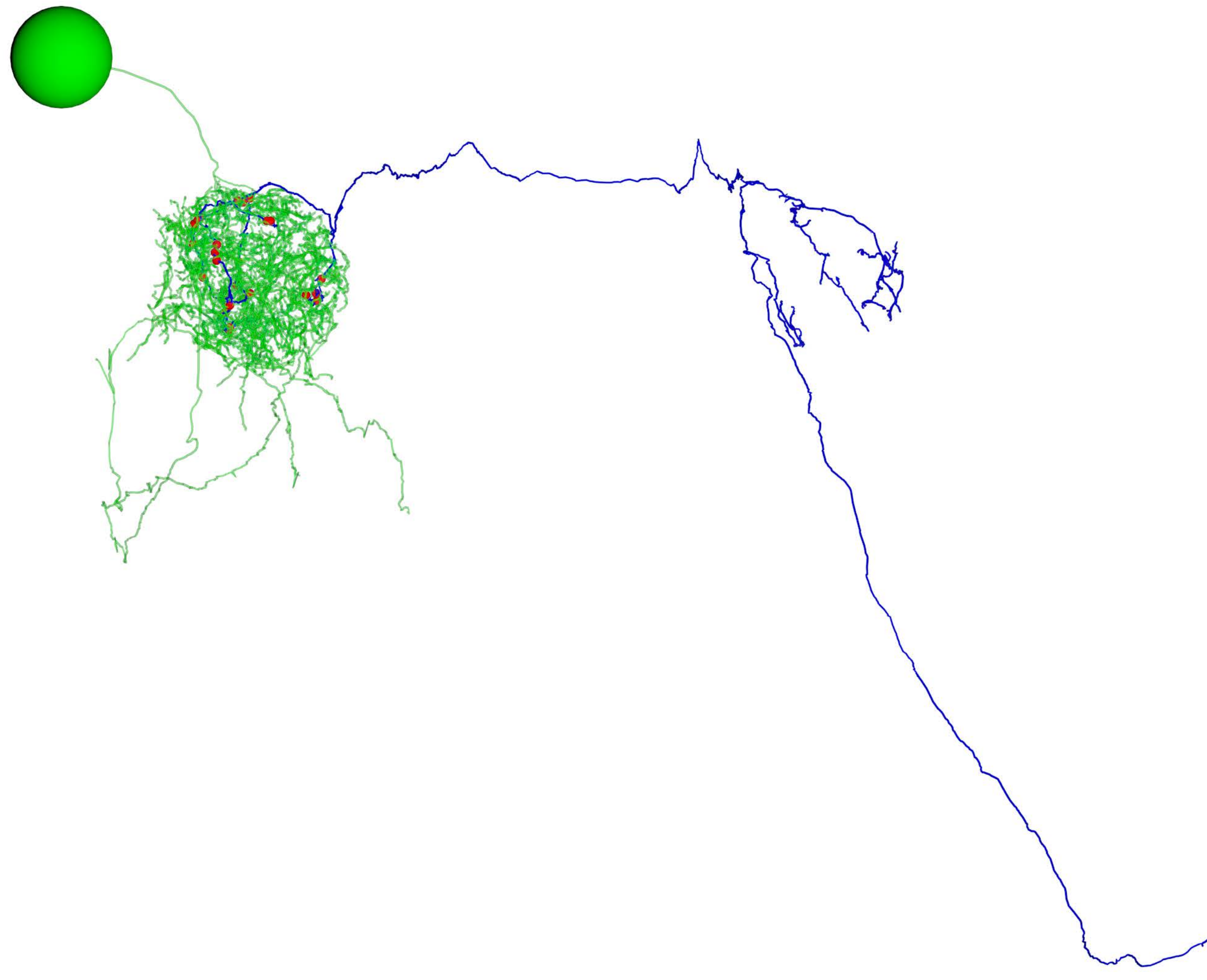


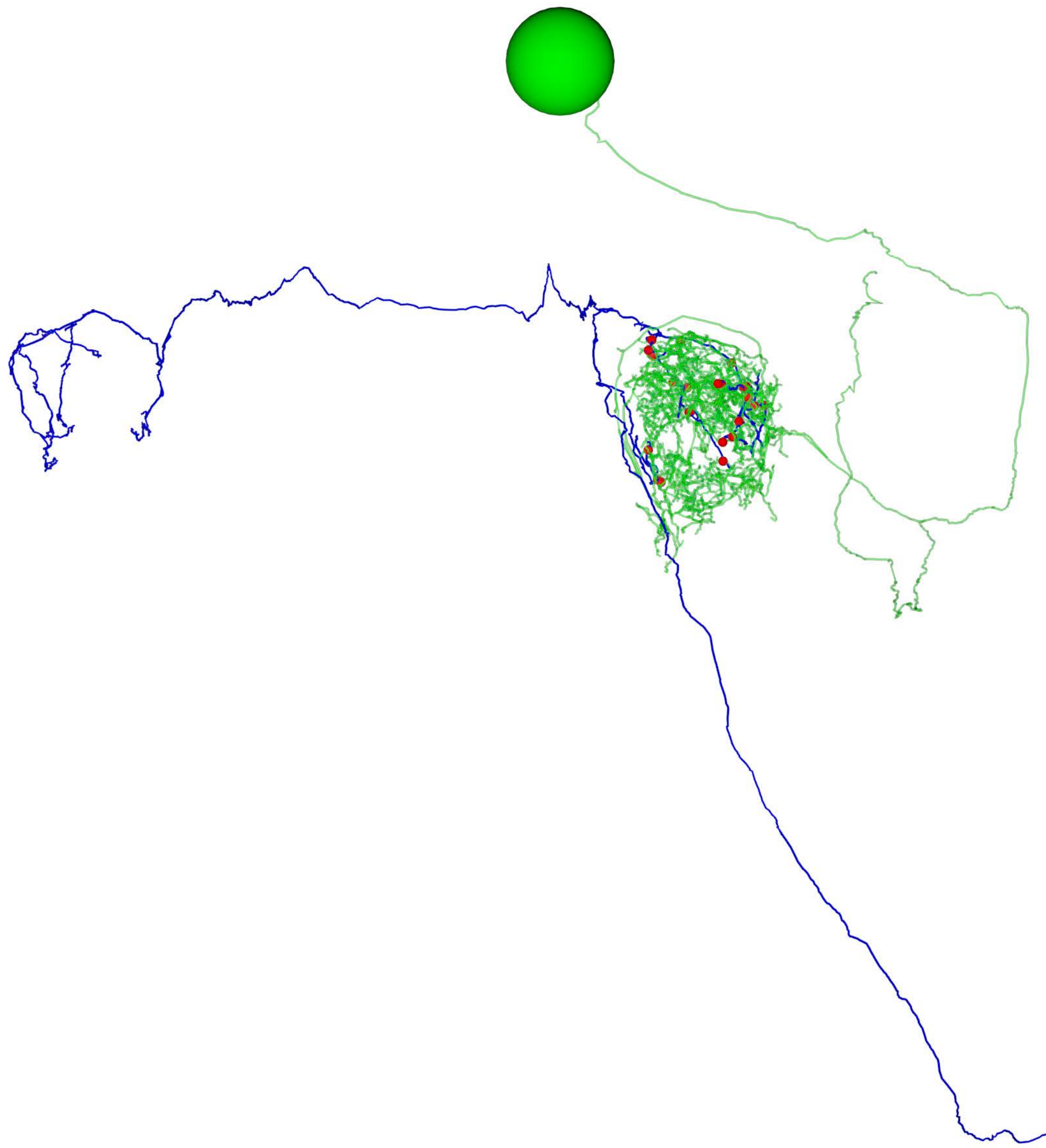


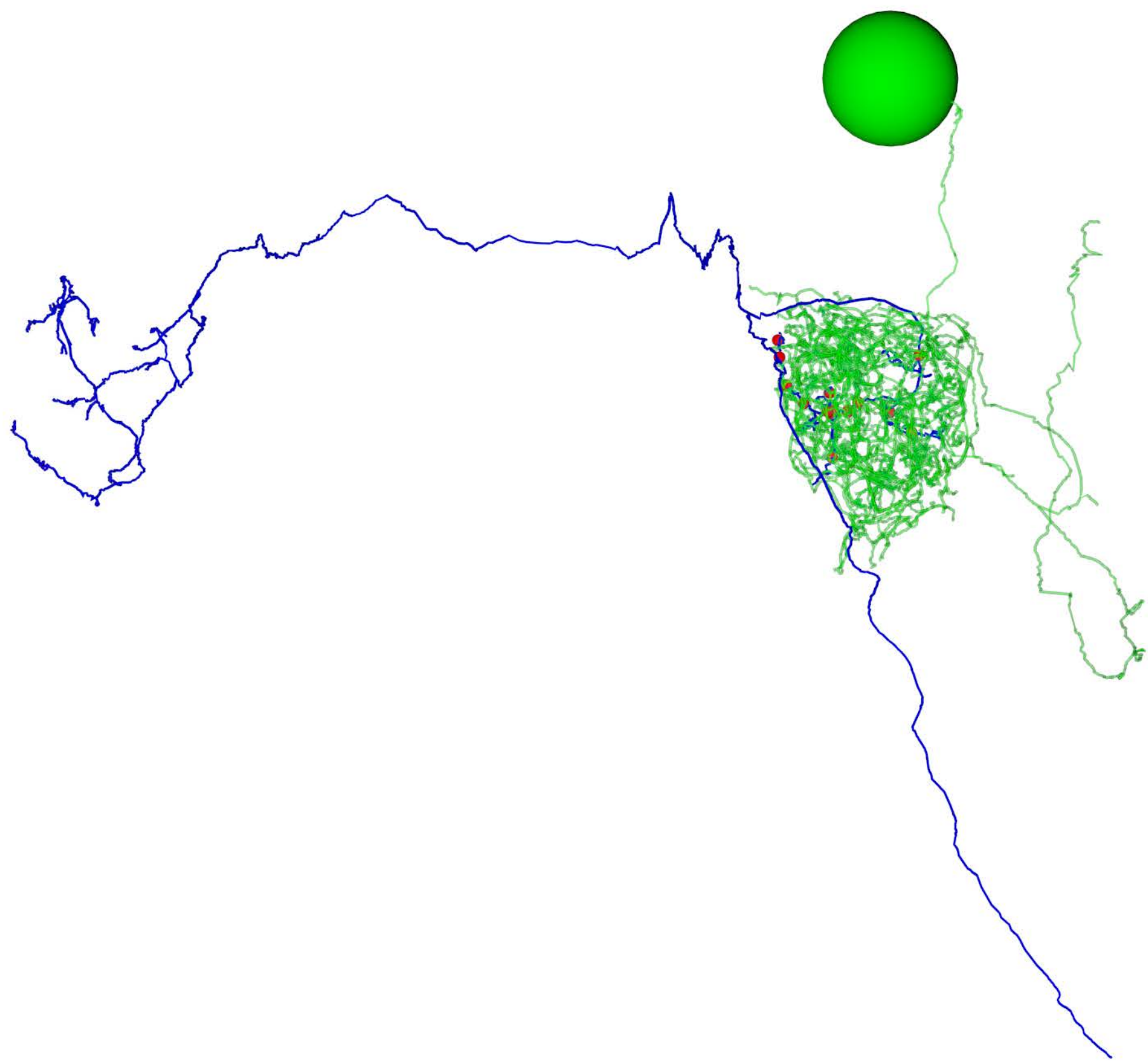


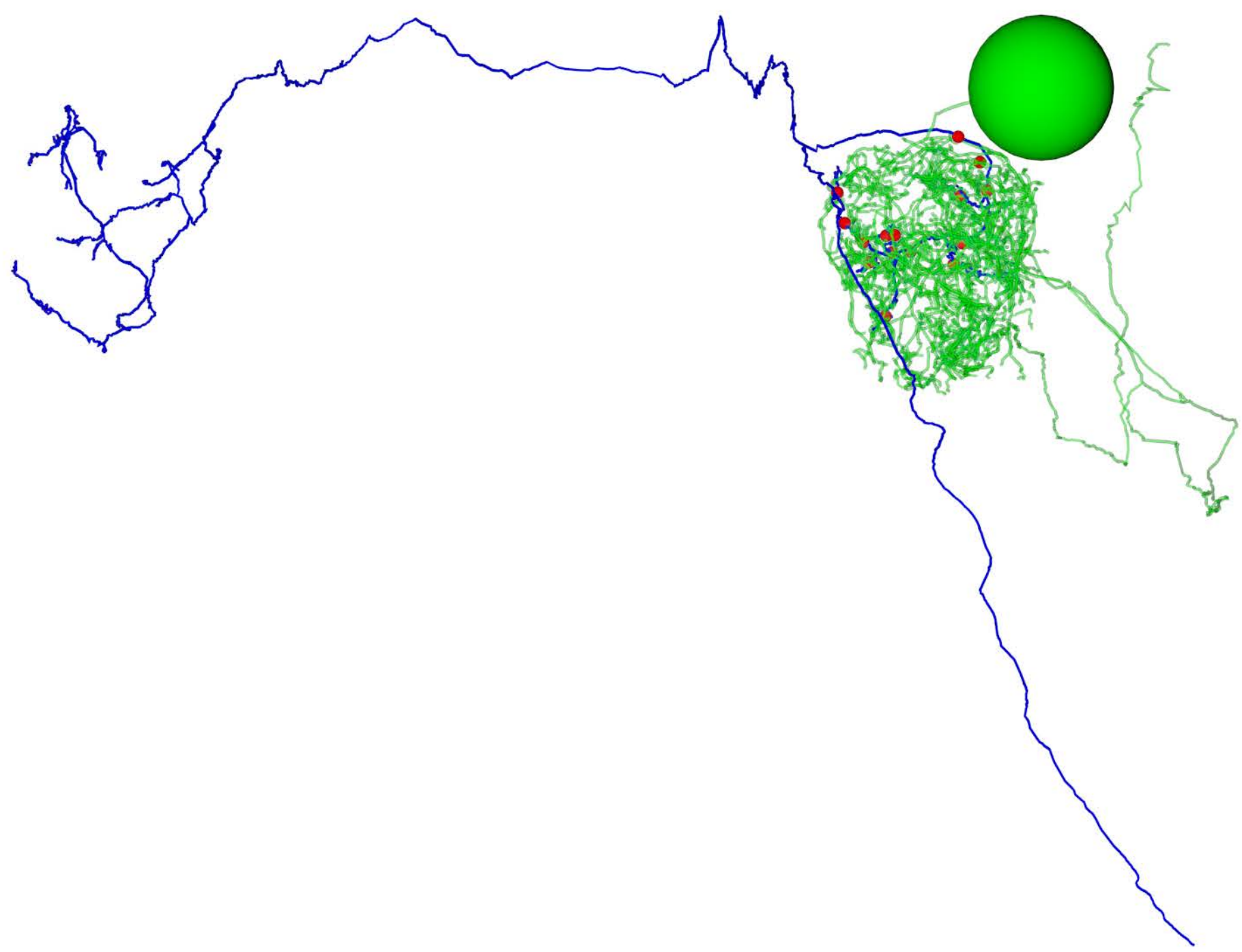


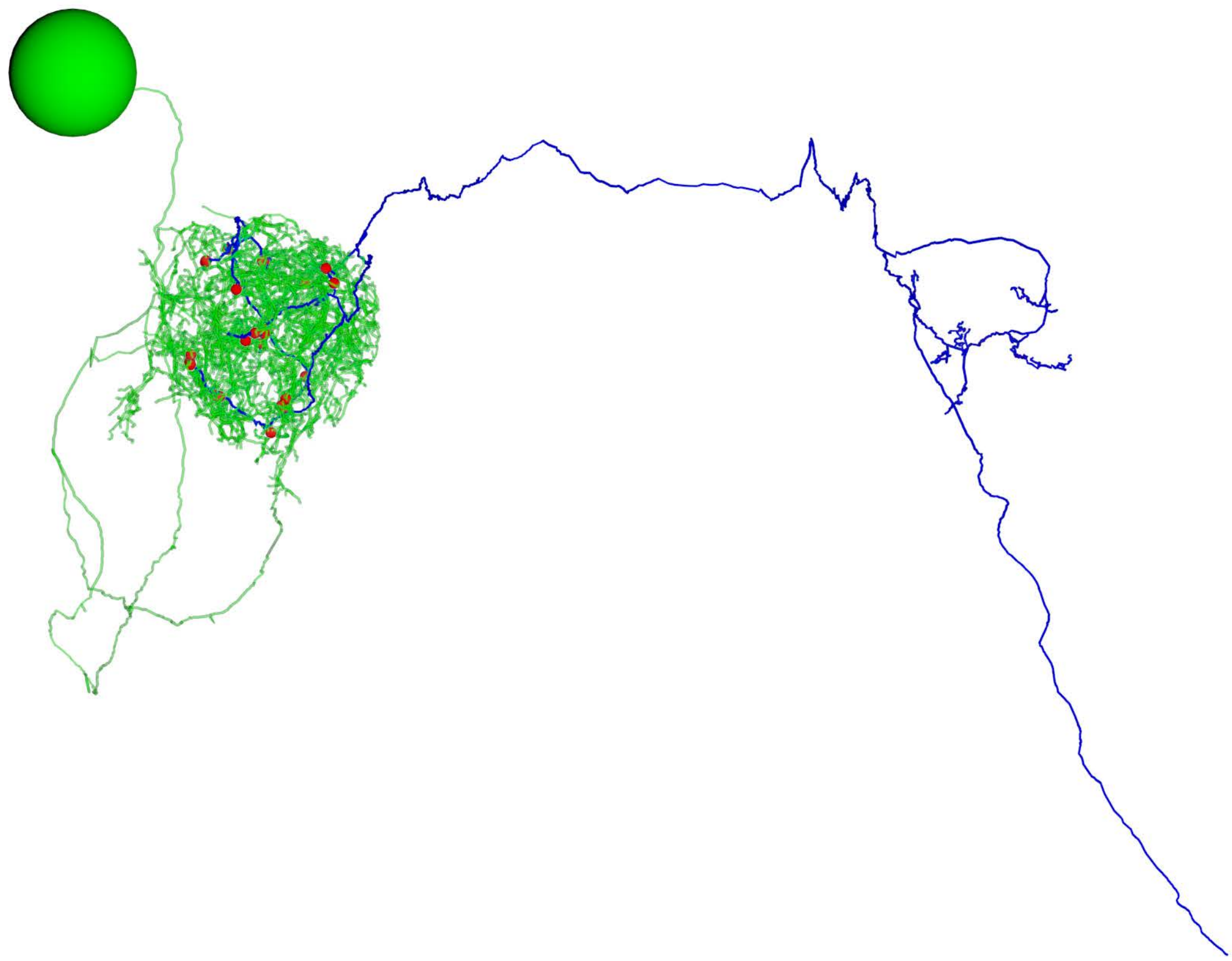


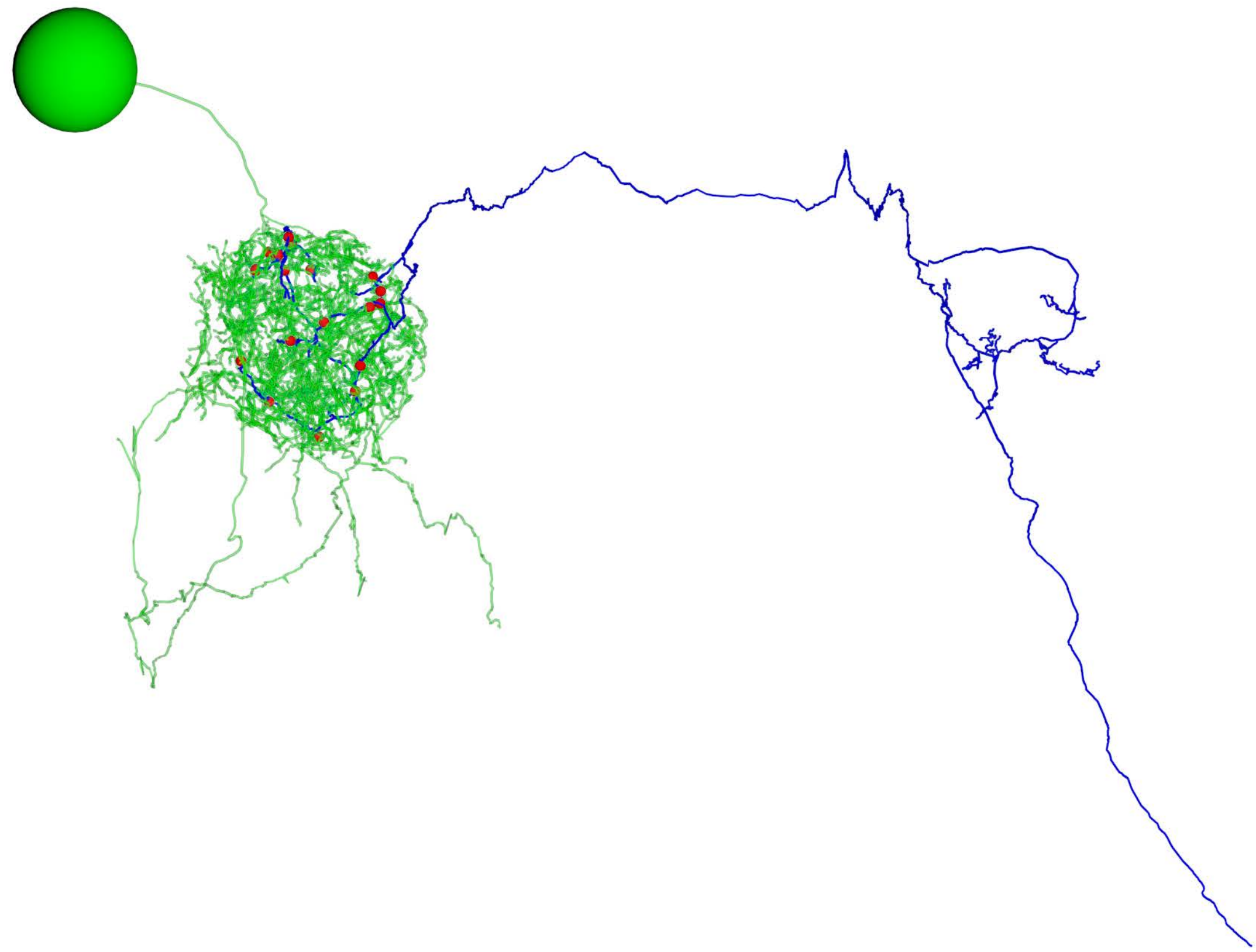


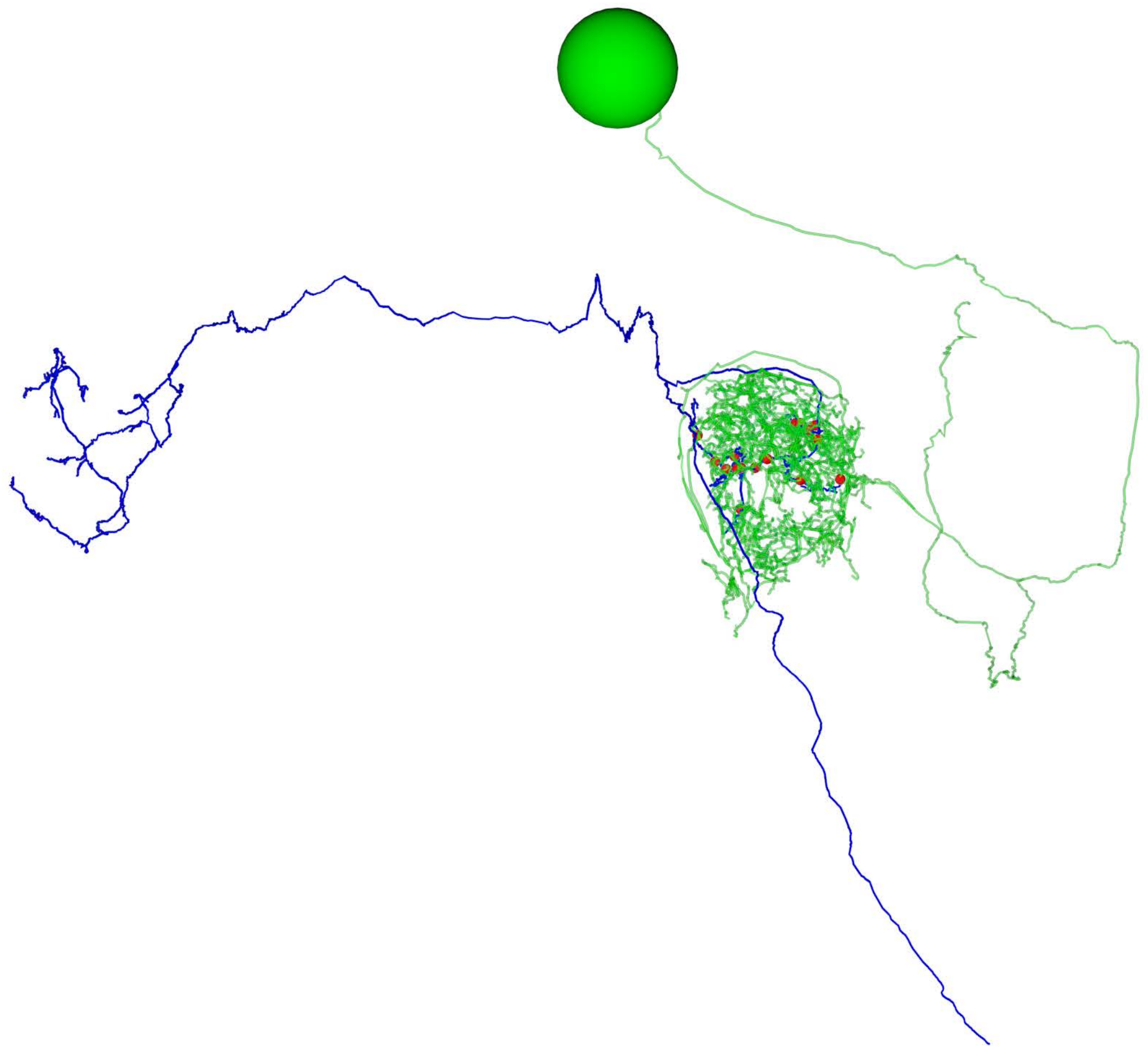


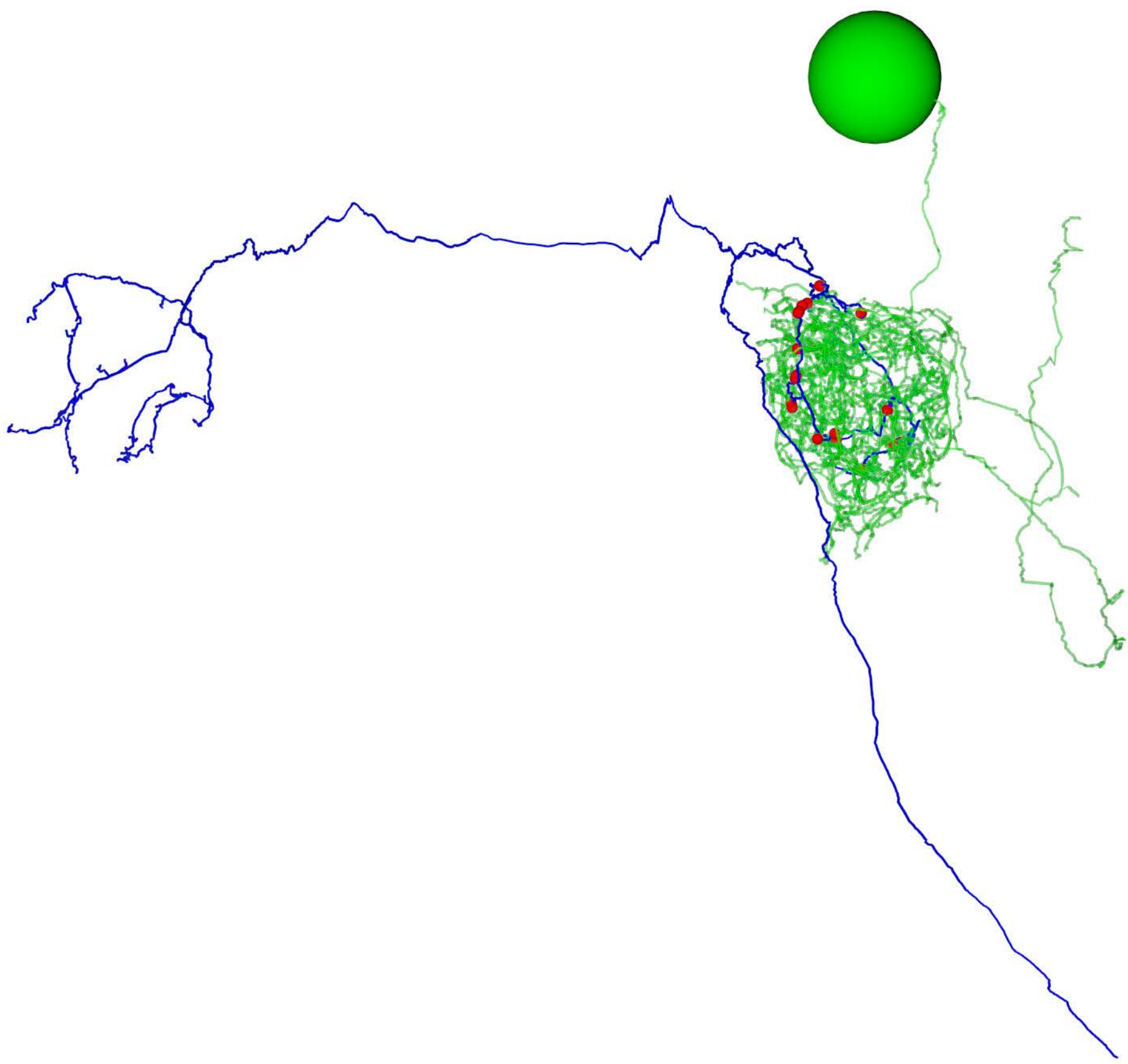


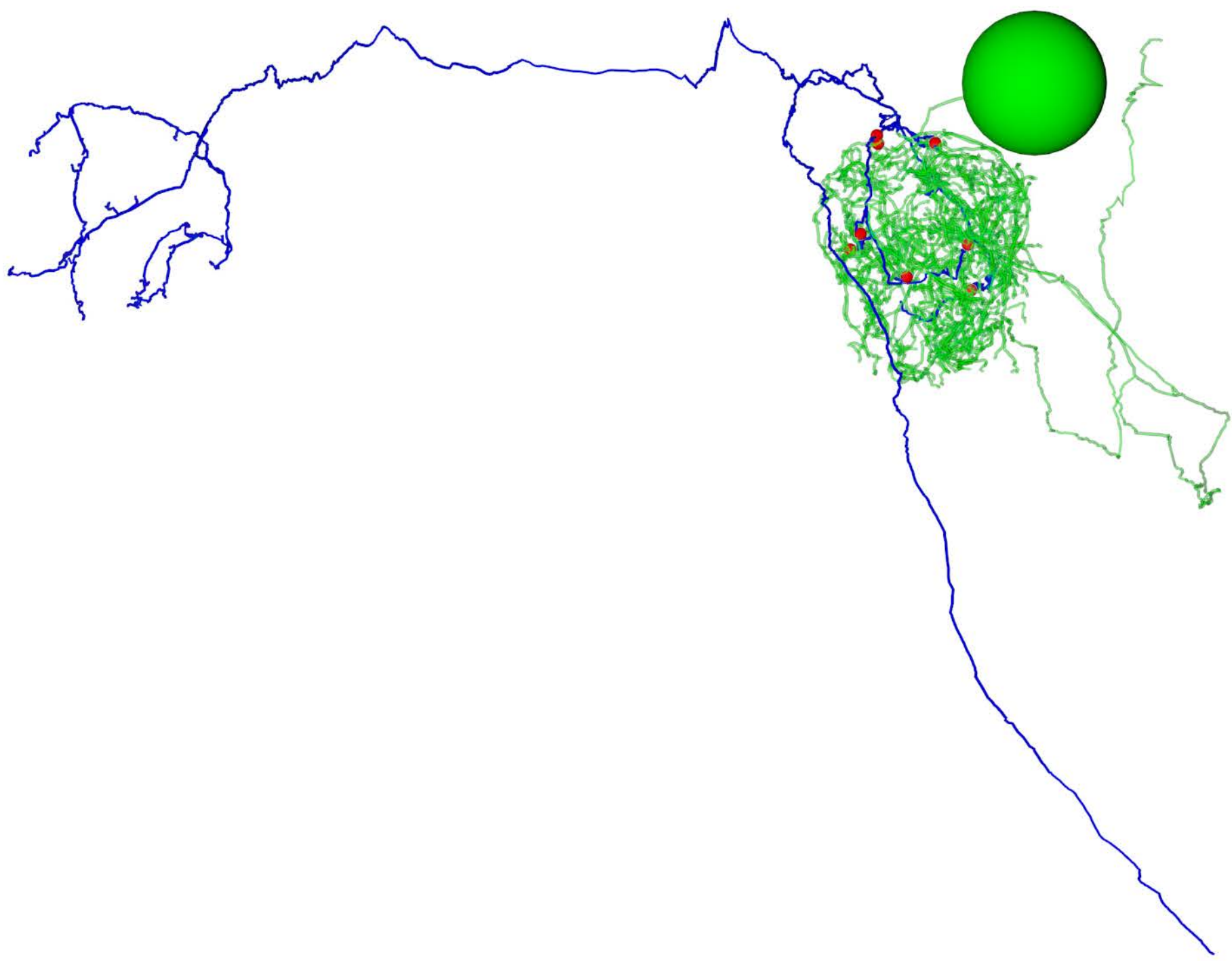


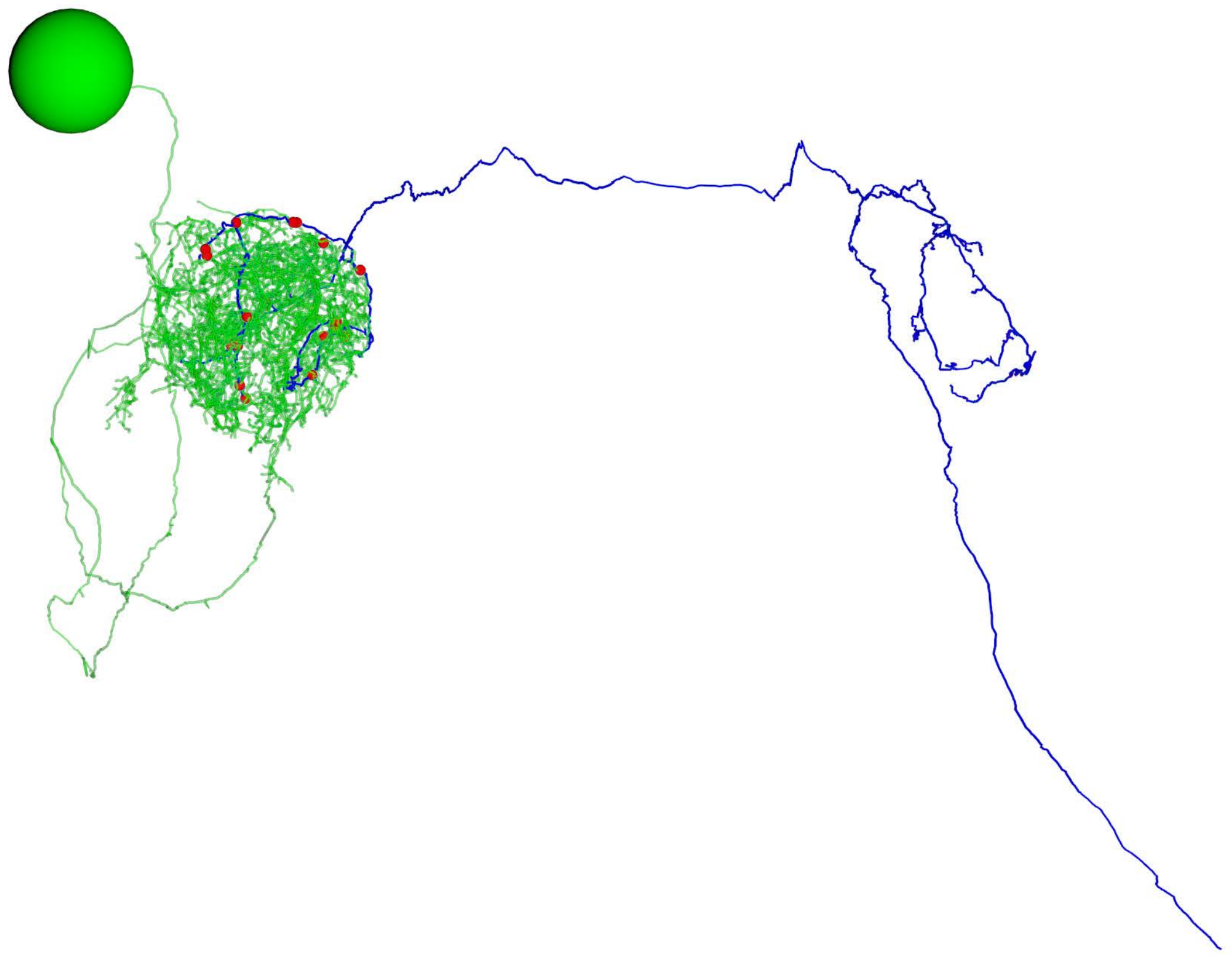


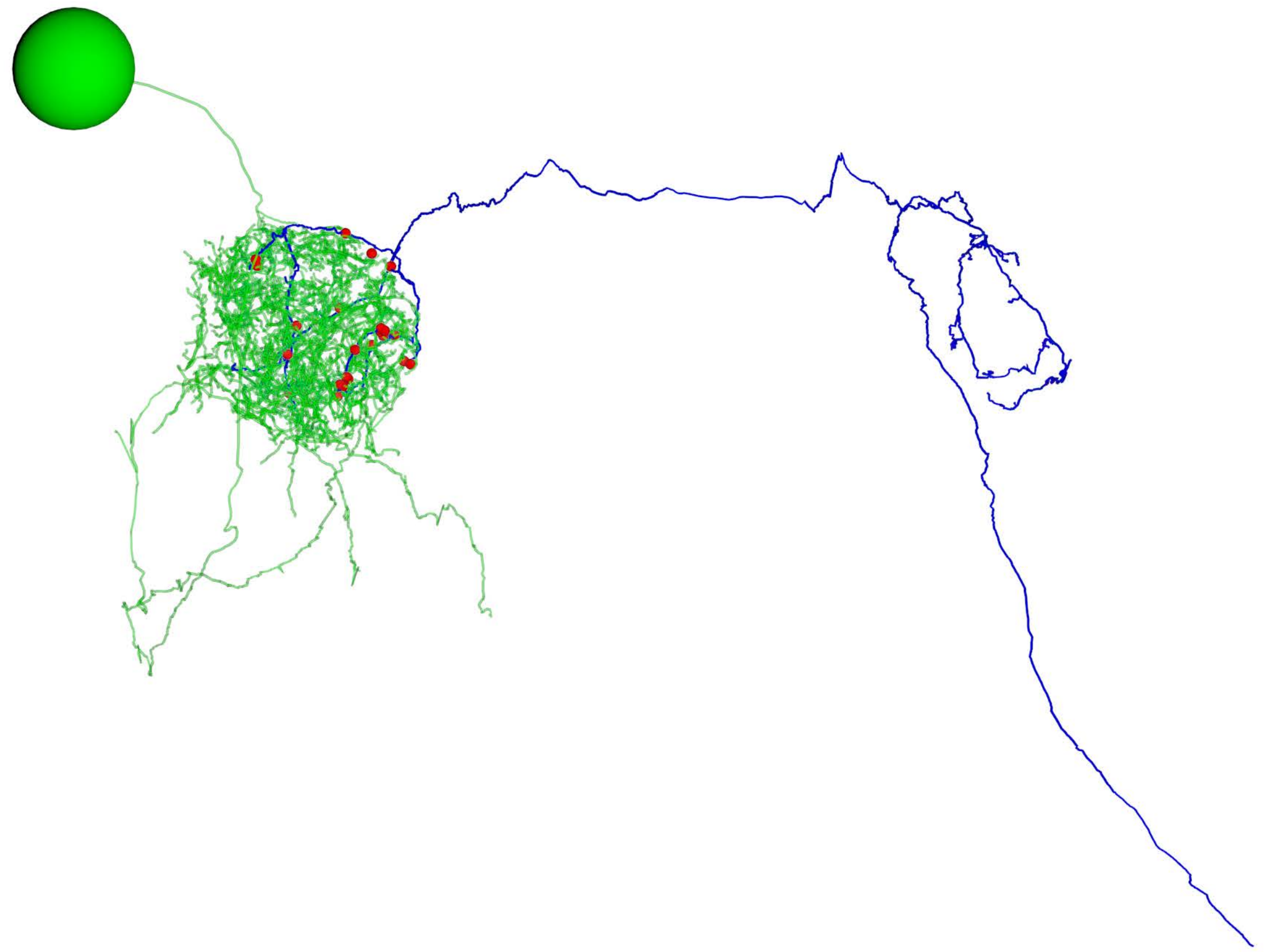


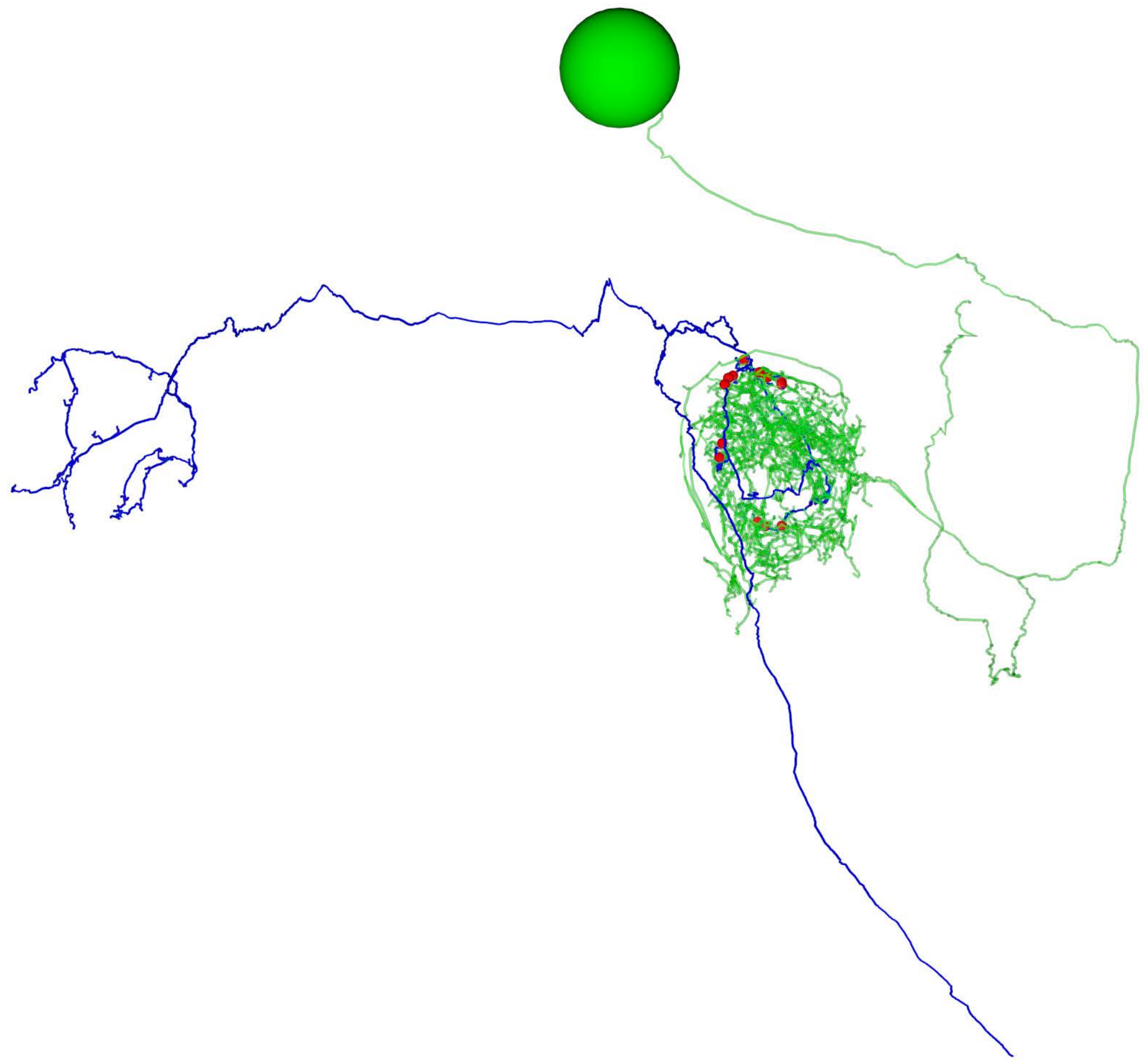


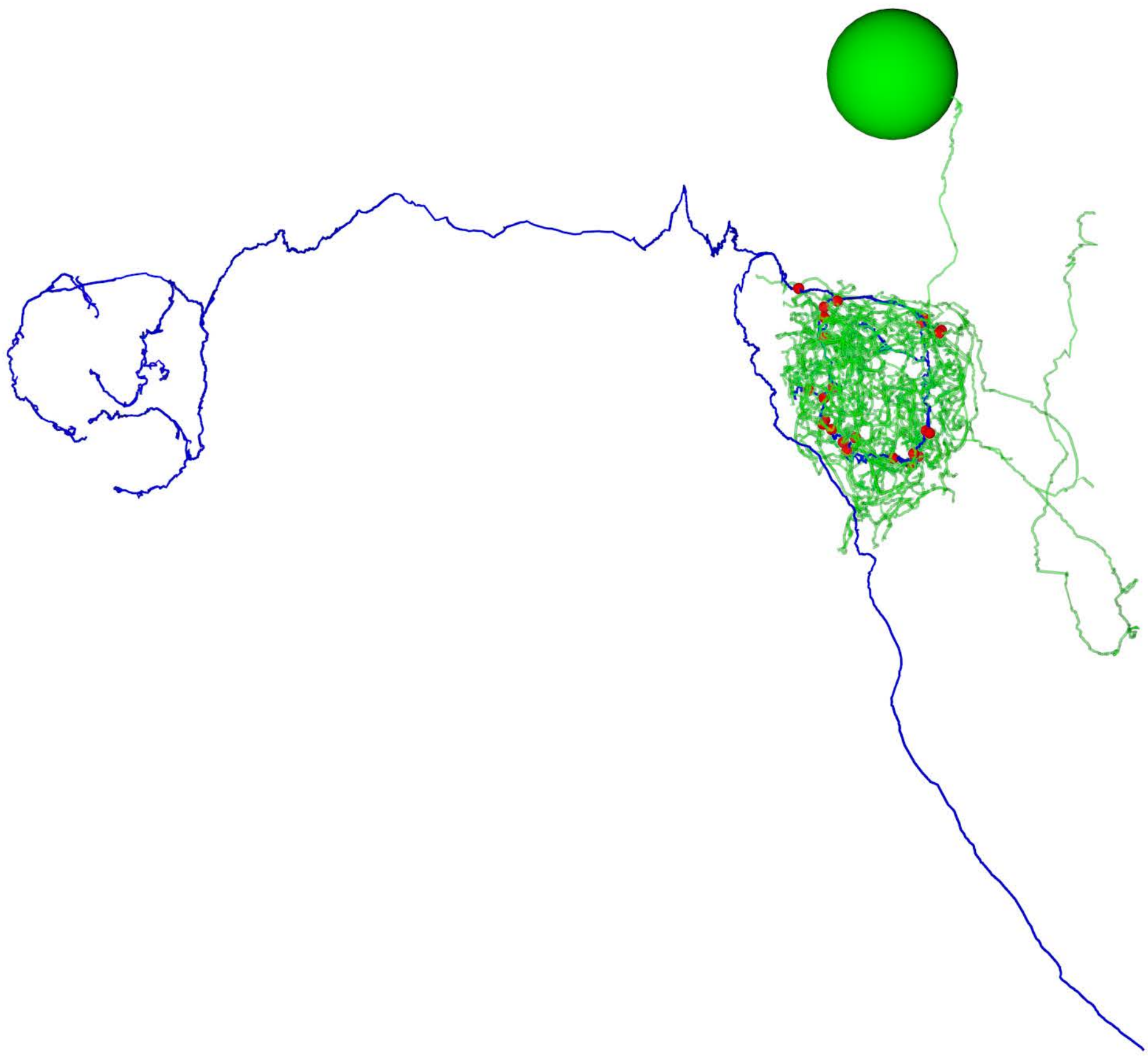


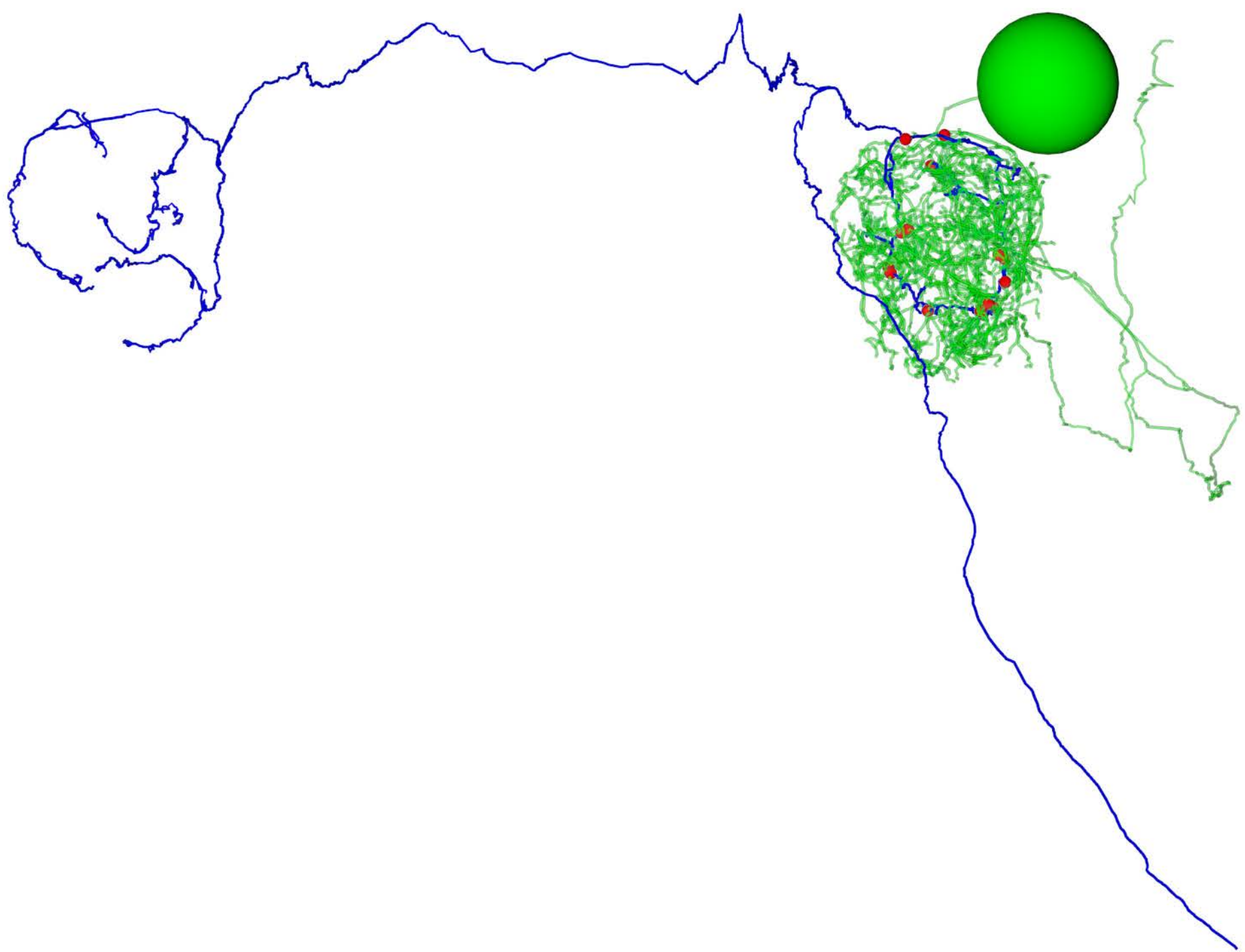


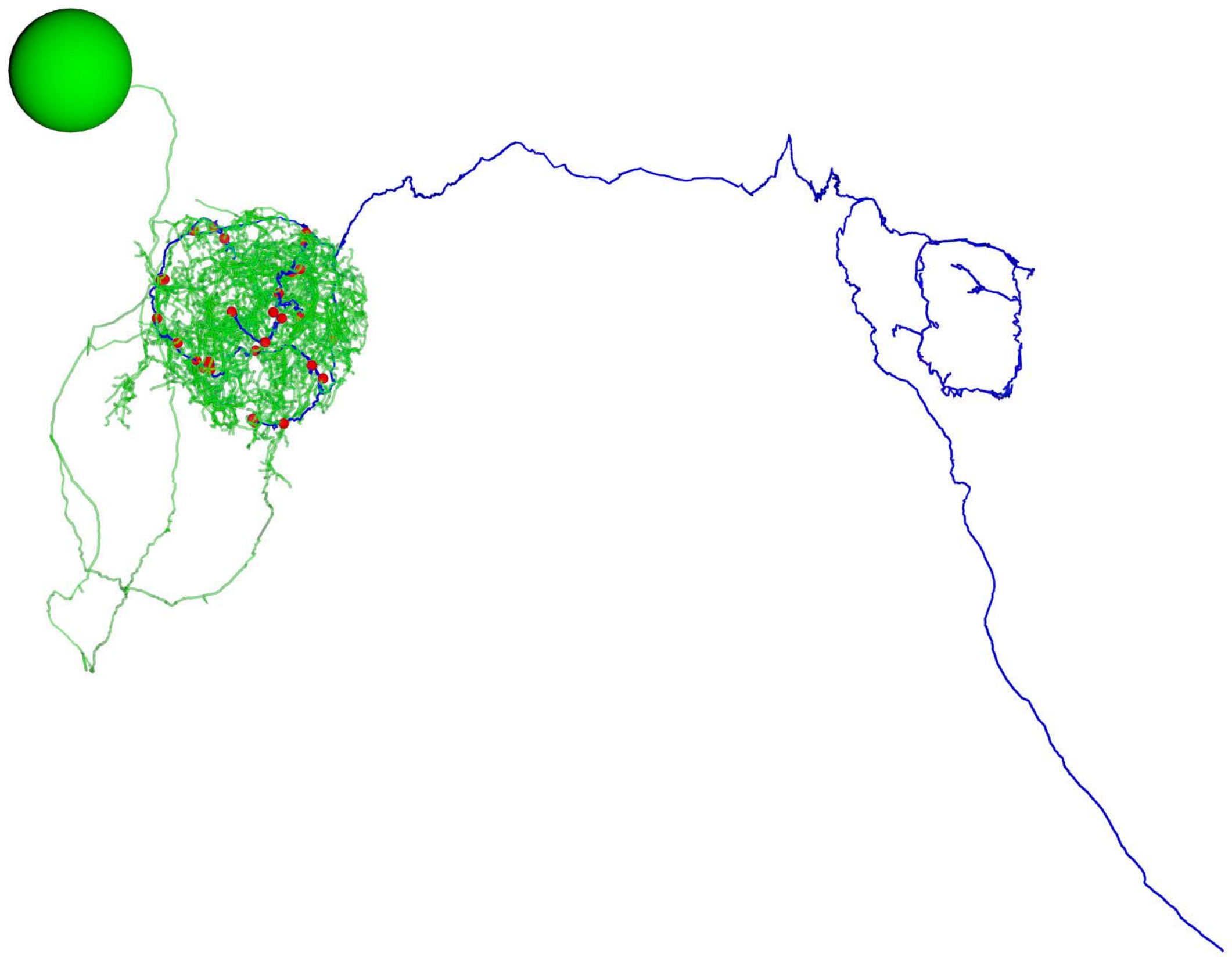


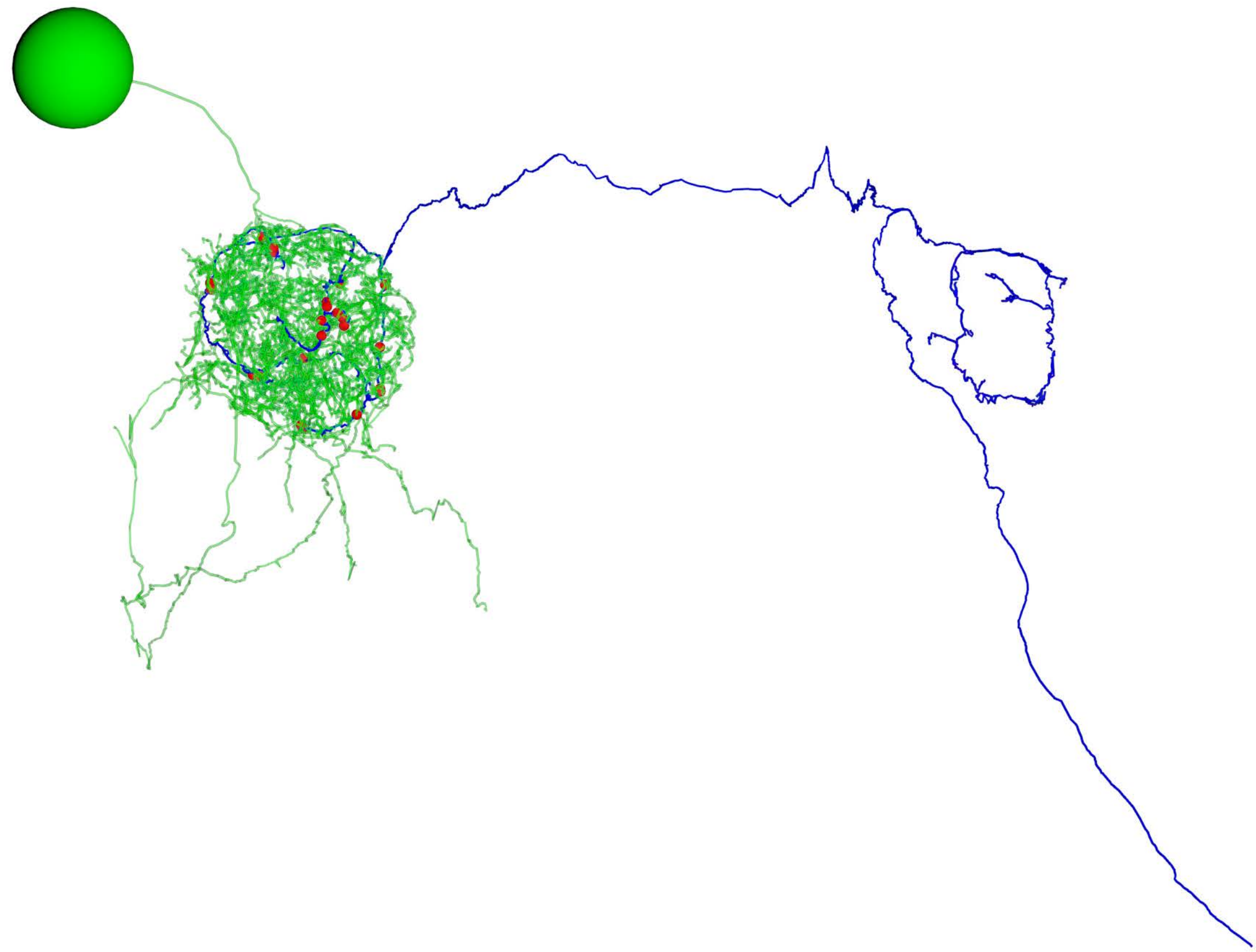


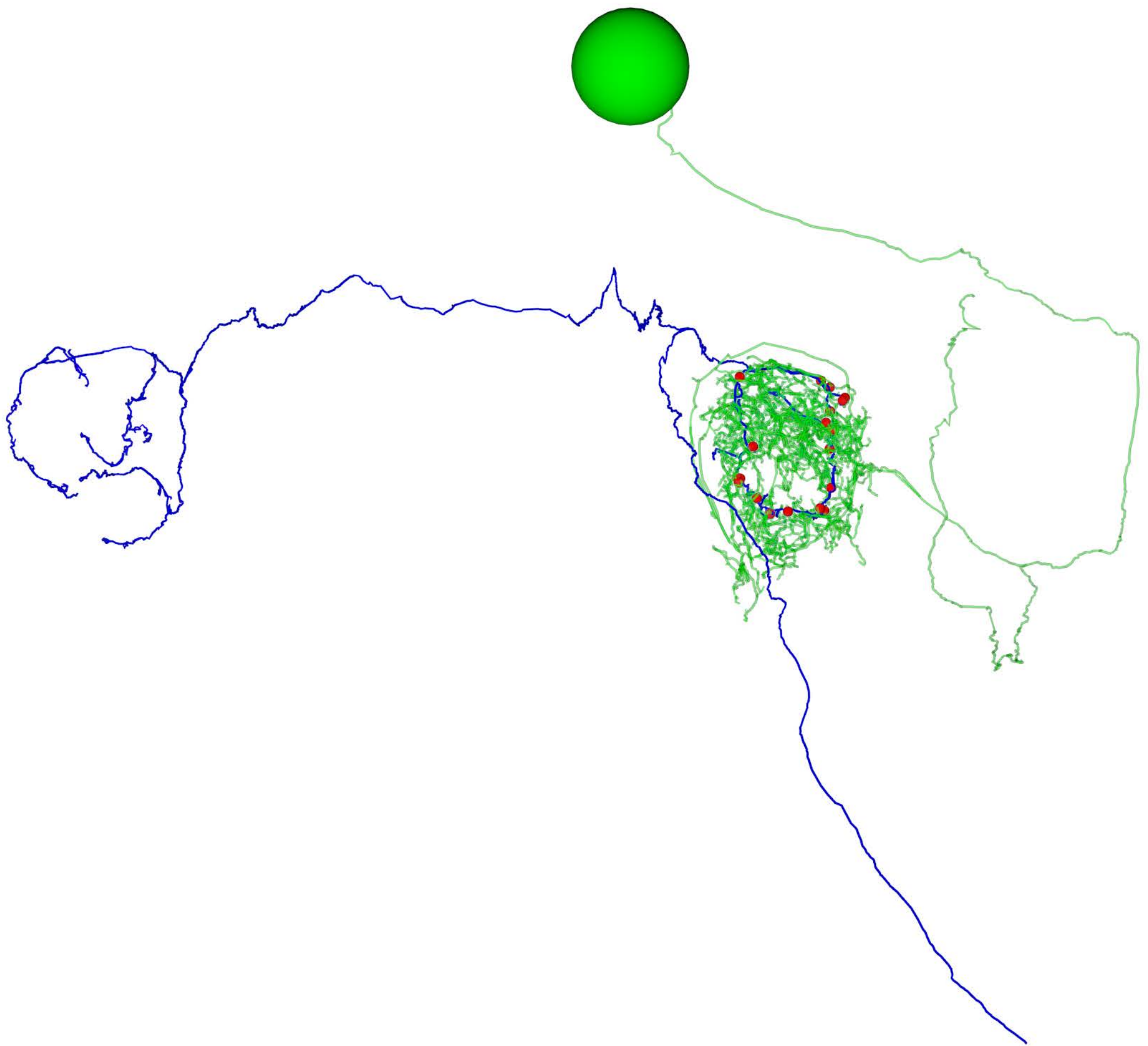


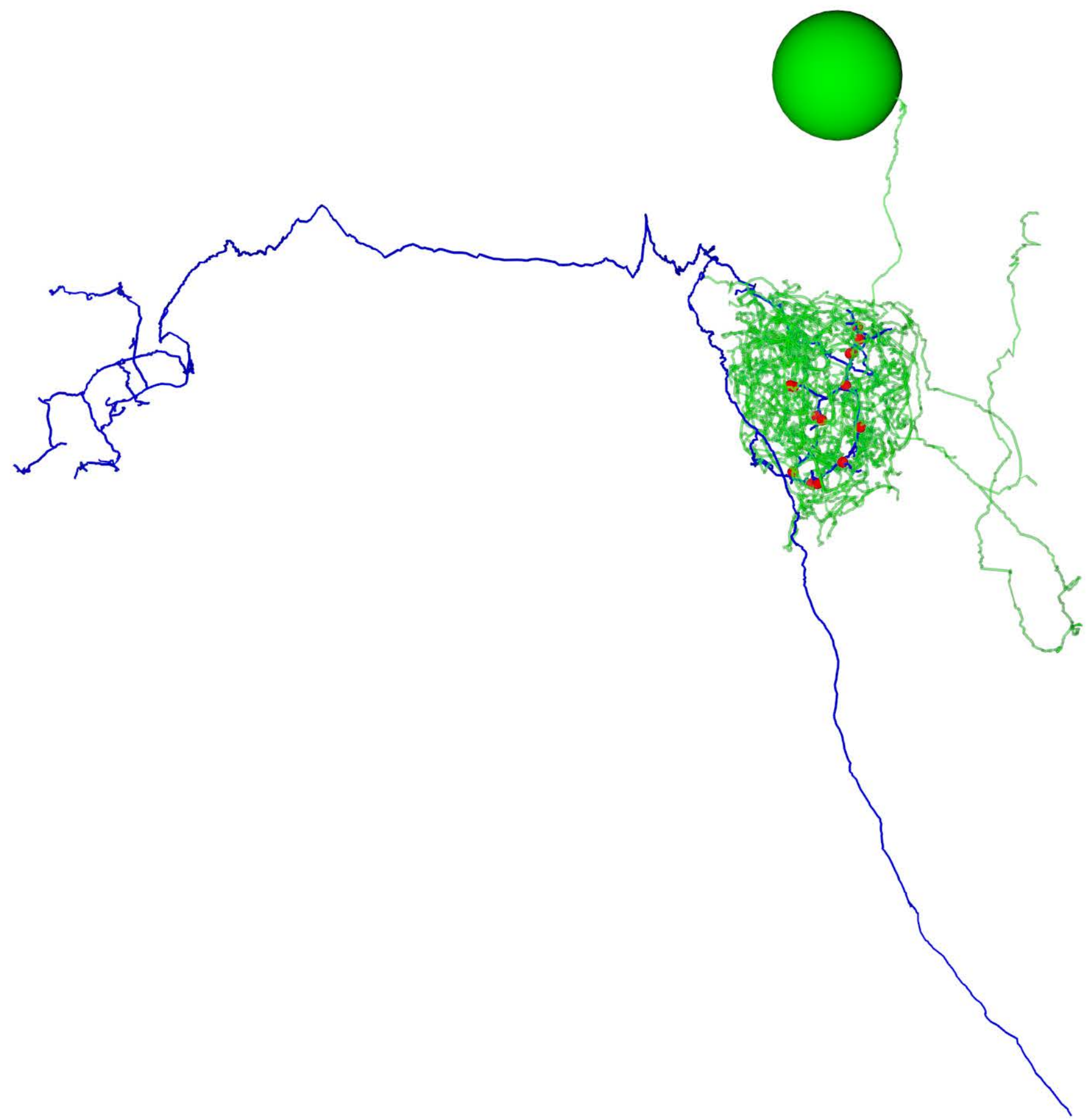


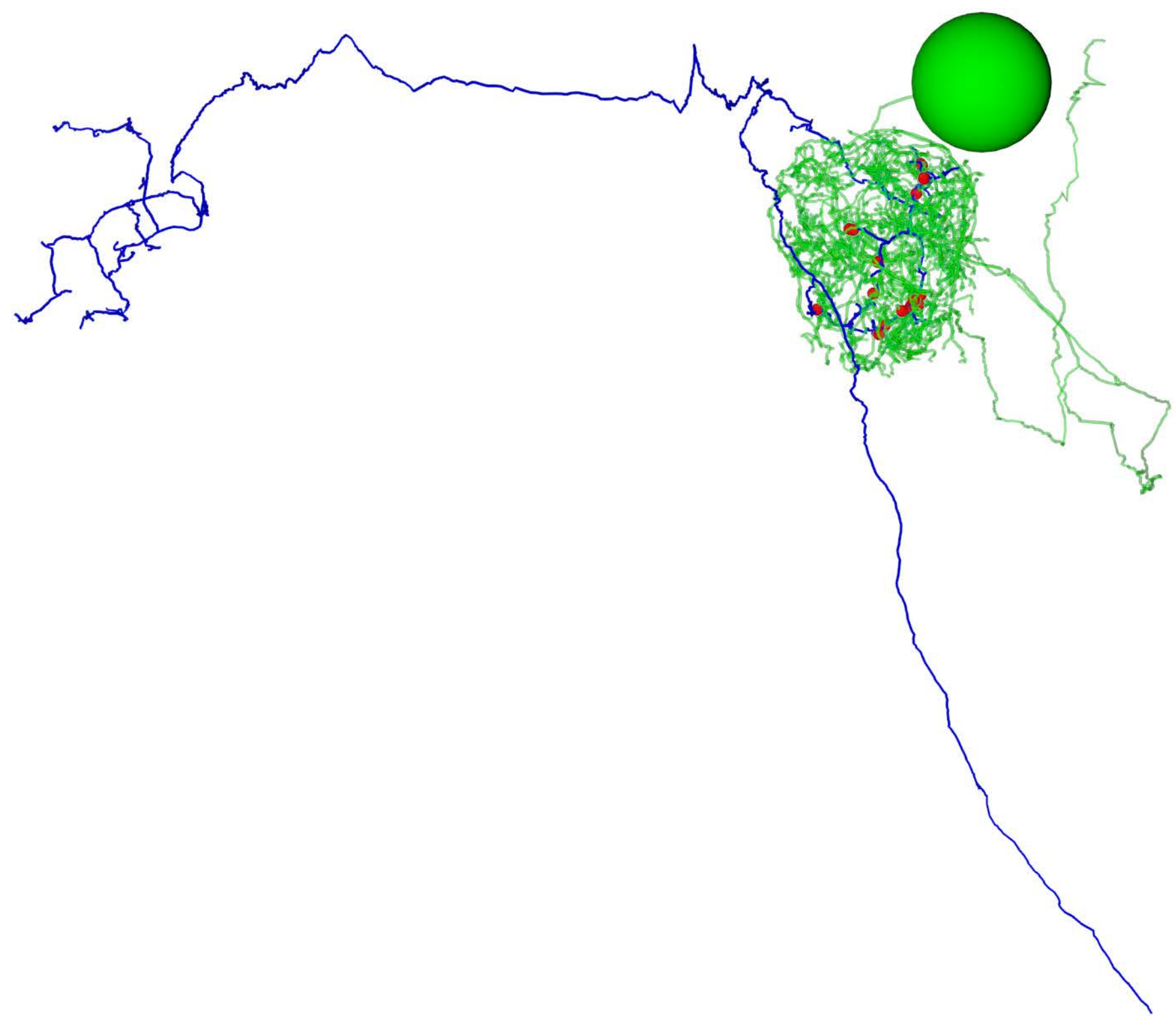


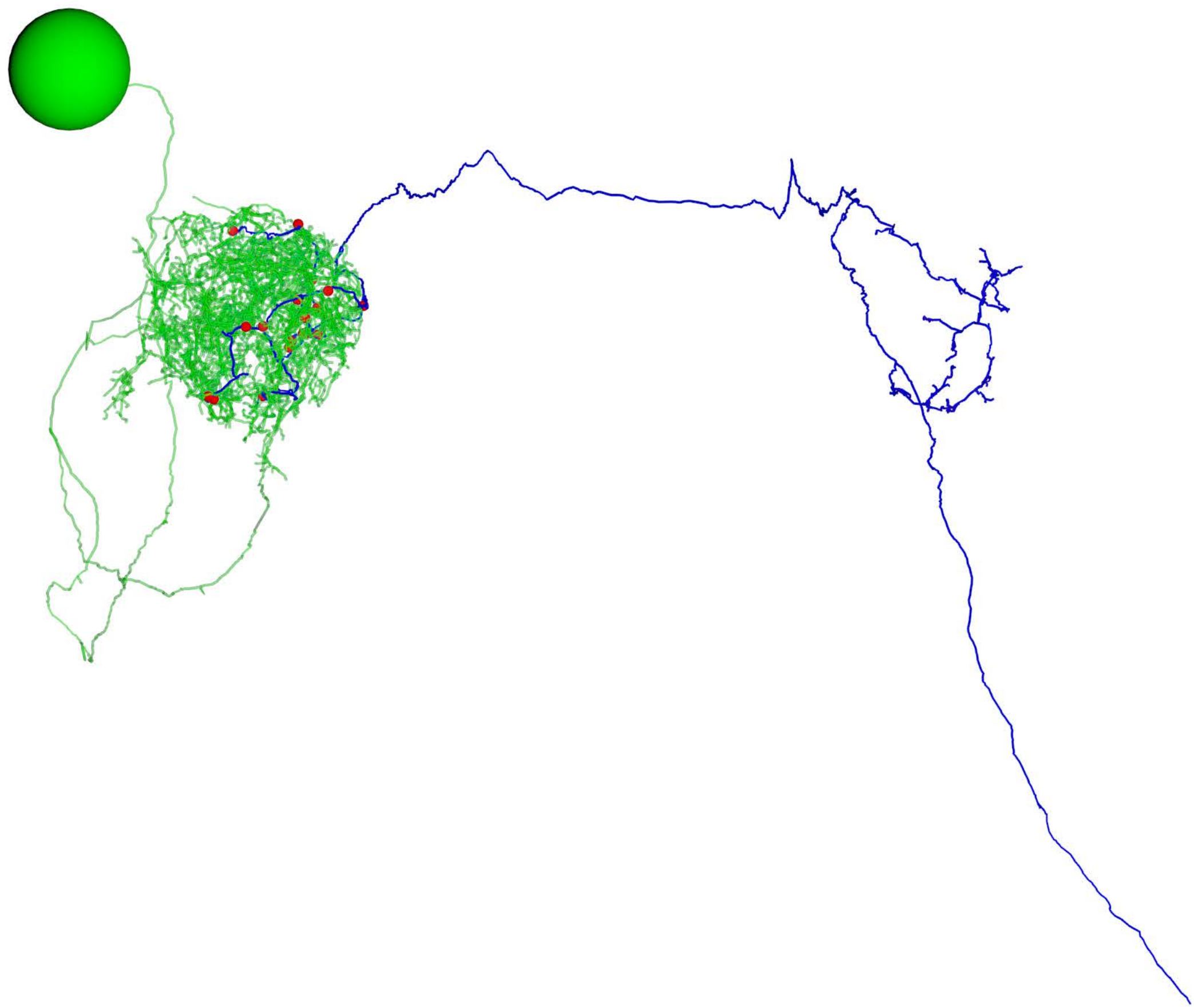


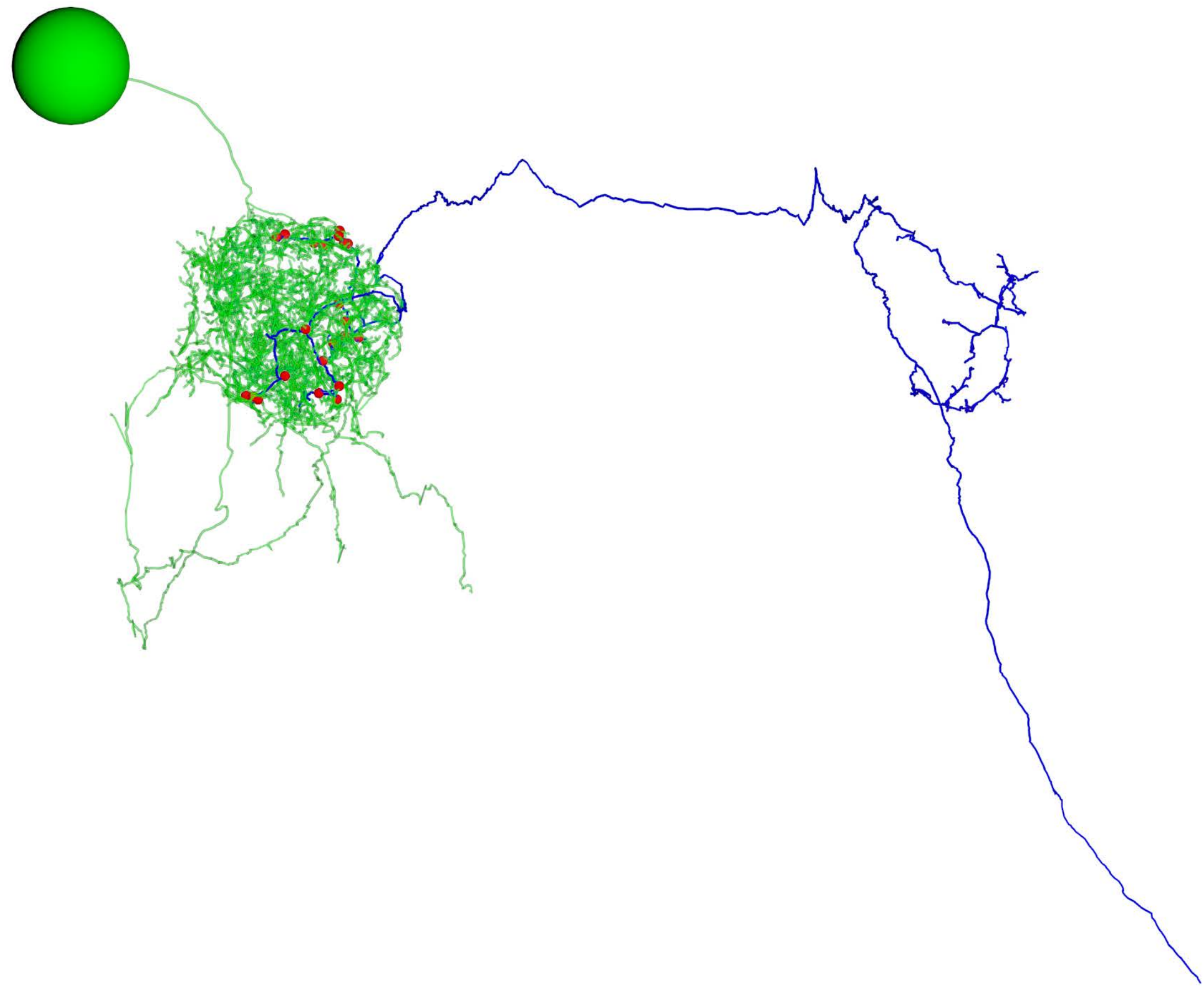


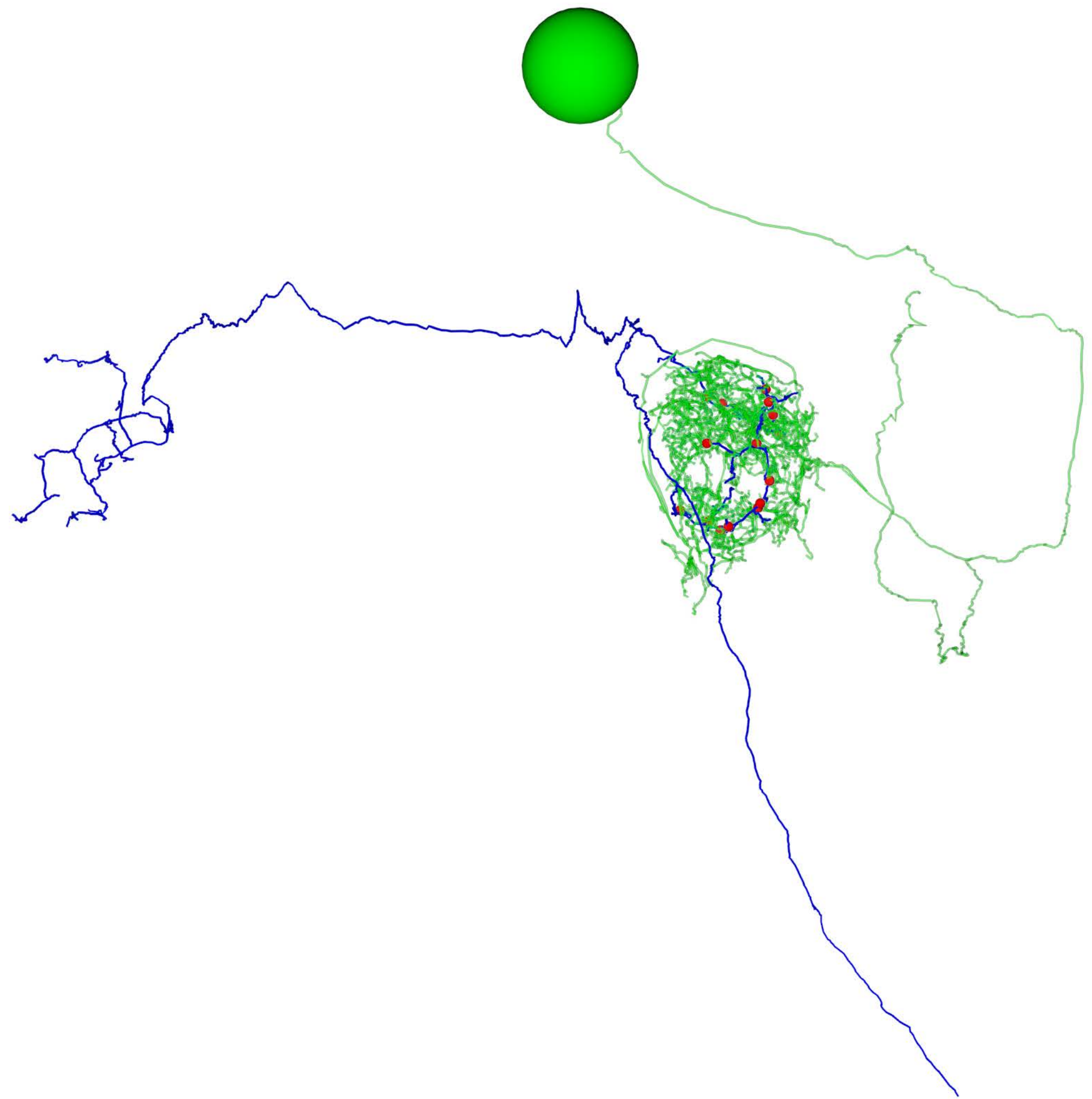


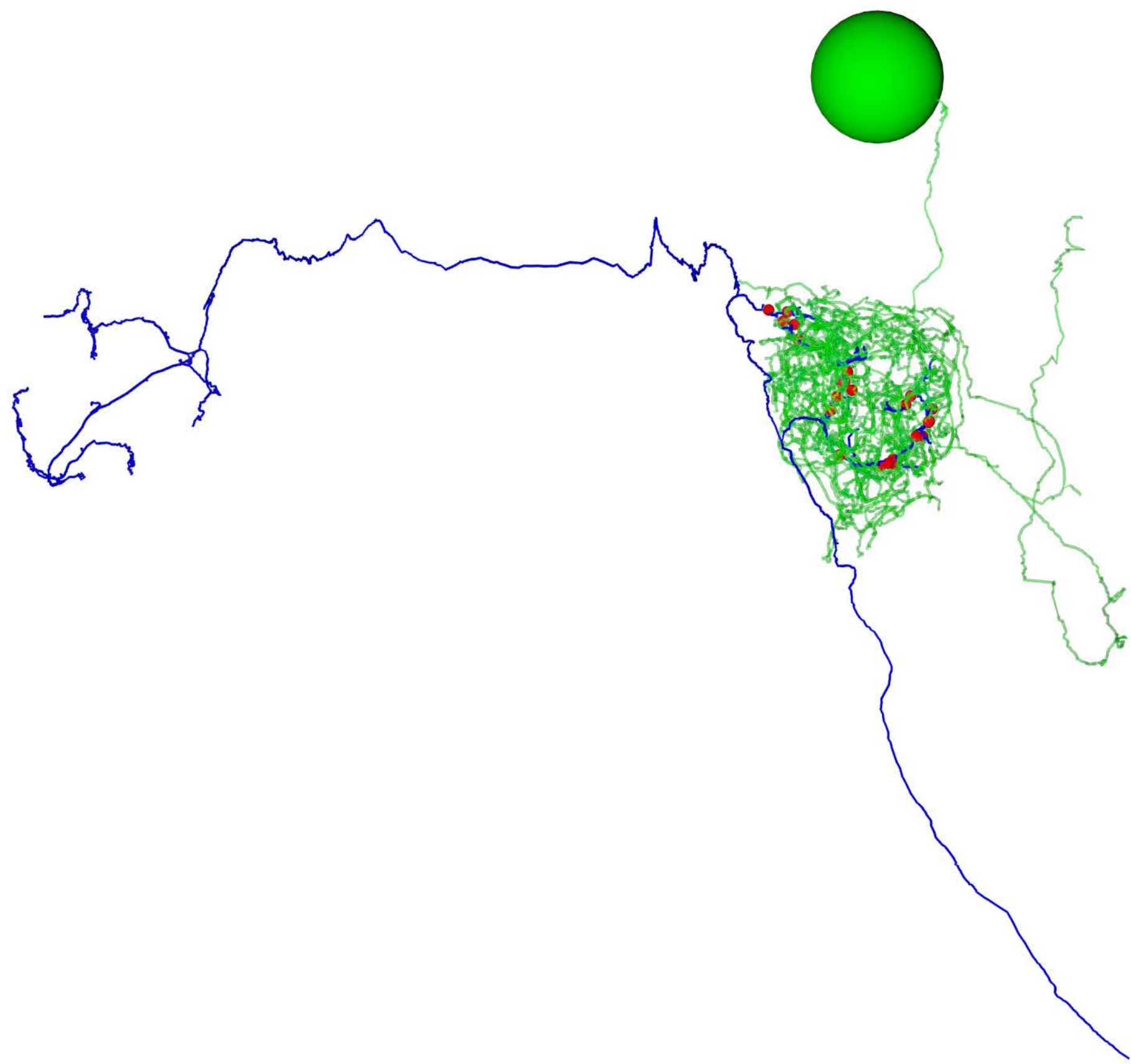


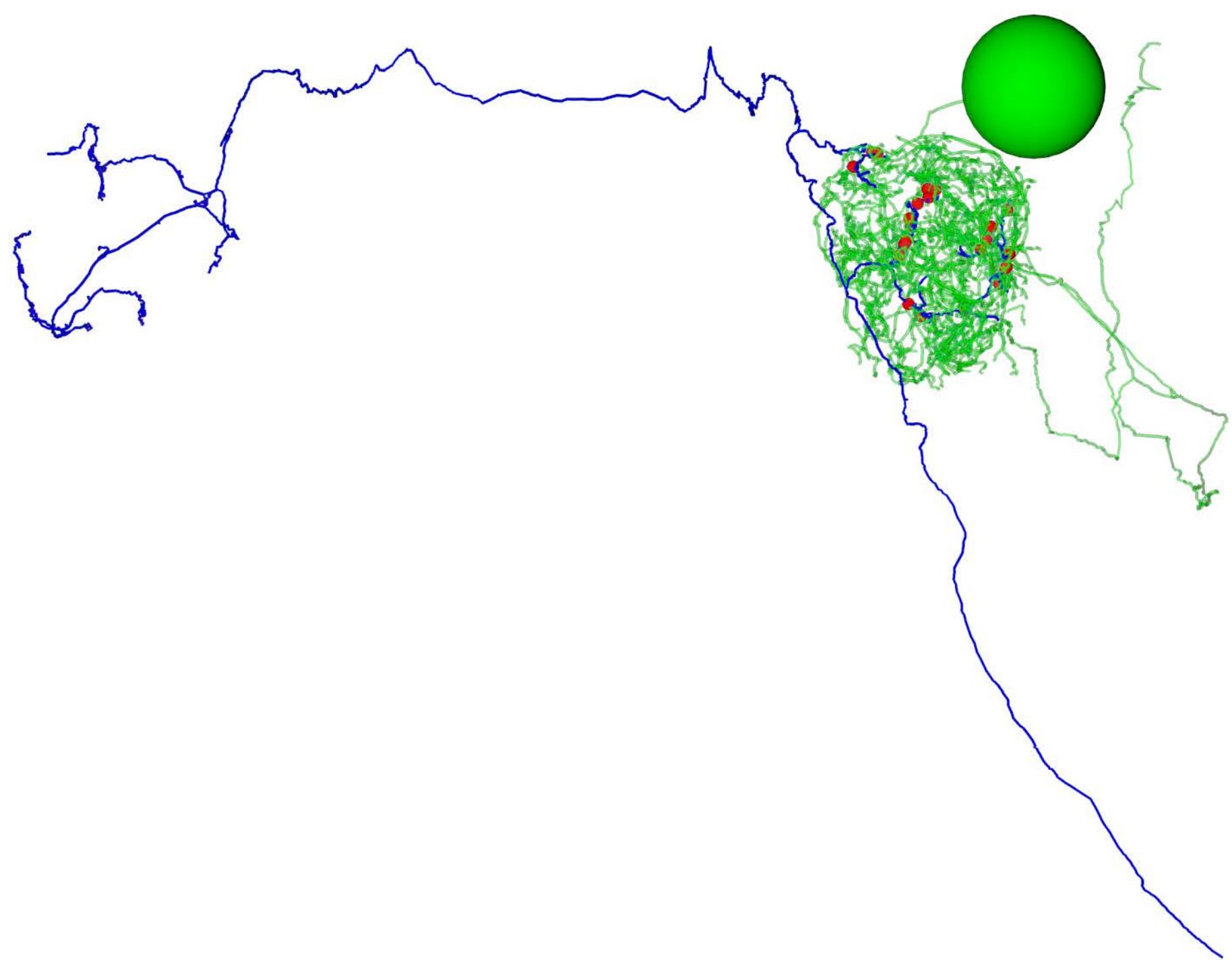


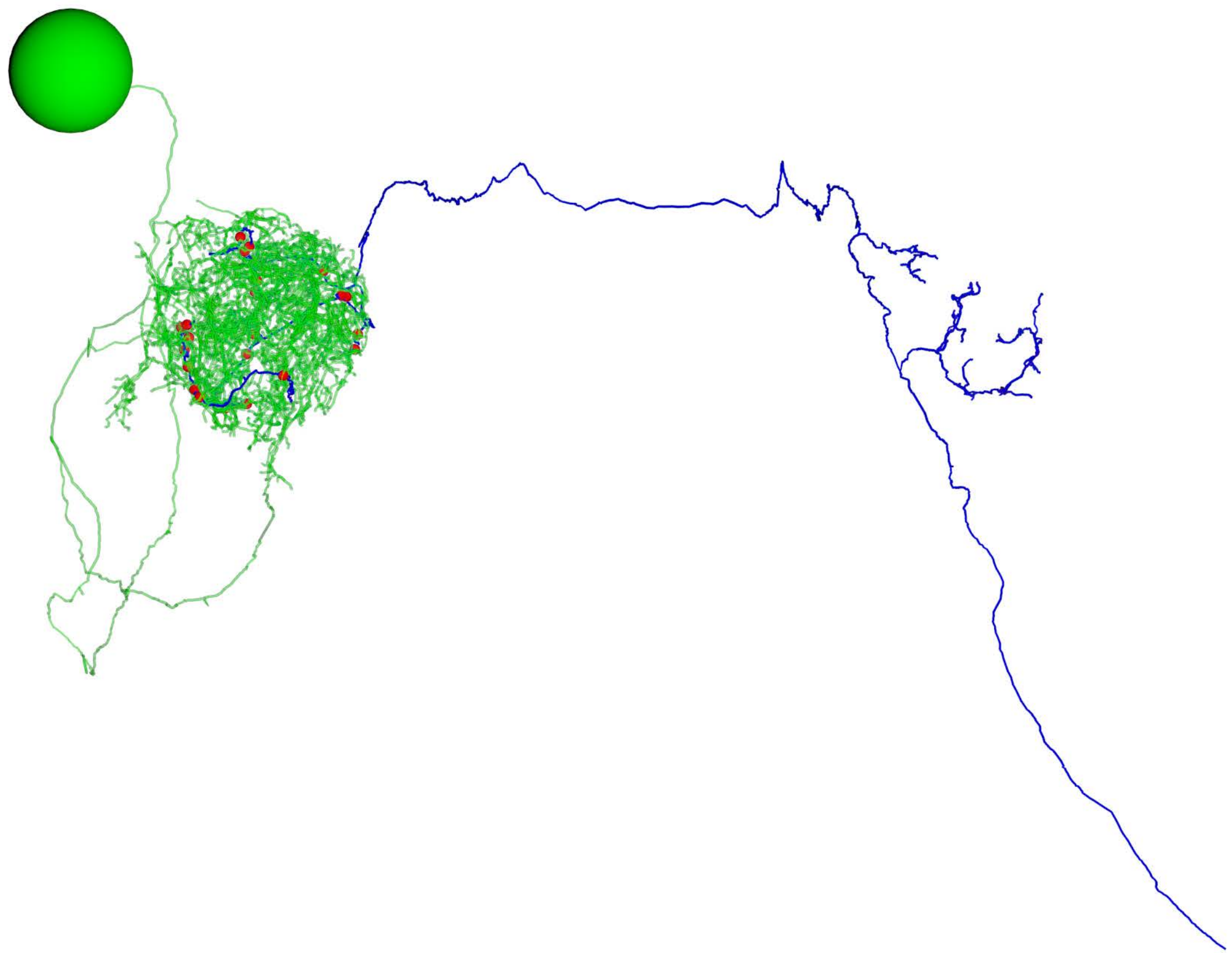


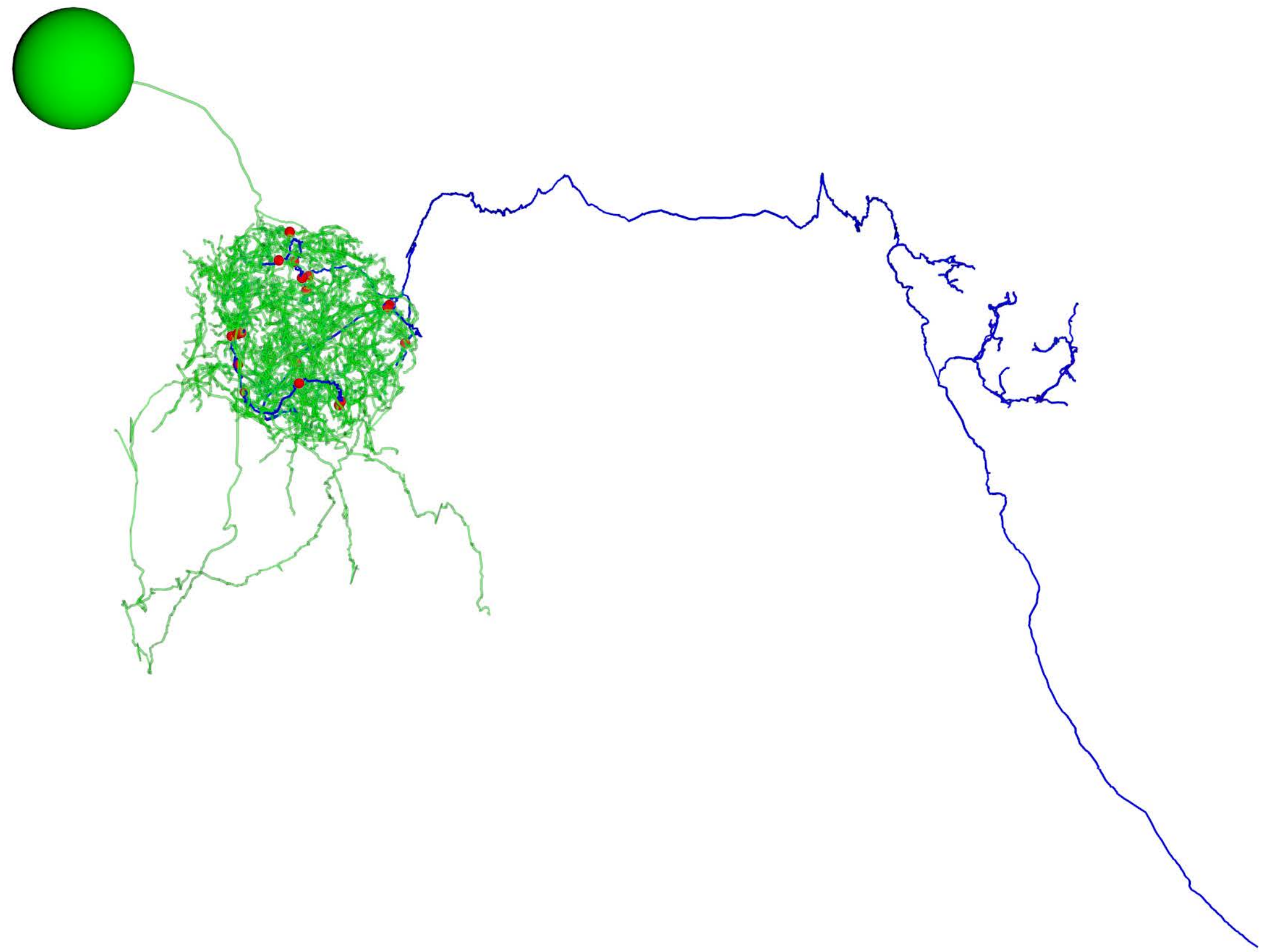


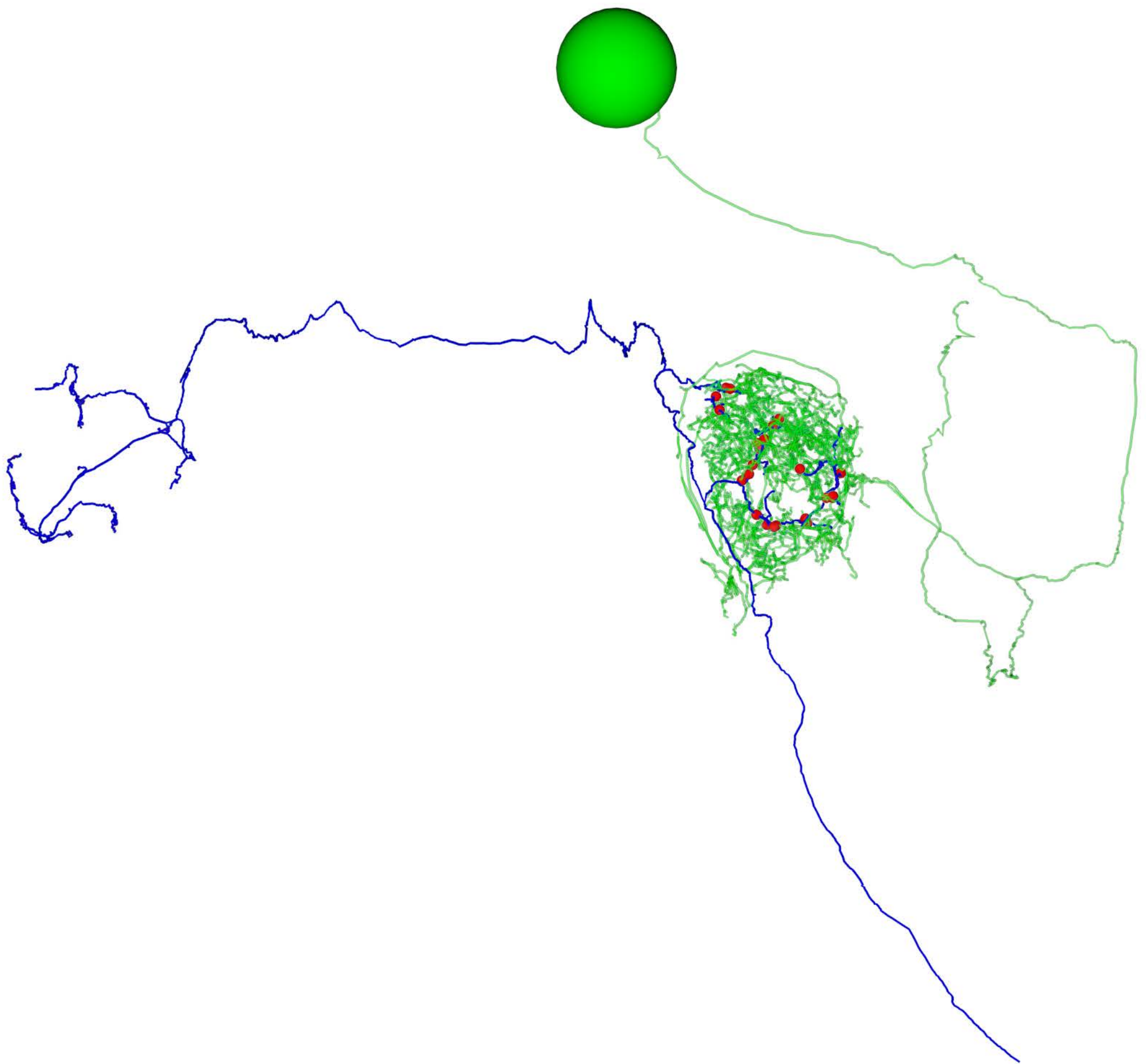


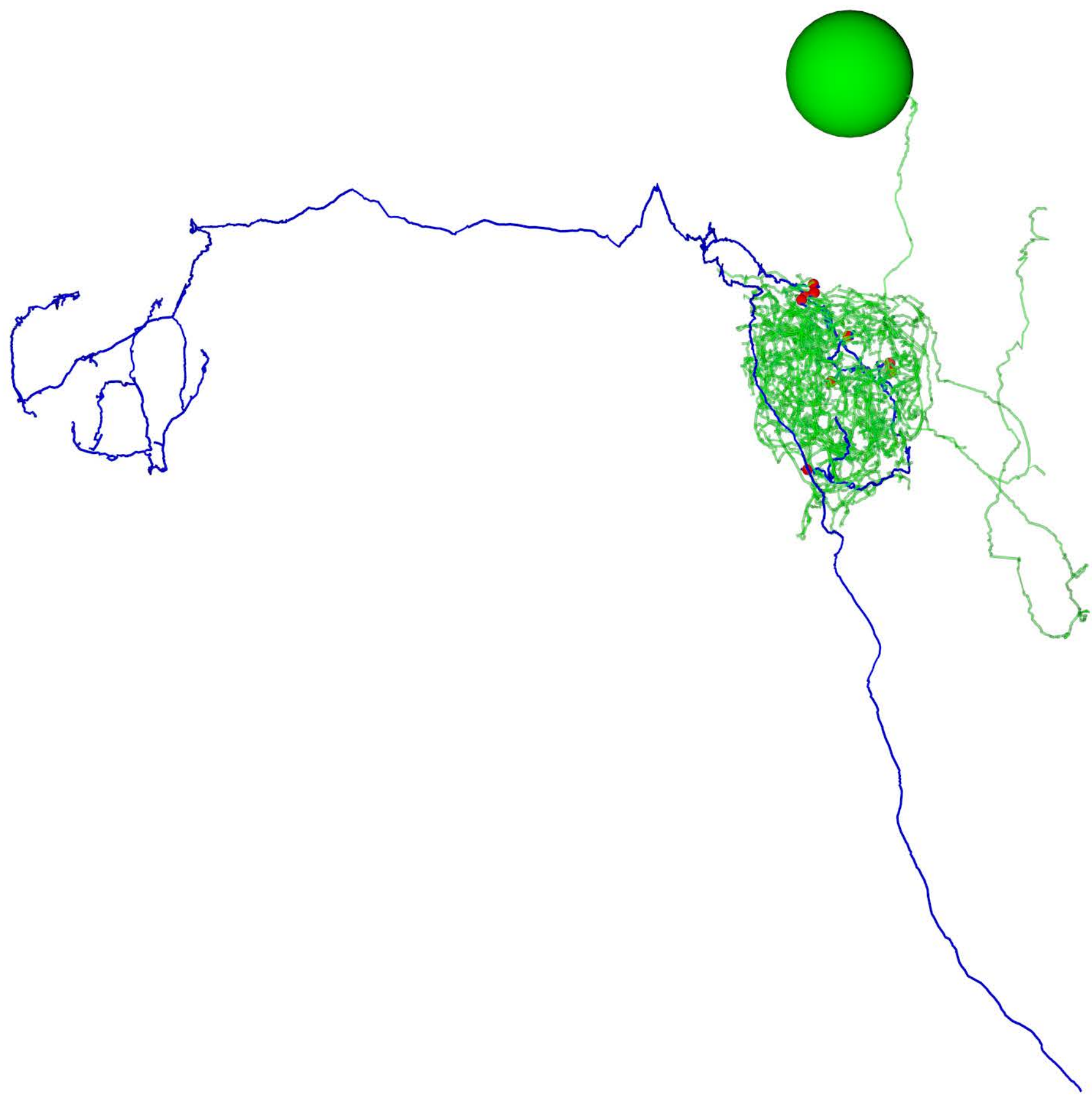


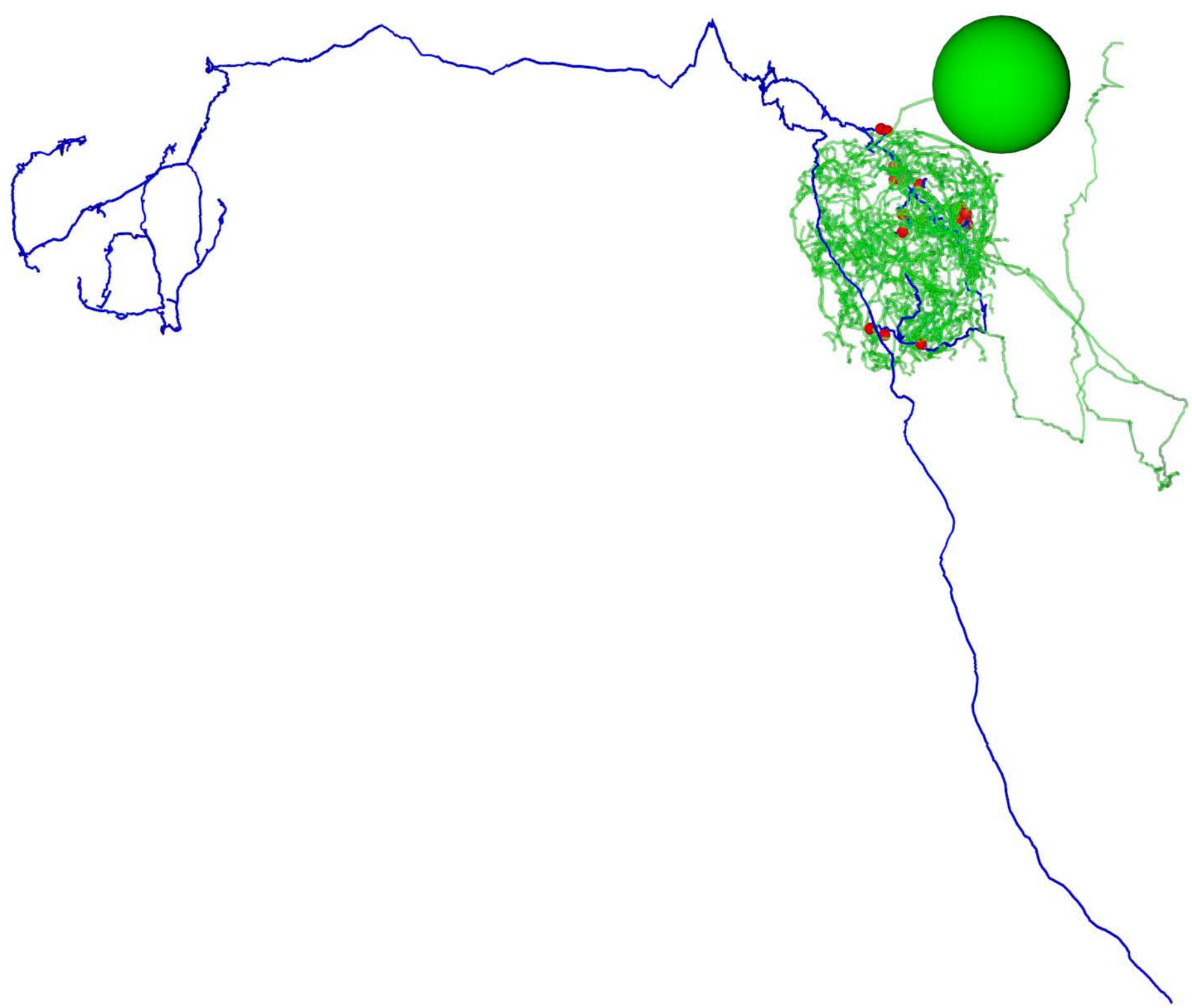


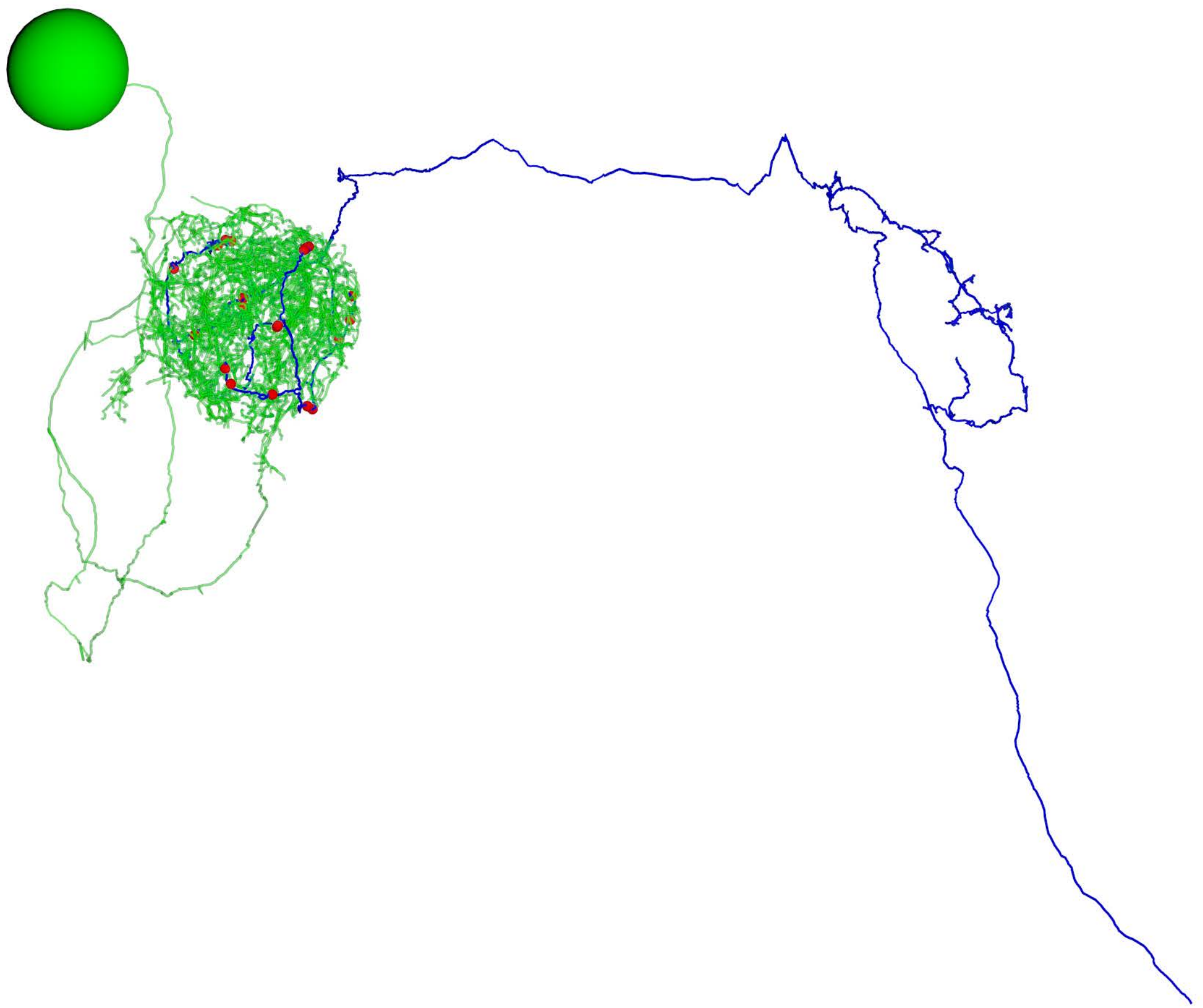


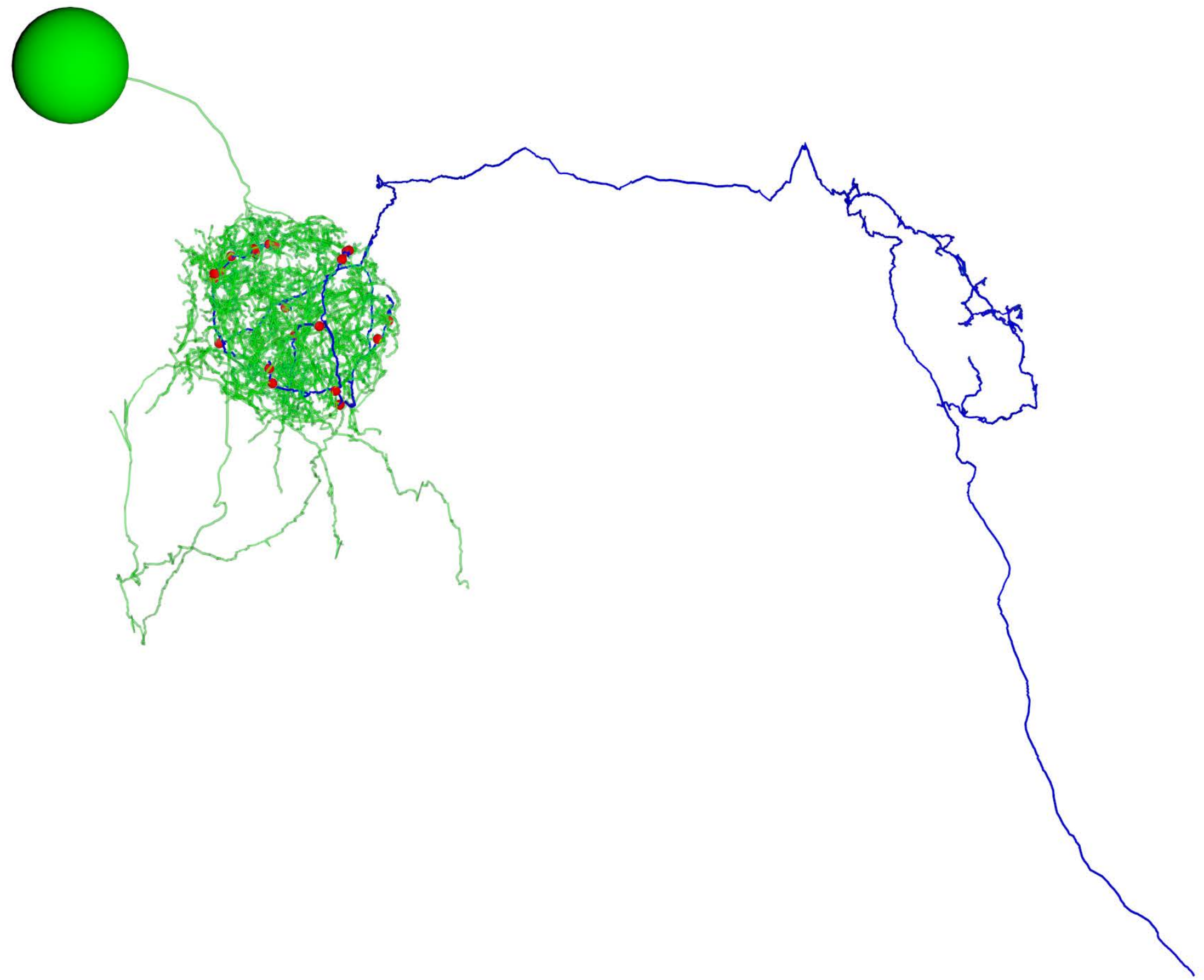


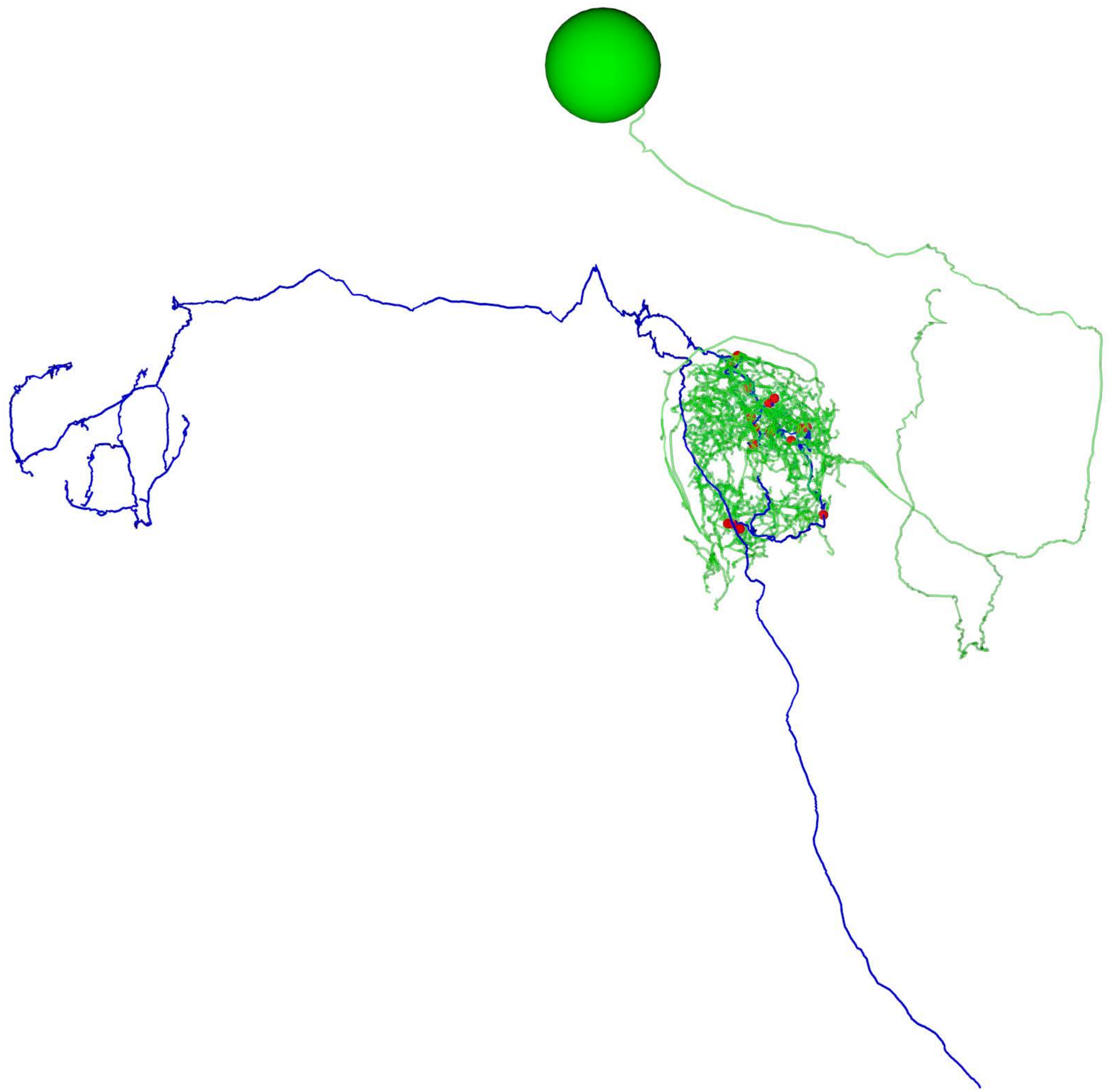


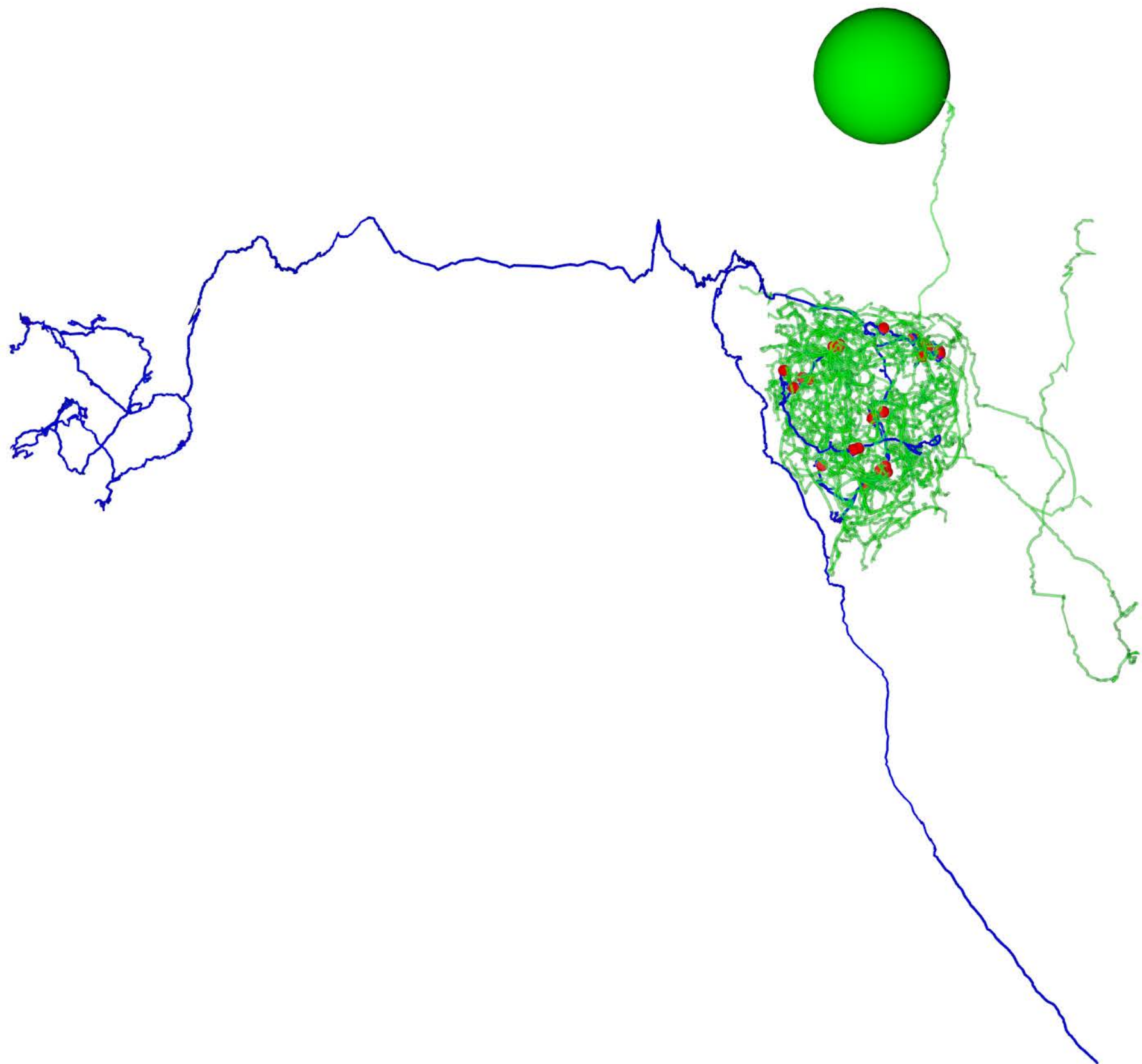


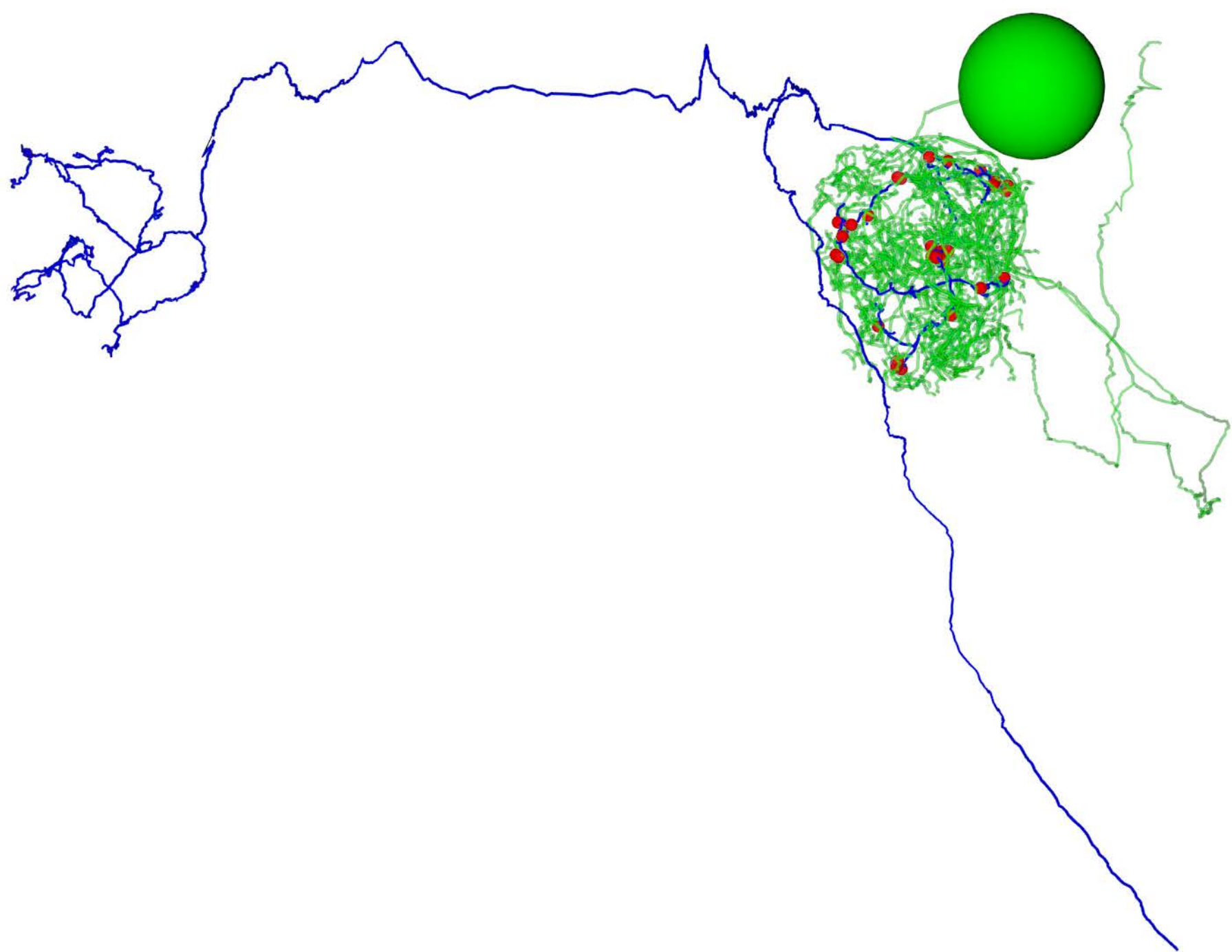


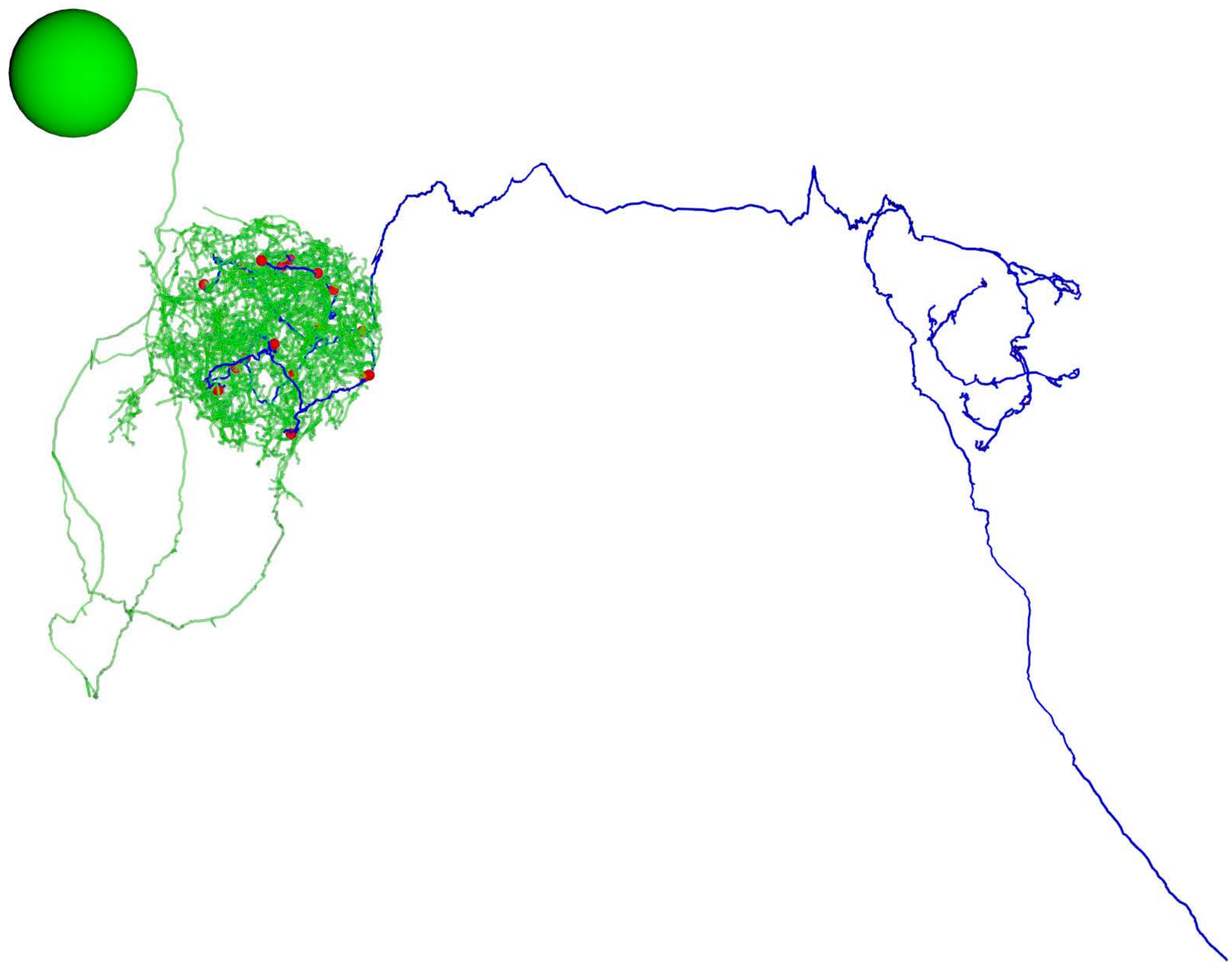


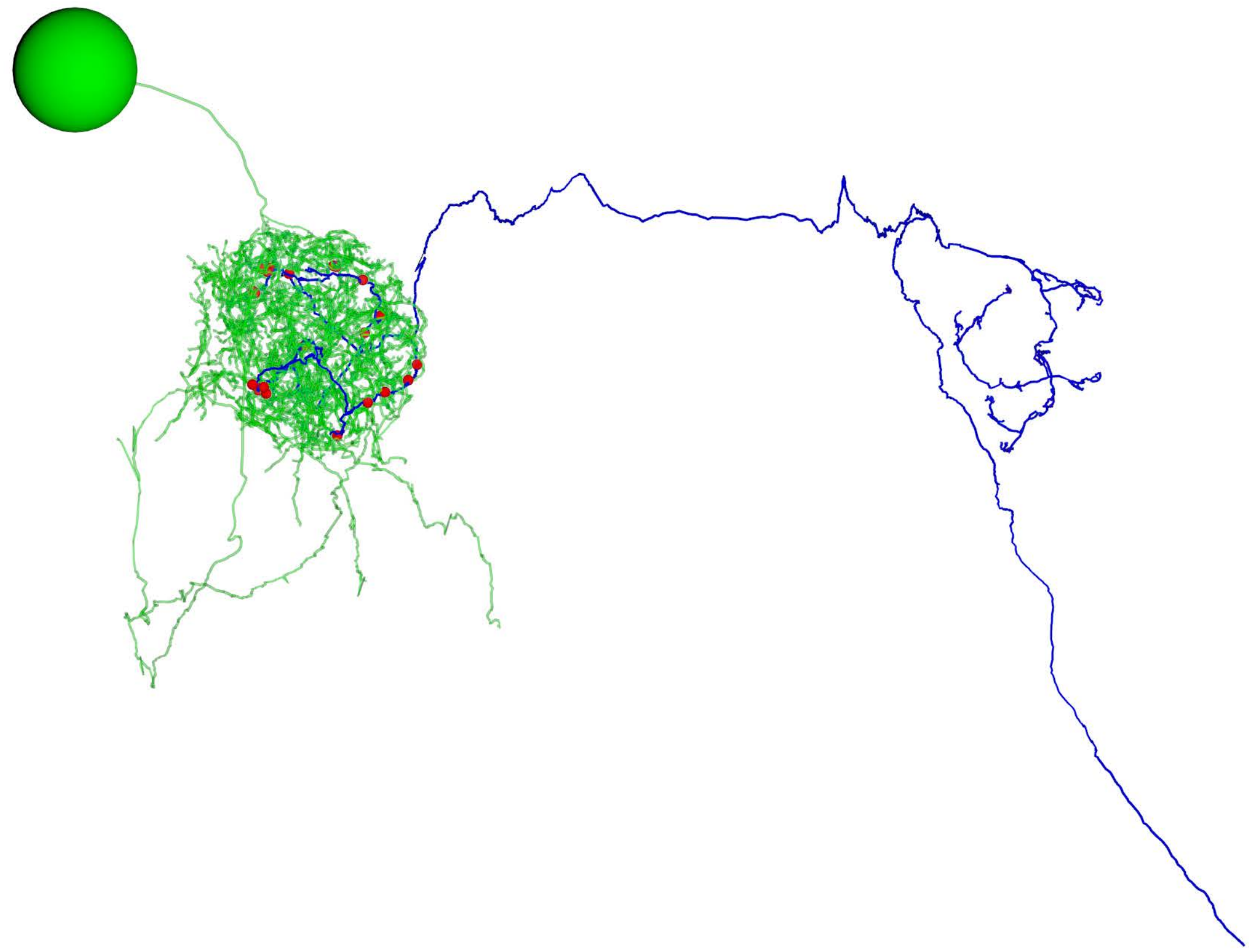


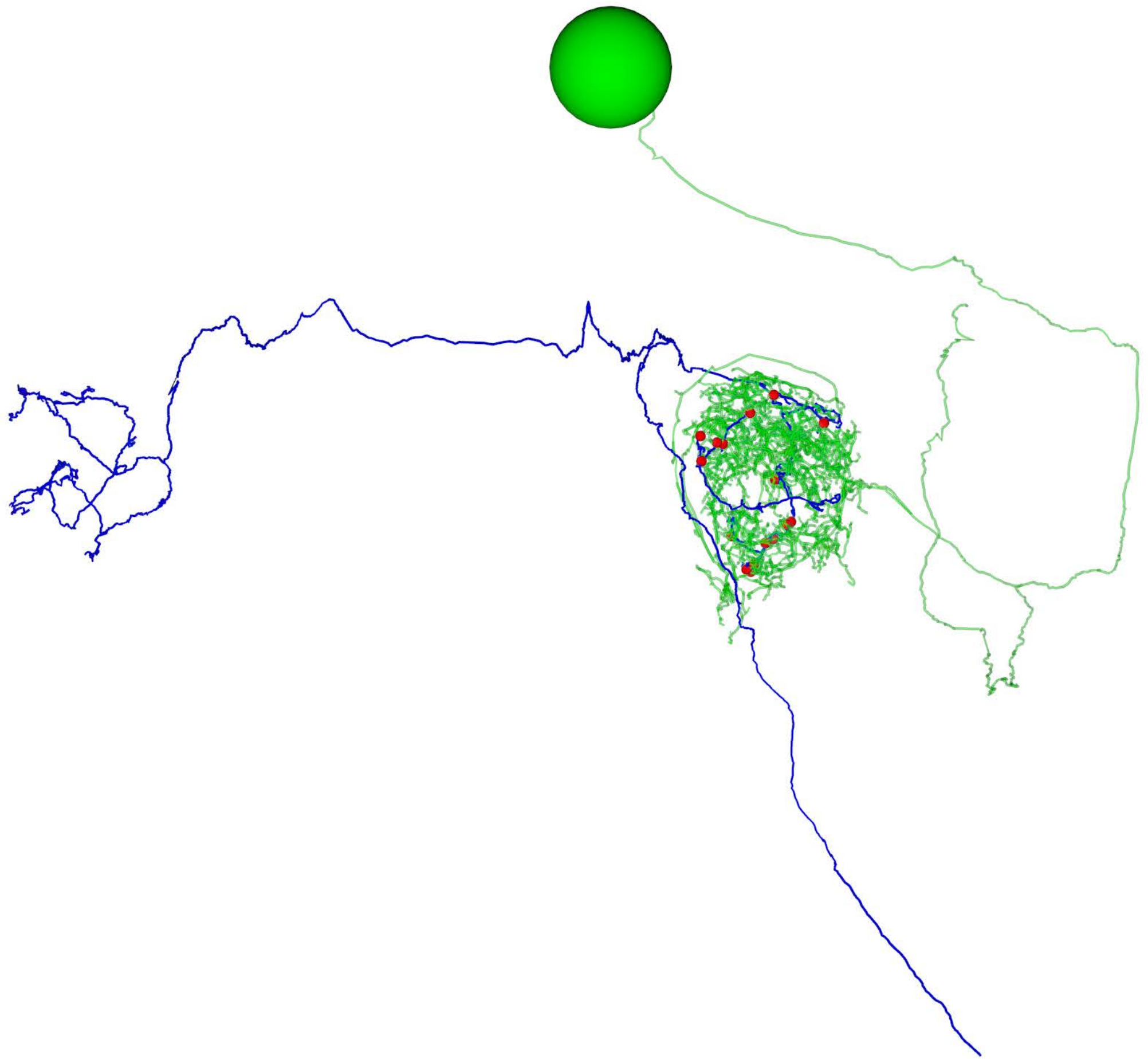


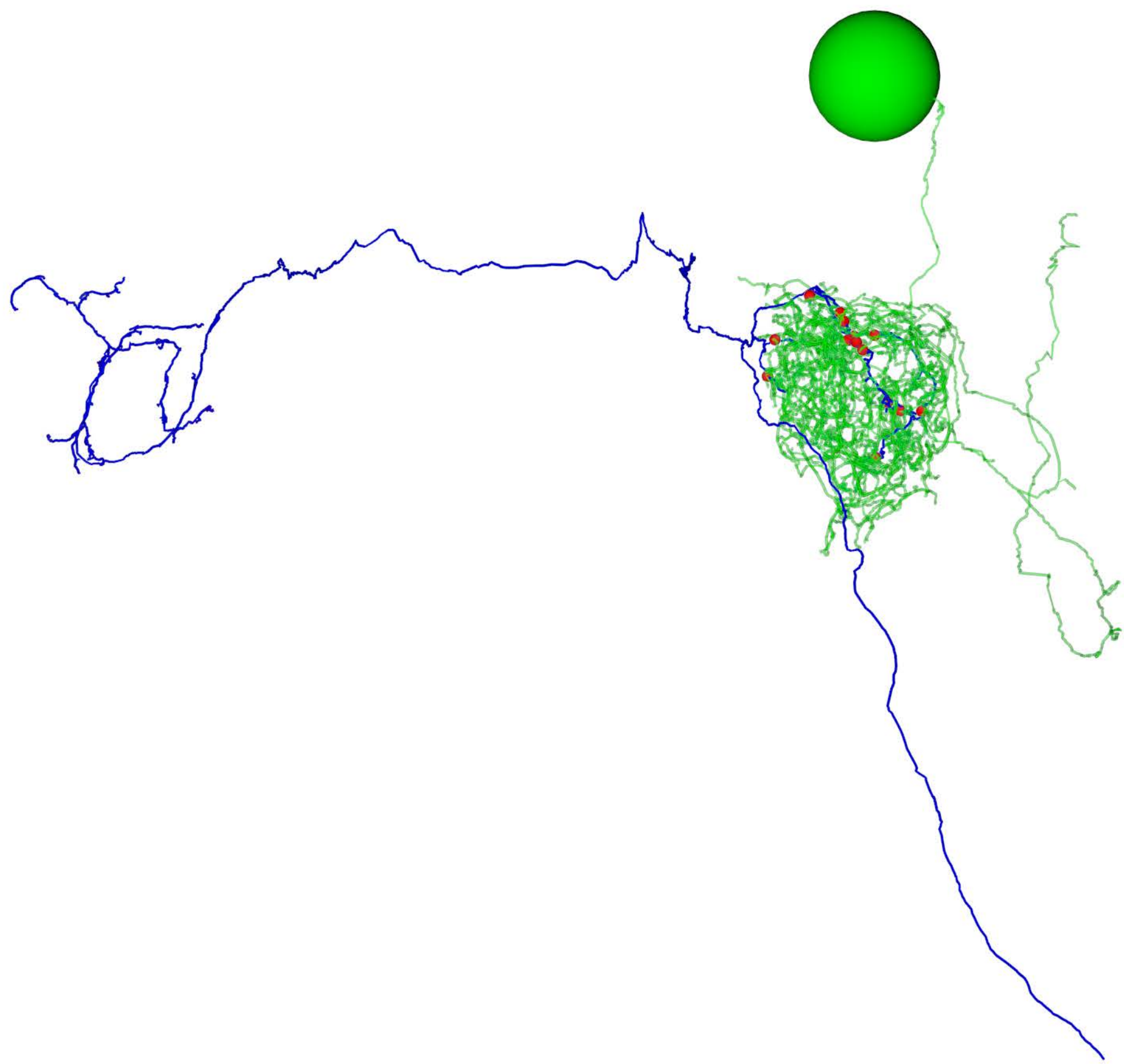


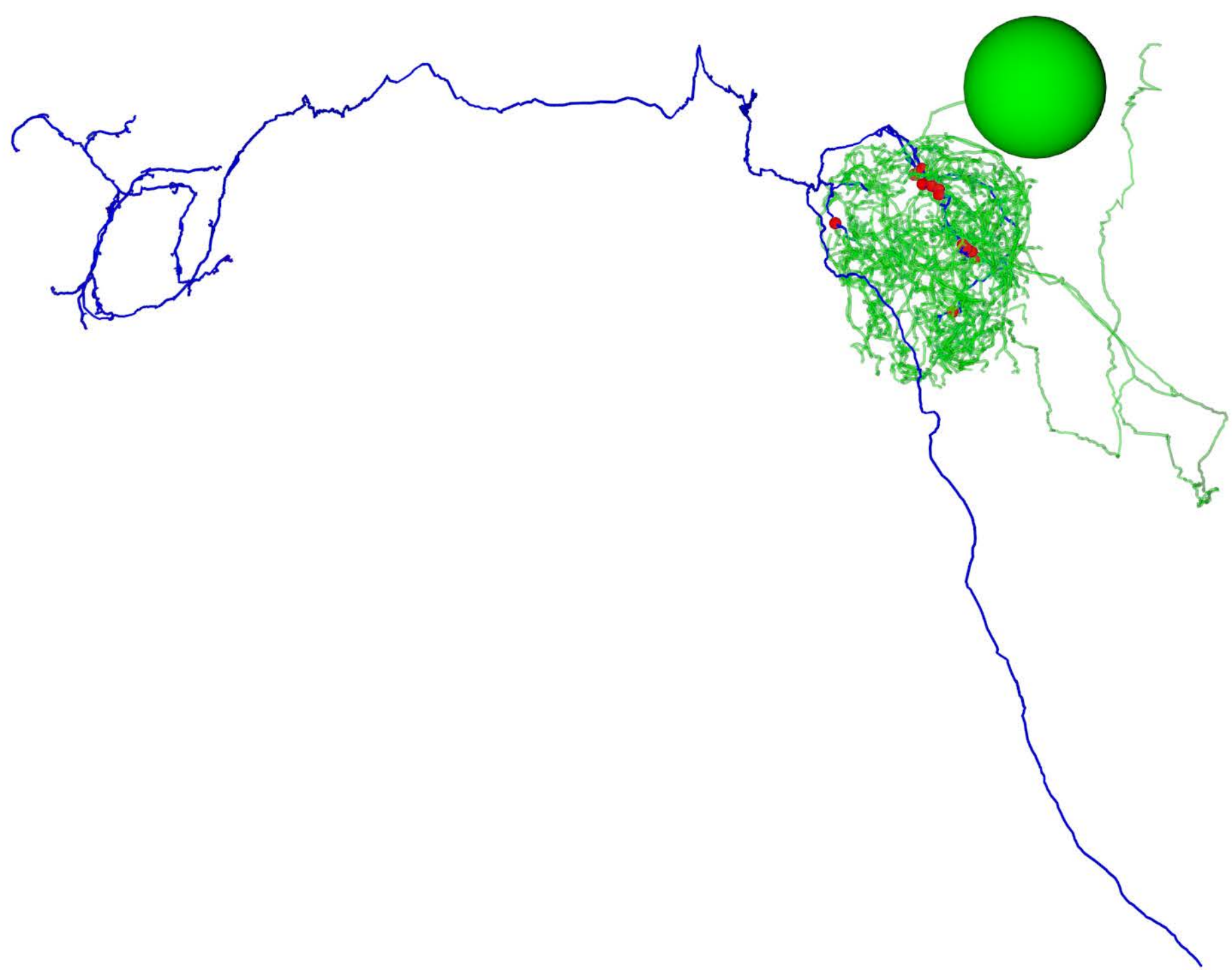


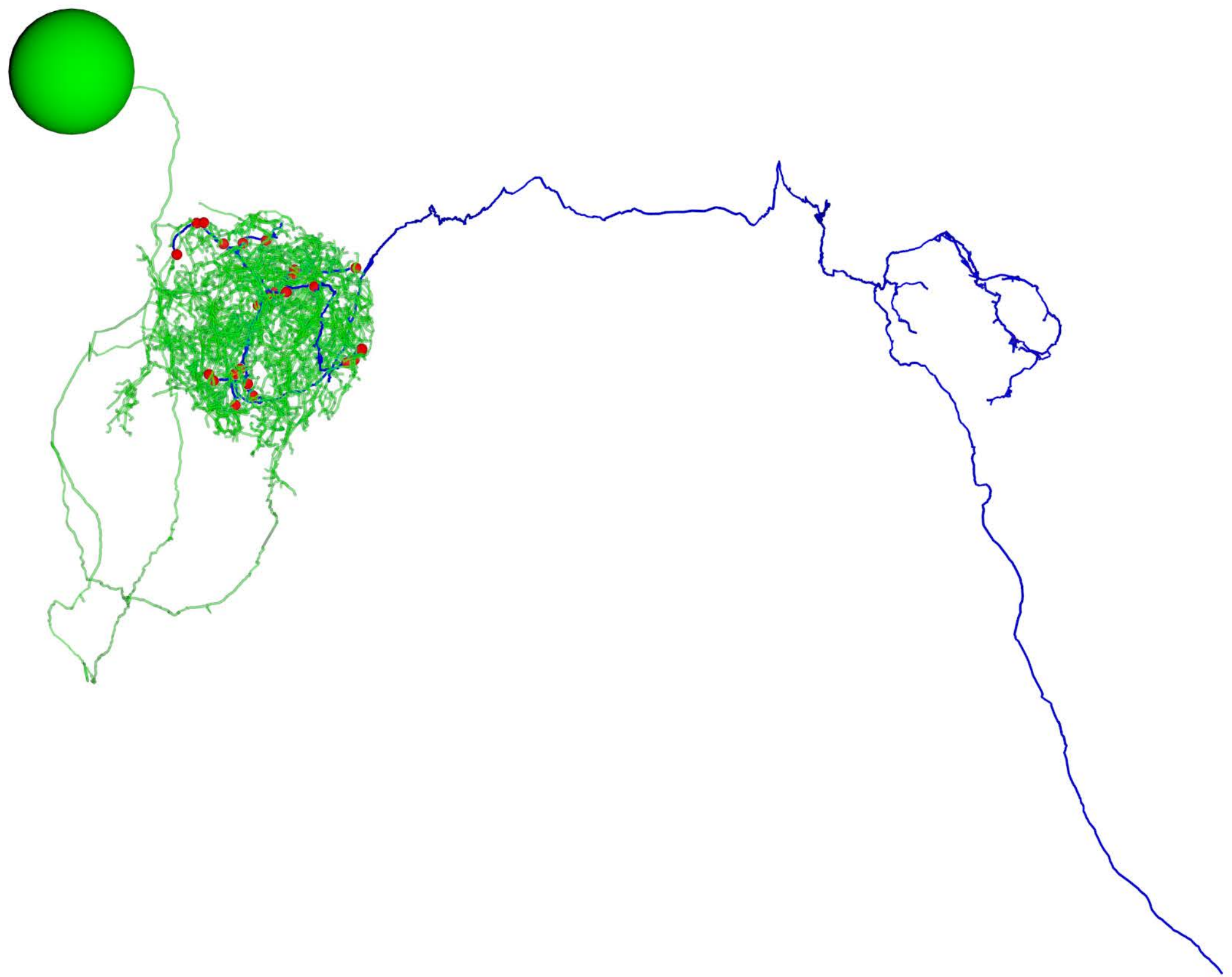


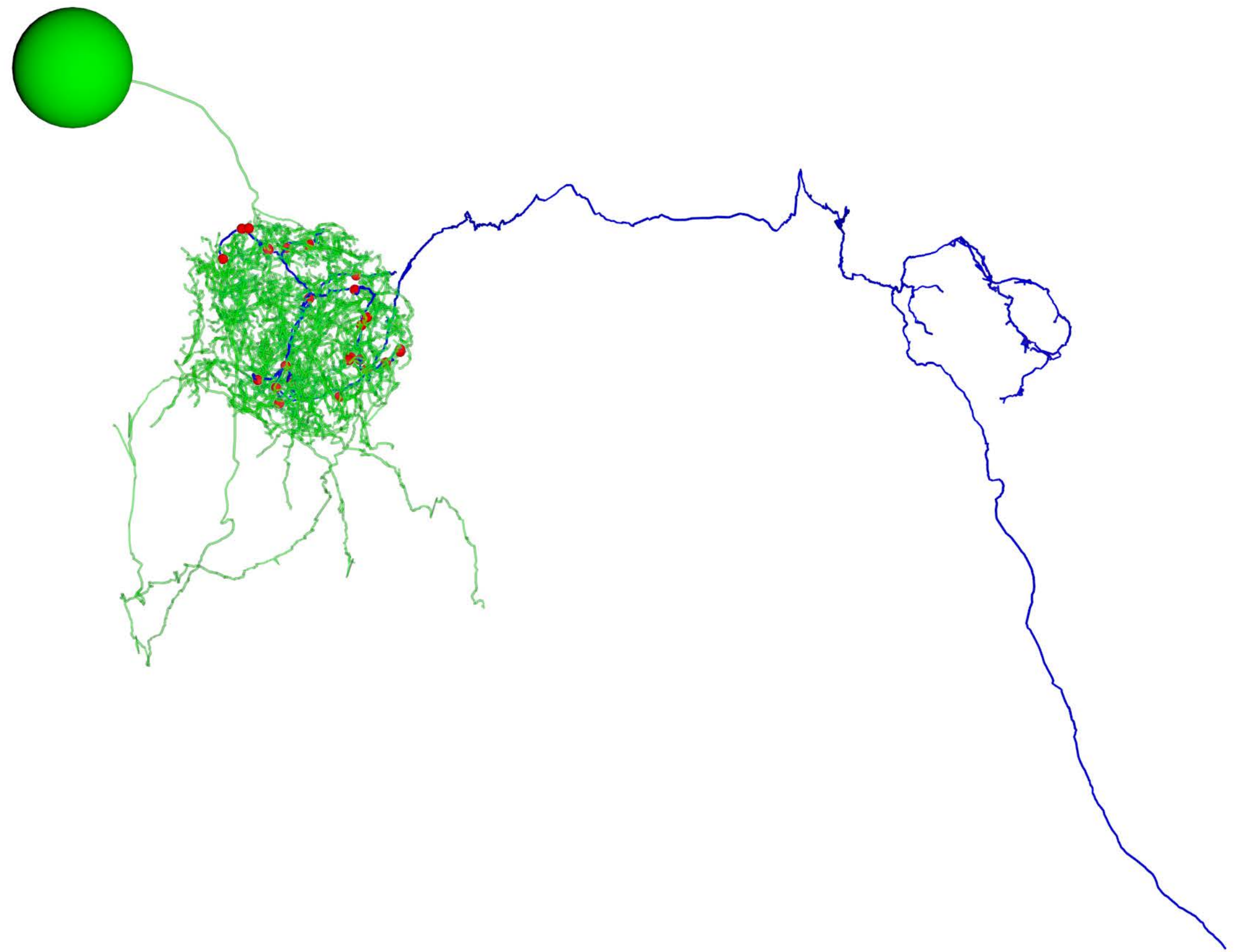


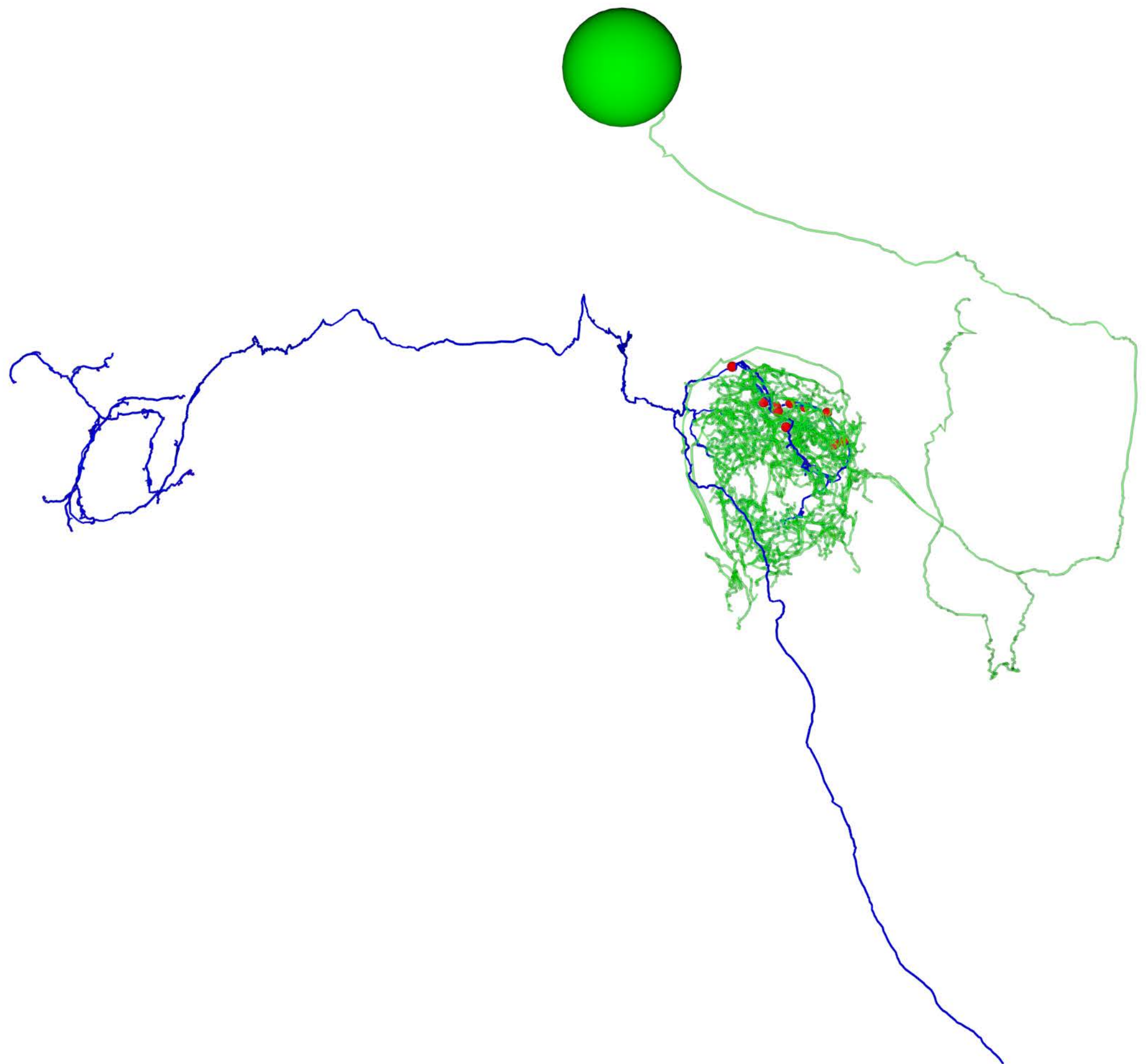


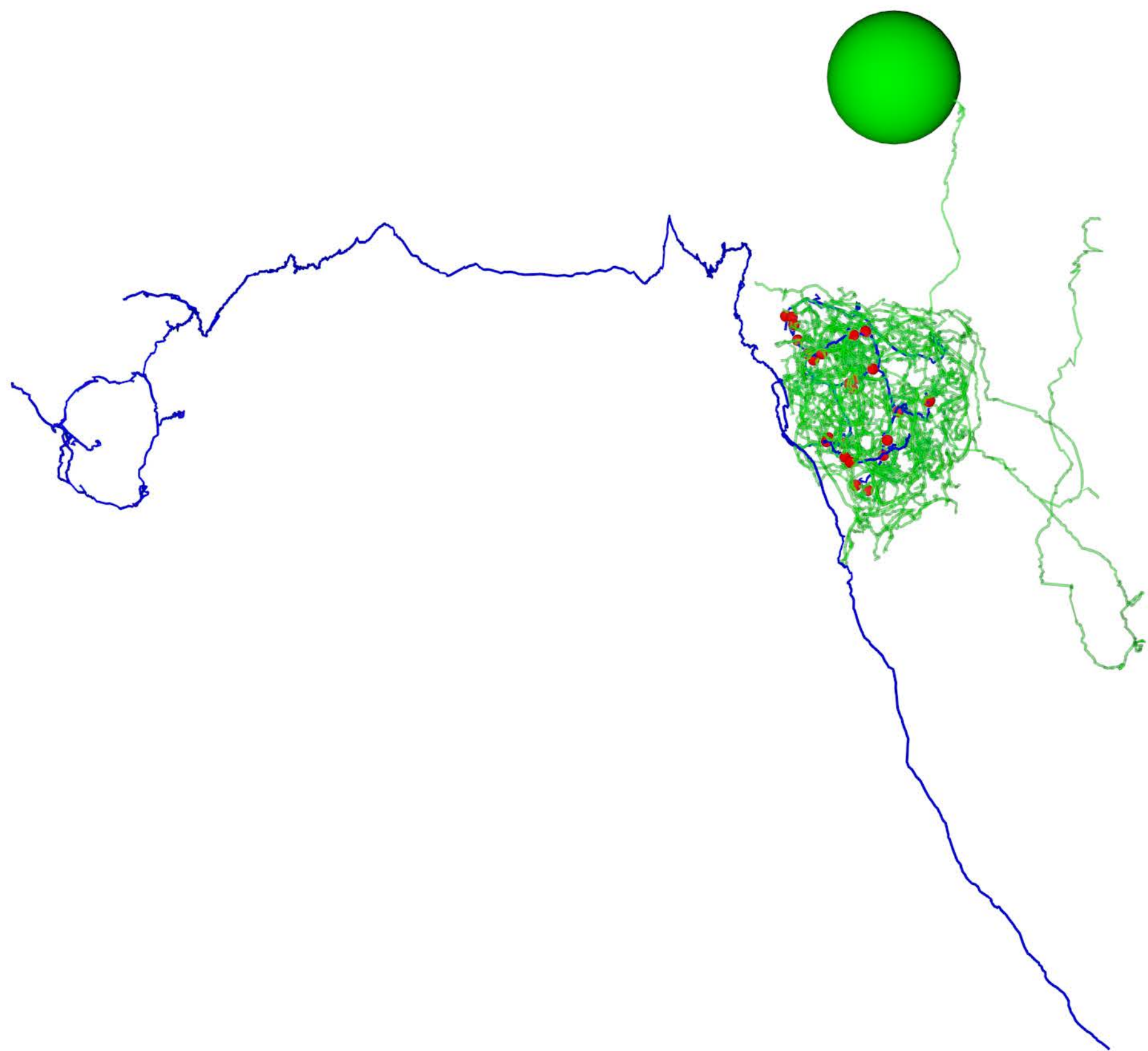


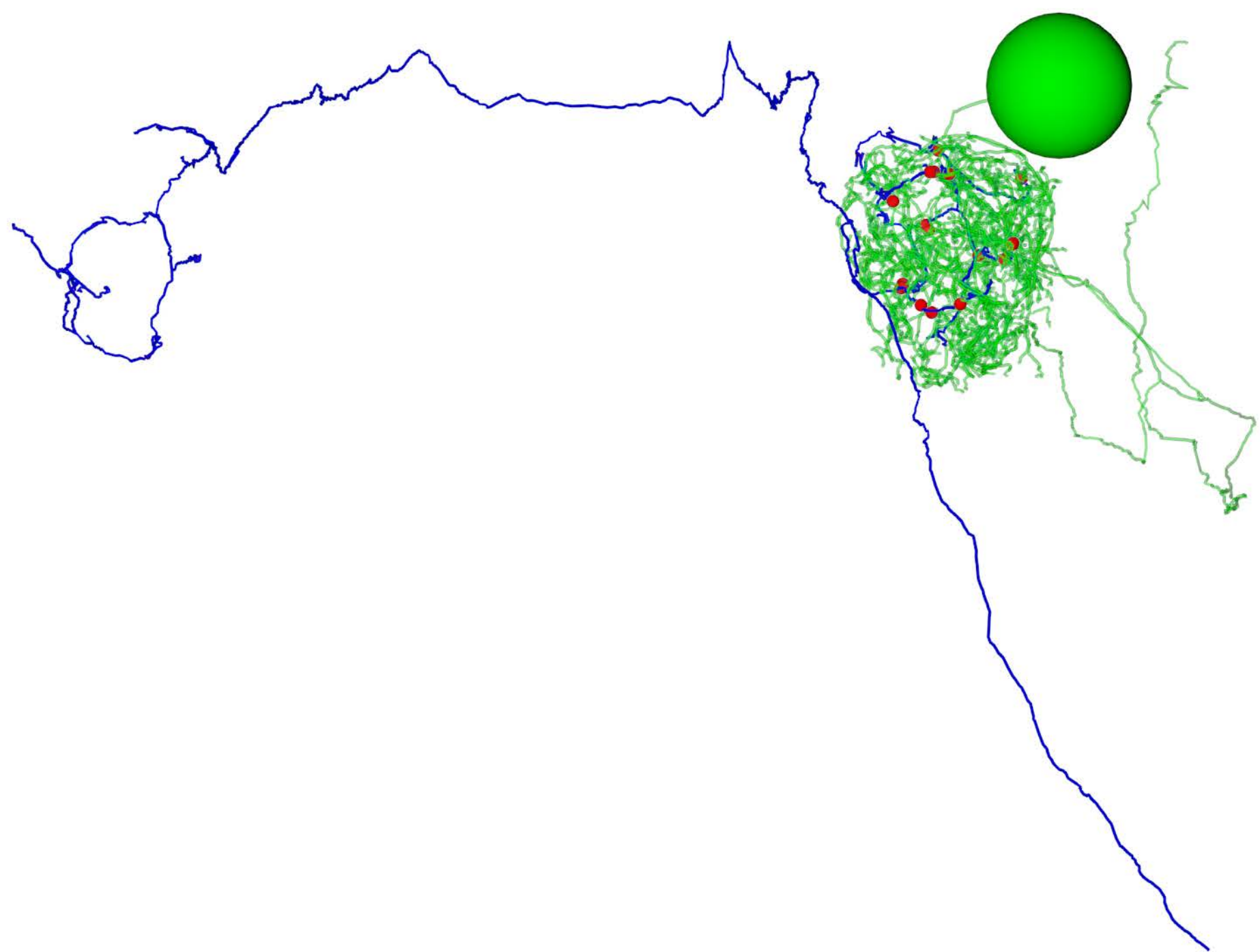


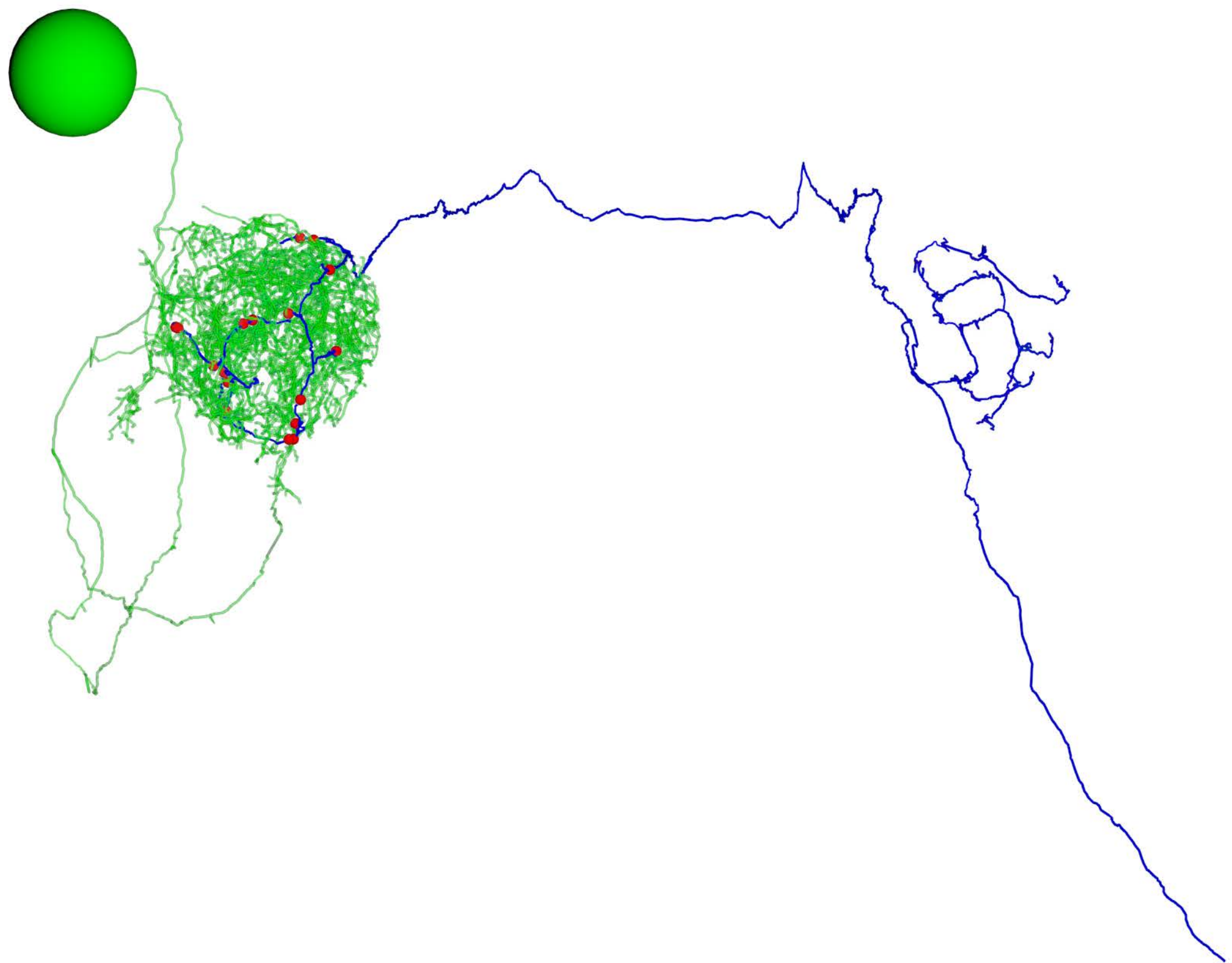


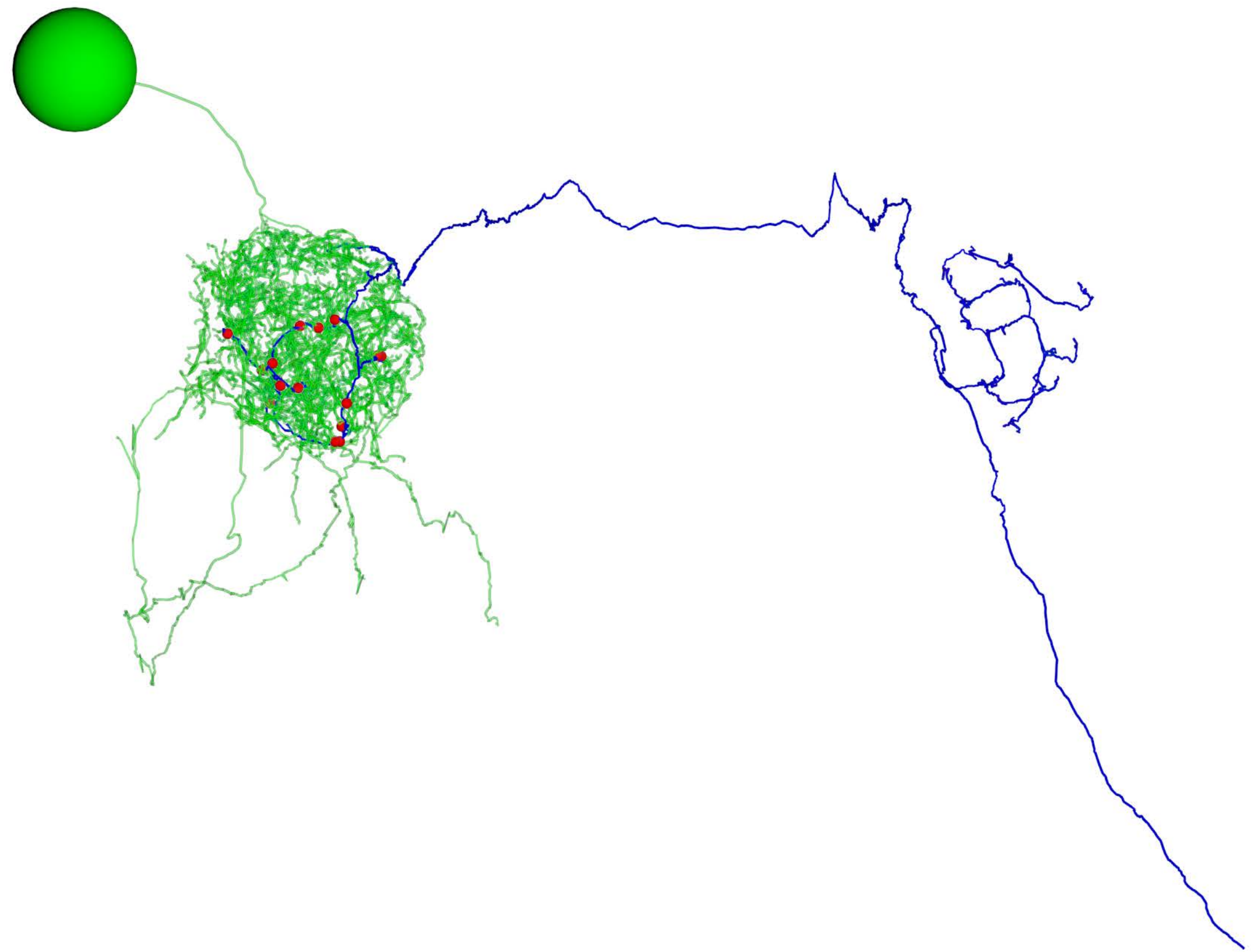


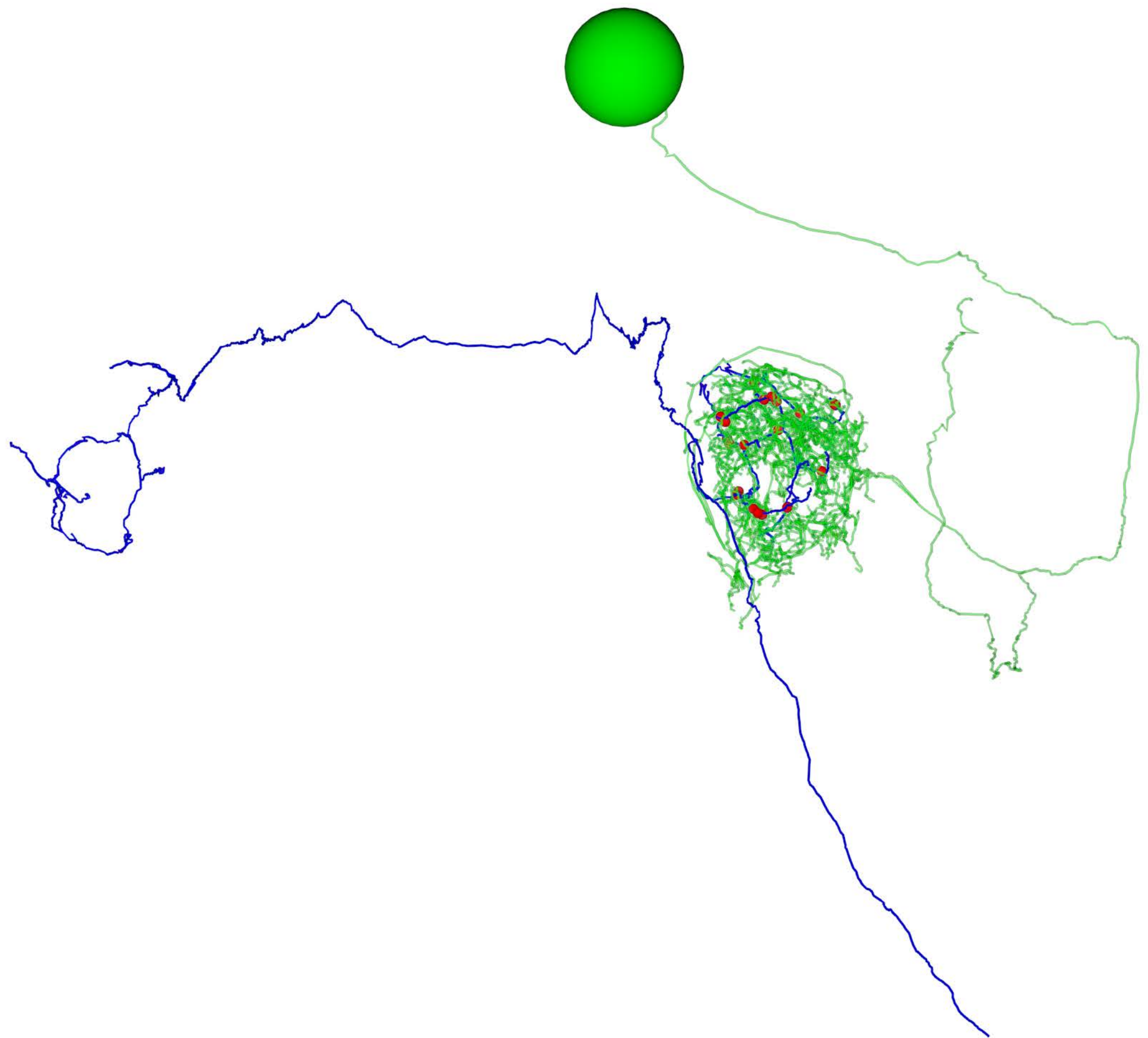


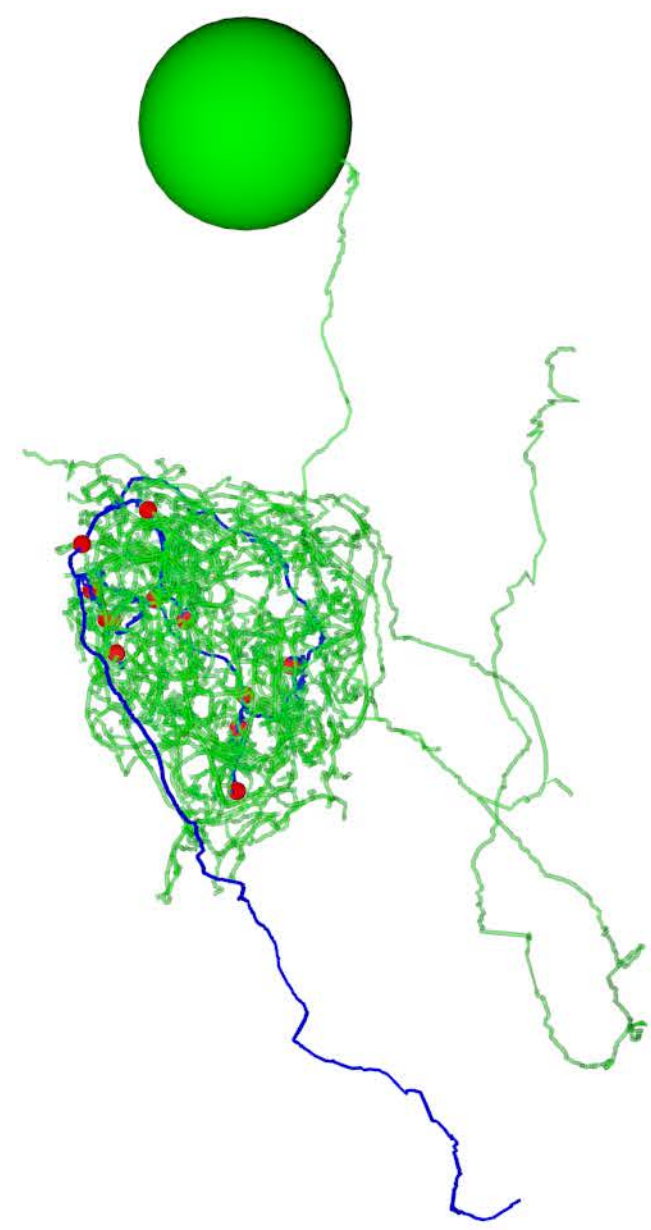


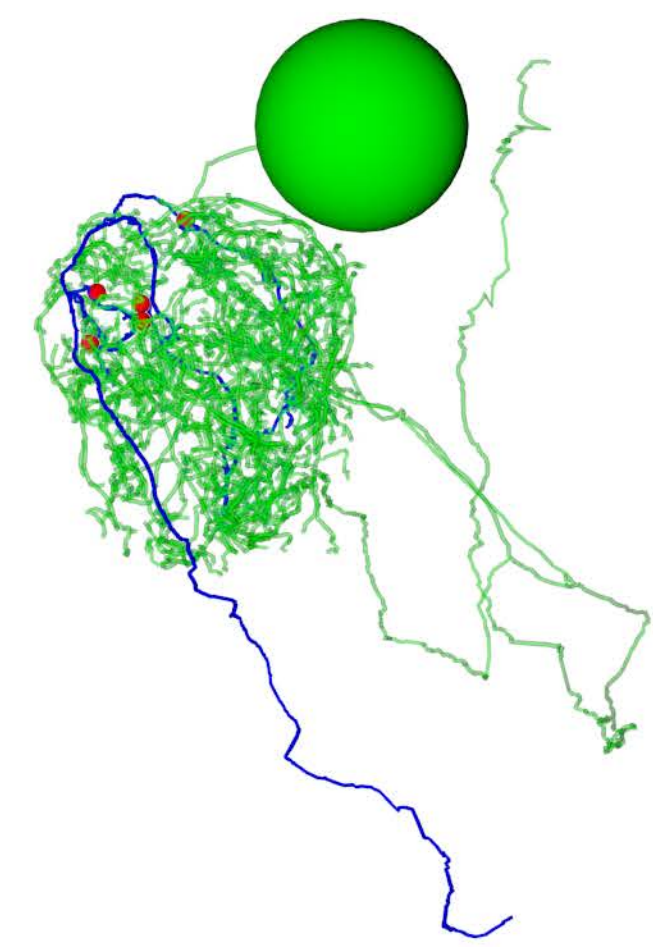


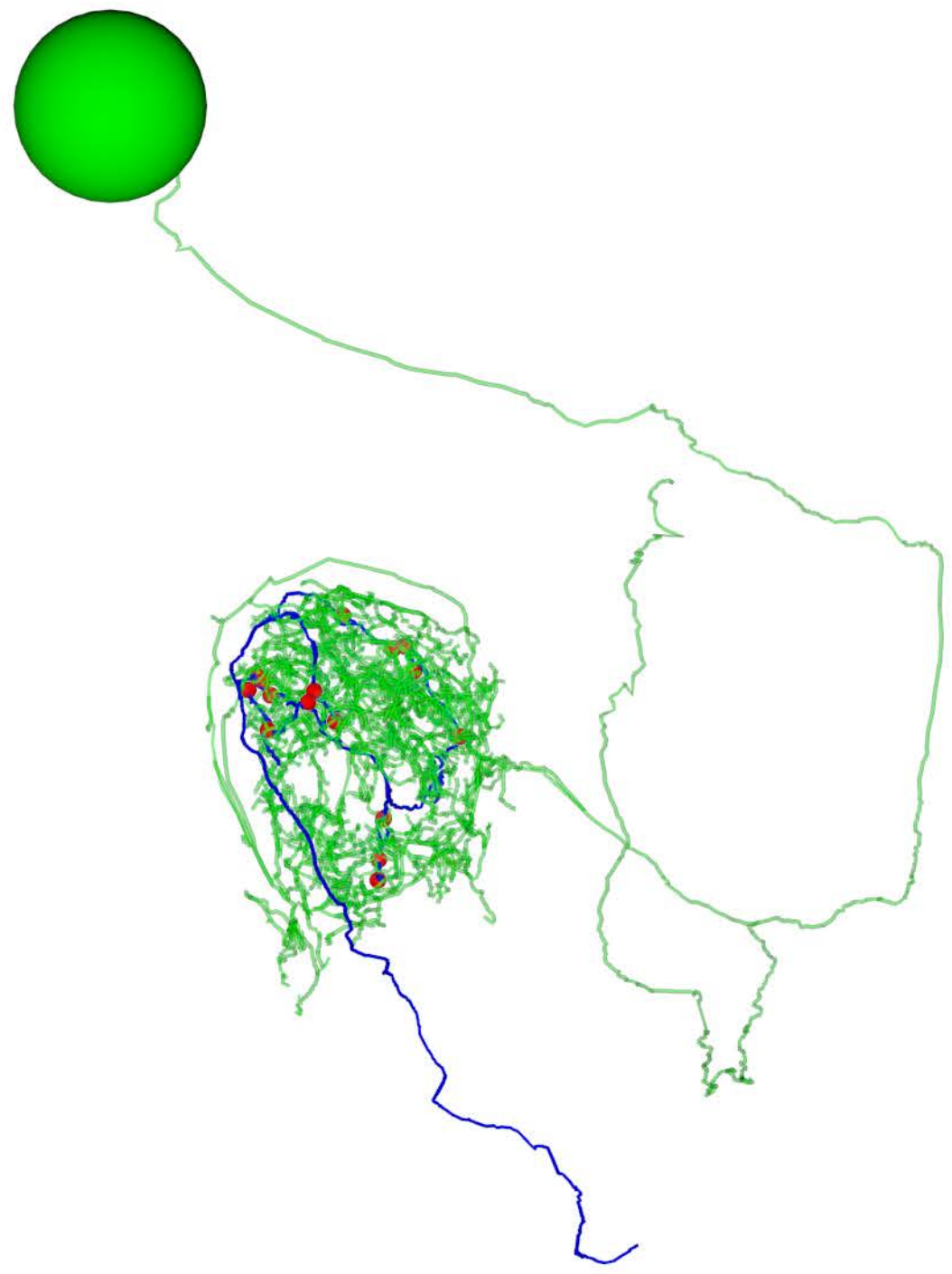


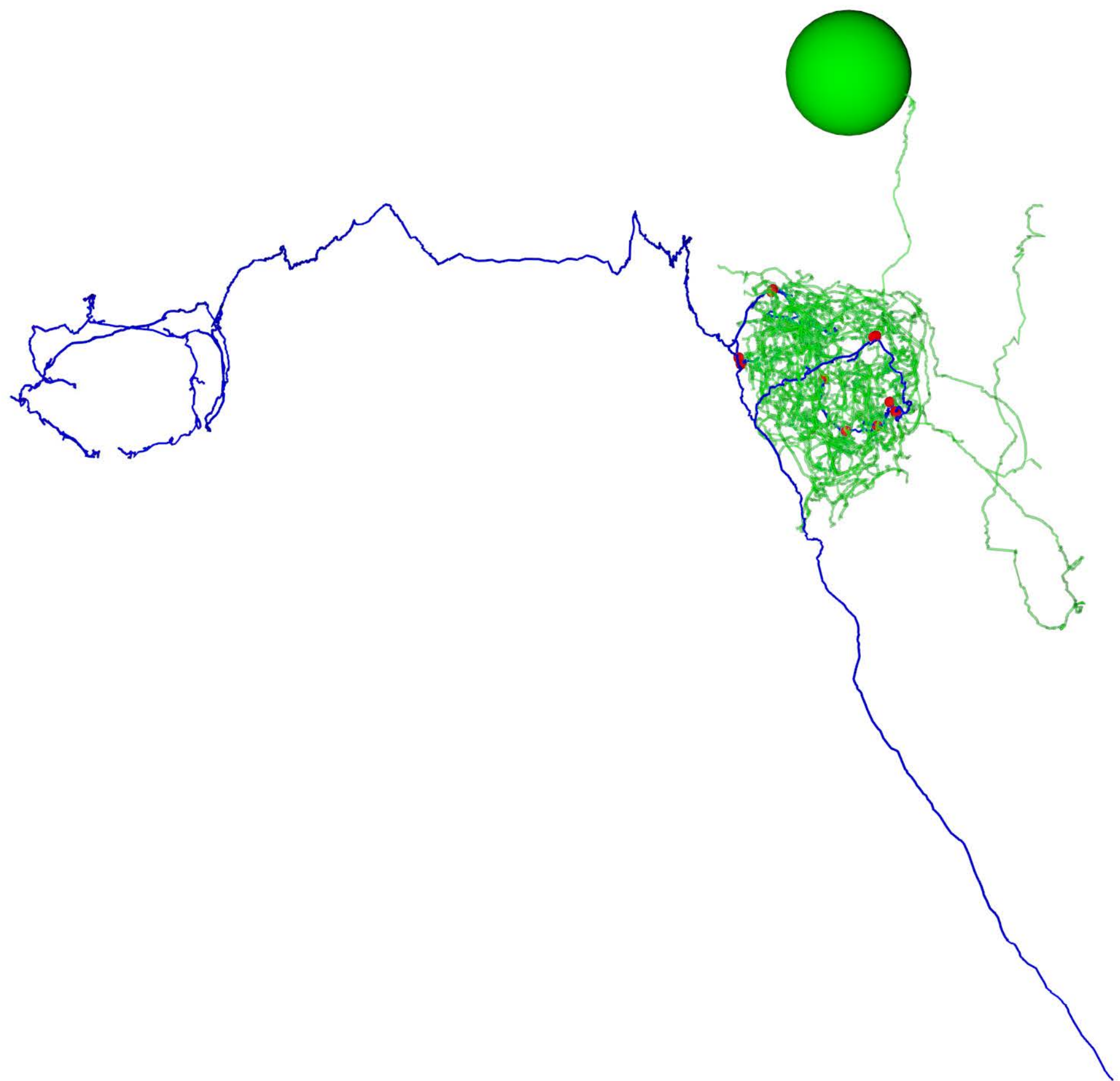


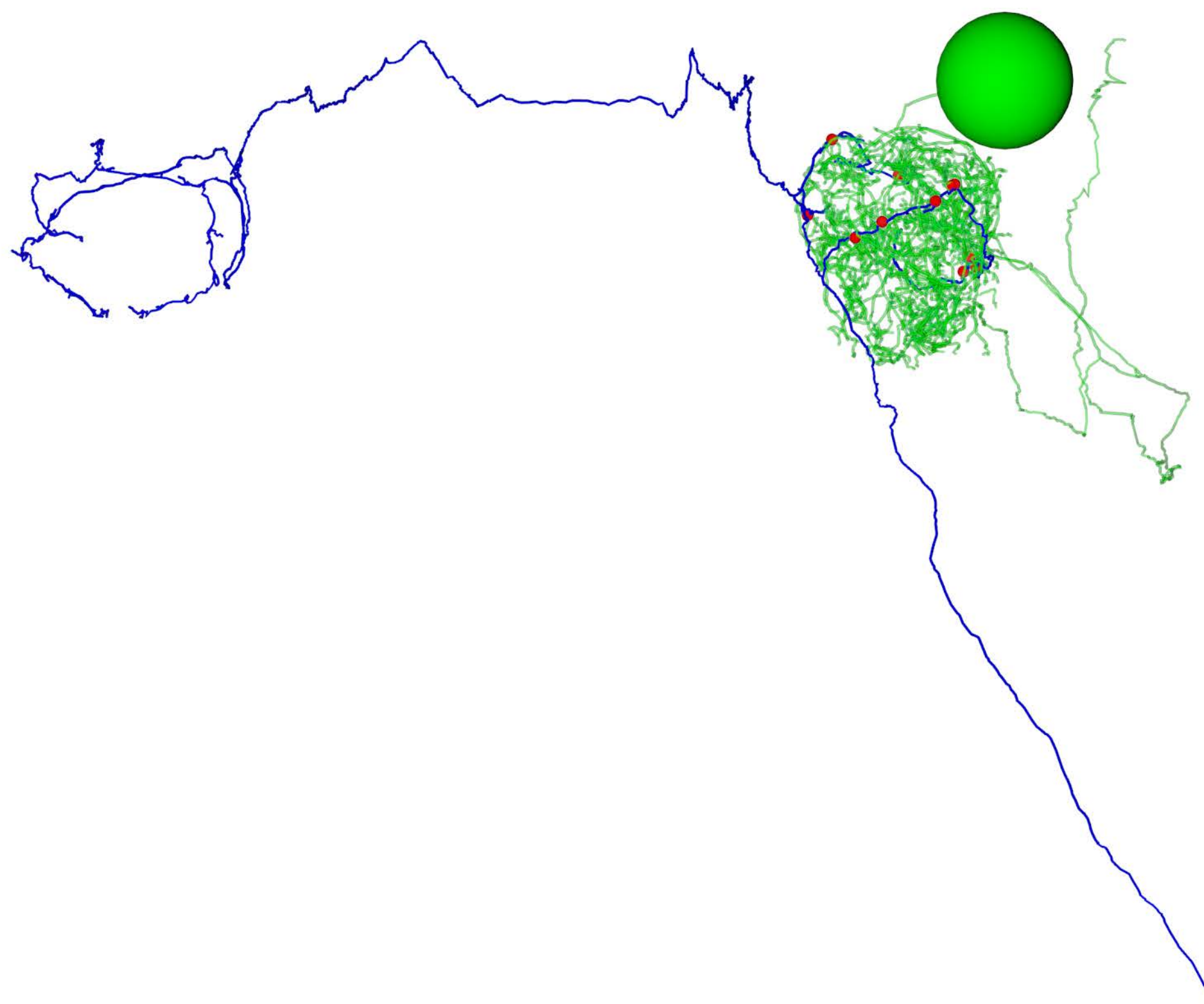


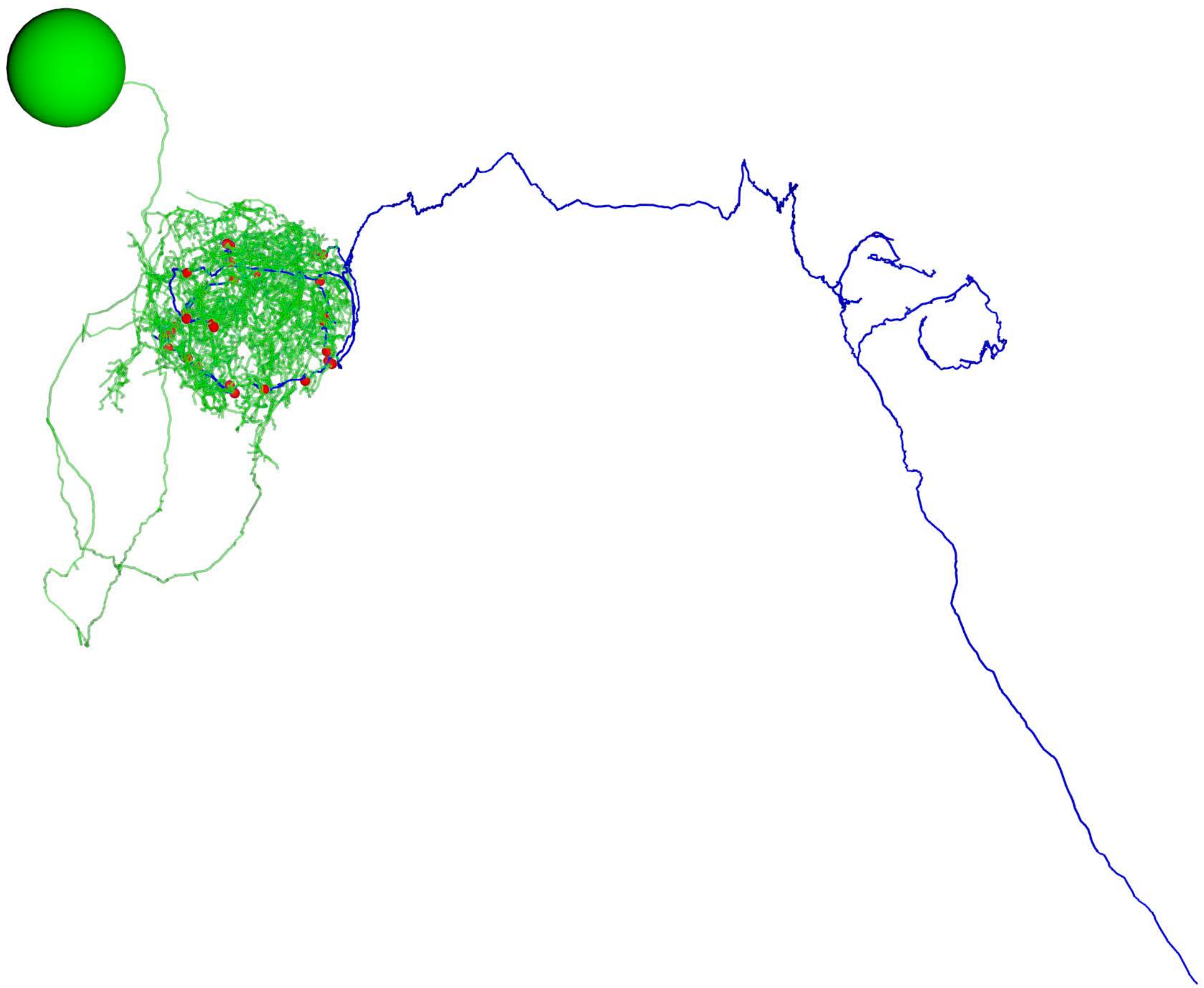


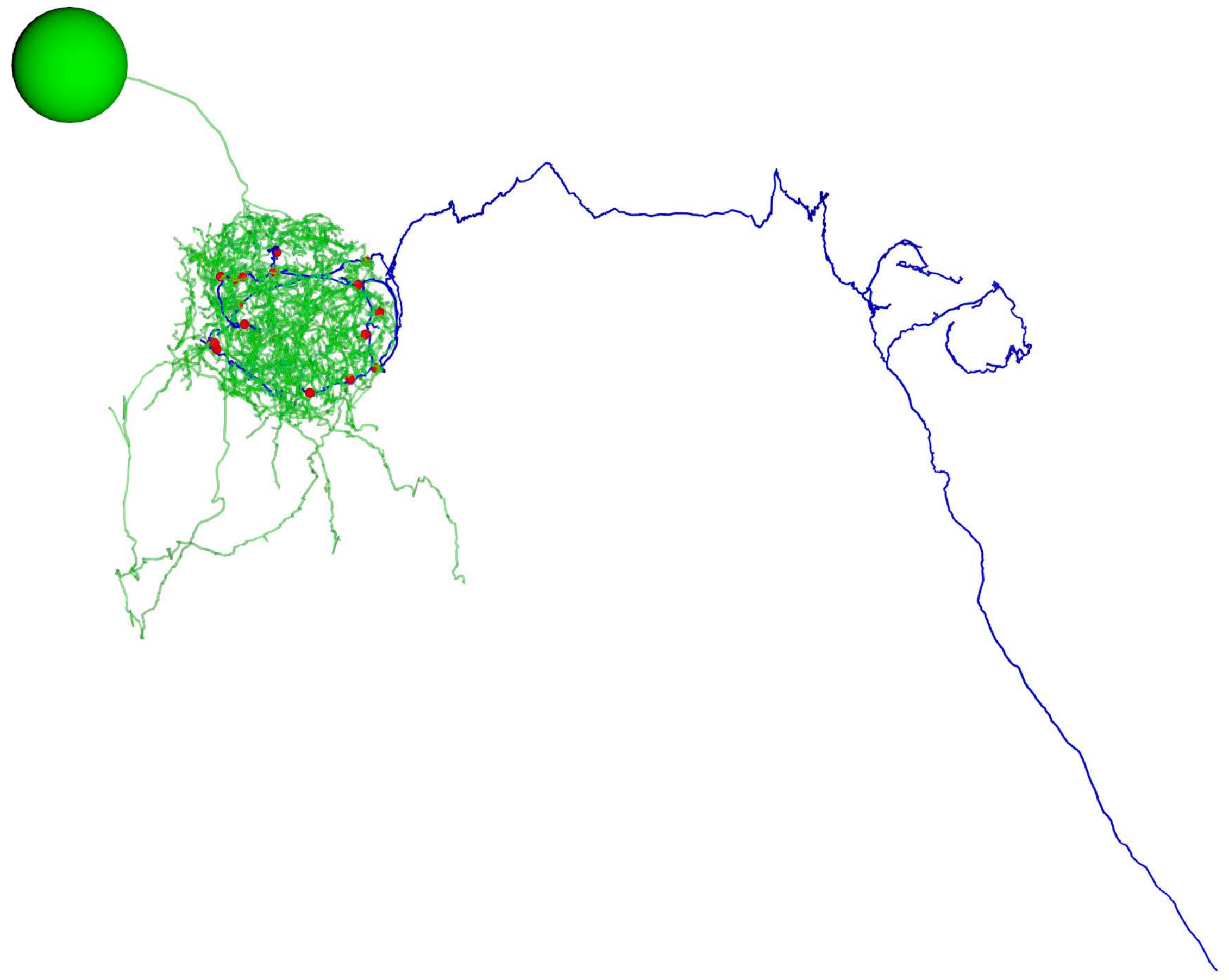


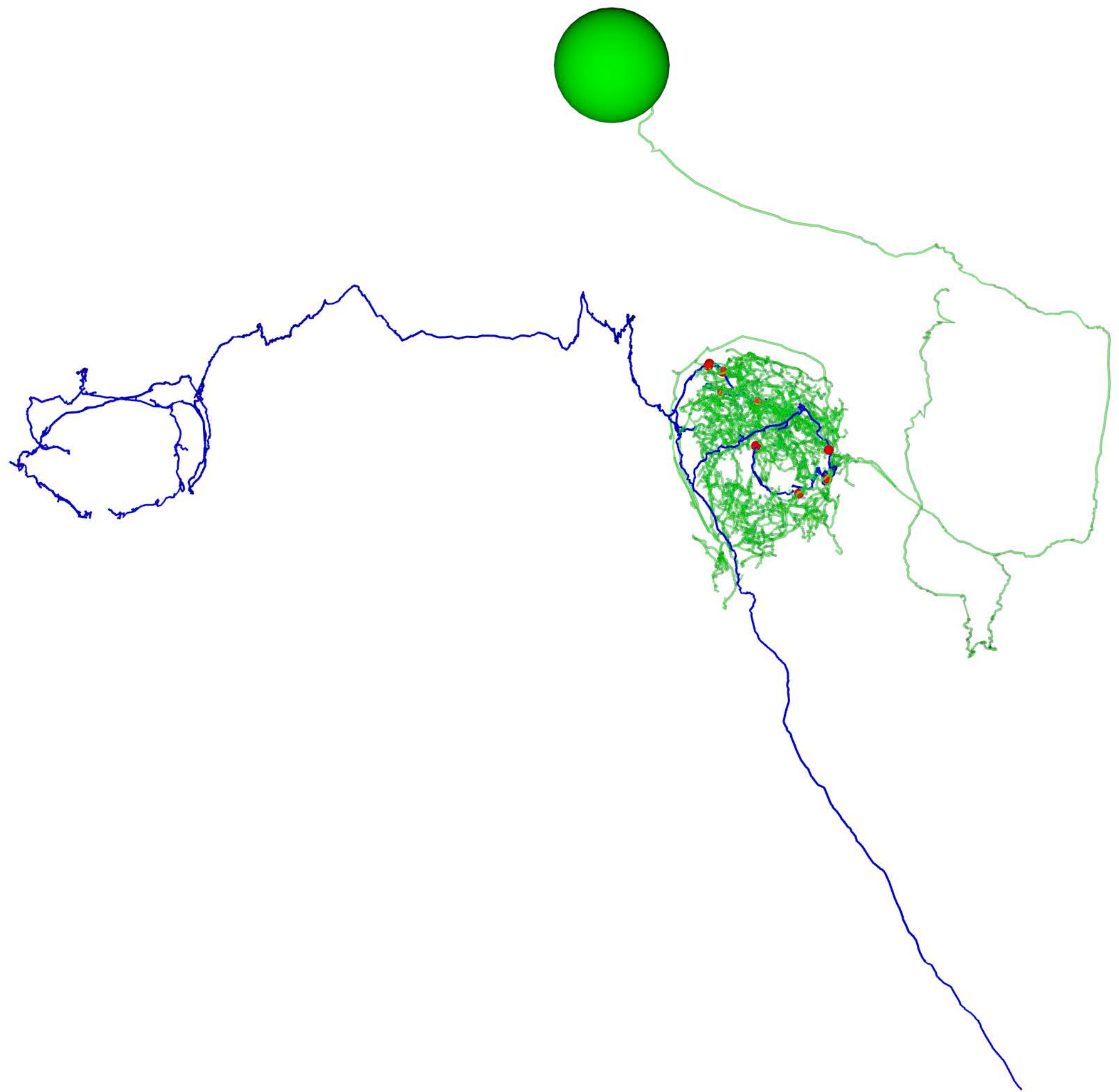


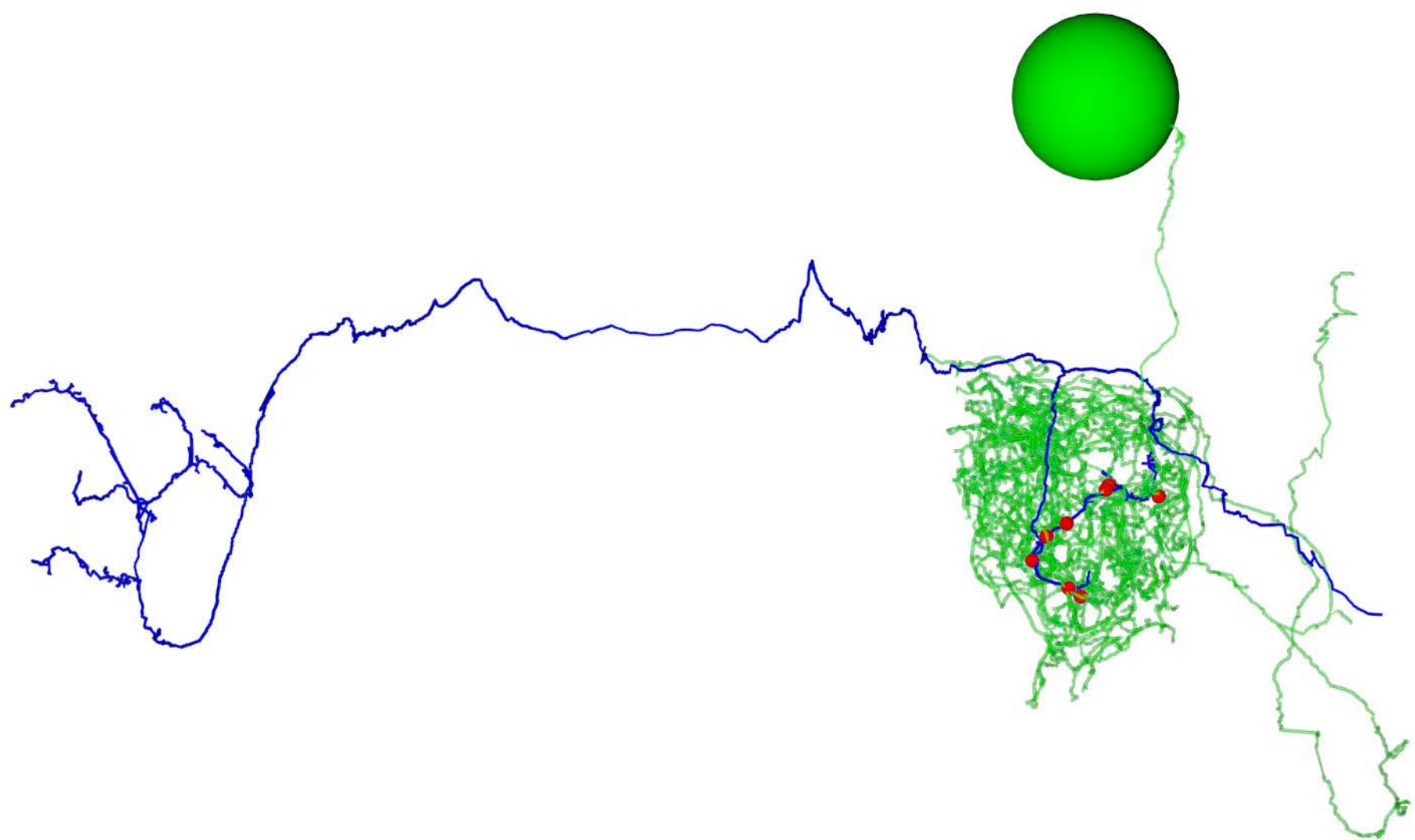


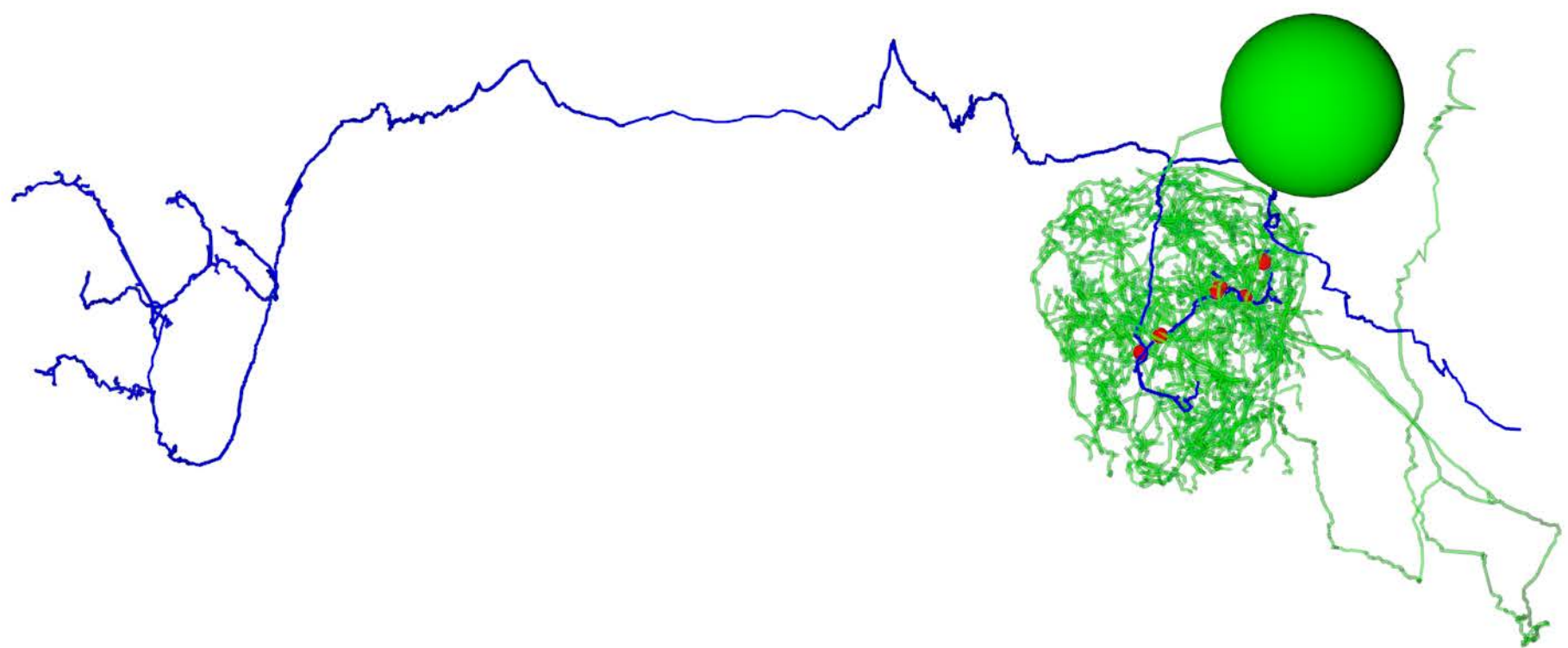


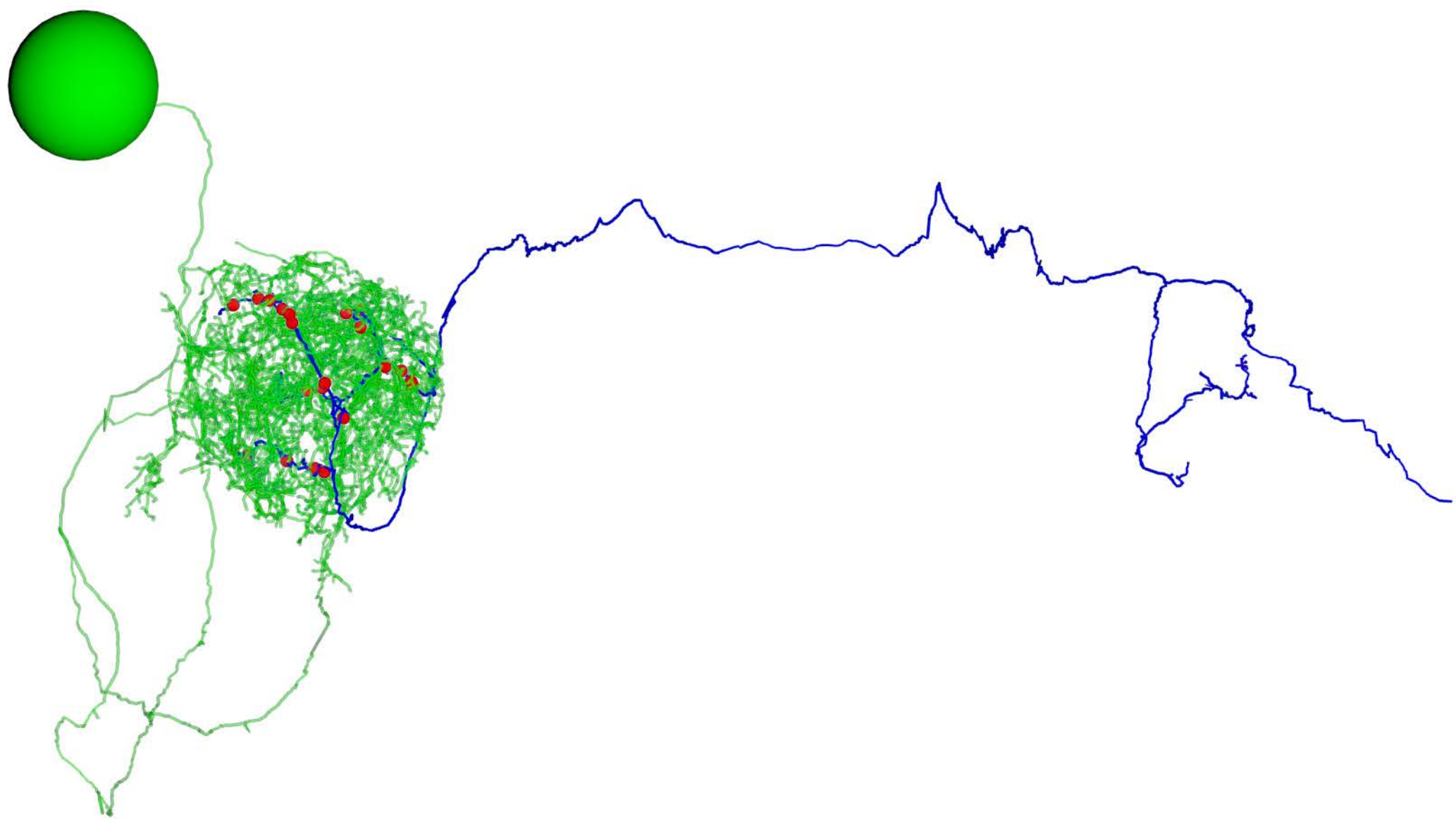


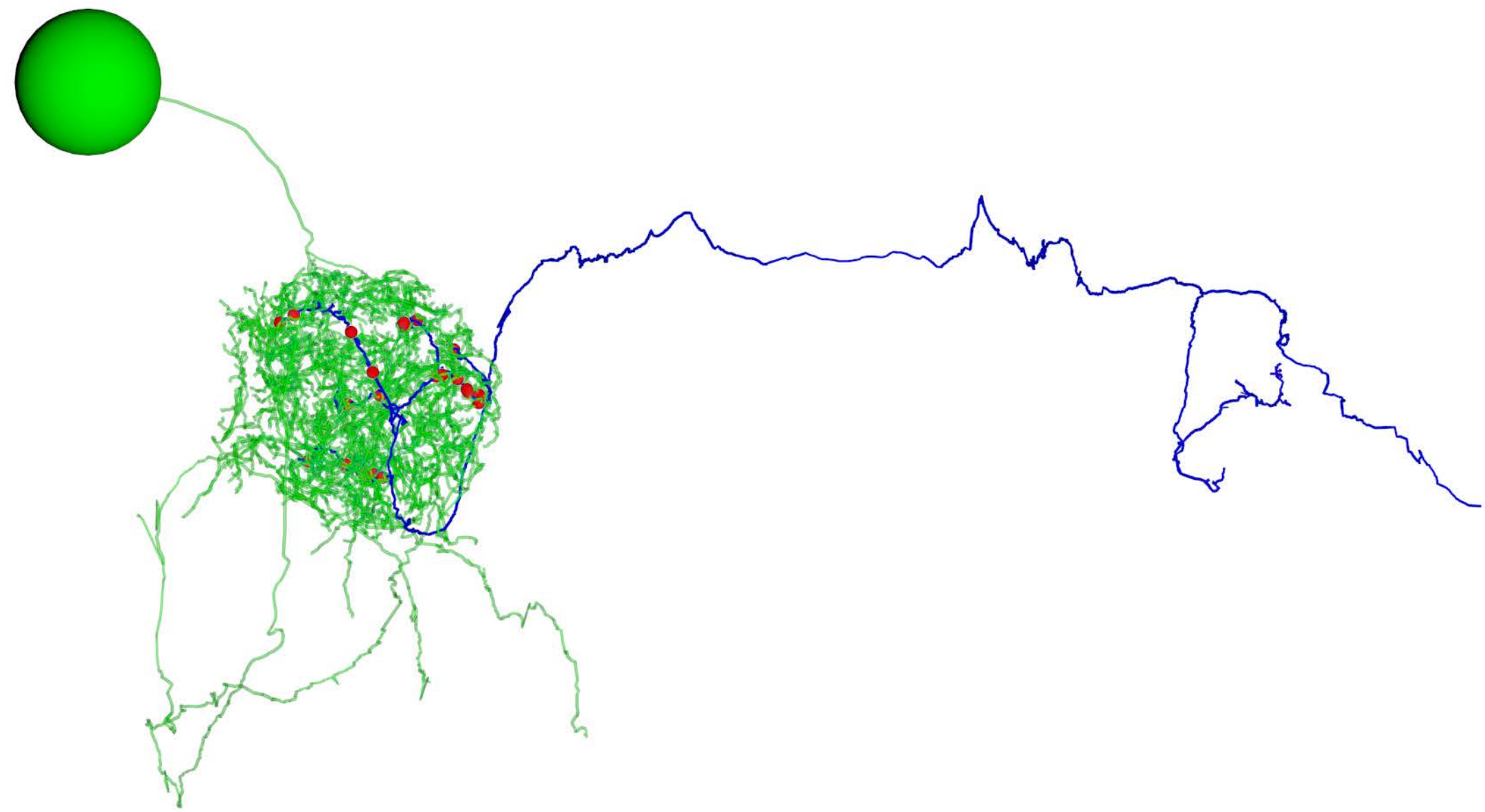


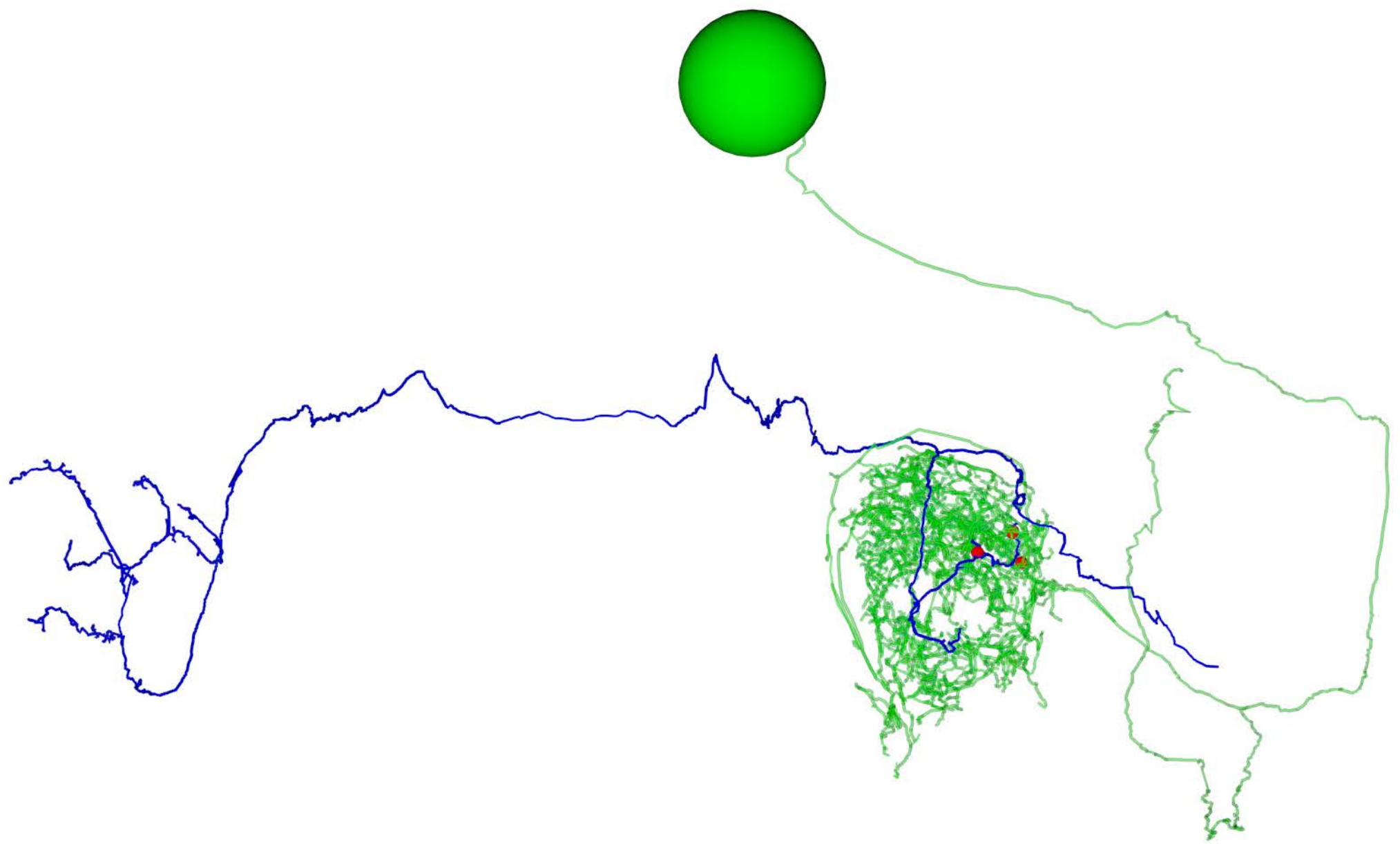


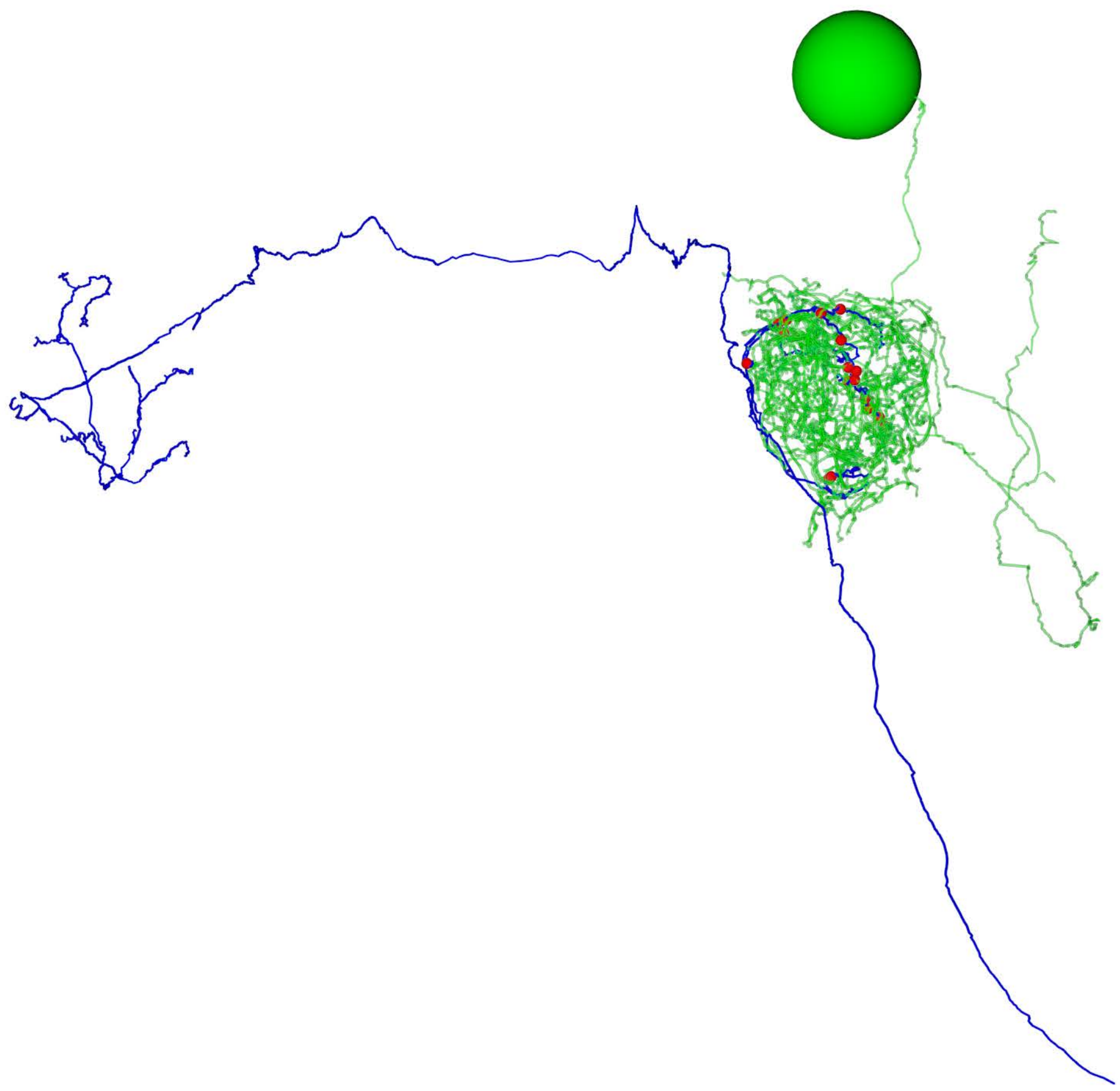


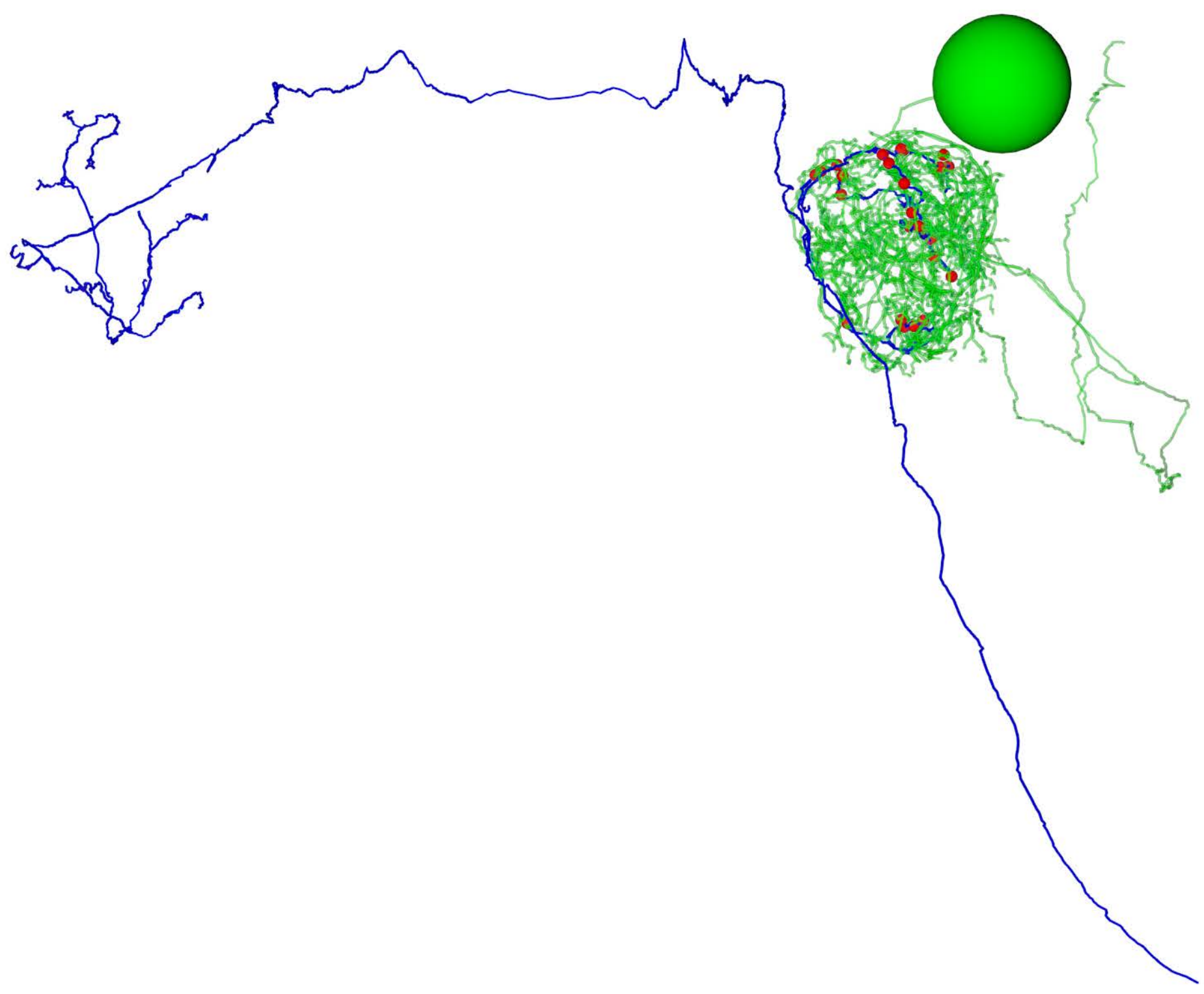


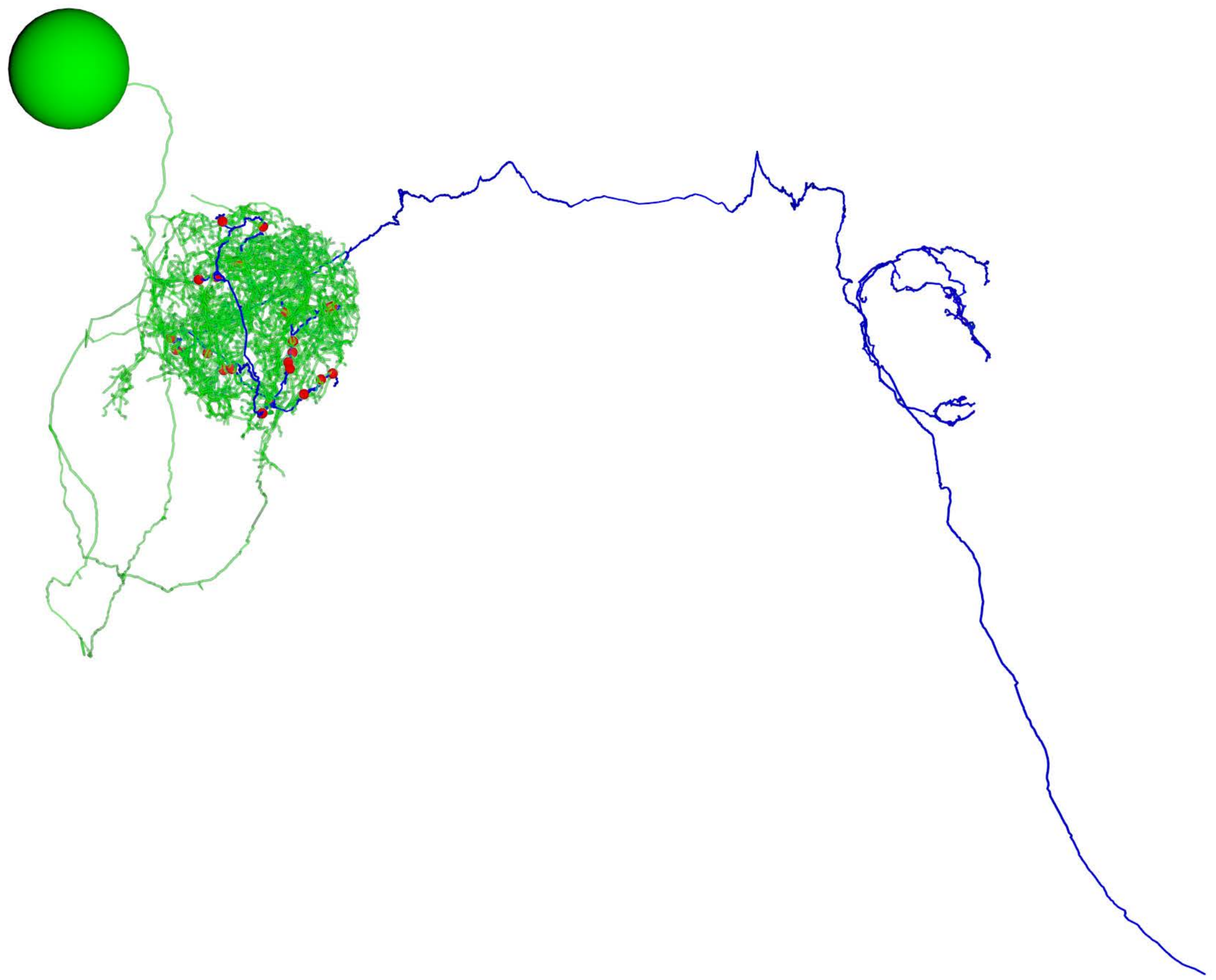


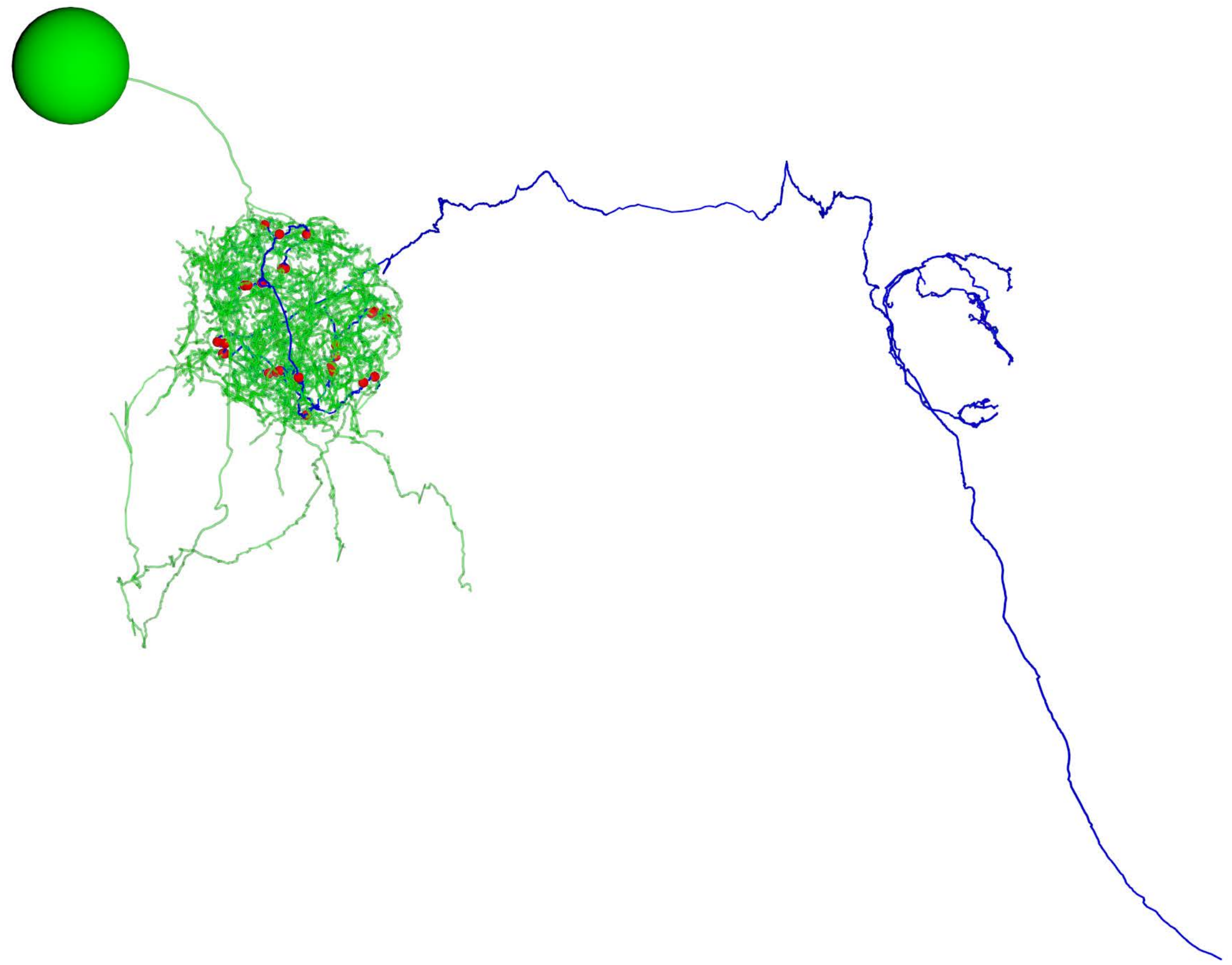


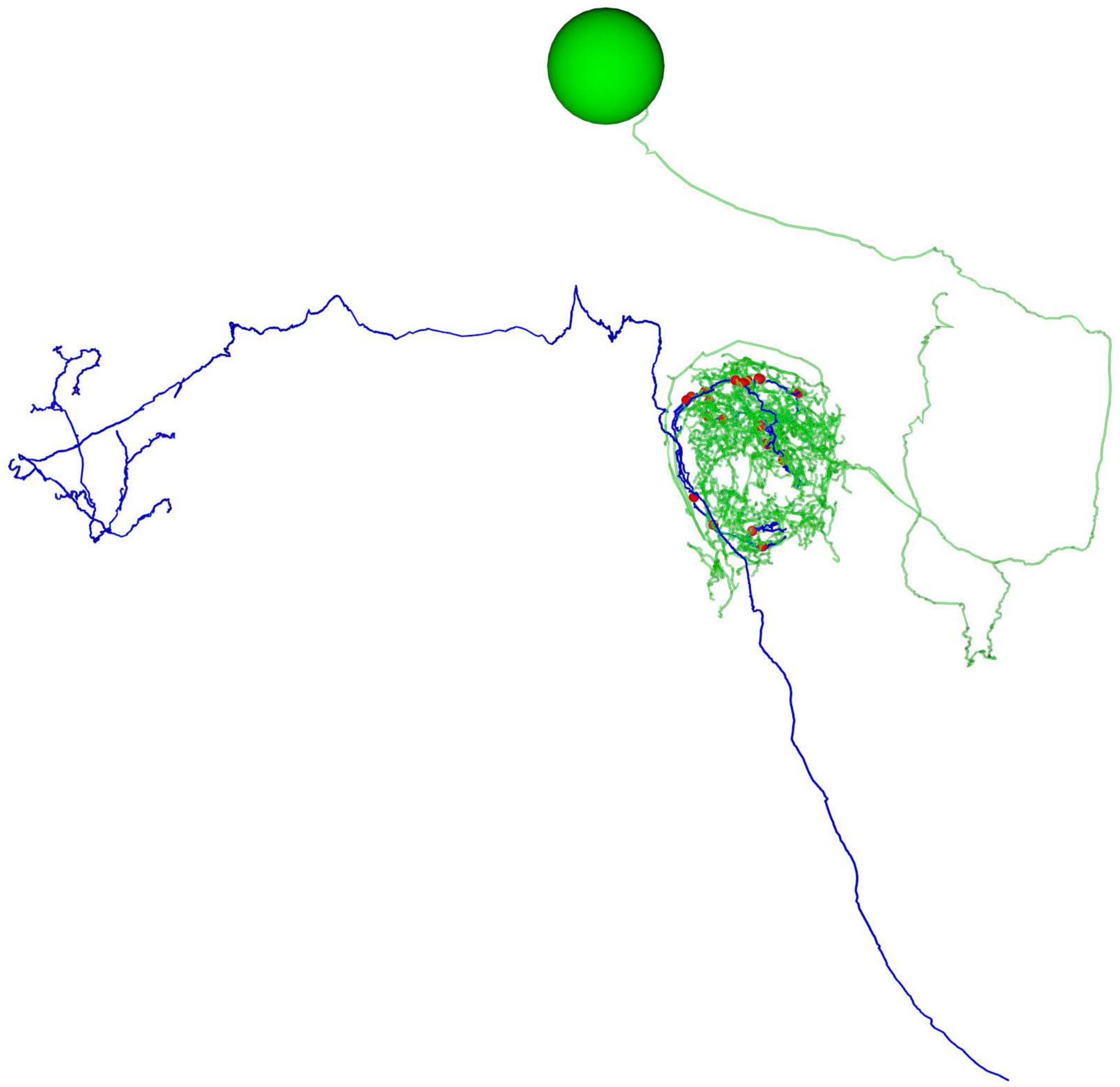


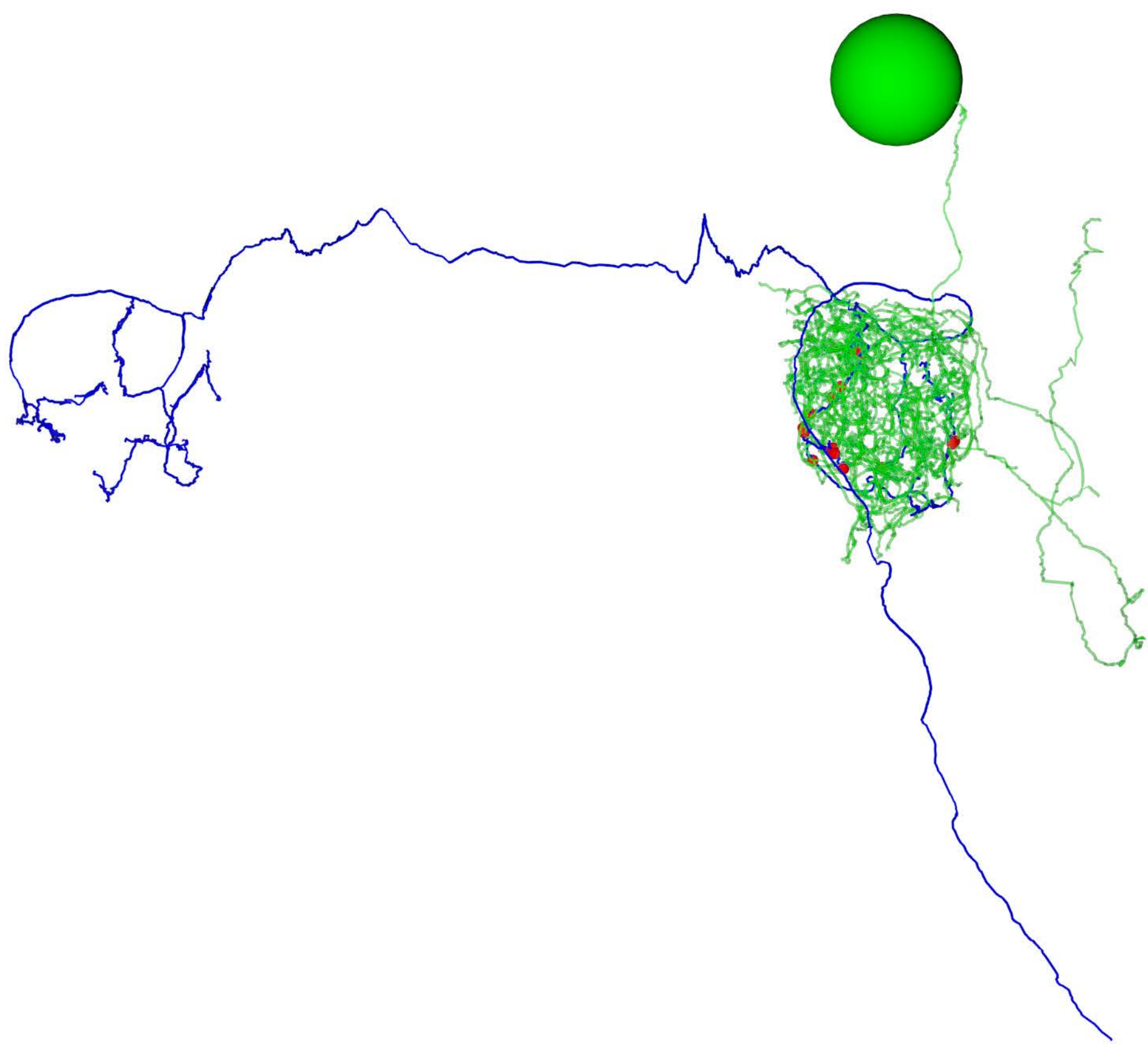


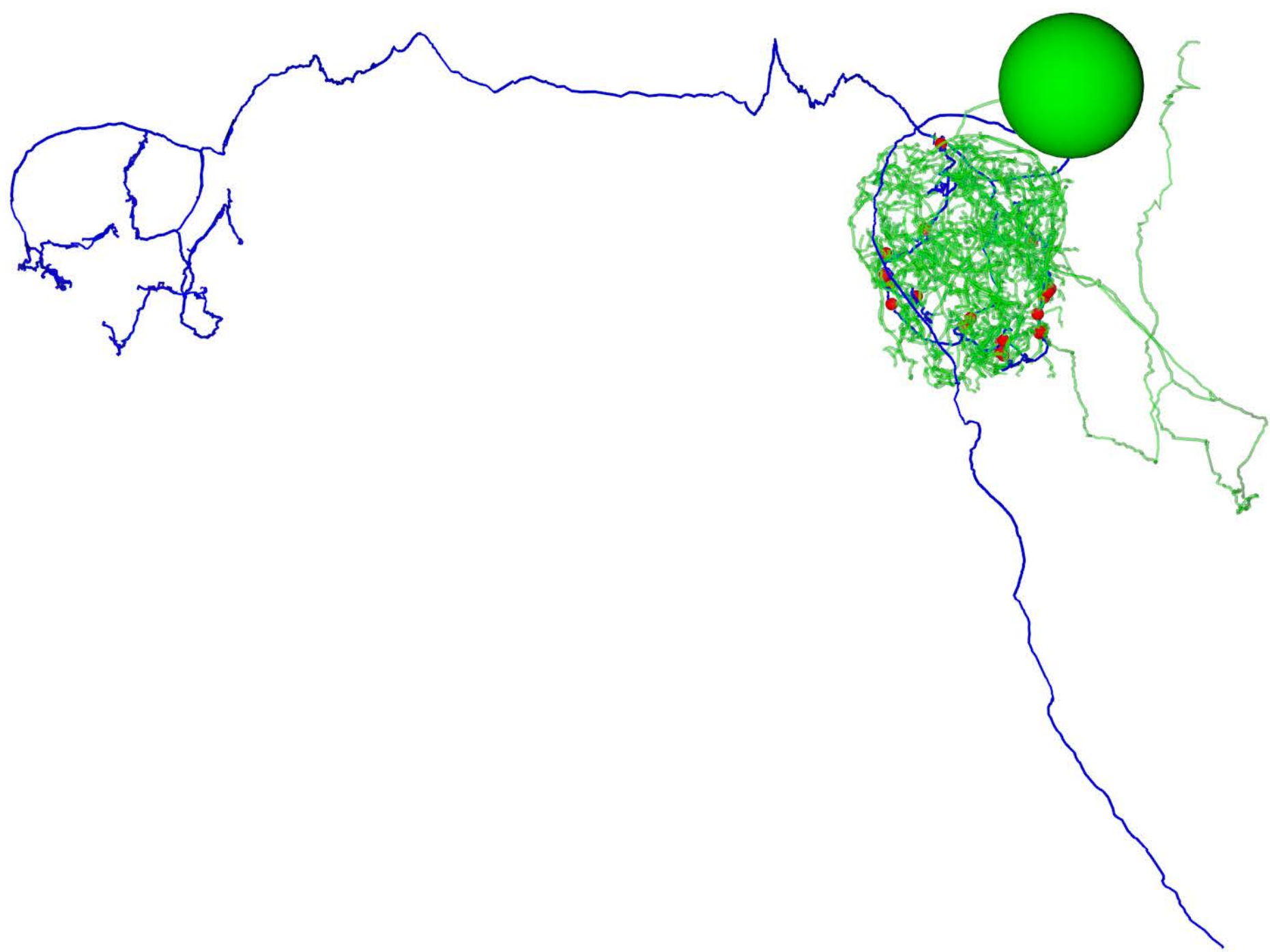


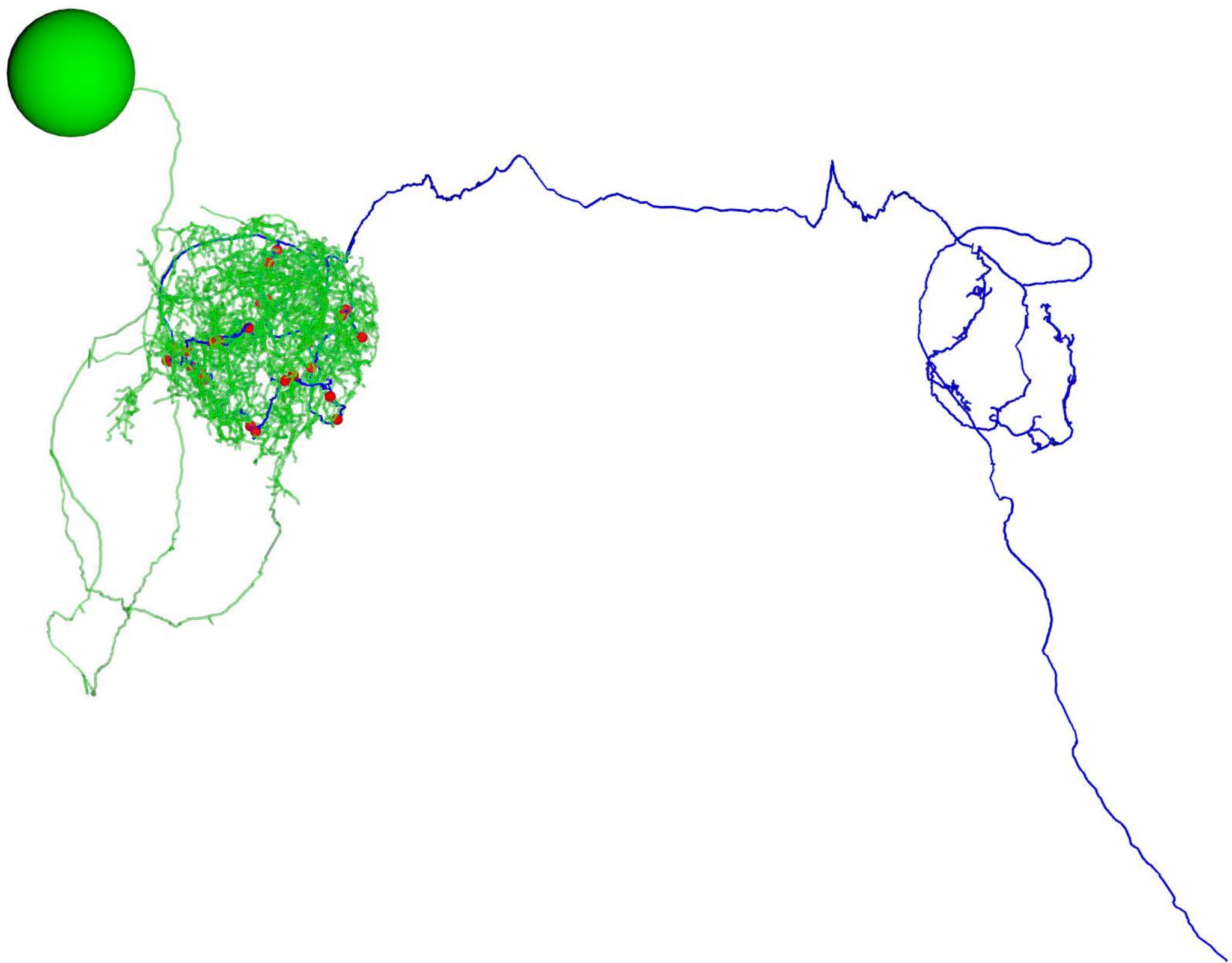


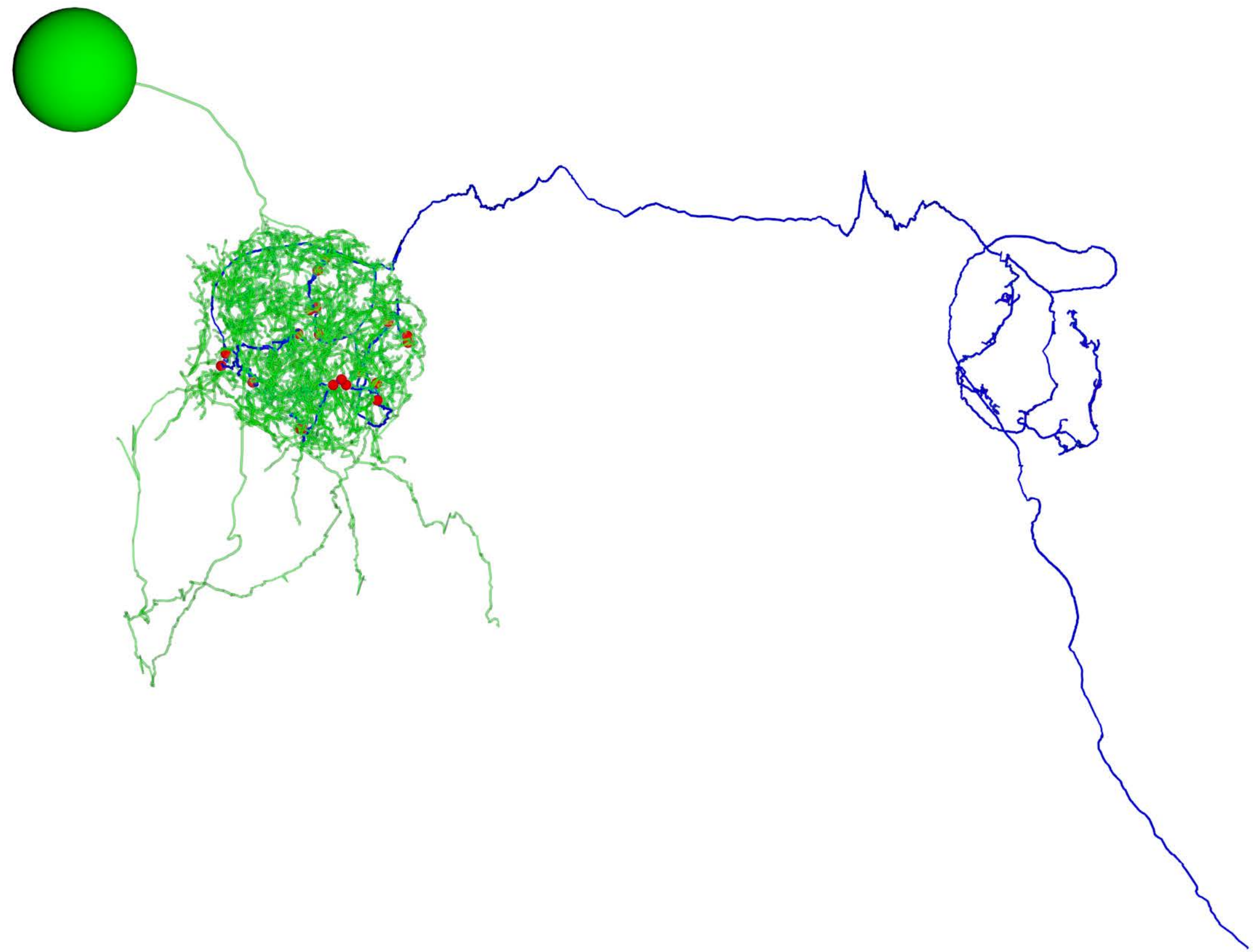


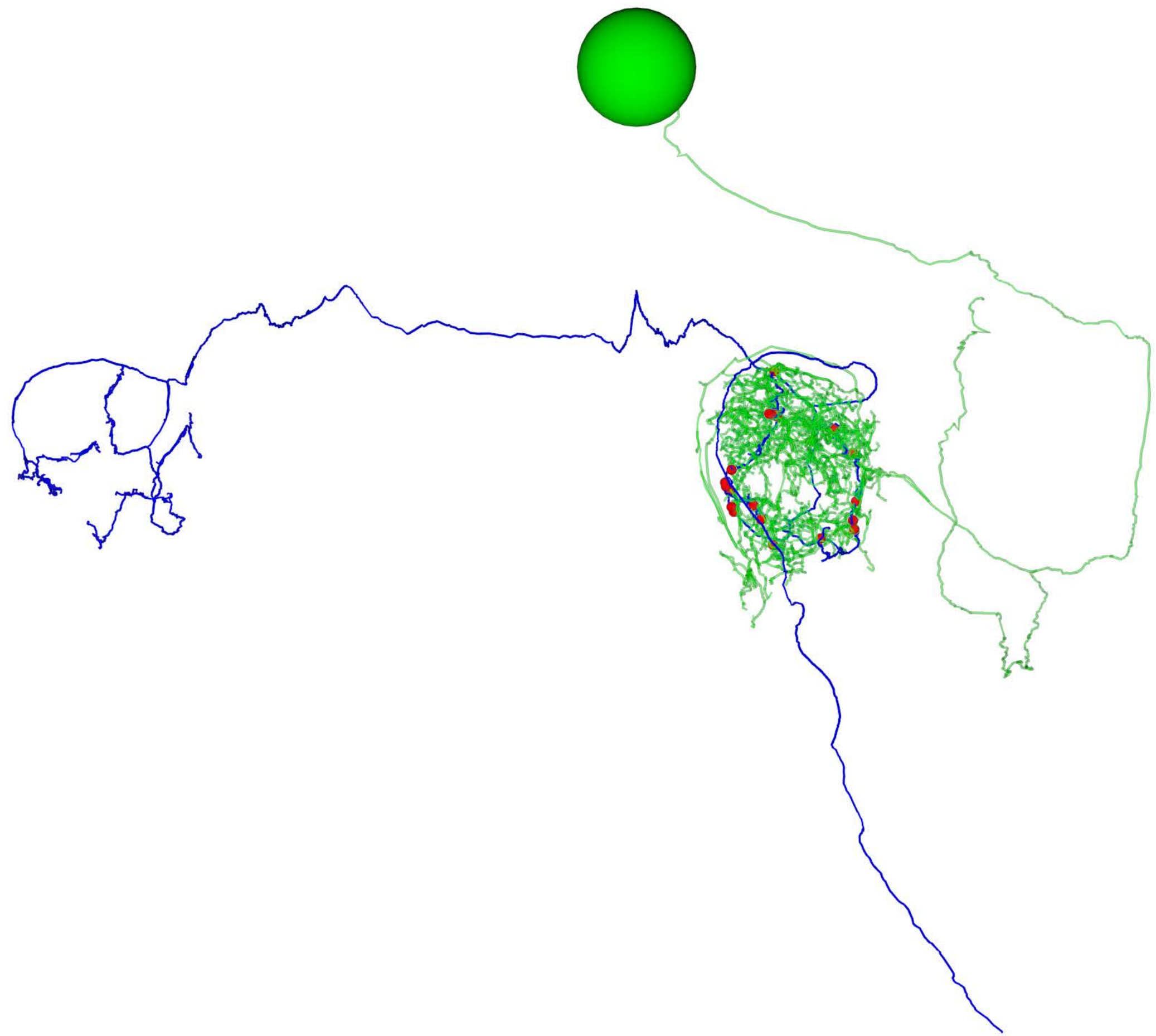


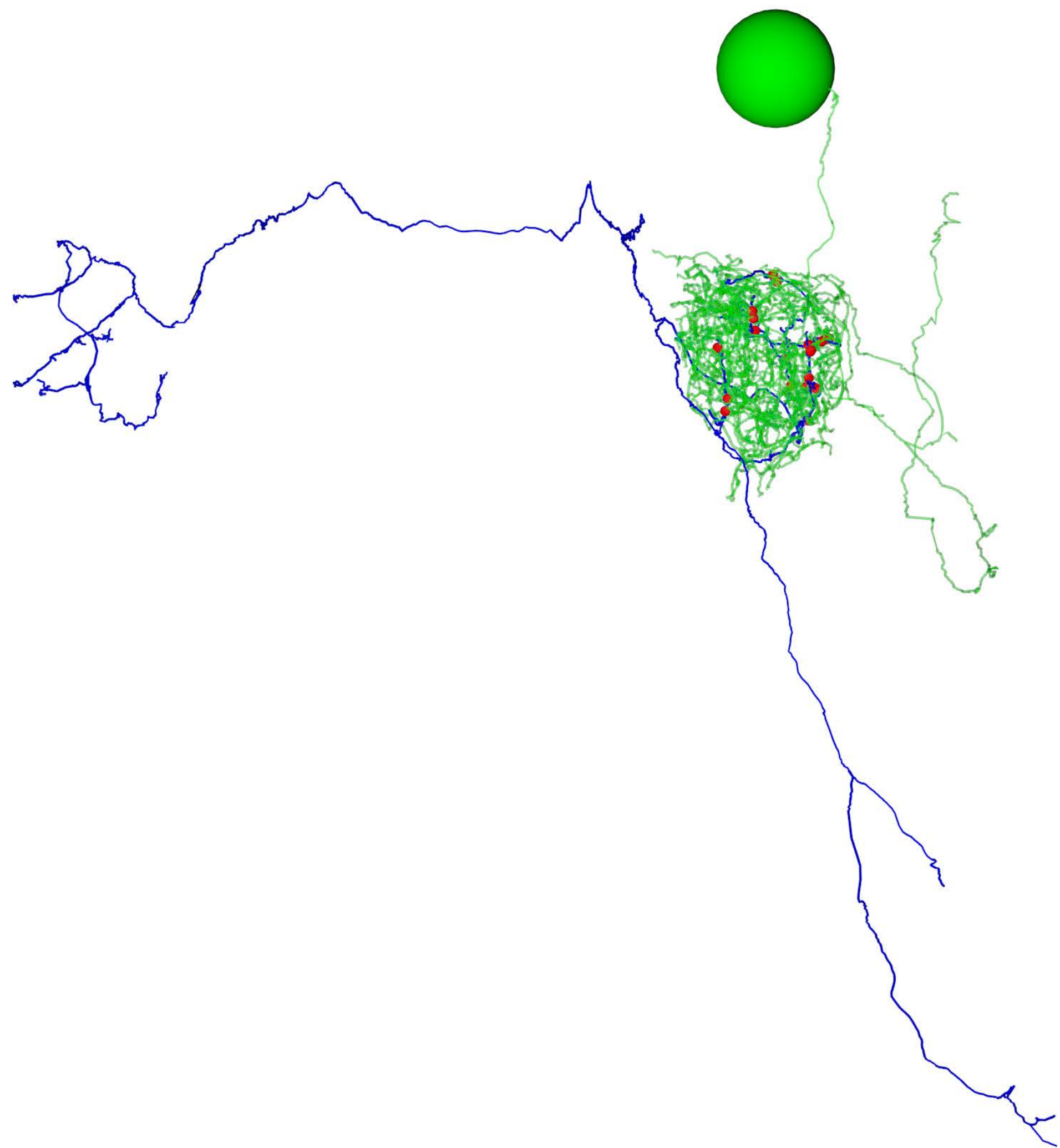


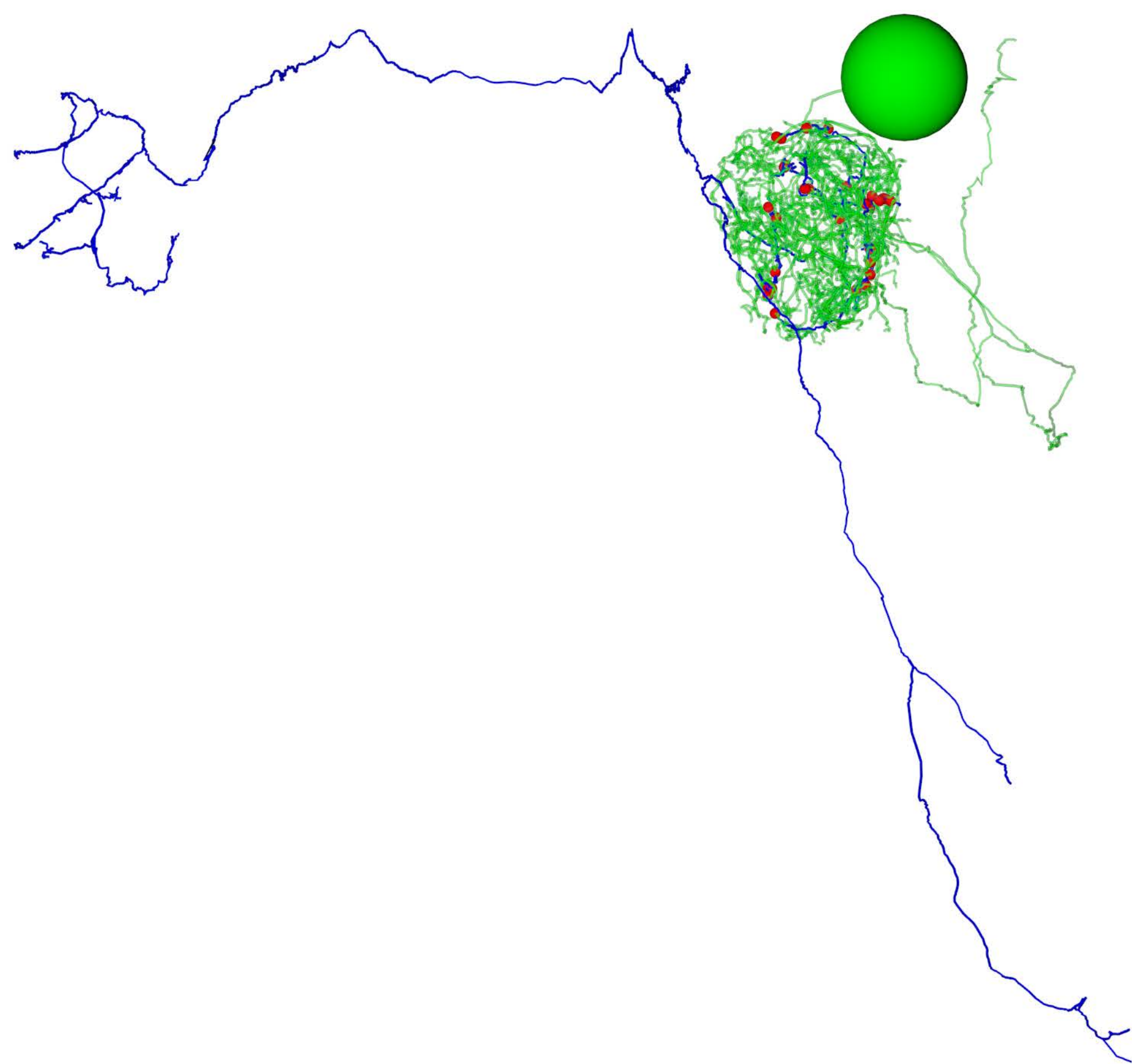


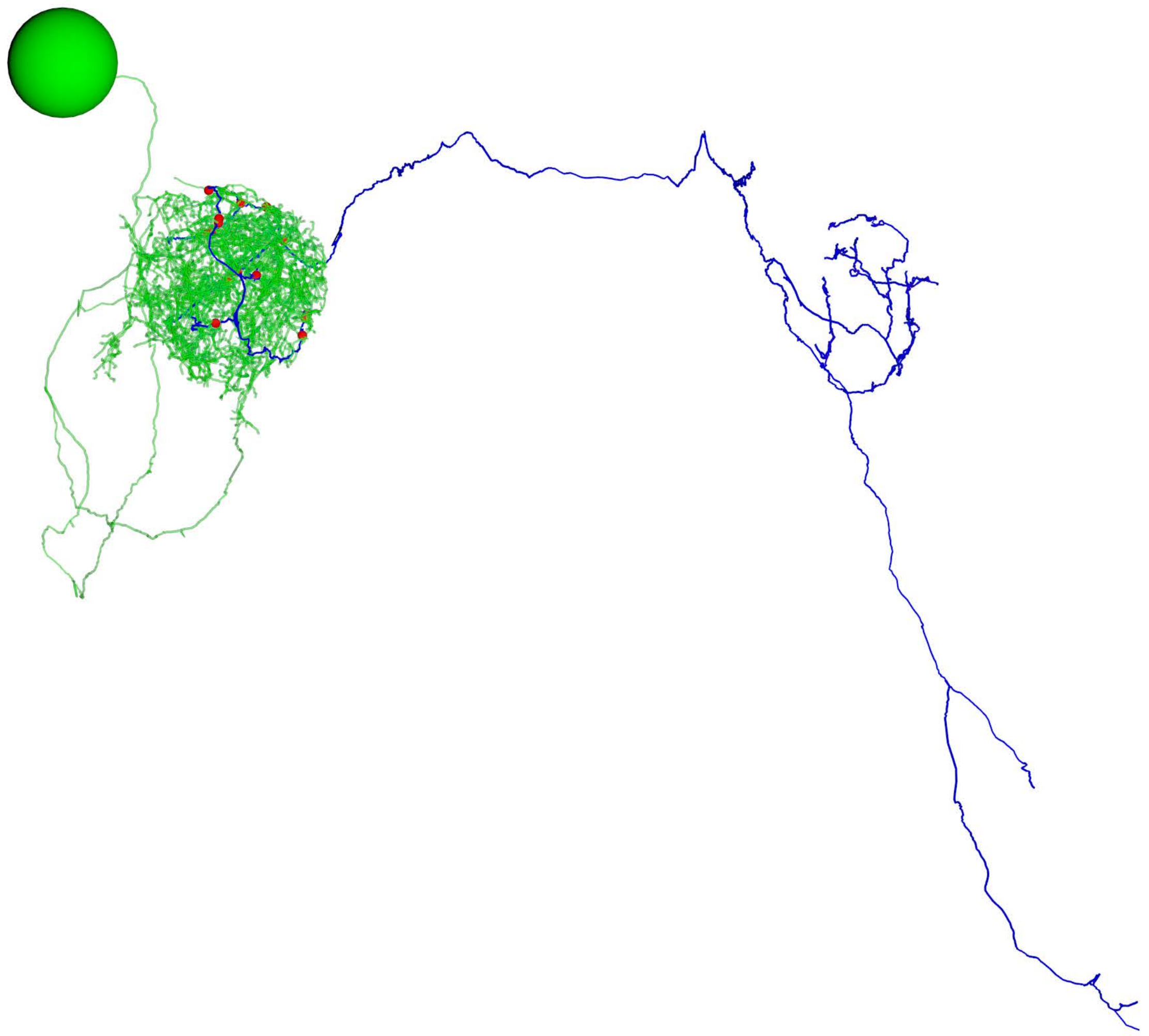


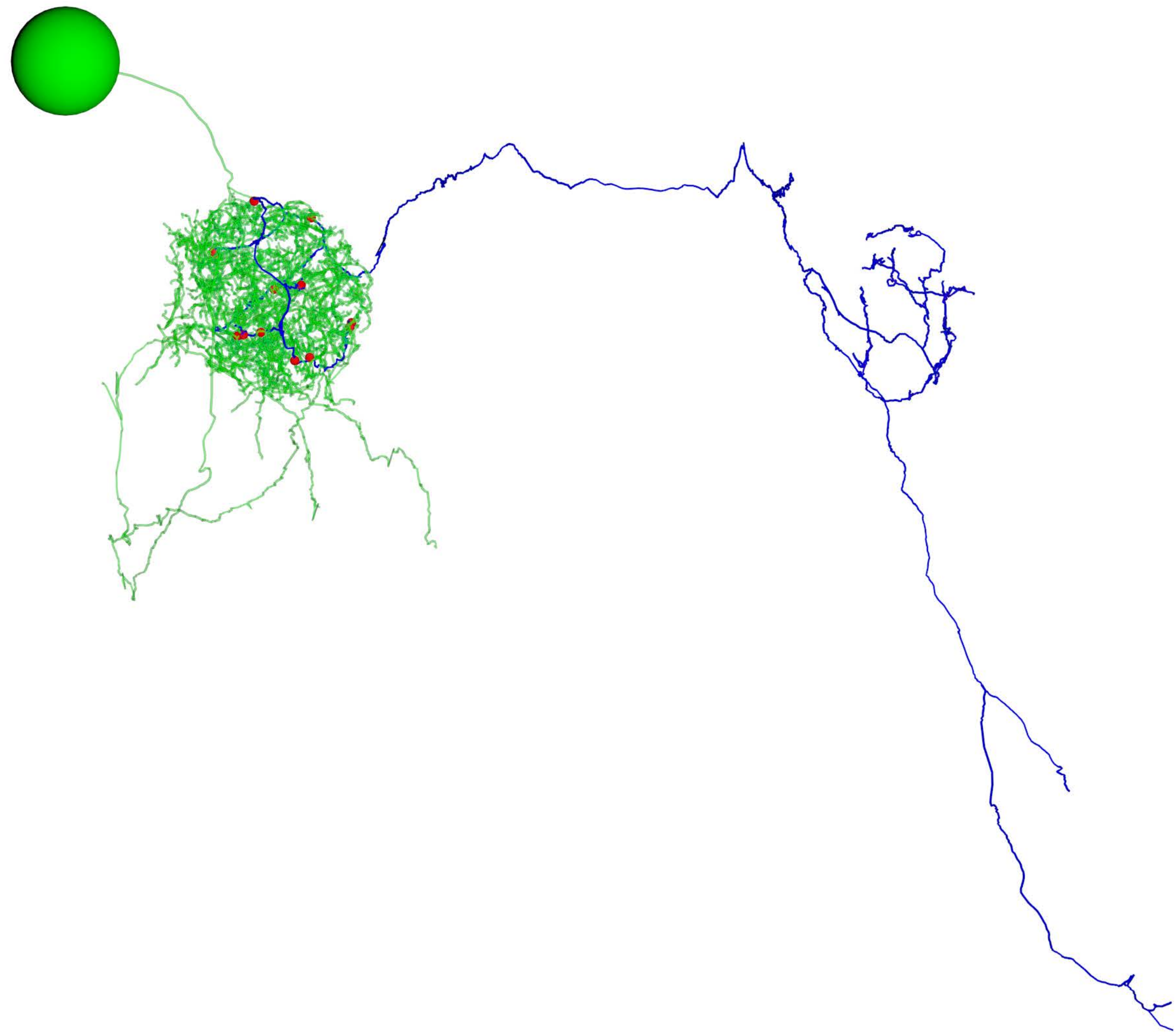


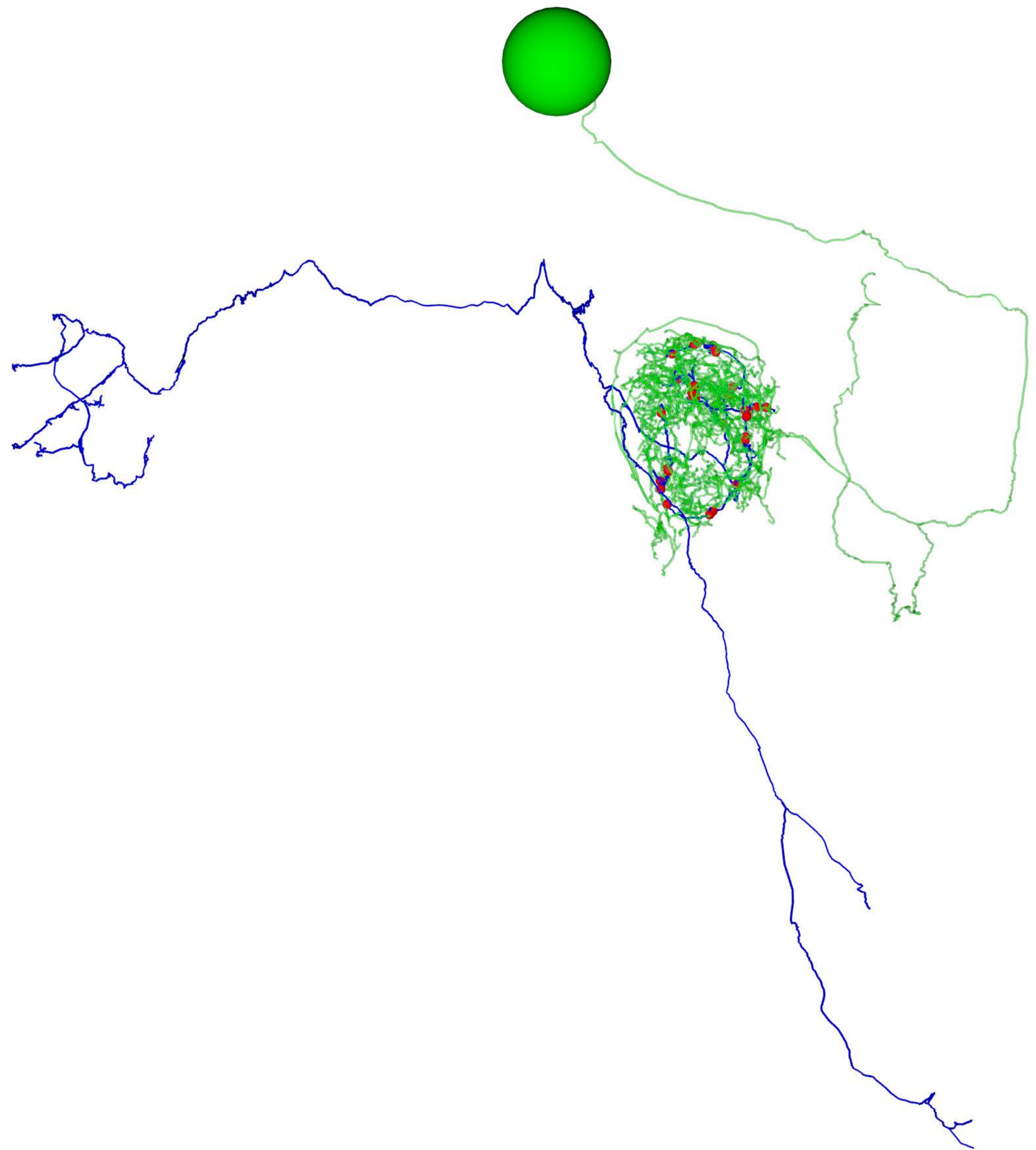


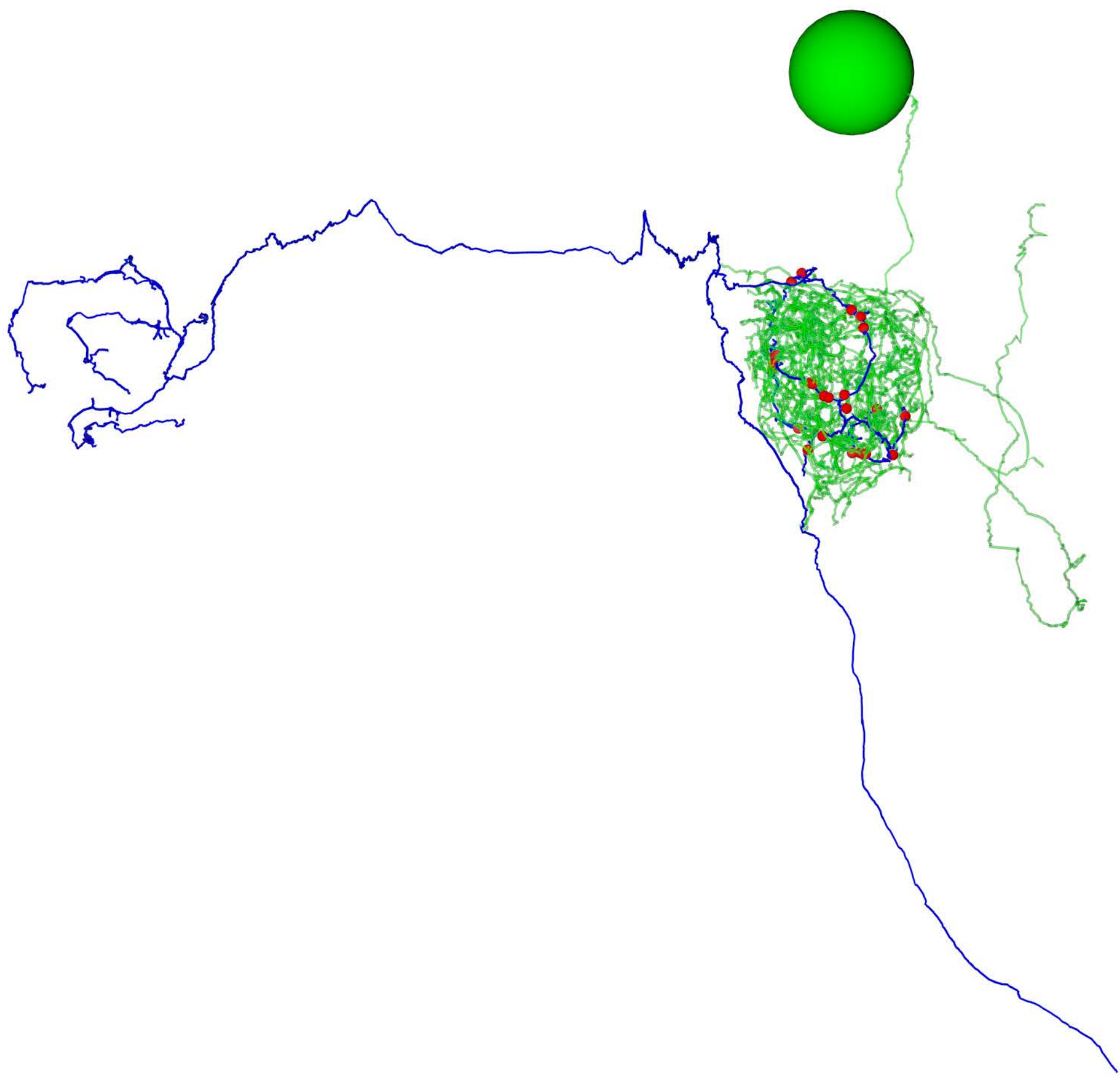


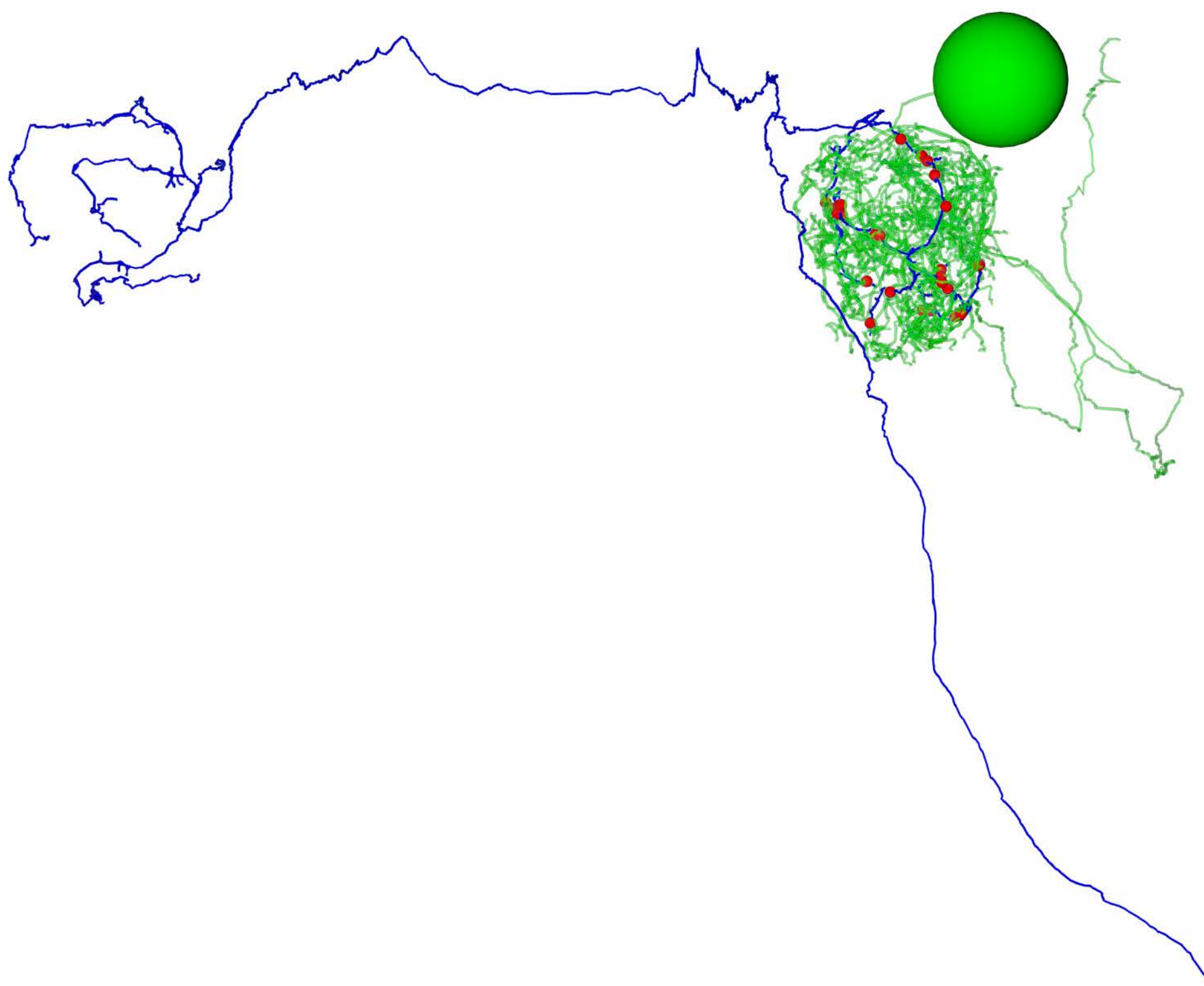


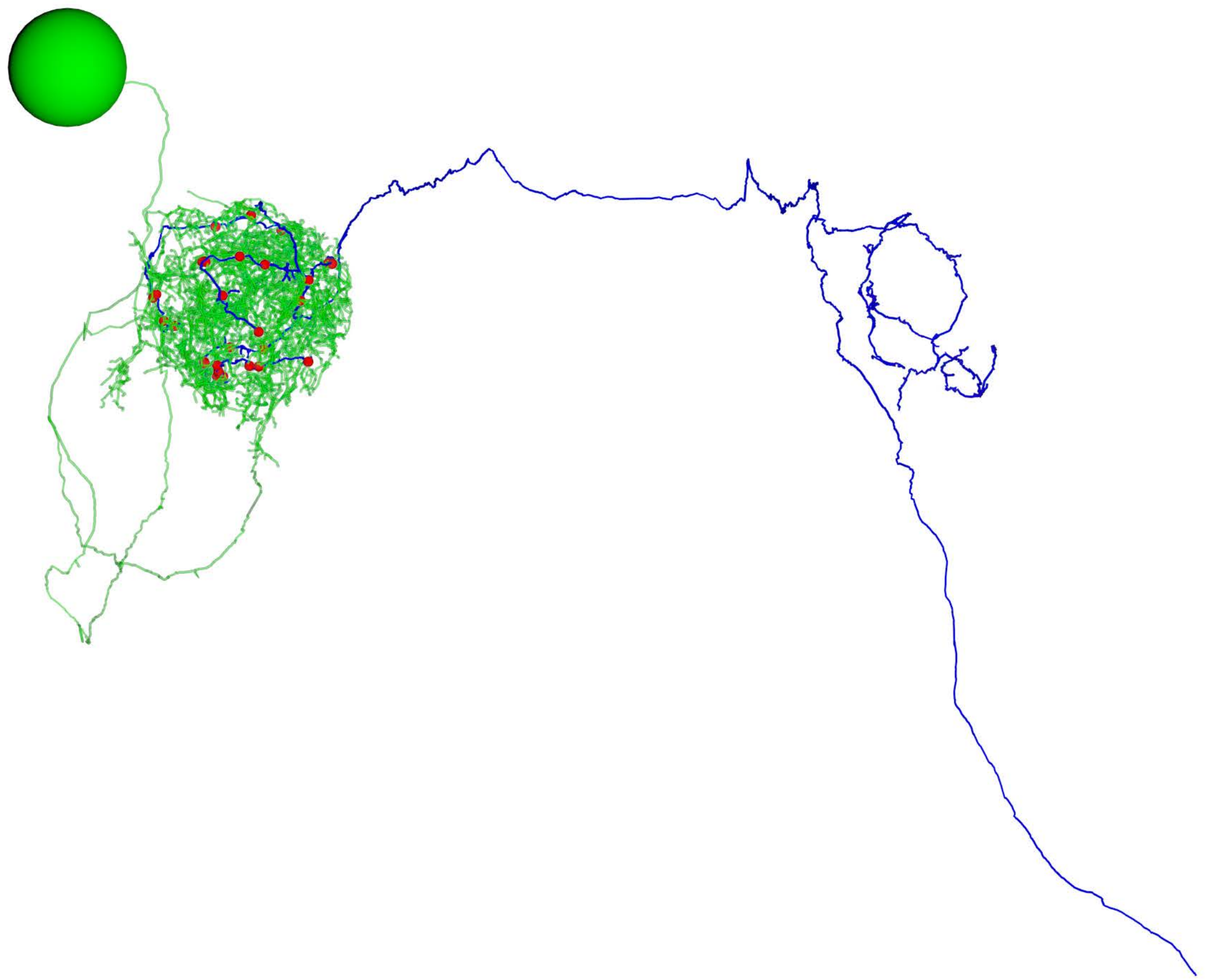


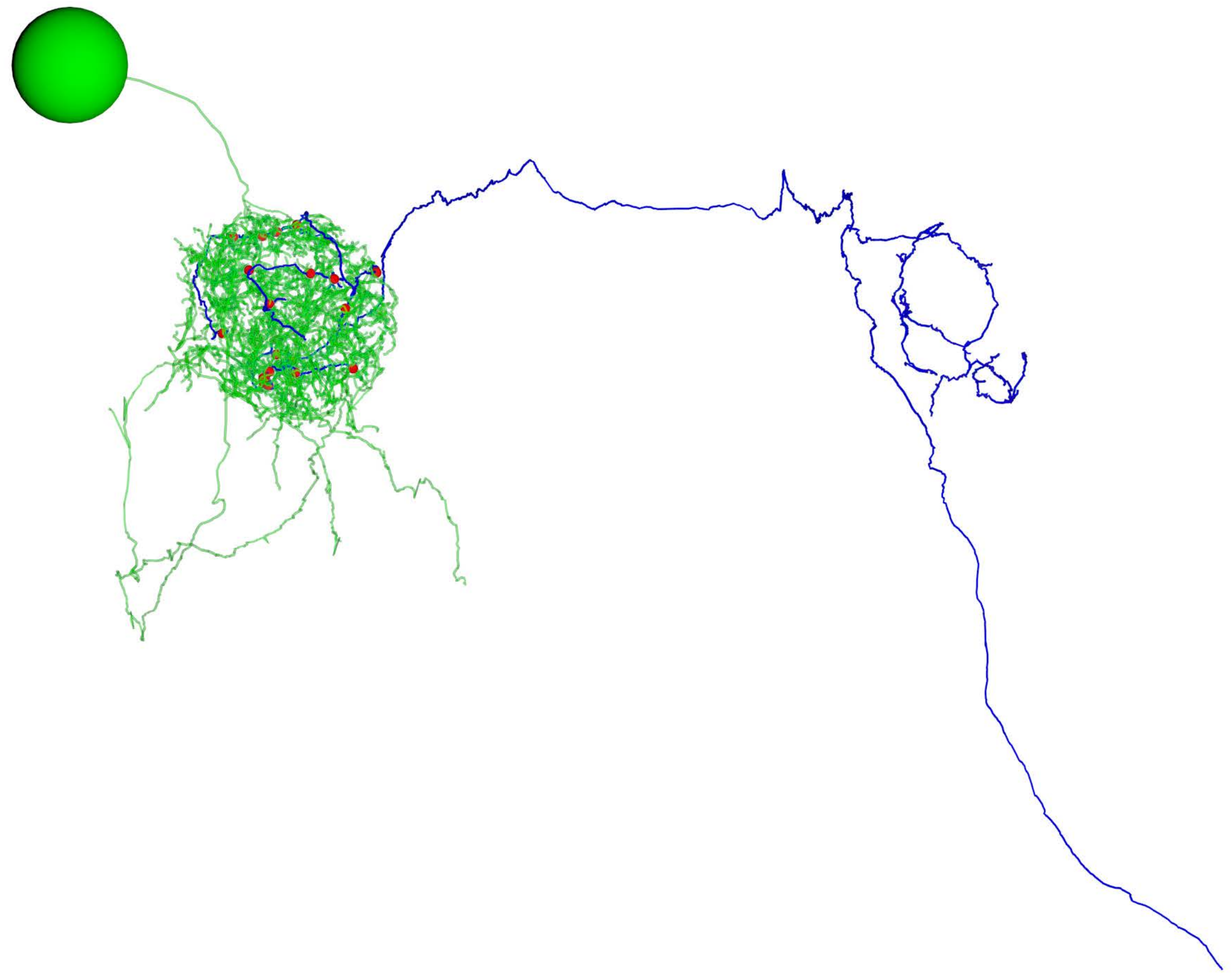


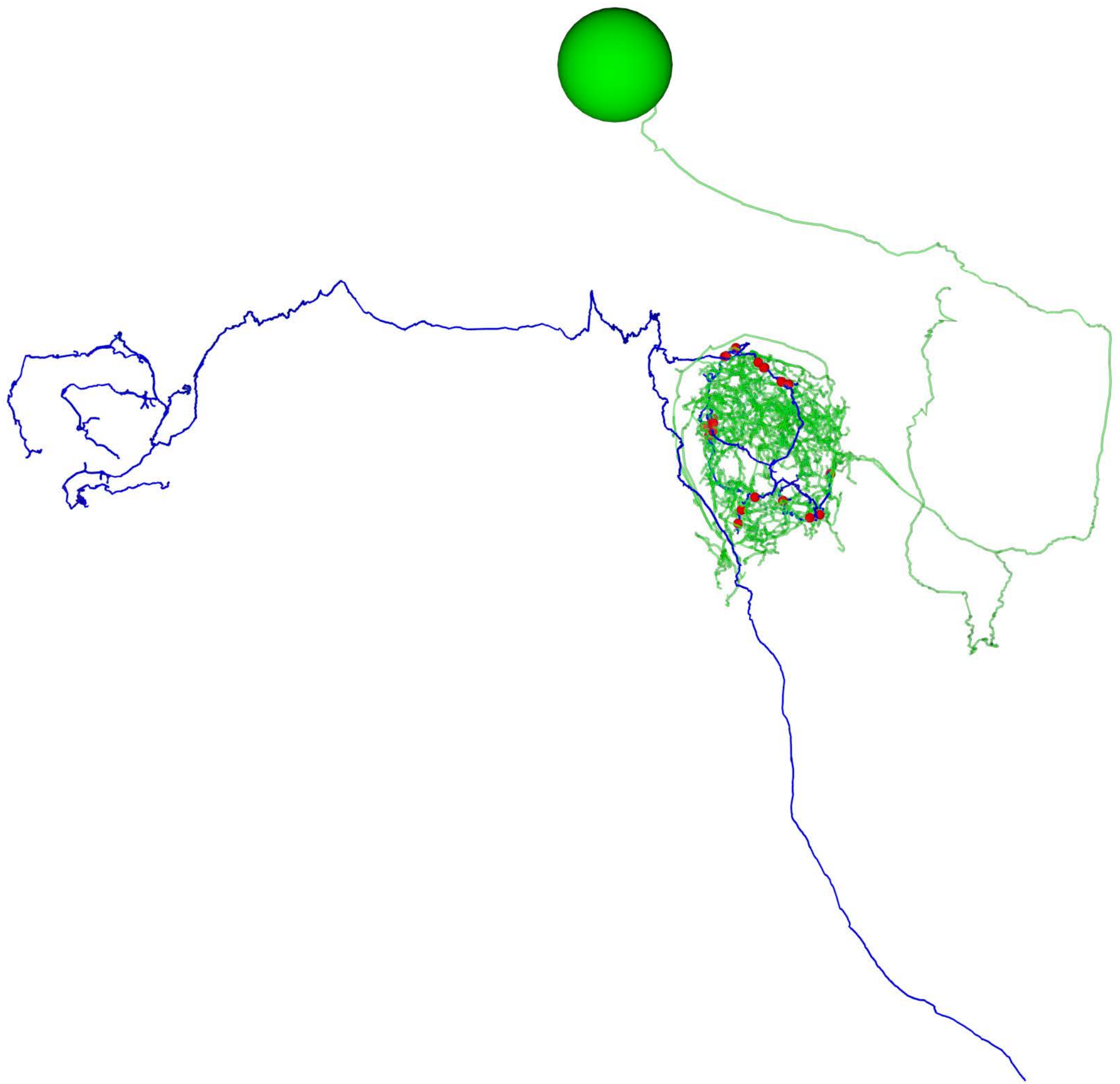


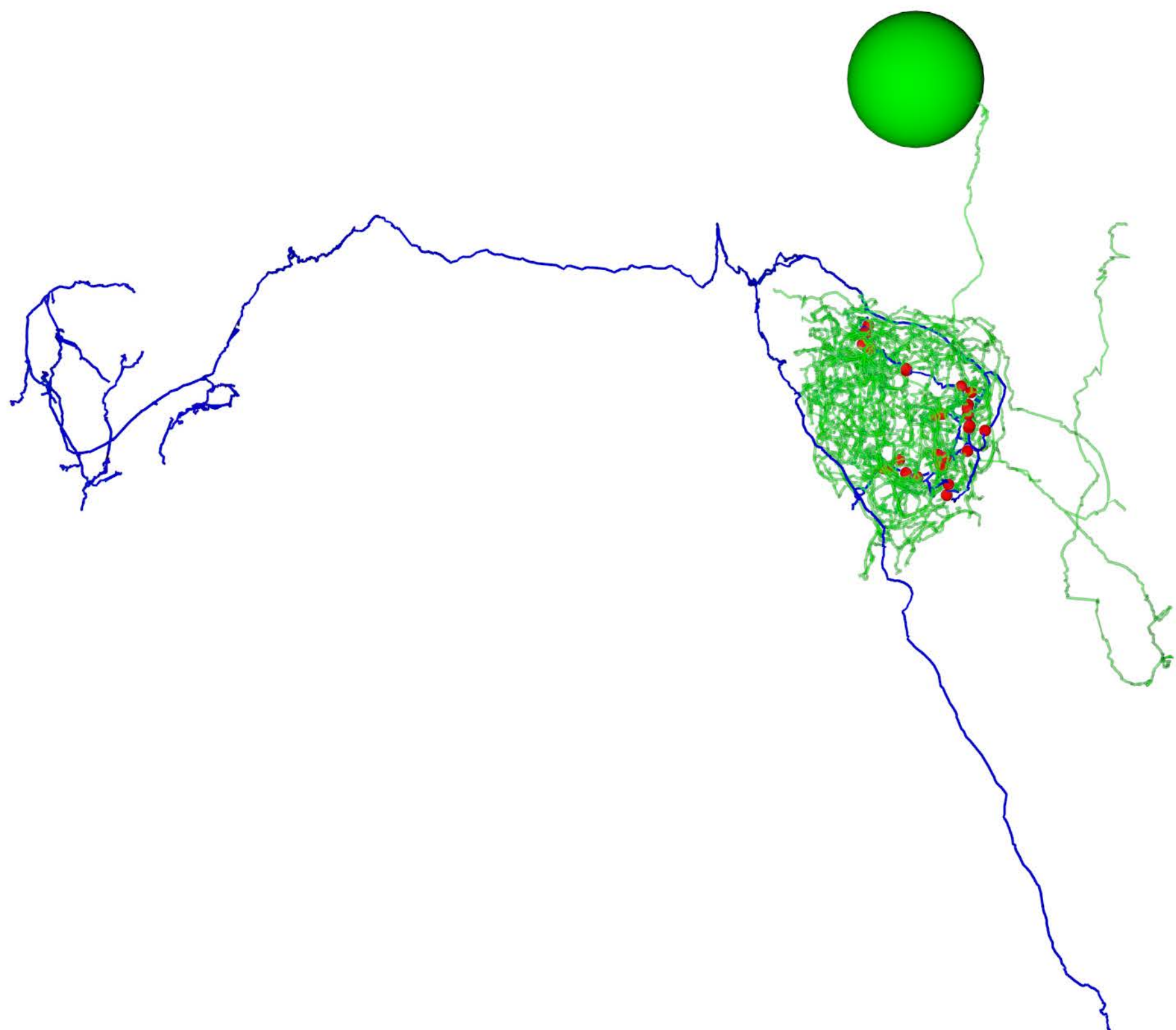


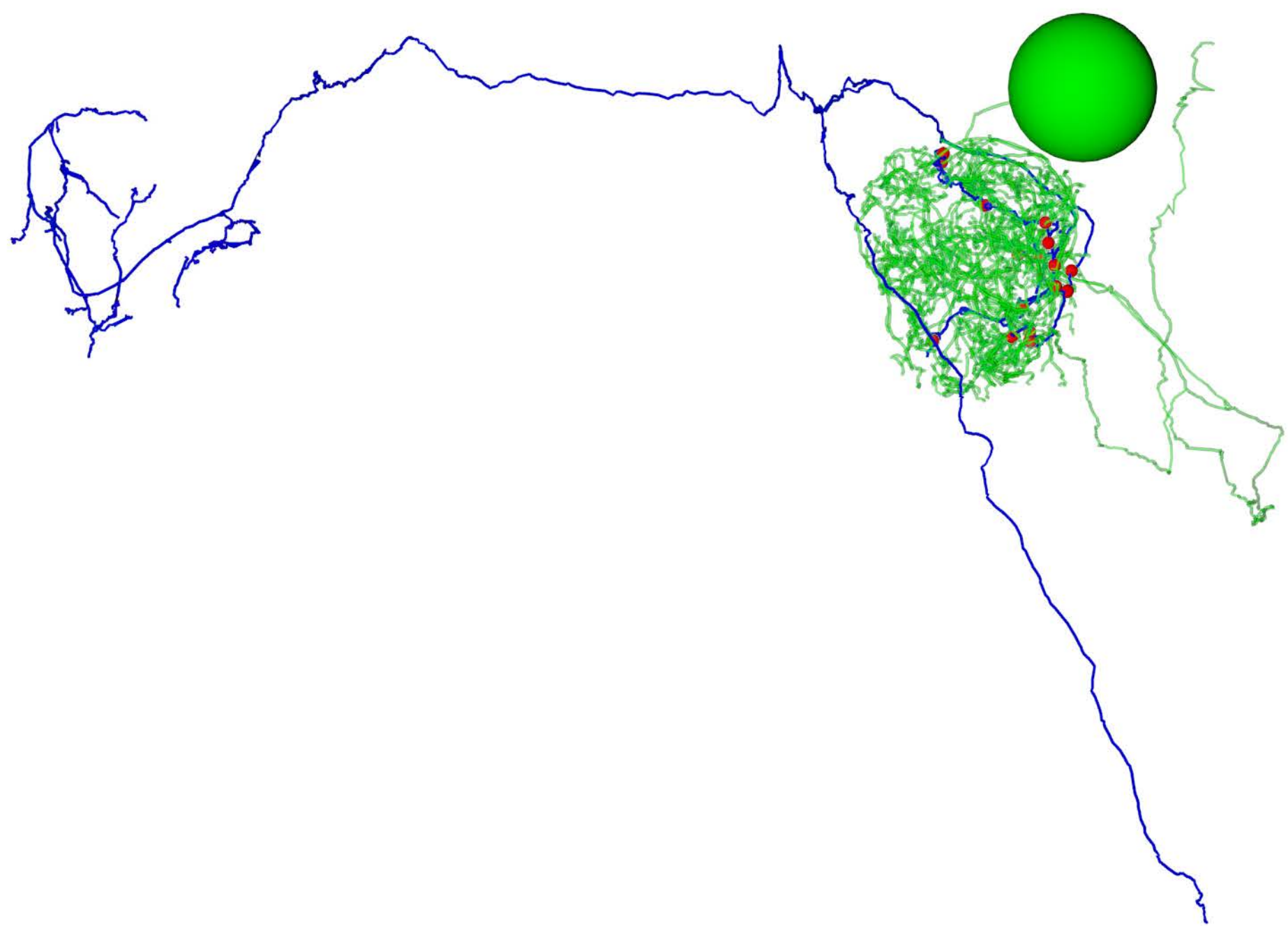


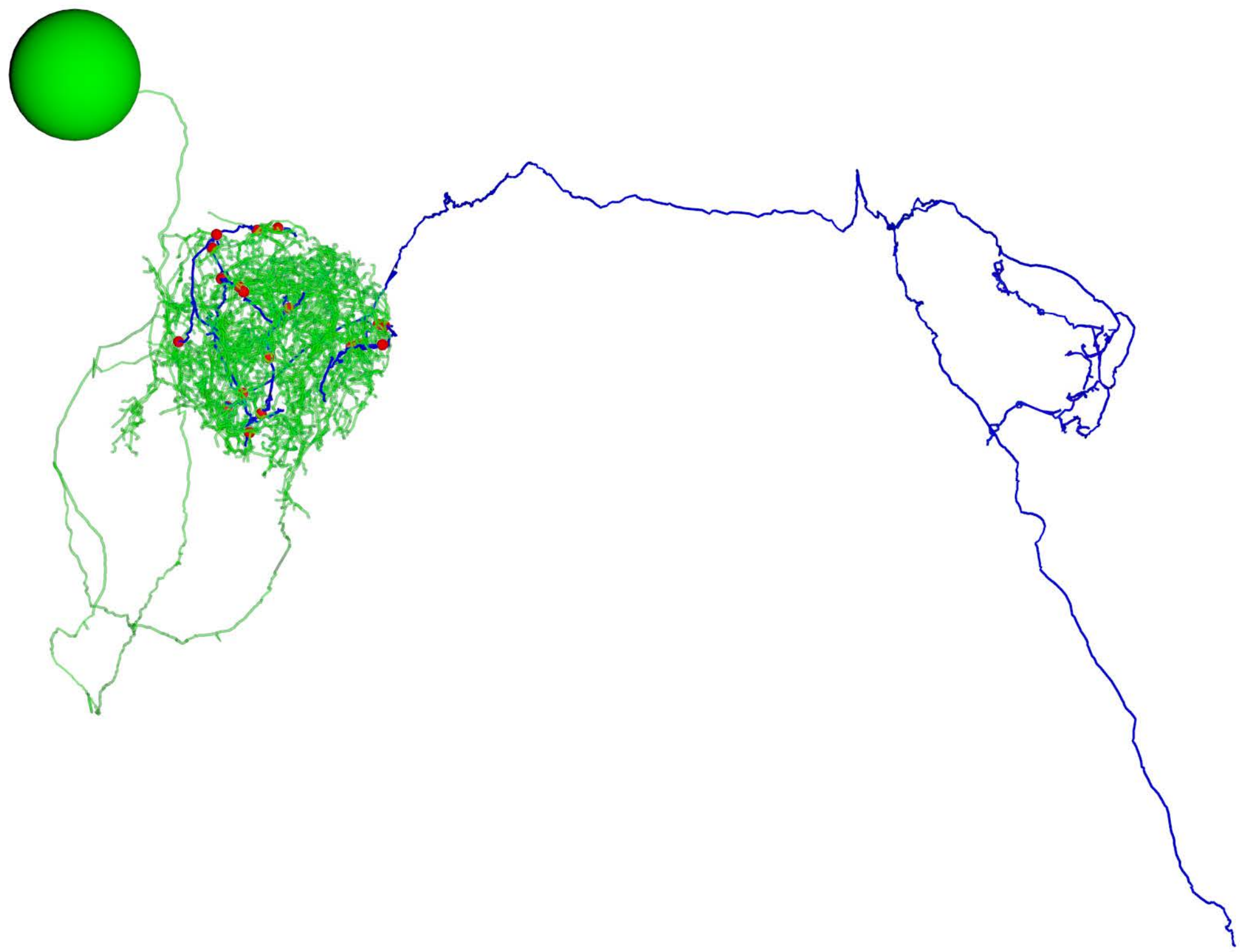


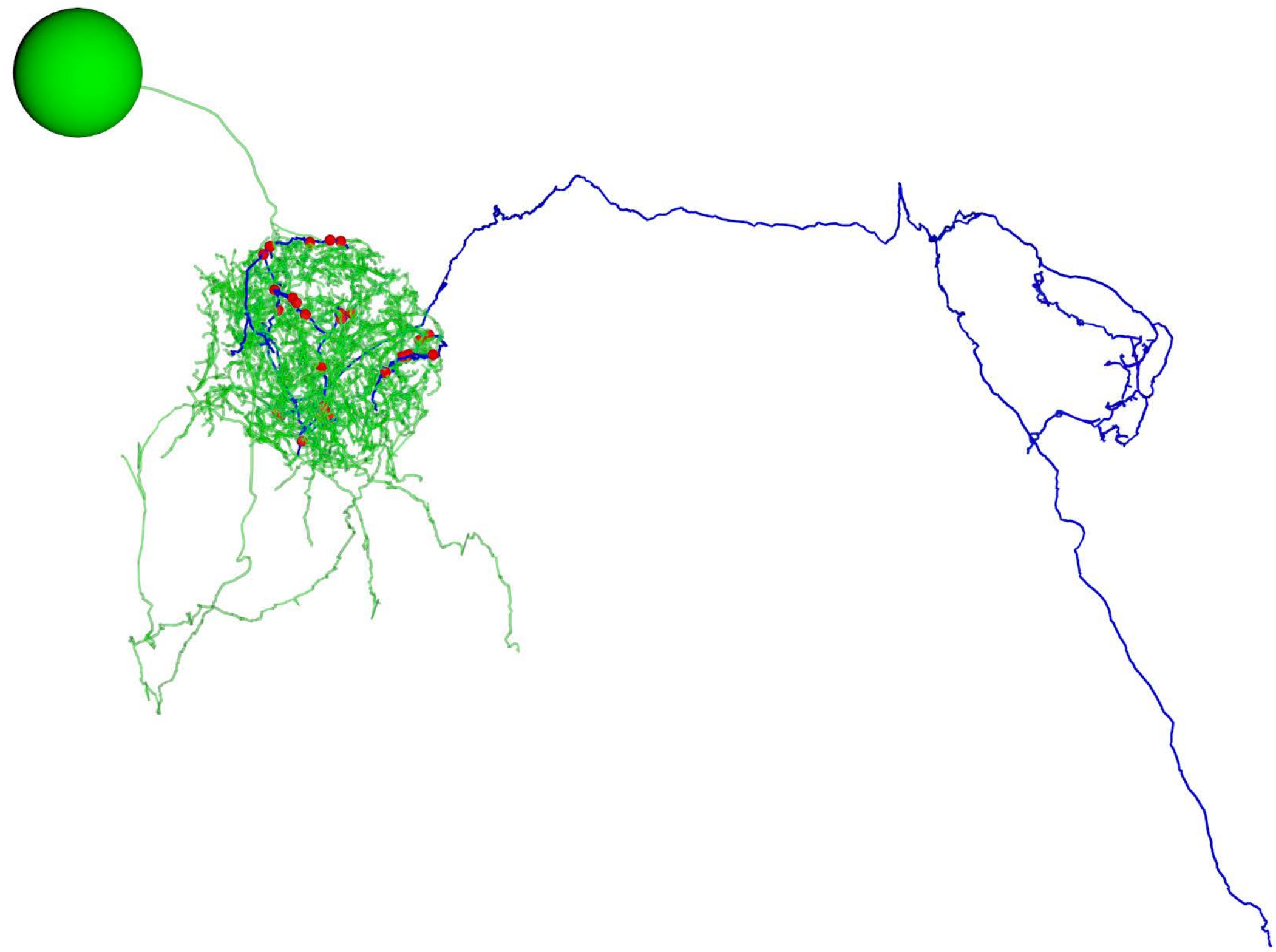


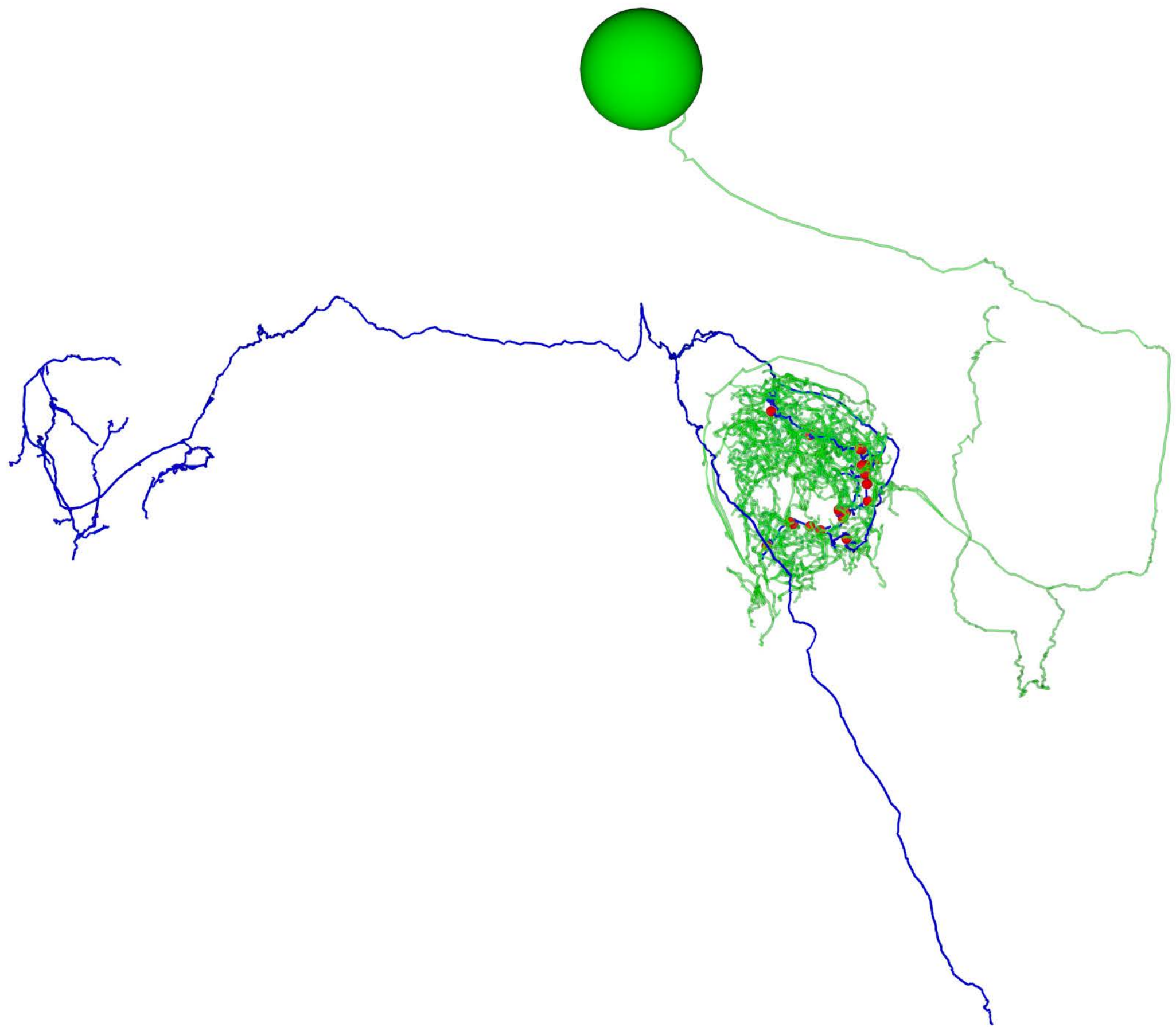


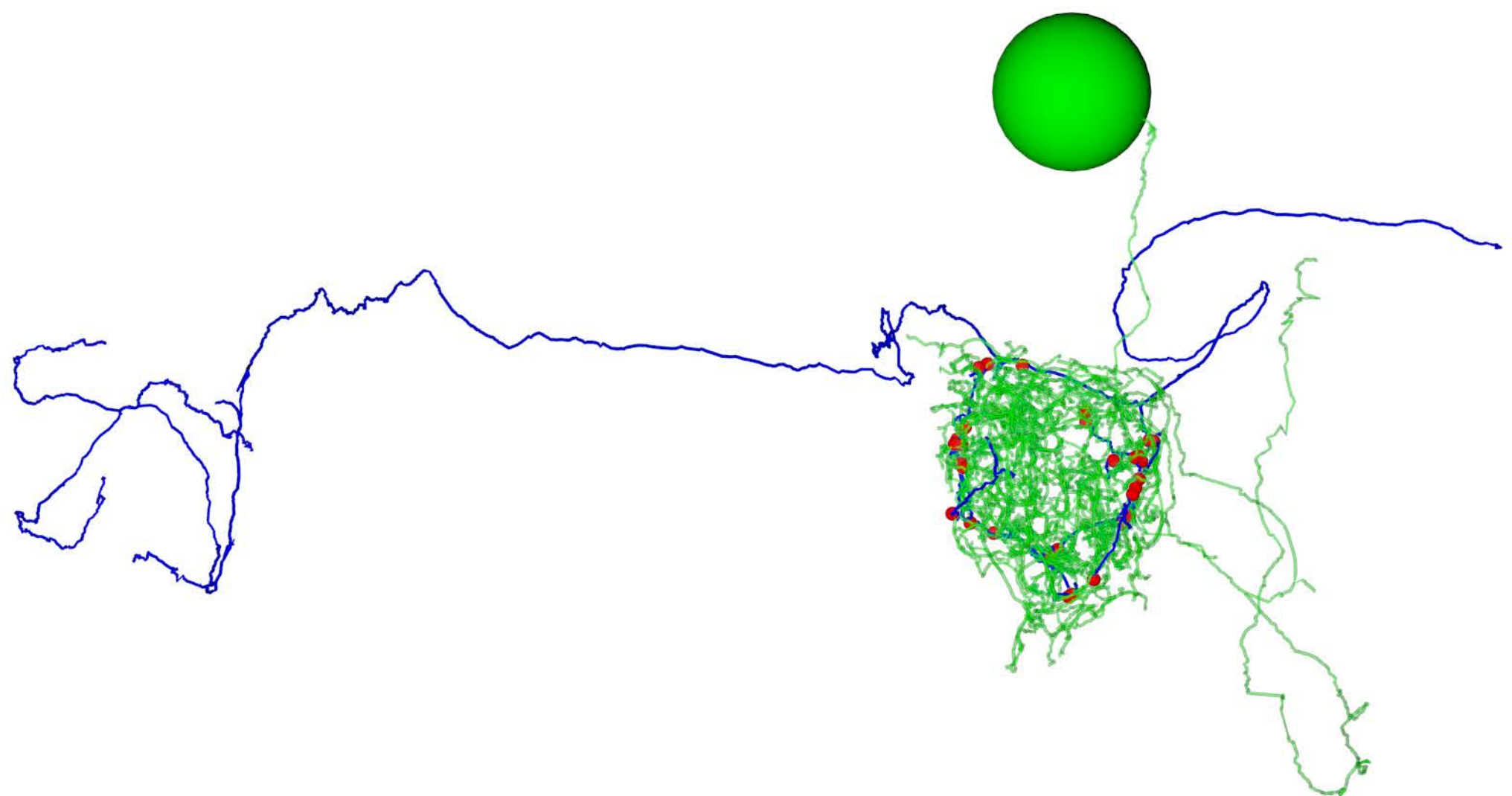


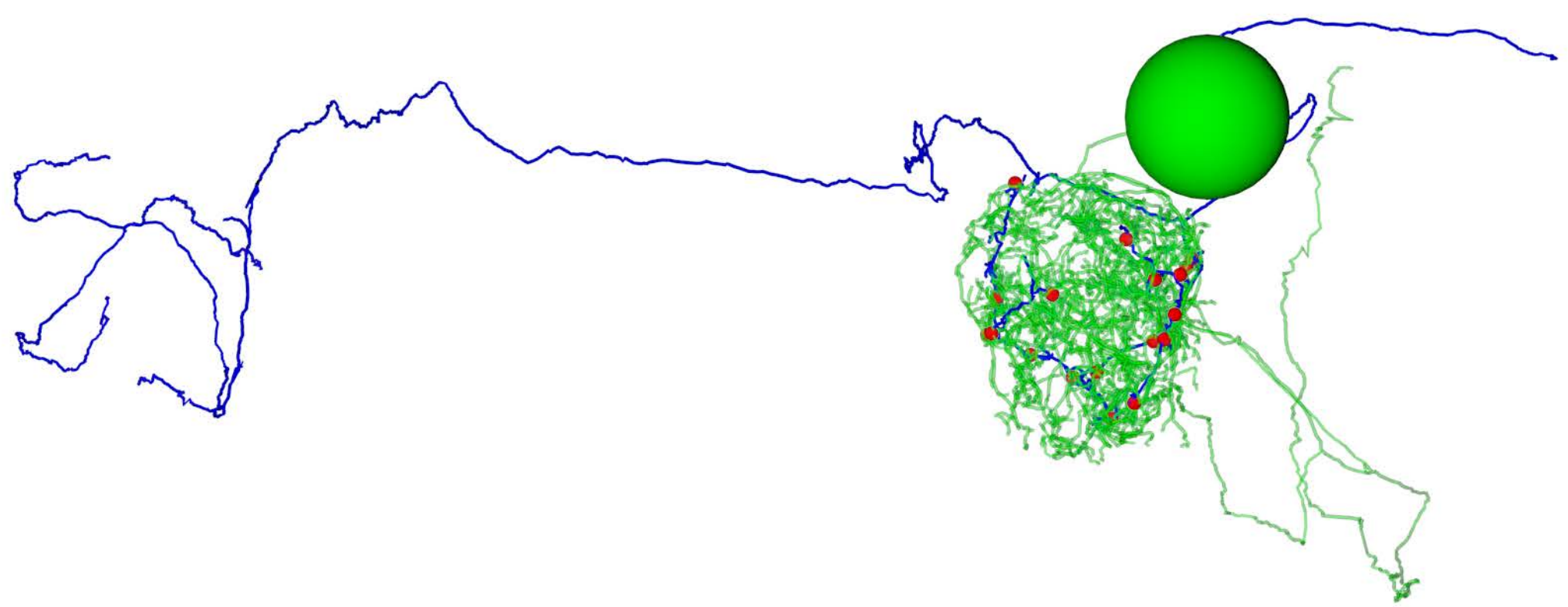


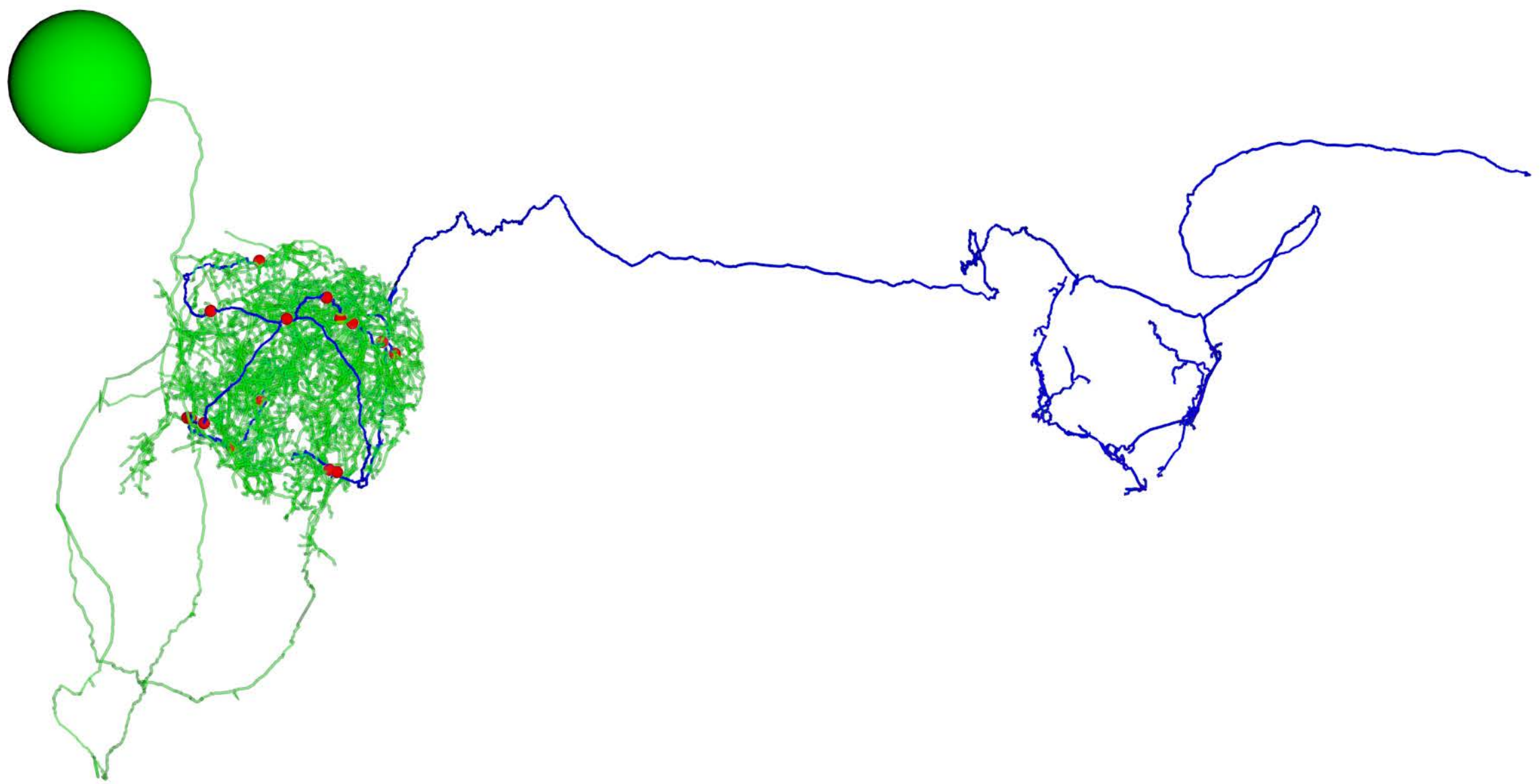


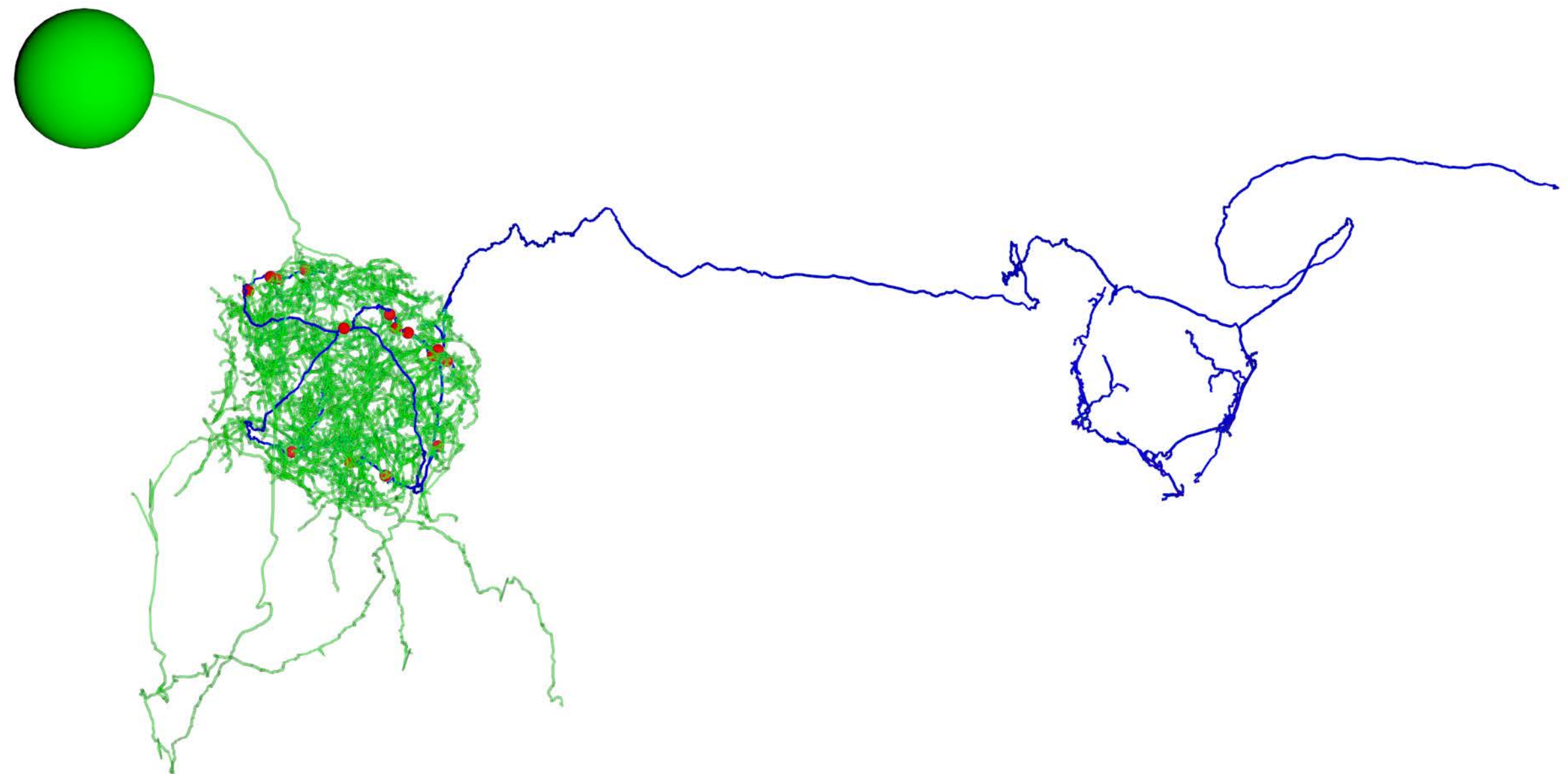


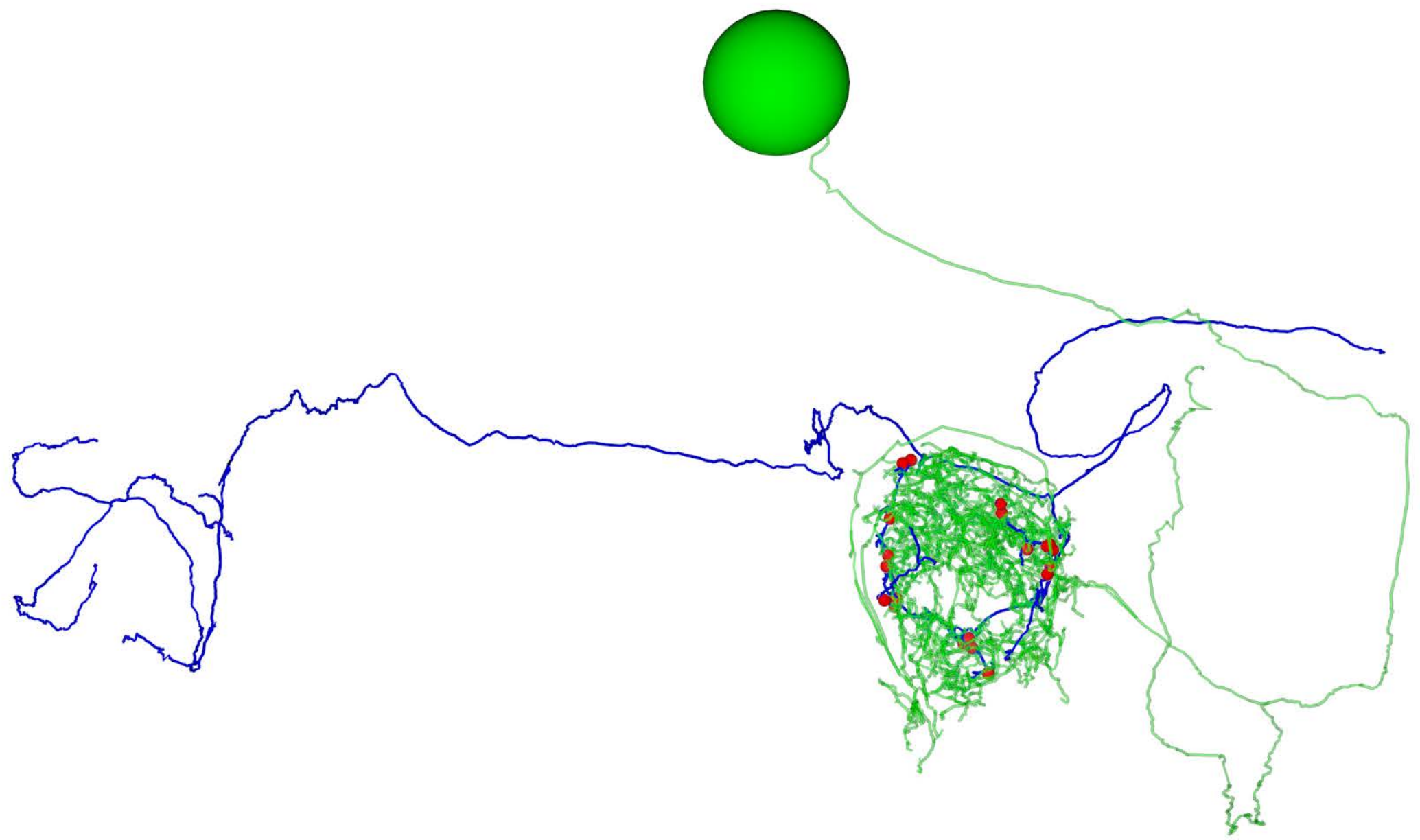


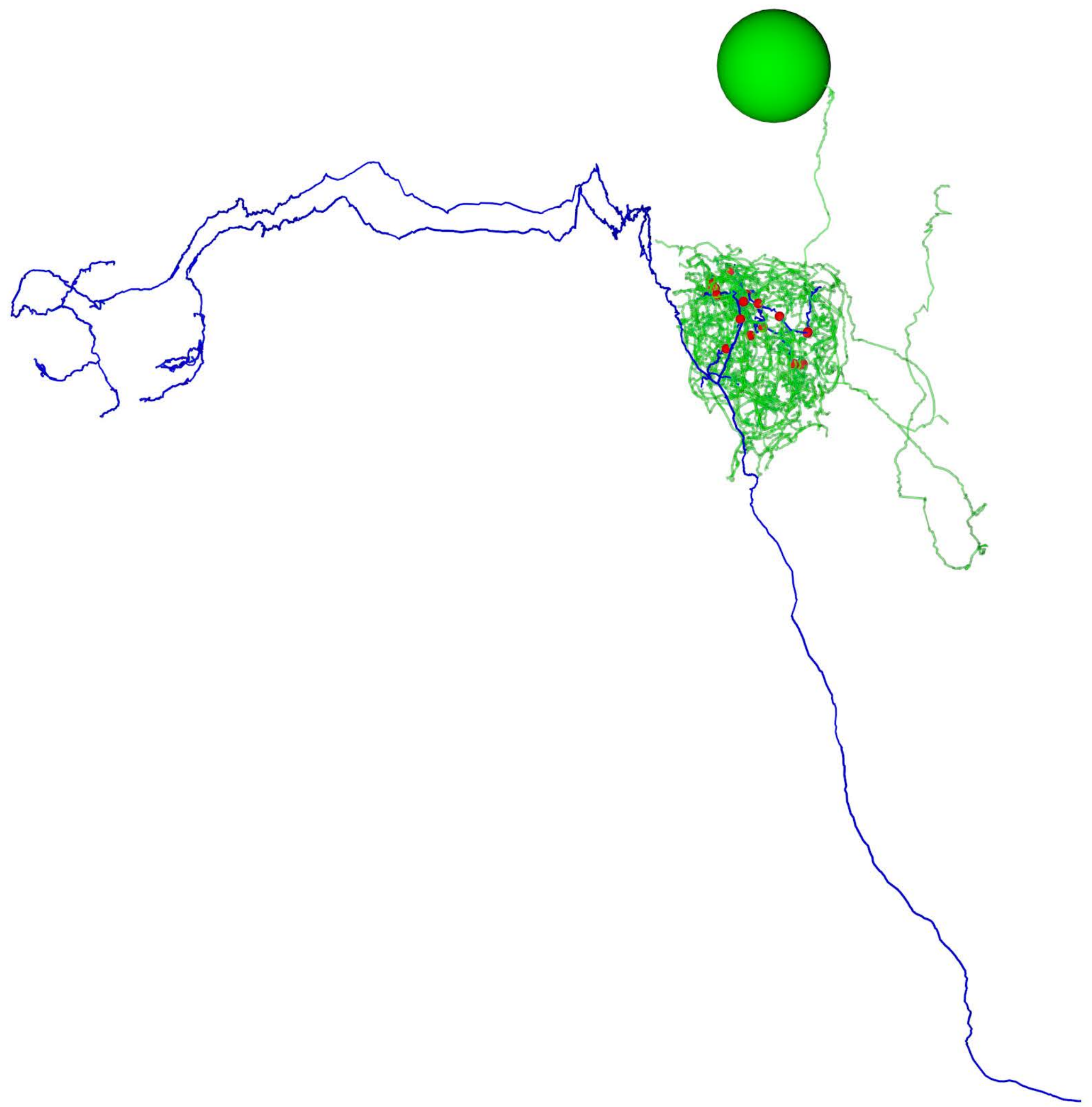


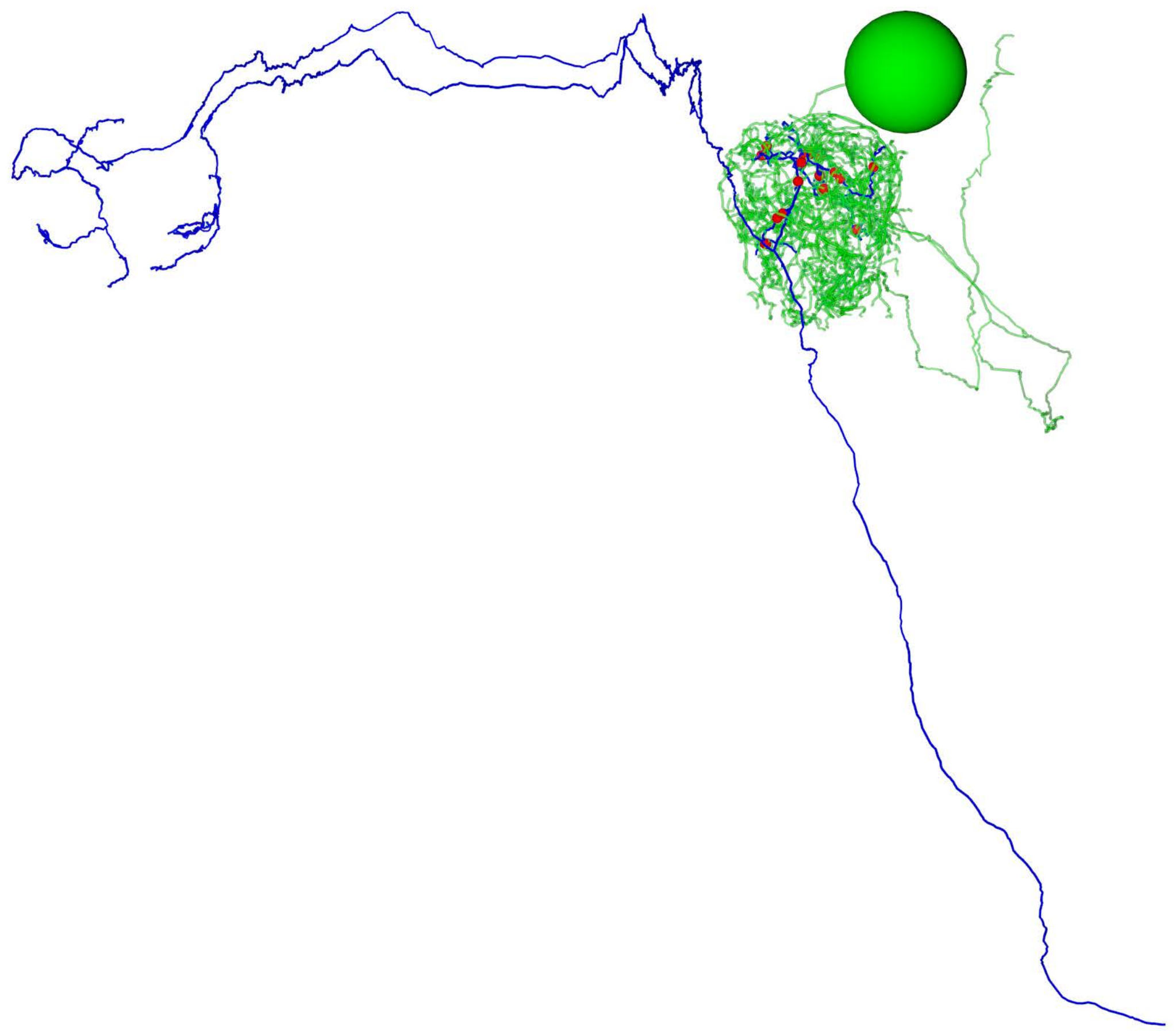


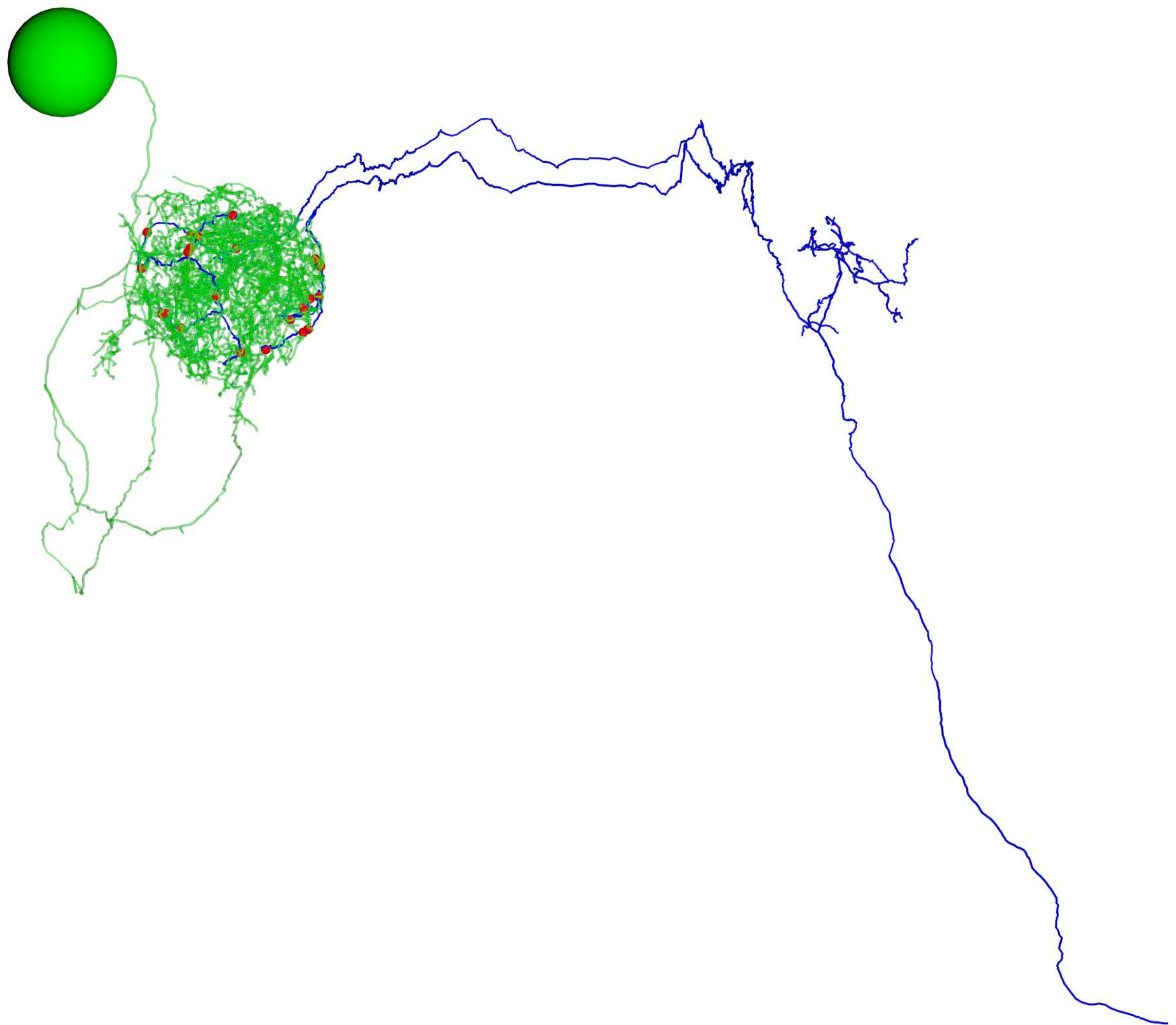


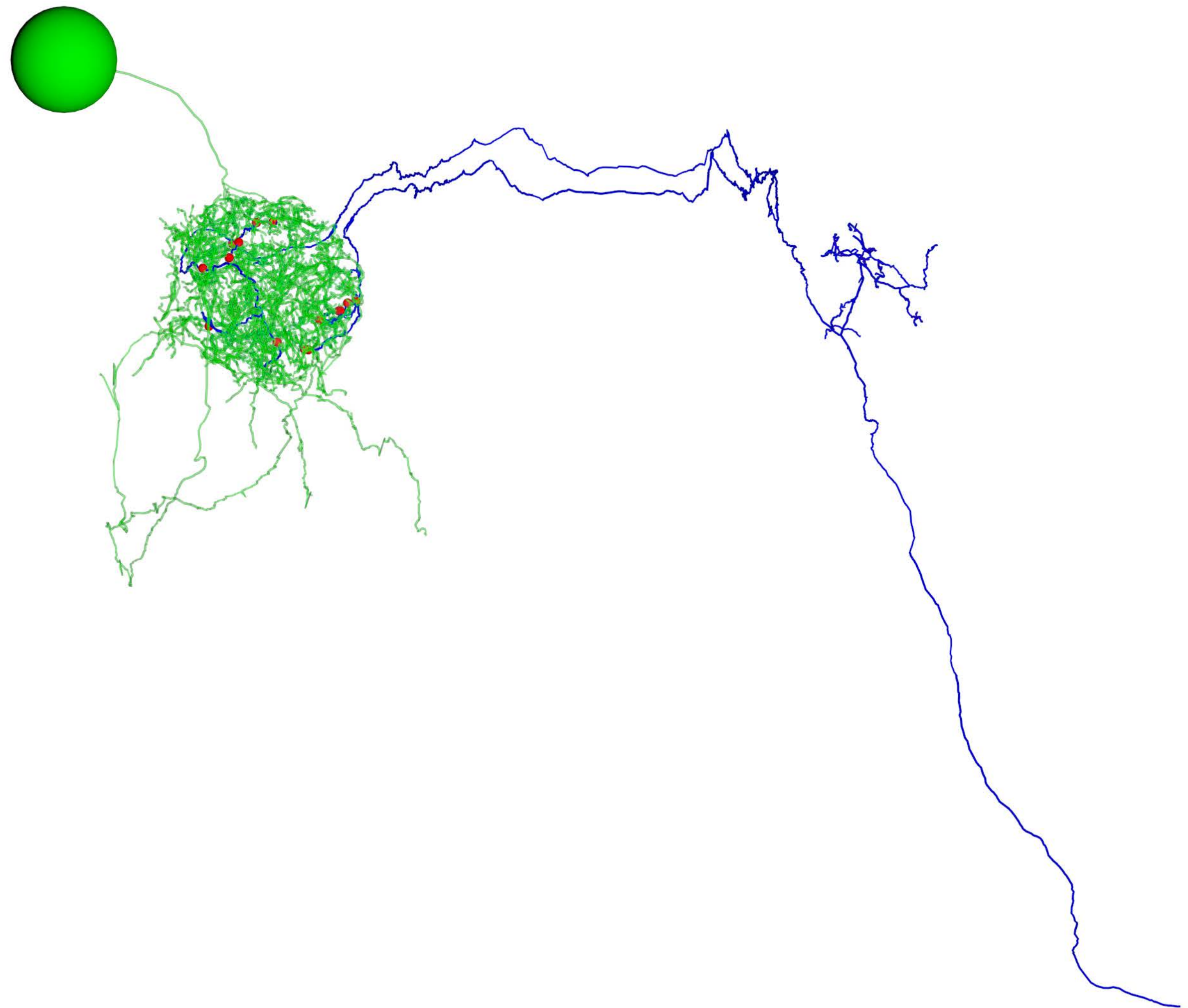


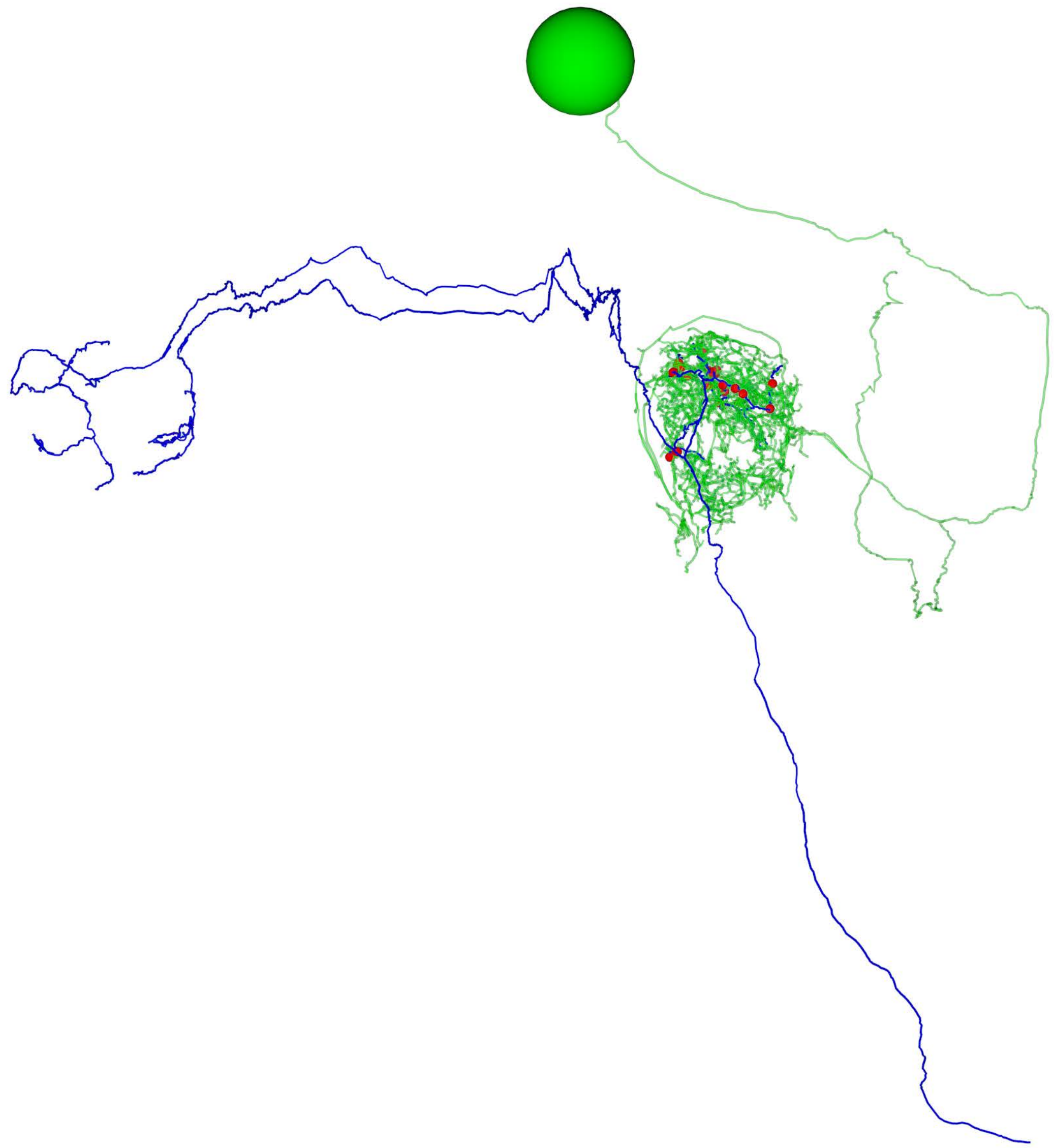


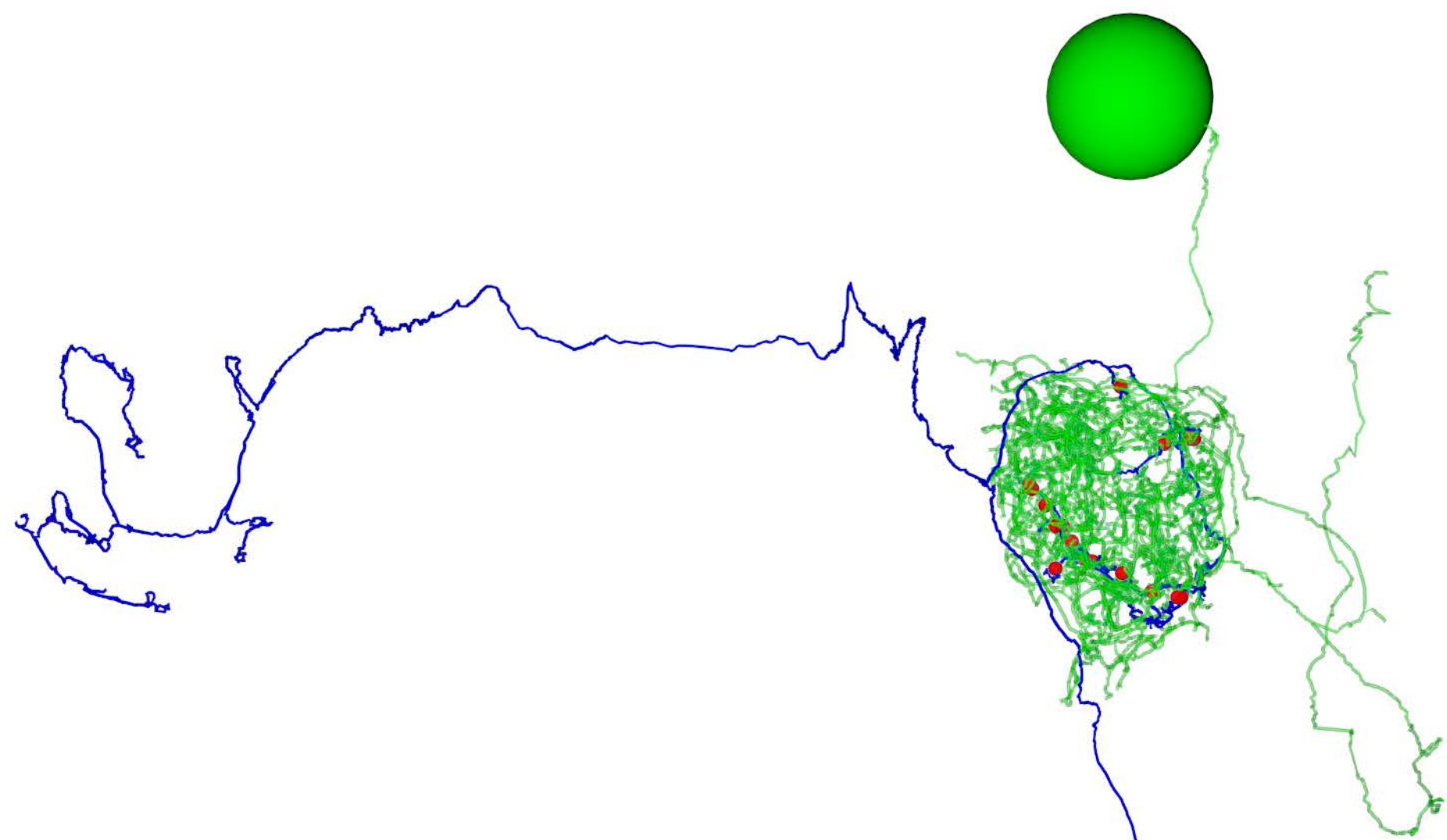


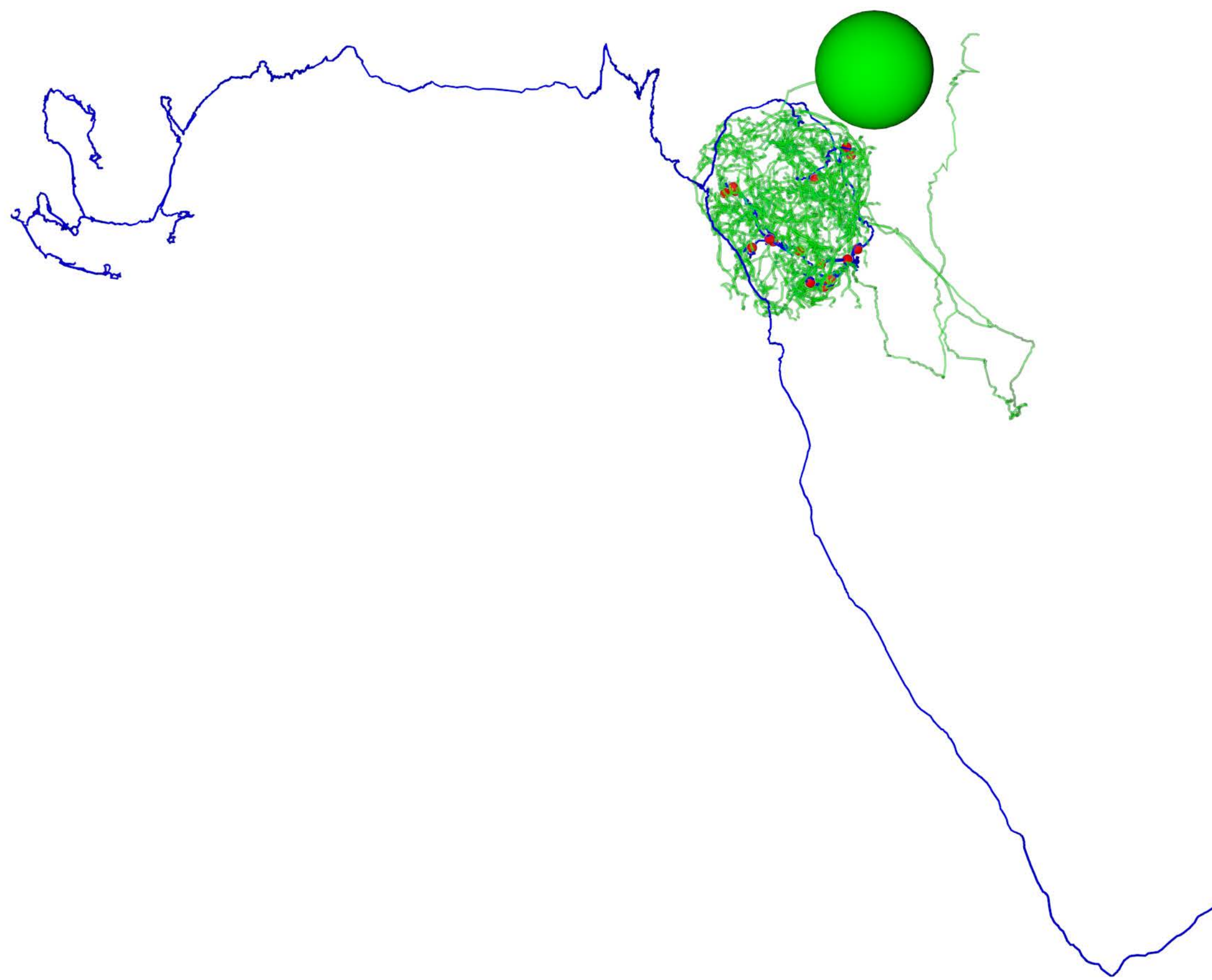


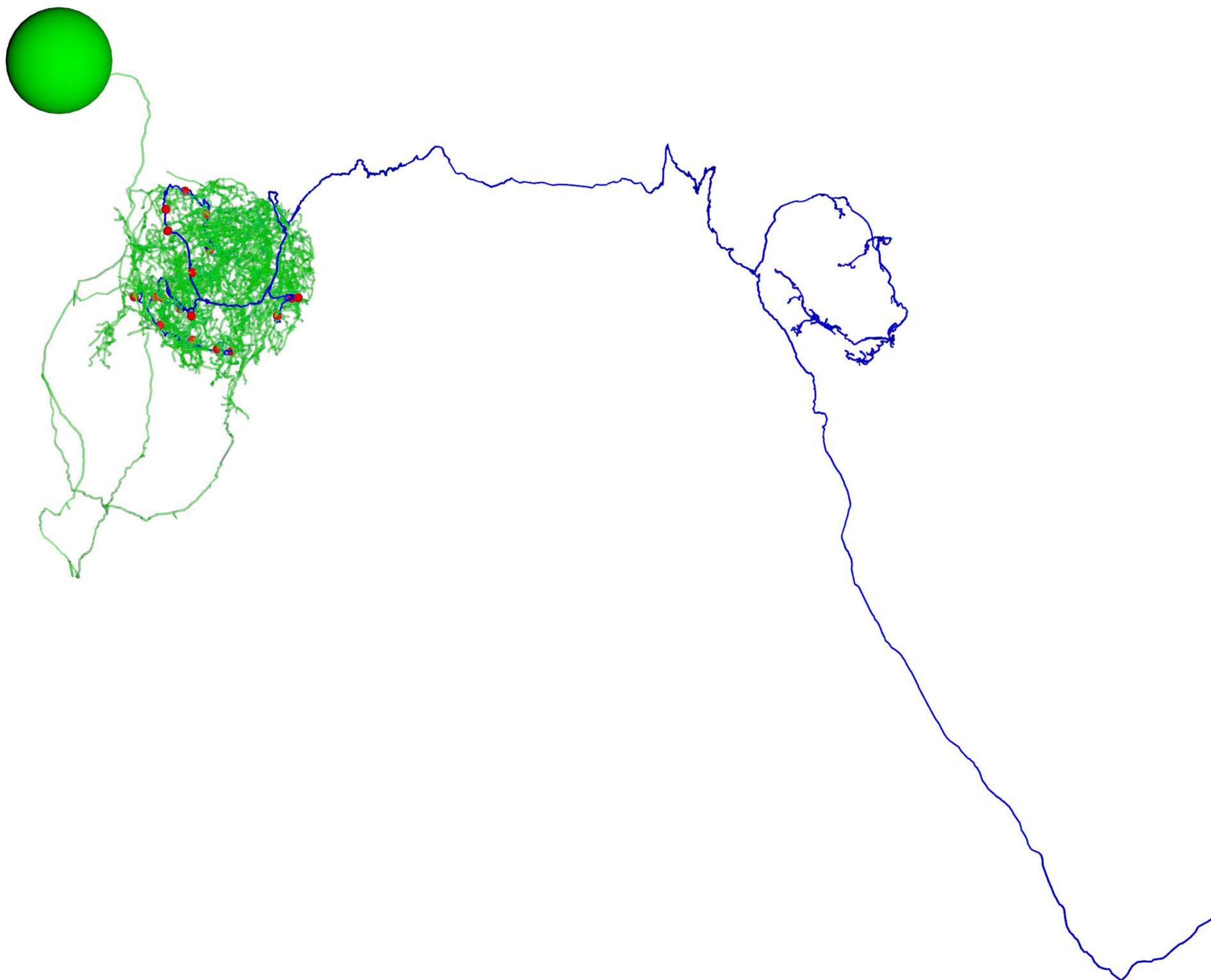


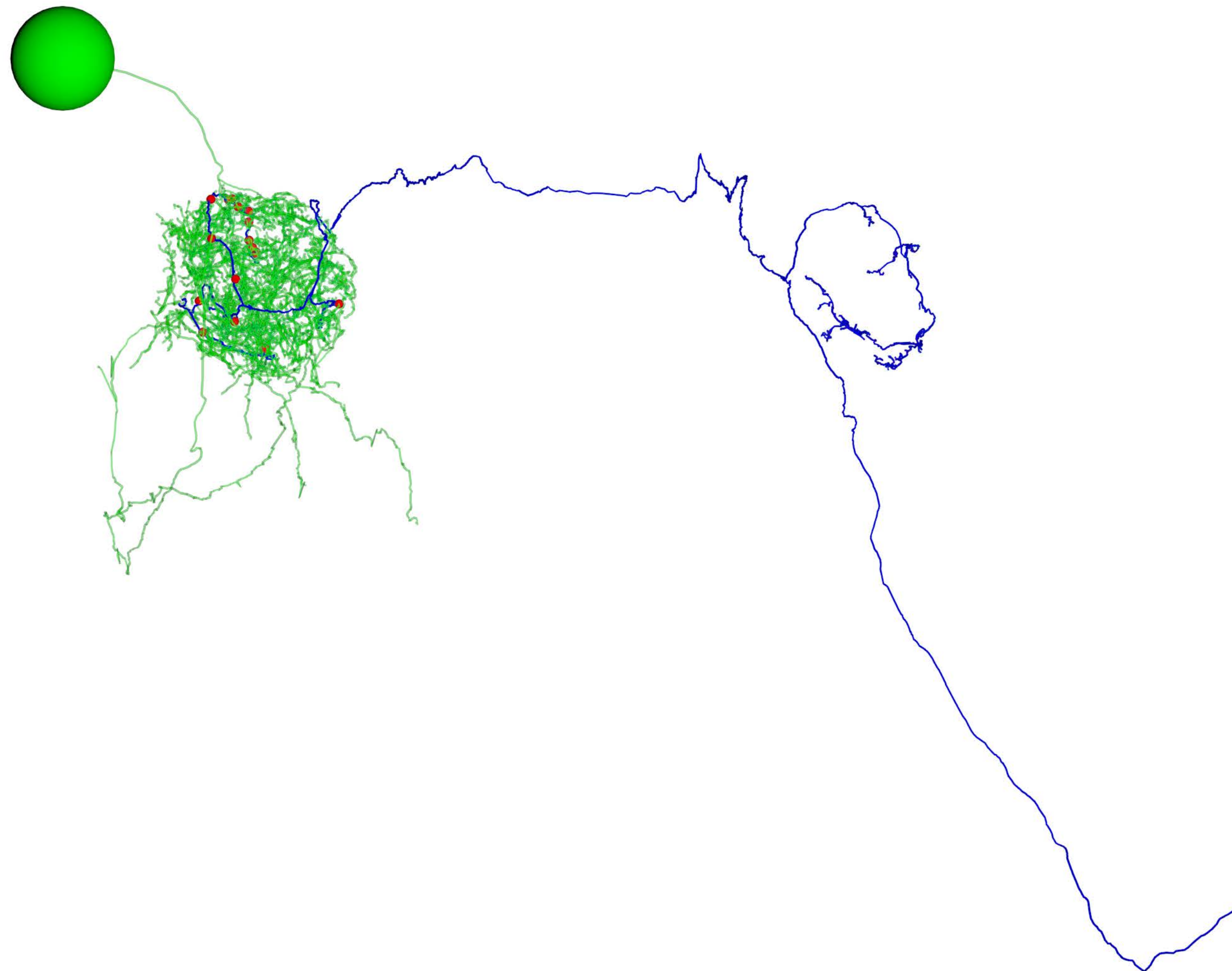


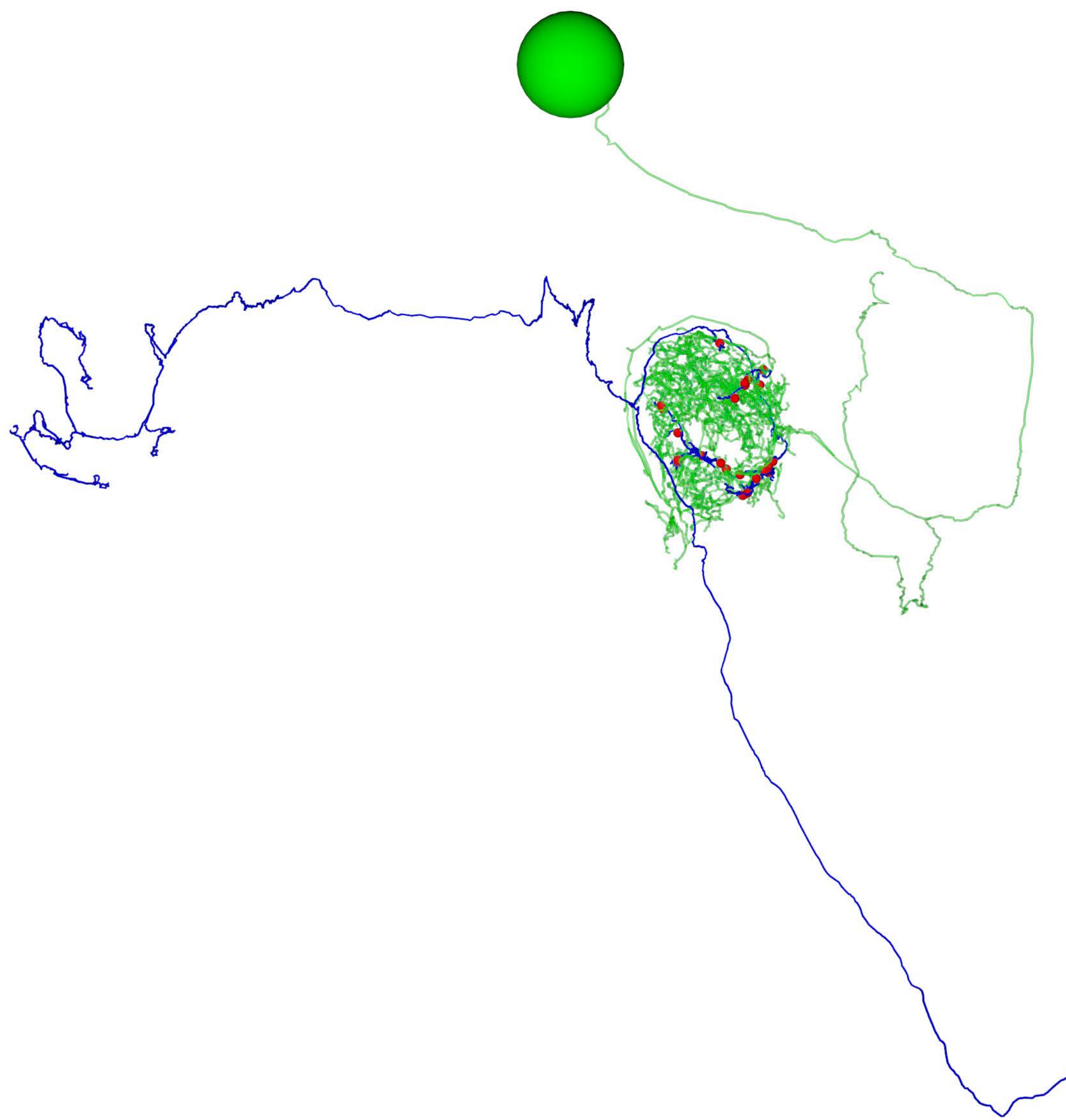


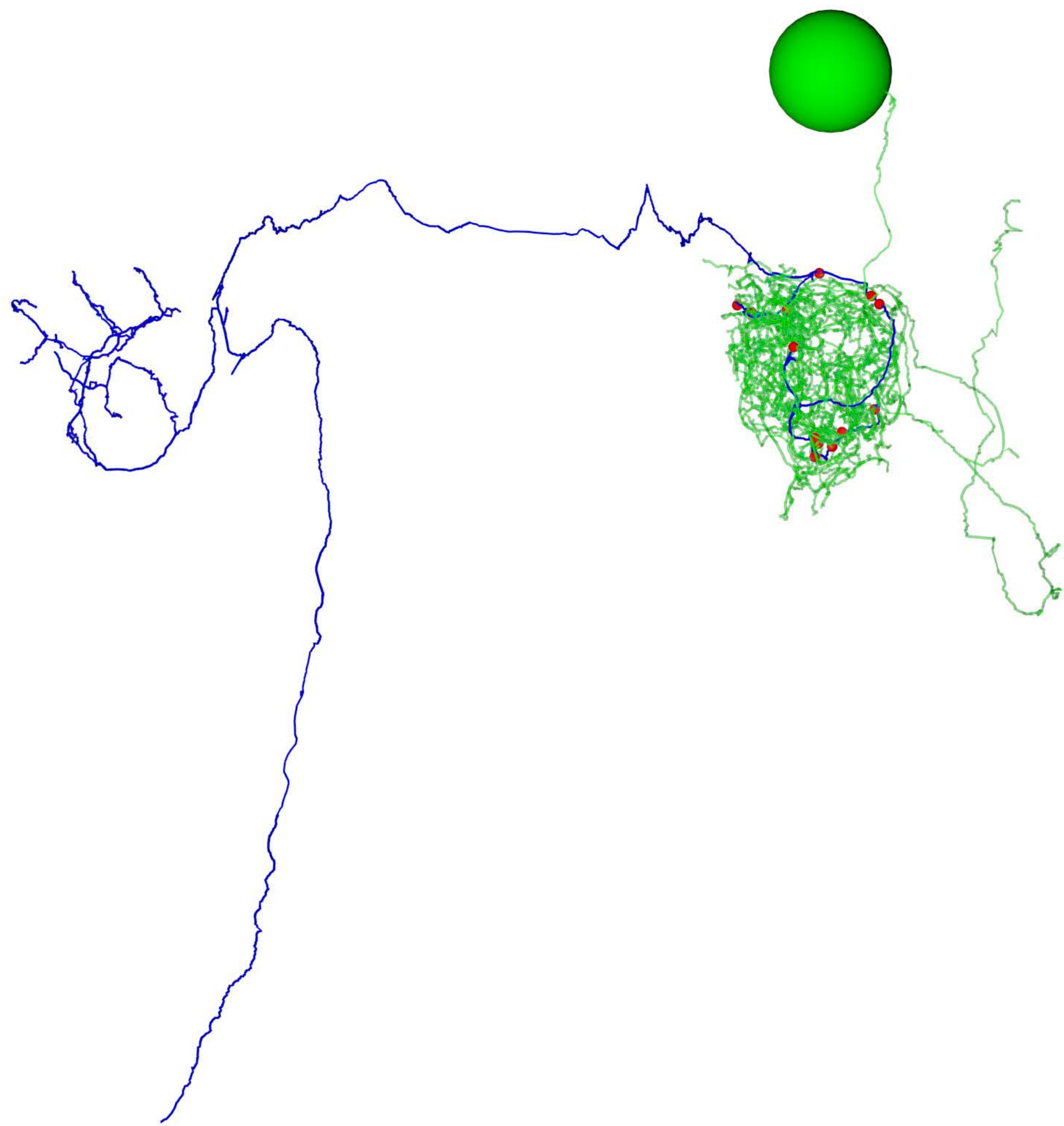


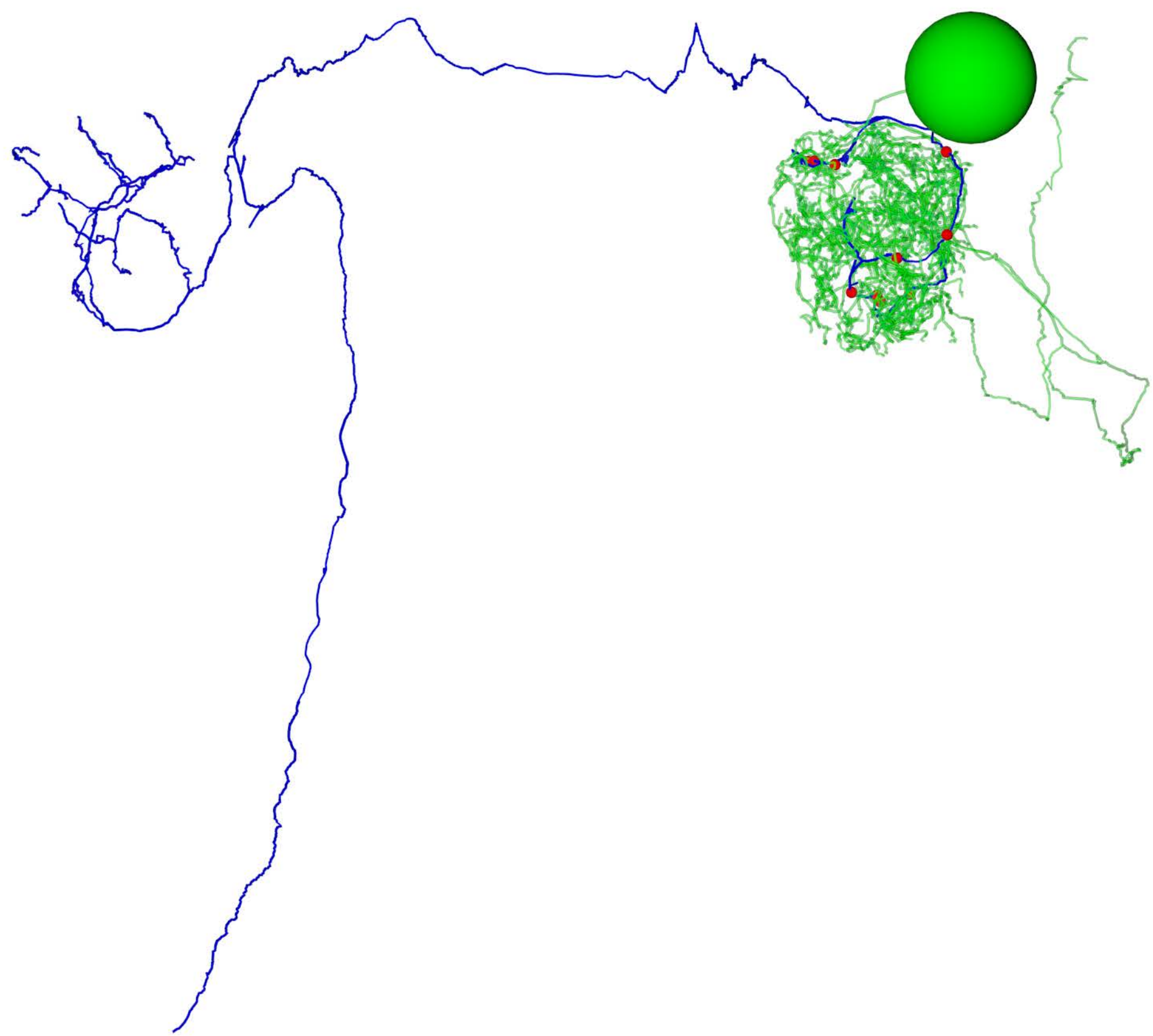


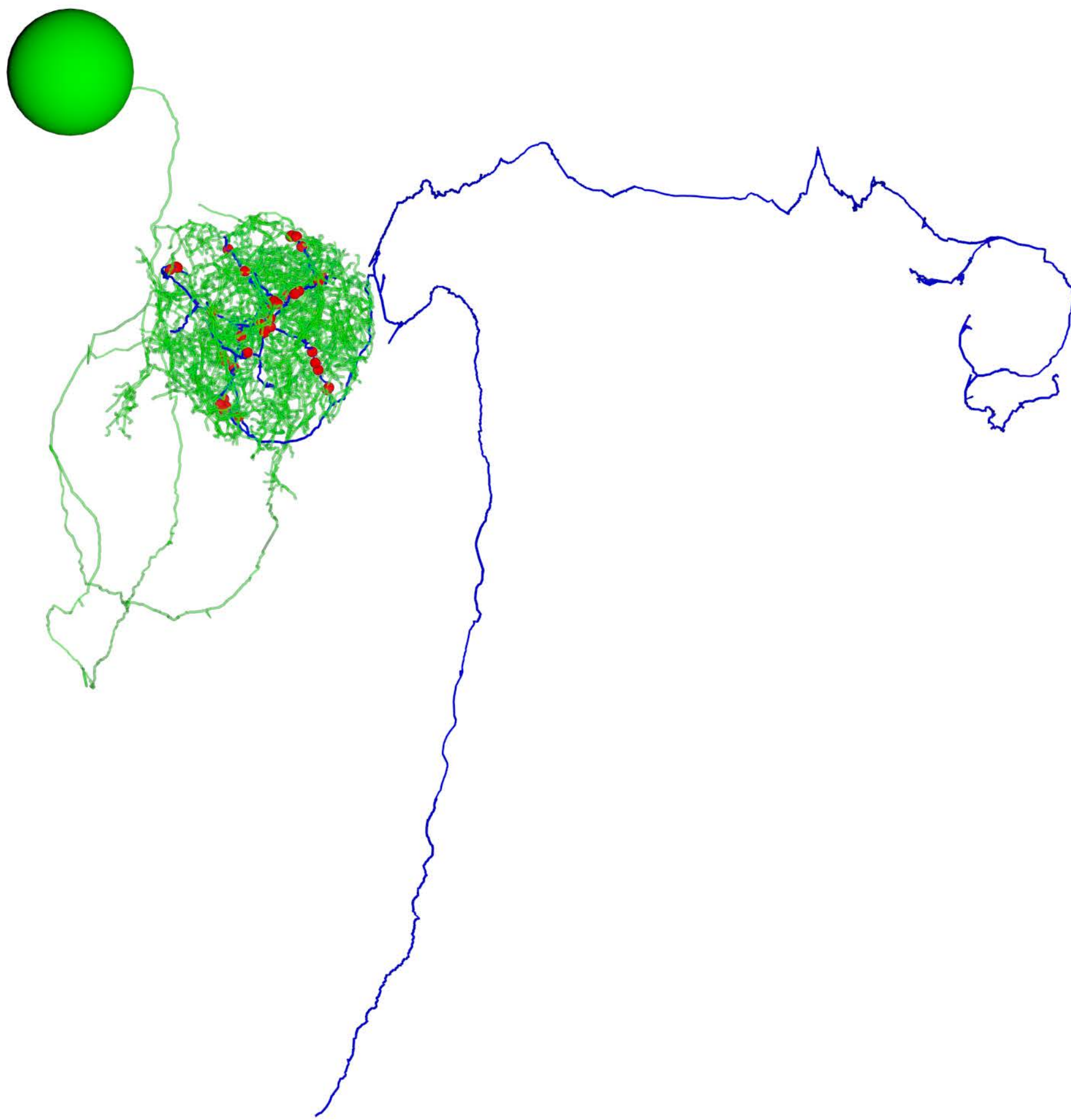


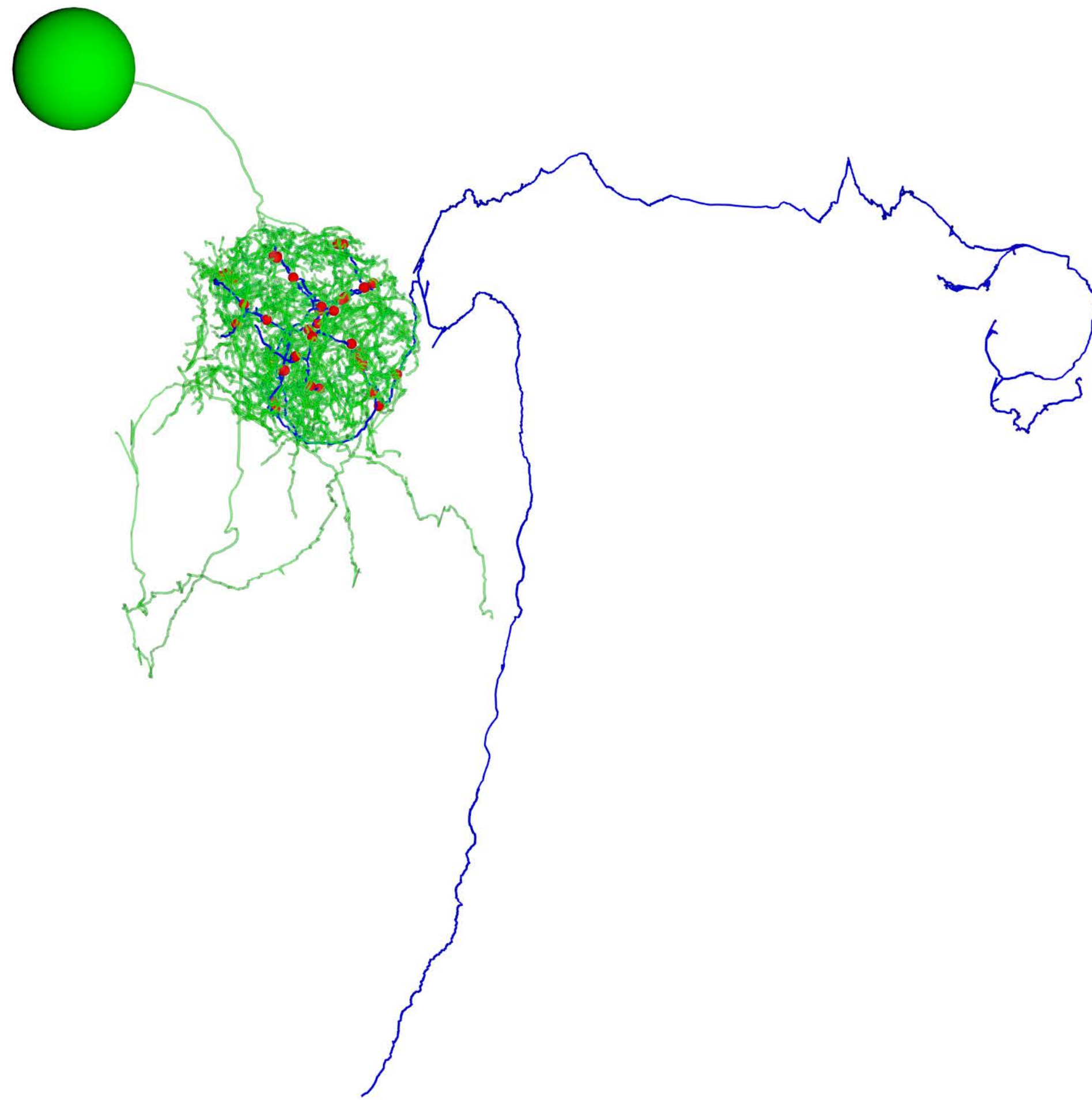


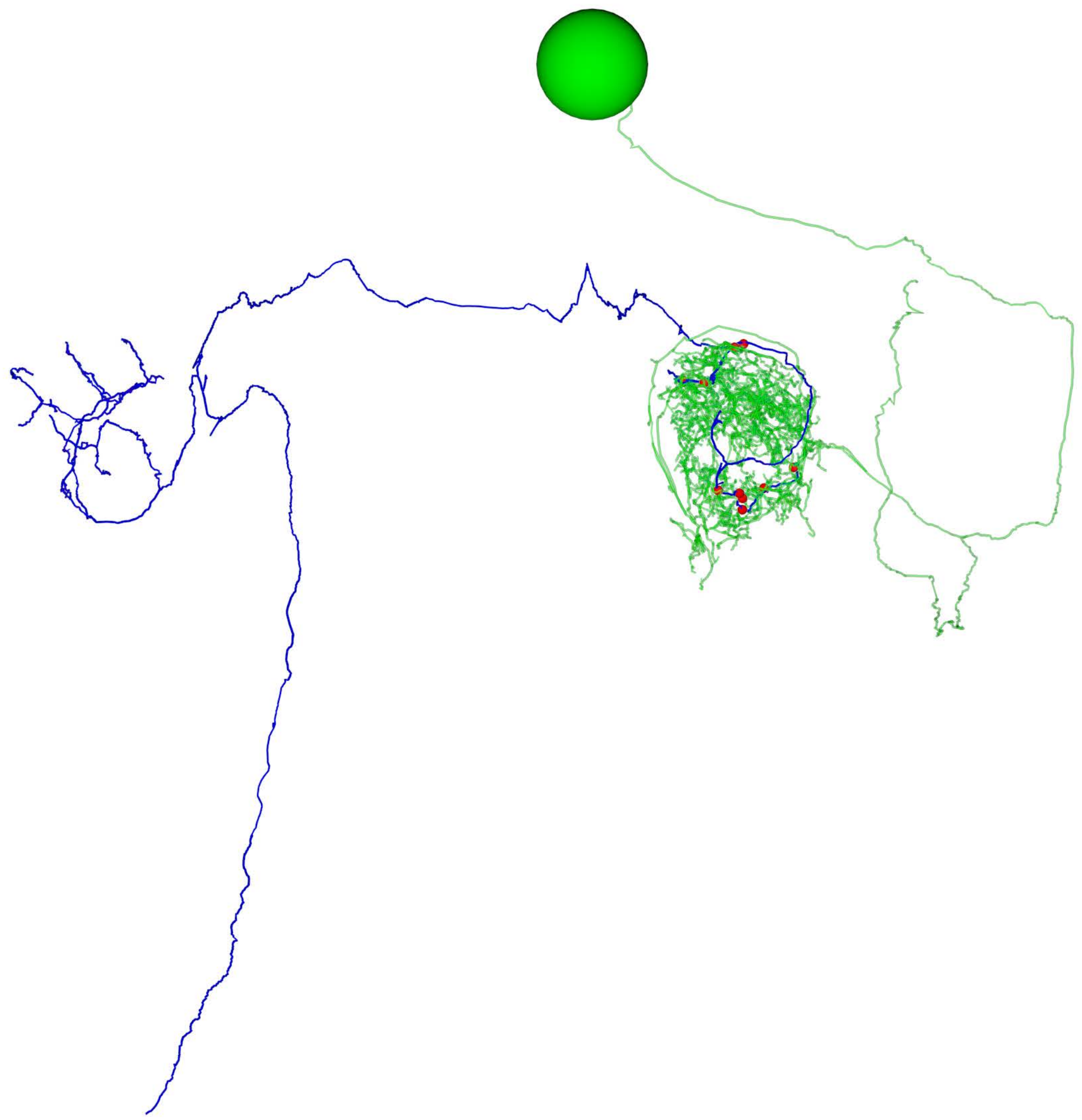


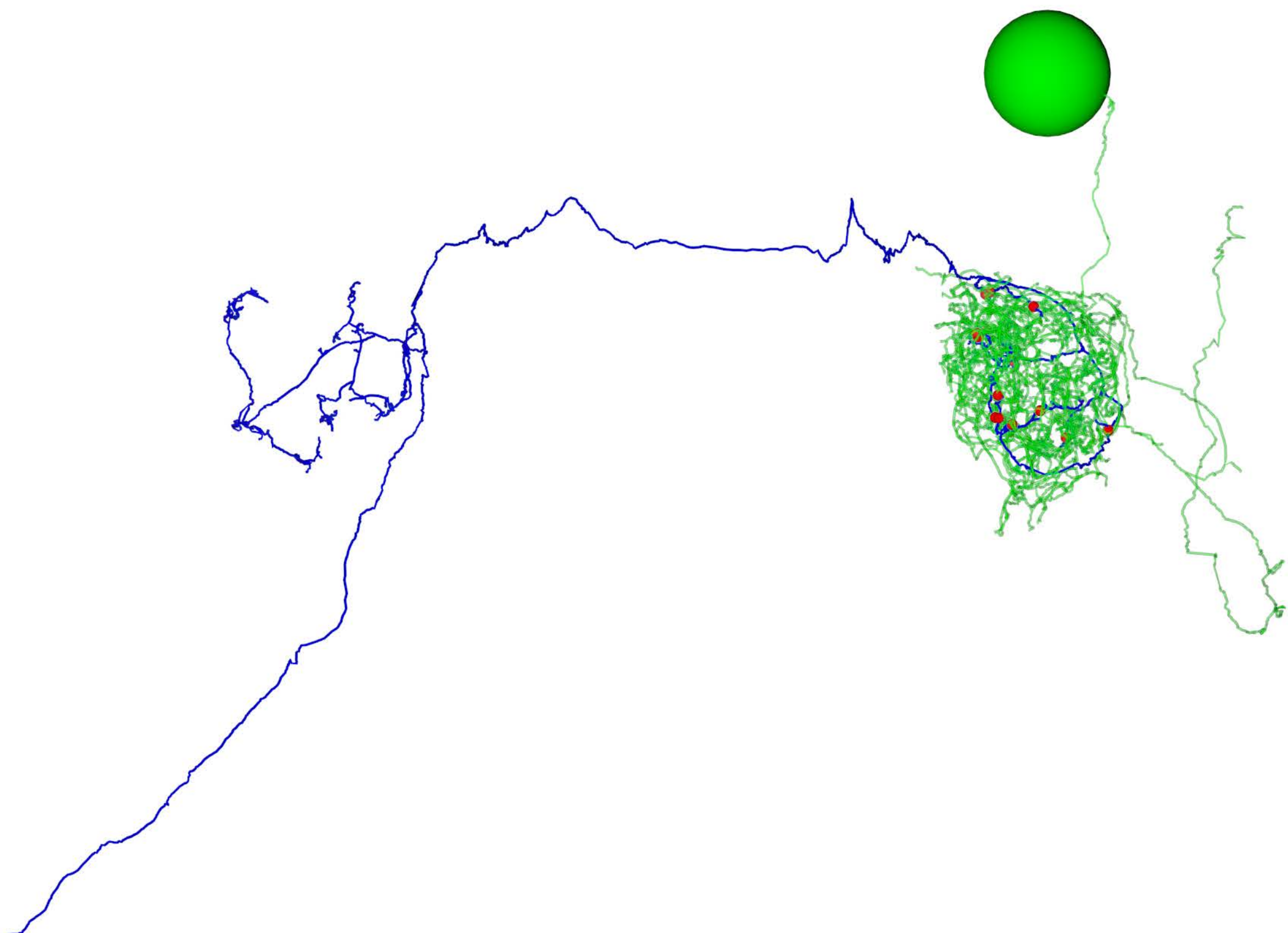


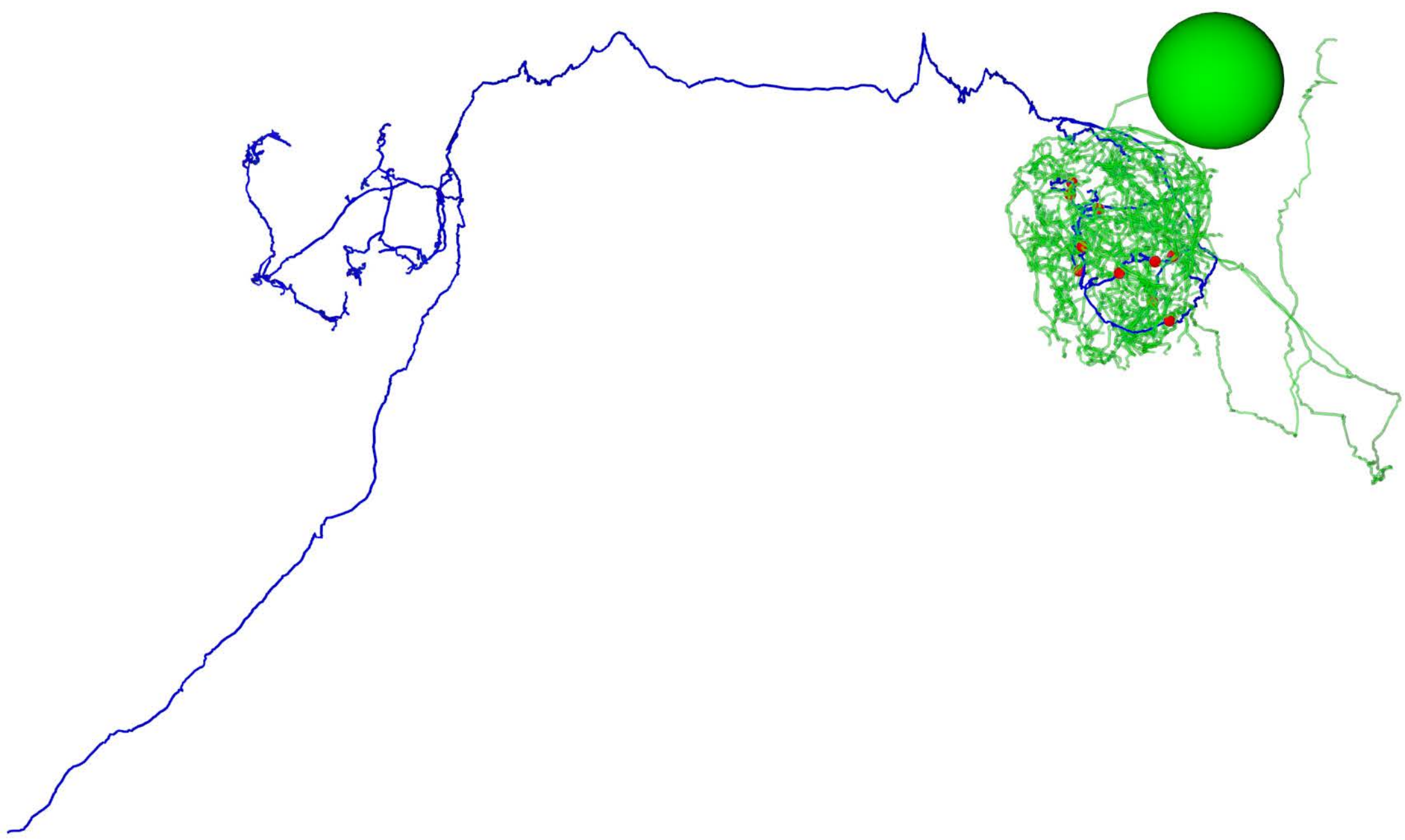


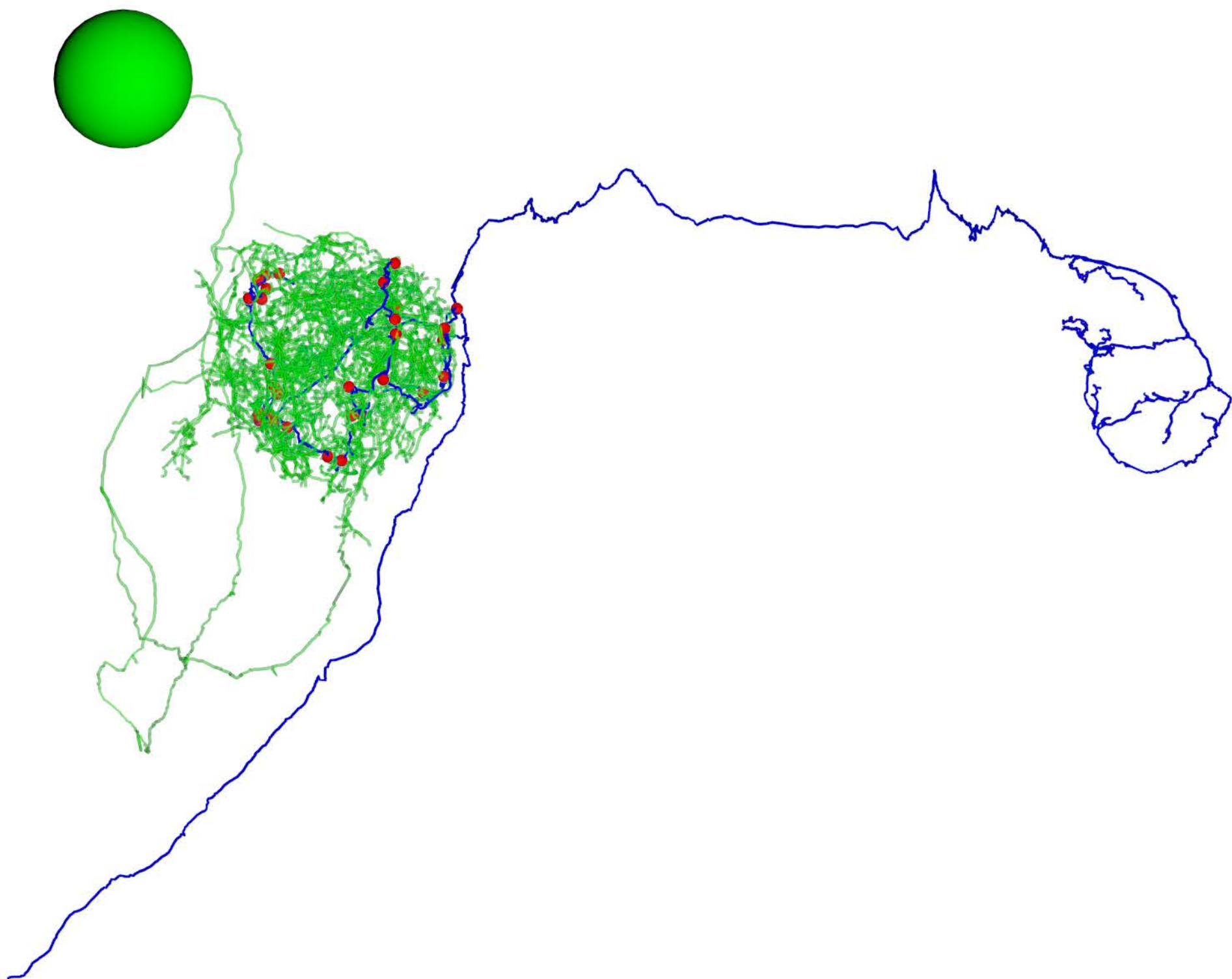


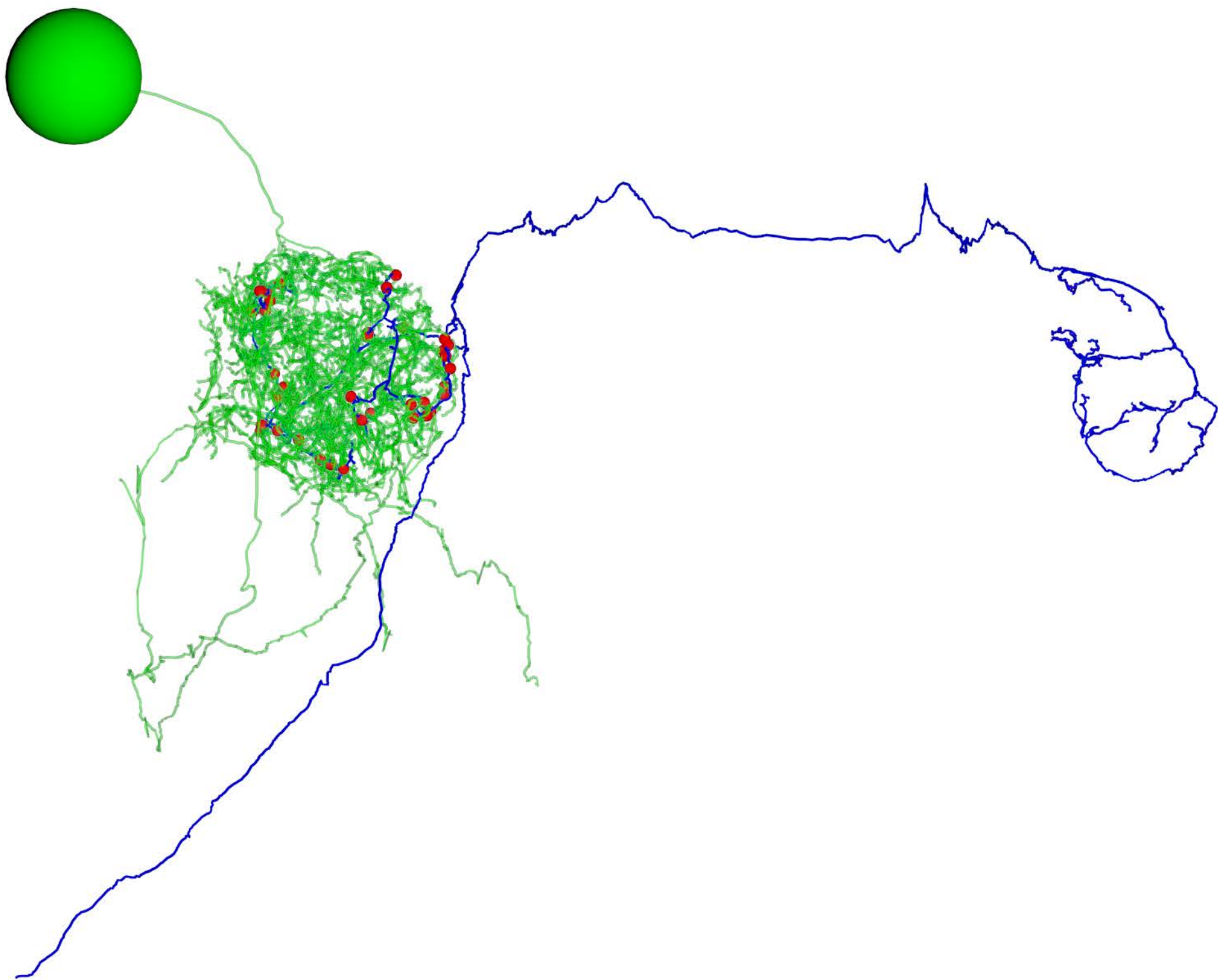


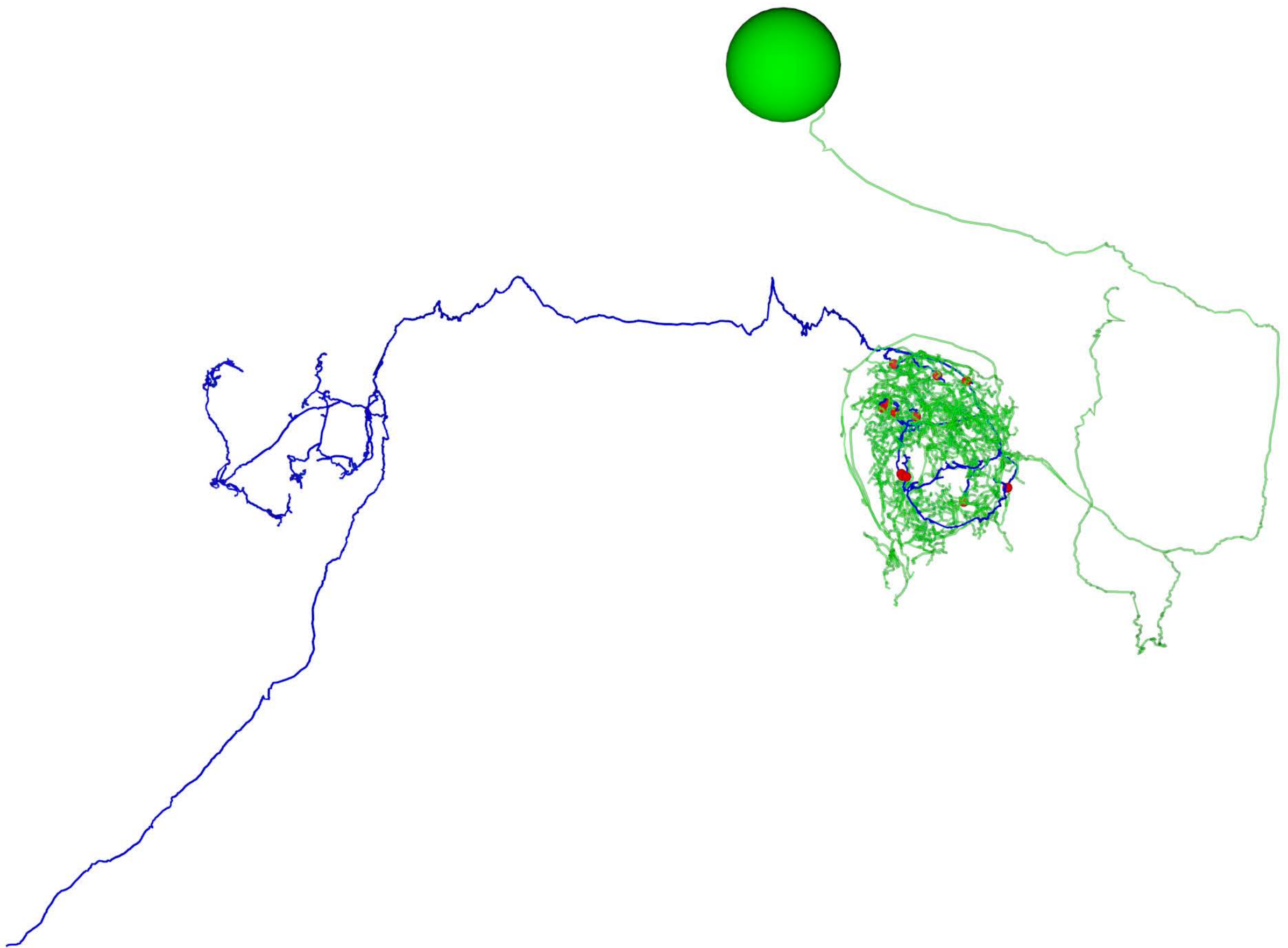


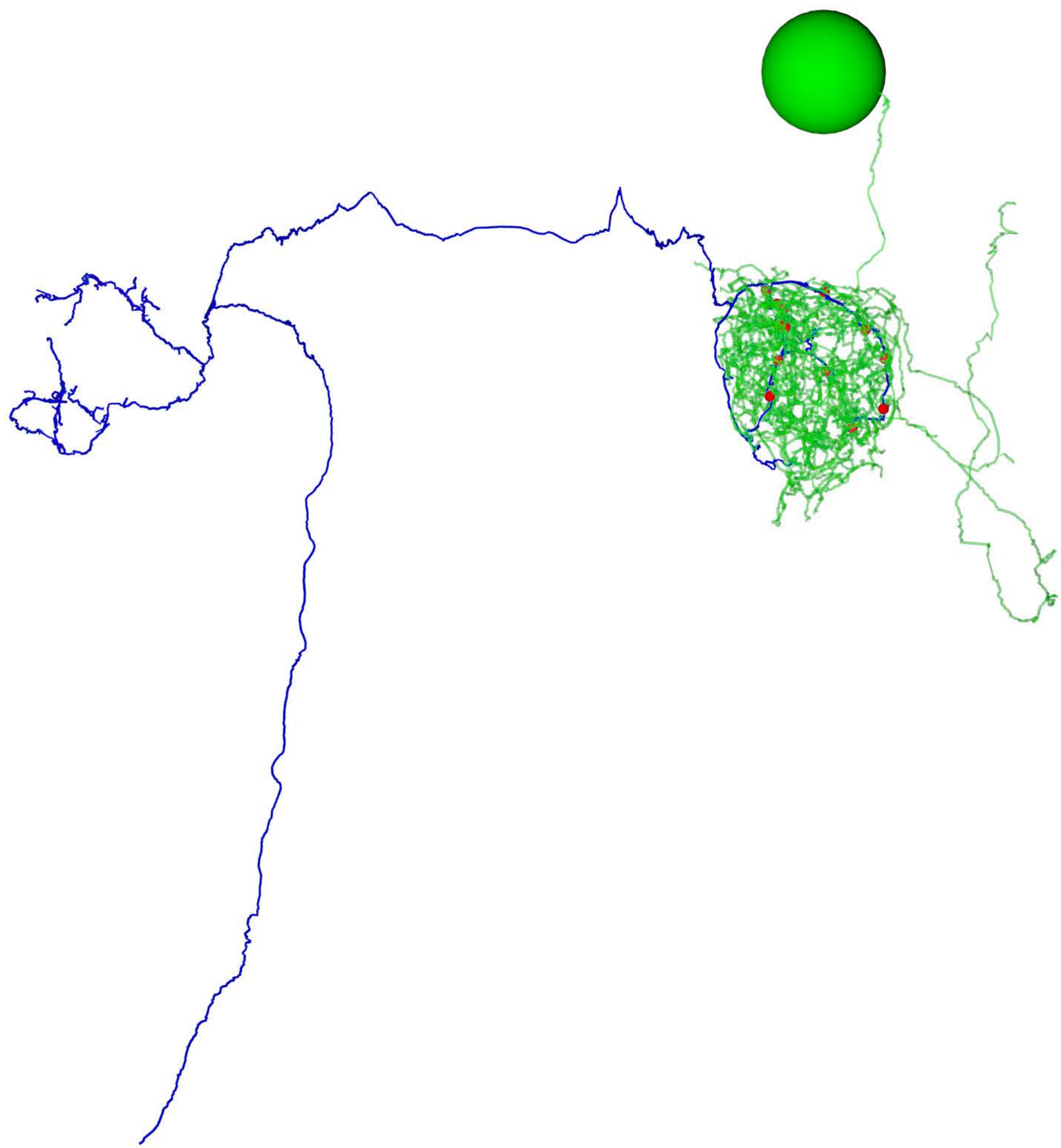


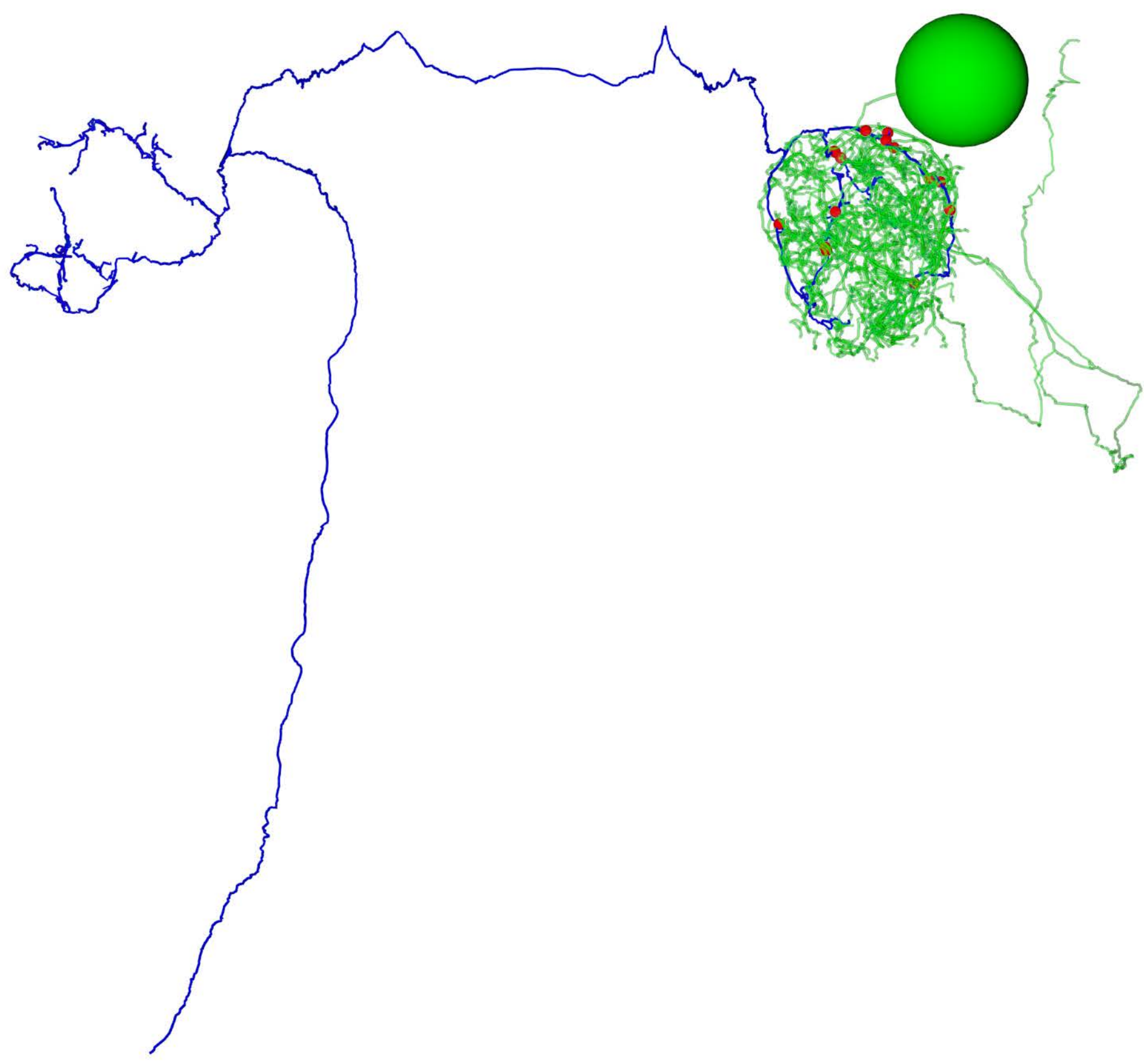


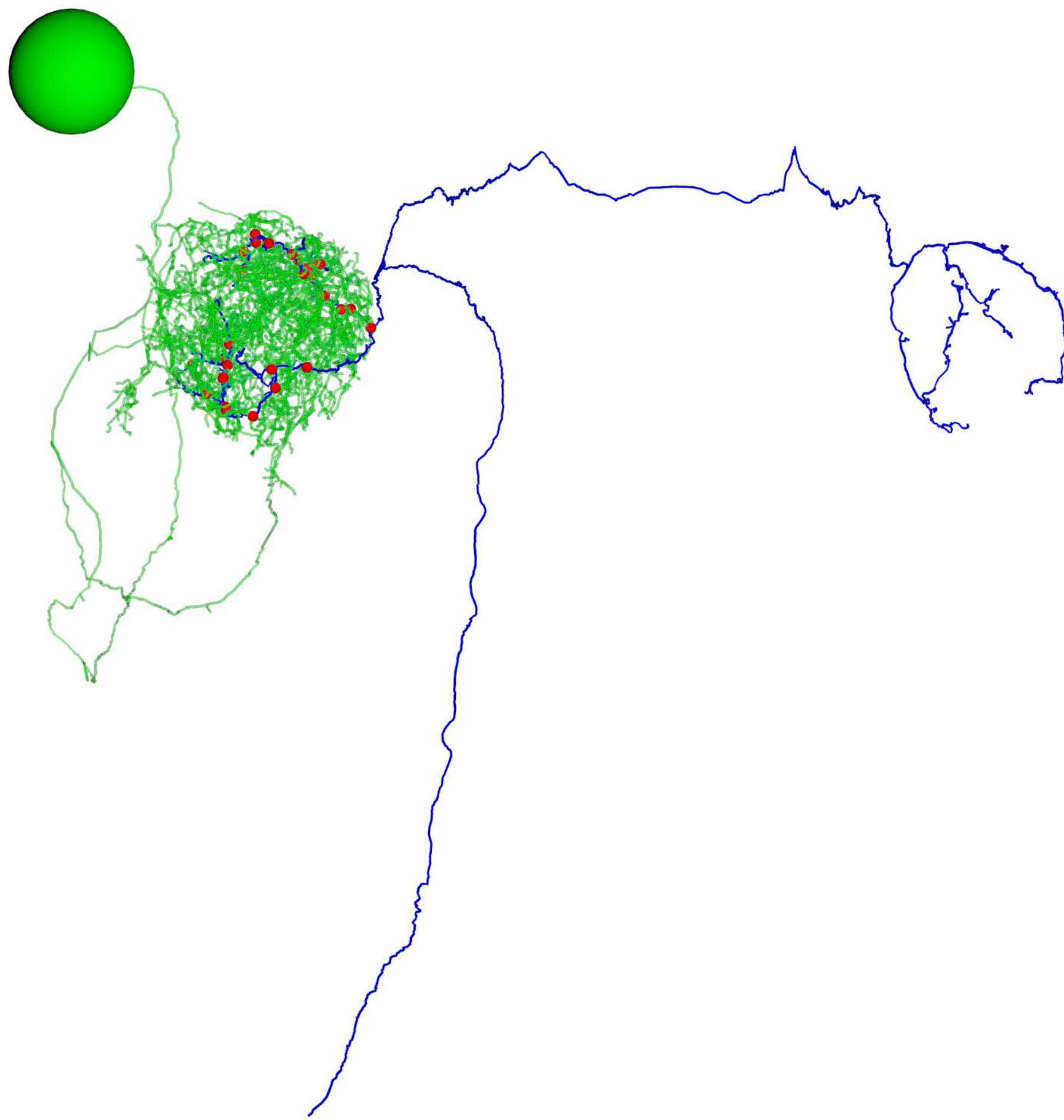


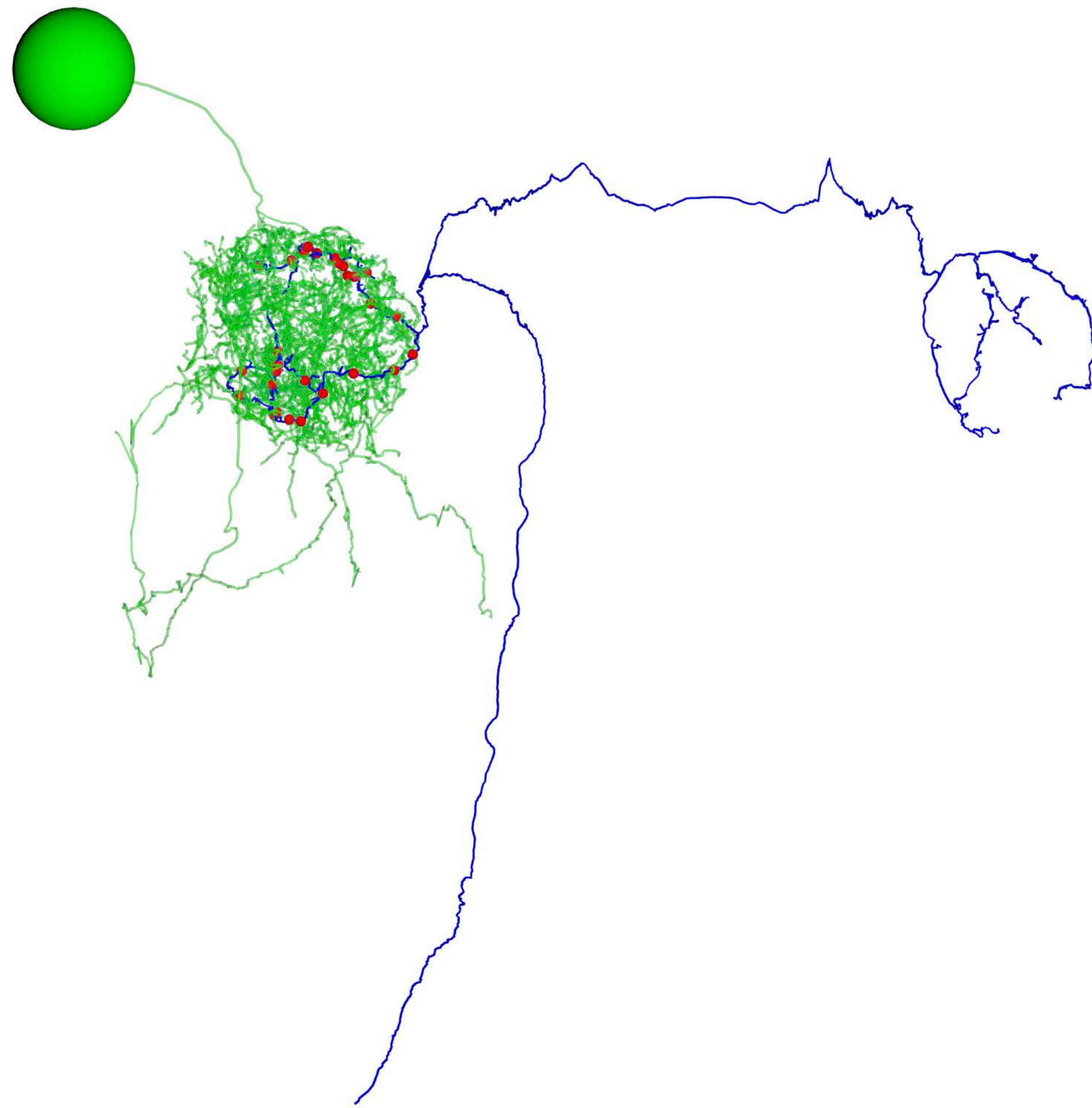


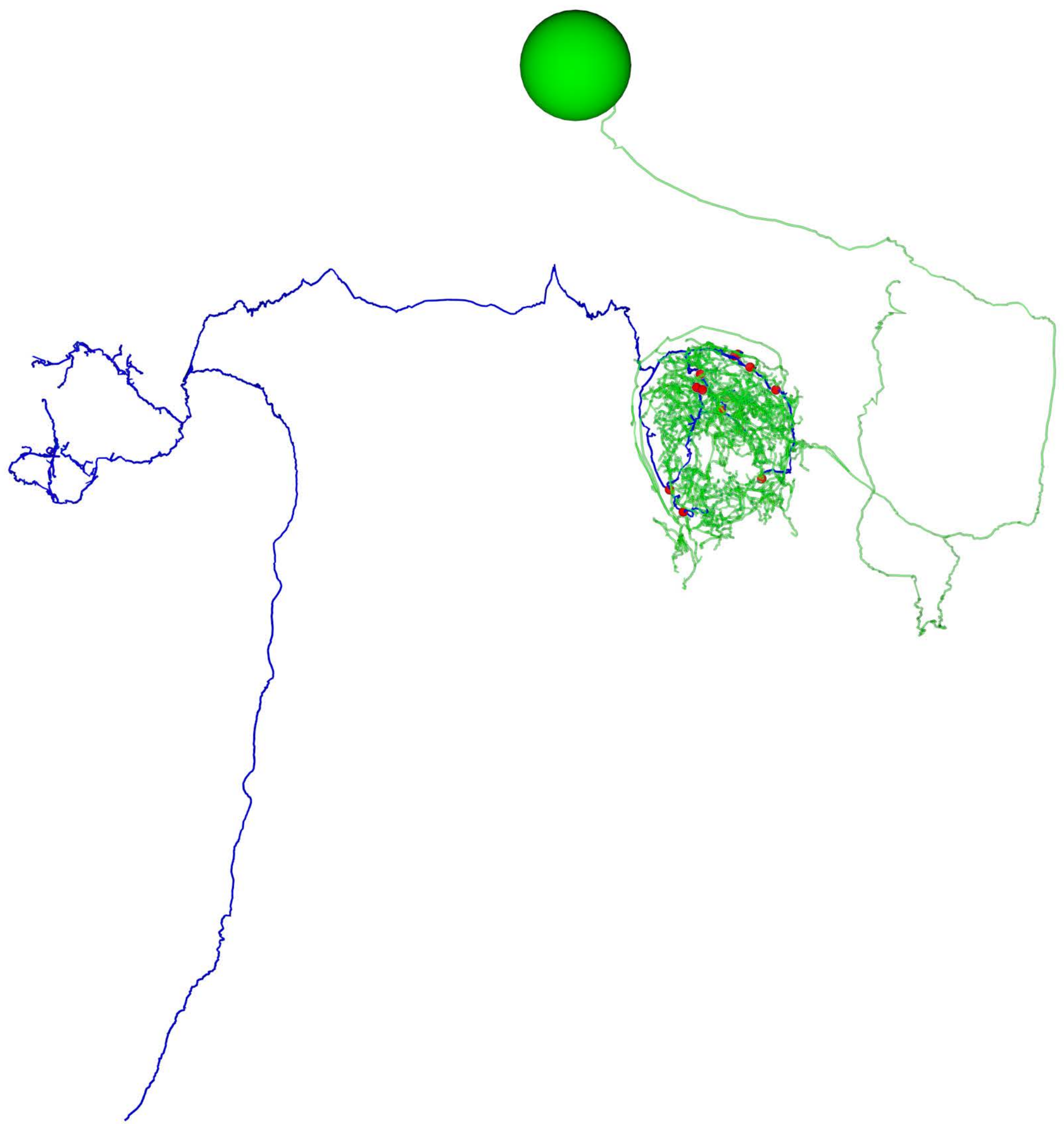


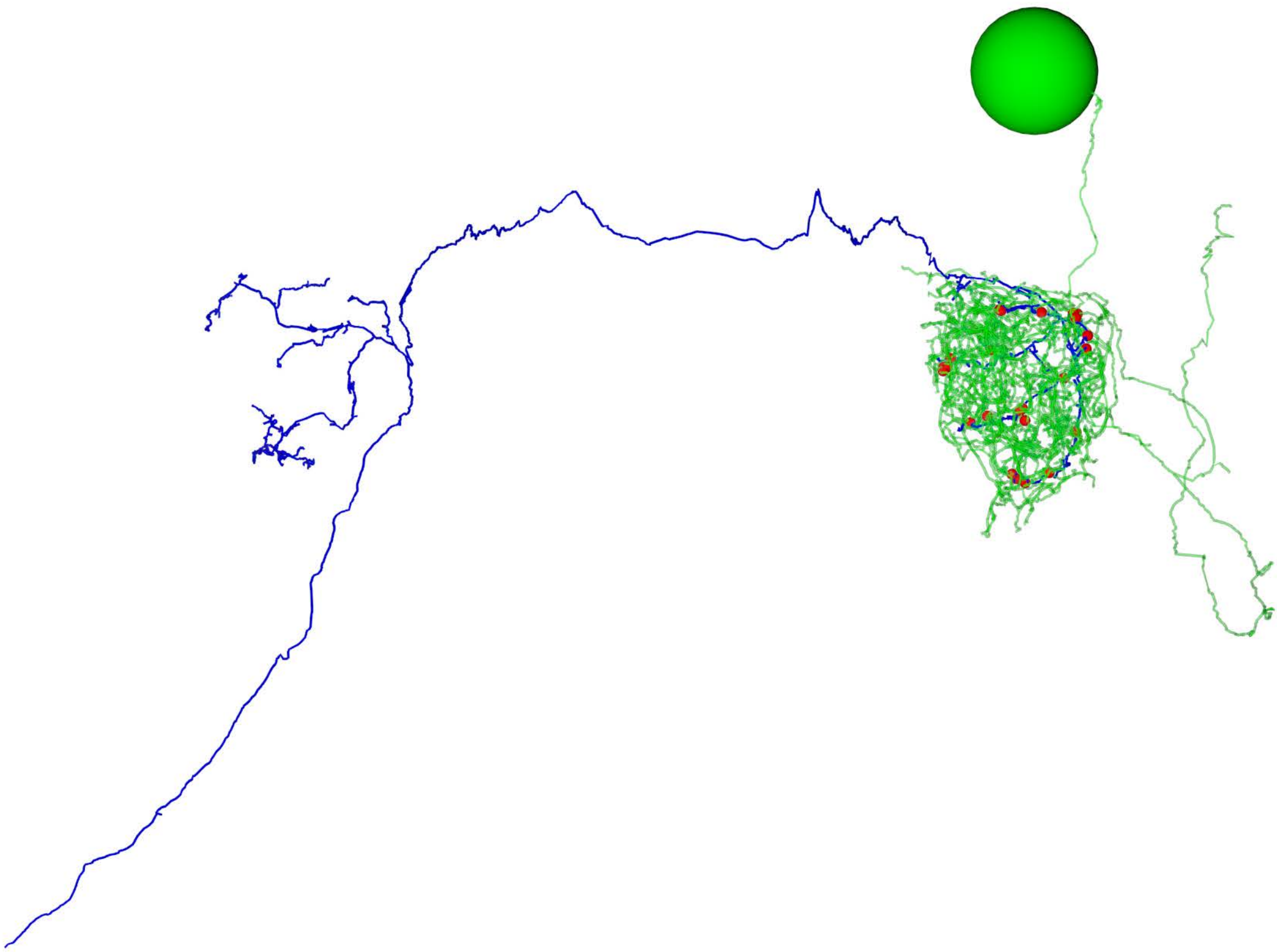


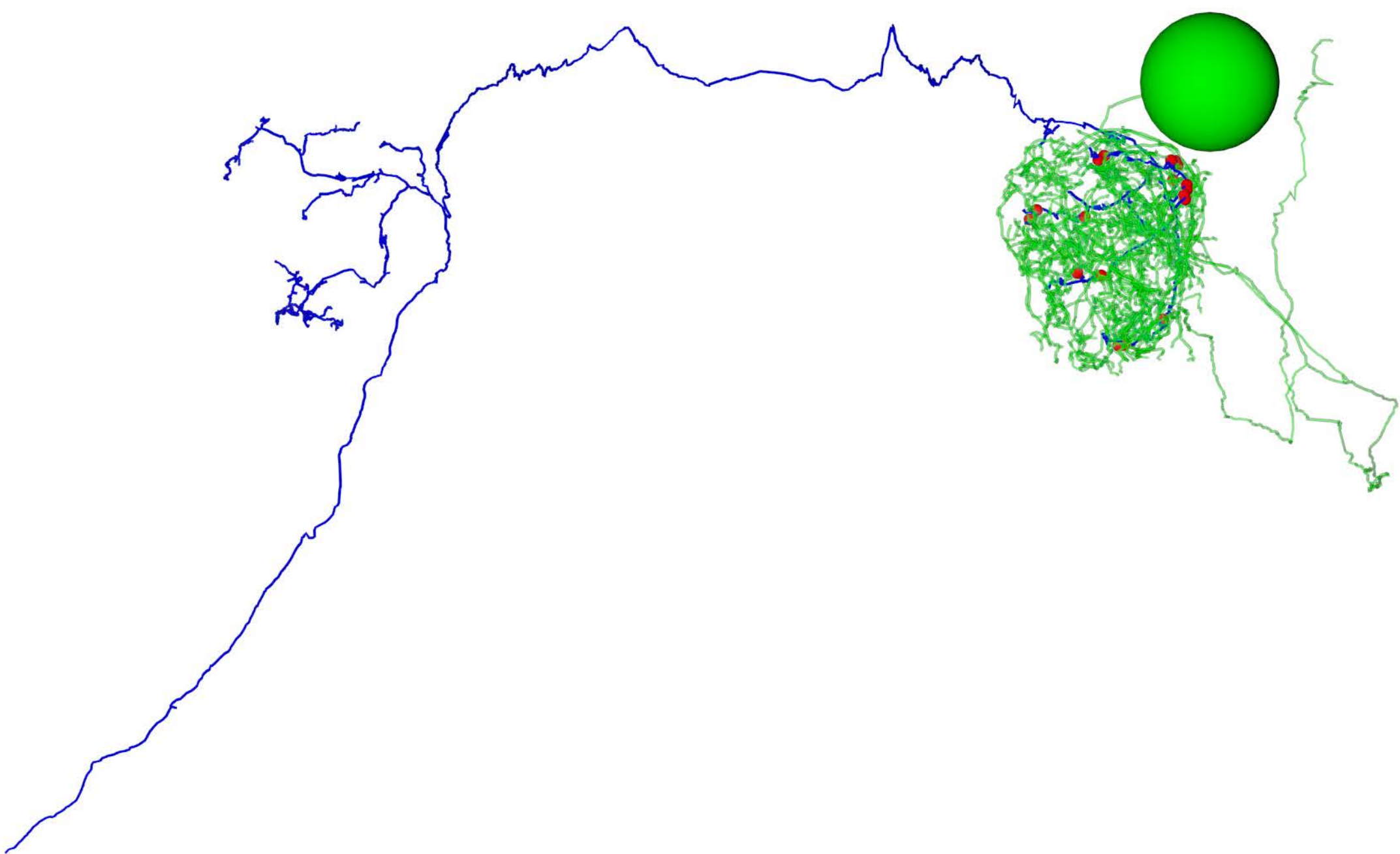


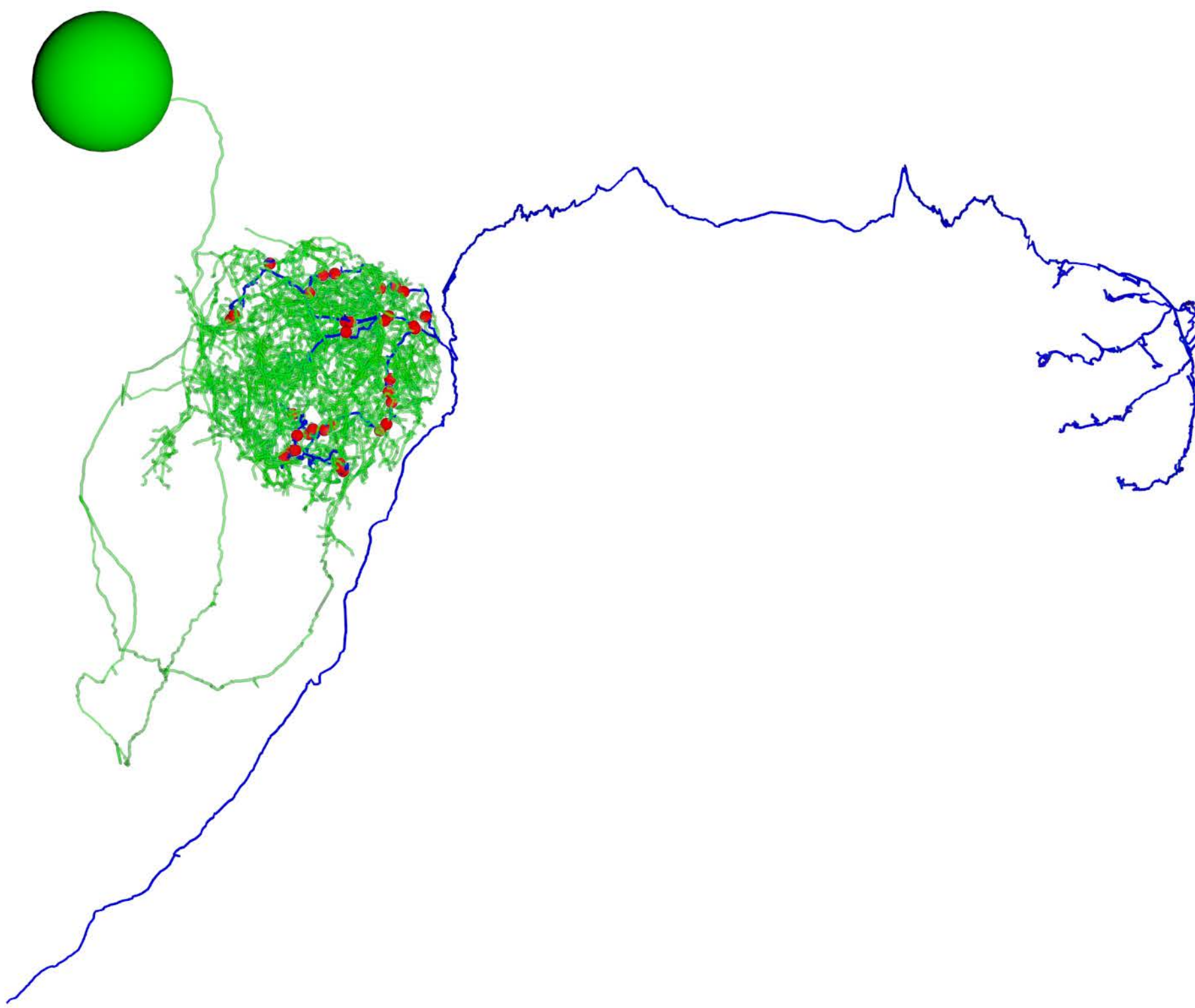


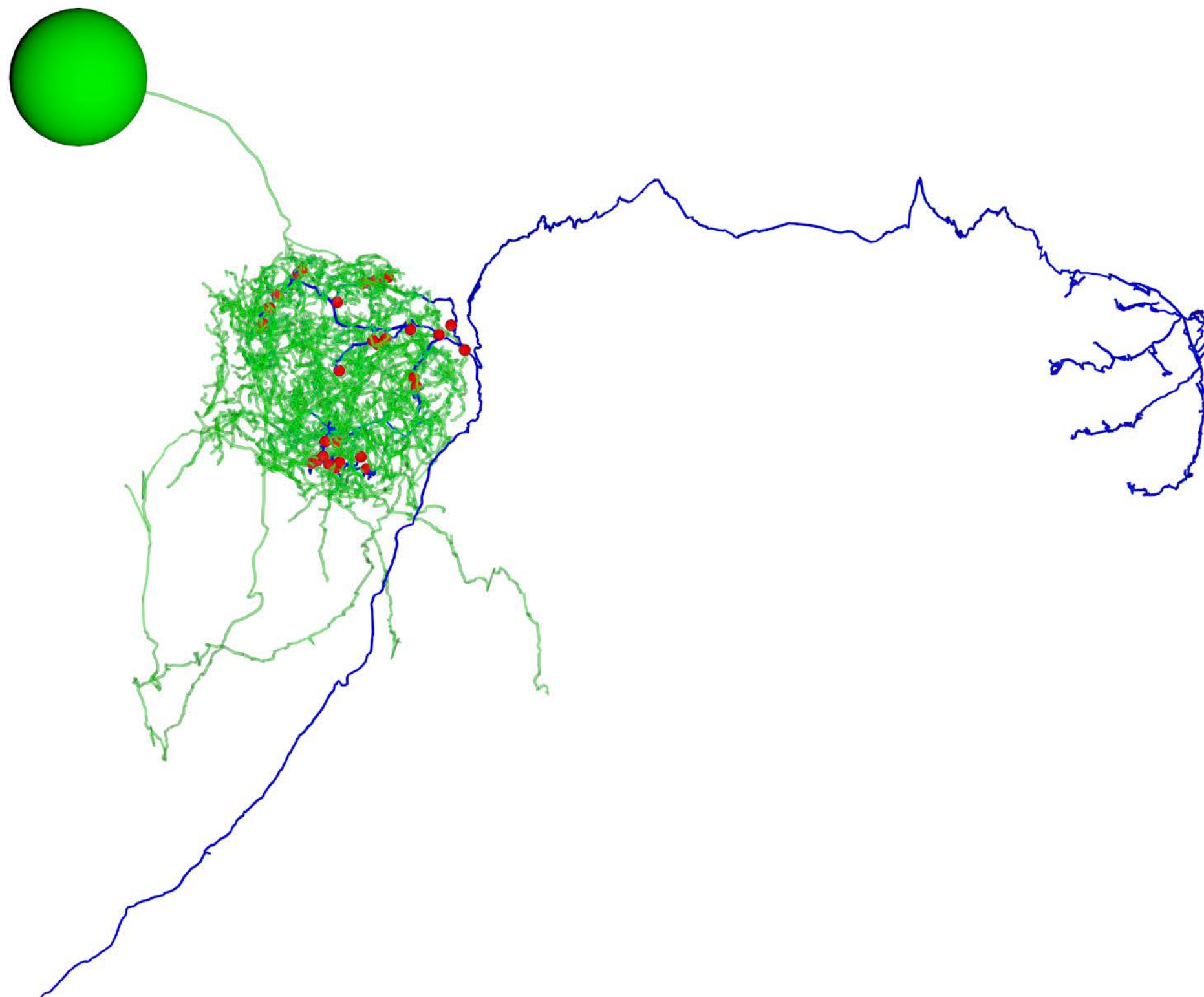


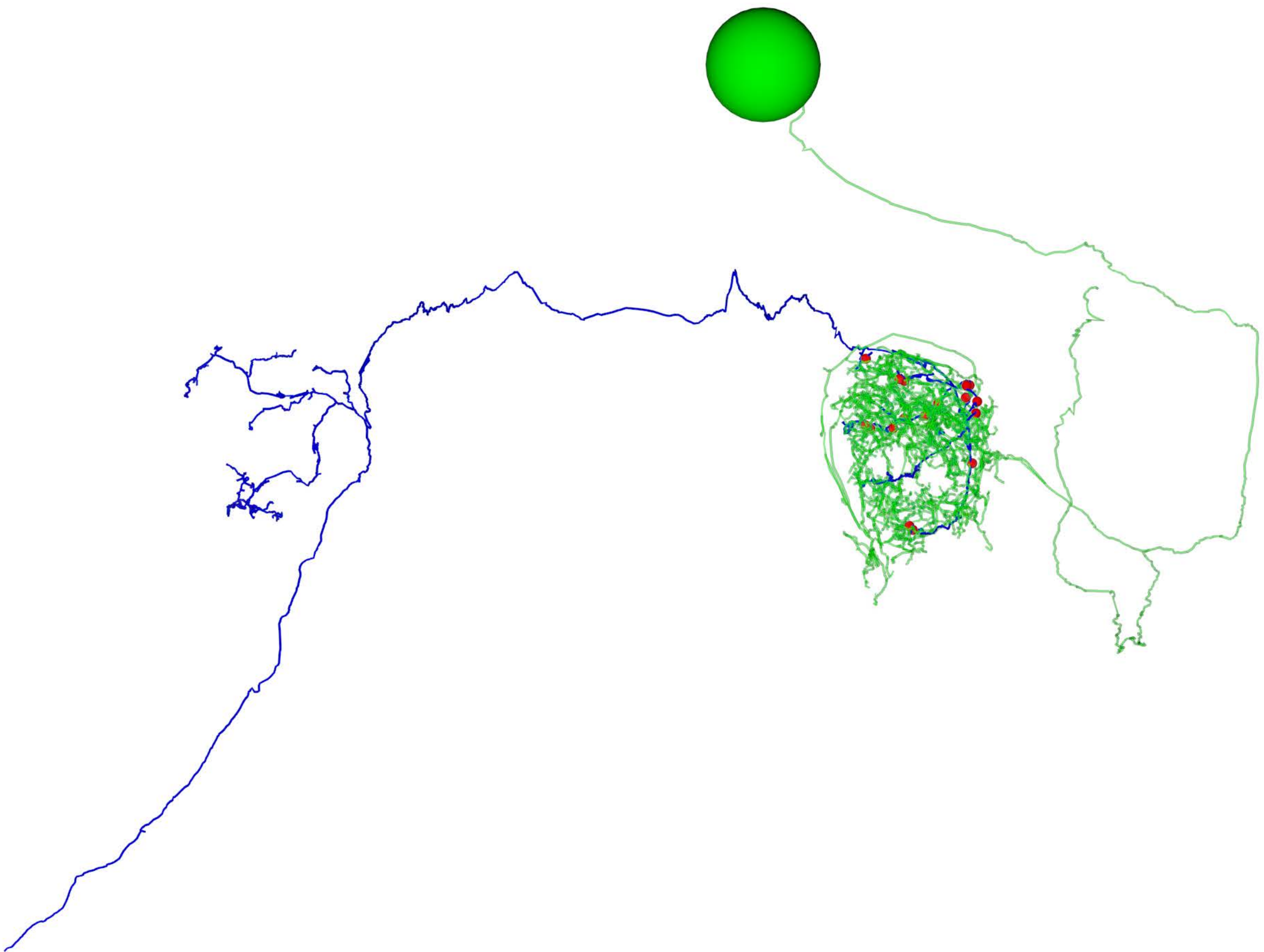


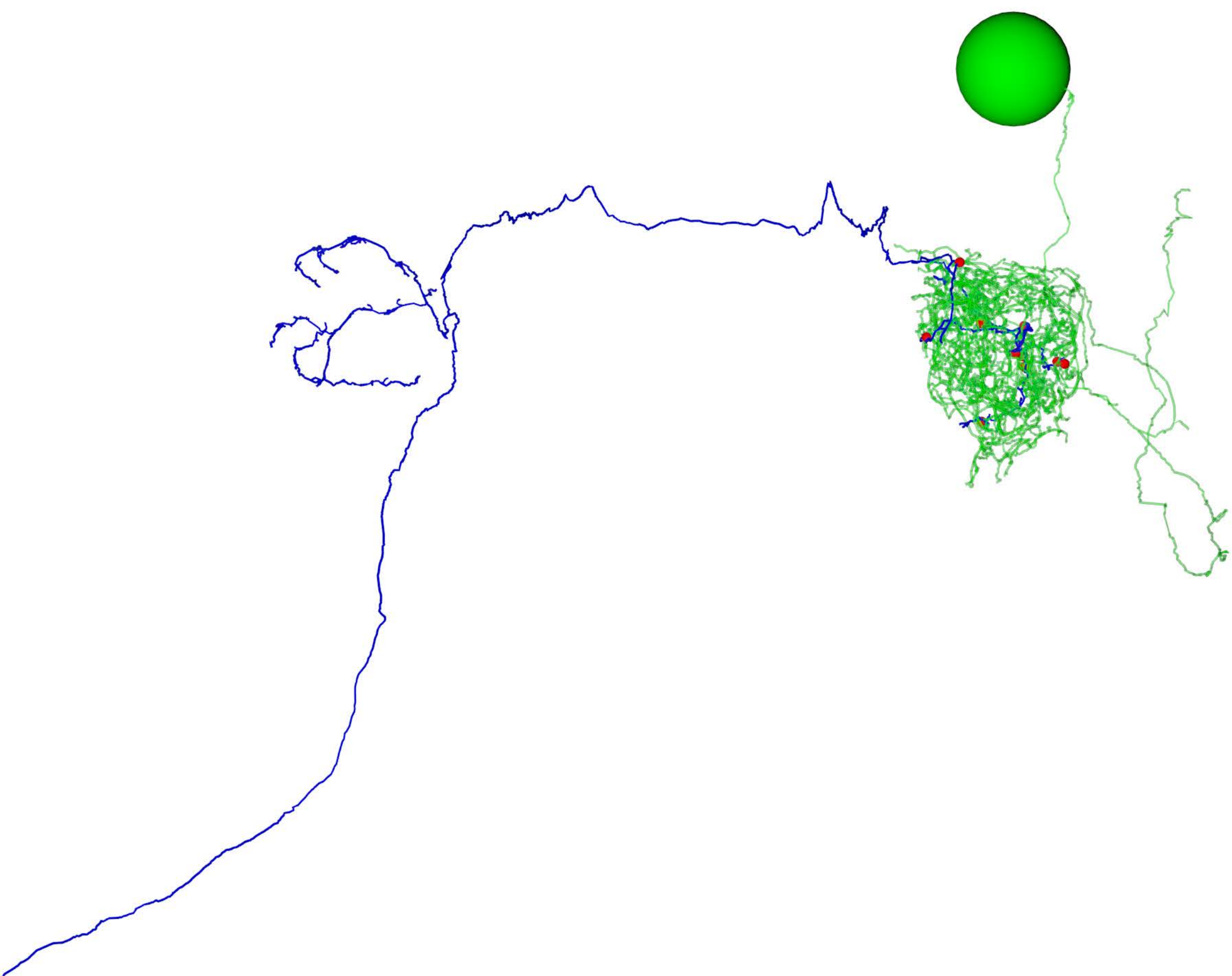


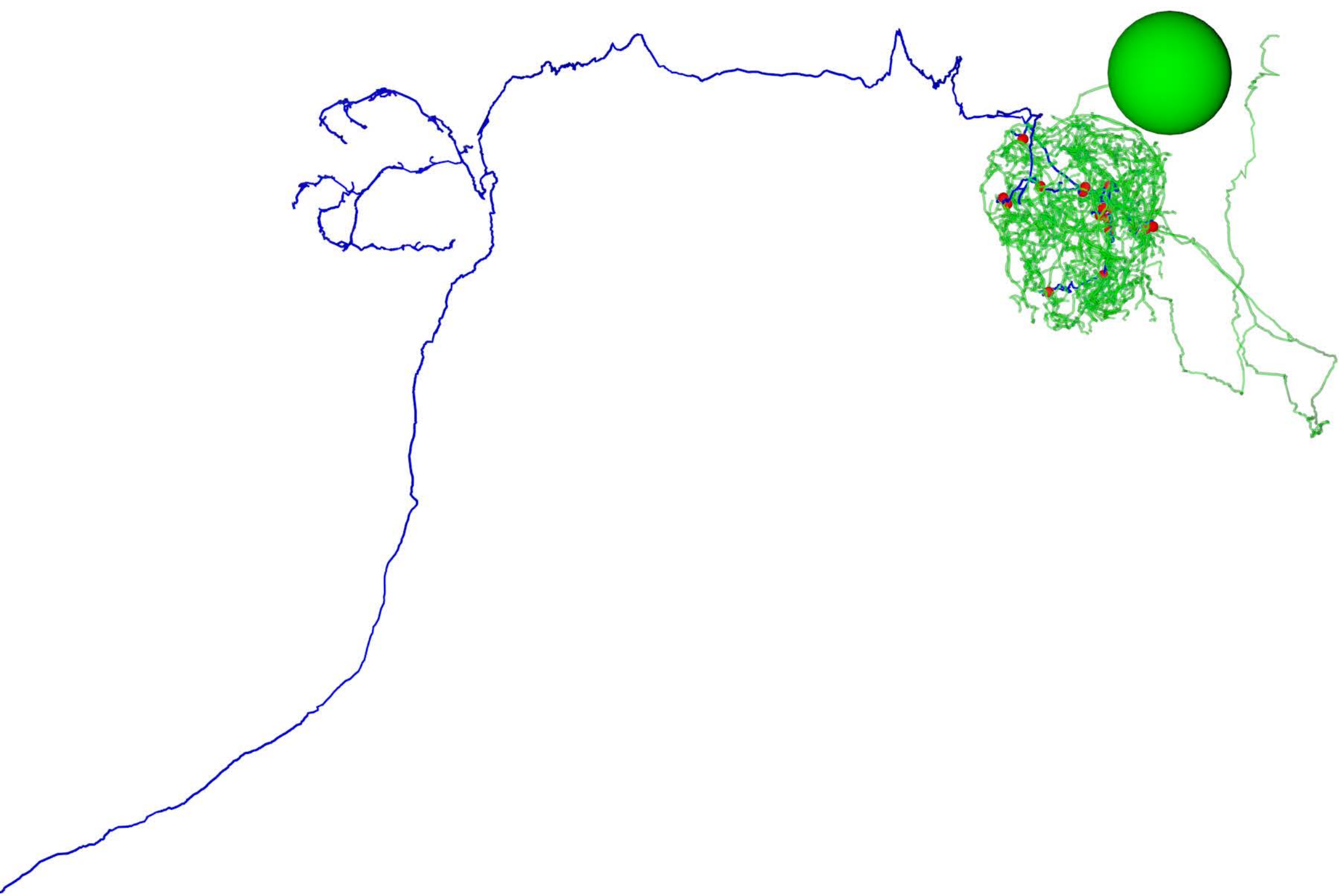


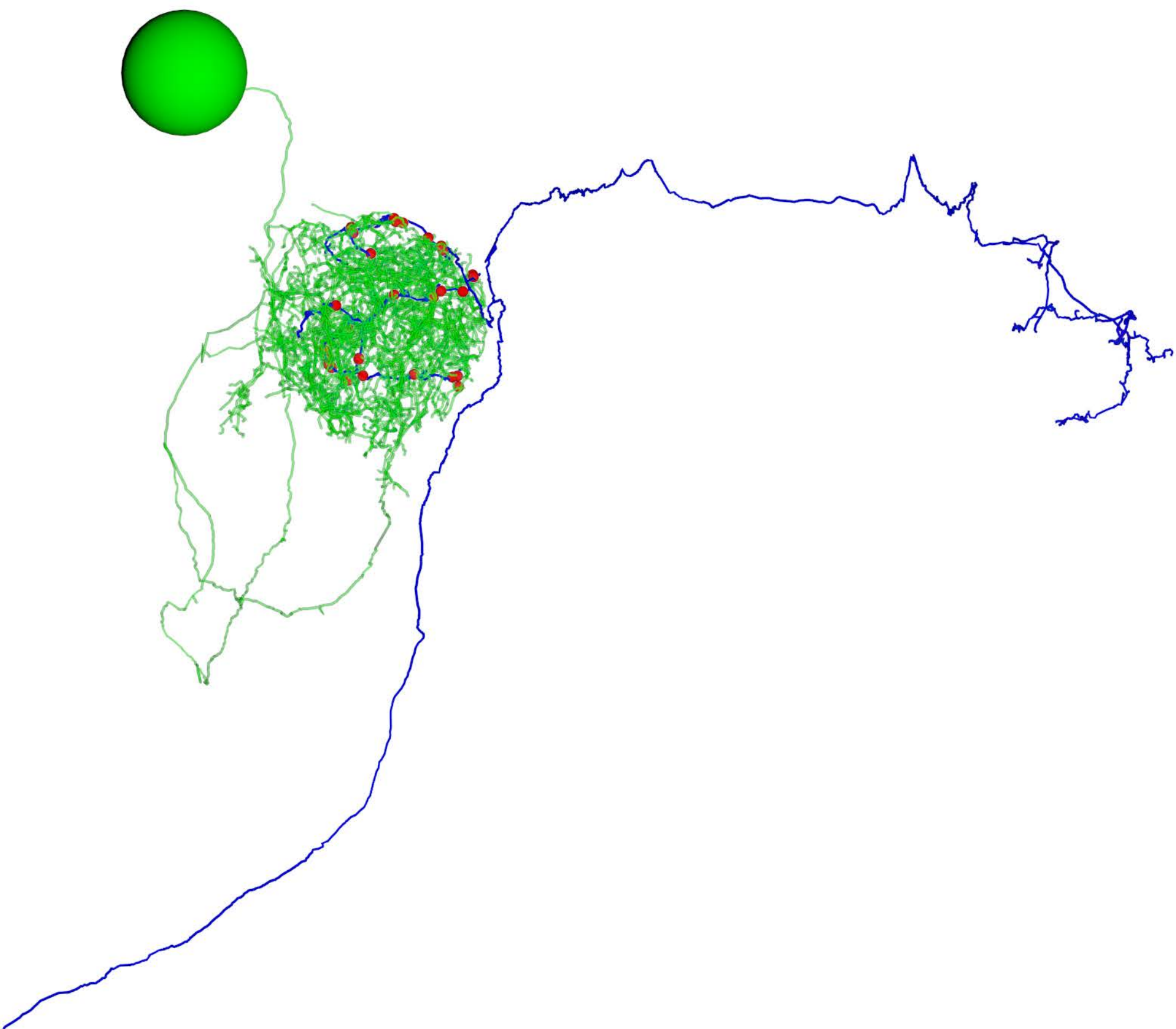


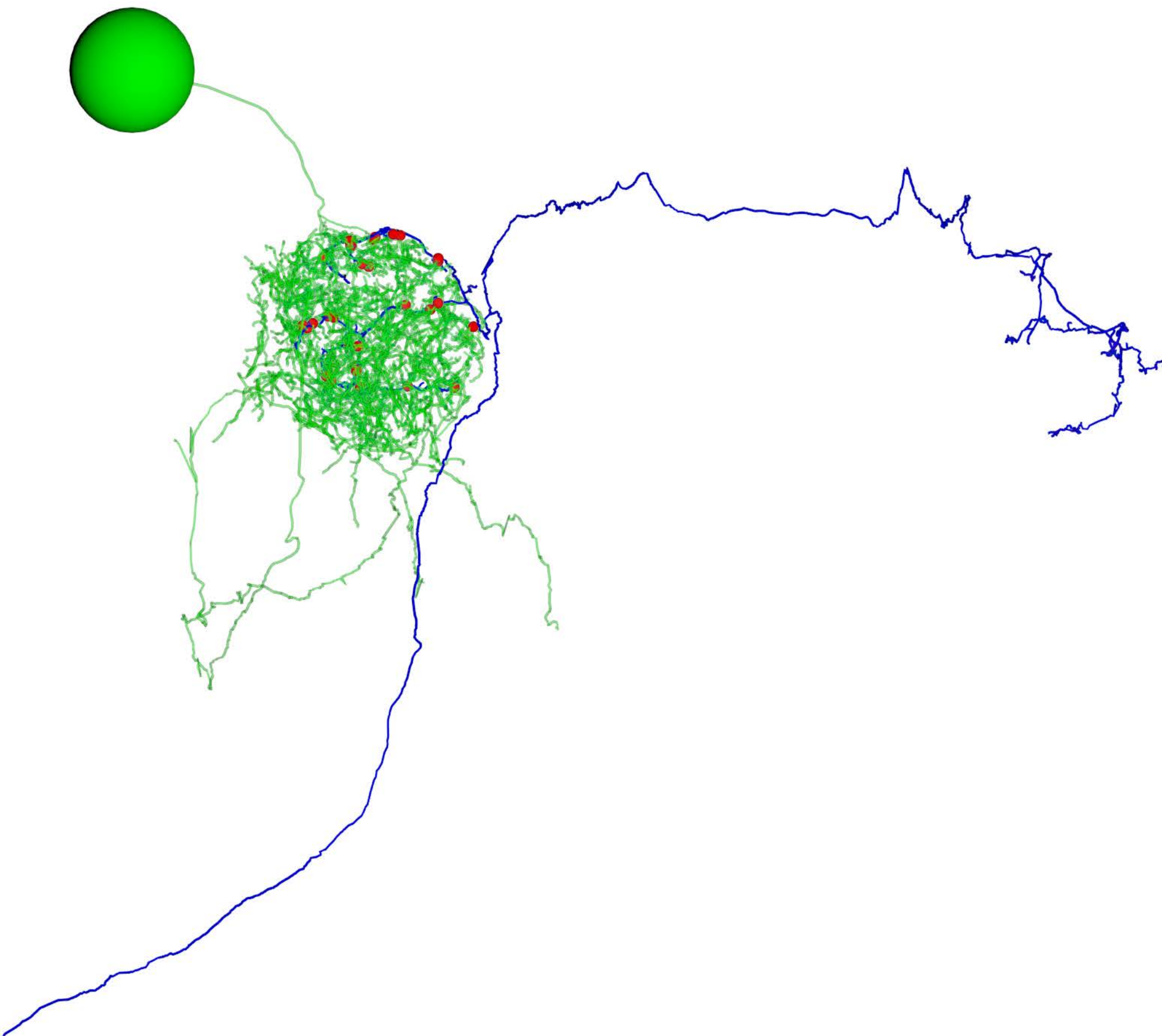


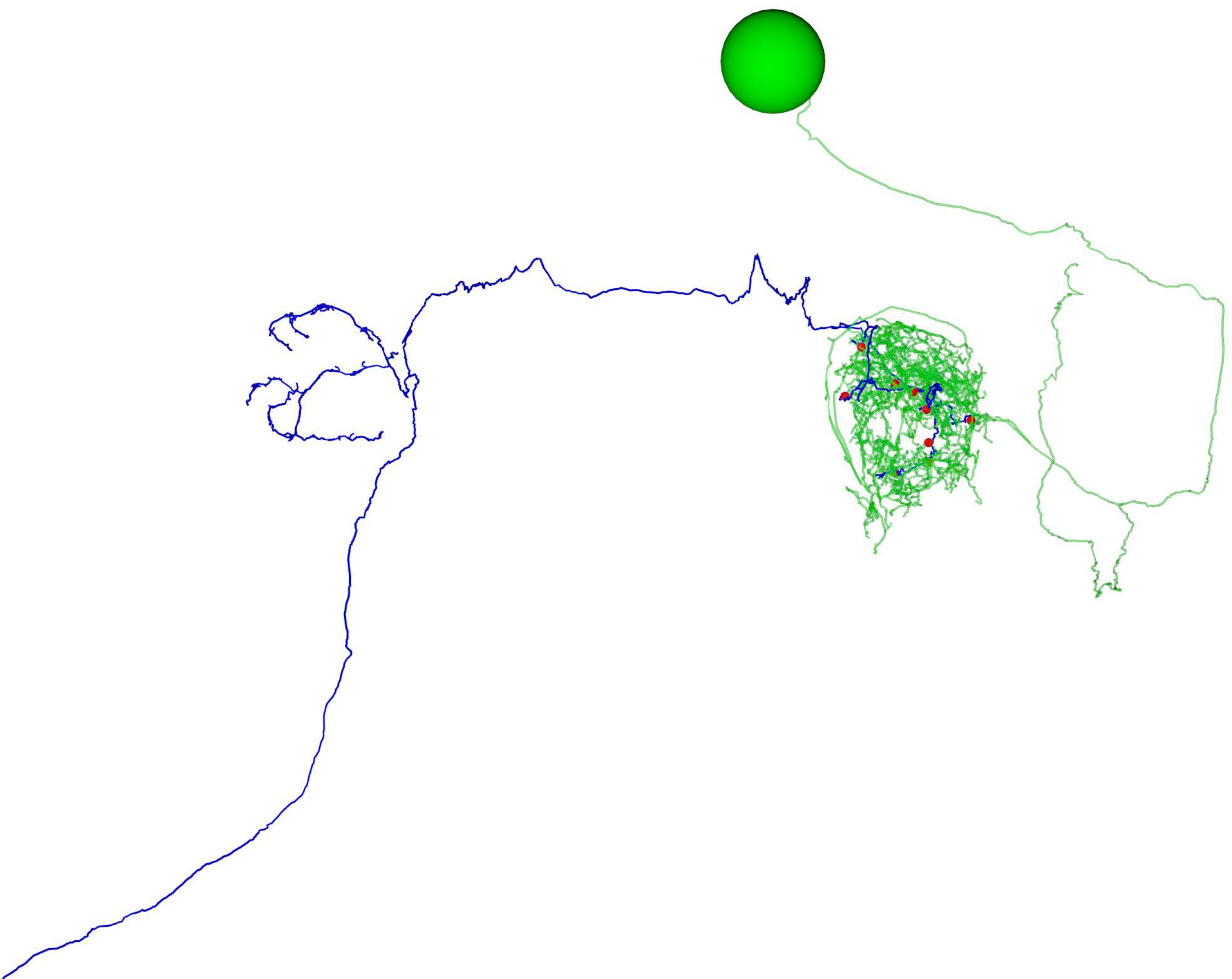


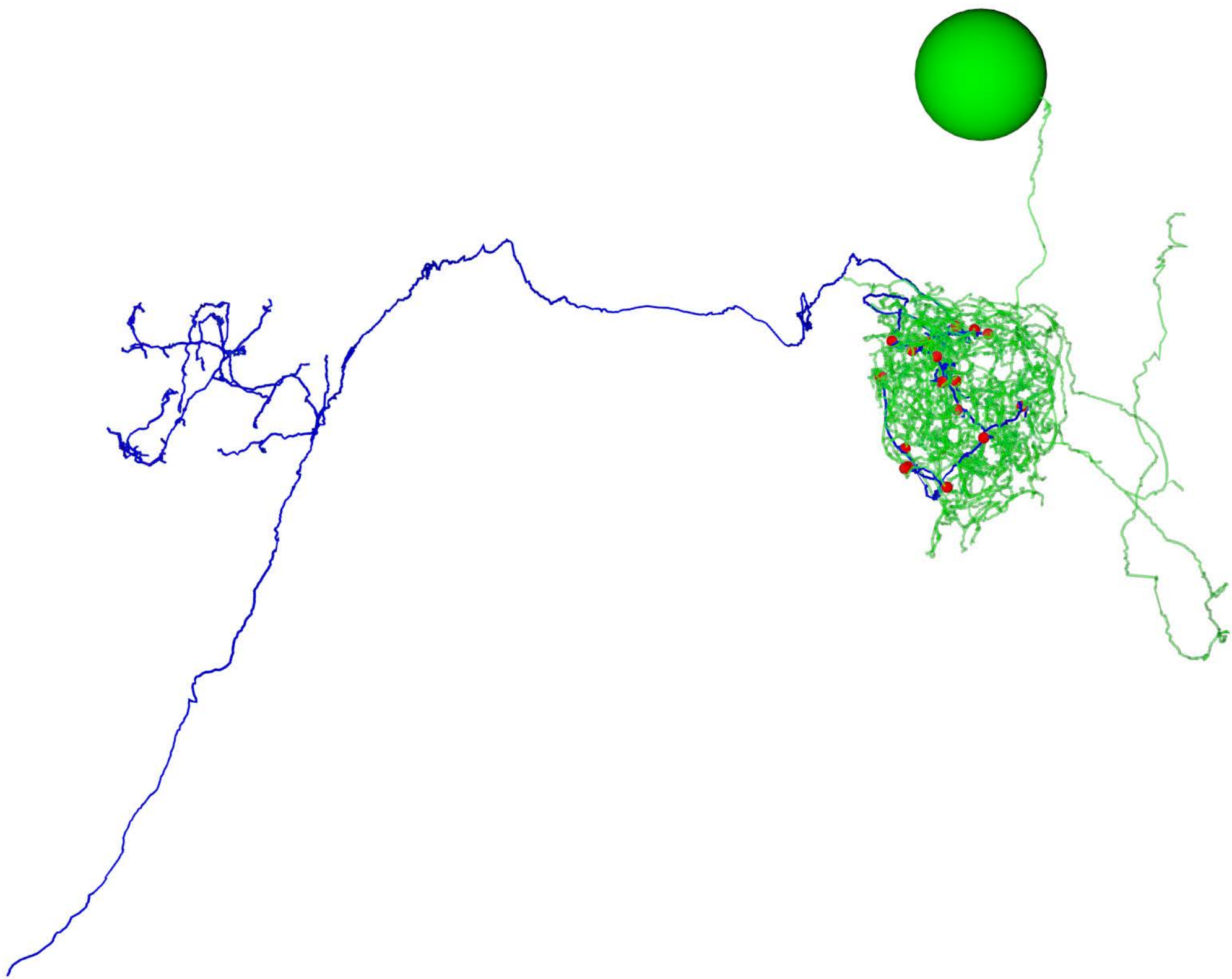


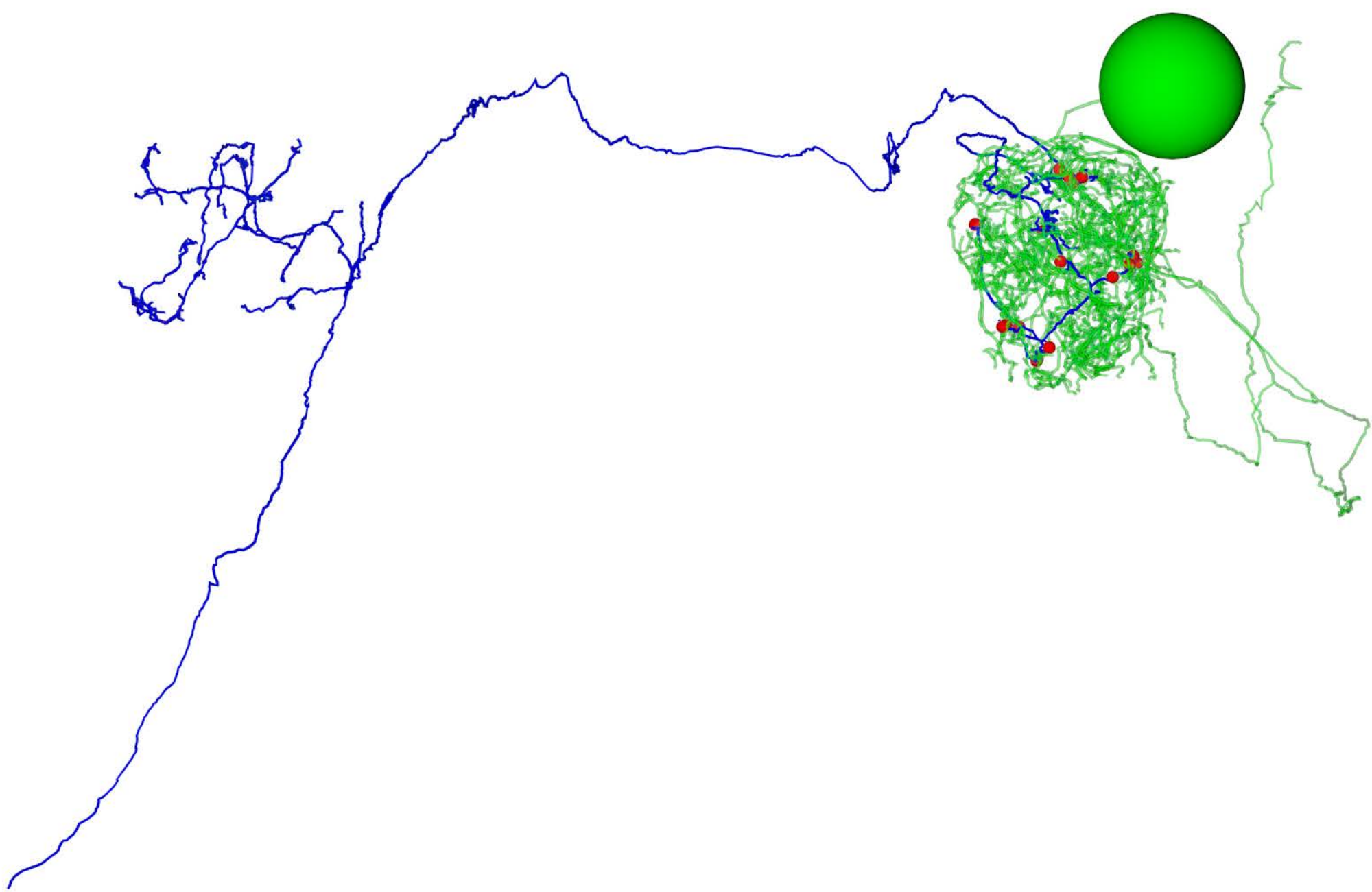


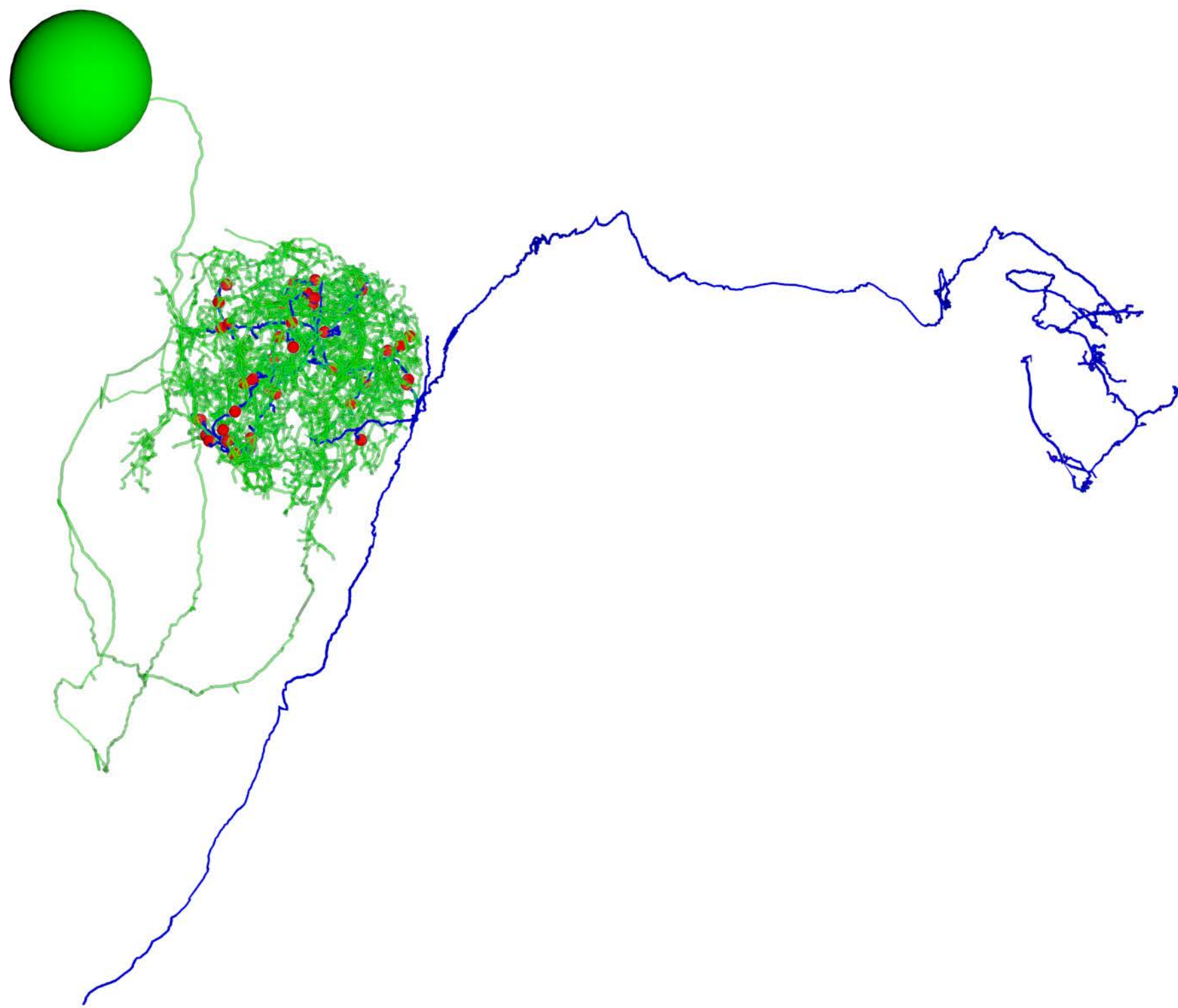


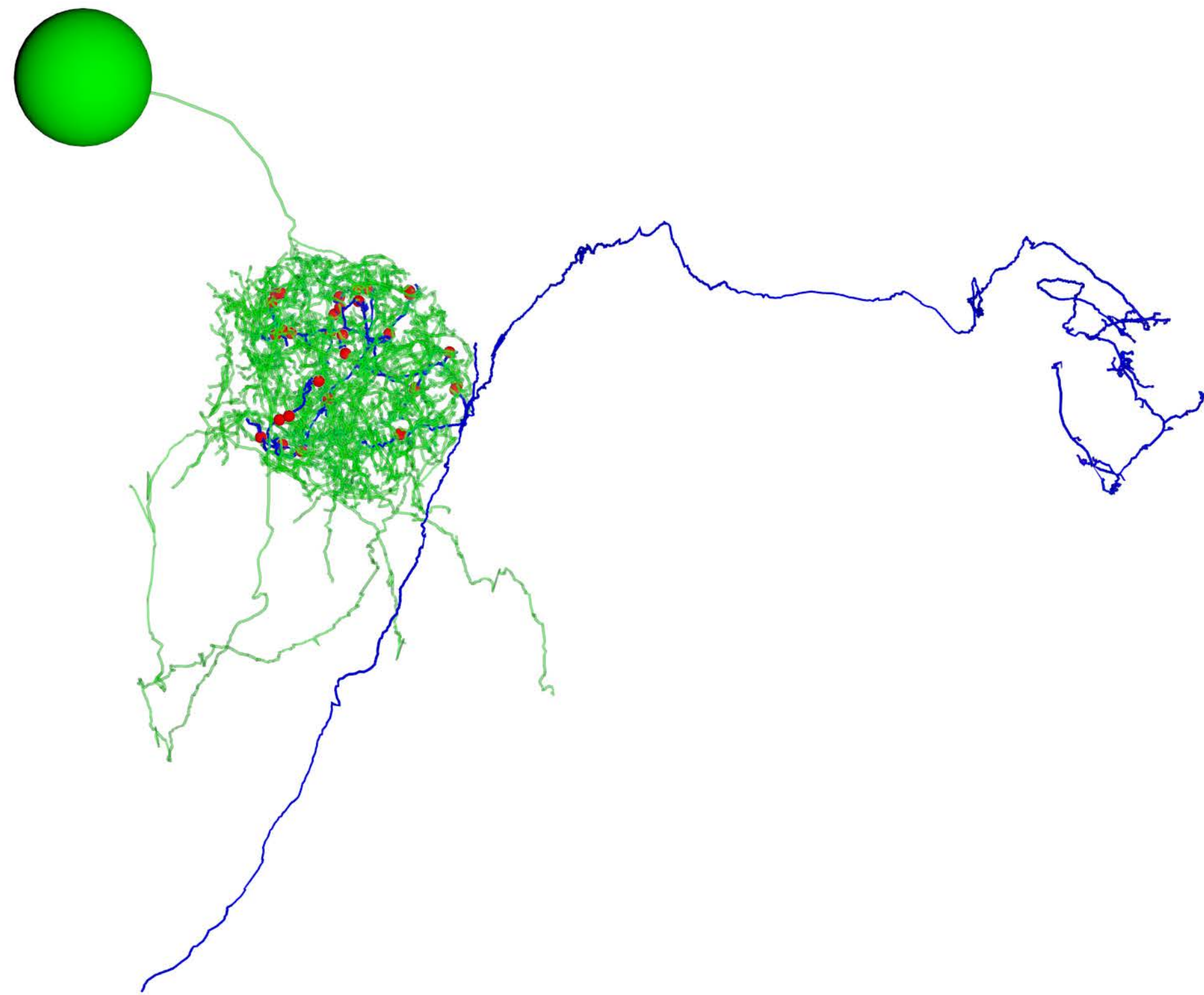


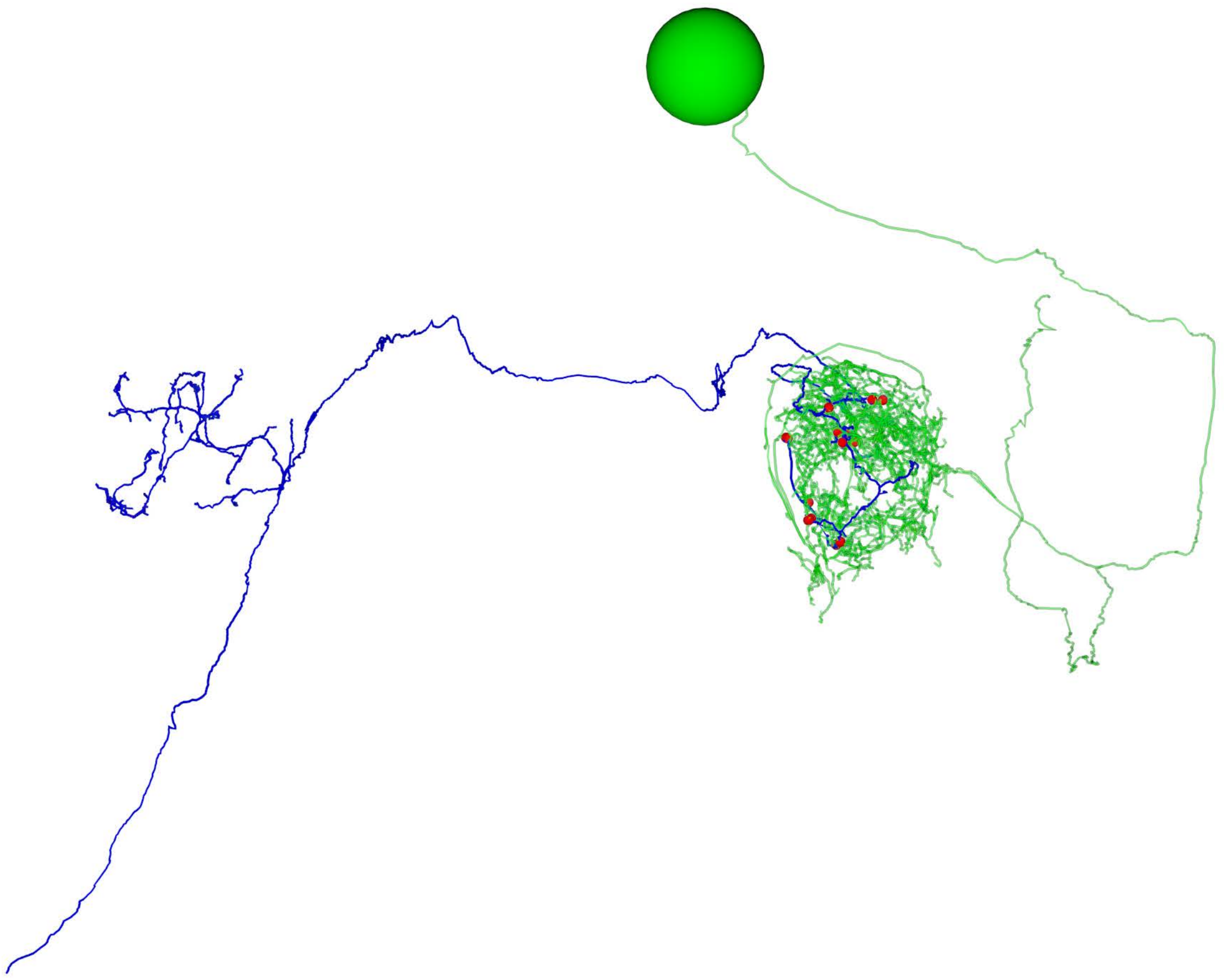


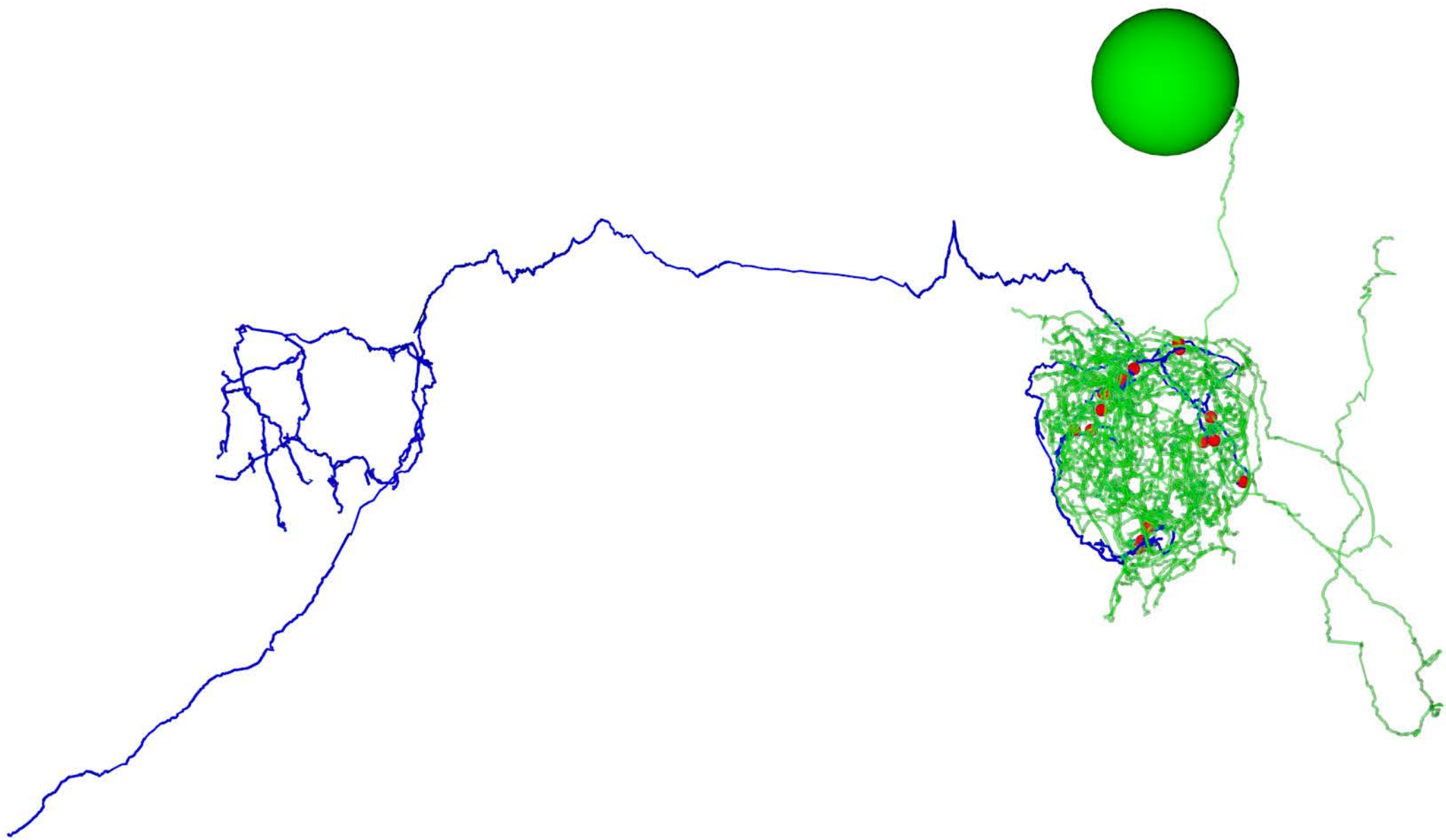


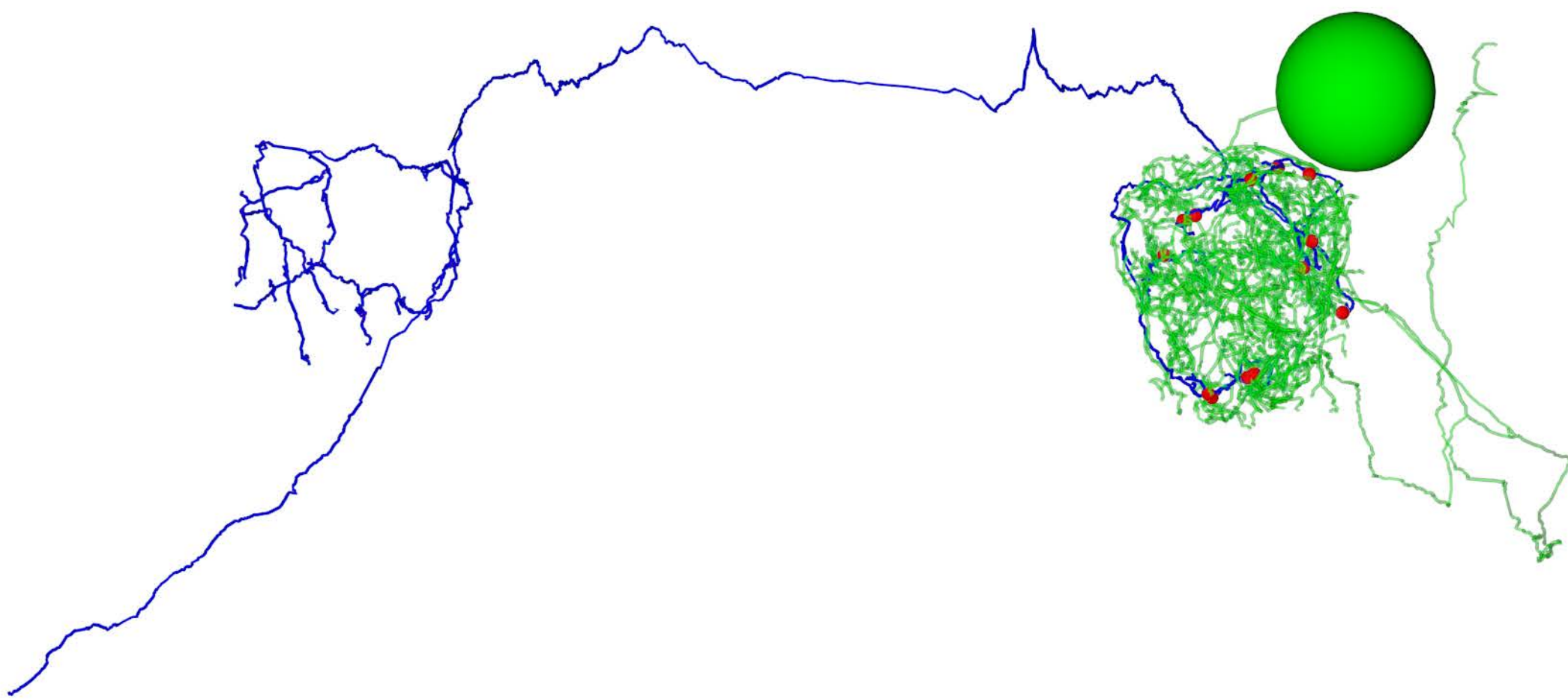


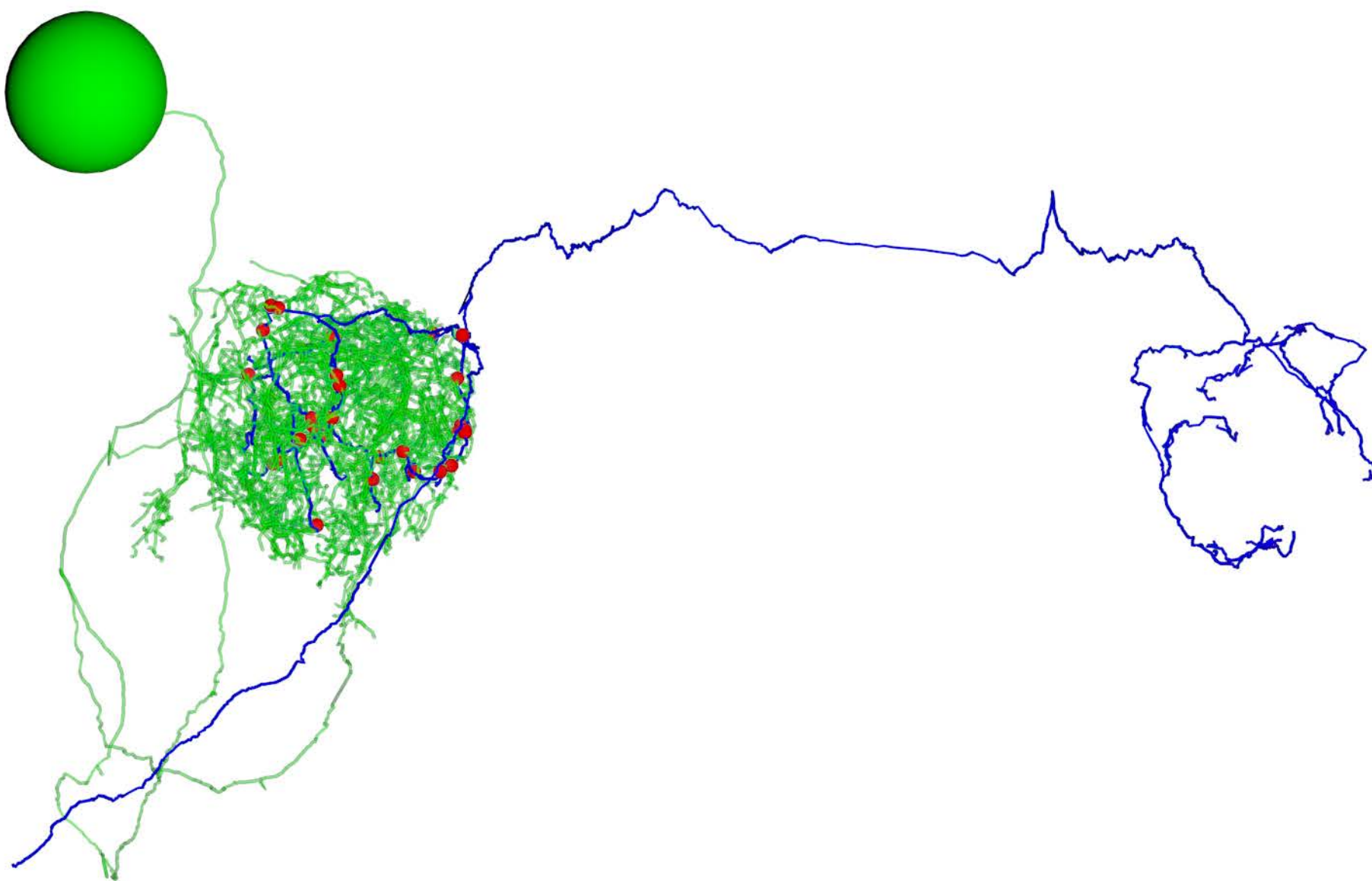


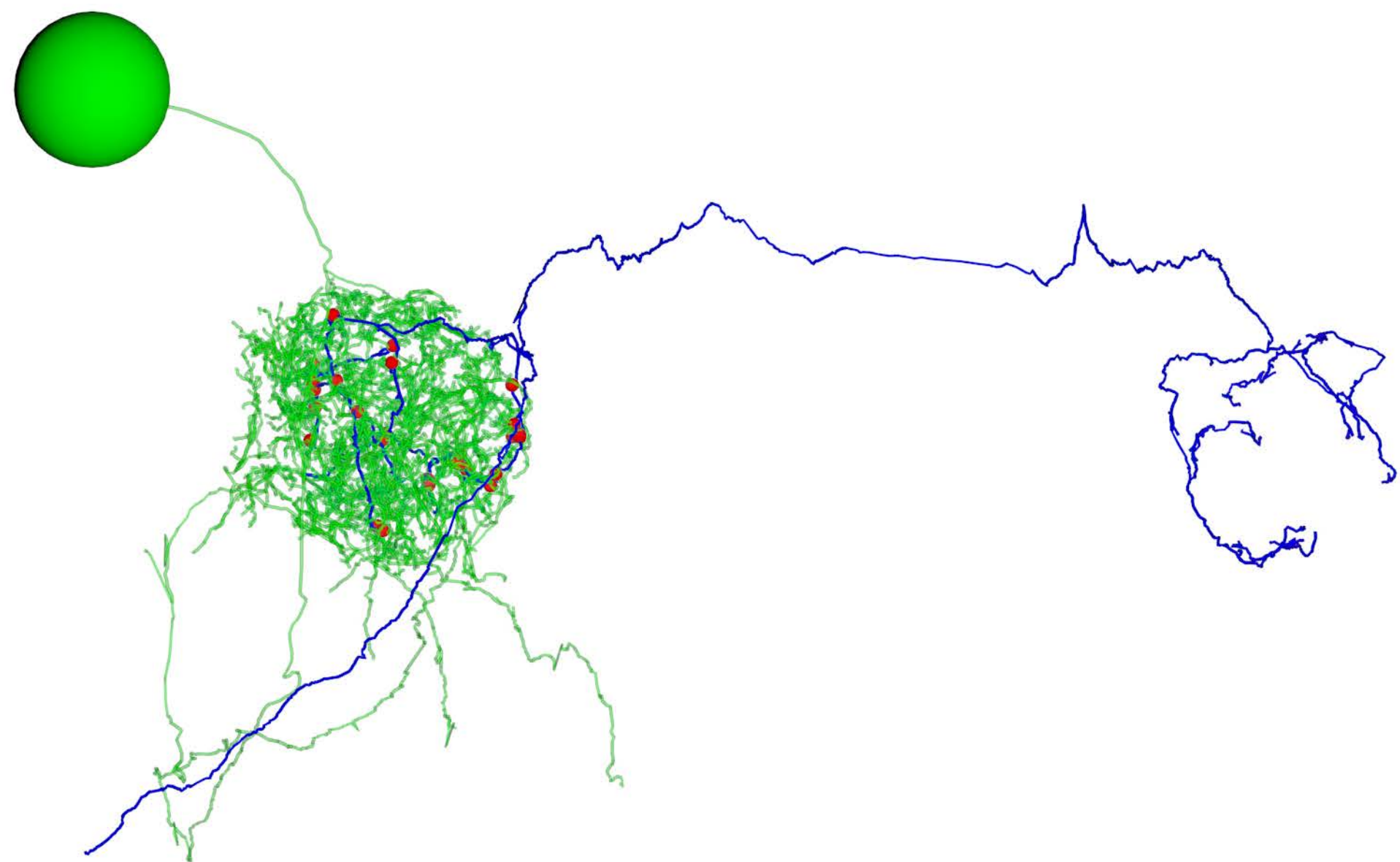


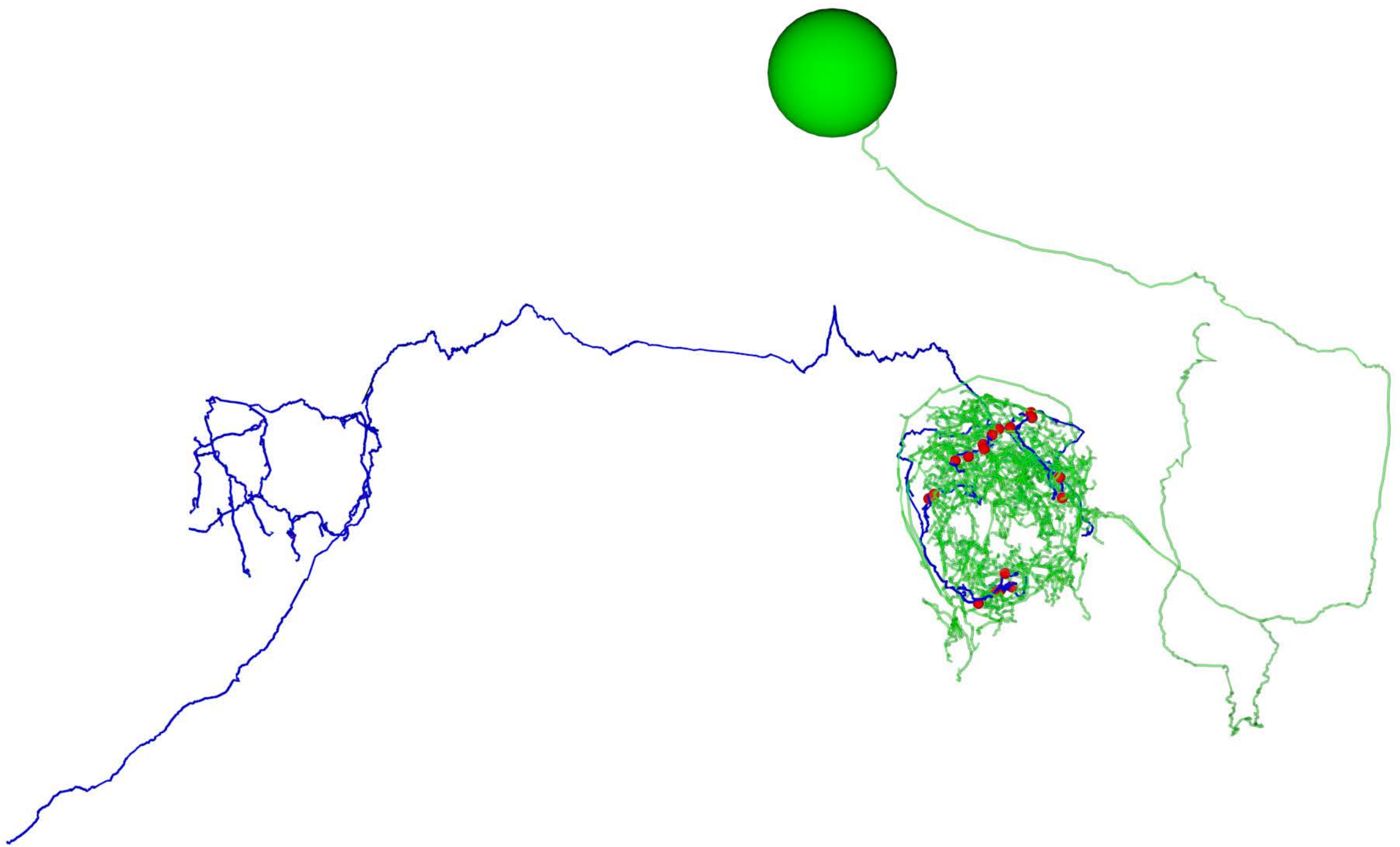


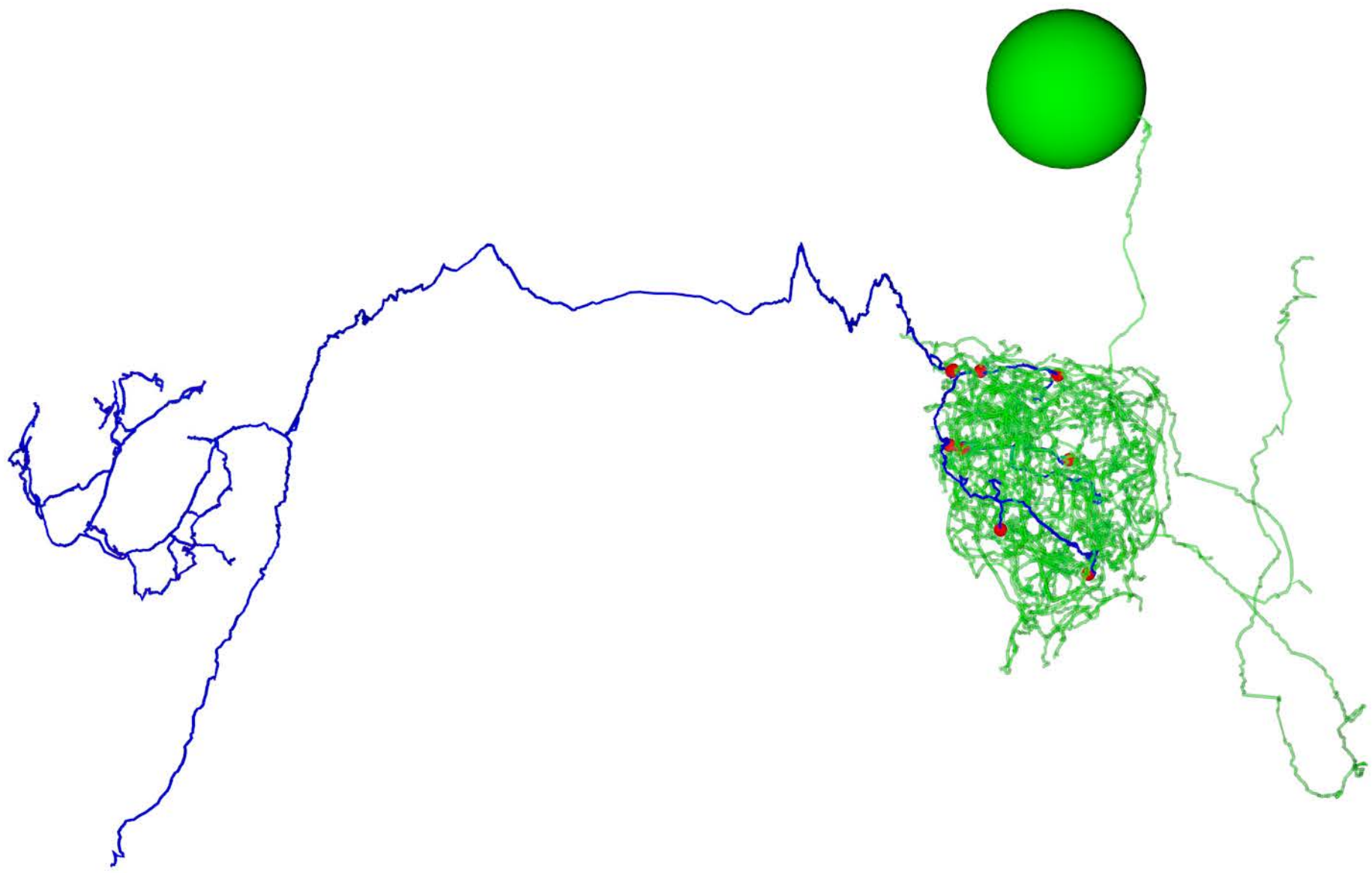


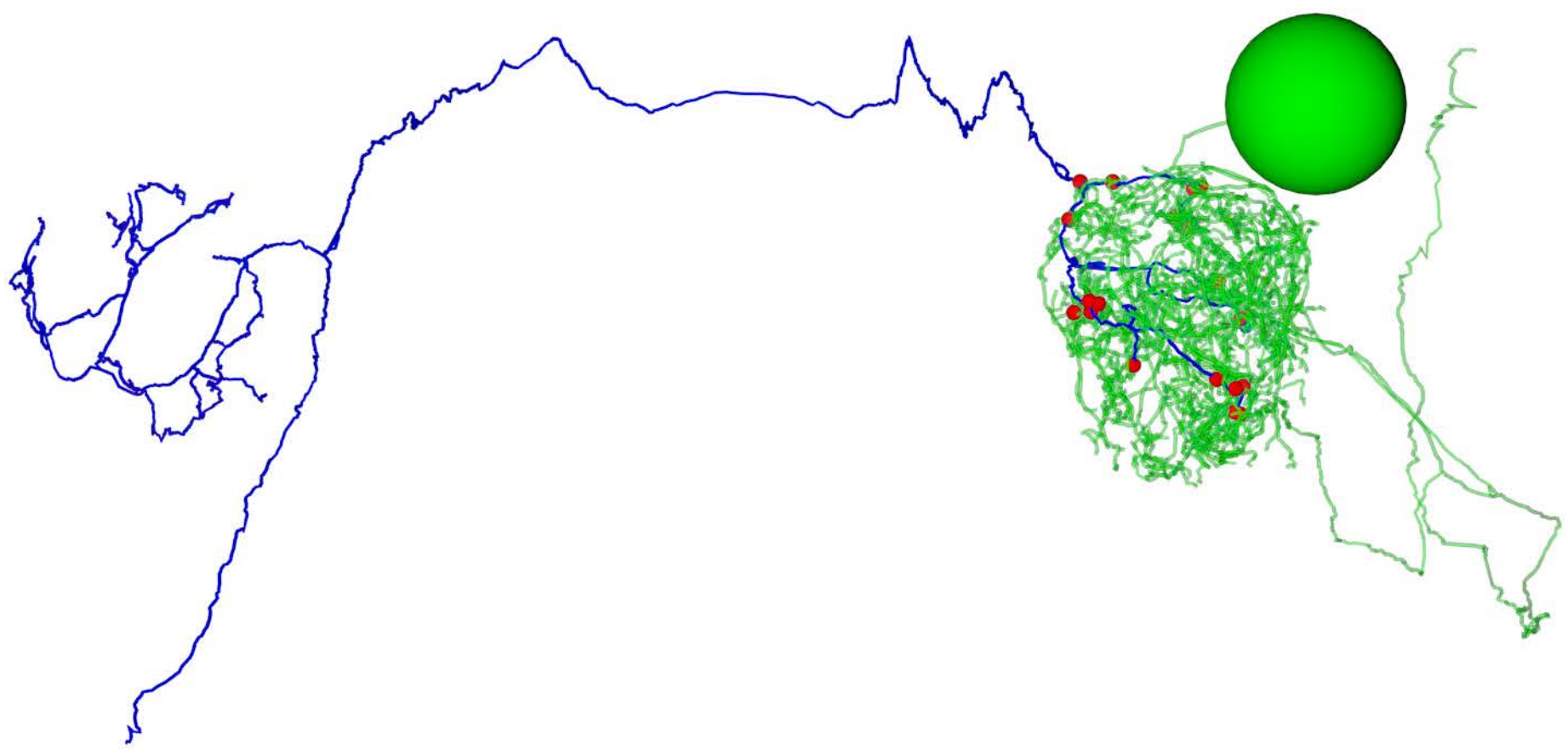


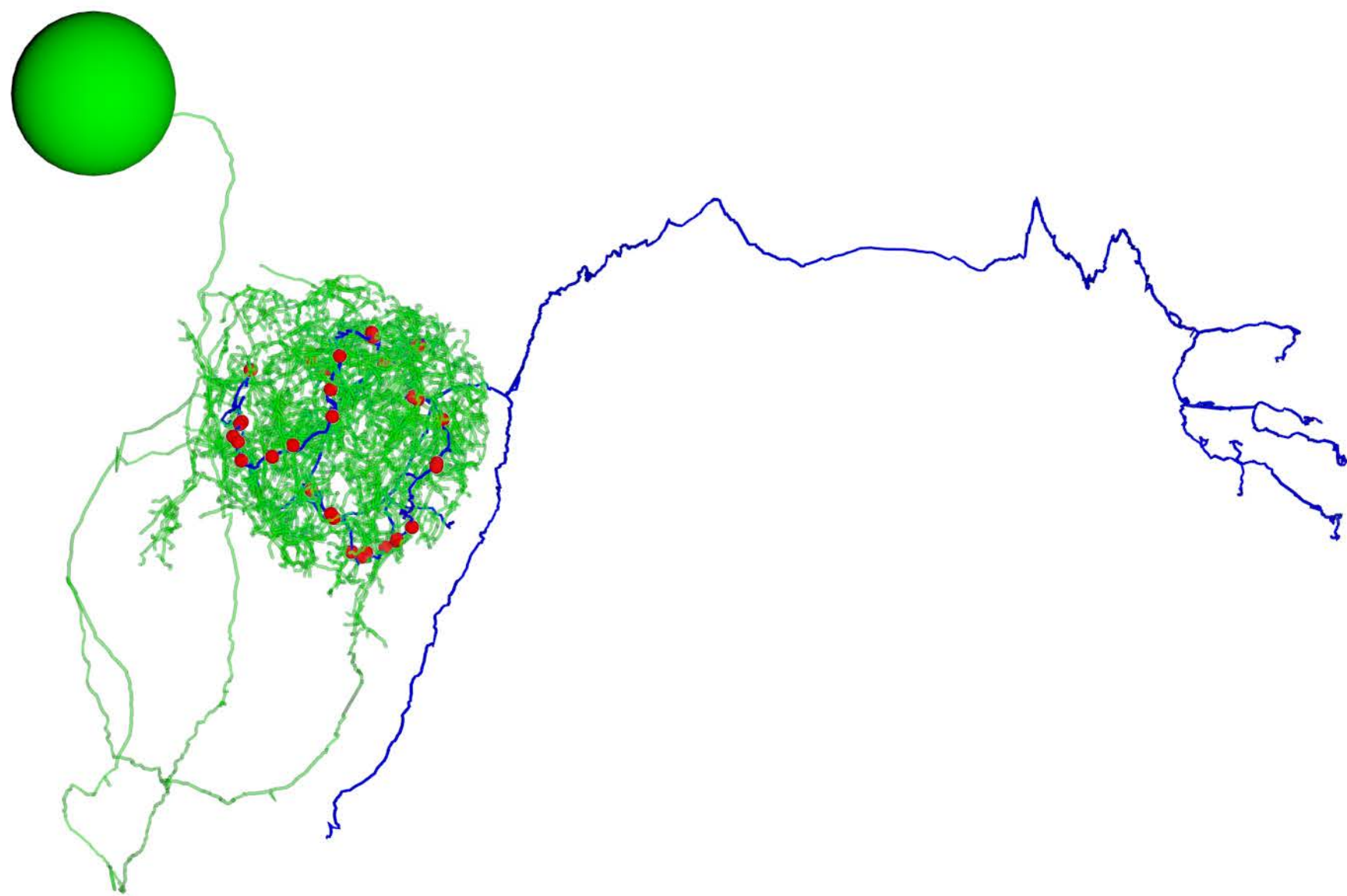


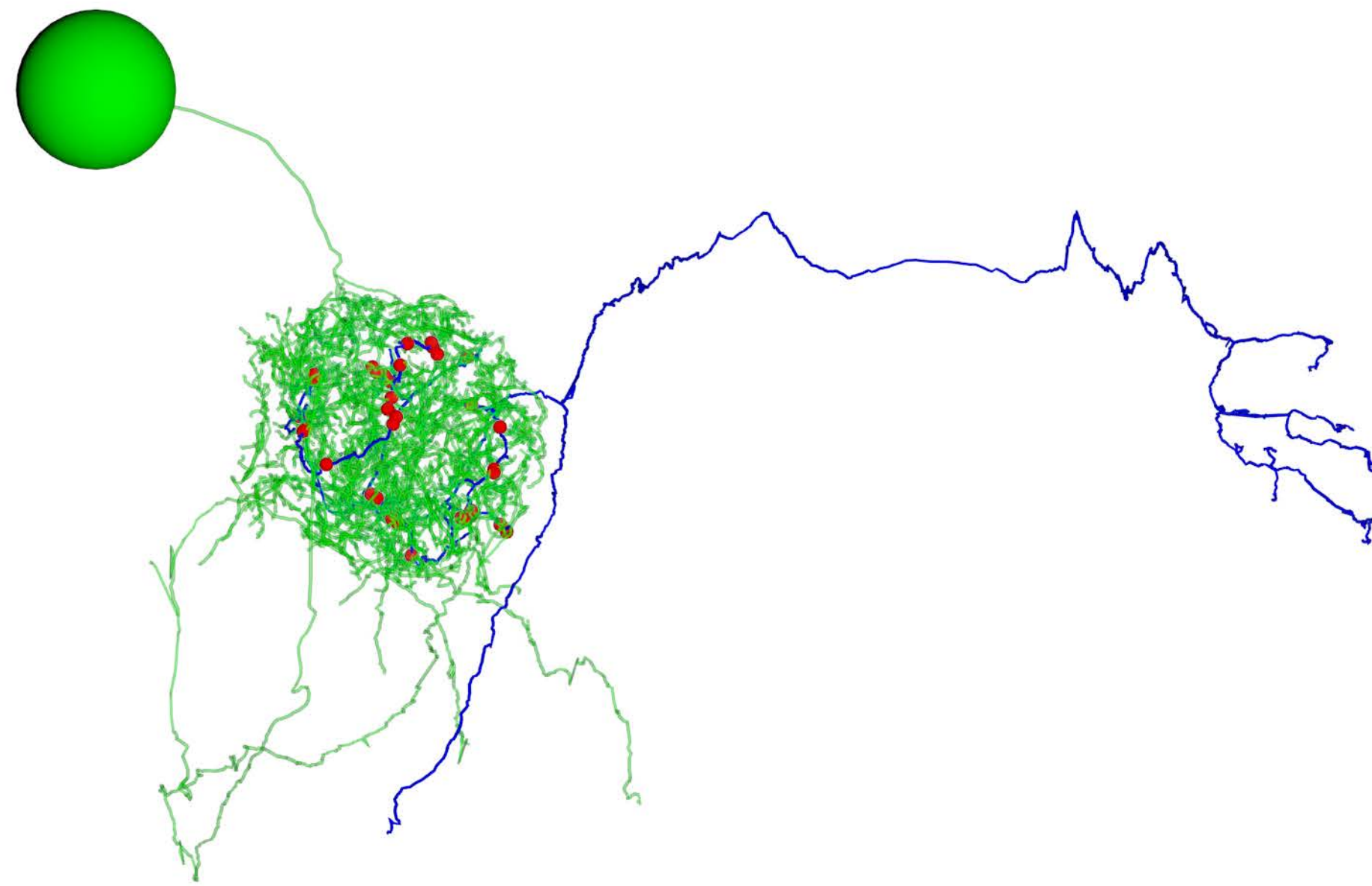


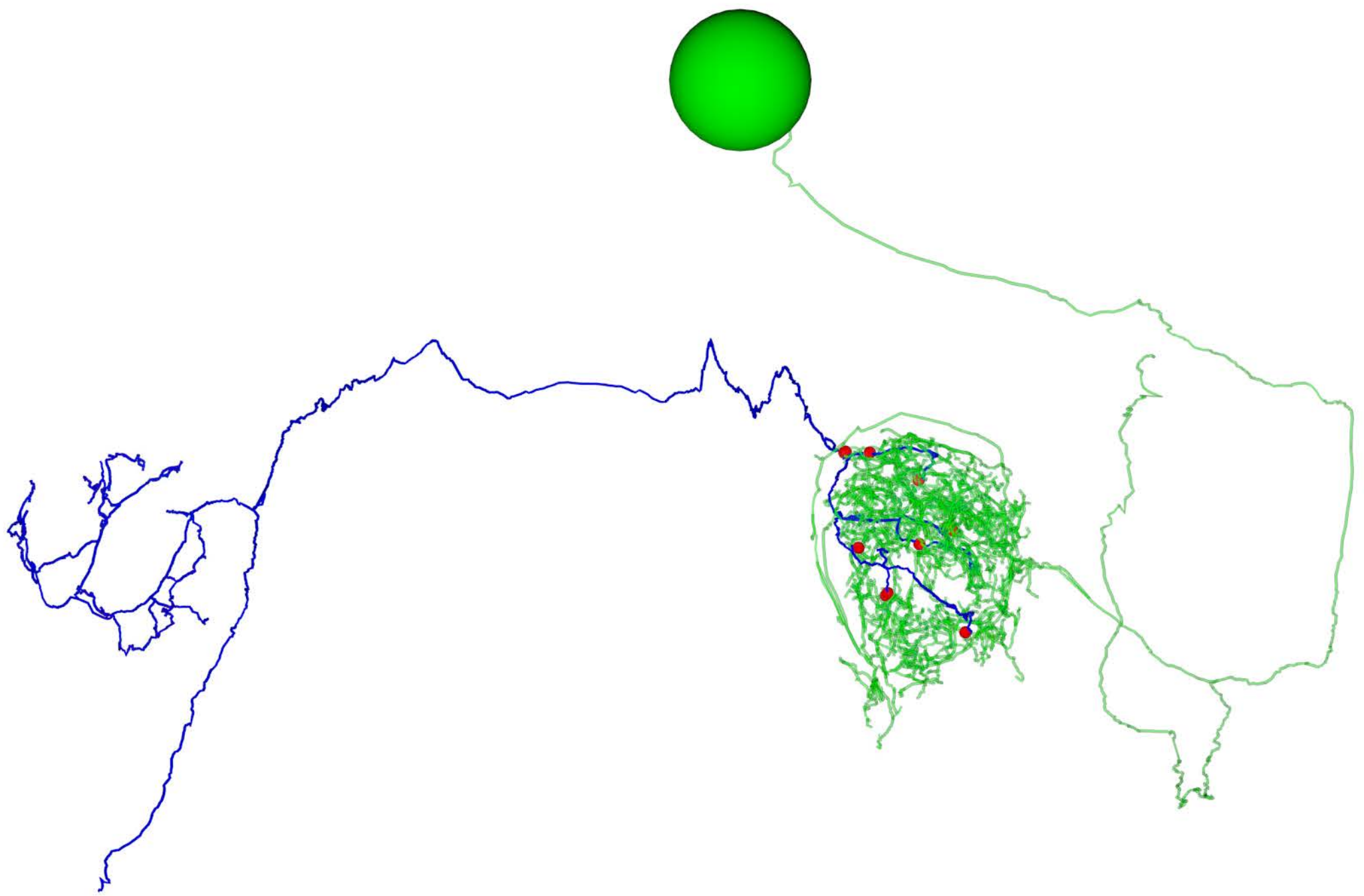


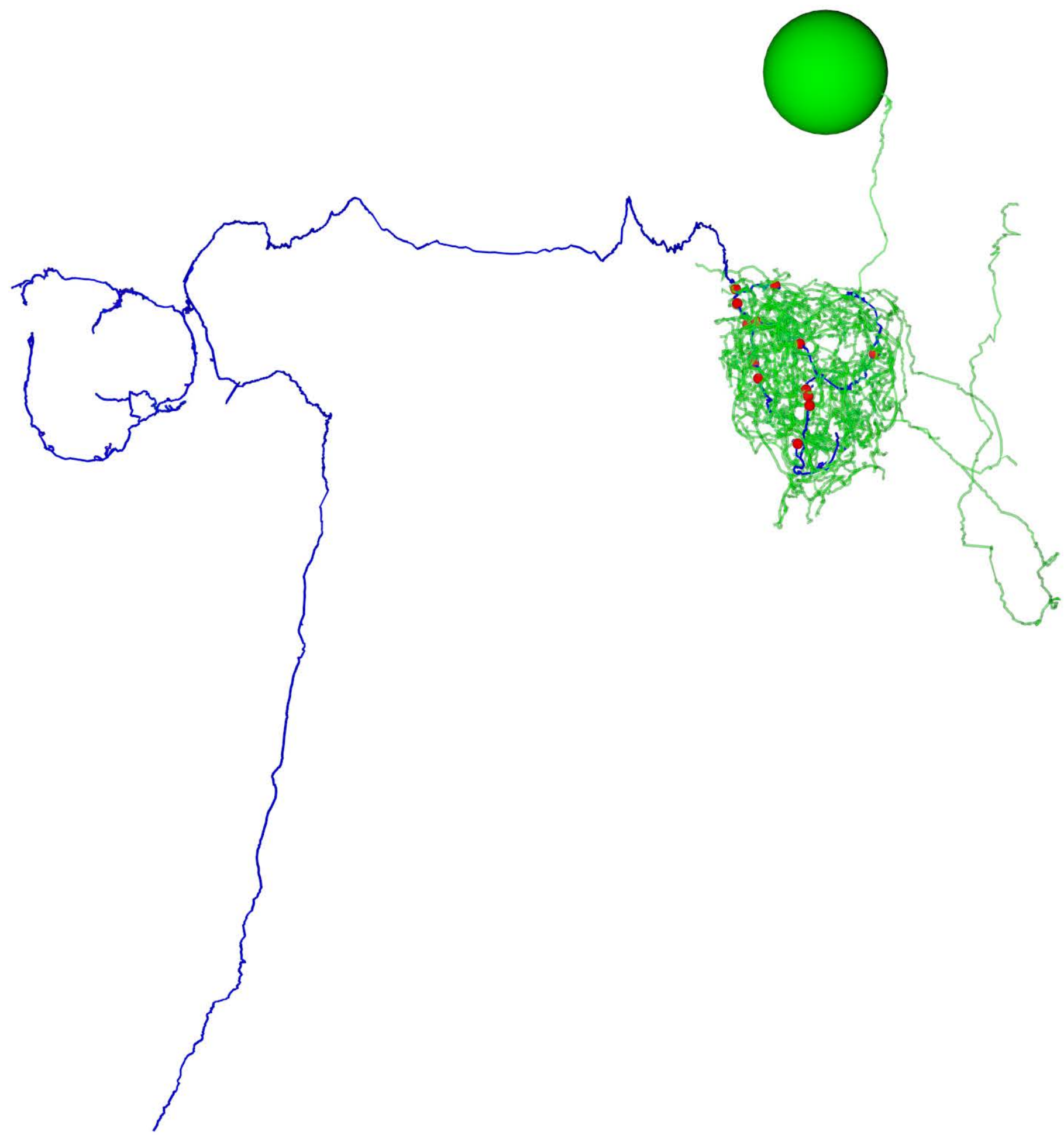


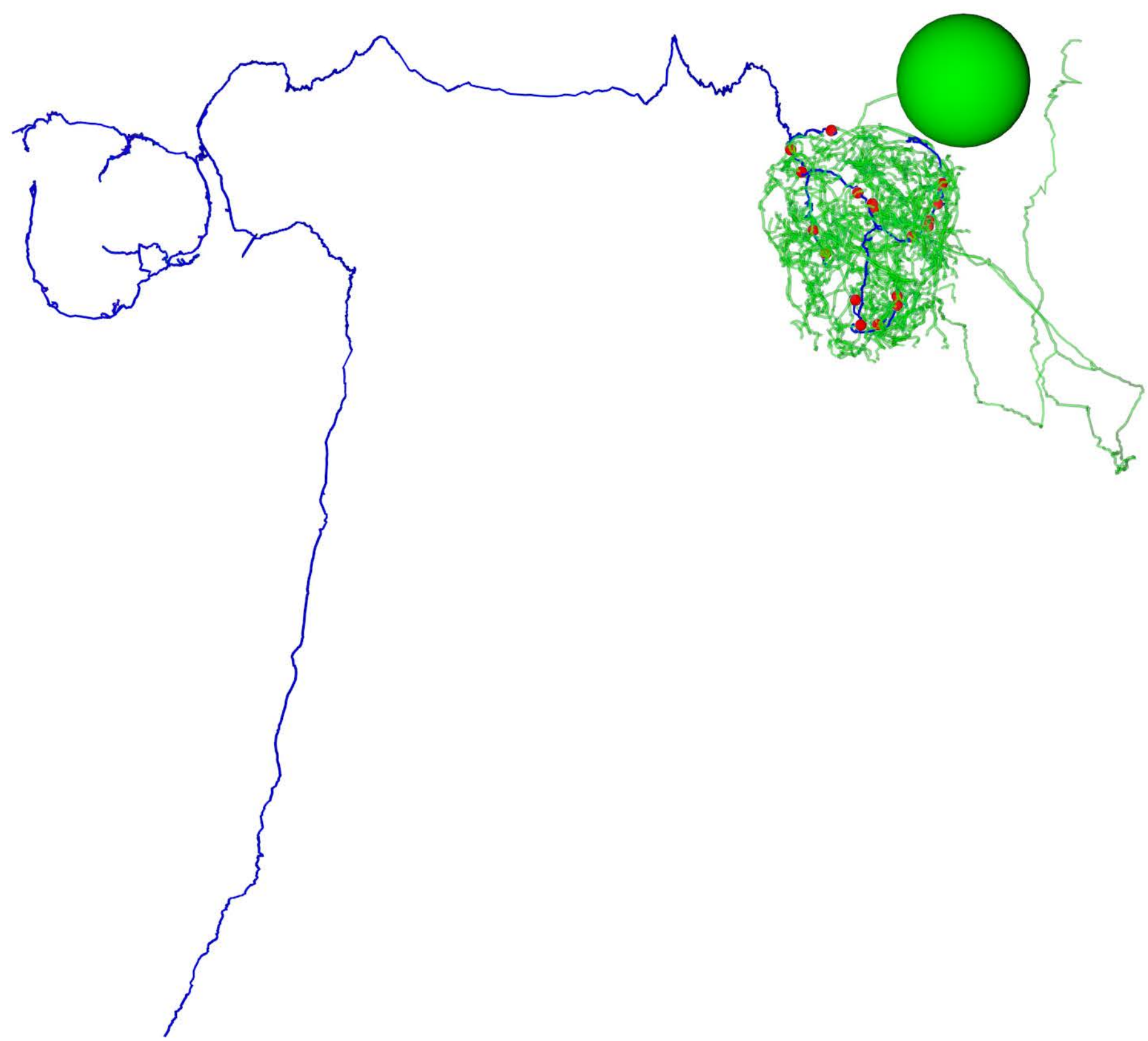


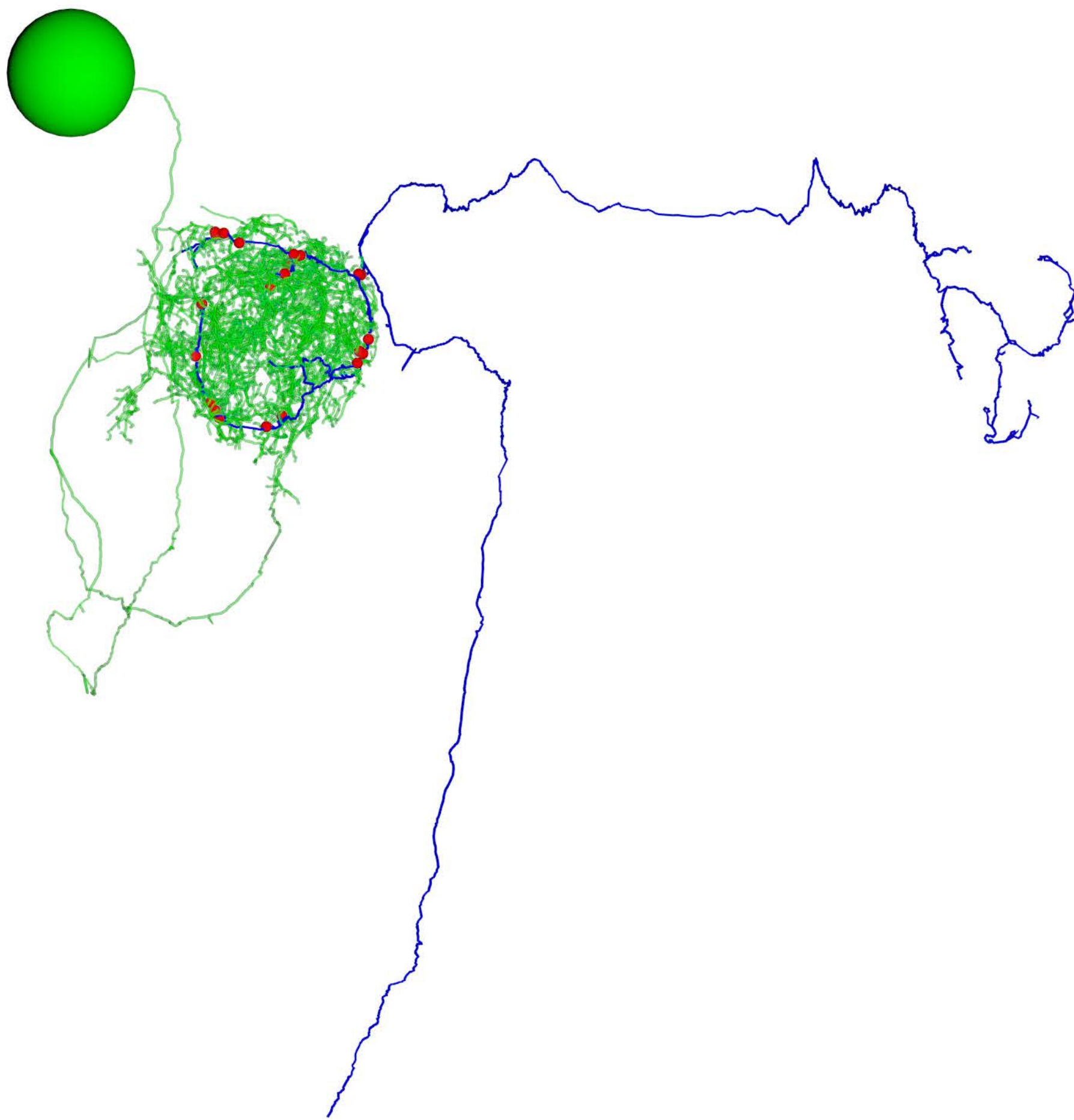


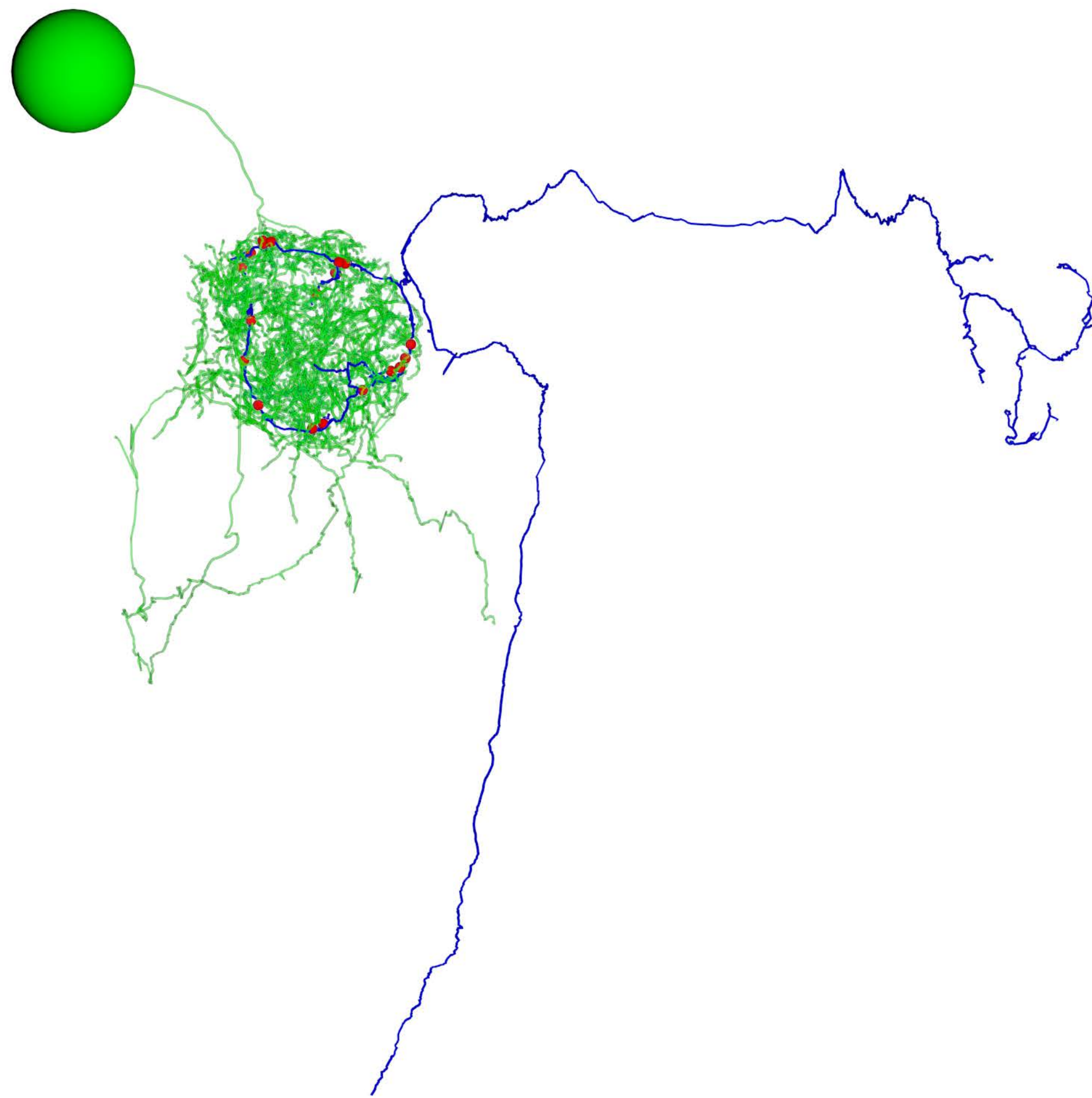


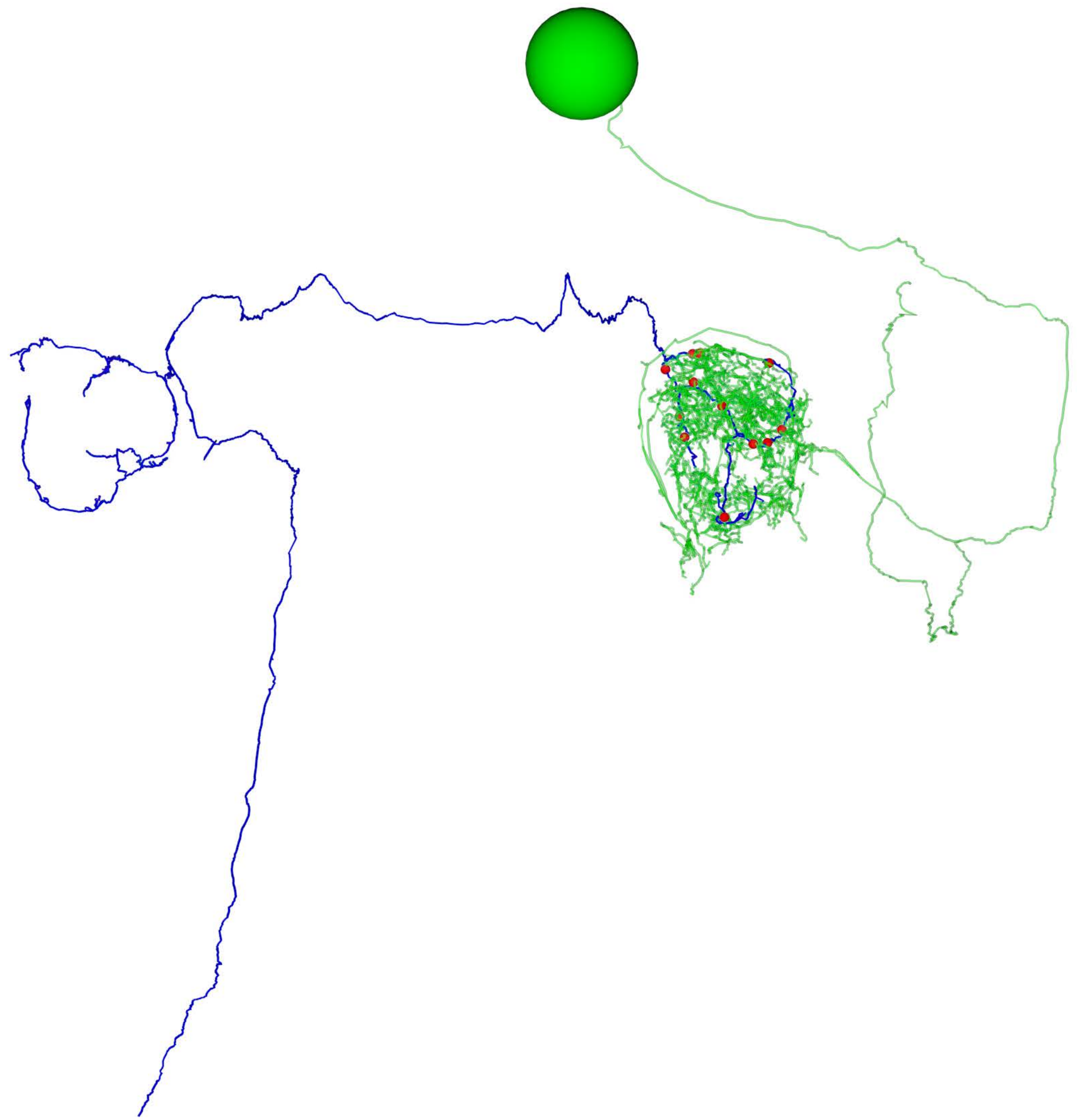


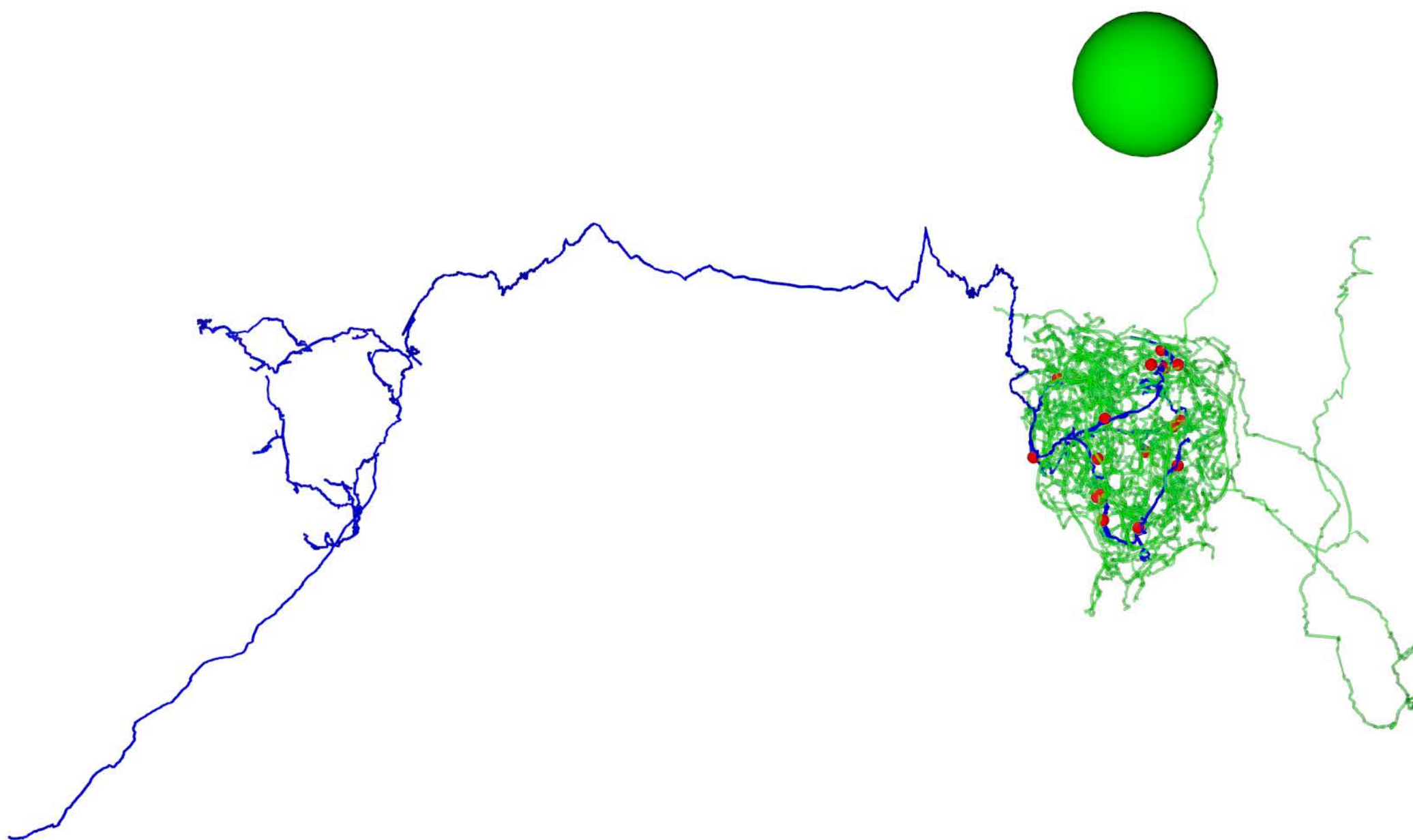


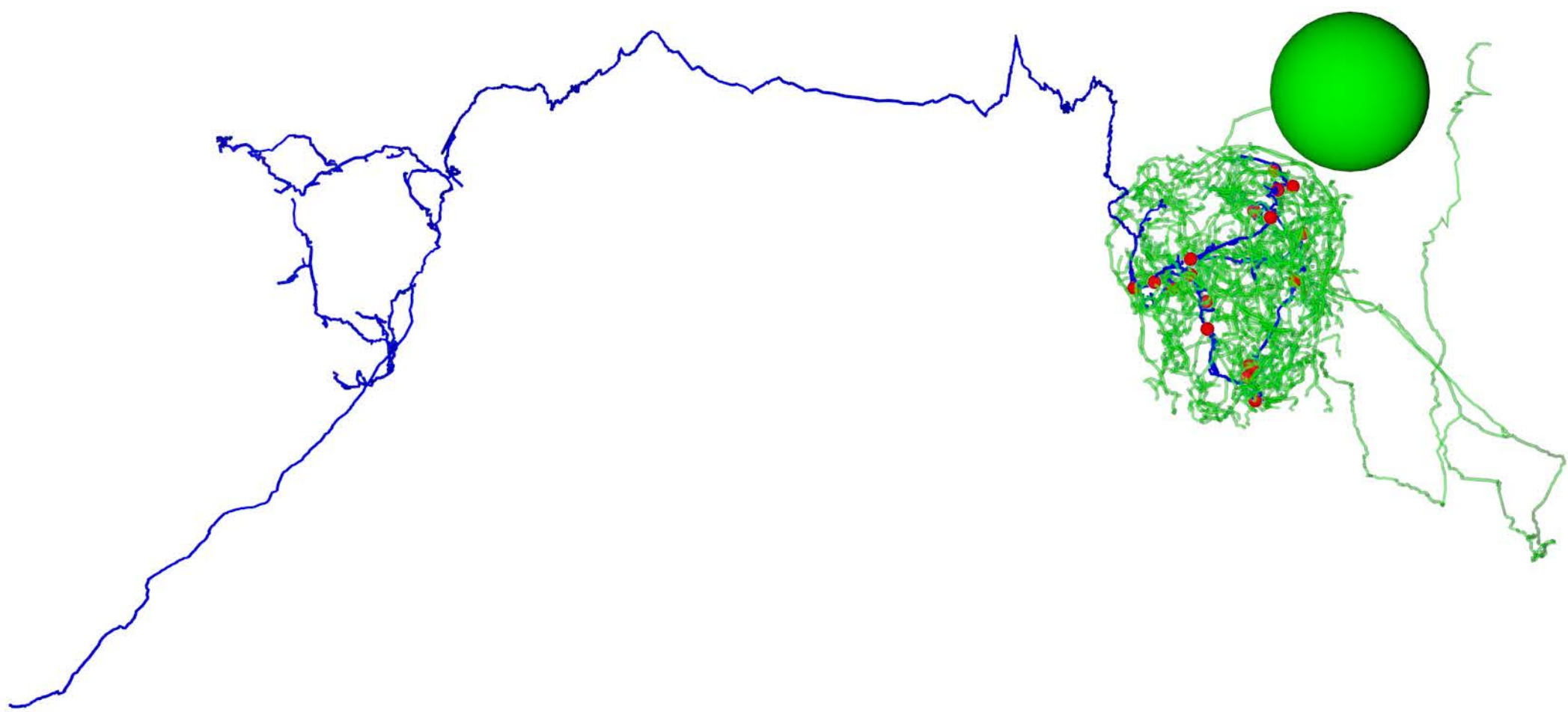


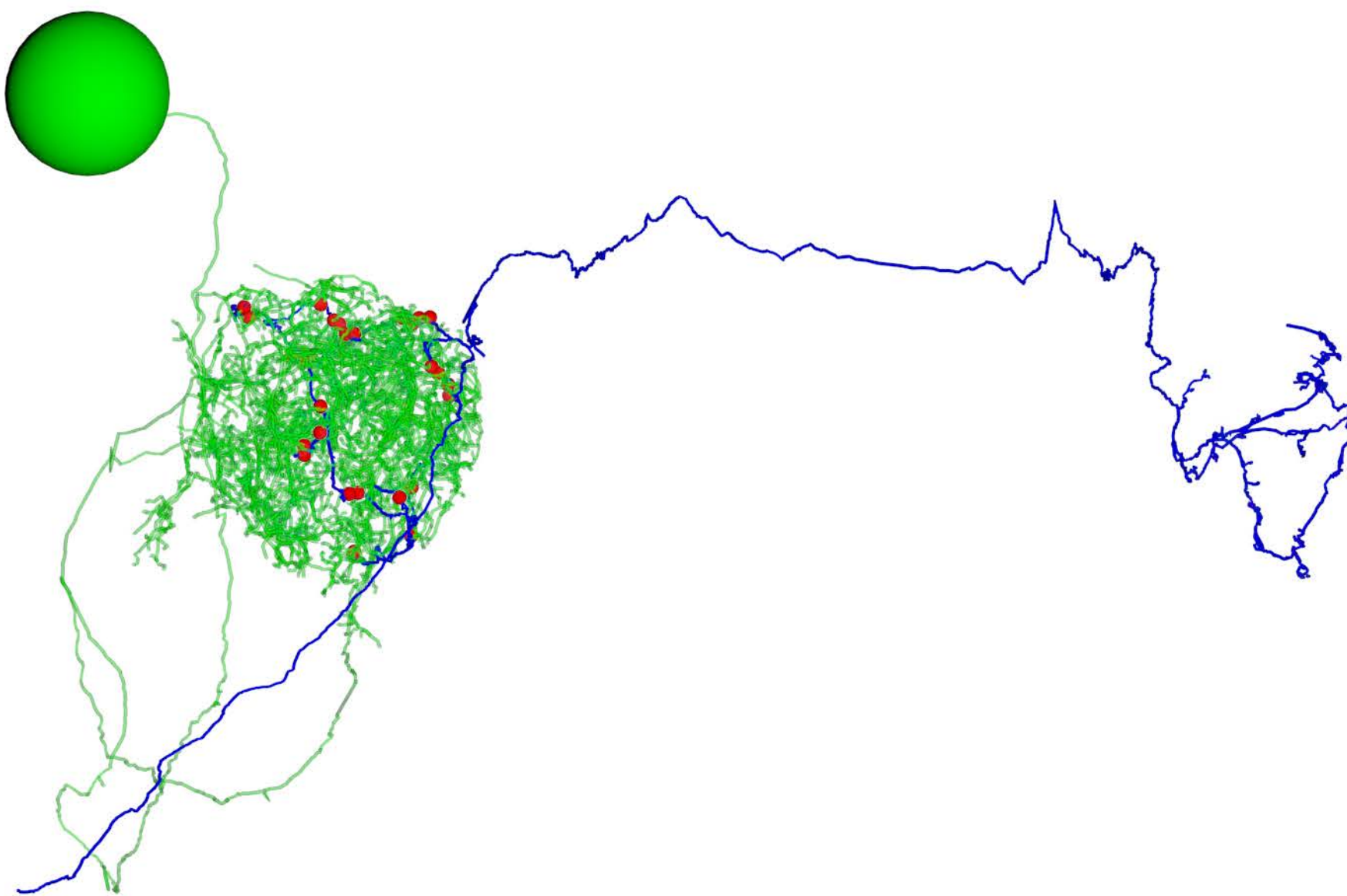


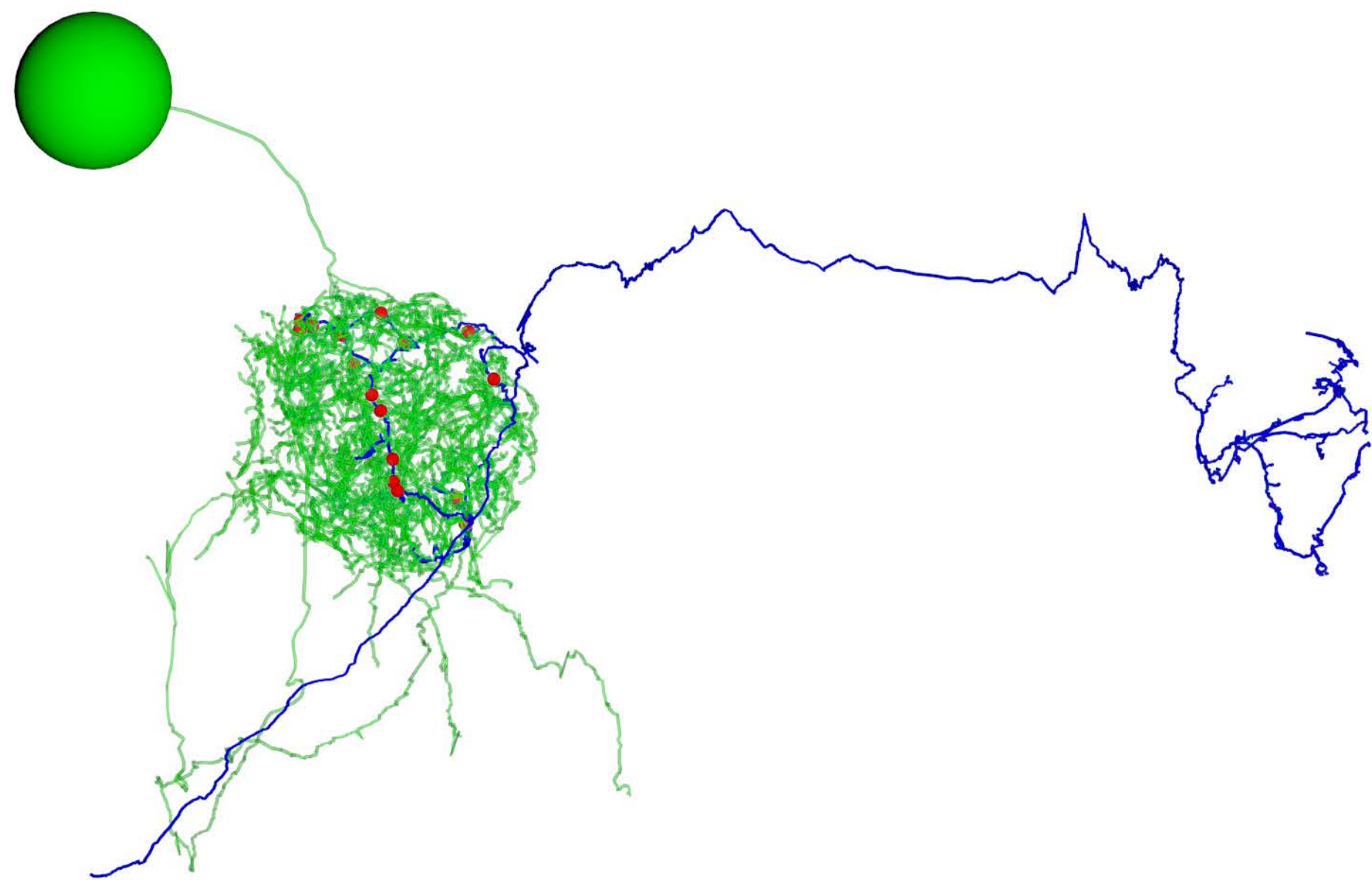


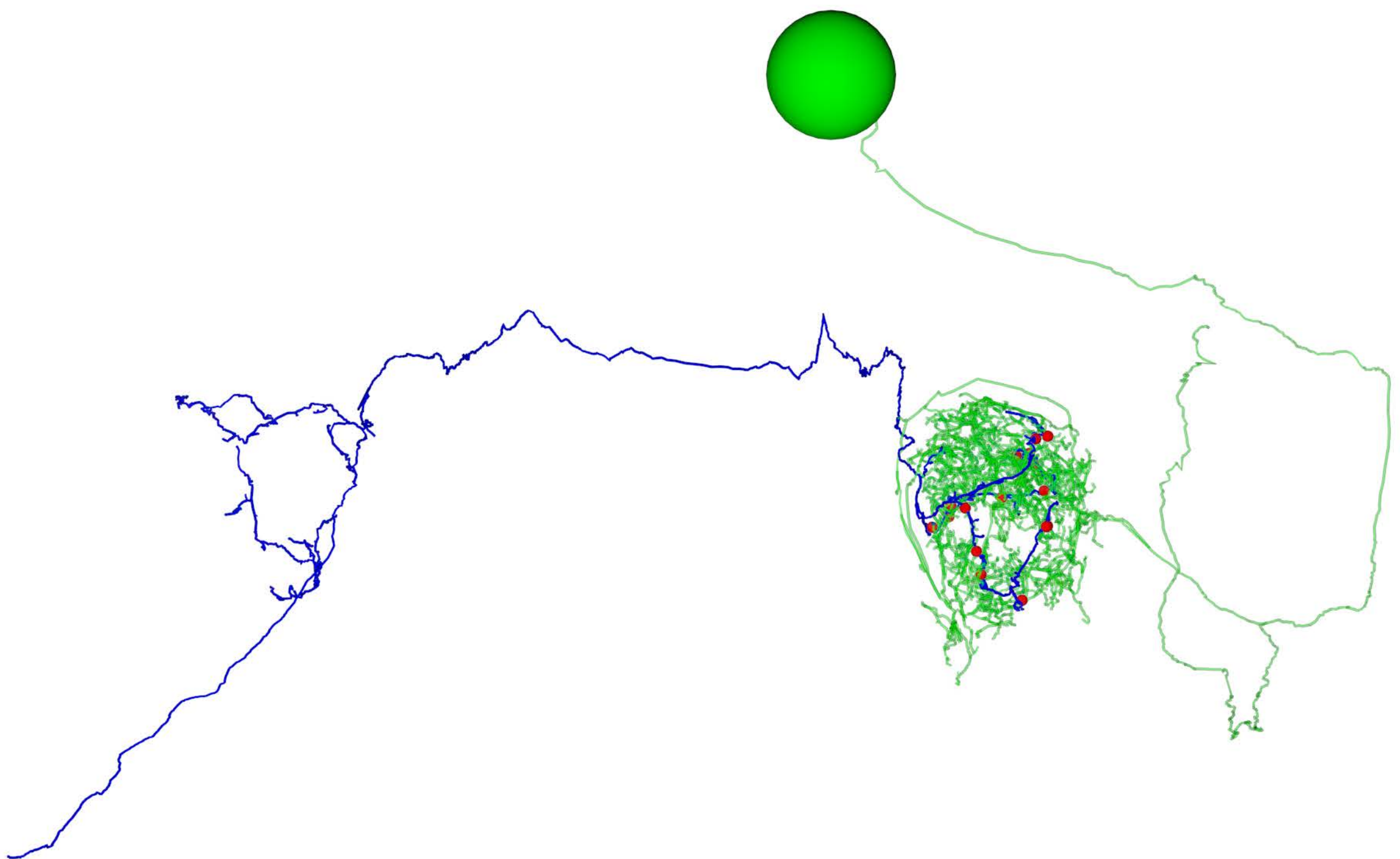


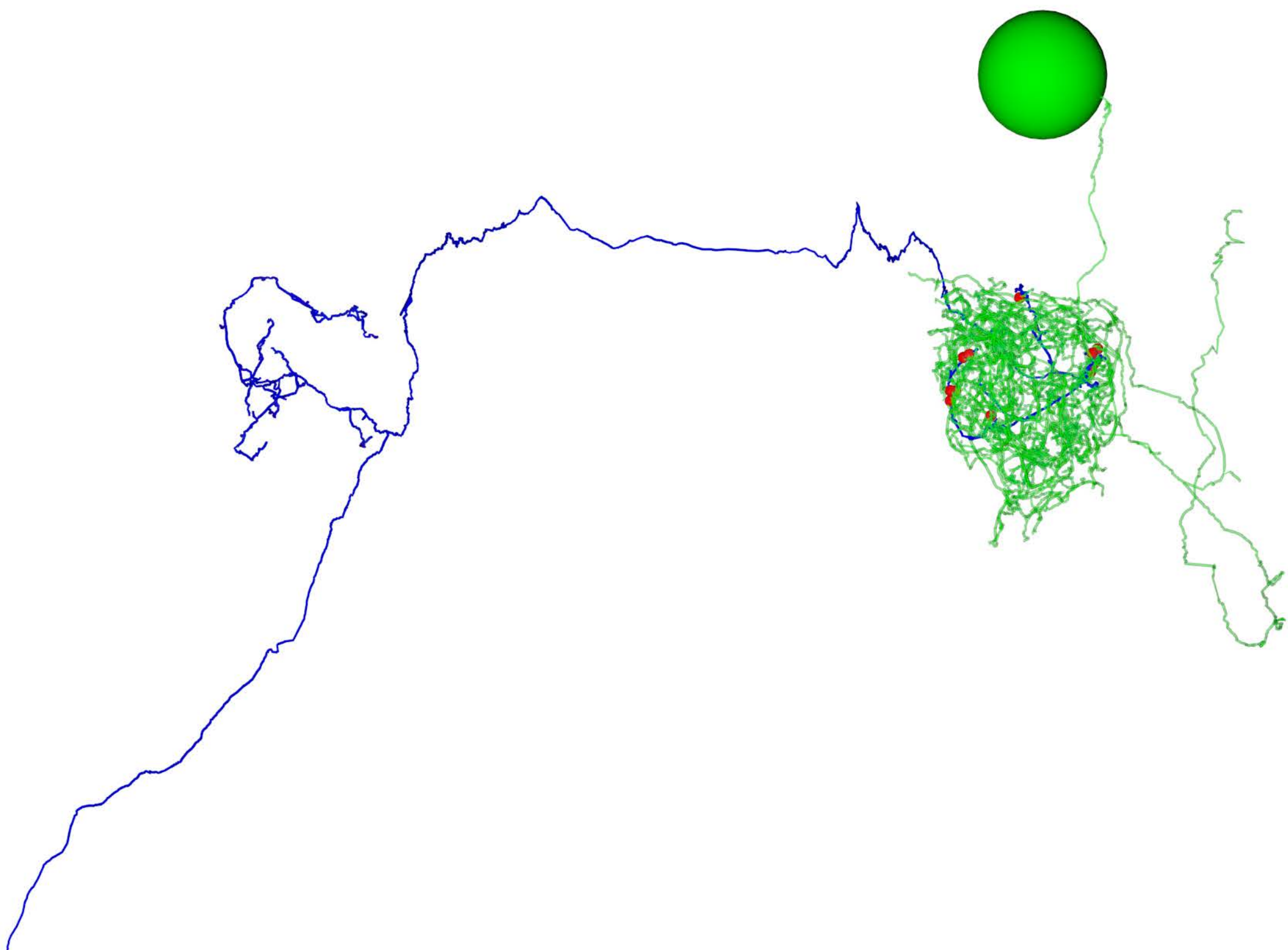


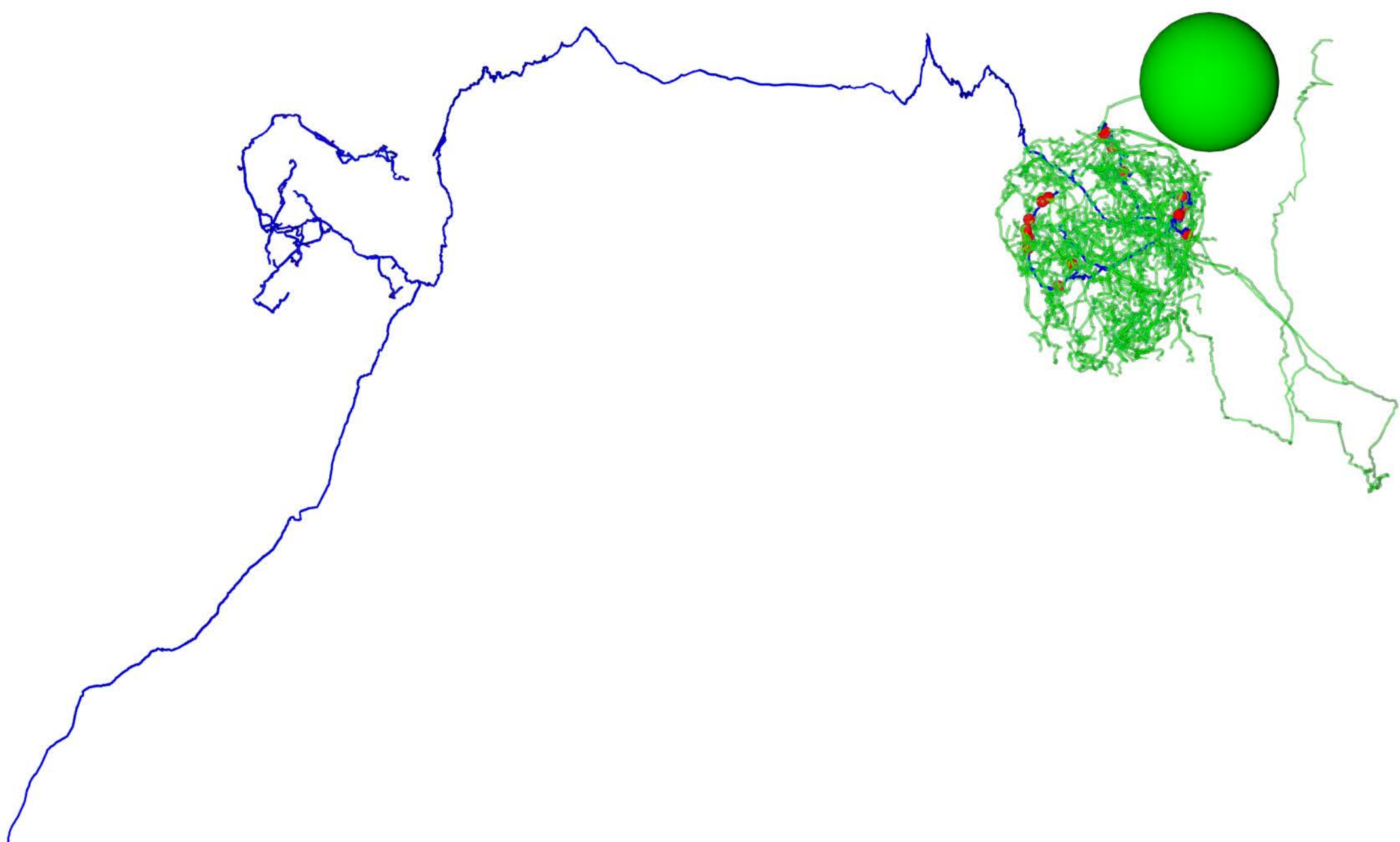


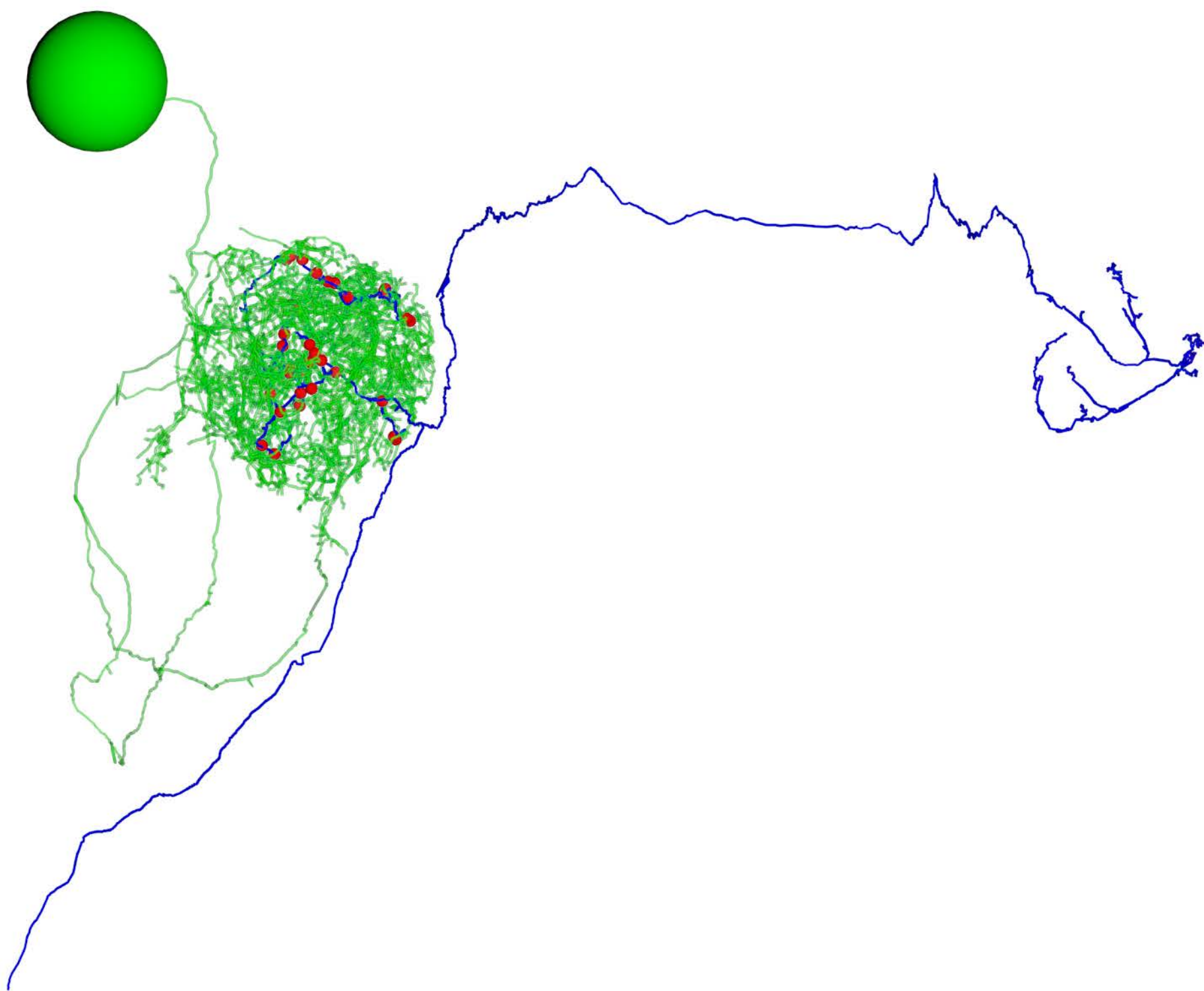


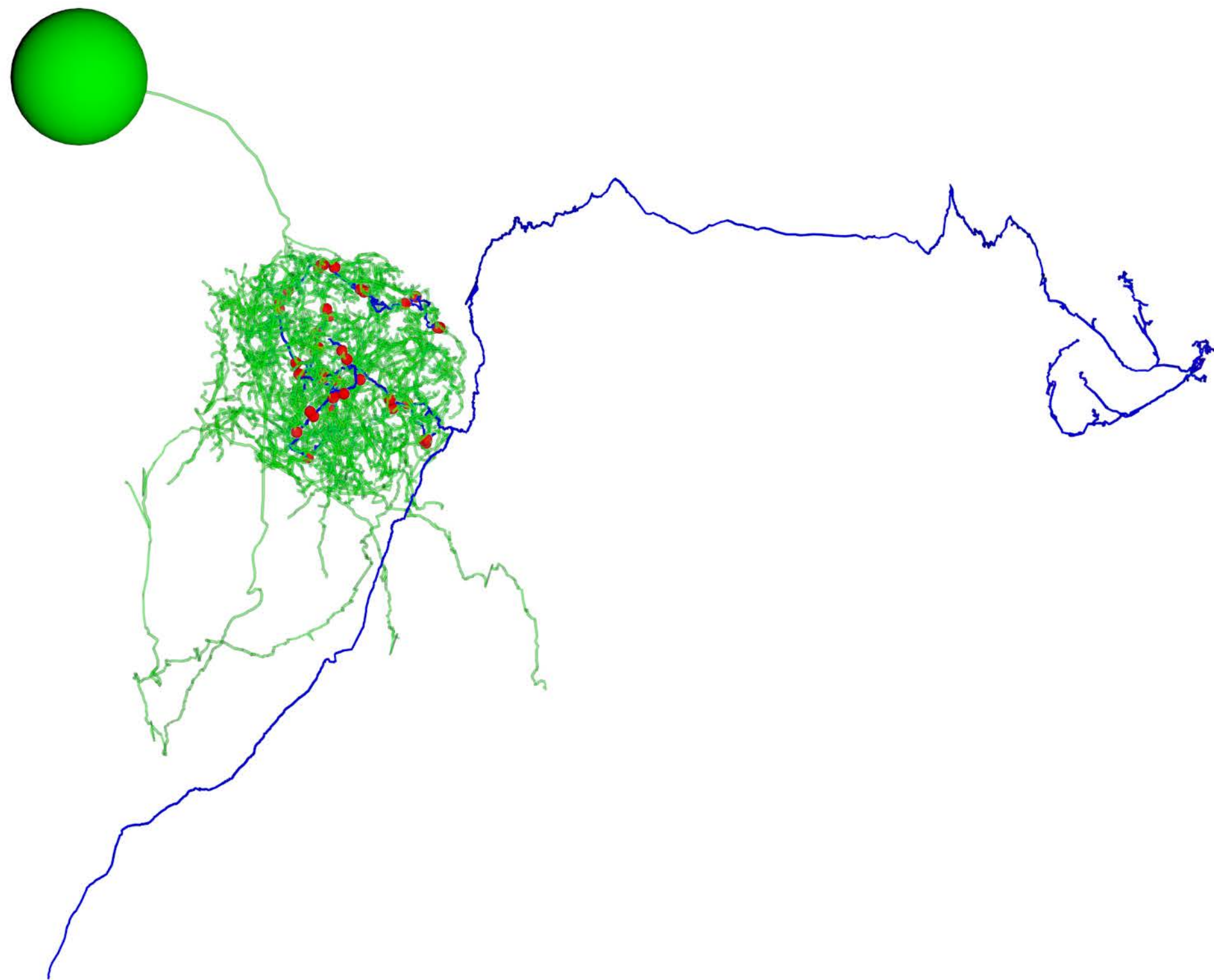


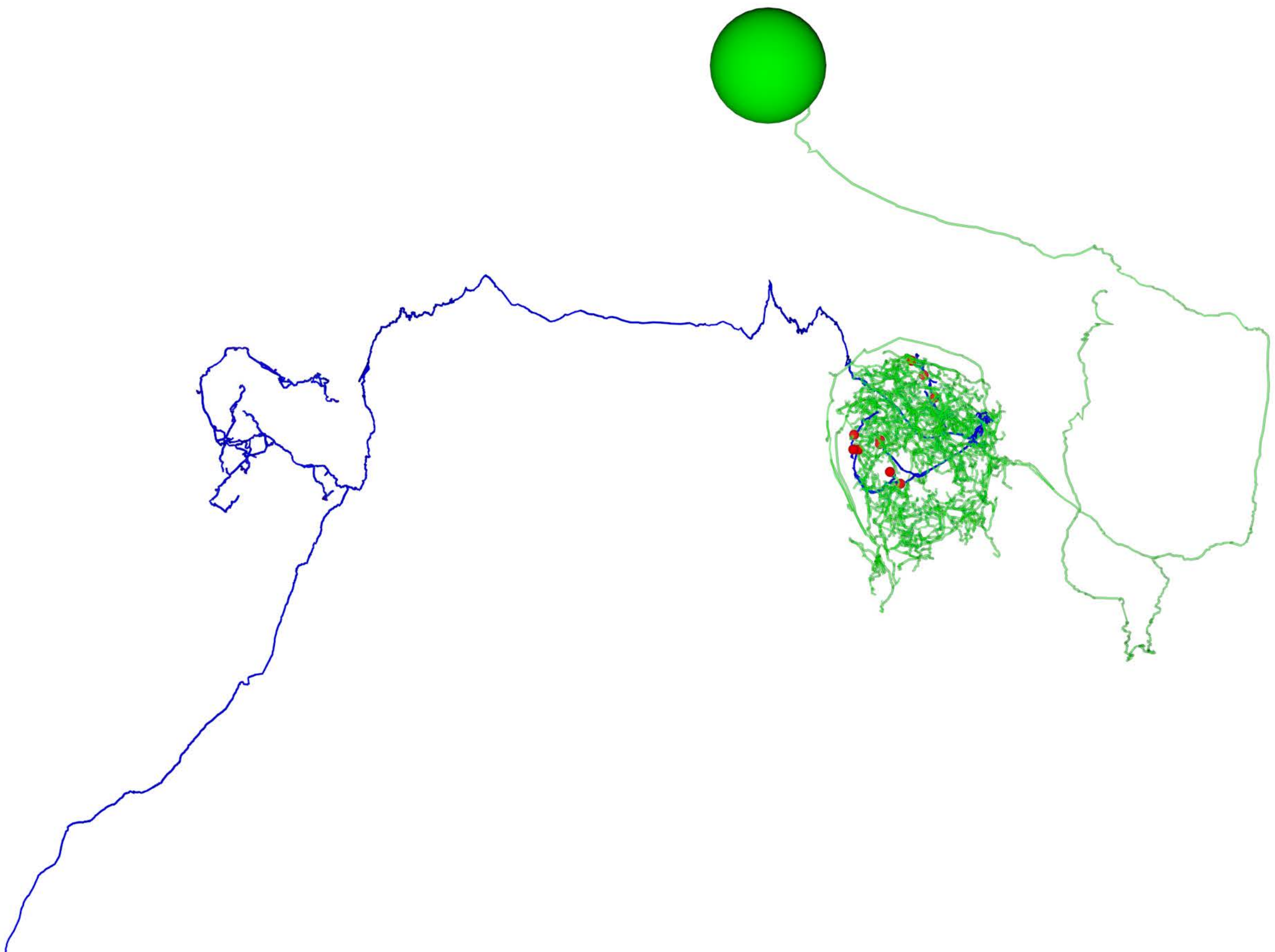


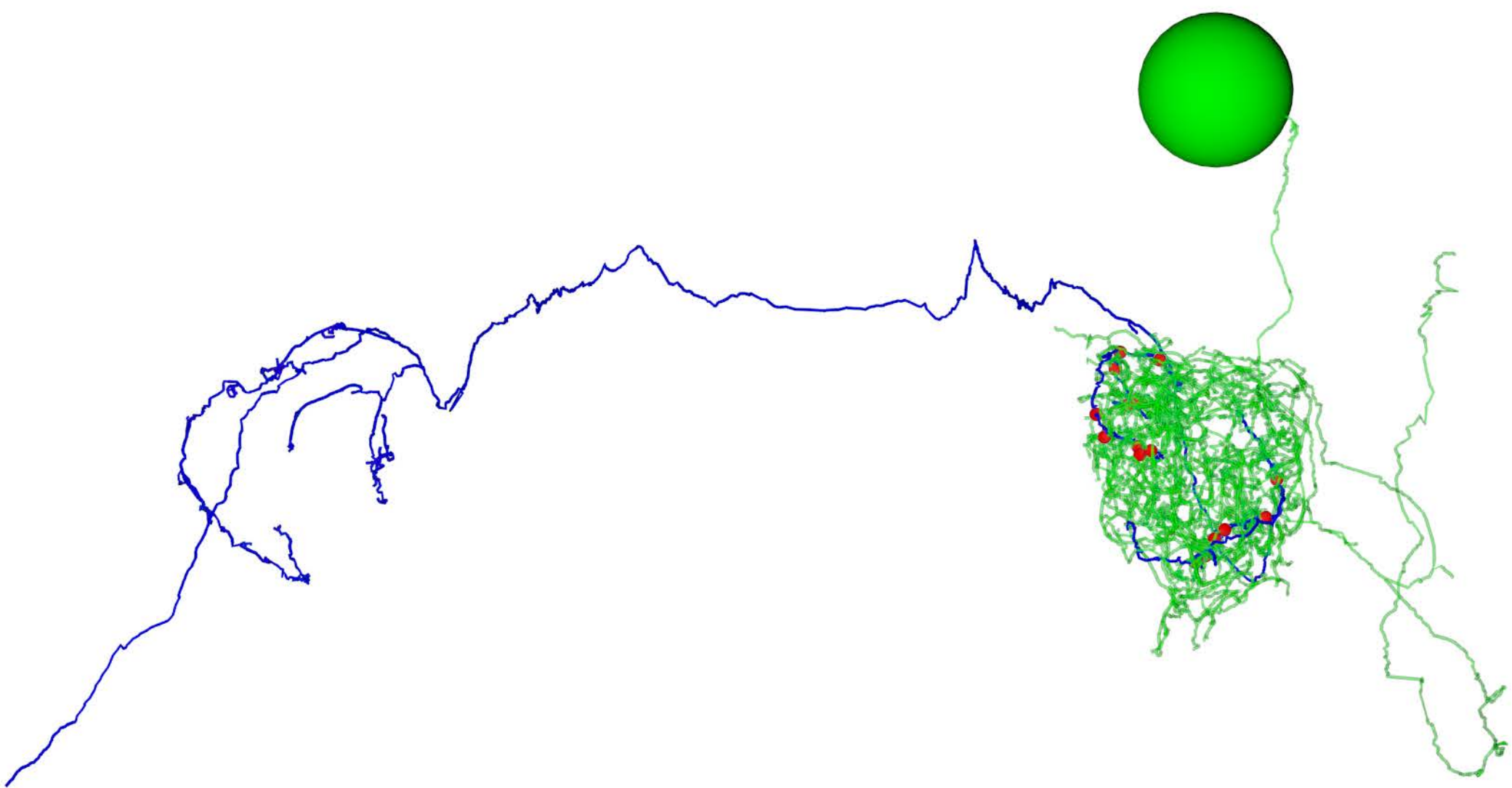


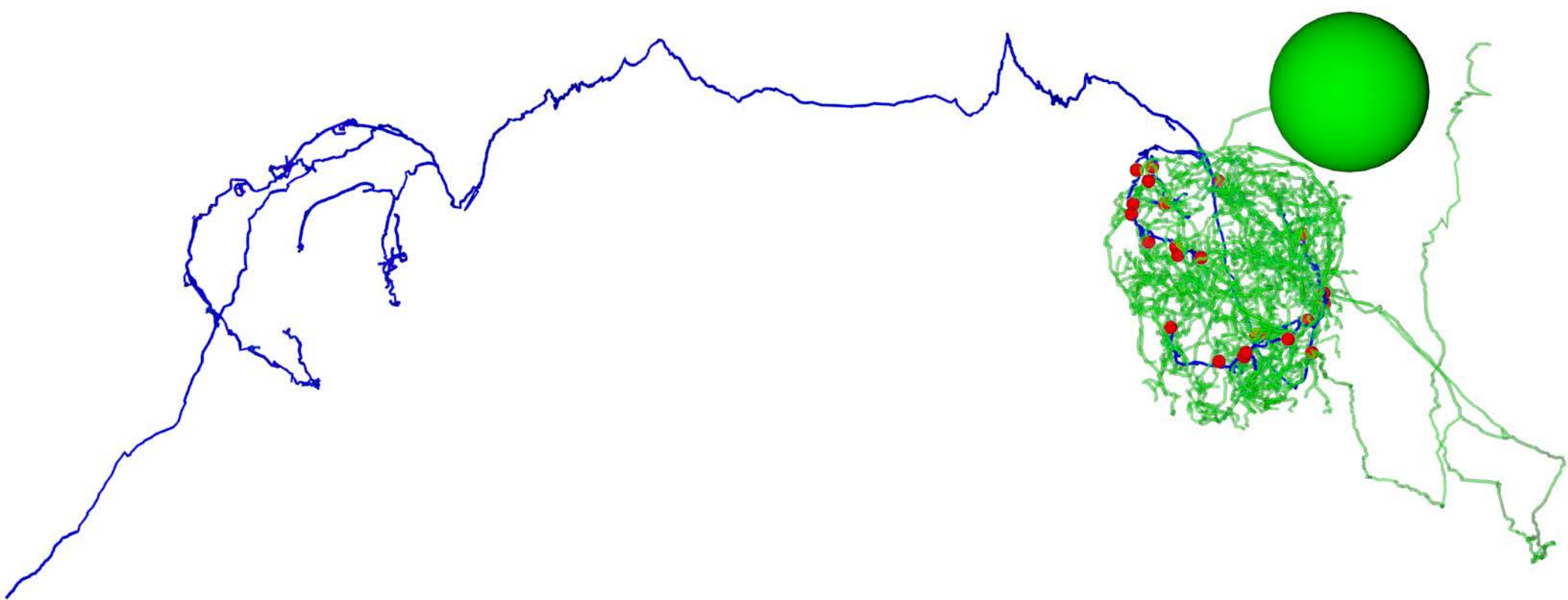


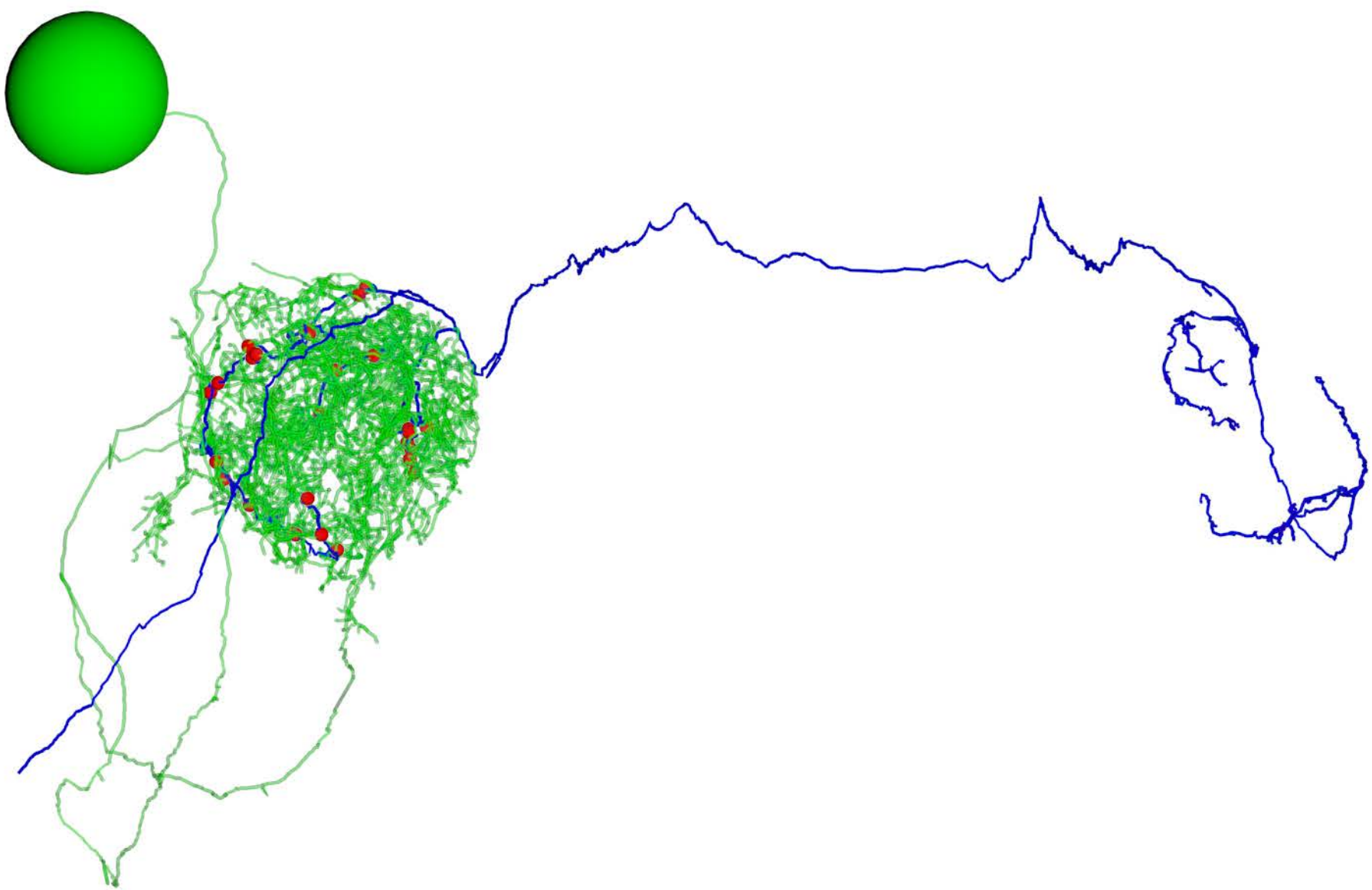


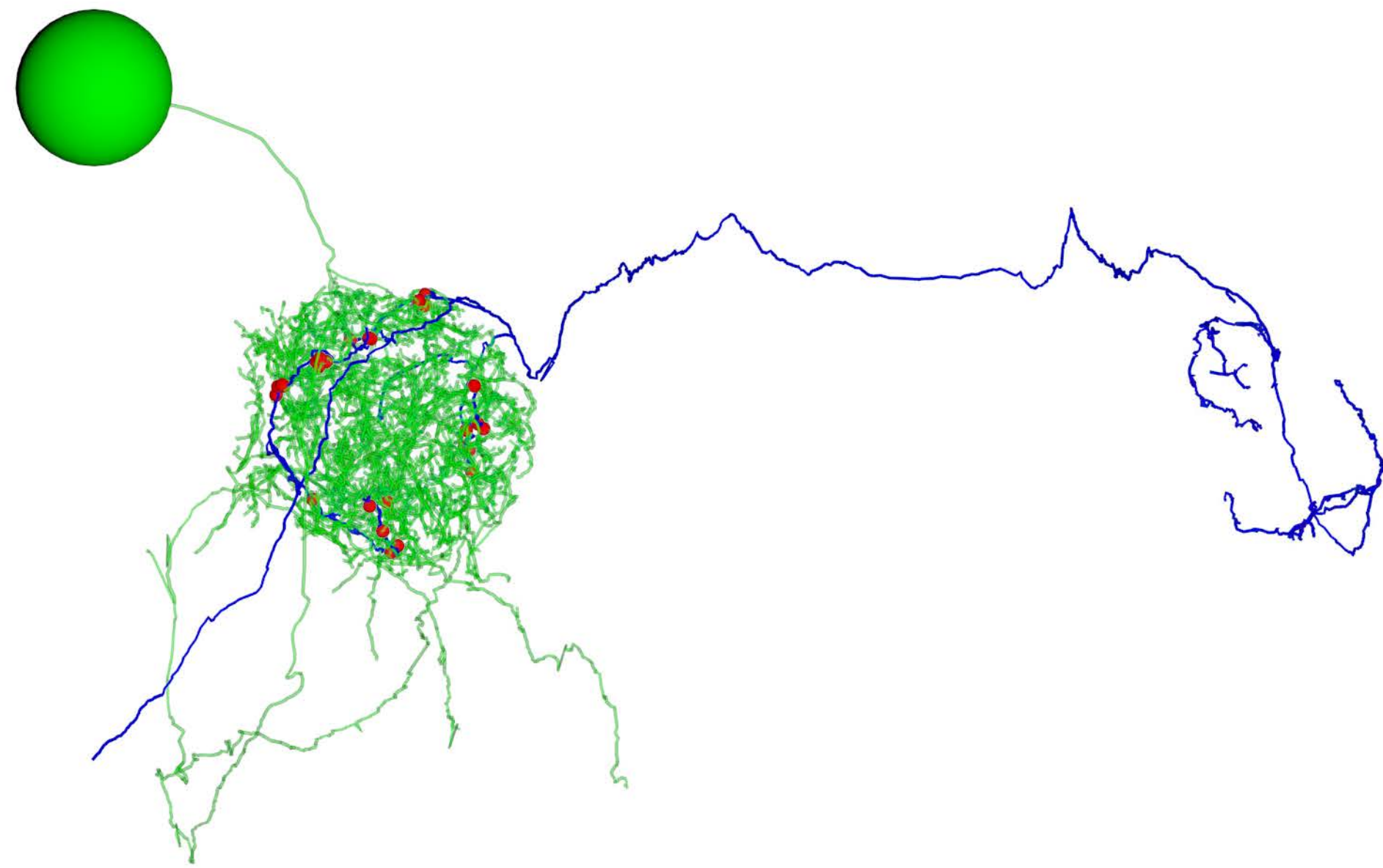


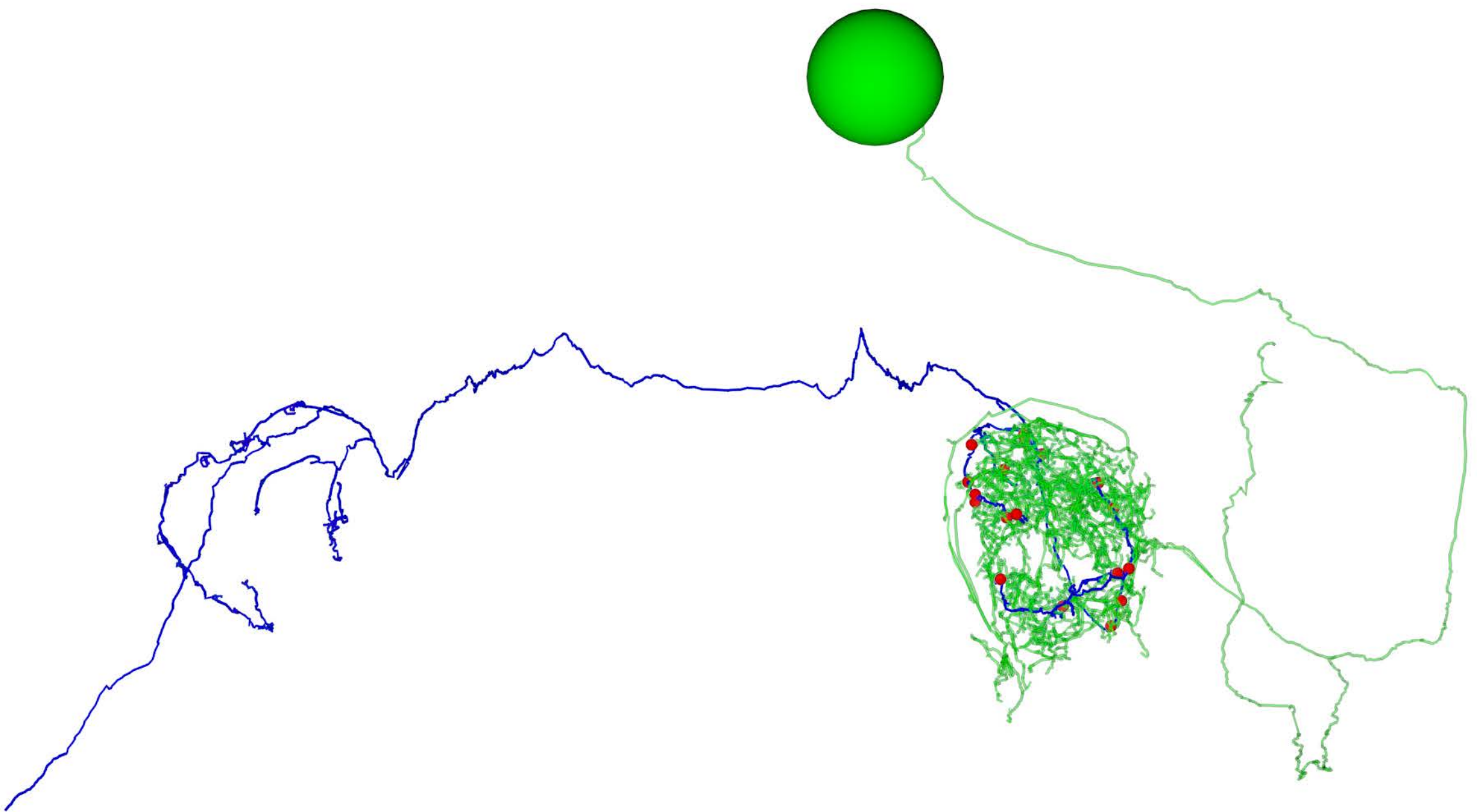


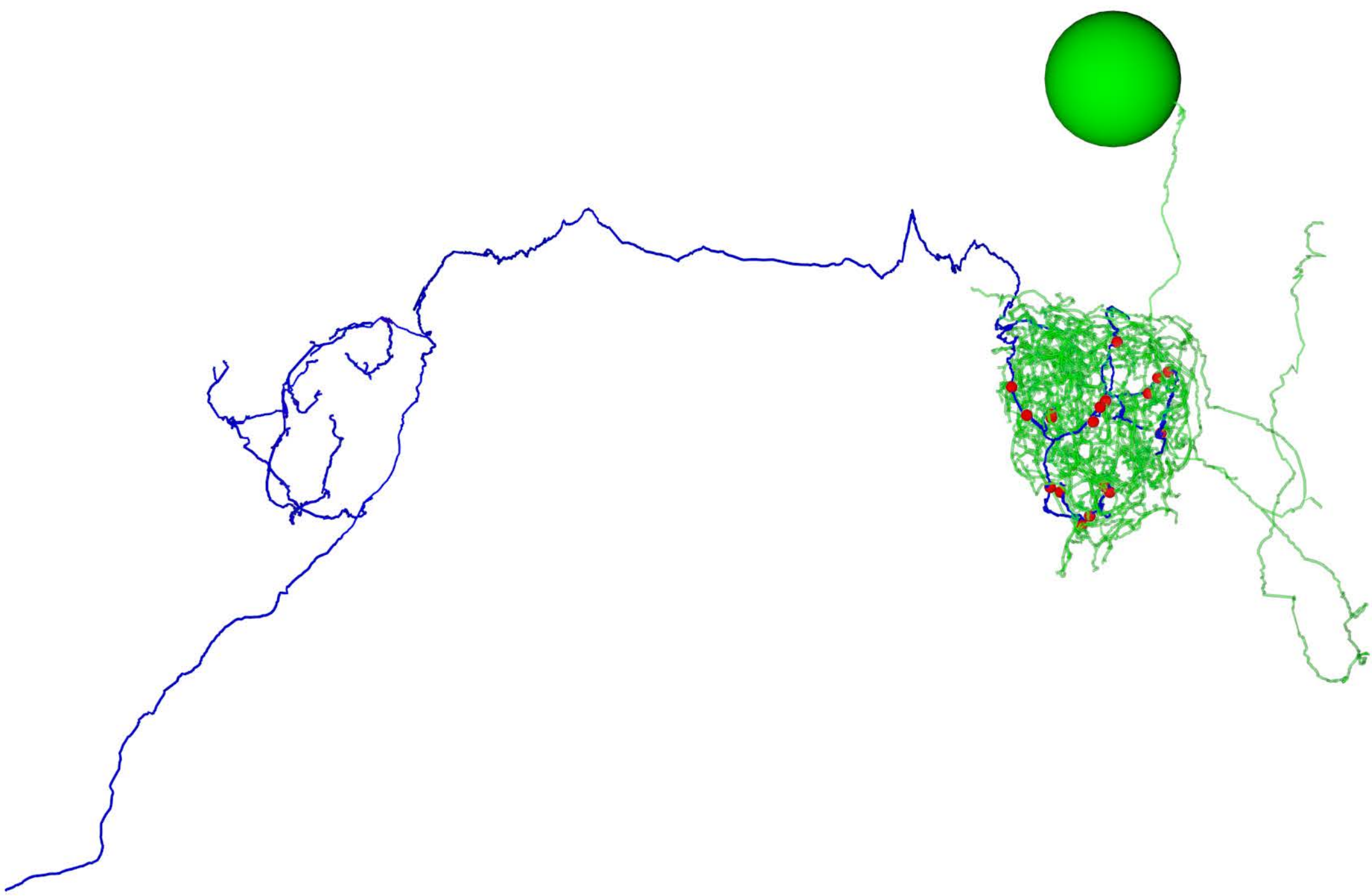


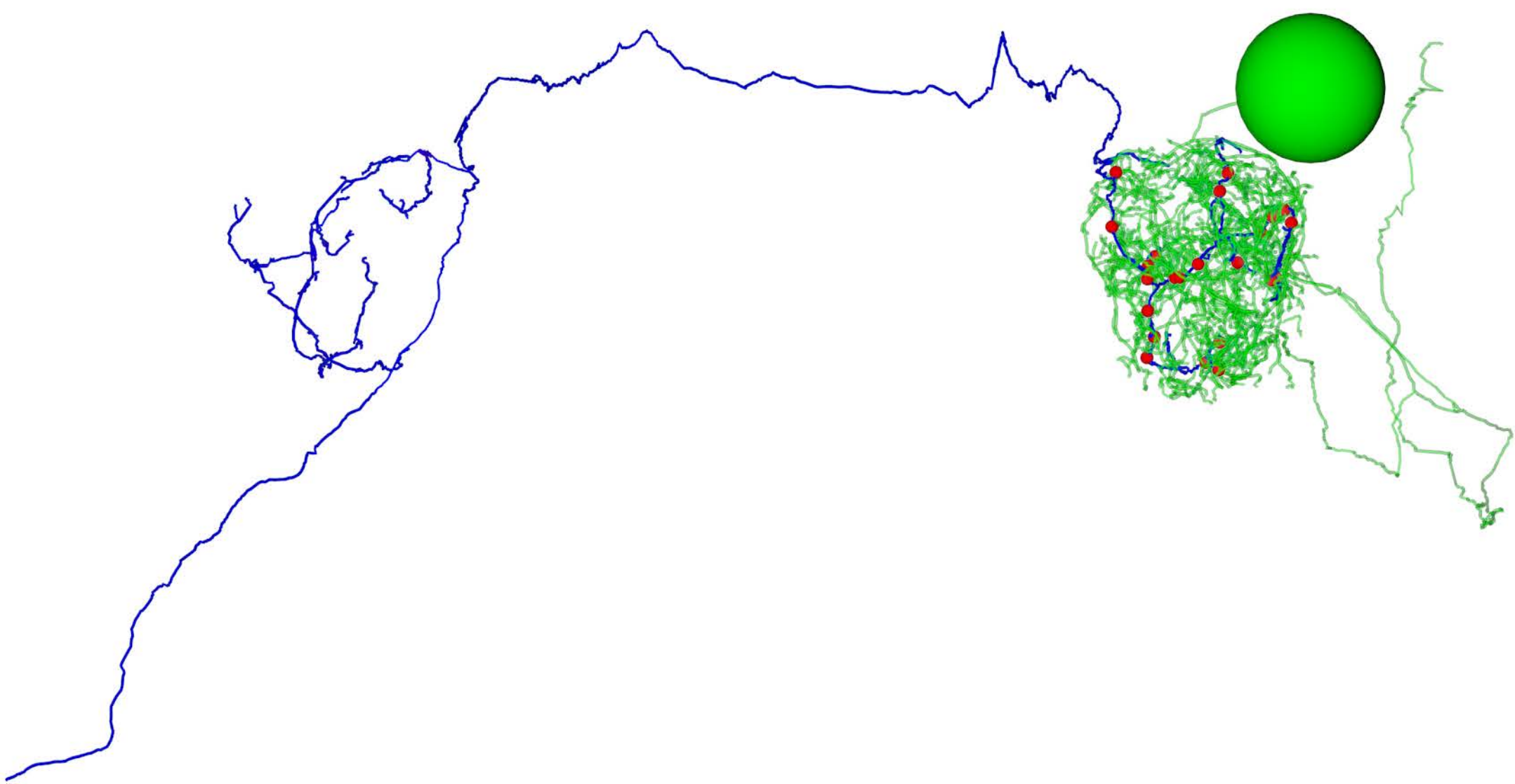


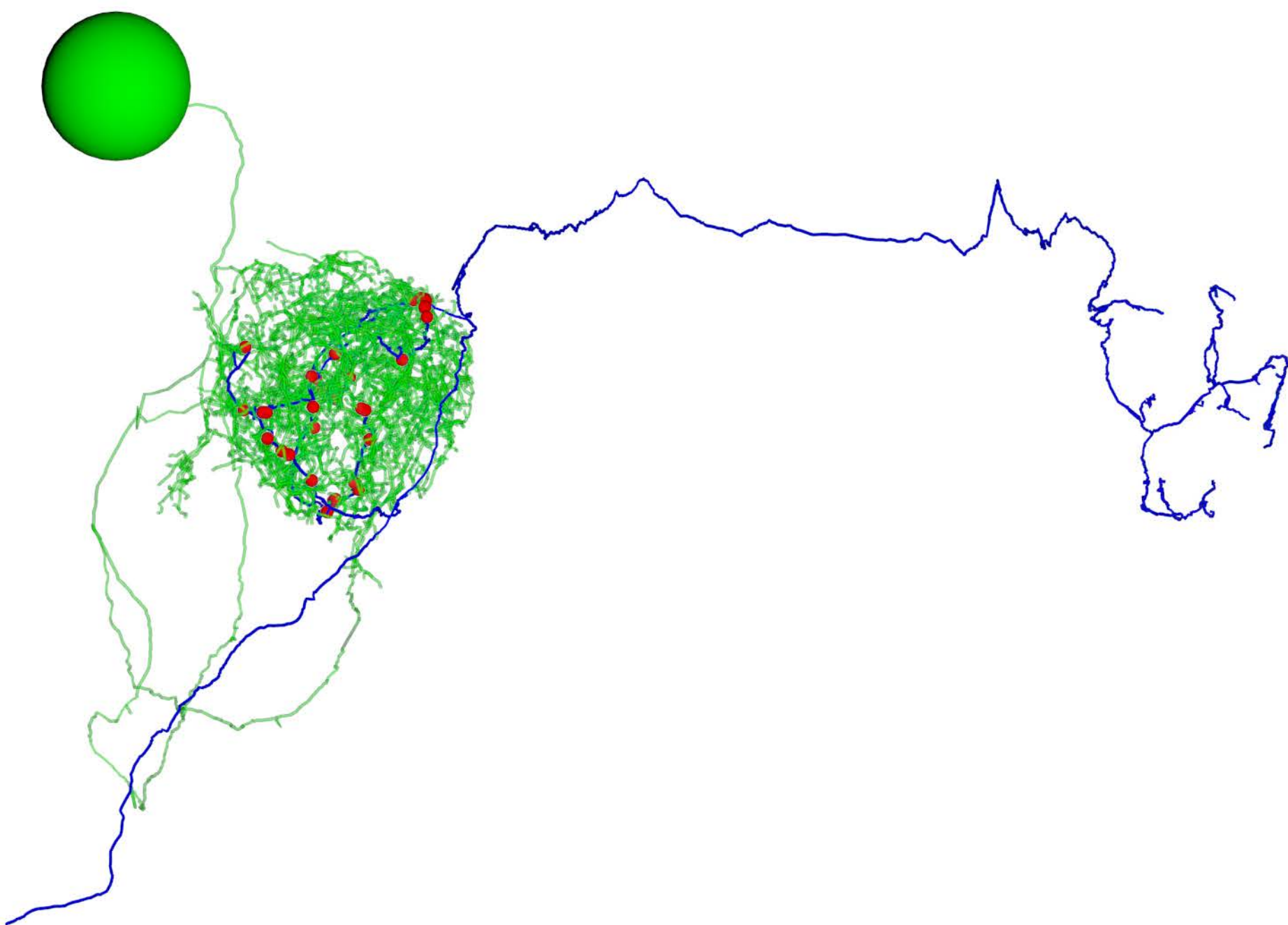


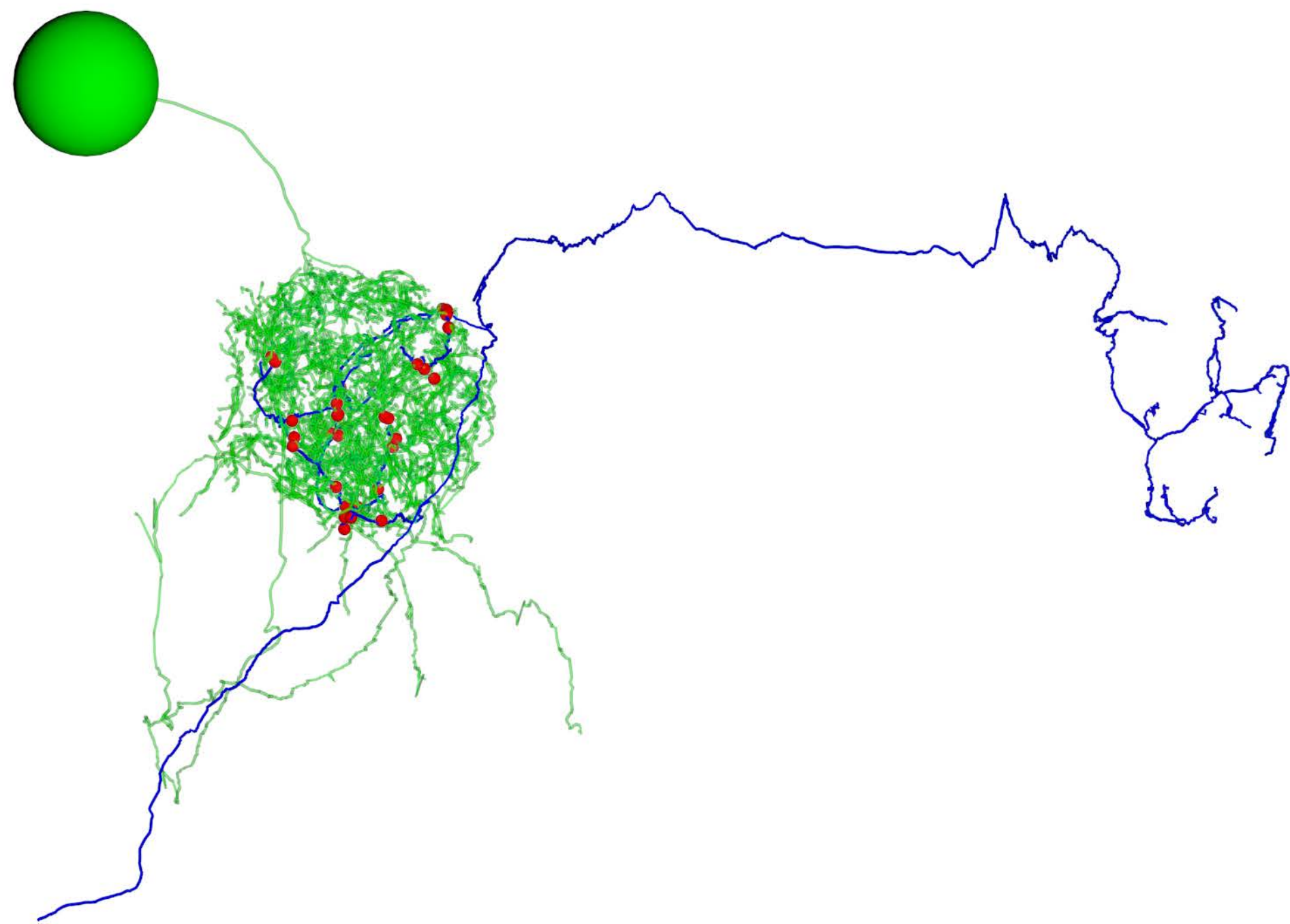


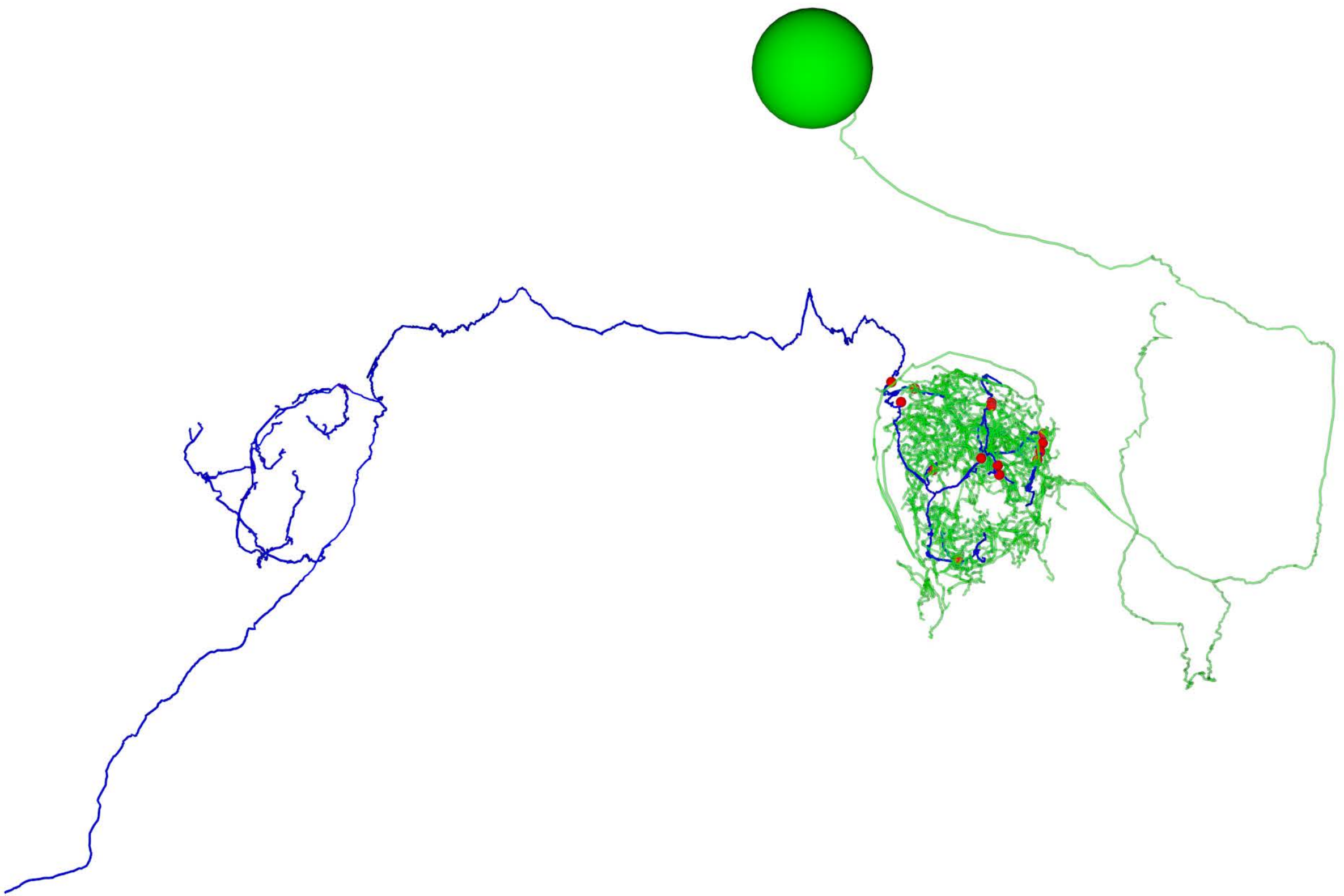


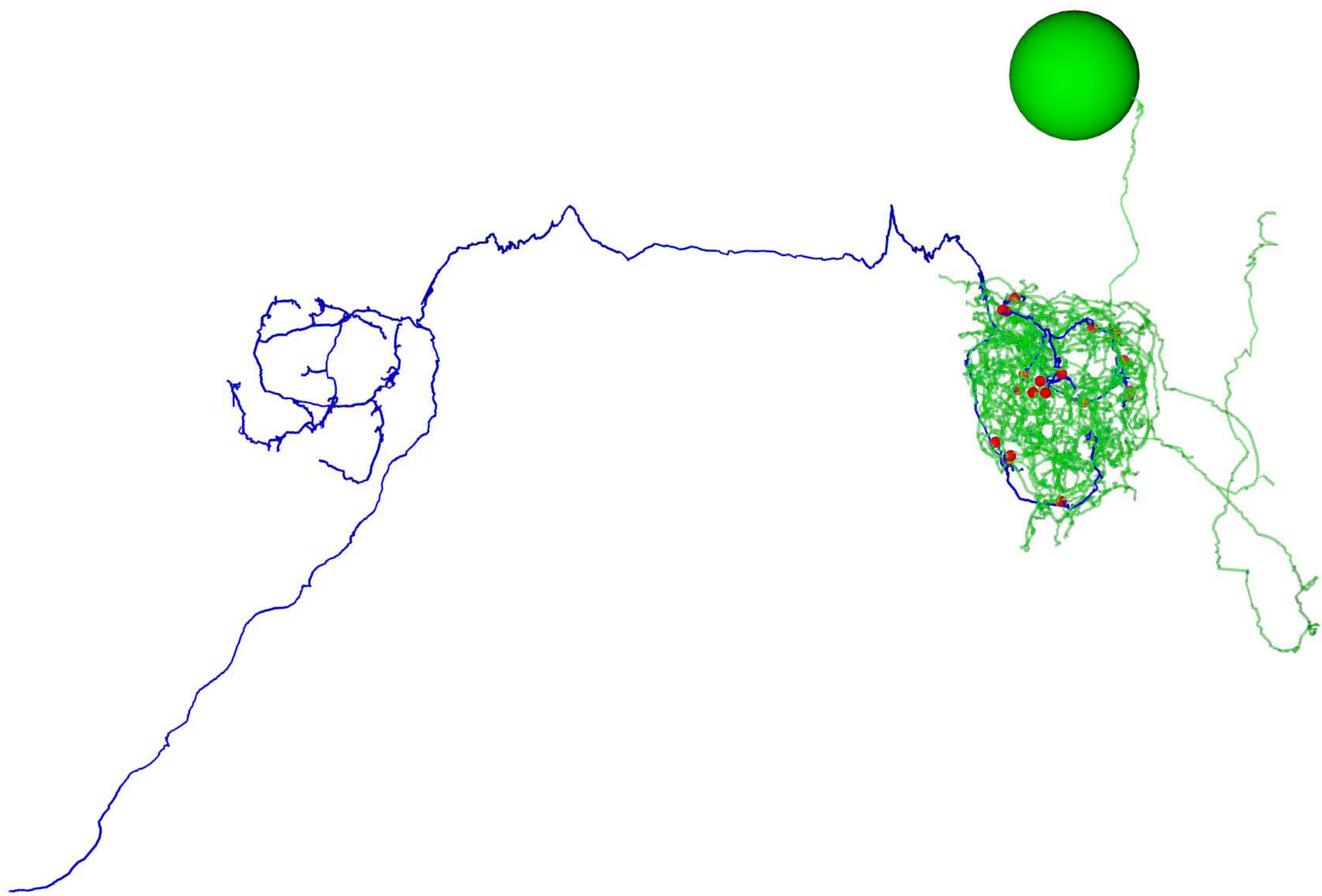


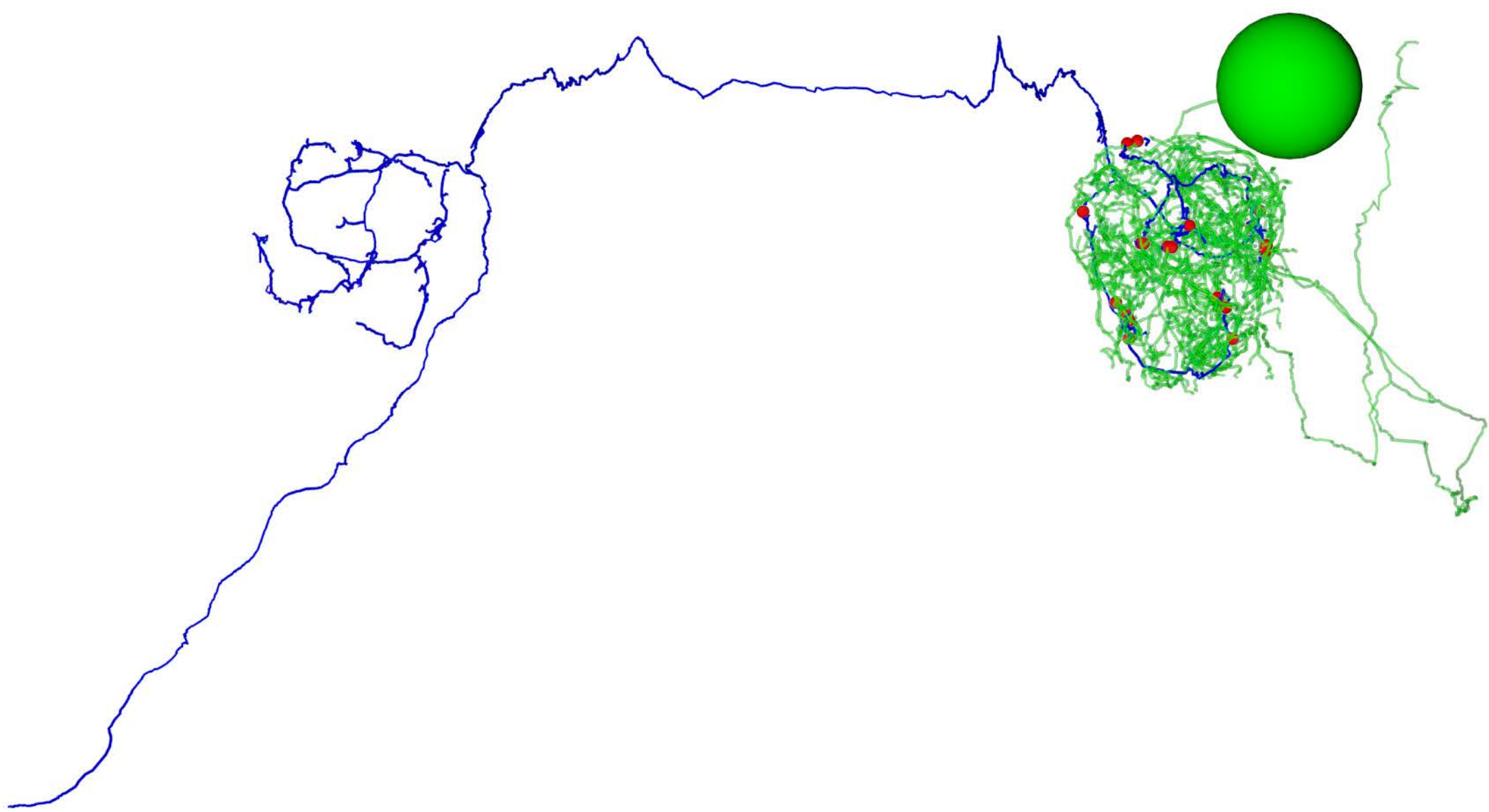


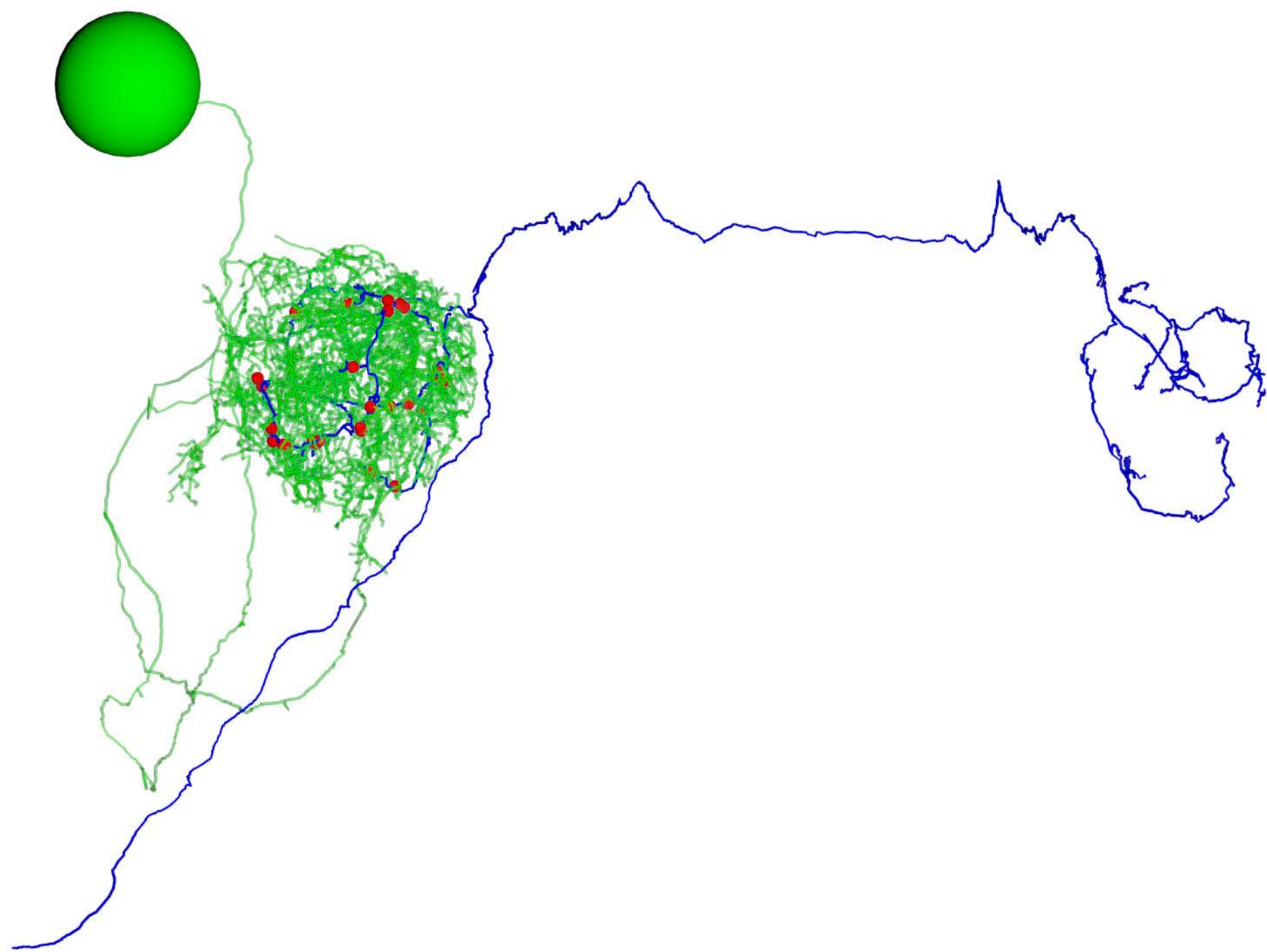


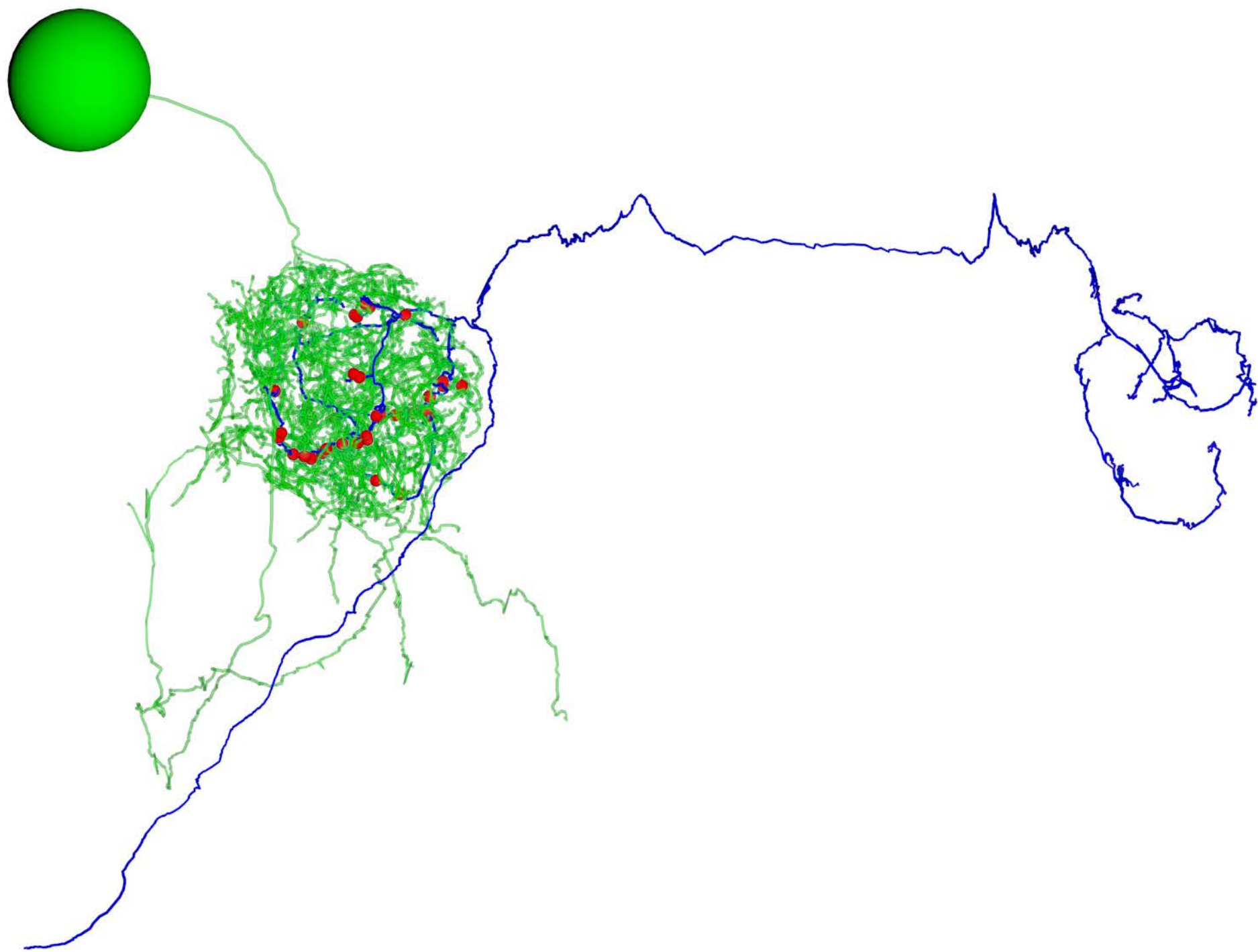


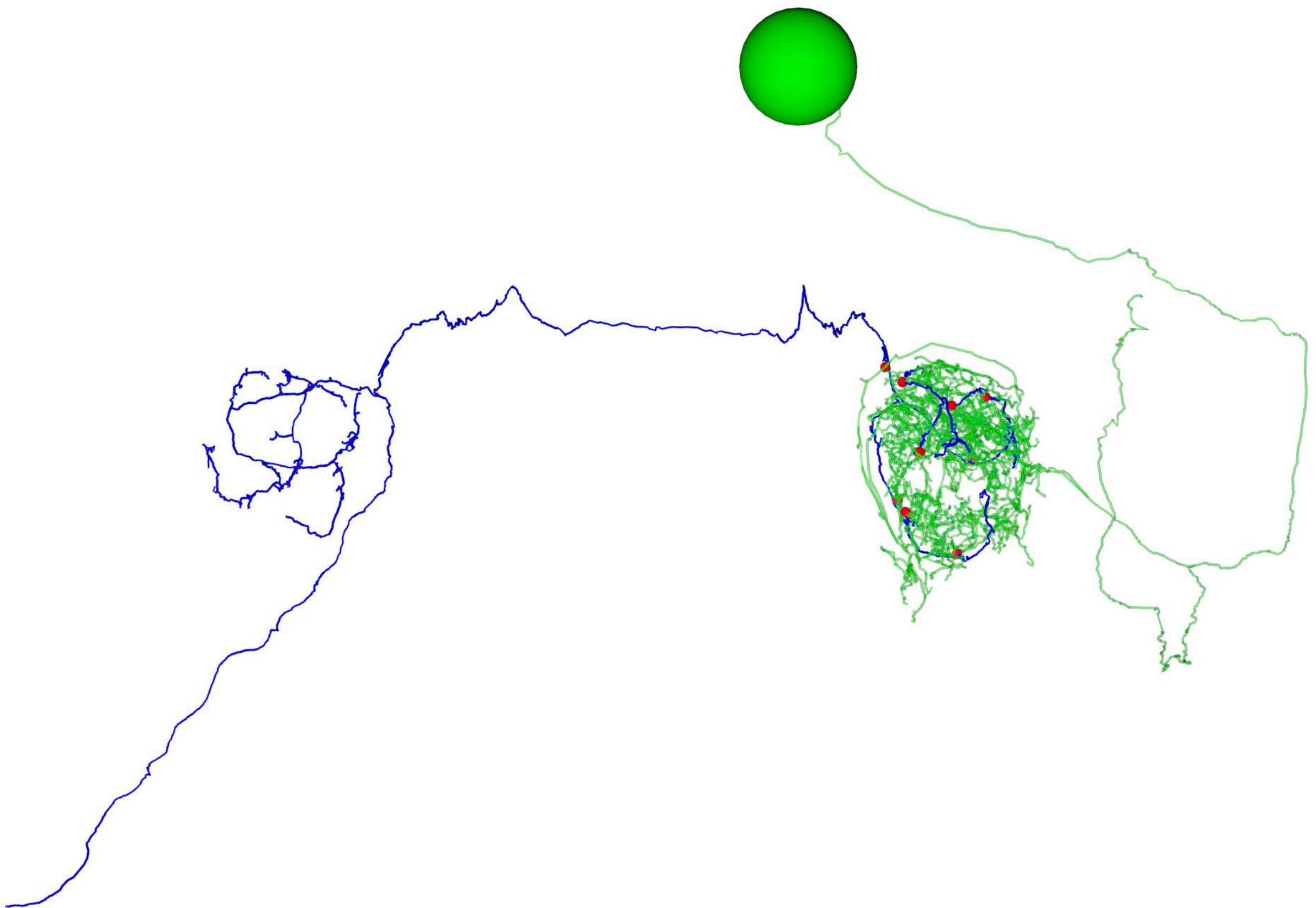


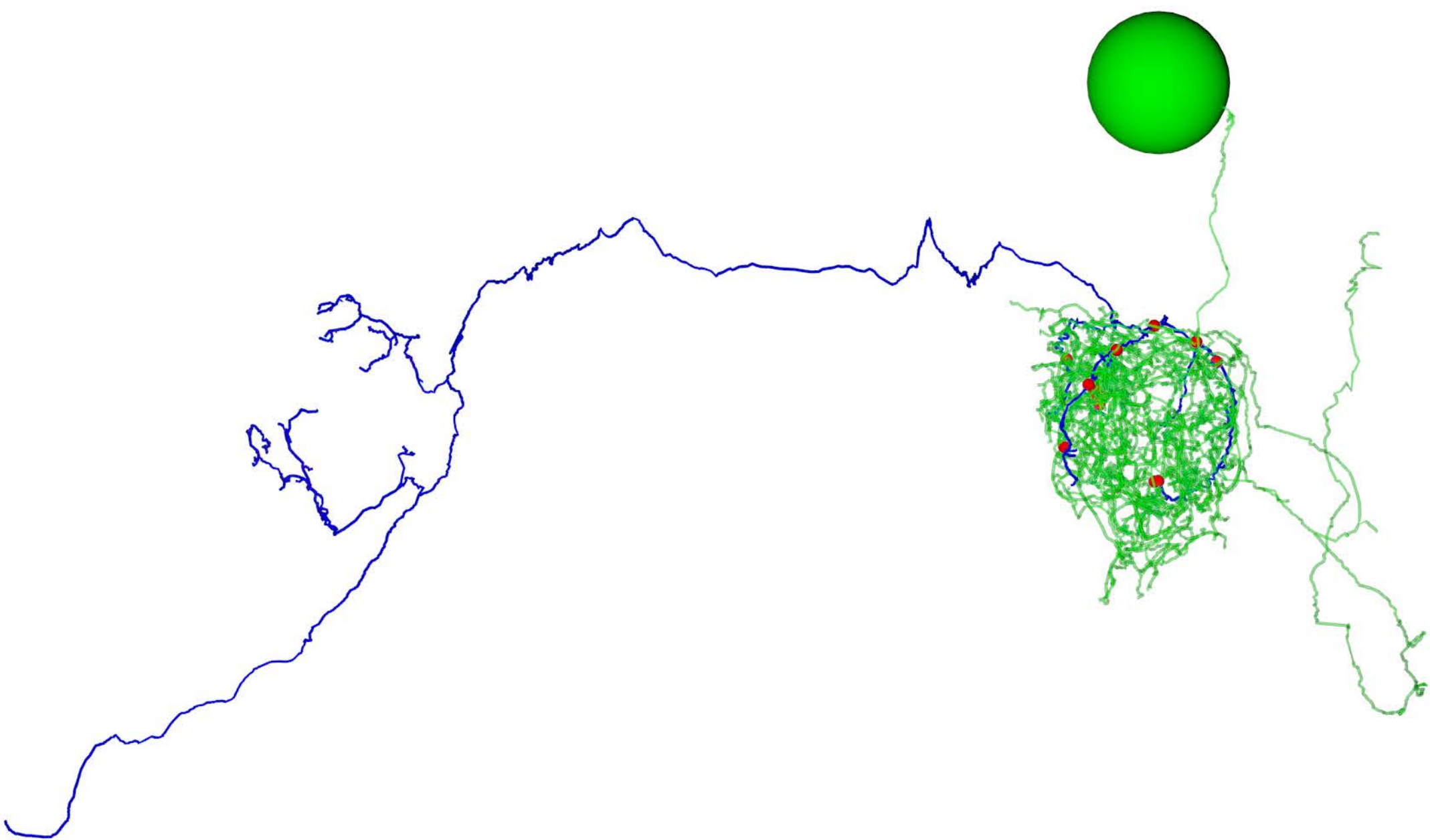


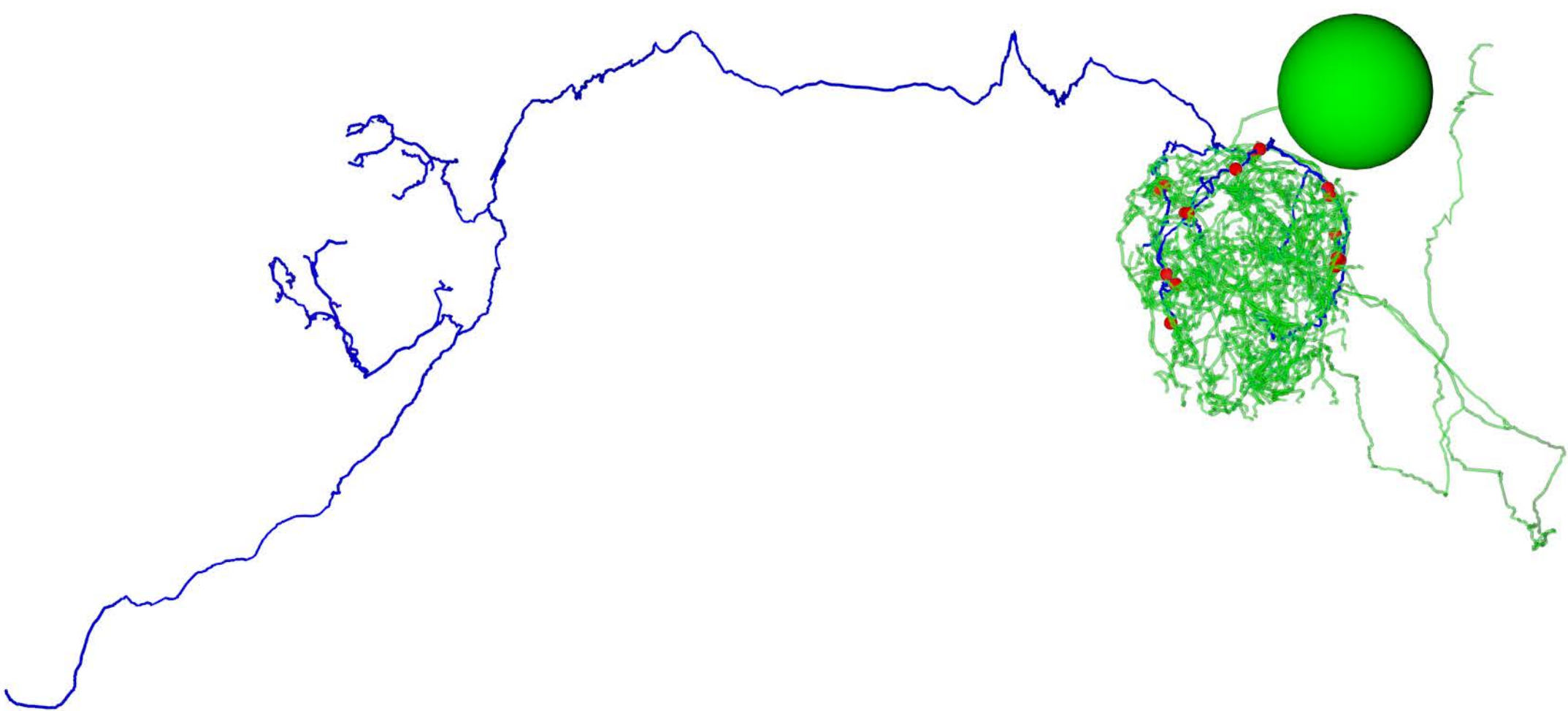


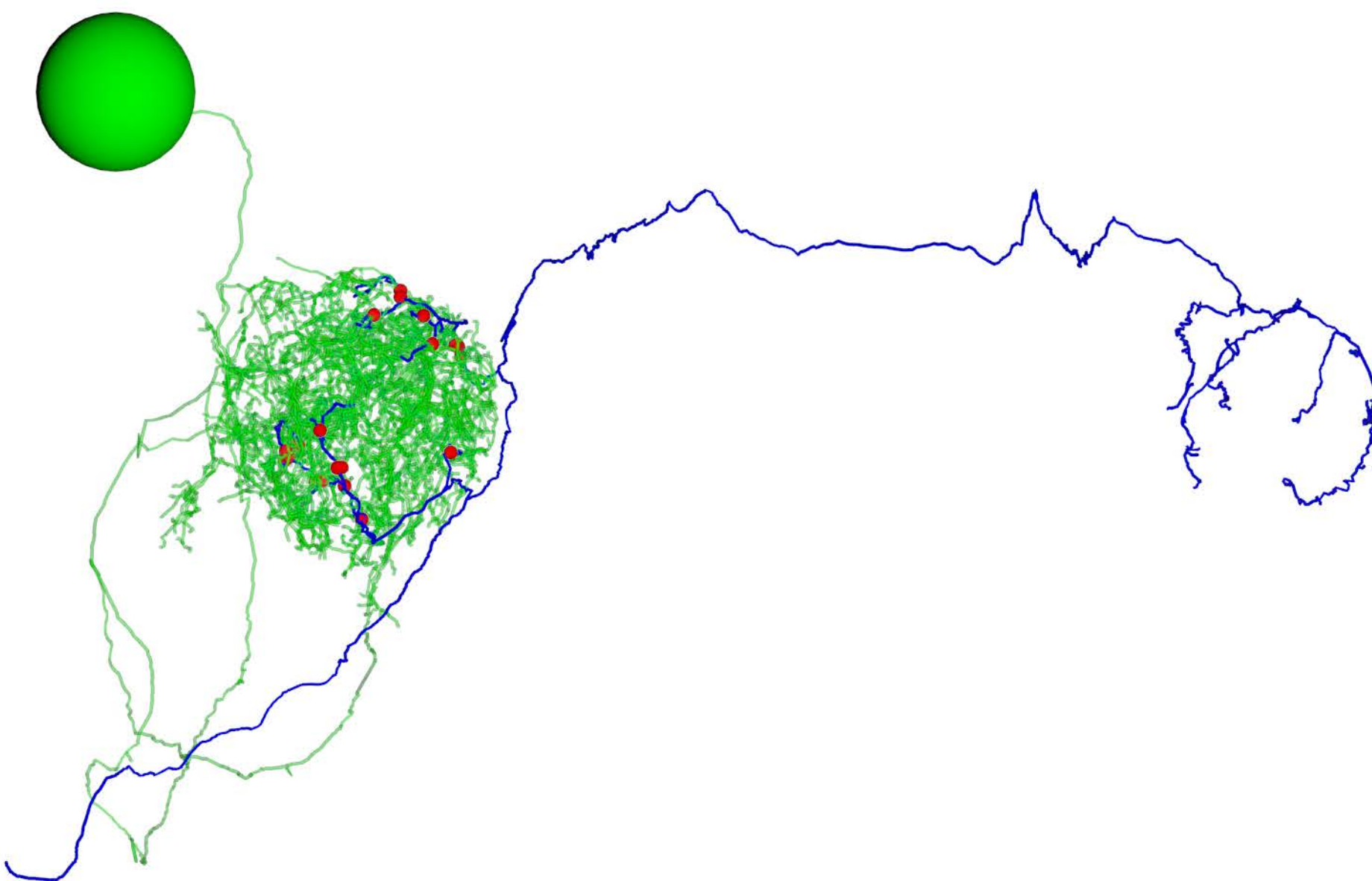


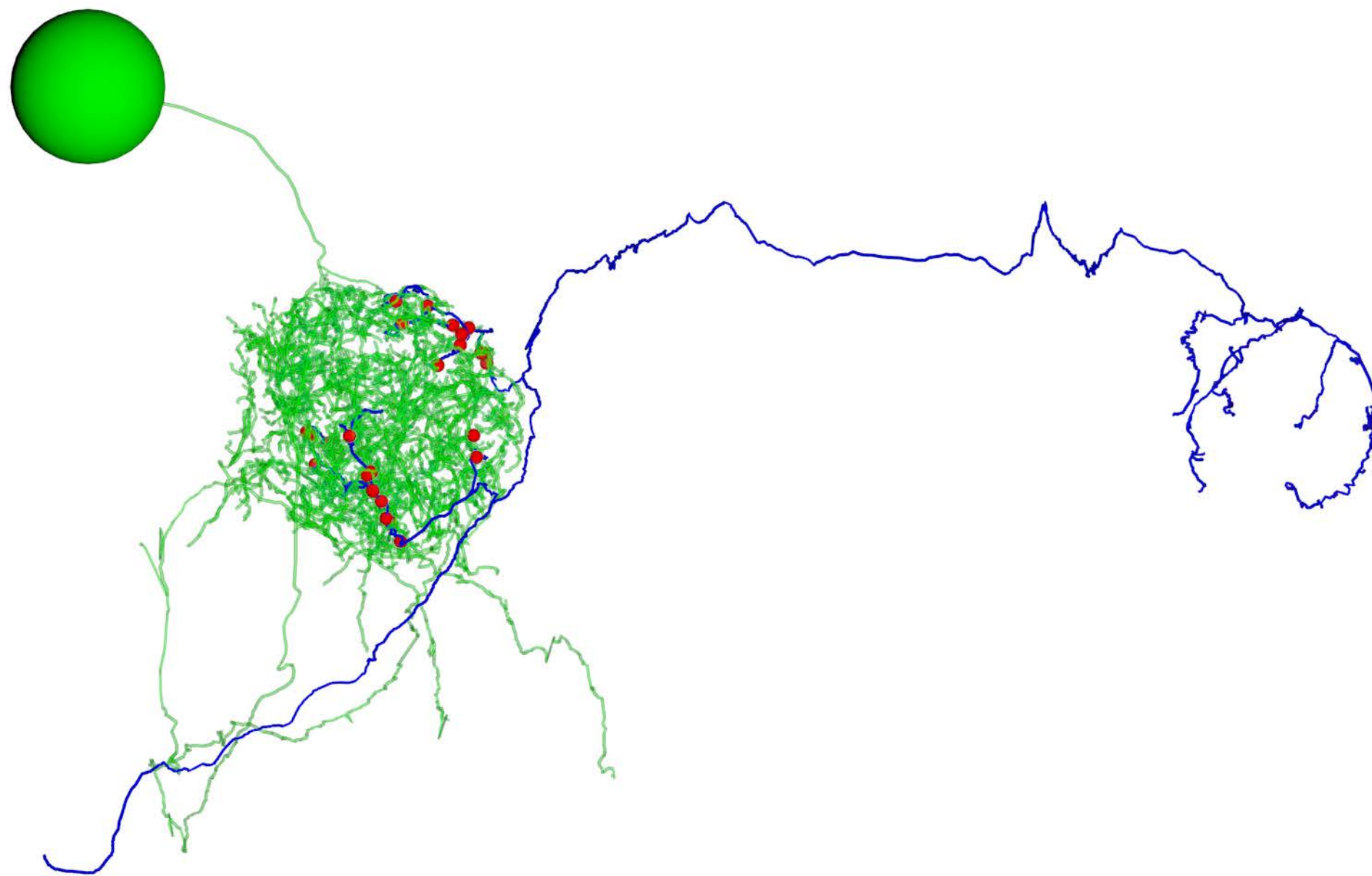


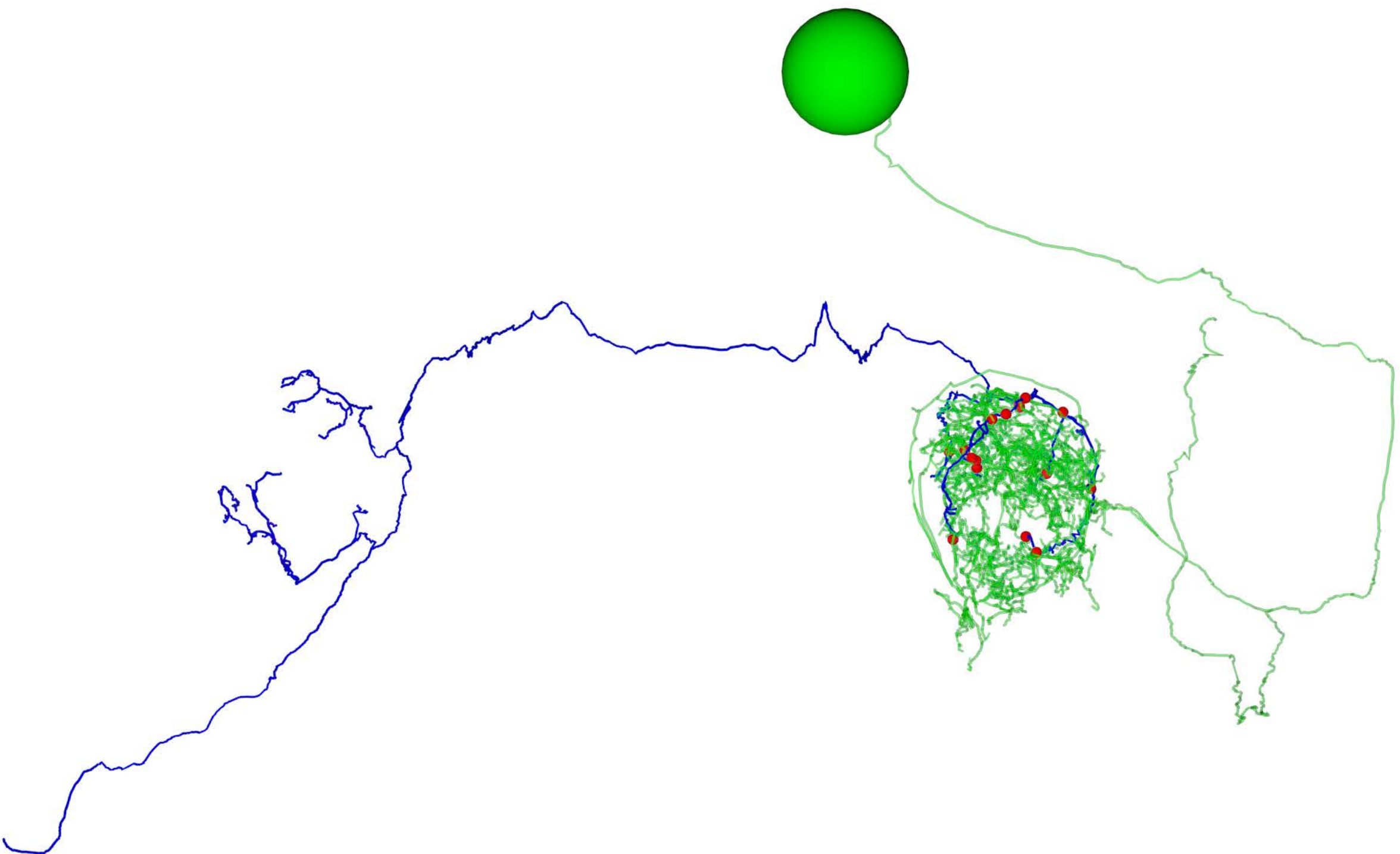


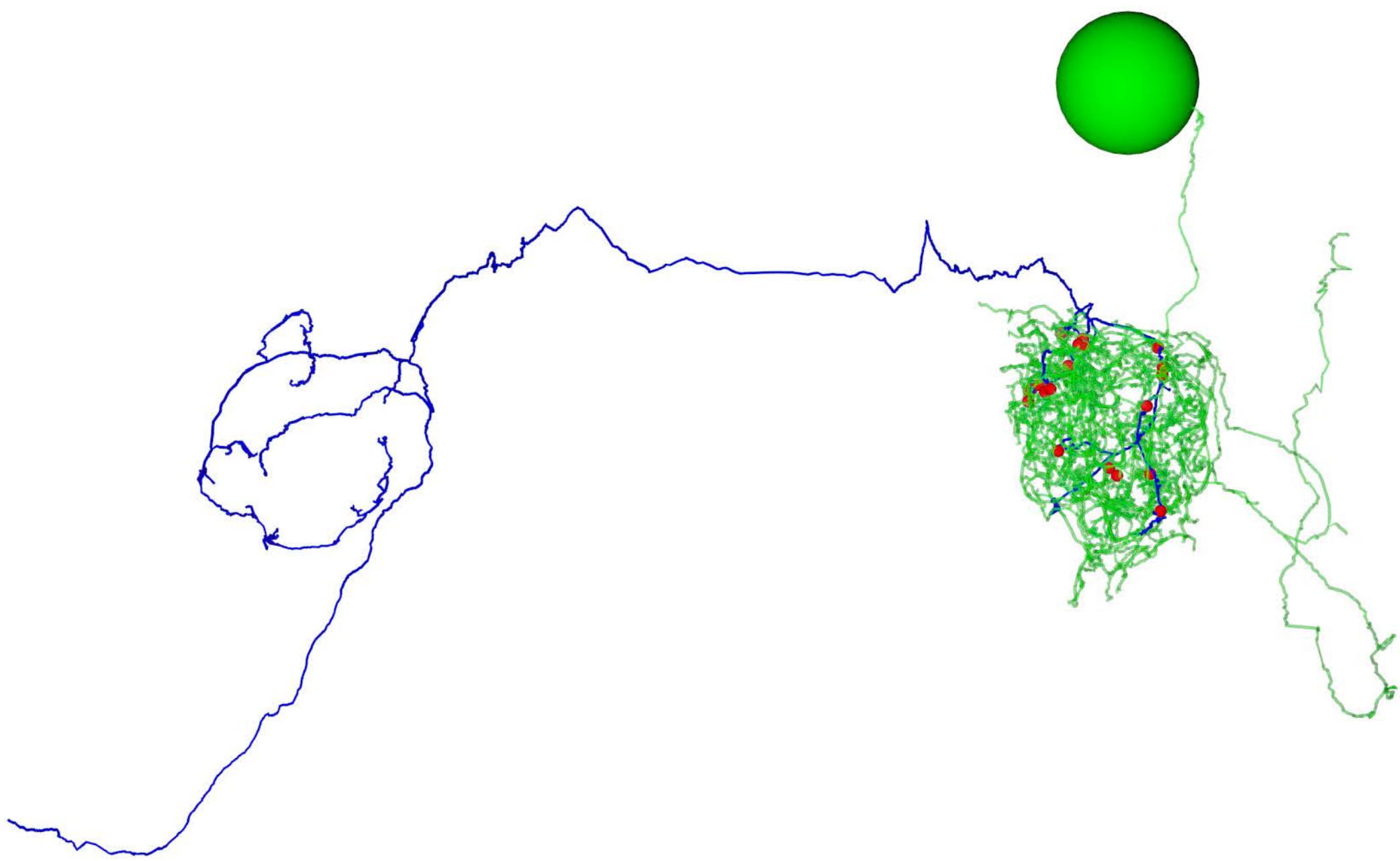




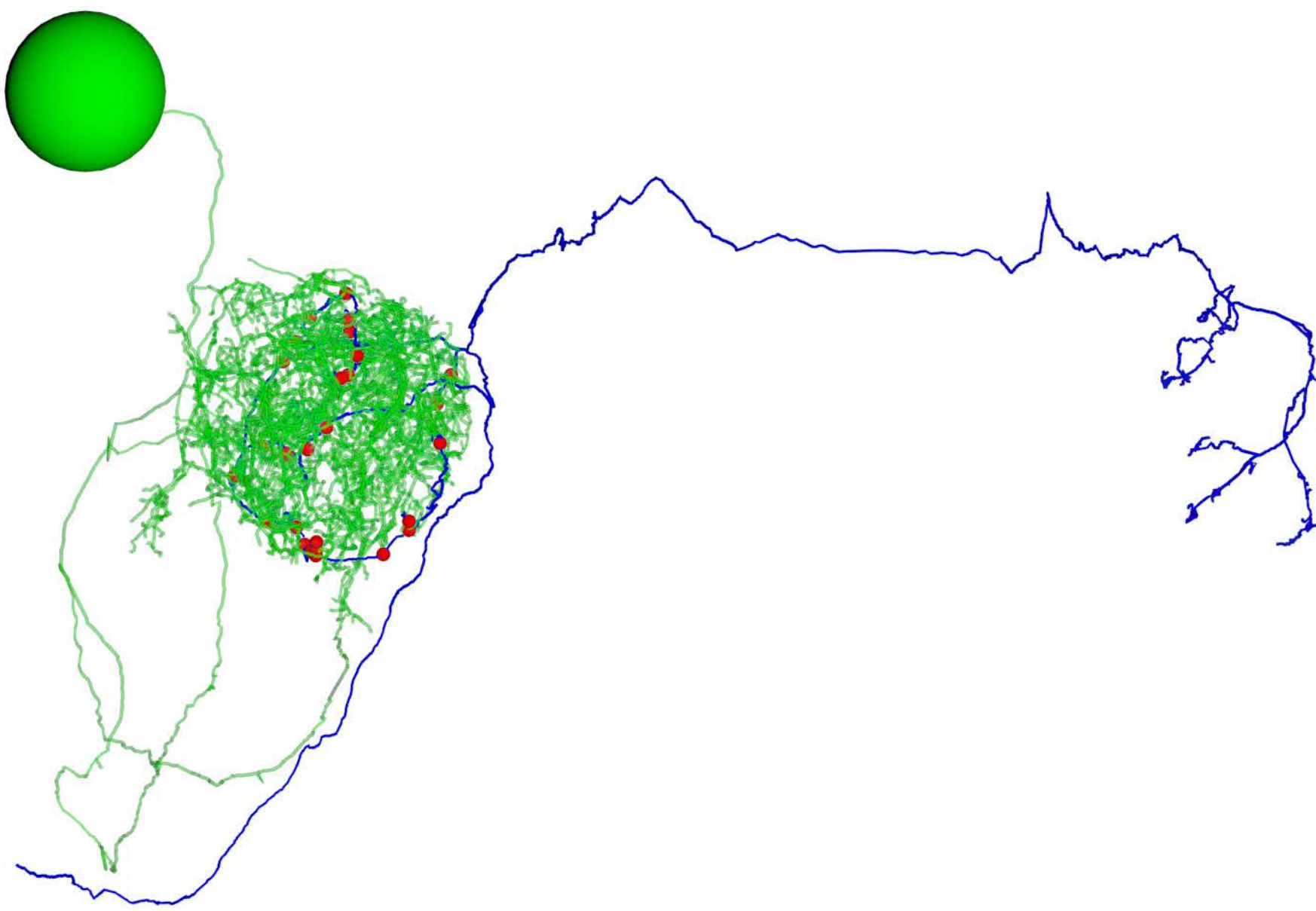


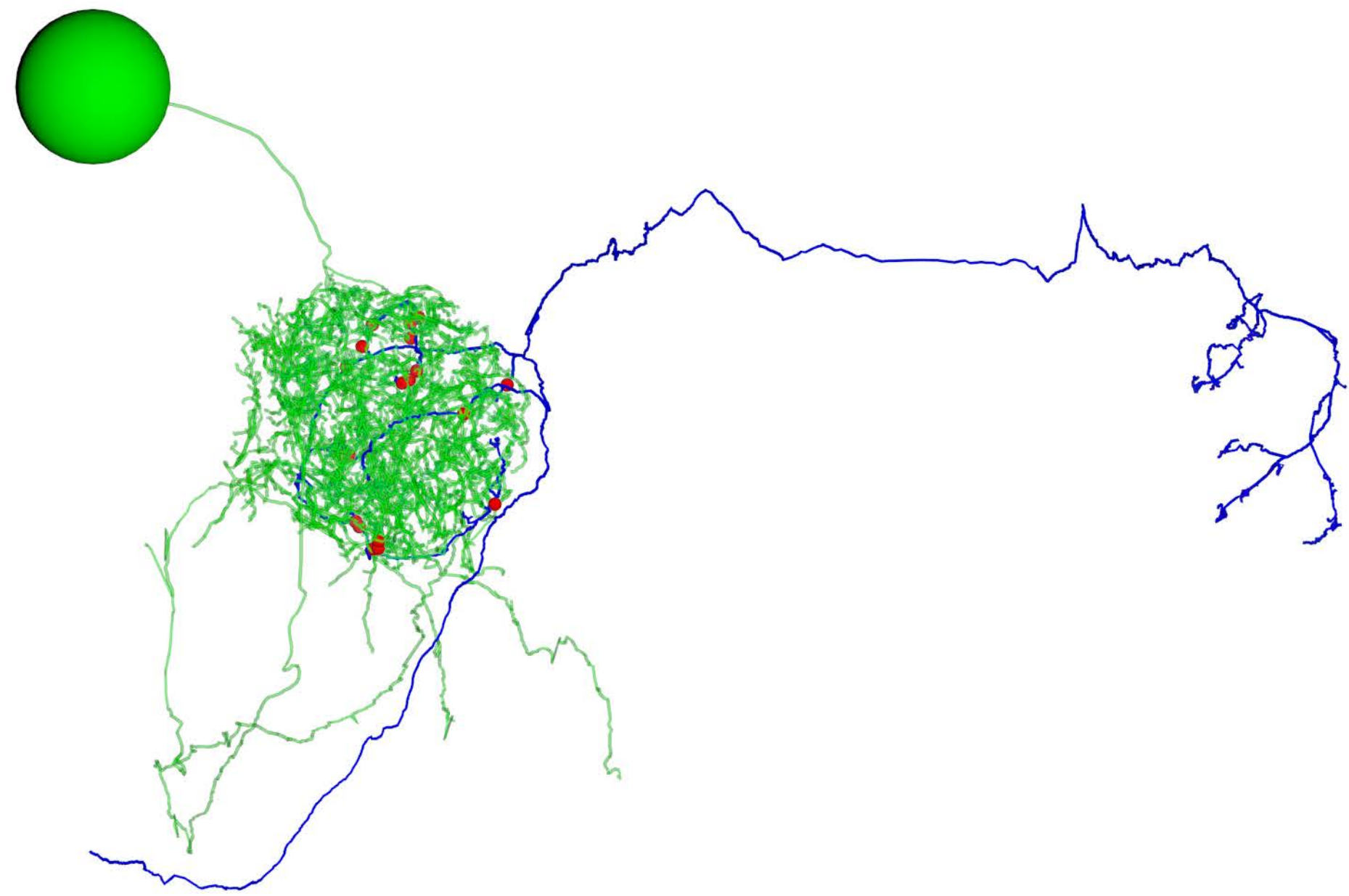


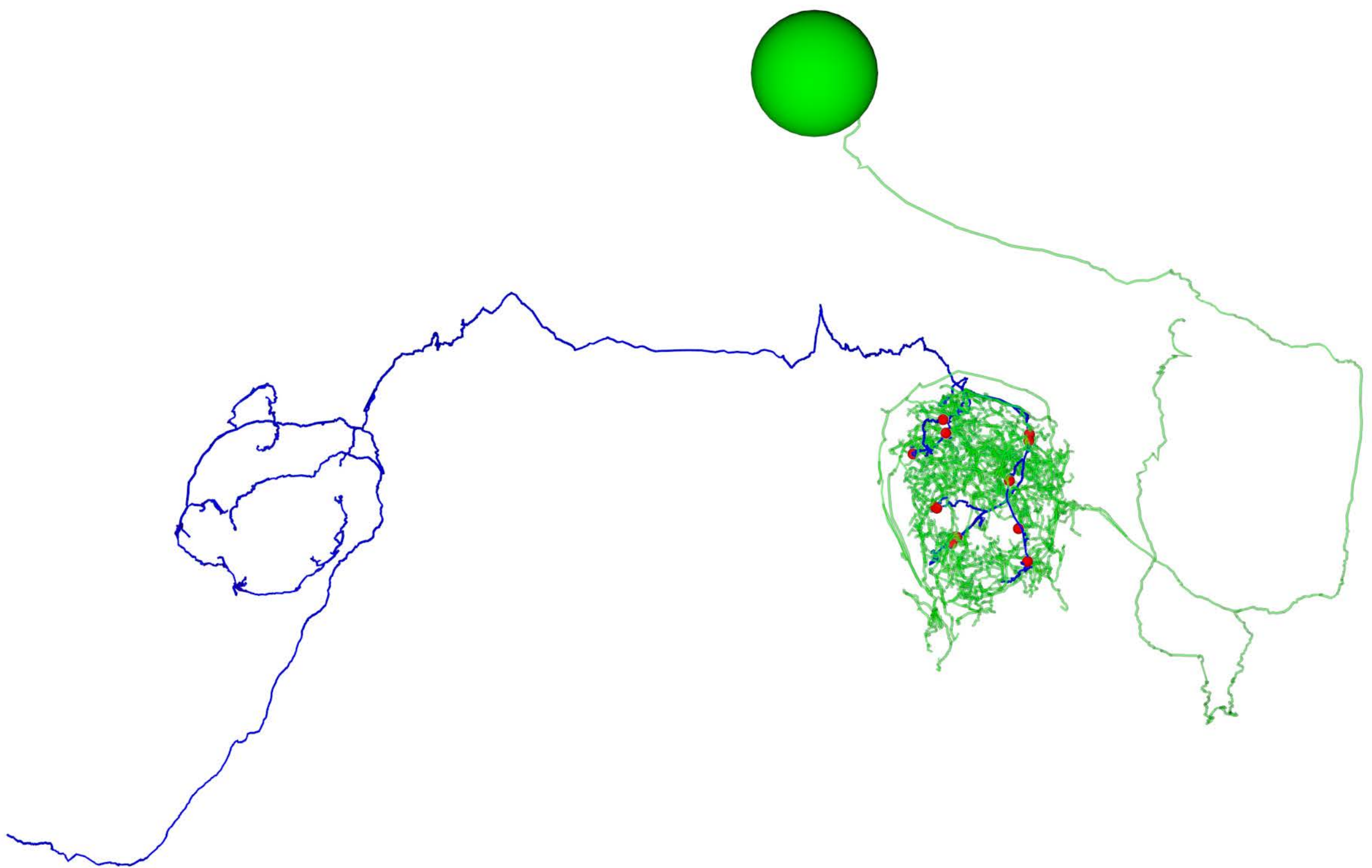


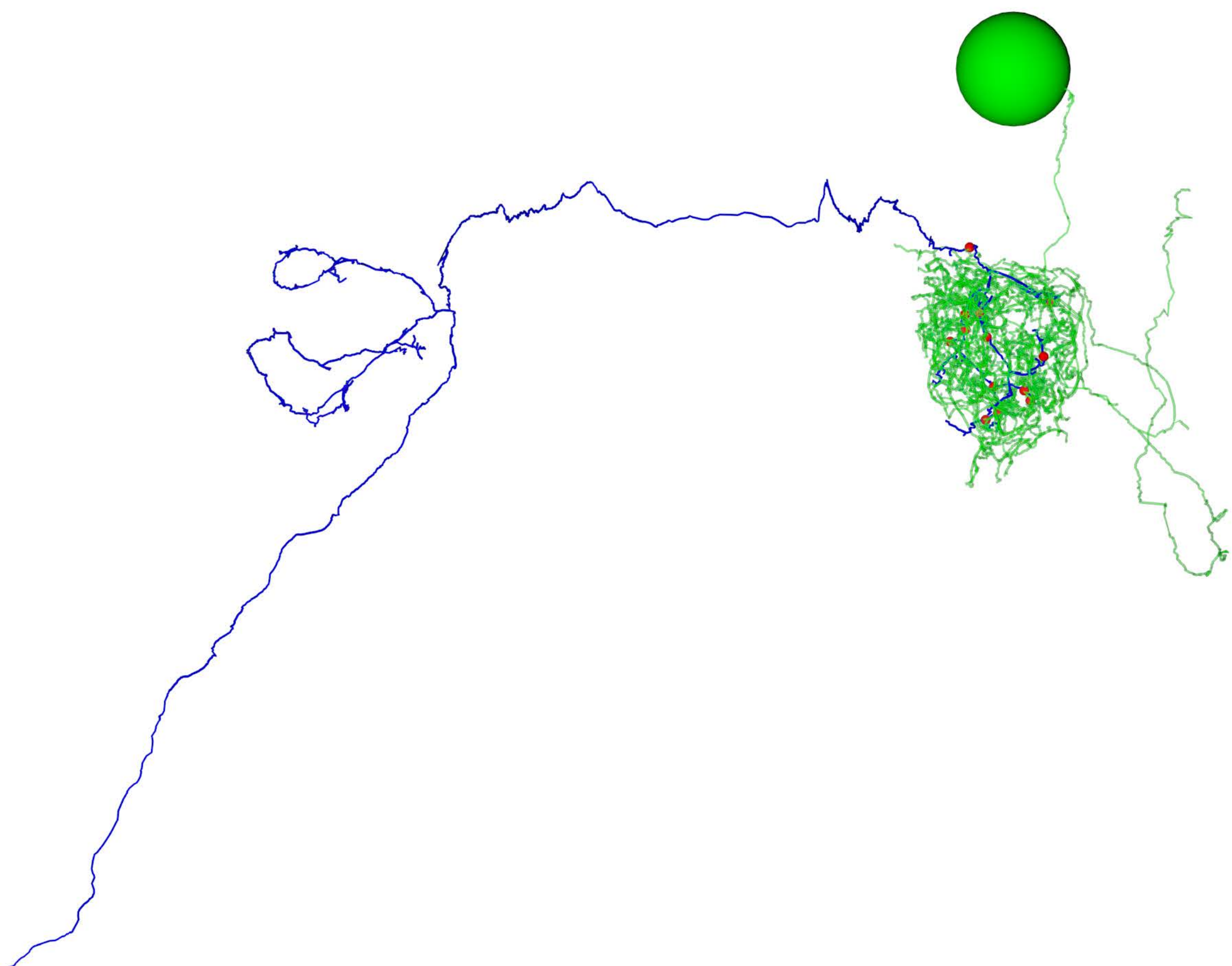


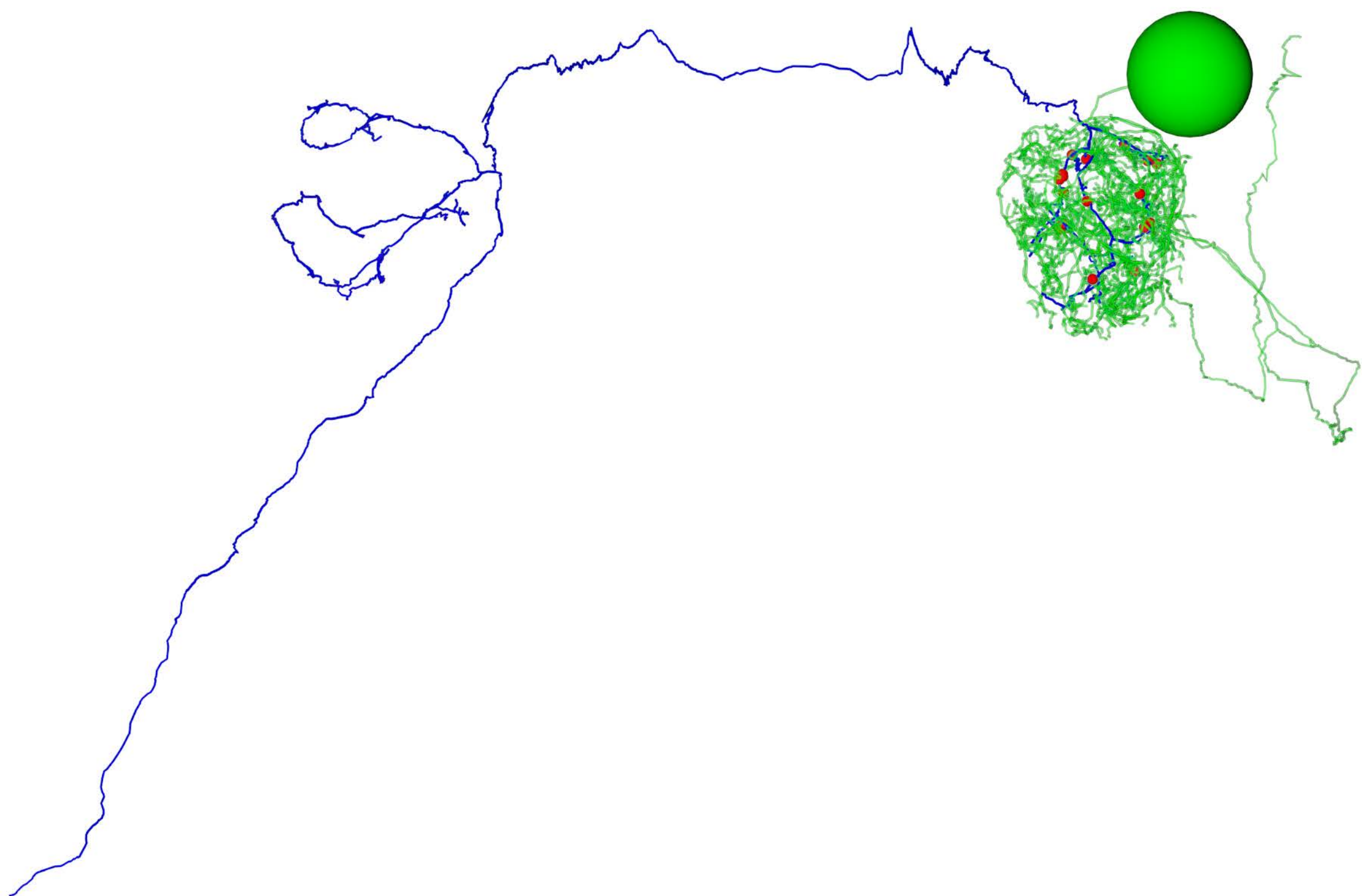


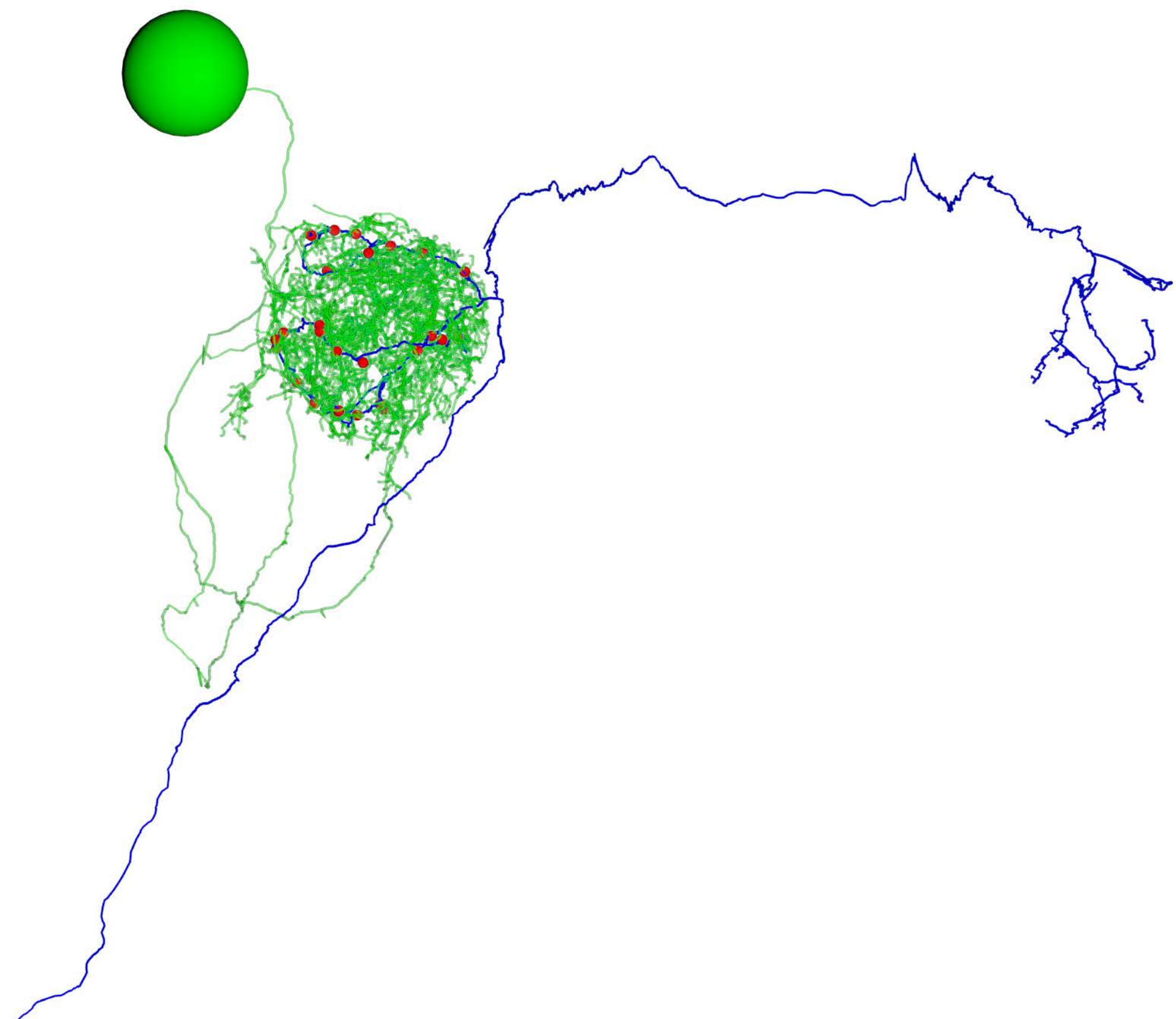


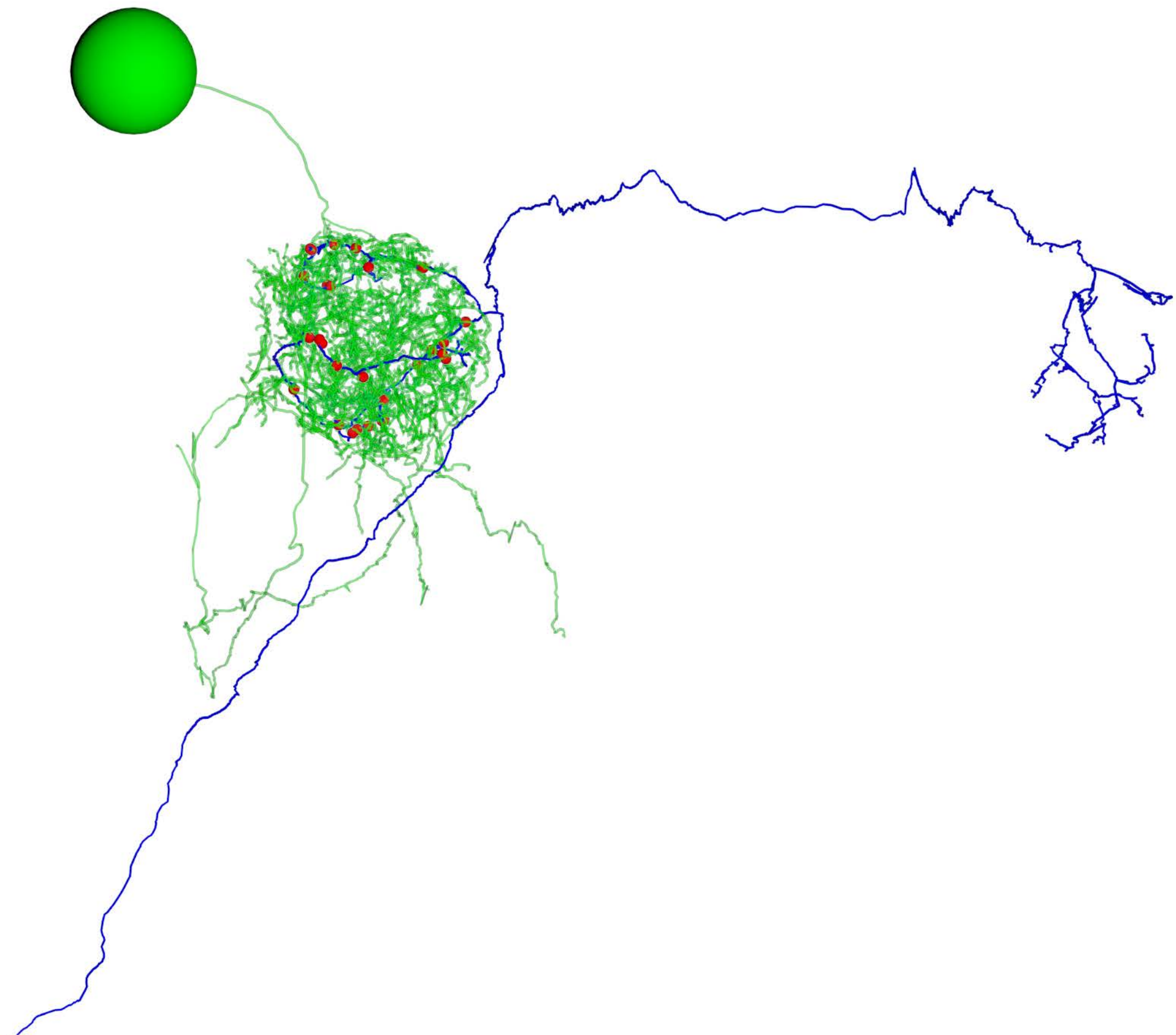


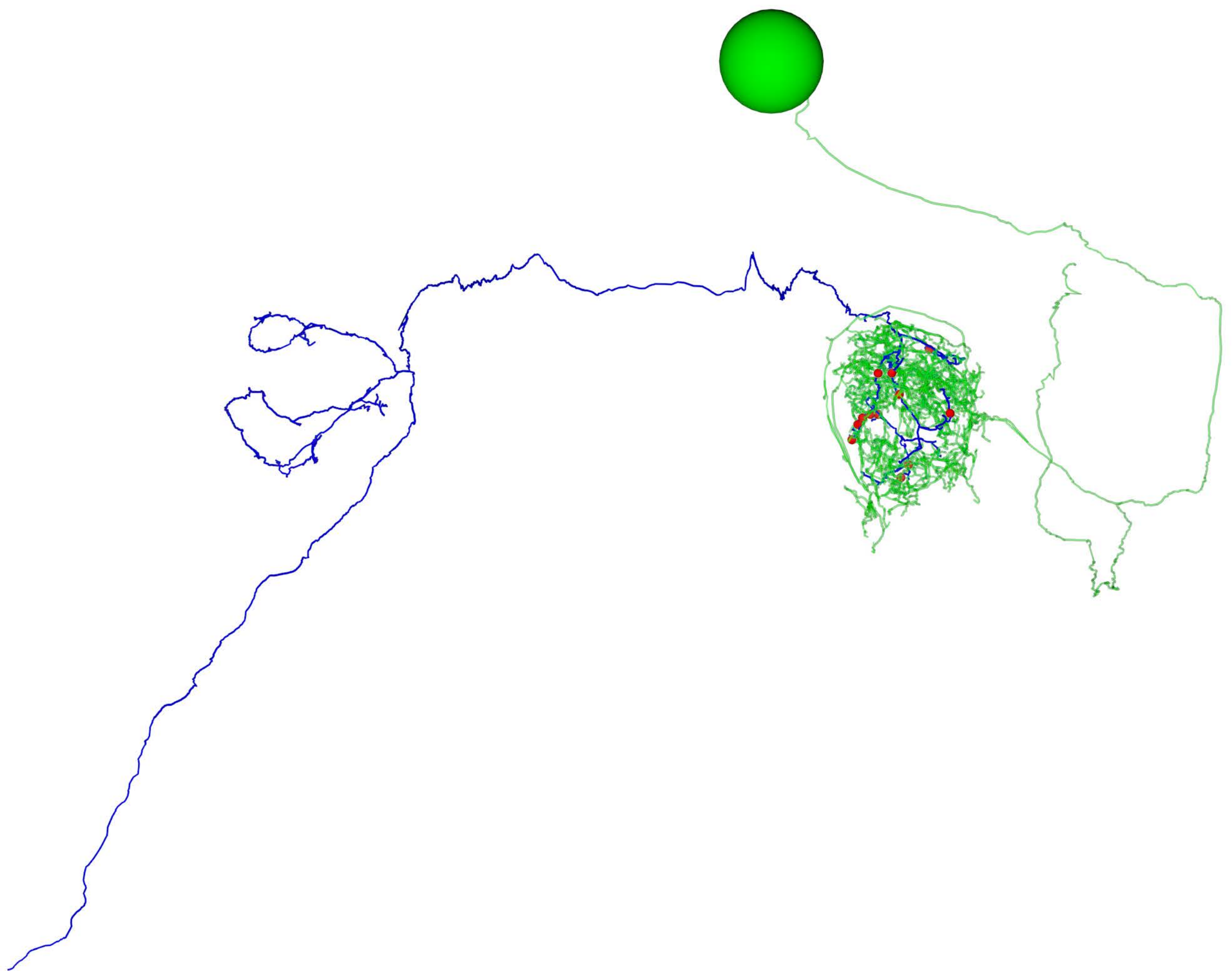


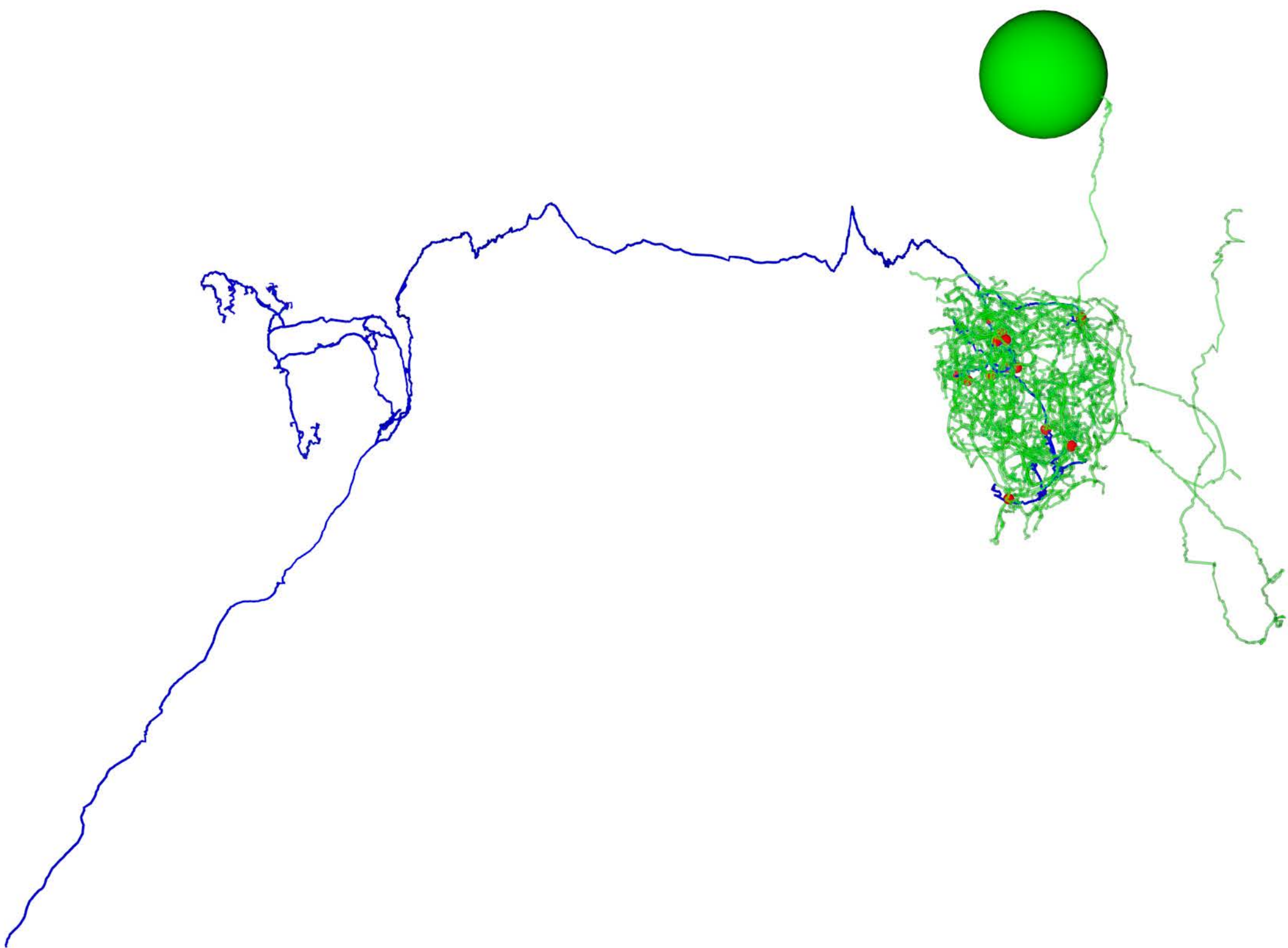


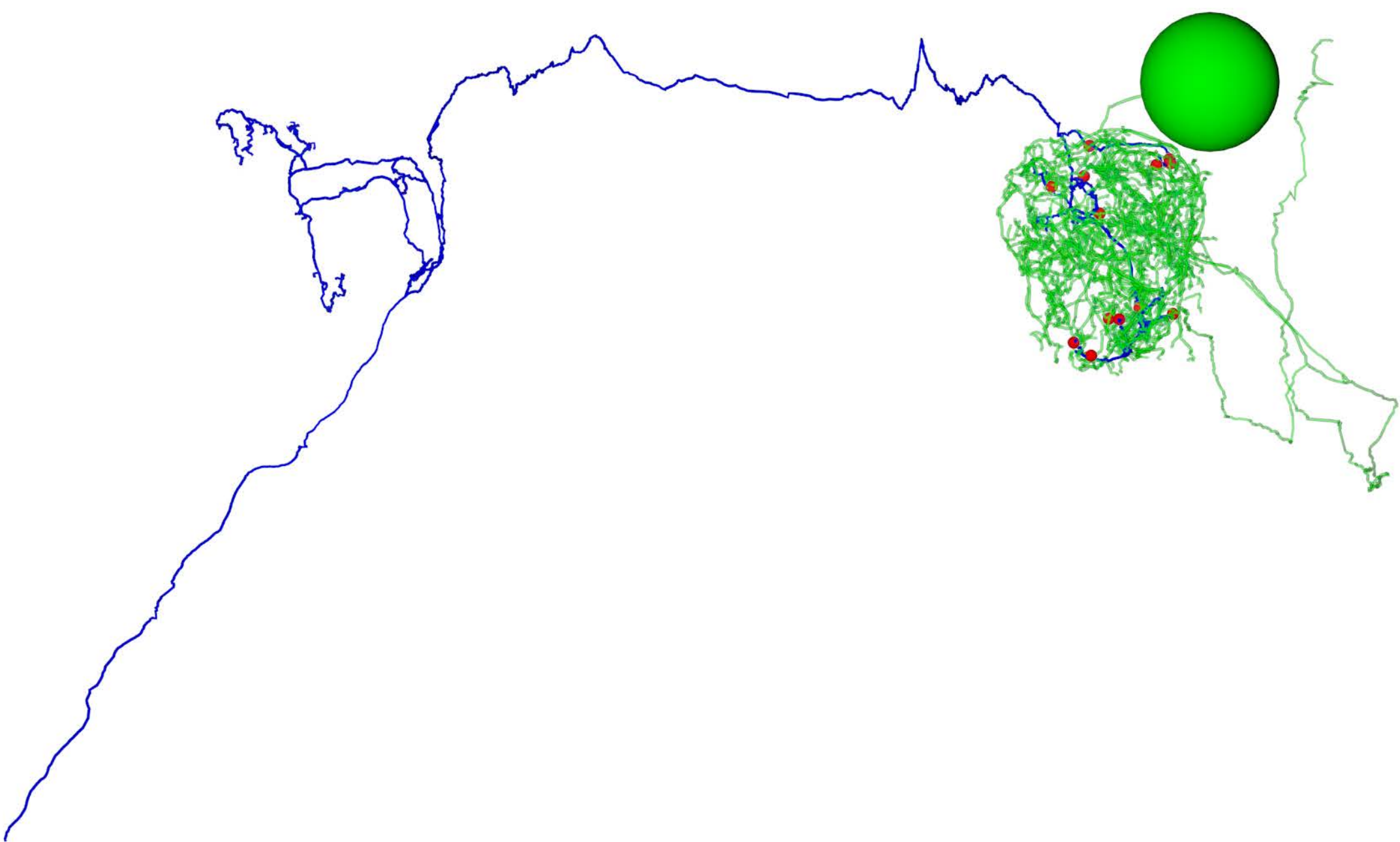


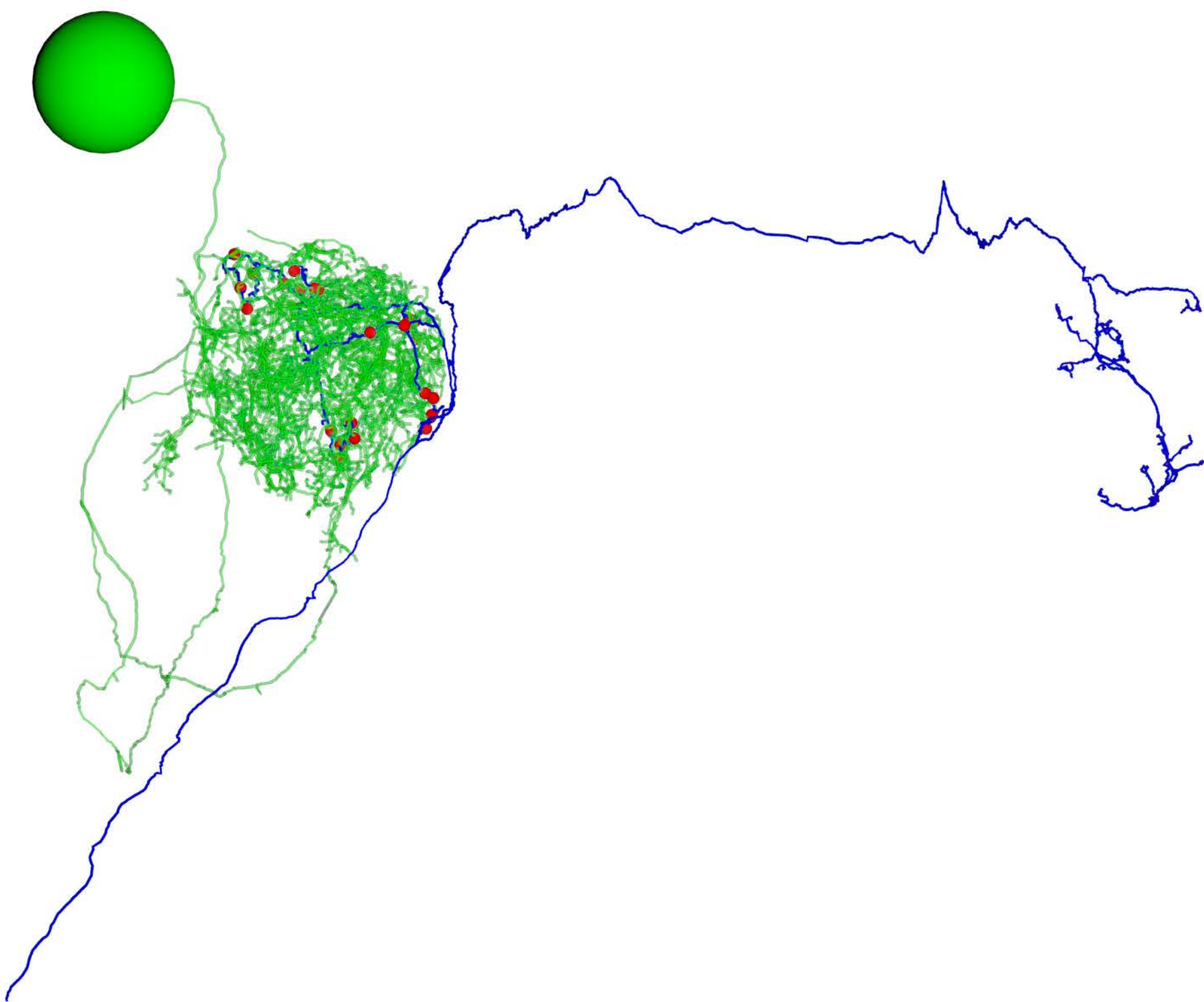


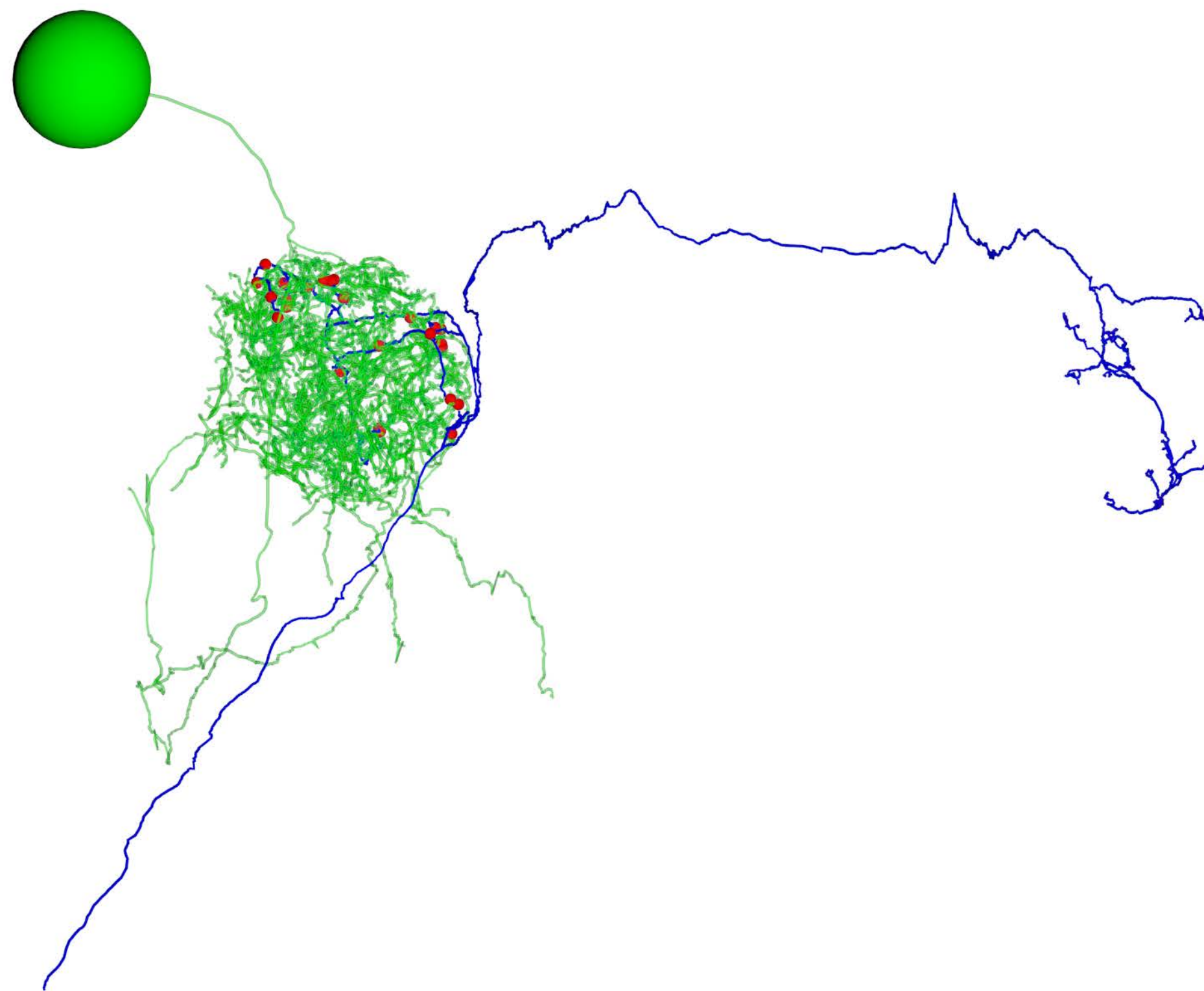


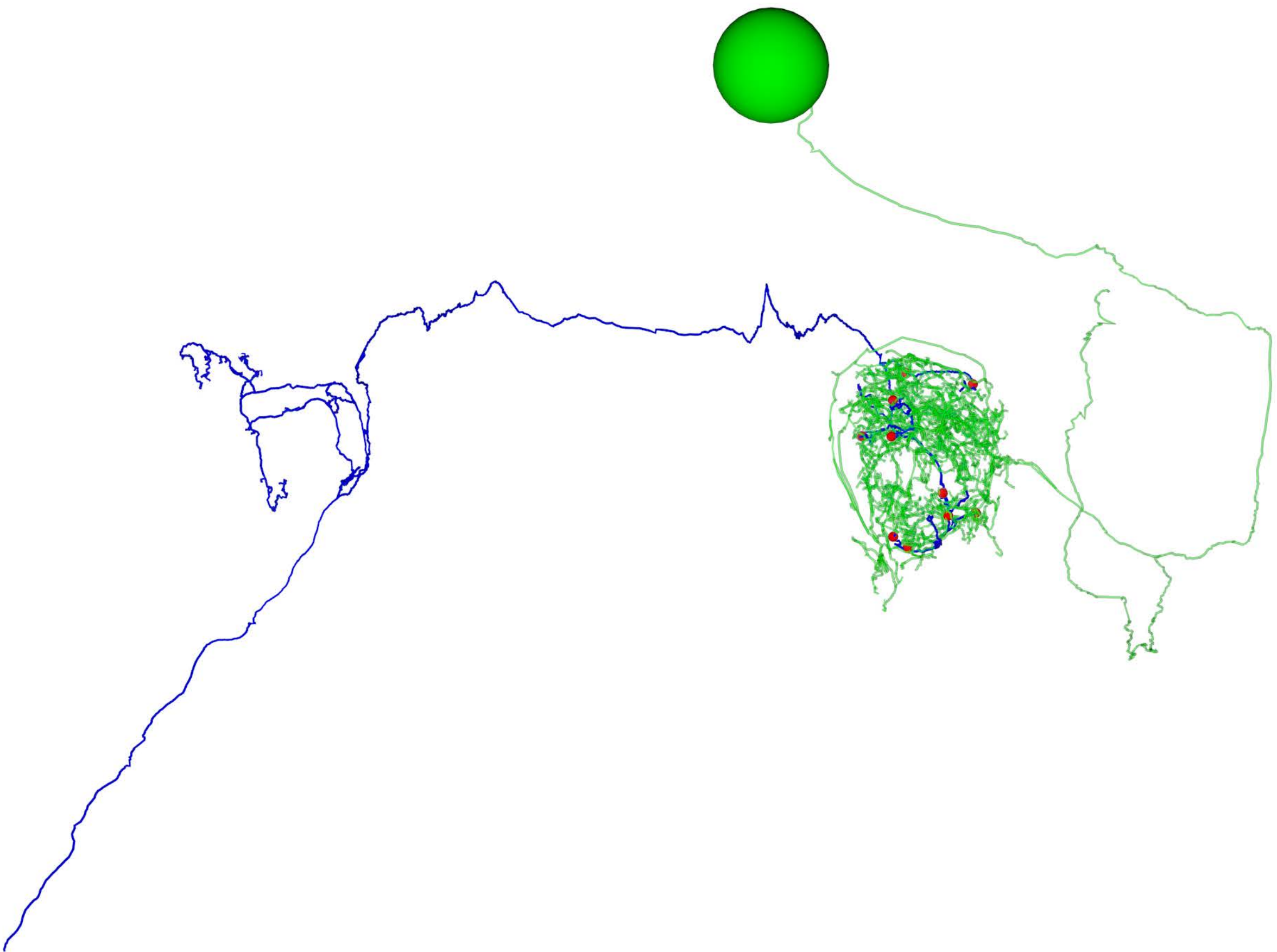


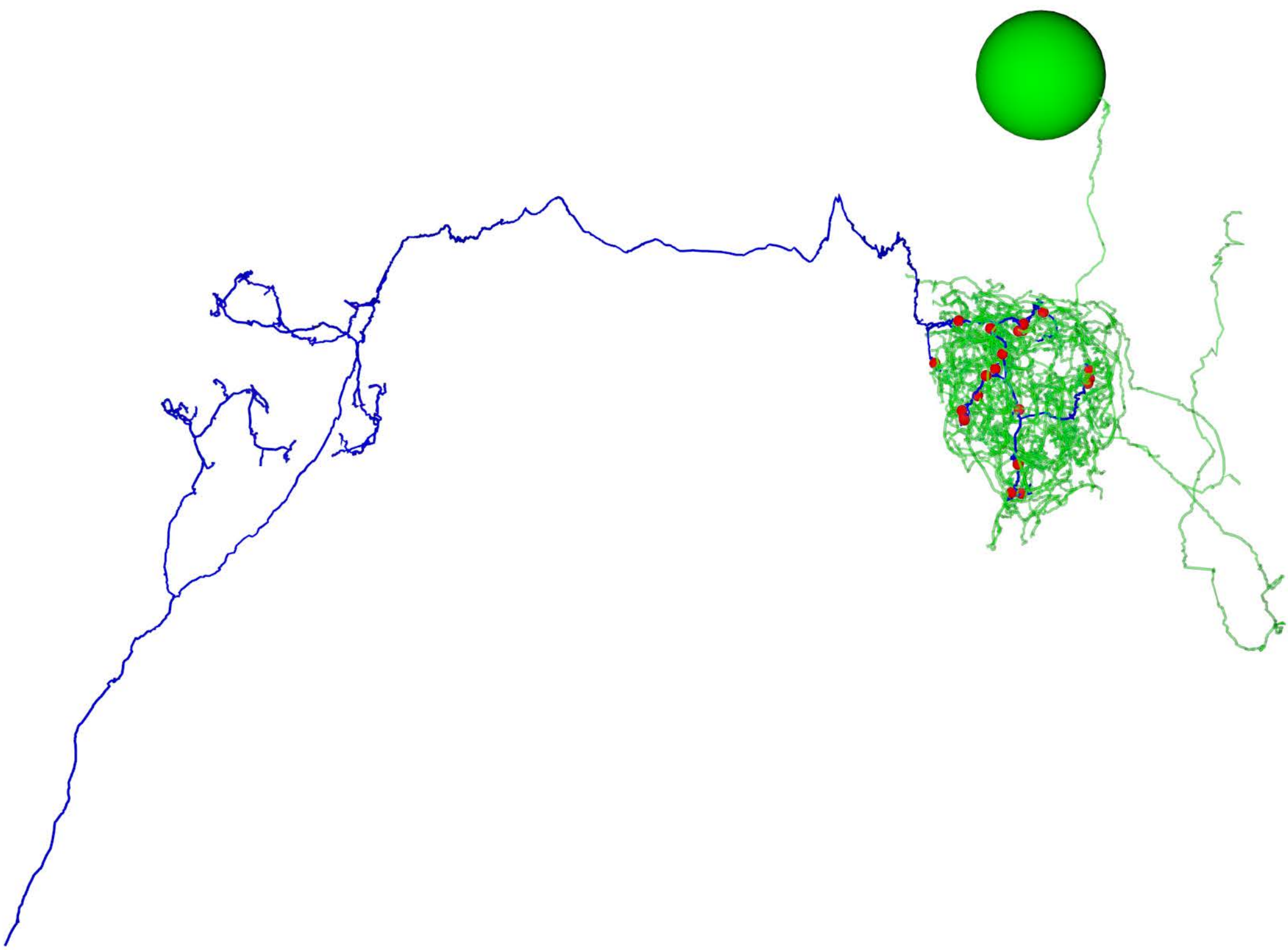


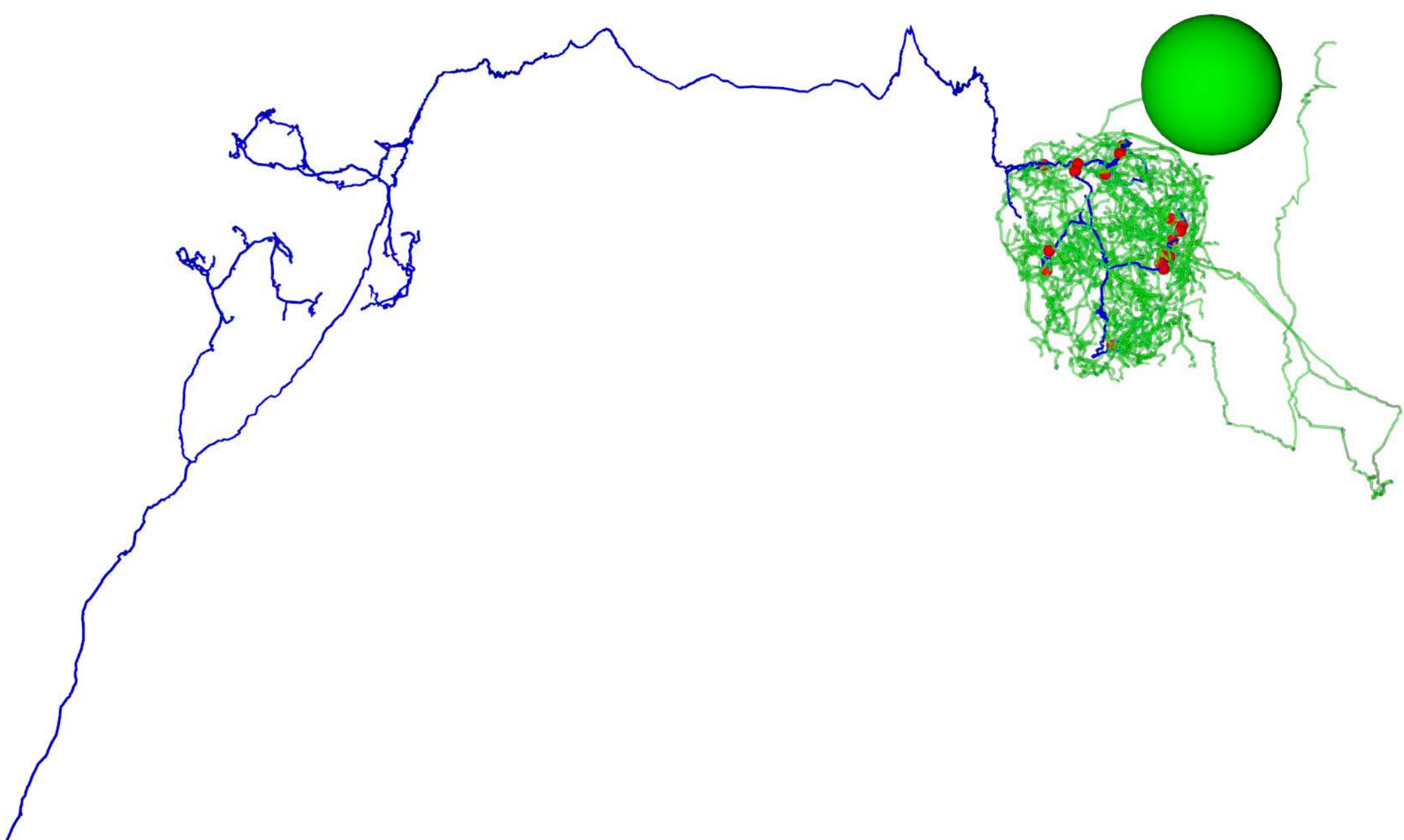


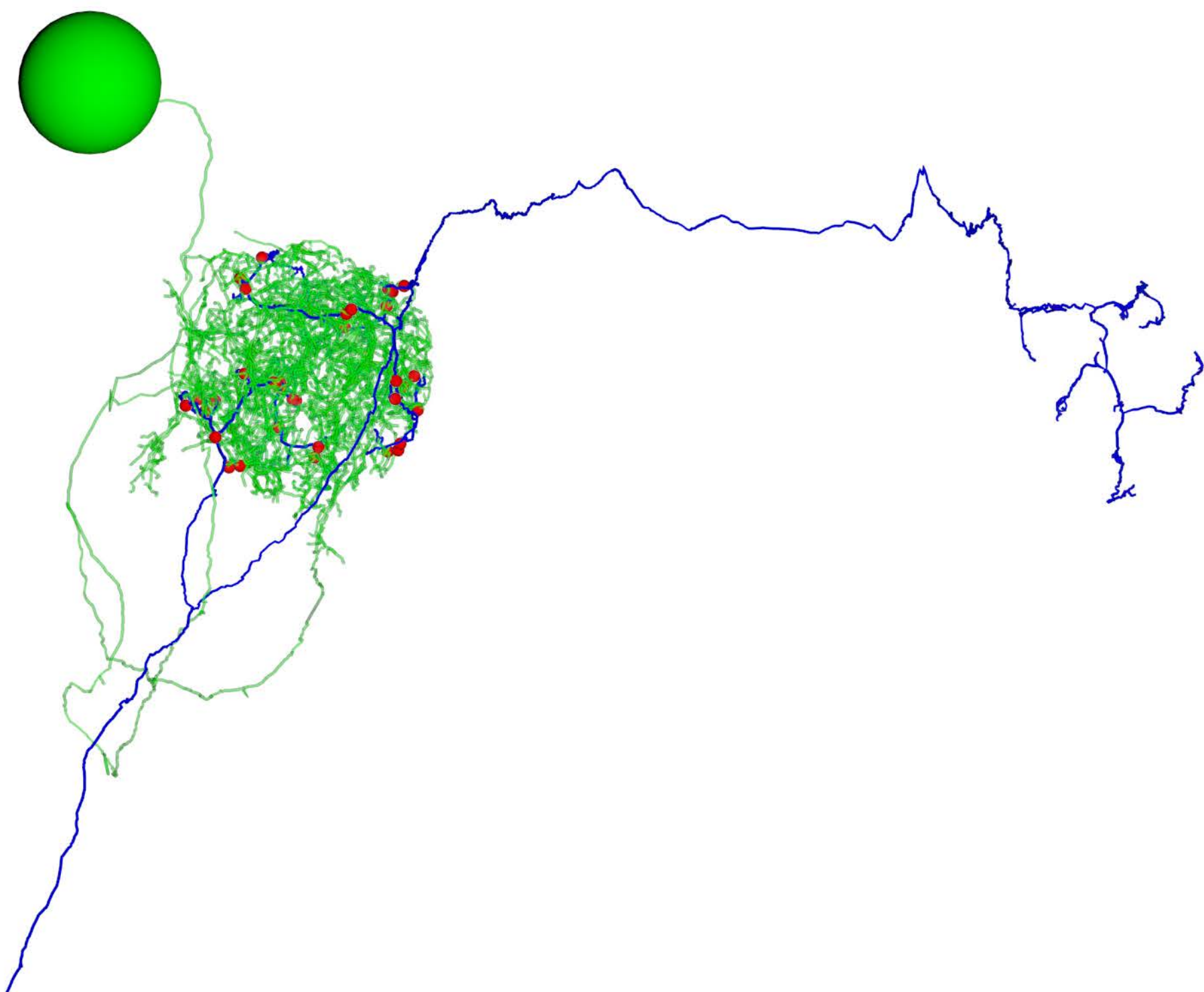


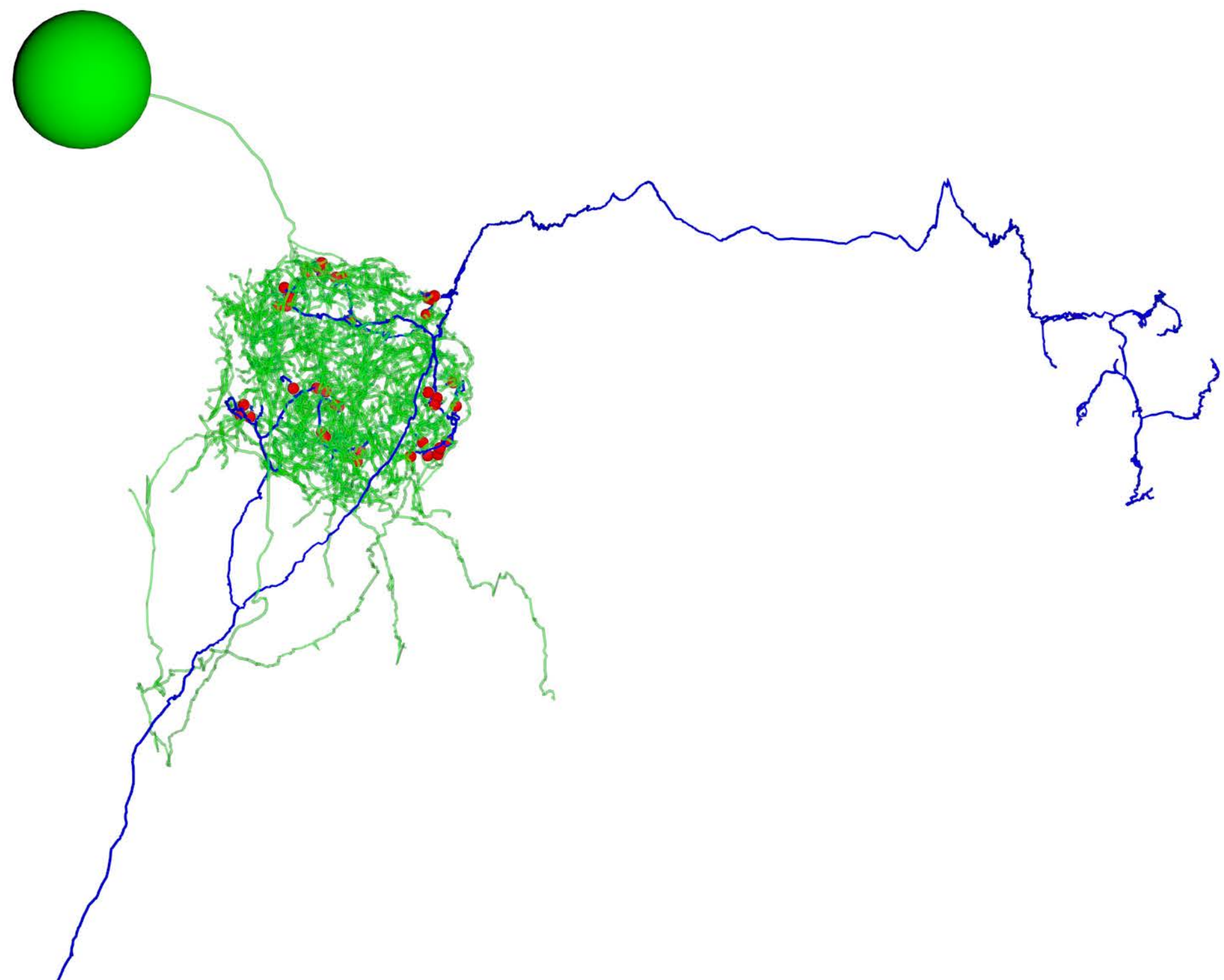


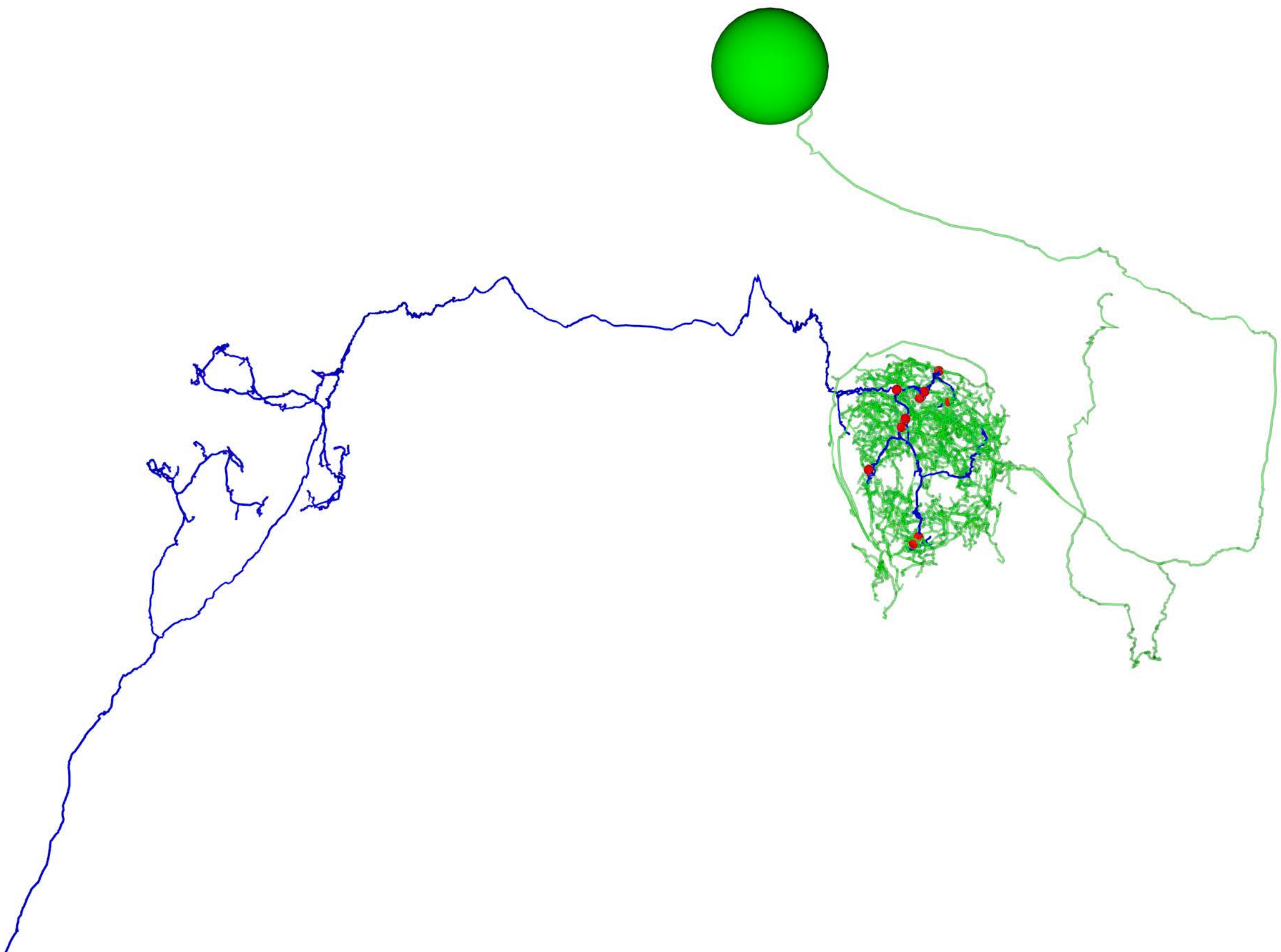


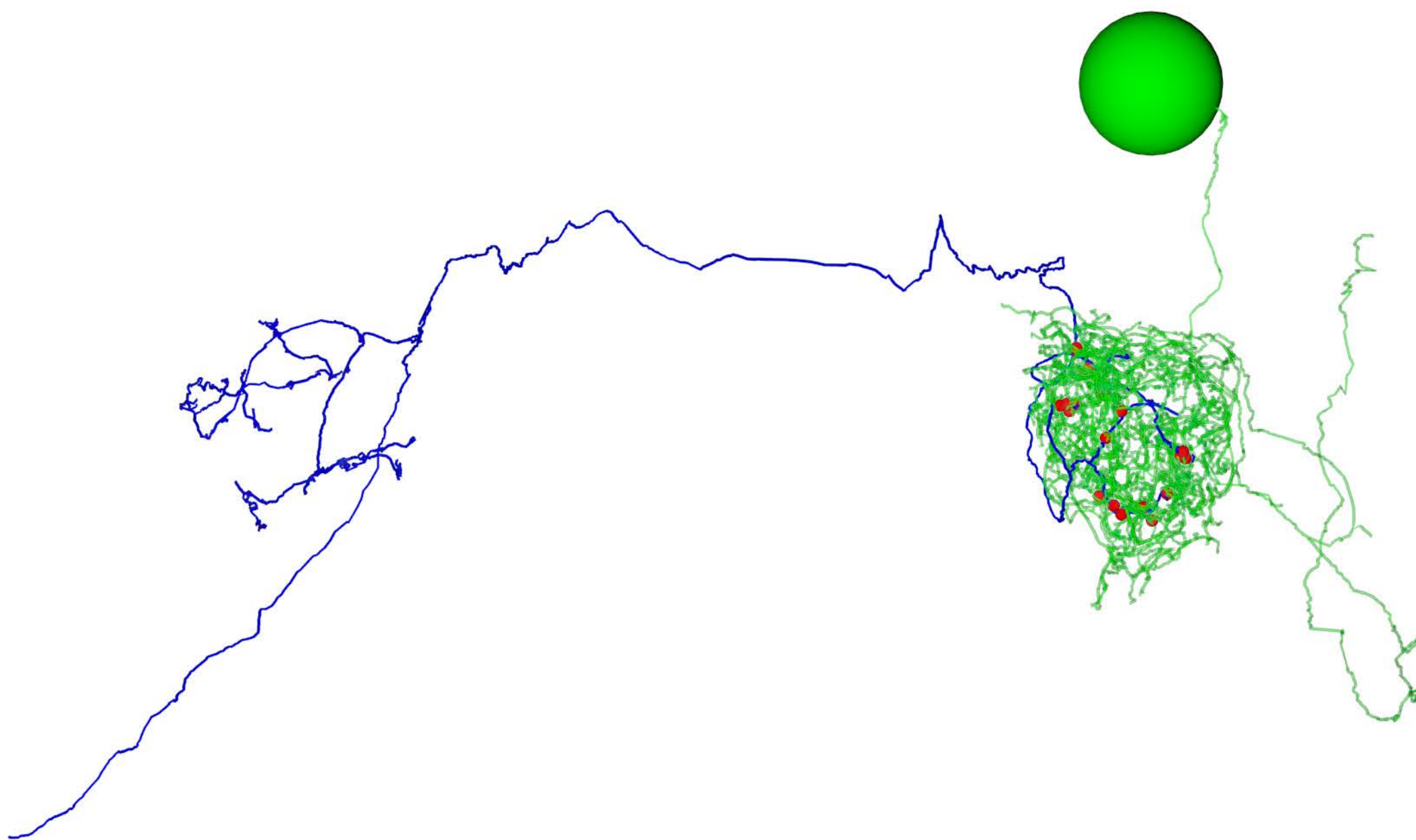


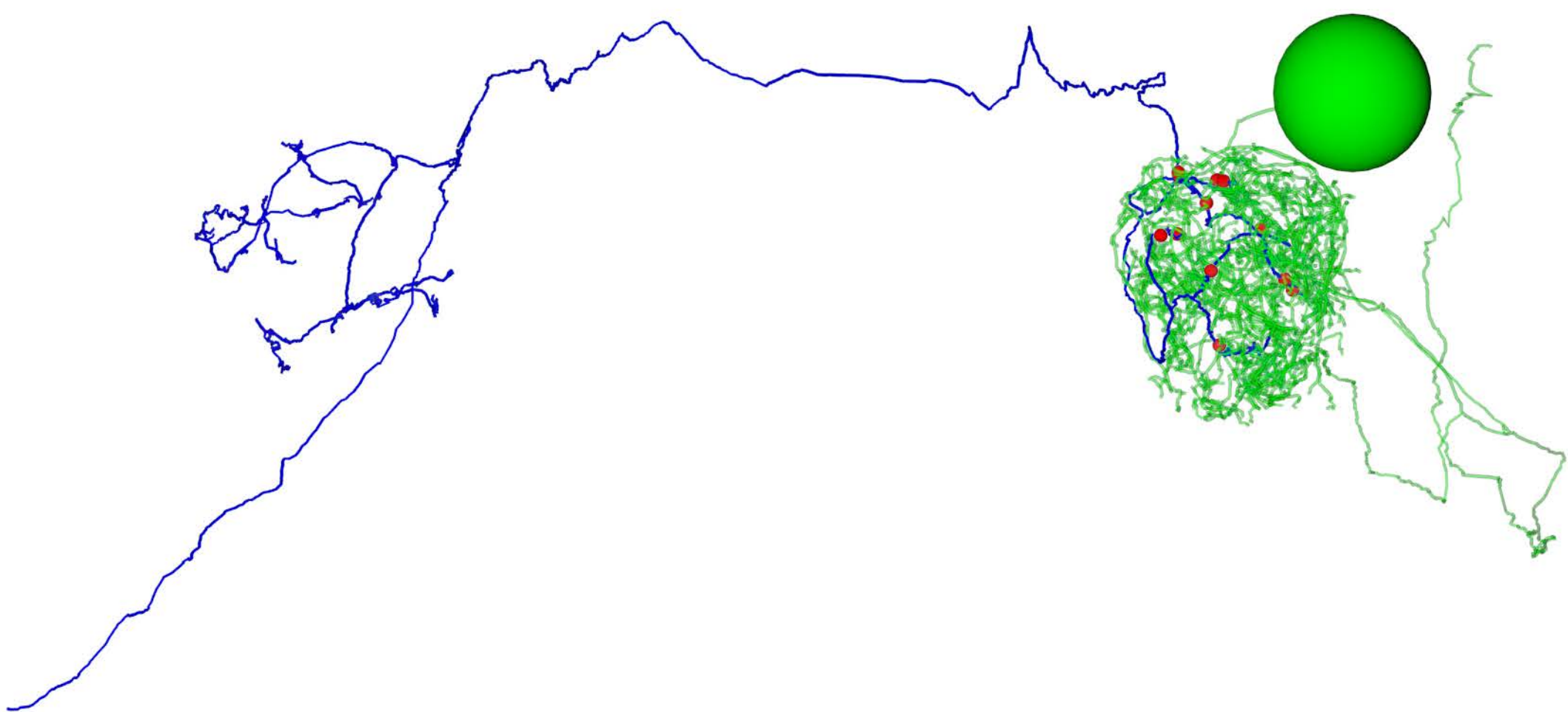


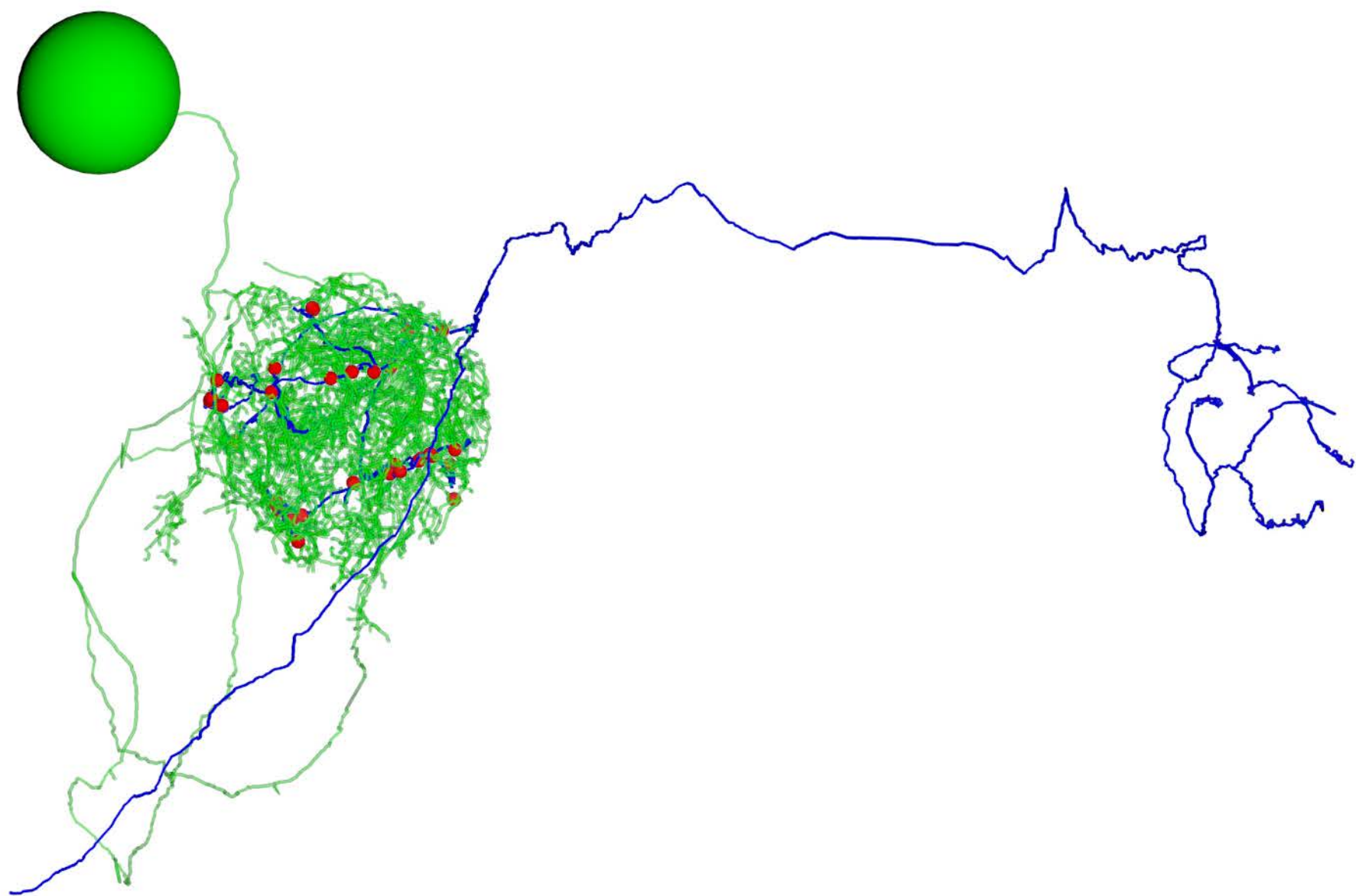


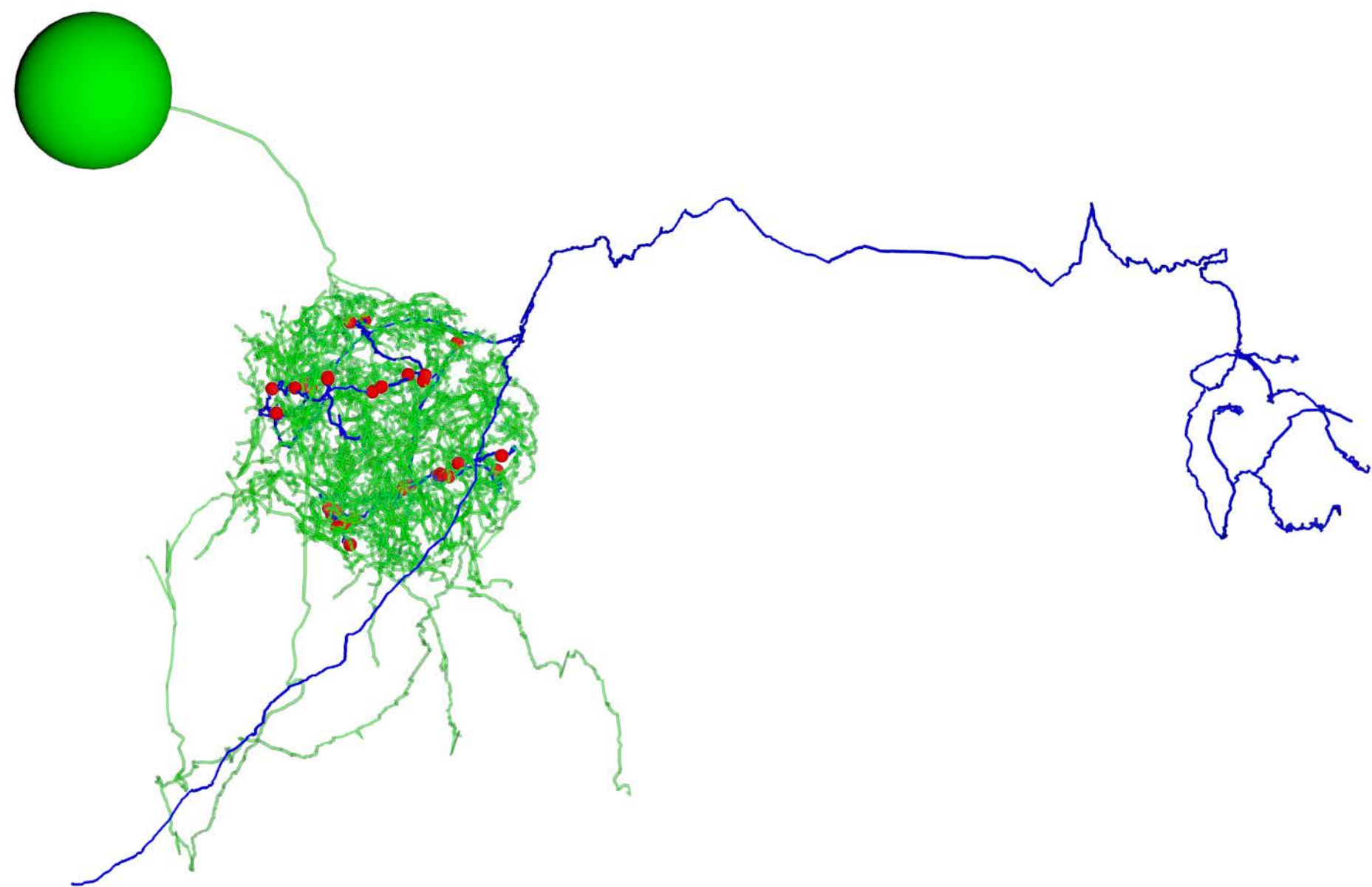


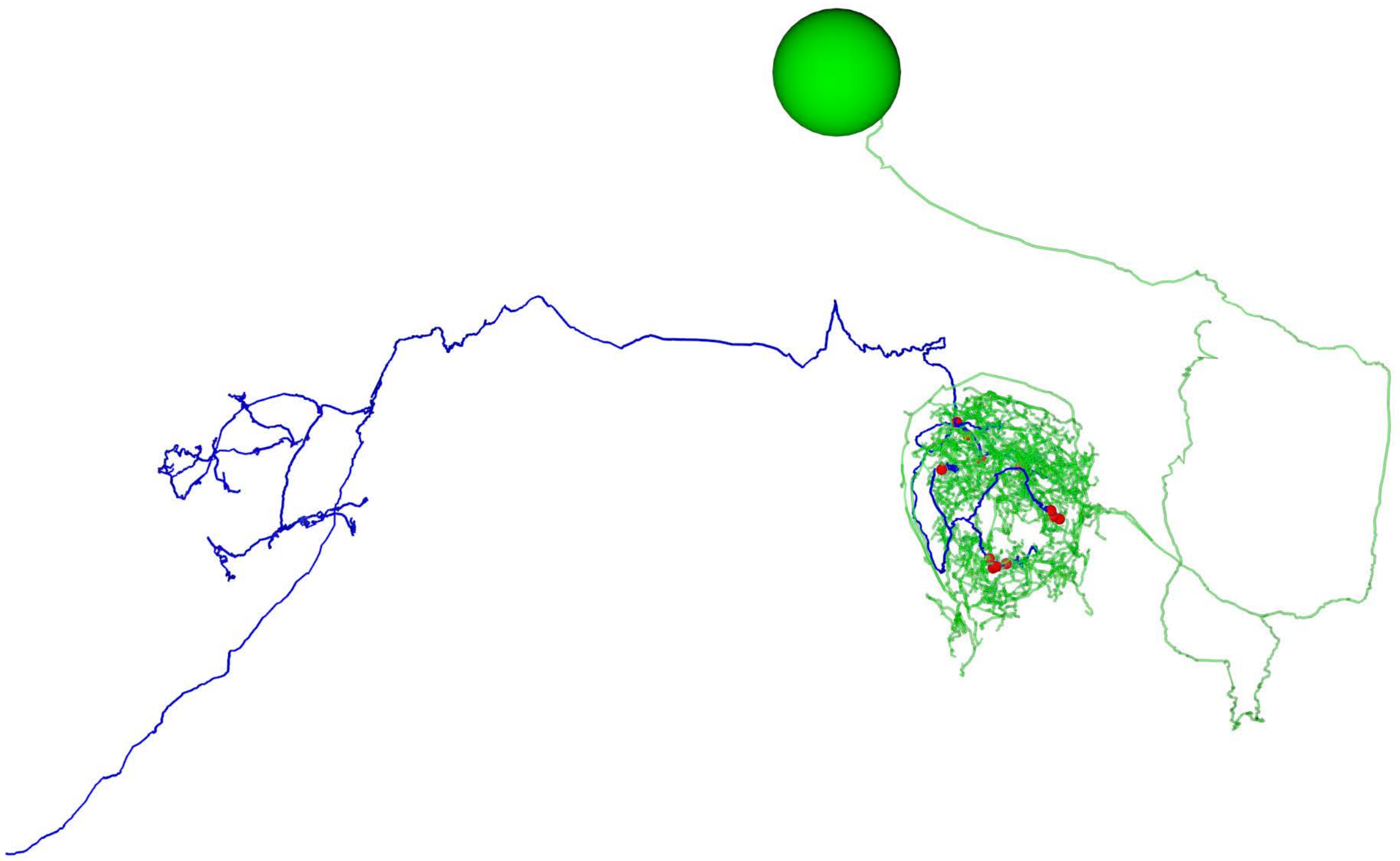


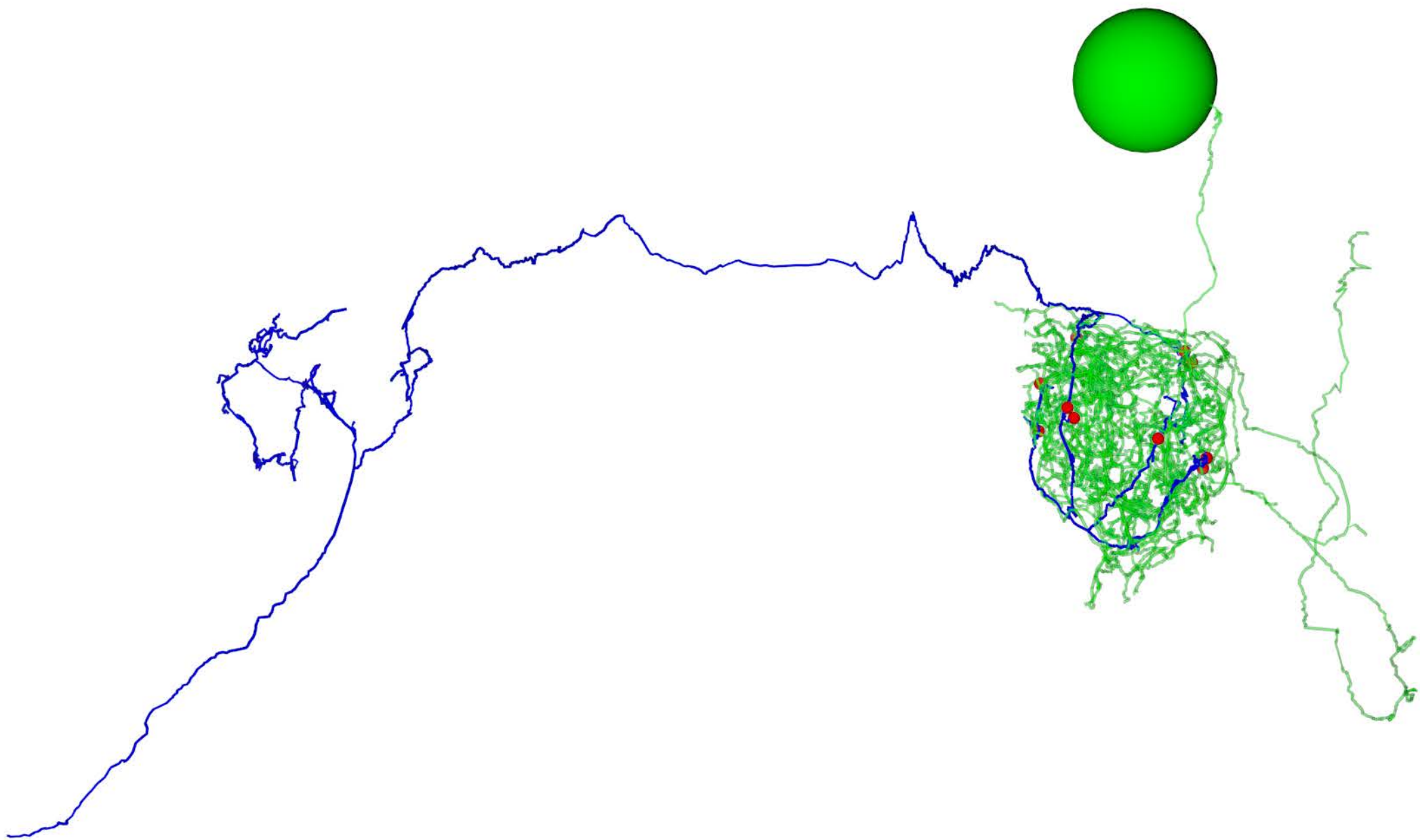




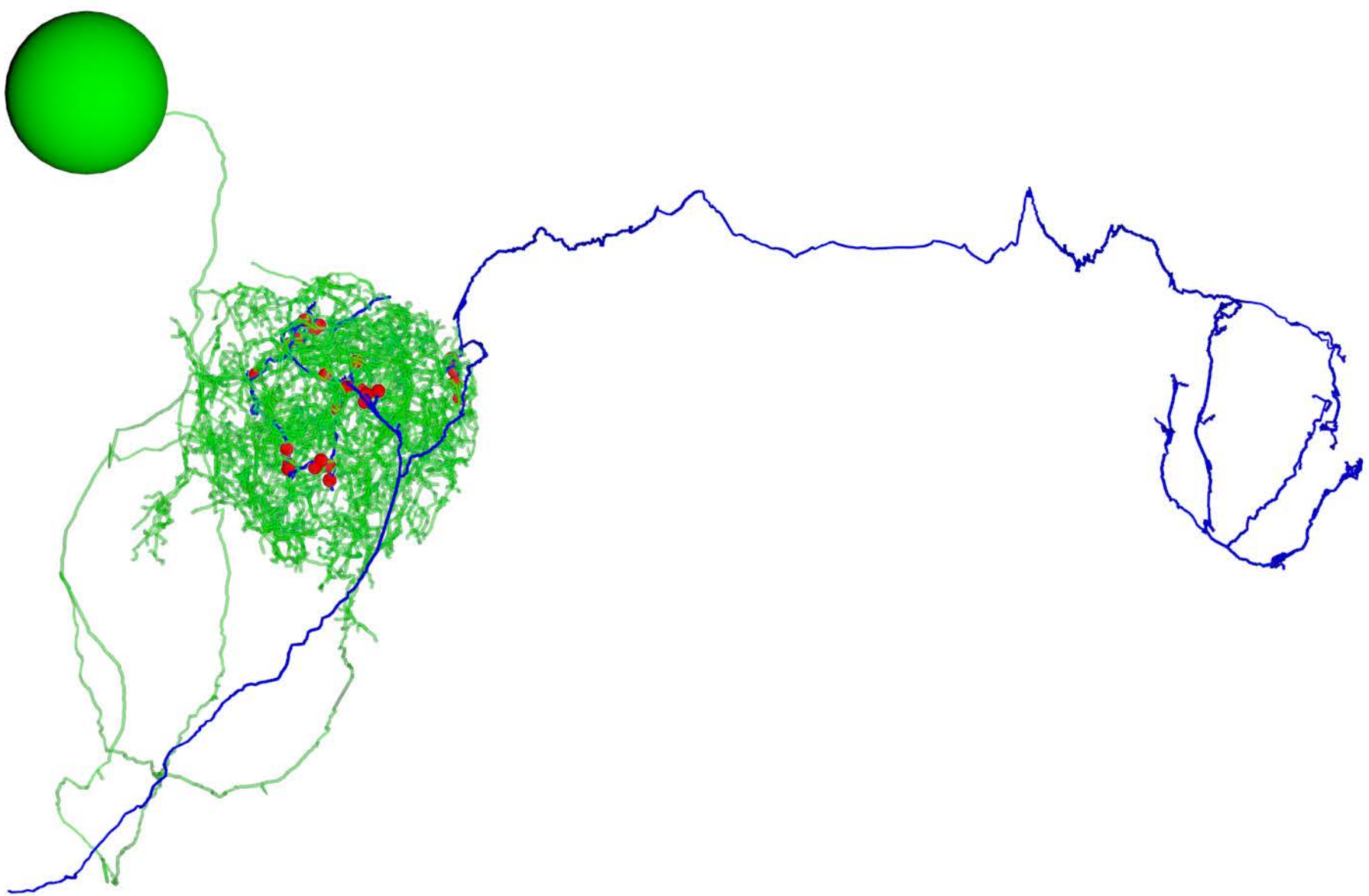


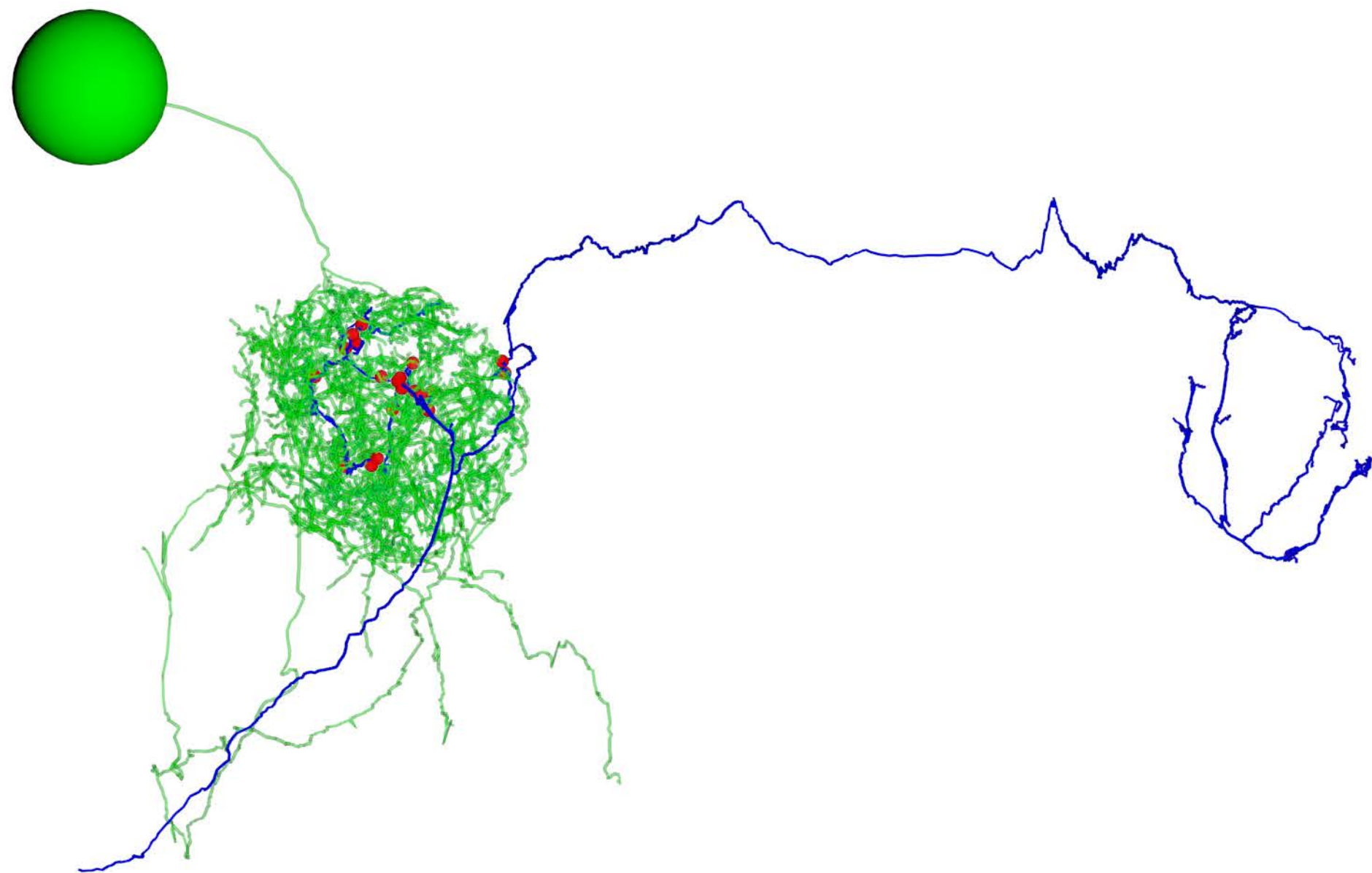


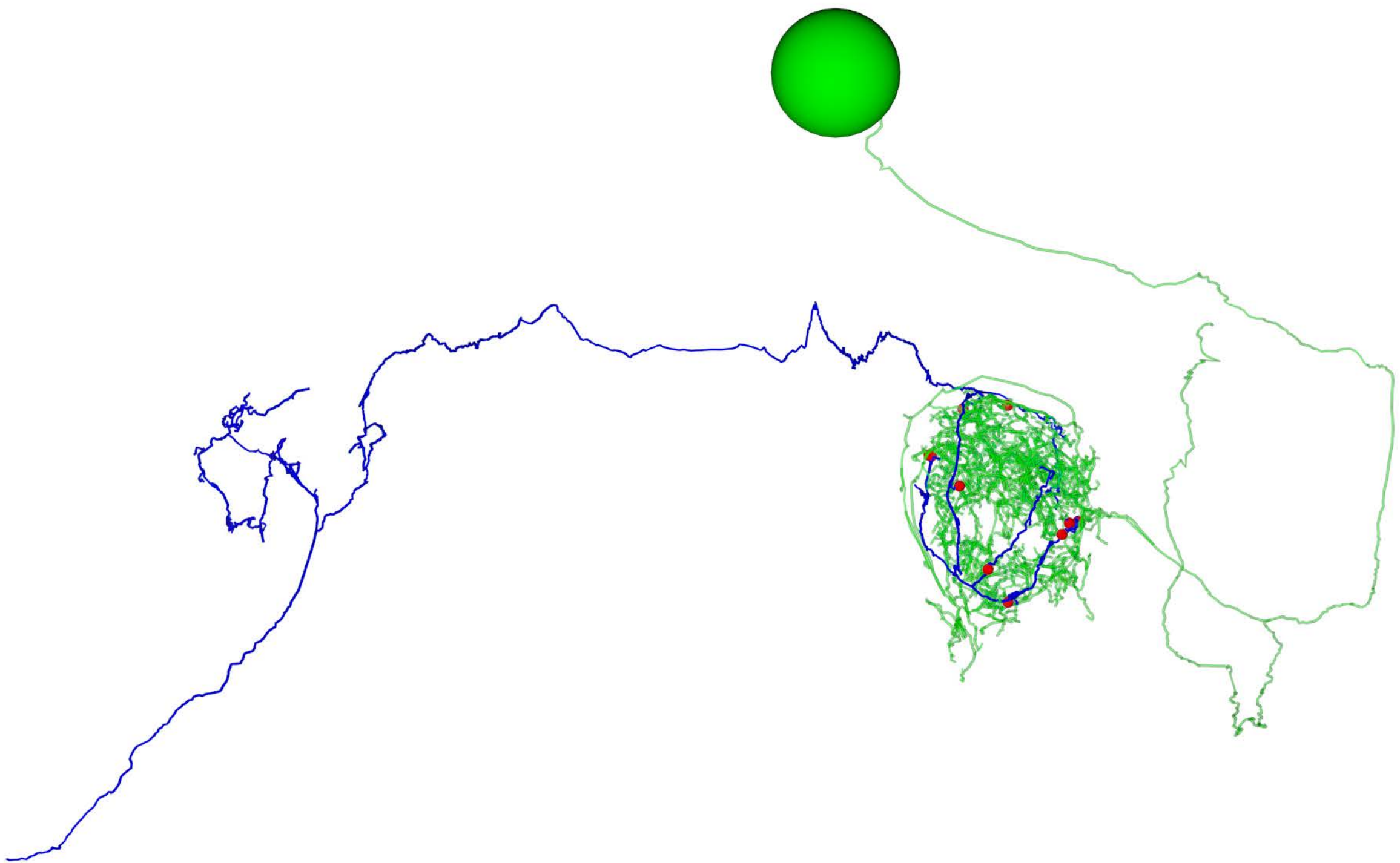


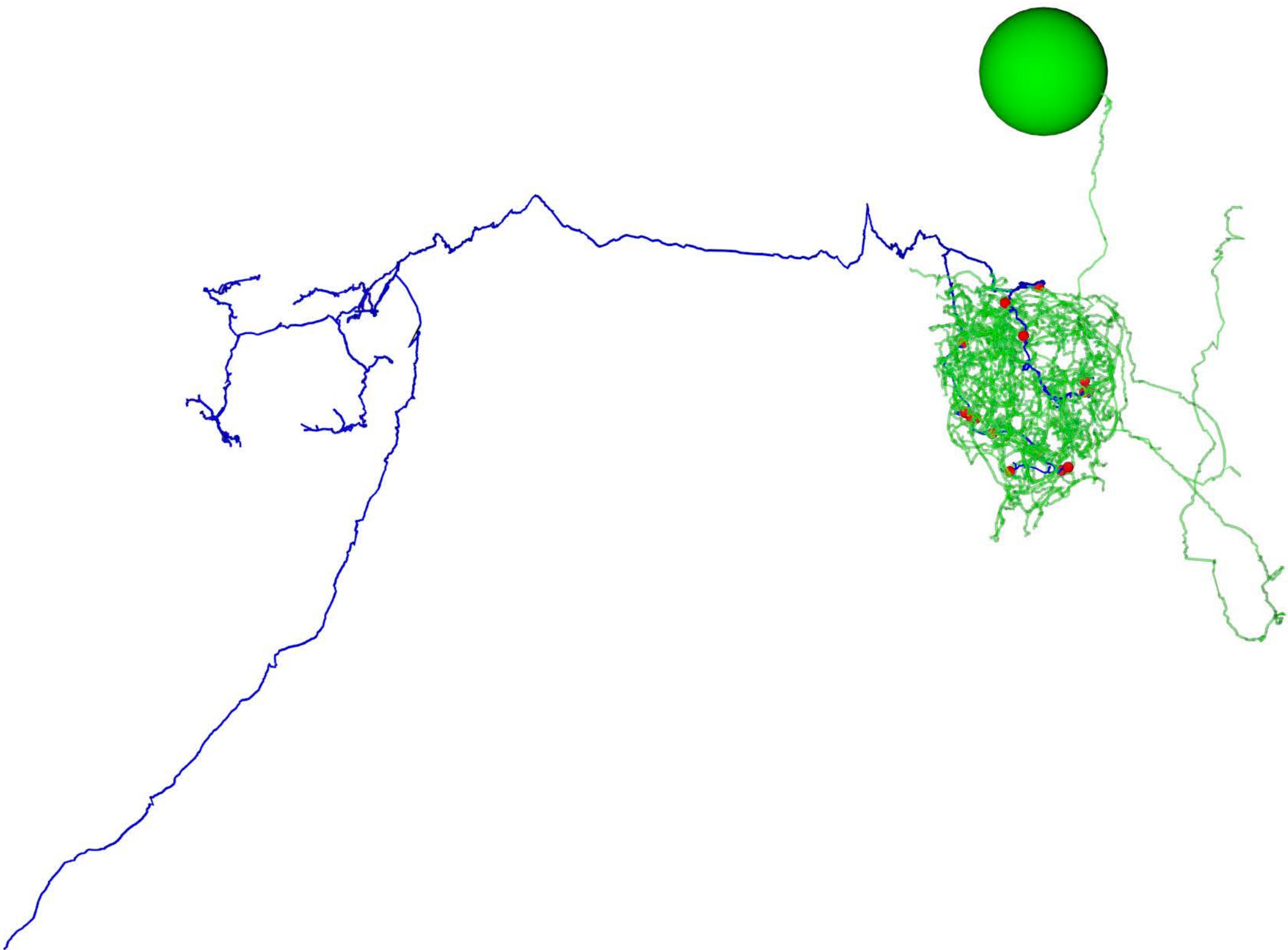


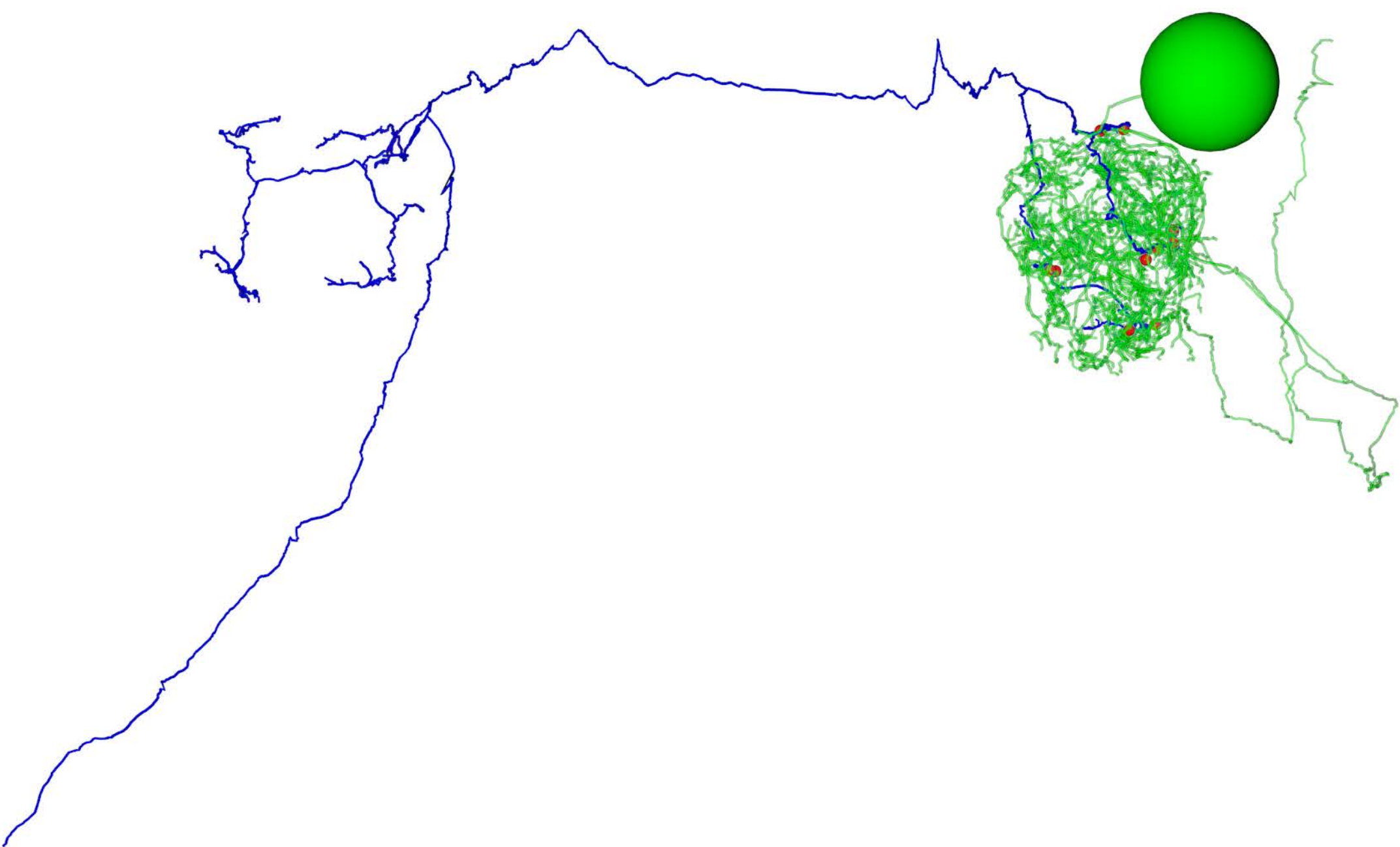


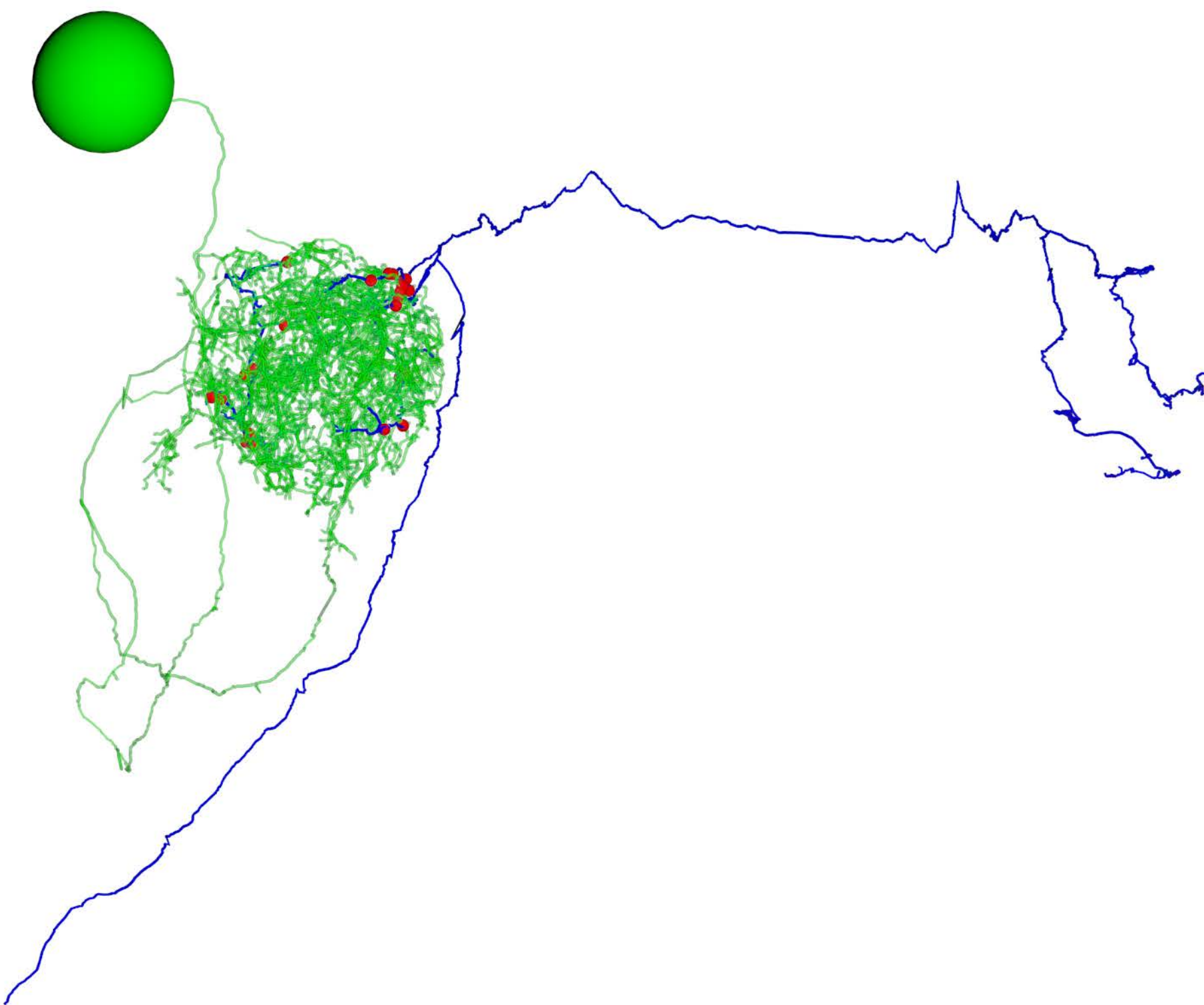


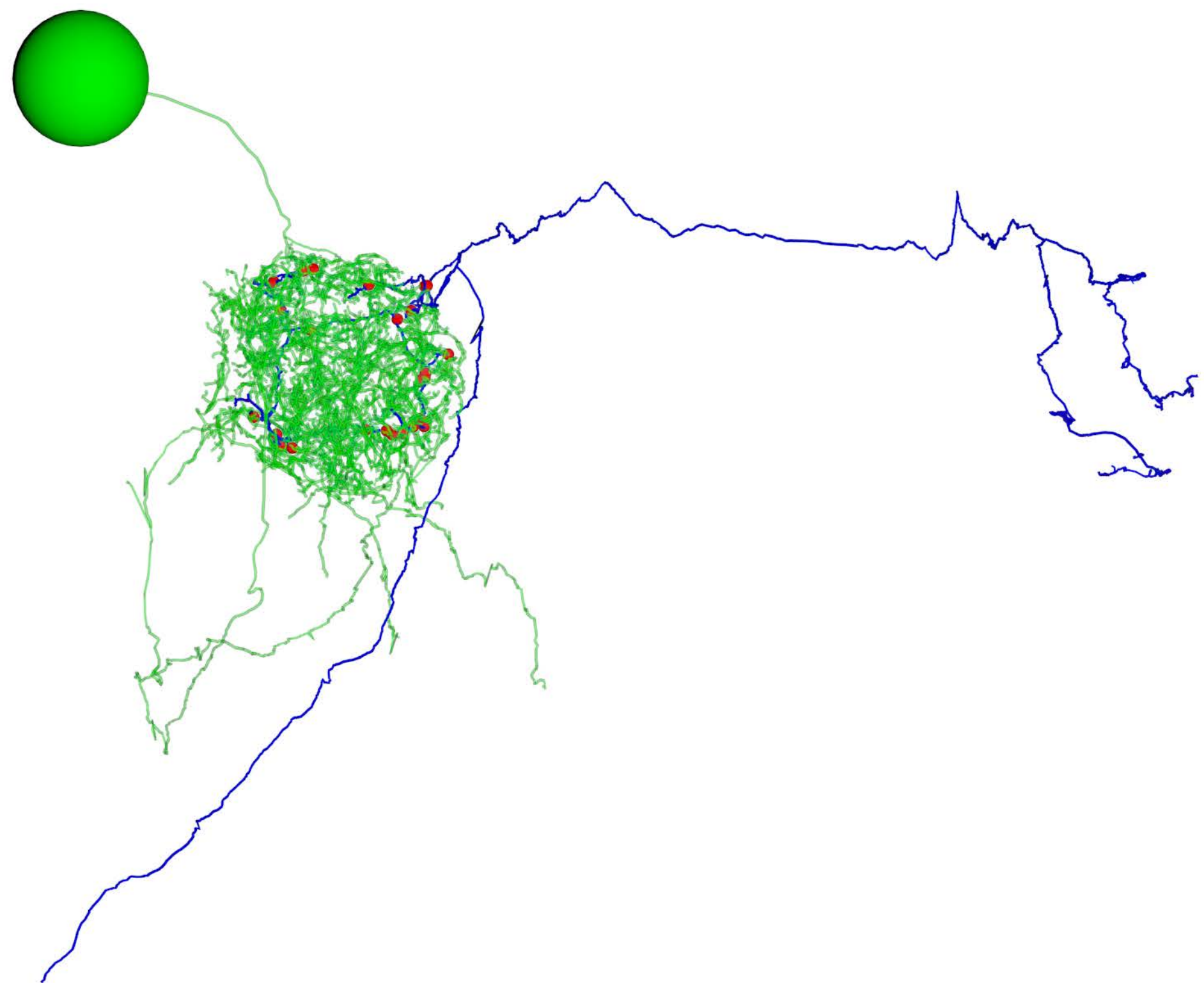


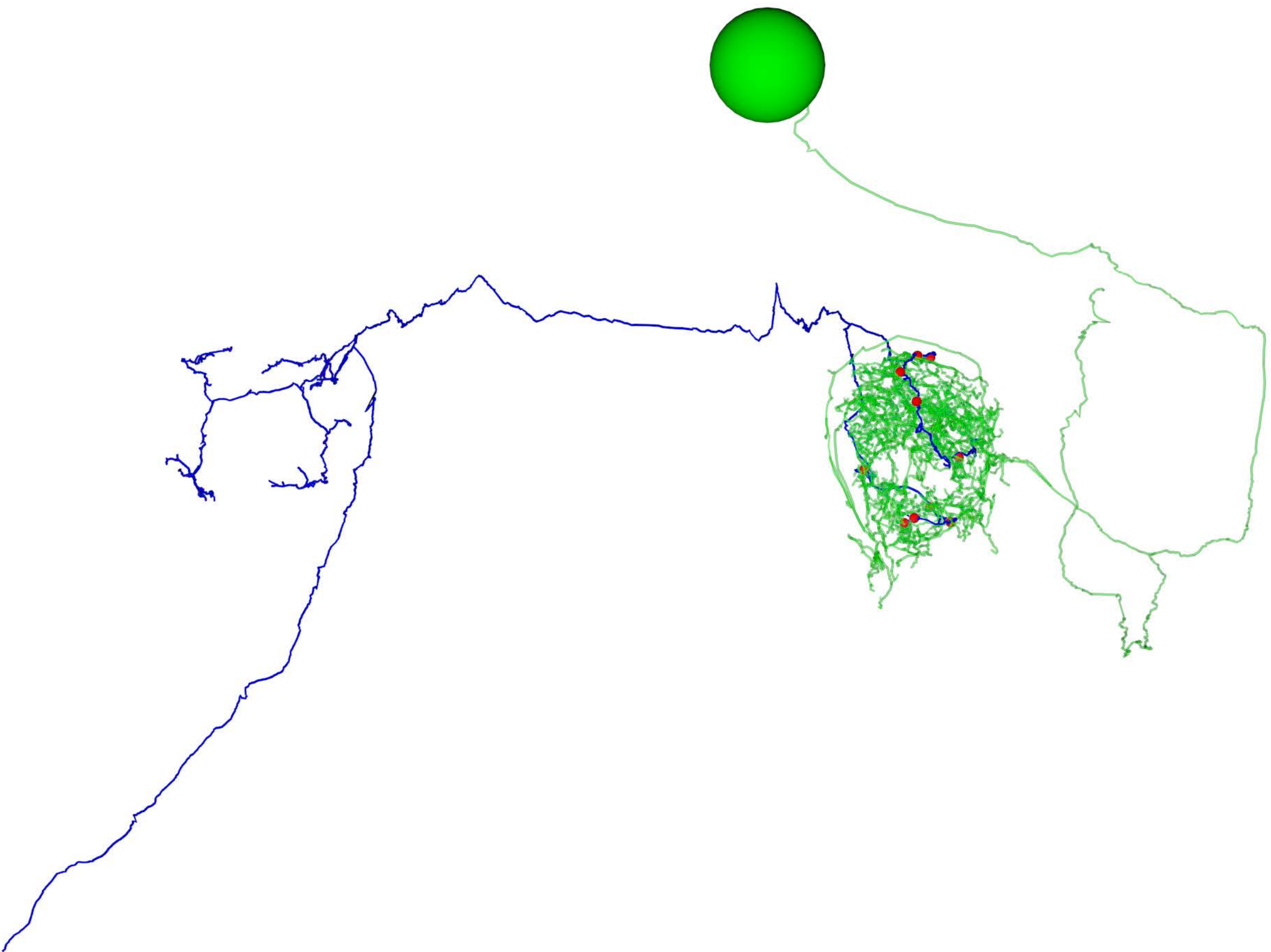


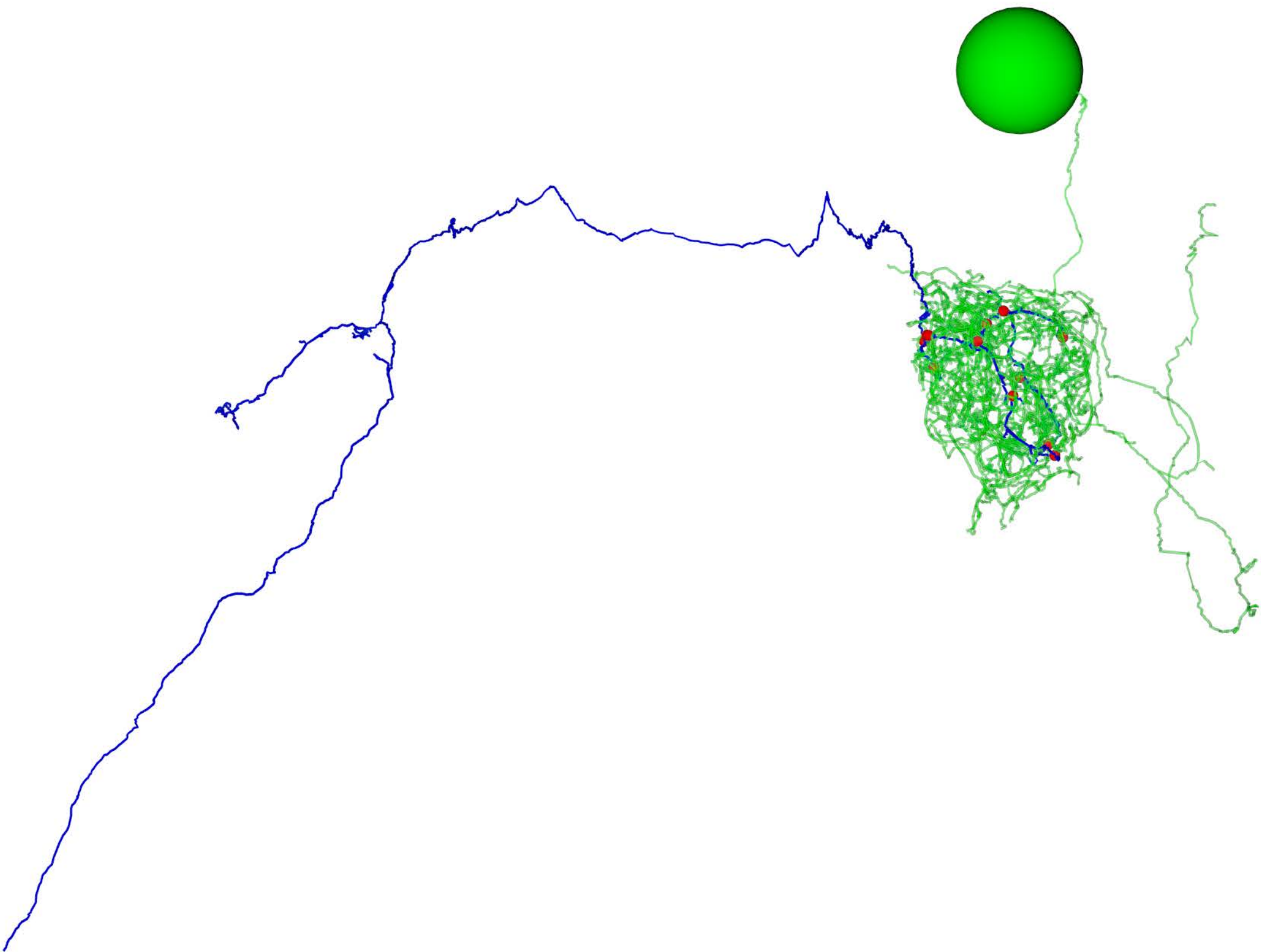


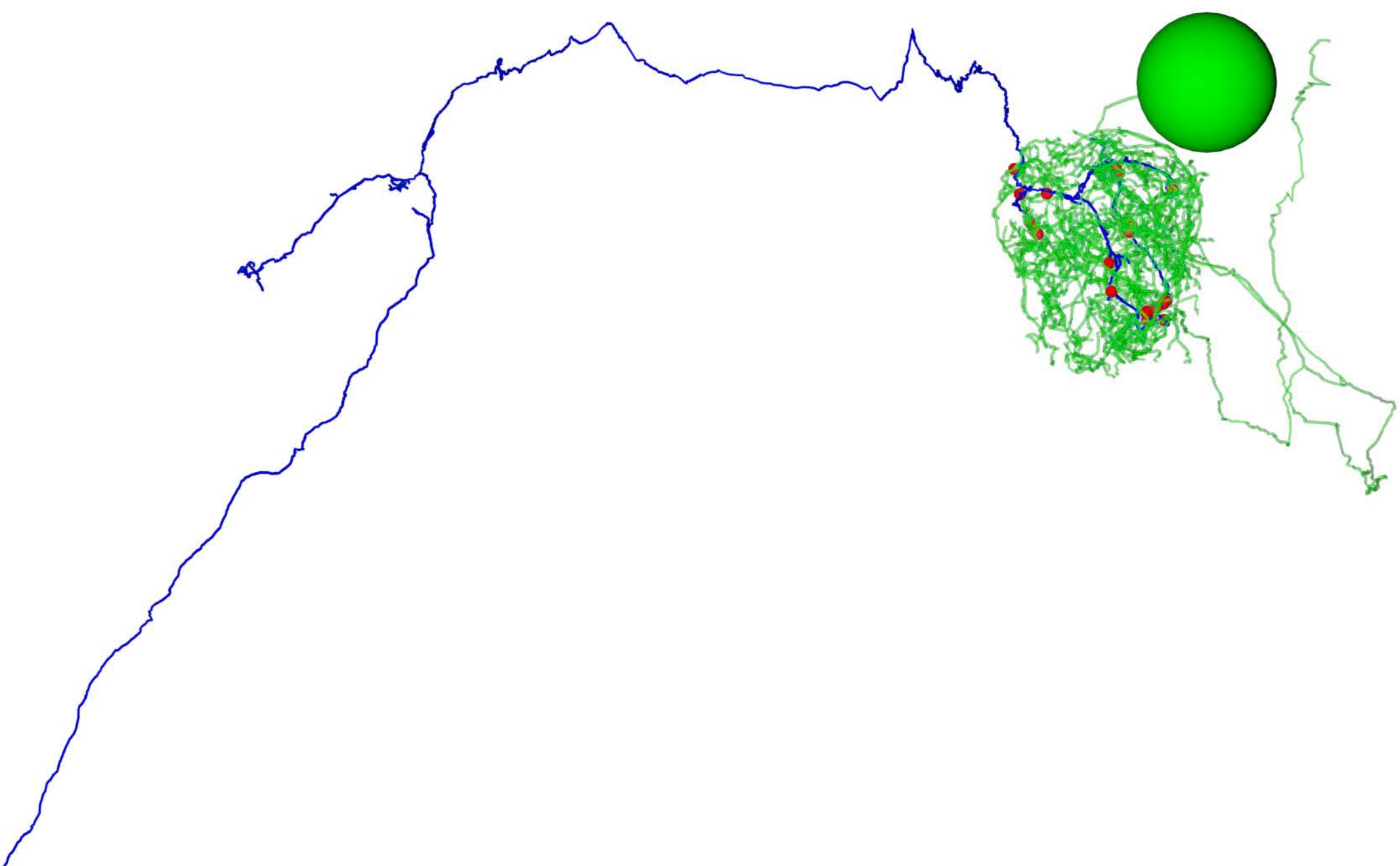


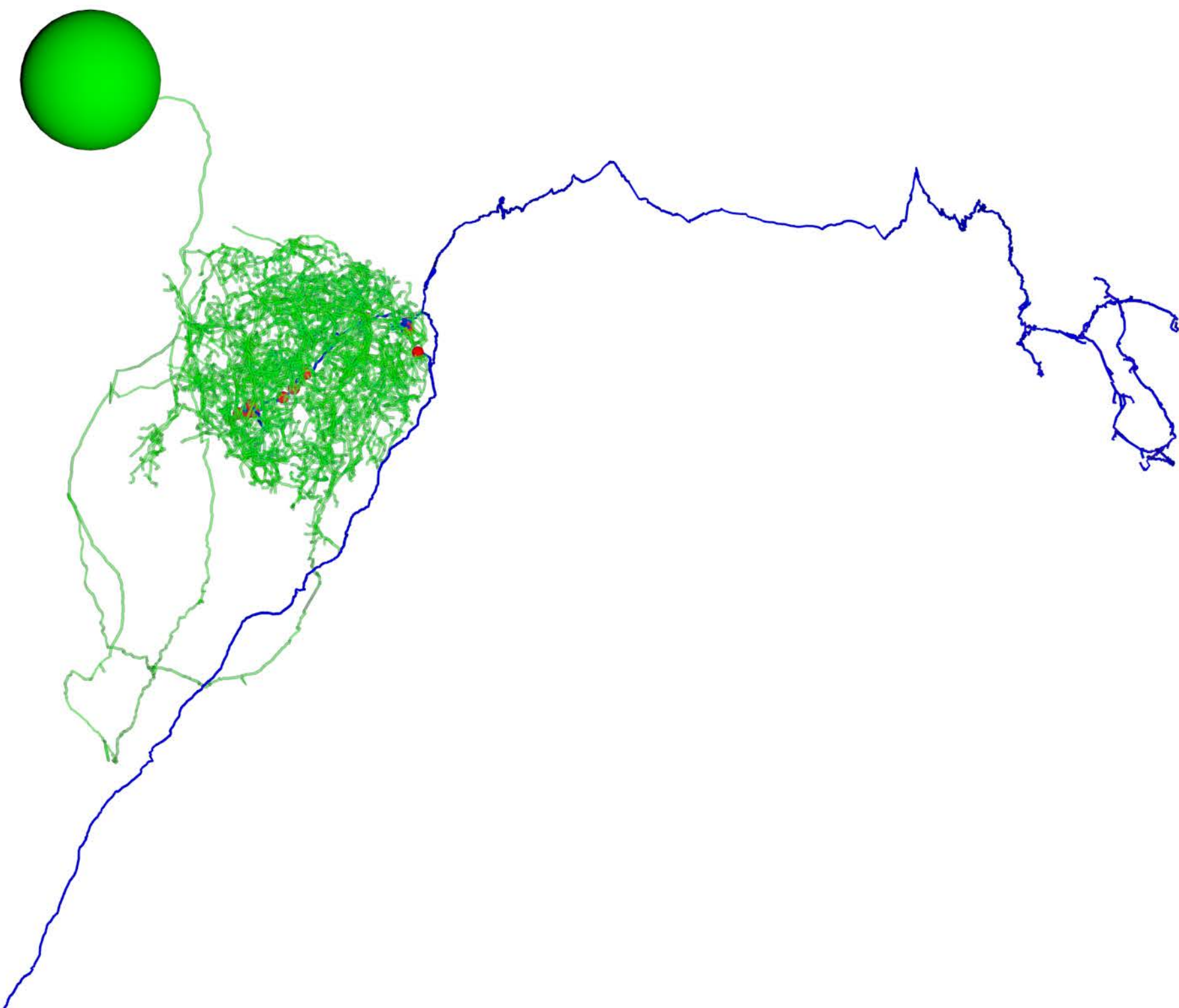


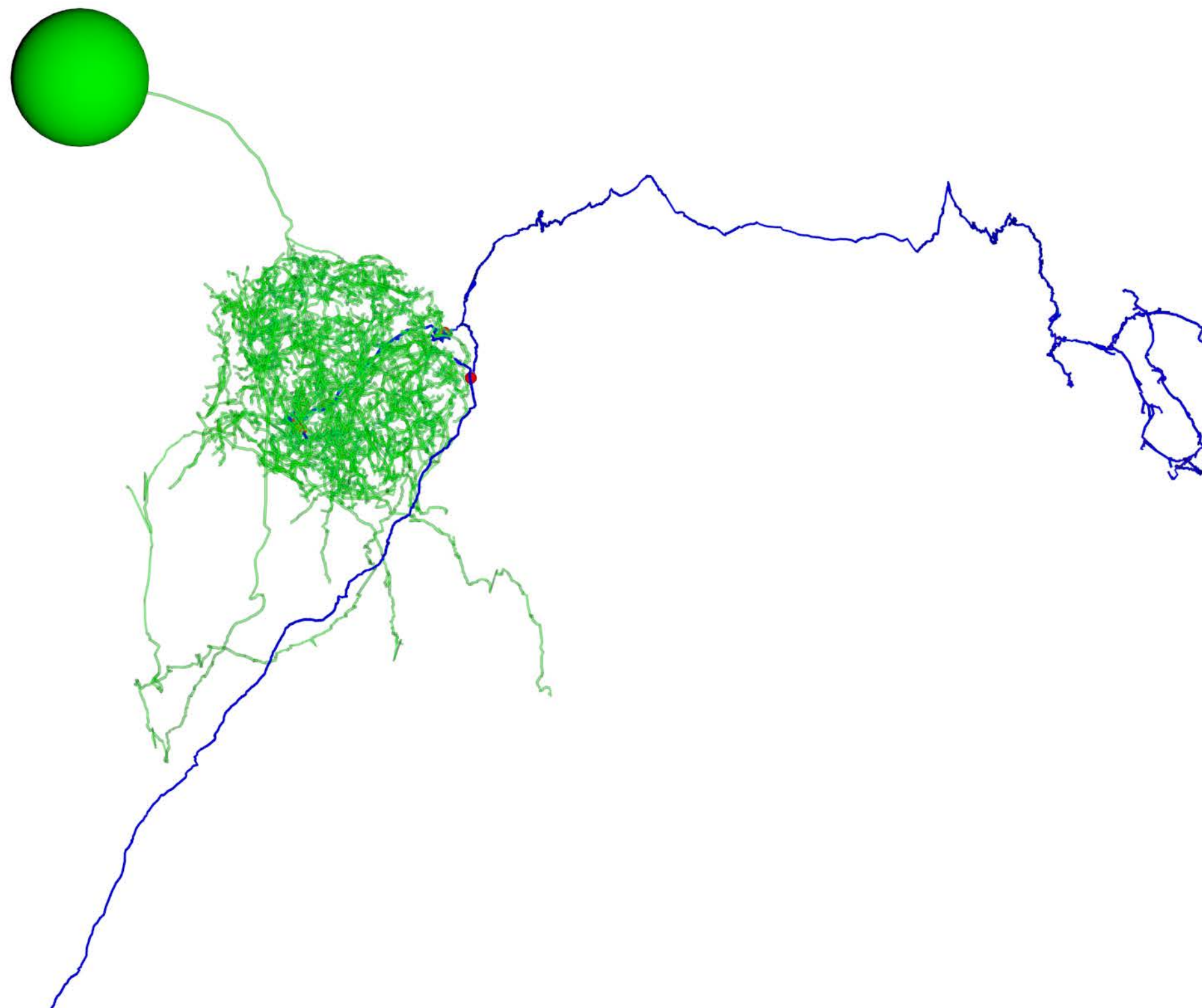


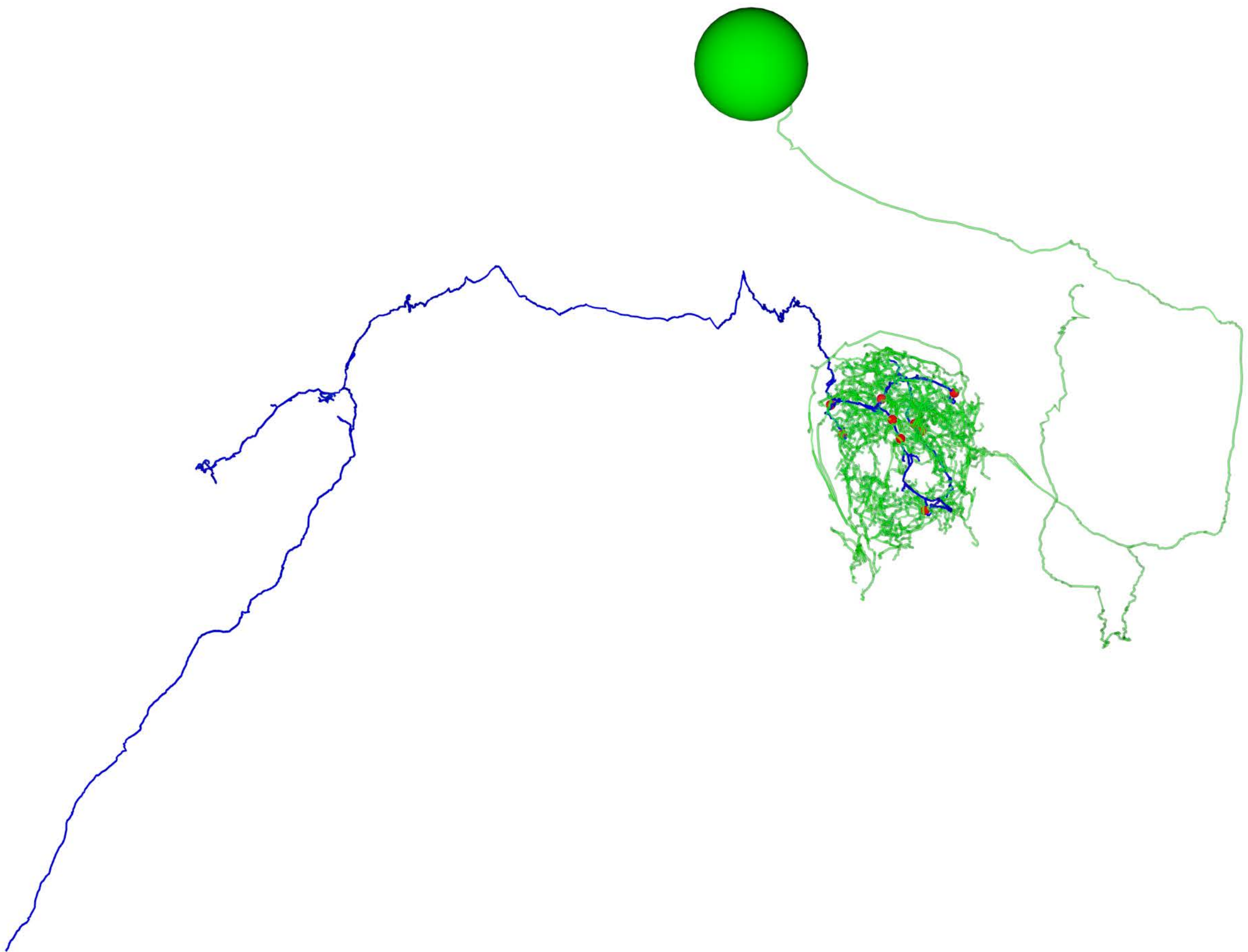


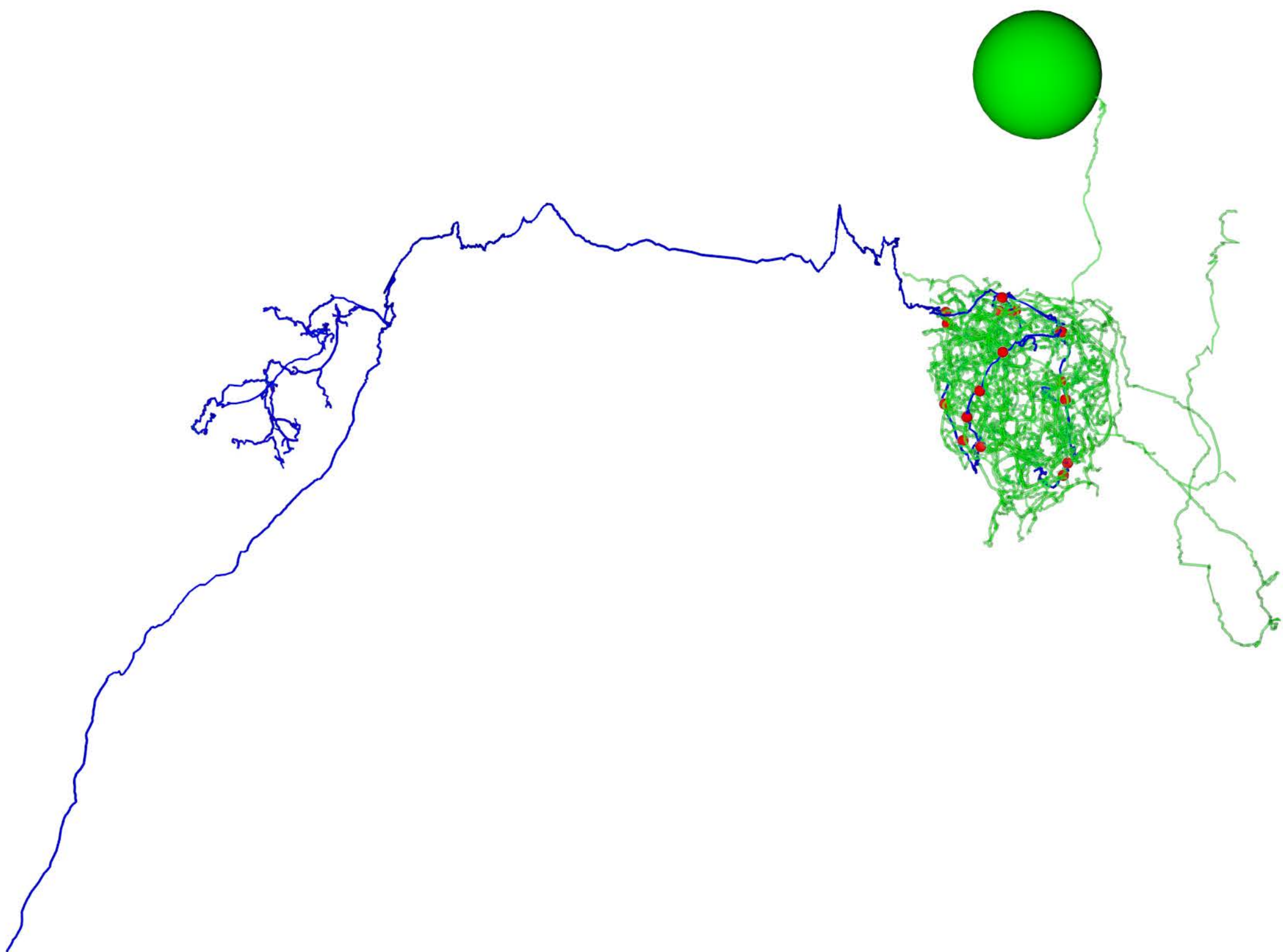


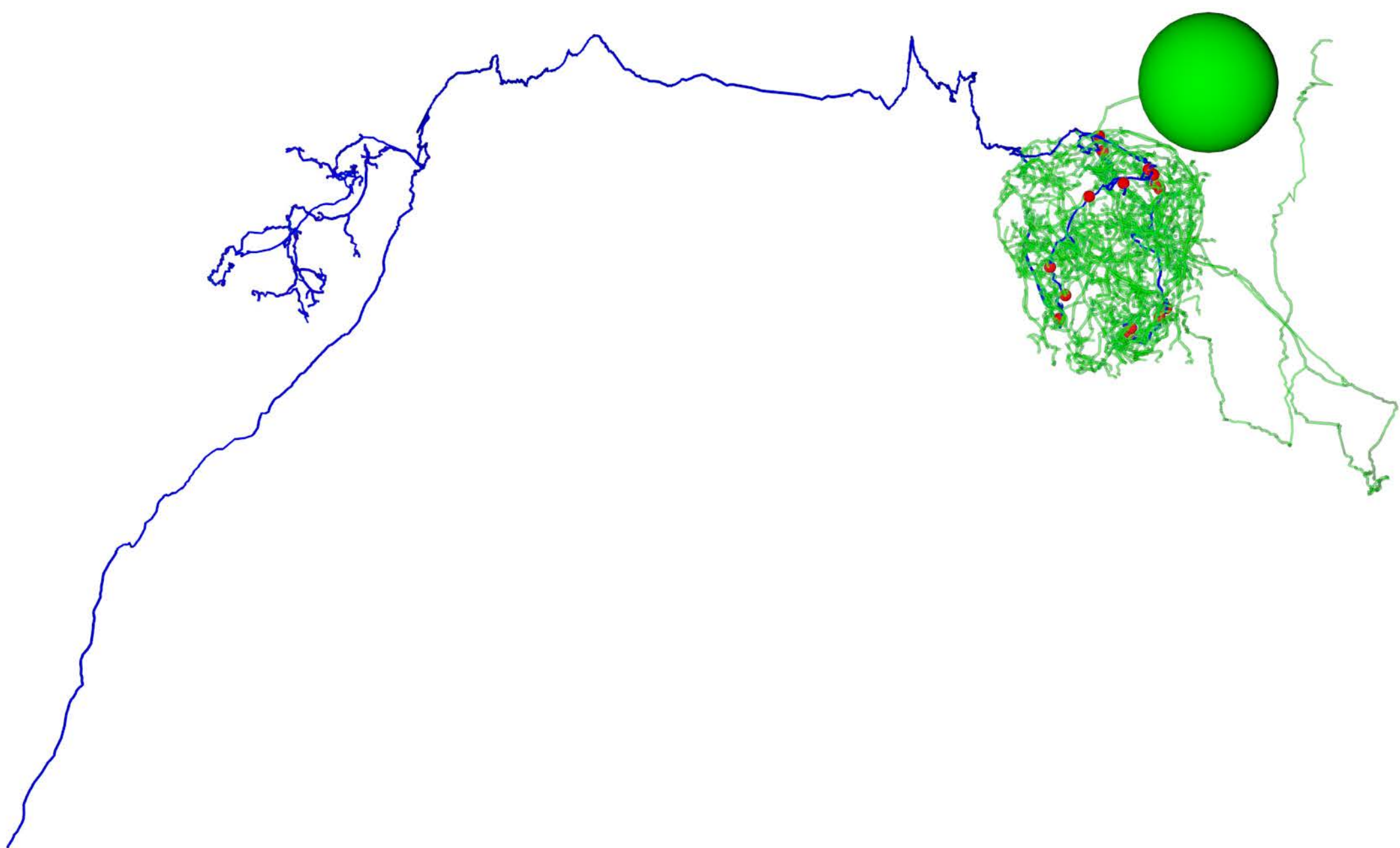


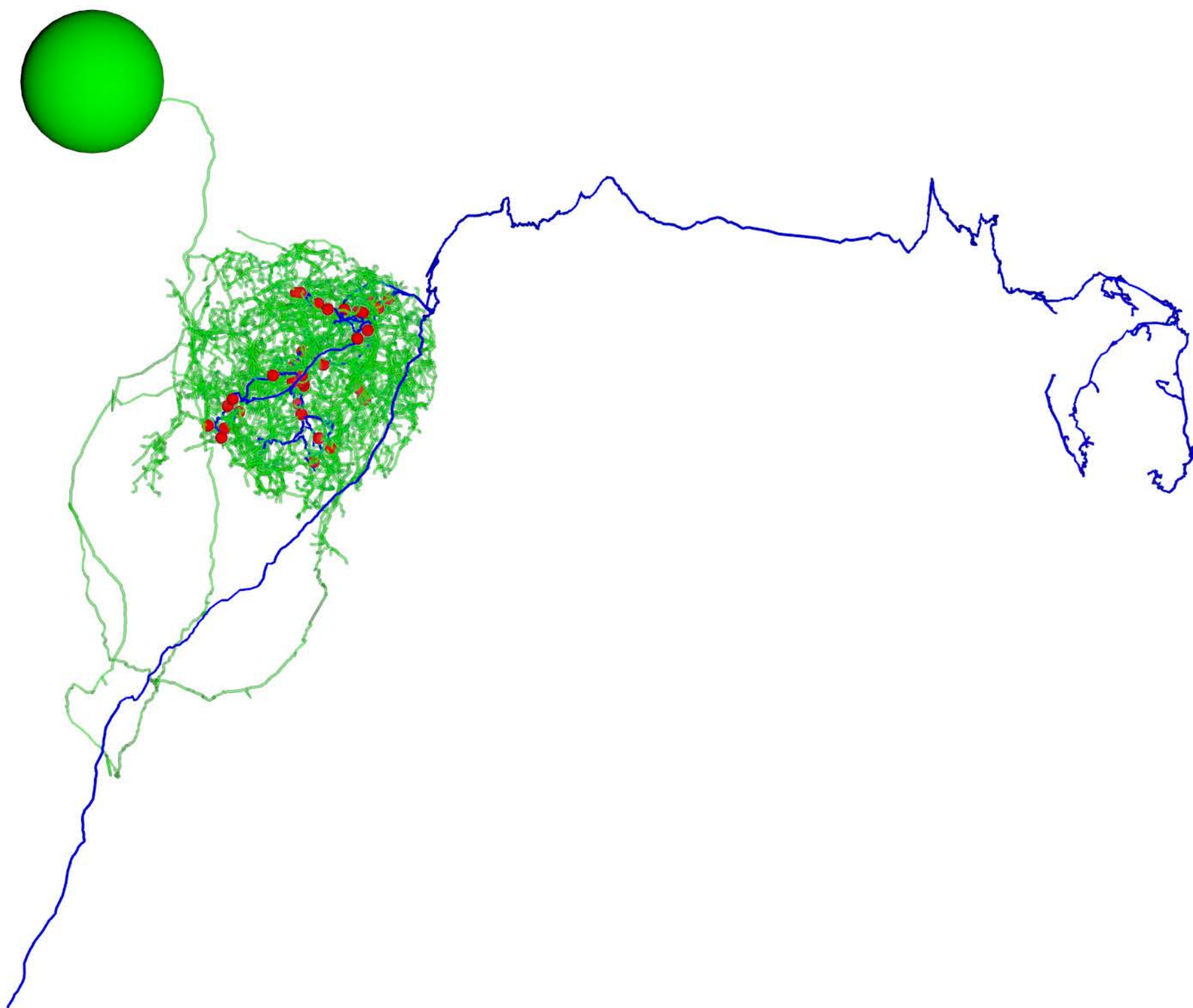


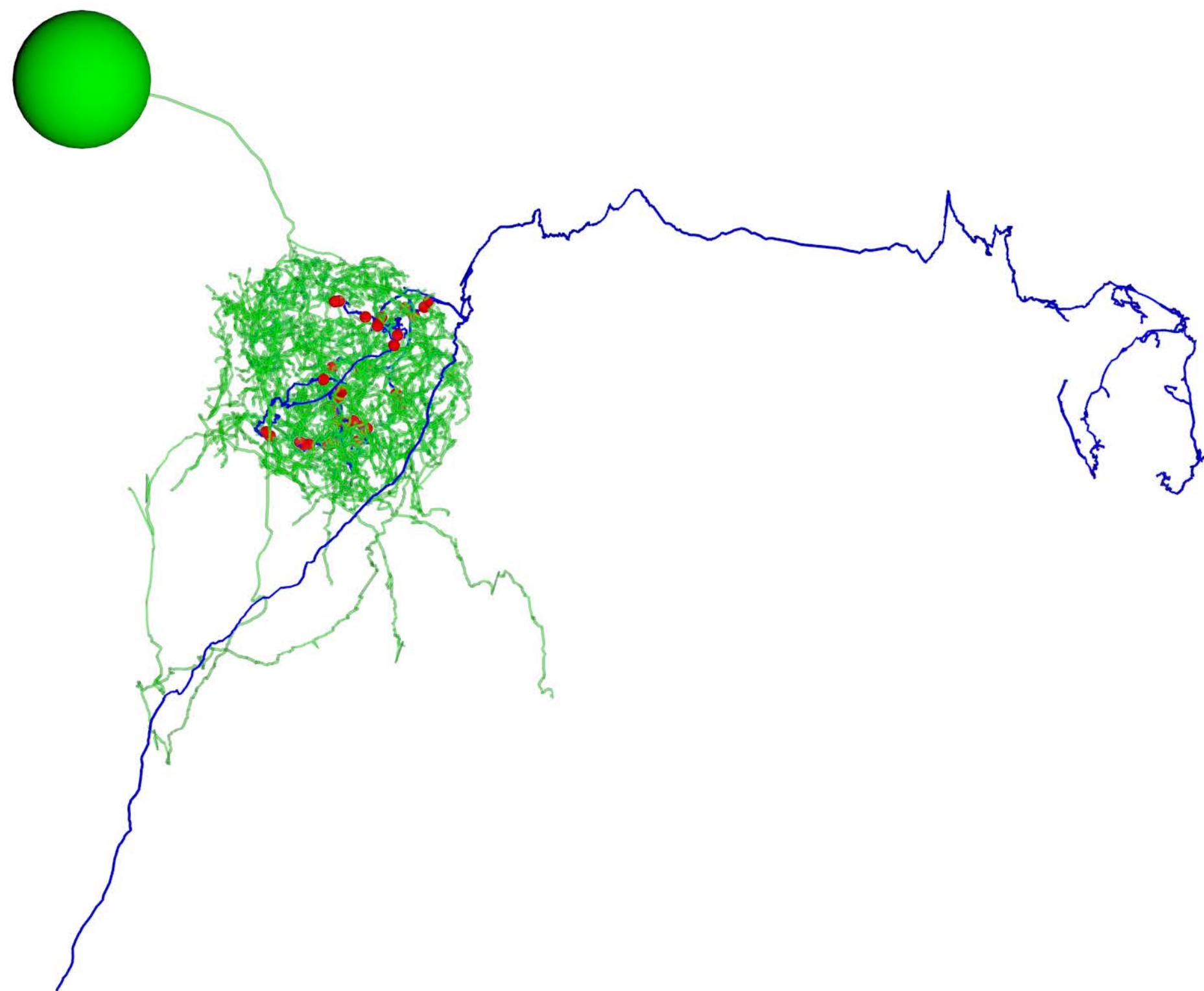


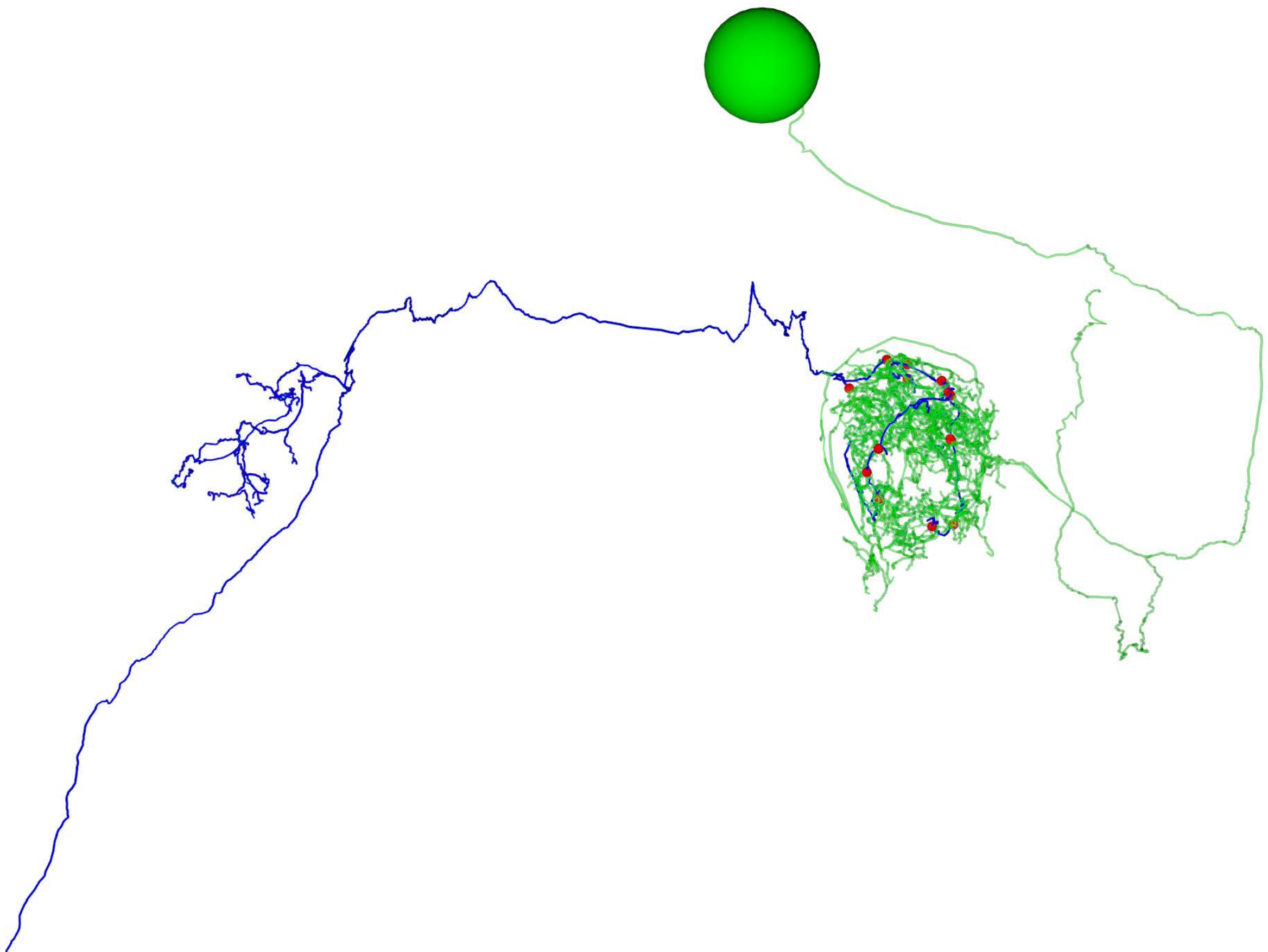


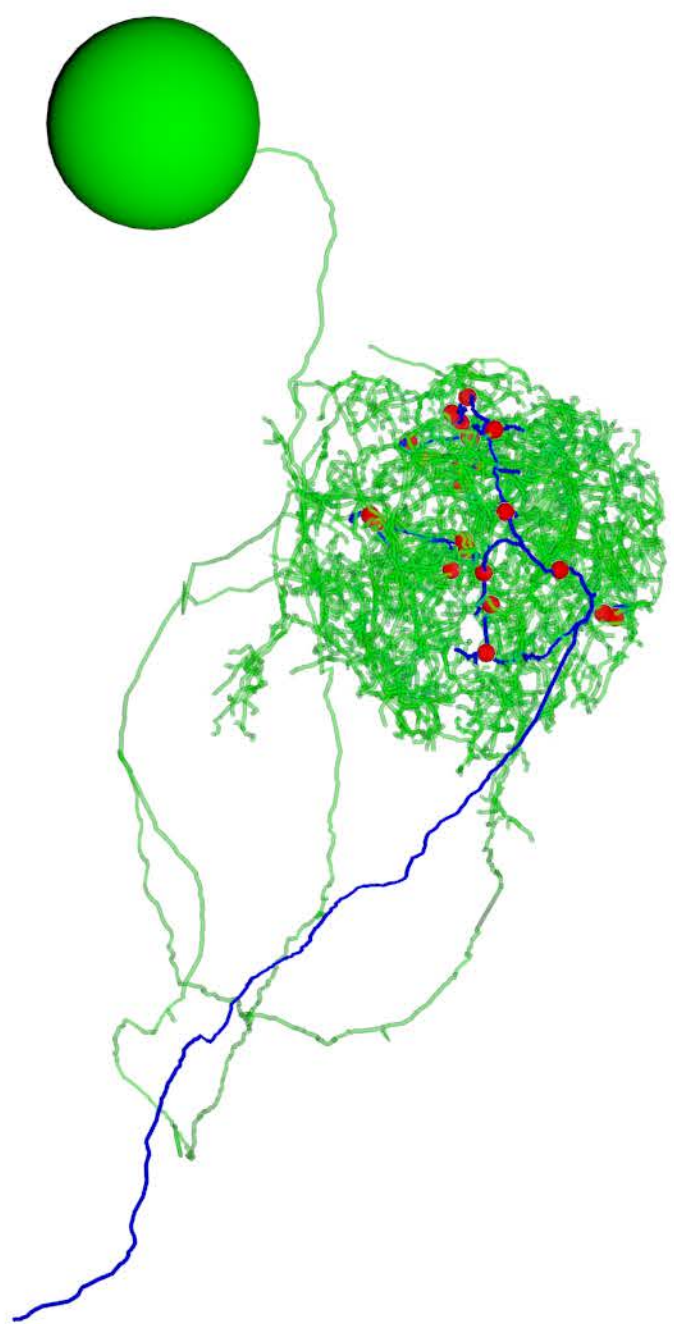


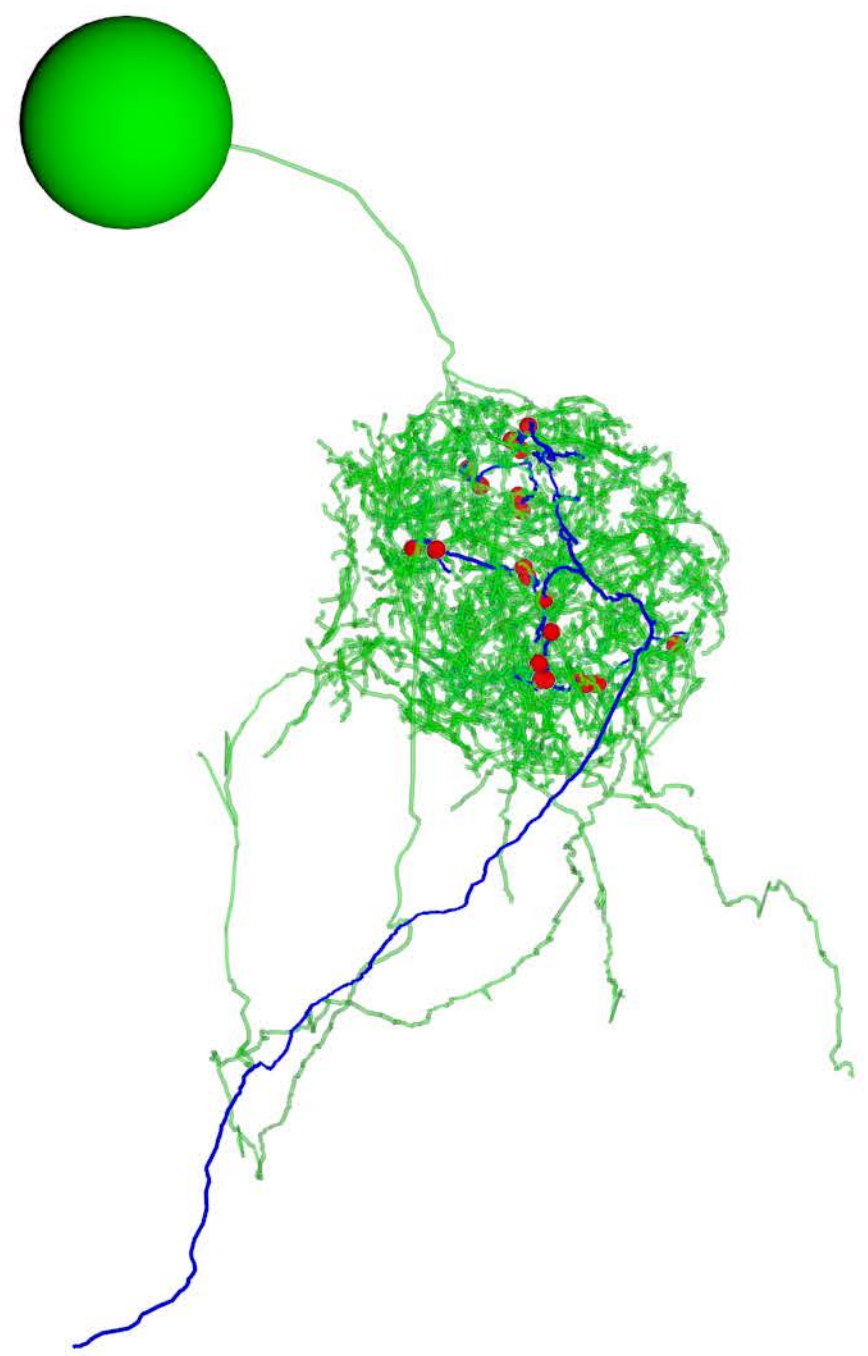




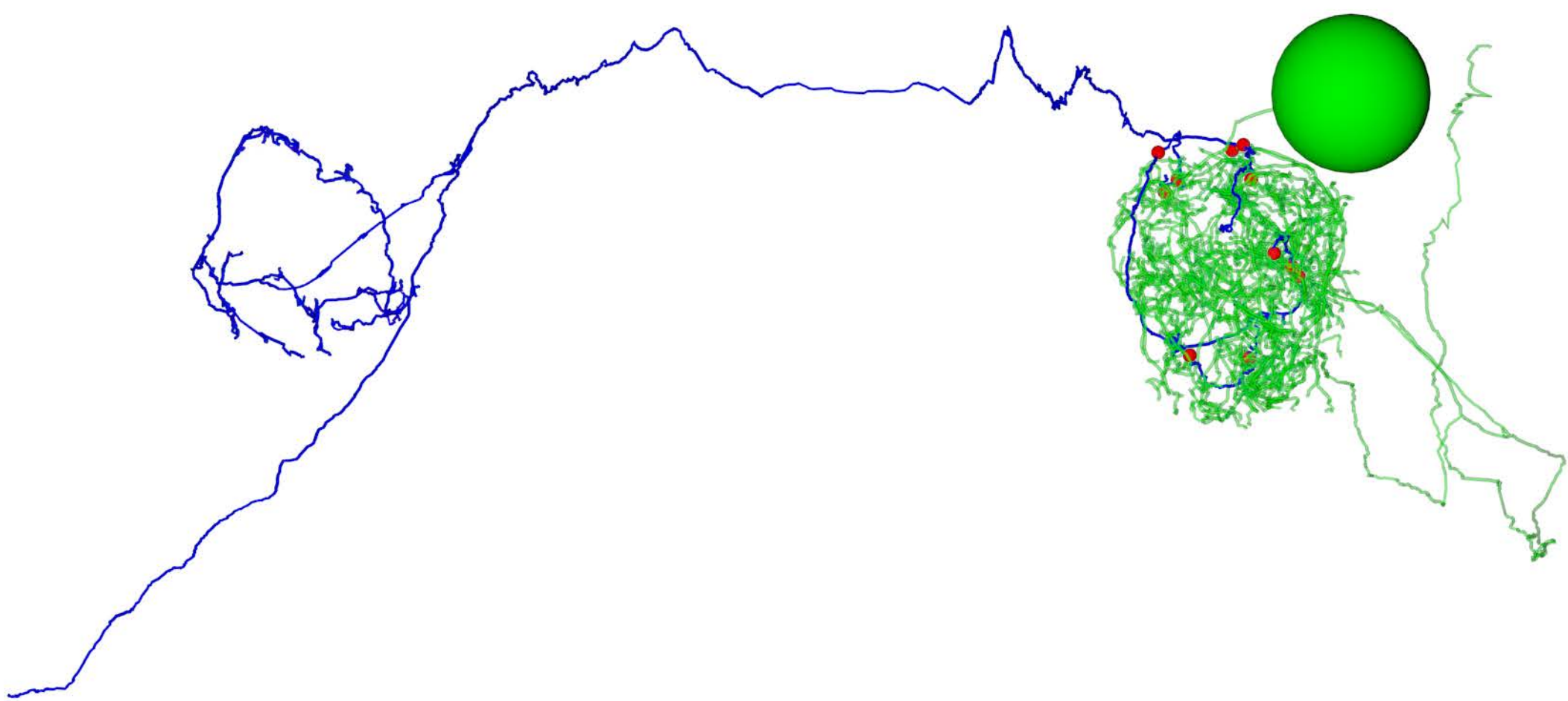


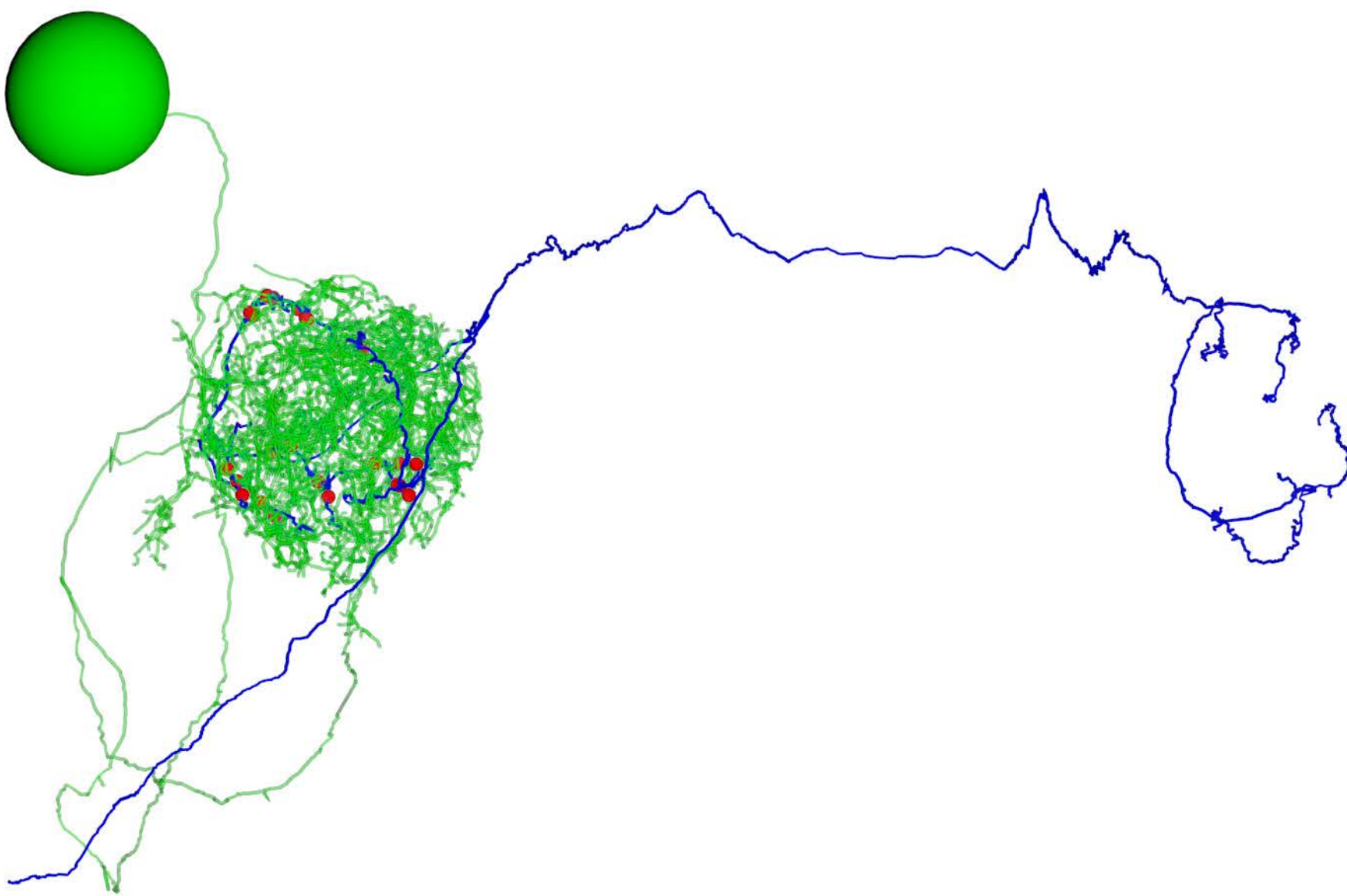


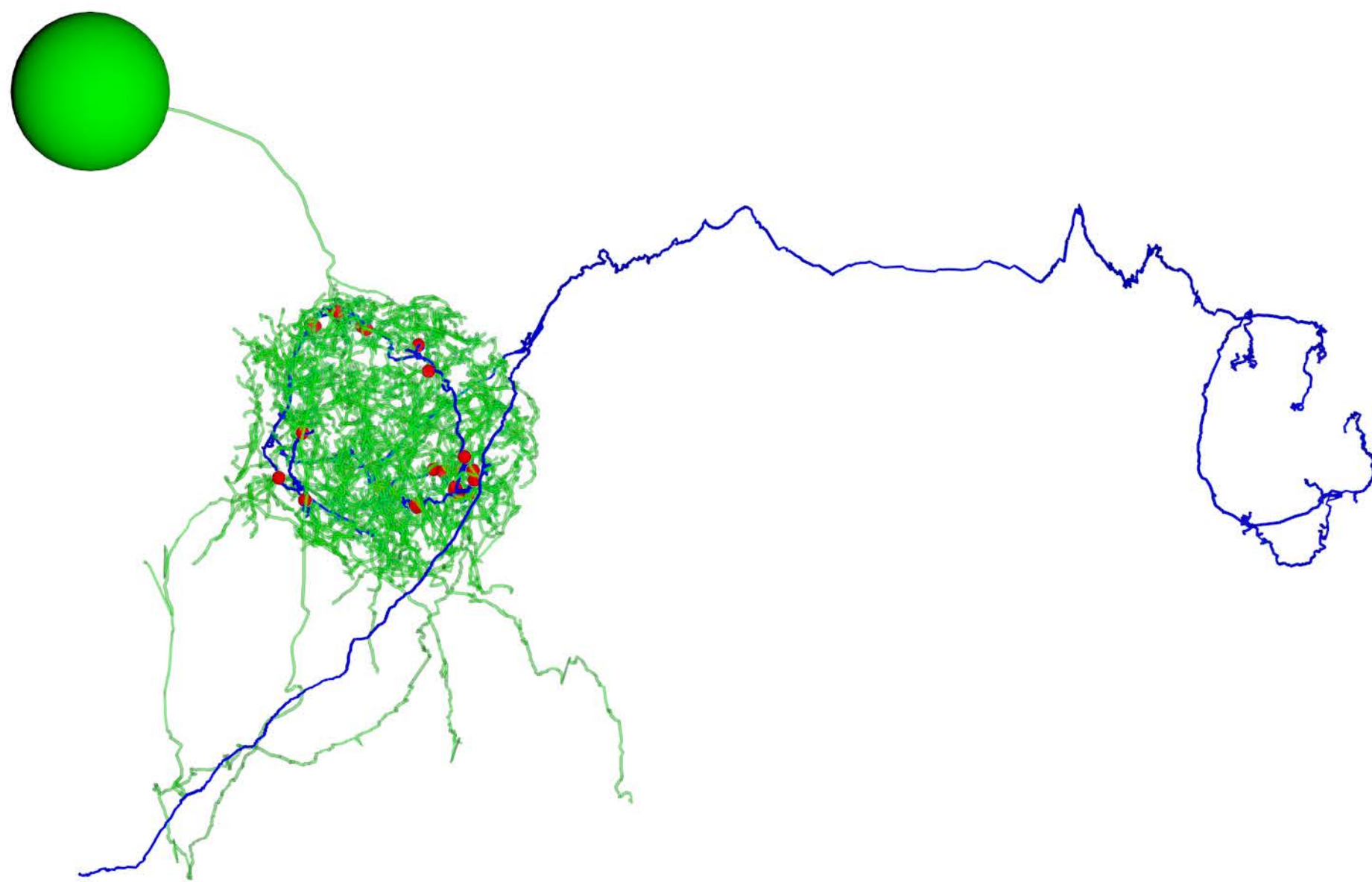


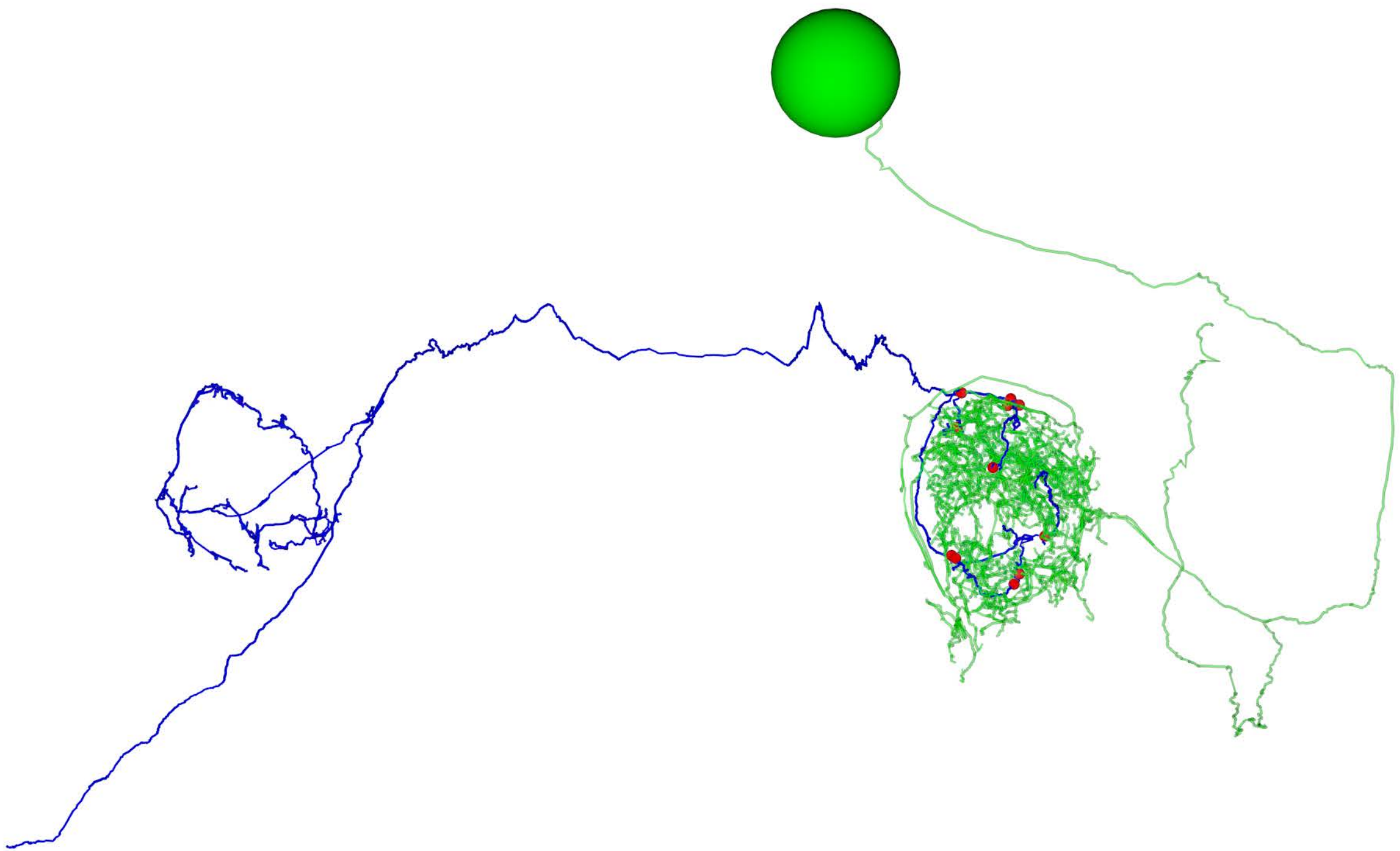












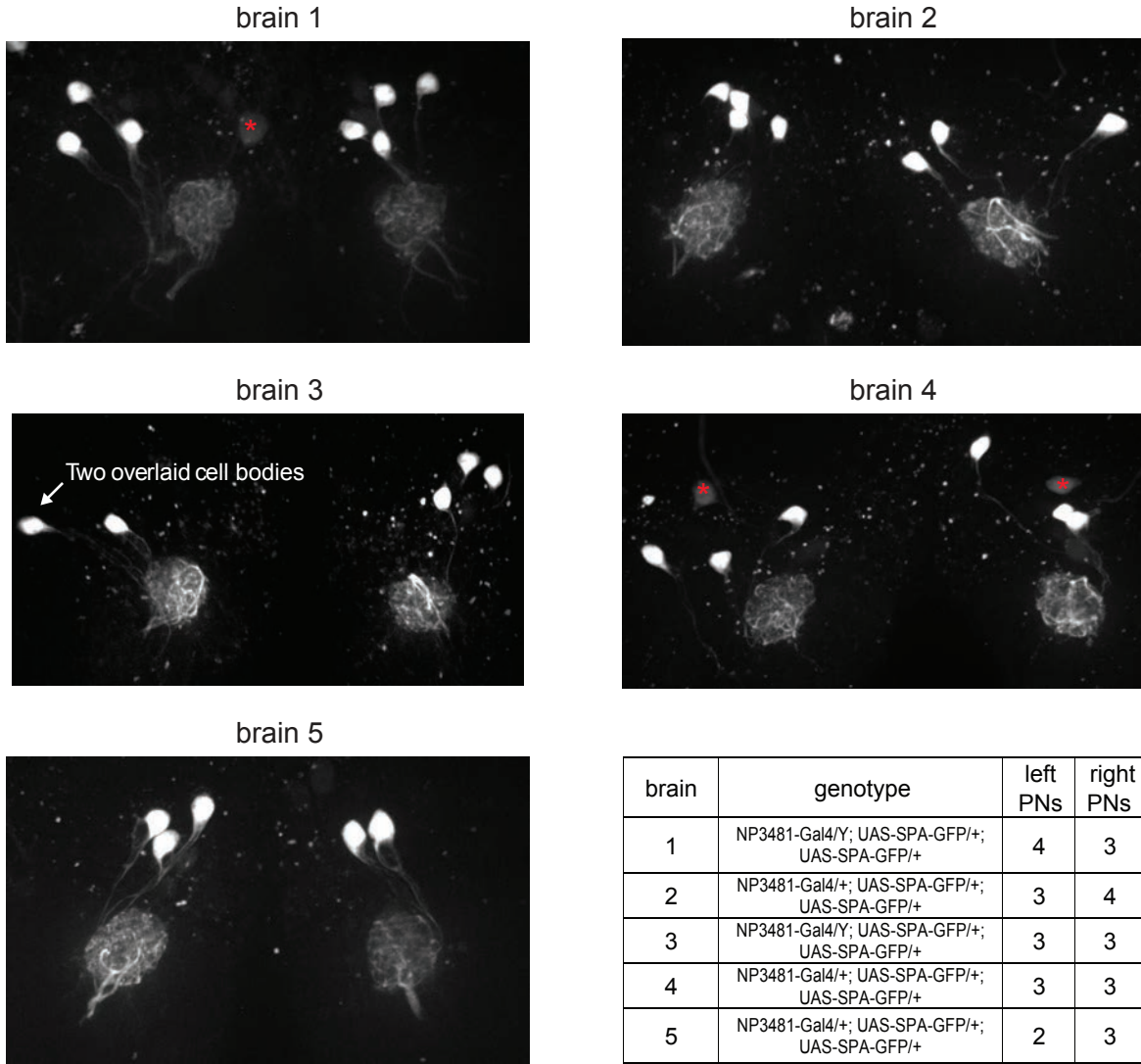


Figure S2: Variations in the number of PNs in glomerulus DM6.

By counting Gal4-expressing PNs in a glomerulus, we can obtain a lower bound on the number of PNs that reside in that glomerulus. No Gal4 line has been identified which drives expression exclusively in DM6 PNs. However, the *NP3481-Gal4* line drives expression in DM6 PNs along with PNs in several other glomeruli (total count is 9.5 PNs on average, according to Tanaka et al., 2012). In order to limit a fluorescent marker to DM6 PNs alone, we used *NP3481-Gal4* to drive expression of photoactivatable GFP (*UAS-SPA*; Datta et al., 2008), and we used 2-photon excitation to specifically photoactivate GFP within the DM6 glomerulus. Because the dendritic arbor of each PN typically ramifies throughout the entire glomerulus, photoactivating within a large fraction of the glomerulus should label each Gal4+ PN. In five experiments, we photoactivated both the right and left copies of DM6. Images shown here are maximum-intensity projections of confocal stacks imaged in a coronal plane (dorsal is up; red asterisks denote dim somata that were not photoactivated and that are not associated with DM6, based on inspection of the 3D stack). Most frequently we found three PNs per glomerulus, but we also occasionally found four or two PNs. The number of PNs was often different on the two sides of the same brain, but there was no systematic difference between right and left. This result implies that the number of Gal4+ DM6 PNs can vary, consistent with variable counts in other glomeruli in the number of Gal4+ PNs (Tanaka et al., 2004). Our EM reconstruction implies that at least some of this variability is due to true variation in PN counts, and is not merely due to variations in Gal4 expression patterns.

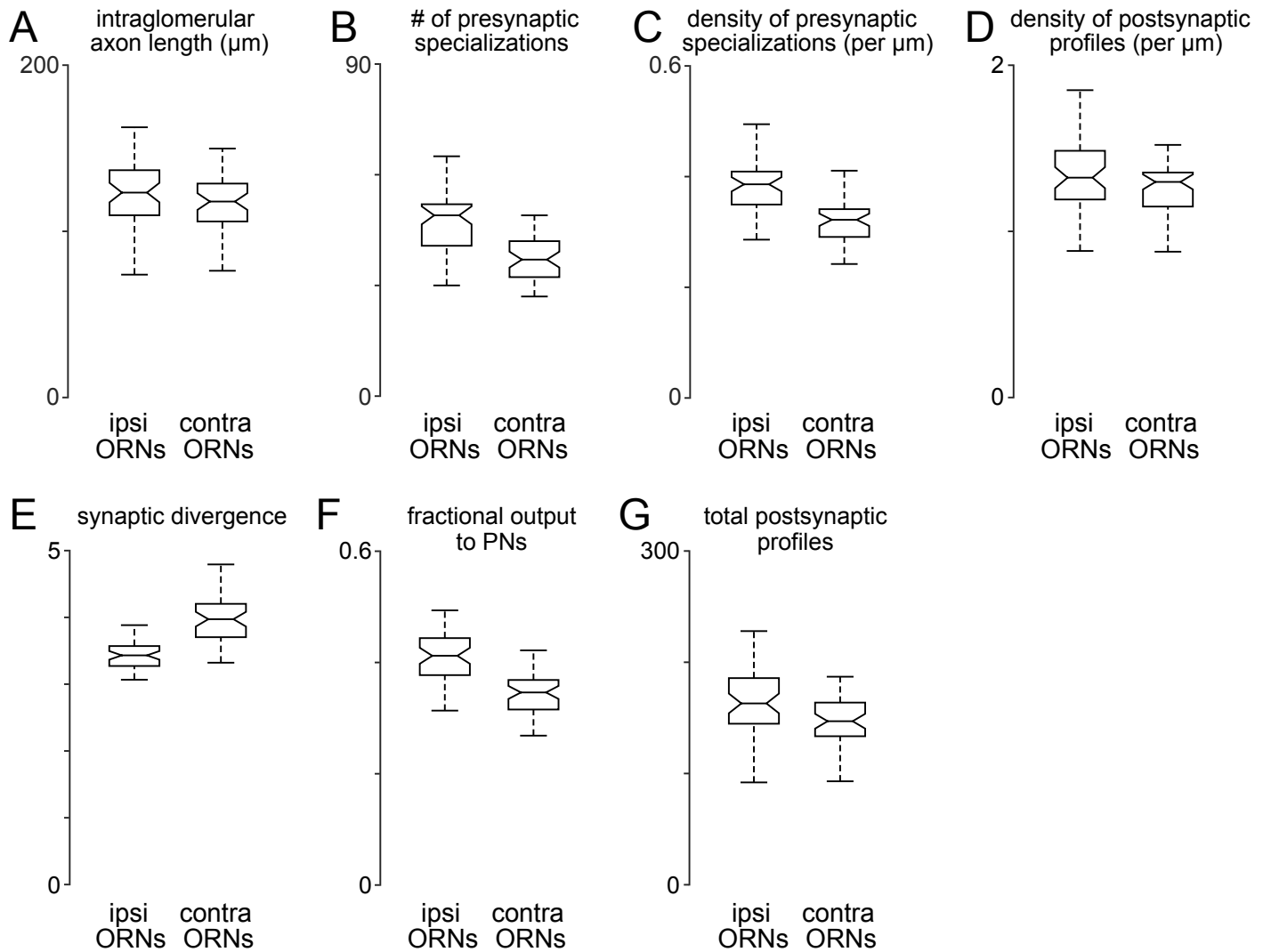


Figure S3: Comparing anatomical features of ipsi- and contralateral ORN axons in glomerulus DM6.

(A) Total path length of each ORN axon within DM6 ($P > 0.11$, permutation test, $n = 106$, because the 52 bilateral axons were each counted 2 times, and the two unilateral 2 axons were each counted 1 time). For each axon, we identified the first node upstream (proximal) to all synapses within the glomerulus, and then we computed the sum of the Euclidean distance between all connected nodes downstream from that node.

(B) Total number of presynaptic specializations (T-bars) for each ORN axon within DM6 ($P < 0.0001$, permutation test).

(C) Density of presynaptic specializations (T-bars) for each ORN axon within DM6 ($P < 0.0001$, permutation test). For each axon, the total number of T-bars was divided by the total cable length.

(D) Postsynaptic profile density ($P < 0.025$, permutation test). We counted the number of cellular profiles postsynaptic to each axon (the number of outgoing edges) within DM6, and then divided this by the total path length of the axon in that glomerulus.

(E) Synaptic divergence (polyady) ($P < 0.0001$, permutation test). We counted the number of profiles postsynaptic to each axon in DM6 and divided this by the number of presynaptic specializations (T-bars) in that axon in that glomerulus.

(F) Fraction of output to PNs ($P < 0.0001$, permutation test). This is the fraction of the profiles postsynaptic to each axon in DM6 that are PN profiles.

(G) Total number of postsynaptic profiles ($P < 0.002$, permutation test). This is the number of profiles postsynaptic to each axon.

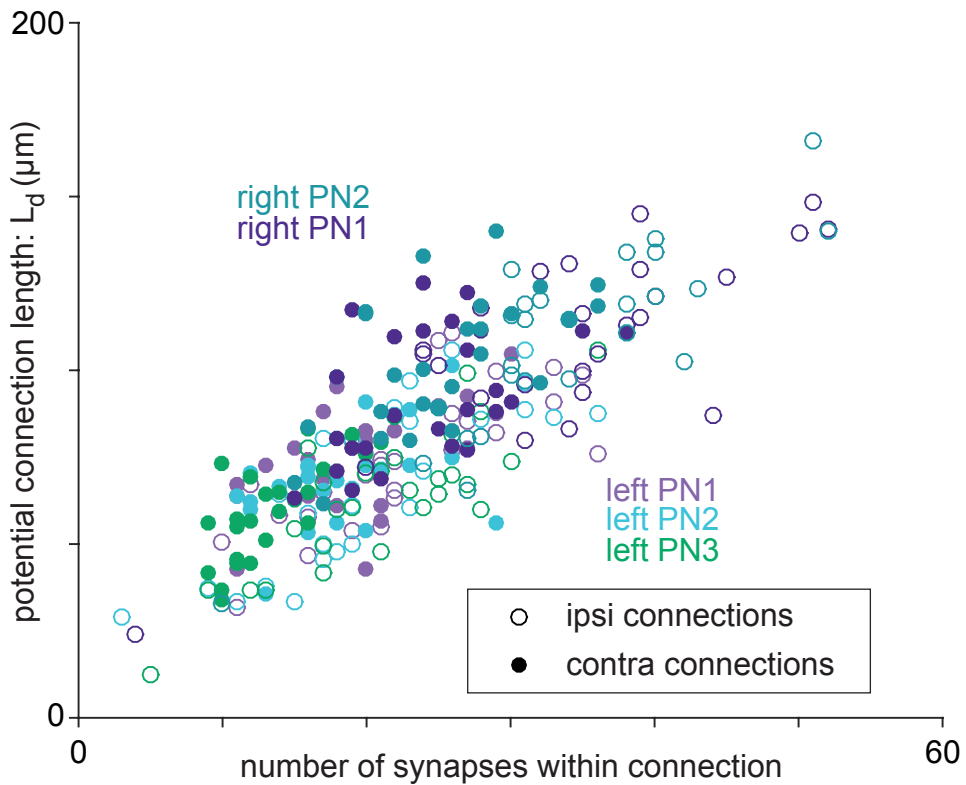


Figure S4: Axon-dendrite proximity correlates with the number of synapses per ORN-PN connection.

For each ORN-PN connection ($n = 260$), we measured the “potential connection length” (L_d) as the total path length of the PN dendrite within 500 nm of the ORN axon (Lee et al., 2016). For every PN, this estimate of proximity was strongly correlated with the number of synapses per connection (Pearson’s r ranges from 0.67 to 0.74; P -values range from 4.95×10^{-8} to 2.46×10^{-9} after Bonferroni-Holm correction for multiple comparisons, $m = 5$ tests).

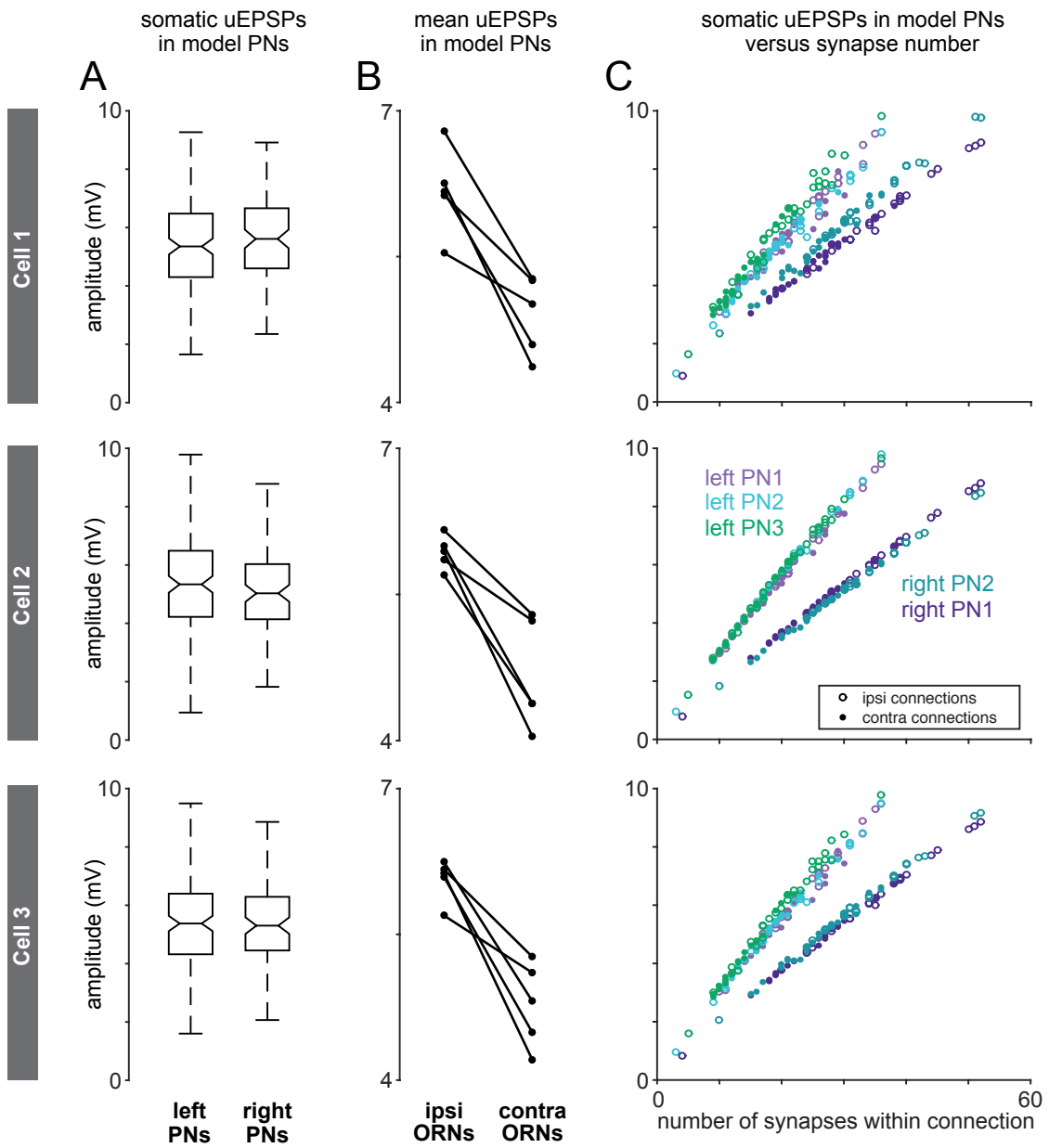


Figure S5: Comparing model output sensitivity to parameter value changes.

Here we explored three sets of models (5 model PNs per set), with each set using specific intracellular resistivity, membrane resistance, and membrane capacitance values obtained from different electrophysiological experiments (Cell 1, Cell 2, and Cell 3 of Gouwens & Wilson, 2009). Cell 3 was intermediate between Cell 1 and Cell 2, so it was used throughout the main figures of our study.

(A) Left-right comparison of uEPSP amplitudes measured at the cell body of modeled PNs. Cell 3 (bottom panel) is reproduced from Figure 3C. Using parameters fit to Cell 1 and Cell 2, we obtain overall similar results, except with Cell 2 parameters we find a very small but statistically significant left-right difference ($P_{Cell\ 1} > 0.07$, $P_{Cell\ 2} > 0.02$, $P_{Cell\ 3} > 0.7$, permutation test, $n = 156$ left and 104 right unitary connections).

(B) Ipsi-contra comparison of uEPSP amplitudes measured at the cell body of modeled PNs. Cell 3 (bottom panel) is reproduced from Figure 4D. The ipsi-contra difference is similar in all three cases ($P_{Cell\ 1} = 0.007$, $P_{Cell\ 2} = 0.006$, $P_{Cell\ 3} = 0.0059$, paired-sample t -test, $n = 5$ PNs).

(C) Correlations between synapse number and mean uEPSP amplitudes are consistently strong. Cell 3 (bottom panel) is reproduced from Figure 5H. Pearson's r ranges from 0.984 to 0.997 (Cell 1), 0.998 to 0.999 (Cell 2), 0.993 to 0.999 (Cell 3). P -values range from 1.59×10^{-39} to 2.94×10^{-56} (Cell 1), 3.85×10^{-60} to 1.22×10^{-72} (Cell 2), 9.78×10^{-48} to 1.34×10^{-65} (Cell 3) after Bonferroni-Holm correction for multiple comparisons, $m = 5$ tests).